IIUM ENGINEERING JOURNAL

Volume 24 **Number 1**

January 2023

IIUM Press

INTERNATIONAL ISLAMIC UNIVERSITY MALAYSIA

ISSN: 1511-788X E-ISSN: 2289-7860

http://journals.iium.edu.my/ejournal

IIUM Engineering Journal

Volume 24, Issue 1, January 2023
https:/doi.org/10.31436/iiumej.v24i1

Copyright Notice

IIUM ENGINEERING JOURNAL EDITORS

AIMS & SCOPE OF IIUMENGINEERING JOURNAL

The **IIUM Engineering Journal**, published biannually (January and July), is a carefully refereed international publication of International Islamic University Malaysia (IIUM). Contributions of high technical merit within the span of engineering disciplines; covering the main areas of engineering: Electrical and Computer Engineering; Mechanical and Manufacturing Engineering; Automation and Mechatronics Engineering; Material and Chemical Engineering; Environmental and Civil Engineering; Biotechnology and Bioengineering; Engineering Mathematics and Physics; and Computer Science and Information Technology are considered for publication in this journal. Contributions from other areas of Engineering and Applied Science are also welcomed. The IIUM Engineering Journal publishes contributions under *Regular papers and Invited review papers*. It also welcomes contributions that address solutions to the specific challenges of the developing world, and address science and technology issues from an Islamic and multidisciplinary perspective.

REFEREES' NETWORK

All papers submitted to IIUM Engineering Journal will be subjected to a rigorous reviewing process through a worldwide network of specialized and competent referees. Each accepted paper should have at least two positive referees' assessments.

SUBMISSION OF A MANUSCRIPT

A manuscript should be submitted online to the IIUM-Engineering Journal website at https://journals.iium.edu.my/ejournal. Further correspondence on the status of the paper could be done through the journal website.

Published by:

IIUM Press

IIUM Press,
International Islamic University Malaysia
Jalan Gombak, 53100 Kuala Lumpur, Malaysia
Phone (+603) 6421-5014, Fax: (+603) 6421-6298

ISSN 1511 - 788X

9 771511 788008

IIUM Engineering Journal

ISSN: 1511-788X E-ISSN: 2289-7860

IIUM ENGINEERING JOURNAL

Volume 24, Issue 1, January 2023

https:/doi.org/10.31436/iiumej.v24i1

Table of Contents

IIUM ENGINEERING JOURNAL

Volume 24, Issue 1, January 2023
https:/doi.org/10.31436/iiumej.v24i1

Table of Contents *Contd.*

https://doi.org/10.31436/iiumej.v24i1.1629

SOLID STATE FERMENTATION OF TURMERIC RHIZOMES WITH *ASPERGILLUS SP.* TO IMPROVE YIELD AND COMPOSITION OF EXTRACTED TURMERIC OIL

MUHAMMAD YUSUF ABDUH[1*], ASRI IFANI RAHMAWATI[1,2], TINTA KOMARIYAH[1,3], AND YOHANES THEDA[1,4]

[1]School of Life Sciences and Technology, Institut Teknologi Bandung, Jl Ganesha No. 10 Bandung 40132, Indonesia
[2]PT Partner Impian Milenial, SOHO Pancoran F16, South Jakarta 12810, Indonesia
[3]Research Center for Vaccine and Drug, National Research and Innovation Agency, Jl Raya Jakarta – Bogor KM. 46, Cibinong, Bogor 16911, Indonesia
[4]PT Cultiva Tunas Niaga, Setrasari Plaza B11, Sukagalih, Sukajadi, Bandung 40164, Indonesia

**Corresponding author: yusuf@sith.itb.ac.id*

(Received: 26th September 2020; Accepted: 30th November 2022; Published on-line: 4th January 2023)

ABSTRACT: This research aimed to determine the role of *Aspergillus awamori*, *Aspergillus niger*, and *Aspergillus oryzae* in degrading starch on turmeric rhizome substrate to increase the yield of turmeric oil. The substrate in the form of turmeric rhizome was given additional yeast extract of 10% weight per volume to meet the nutritional needs of fungal growth. The fungal concentration used in inoculation was 5×10^7 cells/ml. The solid-state fermentation process was carried out in dark conditions (~0 W), temperatures of 25–28 ºC, 99% humidity, and aeration (3.5 L/min). Turmeric oil was extracted using a steam distillation method for three hours, with the substrate moisture content of 68–71% and a substrate–water ratio of 1:5. The biodegradation process was conducted for 11 days. The starch content and turmeric oil yield was determined during the fermentation particularly on days 7, 9, and 11. The results showed that the biodegradation process of starch in solid-state fermentation succeeded in increasing the yield of turmeric oil. *Aspergillus awamori* showed the most desirable starch degradation activity by 62.5% to 2.9% wet weight on the 11th day of fermentation. *Aspergillus oryzae* had the most positive effect, nearly doubling the turmeric oil yield to 3.17% dry weight after 11th day of fermentation. The main constituents of turmeric oil are β-turmerone, α-turmerone, and ar-turmerone.

ABSTRAK: Penelitian ini bertujuan bagi mengkaji peranan Aspergillus awamori, Aspergillus niger, dan Aspergillus oryzae dalam mendegradasikan kanji pada substrat rizom kunyit bagi meningkatkan hasil minyak kunyit. Substrat dalam bentuk rizom kunyit telah diberi tambahan ekstrak yis 10% mengikut berat setiap isipadu bagi memenuhi keperluan nutrisi pertumbuhan kulat. Kepekatan kulat yang digunakan dalam inokulasi adalah 5x107 sel/ml. Proses penapaian berkeadaan pepejal telah dijalankan dalam keadaan gelap (~0 W), suhu 25–28 ºC, kelembapan 99%, dan pengudaraan (3.5 L/min). Minyak kunyit diasingkan menggunakan kaedah penyulingan wap selama tiga jam, dengan kandungan lembapan substrat 68-71% dan nisbah substrat-air 1:5. Proses biodegradasi dijalankan selama 11 hari. Kandungan kanji dan hasil minyak kunyit ditentukan semasa penapaian terutamanya pada hari ke-7, 9, dan 11. Hasil kajian menunjukkan bahawa proses biodegradasi kanji dalam penapaian berkeadaan pepejal berjaya meningkatkan hasil minyak kunyit. Aspergillus awamori menunjukkan aktiviti degradasi kanji yang paling diingini iaitu sebanyak 62.5% hingga 2.9% berat basah pada hari ke-11 penapaian. Aspergillus oryzae mempunyai kesan yang paling positif, iaitu hampir dua kali ganda hasil minyak kunyit kepada 3.17% berat kering selepas hari ke-11 penapaian. Konstituen utama minyak kunyit ialah β-turmerone, α-turmerone, dan ar-turmerone.

KEY WORDS: *Aspergillus sp., biodelignification, starch, turmeric rhizome, turmeric oil*

1. INTRODUCTION

Turmeric (*Curcuma longa* L.) is an herbaceous plant that has been widely used as a condiment and in medicine in Asia since ancient times [1]. The main part of the turmeric plant is the rhizome which contains various types of compounds including curcuminoid compounds, turmeric oil, and oleoresin [1]. It has been reported that the rhizome contains 5-6% essential oil [2] that is commonly used in food, cosmetics, and pharmaceutical applications due to its anticancer, anti-inflammatory, antibacterial, antifungal, and antitumor effects [3-4]. Turmeric is widely cultivated in Indonesia with a total cultivation area of 7,481 ha being reported in 2018 [5]. Nevertheless, valorization of the rhizomes to produce turmeric oil is still considered to be very limited. Based on the data of the Indonesian Central Bureau of Statistics, large-scale turmeric oil processing is still in the development stage since 2018. In 2020, a production plant for producing turmeric oil was built in Pacitan, East Java, Indonesia, with a production capacity of 2.4 tons/year, relatively small as compared to a total rhizome production of approximately 193,000 tons/year [5]. This is due to the difficulty of isolating turmeric oil during the distillation process, which results in low oil recovery of approximately 0.46% [6-7].

Turmeric oil in the rhizome is located in secretory cells surrounded by starch granular parenchymal tissue, which can inhibit the extraction of turmeric oil. Various studies addressing the turmeric oil extraction process have been carried out. One example is a pre-treatment using enzymes to degrade polysaccharide compounds on cell walls so that oil yield can increase by 70% [8]. The enzymes are expensive and, therefore, in the large-scale production of turmeric oil, are considered to cause a significant increase in production costs [9]. Microorganisms, especially fungi, can be an alternative solution to increase the yield of turmeric oil while still saving production costs. Fungi can produce various types of extracellular enzymes that can degrade polysaccharide and consequently increase oil yield without using commercial enzymes [10]. Fungi are used because they have complete enzymatic devices, filamentous bodies that can penetrate the substrate, and accumulated ability [11].

Fungi from genus *Aspergillus*, such as *Aspergillus niger*, *Aspergillus oryzae*, and *Aspergillus awamori*, are capable of being starch-degrading agents in turmeric because they are able to produce polysaccharide-breaking hydrolytic enzymes, such as amylase enzymes [12-16]. These three specific types of fungi were selected because they could survive the antimicrobial compounds of turmeric [4]. Therefore, this study was conducted to determine the species of *Aspergillus* and fermentation time that can degrade starch efficiently and produce a relatively high yield (≥ 2.5%) of turmeric oil. An average yield of 2.5% is considered satisfactory for commercial productions [17].

2. MATERIALS AND METHODS

2.1. Preparations of Turmeric Rhizomes

The turmeric rhizomes used in this study were harvested at the age of 8 months from Cimasuk, Tanjung Sari, Sumedang Regency, West Java, Indonesia. They were then washed and sliced to a thickness of ± 0.1 cm. After that, all rhizomes were stored at room temperature (25-28 ºC) and relative humidity (50-70%).

2.2. Cultivation of *Aspergillus sp.* Inocolum

Stocks of *Aspergillus niger*, *Aspergillus oryzae*, and *Aspergillus awamori* were obtained from the Microbiology Laboratory, School of Life Sciences and Technology, Institut Teknologi Bandung. Each species of fungi was cultivated in a semisolid potato dextrose agar (PDA) medium with a concentration of 39 g/L [15]. The PDA medium was sterilized using an autoclave (121 ºC, 1.5 atm). The fungi were cultivated for 4 days in a test tube at room temperature until the active fungi spores covered the entire surface of the medium.

2.3. Preparation of *Aspergillus sp.* Inocolum

The 4-day old *Aspergillus* sp. cultures were harvested with harvesting solution (0.85% NaCl + Tween80 0.1%) to obtain a 600 mL inoculum solution with a concentration of $5x10^7$ spores/ml [16, 18]. Measurement of the spore concentration was conducted using a hemocytometer under a microscope. The cell chamber of the hemocytometer was filled with a 1 mL aliquot of the spore solution. Appropriate dilutions of the aliquot were done when there were too many spores to count by eyes. The resulting number from cell counting was then multiplied by the dilution factor.

2.4. Solid-state Fermentation of Turmeric Rhizome with *Aspergillus sp.*

The fermentation process was carried out under aseptic conditions. The inoculum solution and yeast extract solution were mixed with the sterilized turmeric rhizome in the following proportions: 1 ml inoculum solution, 1 ml yeast extract solution, and 10 g turmeric rhizome [18]. The fermentation process took place in a fermenter tray (50 × 30 ×15 cm) with perforation to remove excess liquid. The fermenter tray was sealed with plastic wrap and black color plastic, so that fermentation could take place at a light intensity of ~0 W [16]. Aeration was given every 2 days for 5 minutes, at a rate of 3.5 L/min. Samples were stirred every 2 days. The fermentation process was carried out by varying the incubation time of 7, 9, and 11 days.

2.5. Extraction of Turmeric Oil using a Steam-Distillation Method

Fermented turmeric rhizome was dried using an oven at 50 ºC for 24–26 hours to reach a moisture content of 68–71% [19]. Moisture content was measured using a Mettler Toledo Infrared Moisture Content Analyzer. Turmeric oil was extracted using a steam distillation method with a ratio of 100 g substrate to 500 mL of distilled water for 3 hours [20-23]. Distillates were collected in a 500 mL separating funnel, and the oil and hydrosol were separated. The obtained turmeric oil yield was calculated using Eq. (1):

$$Yield\ (\%w_d) = \frac{m_{m\,(g)}}{w_d(g)} \times 100 \tag{1}$$

where m_m is the mass of oil in grams, and w_d is the dry weight of the substrate in grams. The value of w_d can be calculated using Eq. (2):

$$w_d(g) = (1 - moisture\ content) \times m(g) \tag{2}$$

where moisture content is in percent, and m is the substrate mass in grams at the initial moisture content (~90%).

2.6. Determination of Turmeric Rhizome Starch Content

The starch content was determined using a Luff Schoorl method (SNI 01-2891-1992). The preparation of the Luff Schoorl reagent was carried out by mixing the following: 143.8 g of anhydrous Na_2CO_3 in 300 mL of distilled water, 50 g of citric acid in 50 mL of distilled water, and 25 g of $CuSO_4.5H_2O$ in 100 mL of distilled water. The solution was stirred until homogeneous.

Next, 3% HCl (200 mL) was added to 5 g of fermented turmeric rhizome. The mixture was boiled using a reflux extractor for 3 hours and then cooled down, and the pH was adjusted to 7.0 using a 30% NaOH solution. The solution was diluted to a volume of 500 mL and filtered. 10 mL of this filtrate was mixed with 25 mL of the Luff Schoorl reagent and 15 mL of distilled water and then boiled for 10 minutes using an upright cooler. 15 mL of KI 20% and 25 mL of 25% H_2SO_4 were slowly added. The final solution was titrated with $Na_2S_2O_3$ (0.1 N), and its volume increase was measured. Starch solution 0.5% weight–volume (w/v) was used as an indicator.

The calculation of starch content was carried out using Eq. (3), where w_1 is the sample mass of turmeric rhizome (mg), w is glucose (mg) contained for every milliliter of $Na_2S_2O_3$ used, f_p is a dilution factor, and the value 0.9 is a glucose conversion factor for starch. The value of w was determined using the sugar conversion table according to SNI.

$$\text{Starch content (\%)} = \frac{0.9w_1\ (mg) f_p}{w\ (mg)} \times 100\% \quad (3)$$

2.7. Characterization of Turmeric Oil

The oil characteristics were determined particularly color, refractive index, and density. The color of turmeric oil was observed subjectively by eye. The refractive index value of turmeric oil was tested using a refractometer. The density was determined by measuring the volume v of oil (mL) using a measuring cup and oil mass m (g) on the analytic balance and calculated using Eq. (4).

$$\text{Density} = \frac{m_{turmeric\ oil}\ (g)}{V_{turmeric\ oil}\ (mL)} \quad (4)$$

2.8. Determination of composition using a Gas Chromatography-Mass Spectrometry

The composition of turmeric oil was analyzed using a gas chromatography–mass spectrometry (GC–MS) device. The initial temperature was set at 60 ºC, then raised to 280 ºC at a rate of 8 ºC/min. The samples were injected in split mode with a split ratio of 200. The rate of the column was set to 1.31 mL/min with a linear speed of 41.7 m/s. The analysis was carried out at the Instrumental Chemistry Laboratory, Universitas Pendidikan Indonesia, Bandung, Indonesia.

3. RESULTS AND DISCUSSIONS

3.1. Effects of Moisture Content on Turmeric Oil Yield

The effects of moisture content on the yield of turmeric oil are shown in Fig. 1. A dry weight base was used for this study so that the values of different moisture content could be compared. The results indicate that the yield of turmeric oil increases with decreasing moisture content of the material before decreasing after reaching an optimum moisture content. A lower moisture content requires longer drying time and consequently more turmeric oil is susceptible to evaporation during the drying process. The turmeric oil yield with 87.9% moisture content was 1.27% dry weight (dw). Lower moisture content in the range of 74–78% resulted in more turmeric oil. Specifically, the yield of turmeric oil at 77.9% moisture content was 1.70% dw, and at 74.3% moisture content, it was 1.69% dw. The optimum moisture content was at 69.2% (obtained after drying for 24 hours) which resulted in a yield of 1.89% dw.

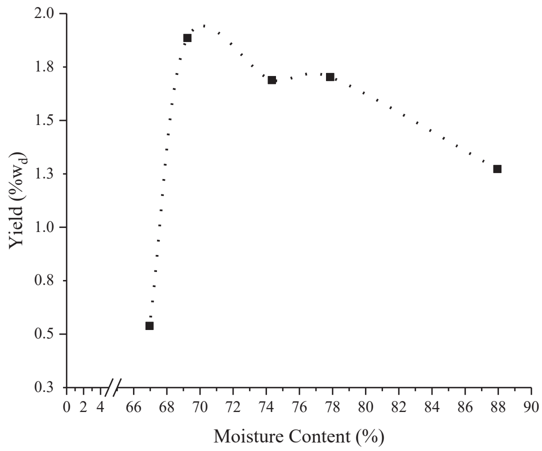

Fig. 1. Effects of moisture content on turmeric oil yield.

The drying process was carried out using an oven at 50 ºC. The selection of the drying method considered two important parameters that affected the extraction of essential oils, namely drying time, and temperature [24]. The higher the temperature in the drying process, the lower the yield of essential oil due to evaporation. According to Hamrouni-Sellami et al. [25], the drying process at a temperature of 50 ºC can produce a high amount of volatile oils, while temperature above 50 ºC will reduce their yield. For medicinal plants, high temperatures (>50 ºC) may cause a drastic decrease in their essential oil yield. An increase in temperature by 20 ºC can cause the loss of essential oils up to 92.3% [25]. This is because high temperatures can damage the biological structure of oil glands and epithelium cells in medicinal plants and reduce the permeability of plasma membranes [25].

The effect of drying time on the yield of essential oils is related to the rate of evaporation of essential oils, which is greater with the length of the drying time. For example, the process of drying *Tymus* subsp. *Doenensis* leaves uses the shade drying method, which causes the reduction of essential oils to increase. The yield of essential oils by drying treatment using an oven at 50 ºC amounted to 1.46%, while the yield by shade drying was only 0.91%. This is due to the long drying time that caused the loss of essential oils as they diffused into the air [24].

The moisture content measured in this study ranged from 66–87% (Fig. 1). A moisture content of 69.24% resulted in the optimal yield of turmeric oil of 1.89%. After reaching the optimum yield at 69% moisture content, the oil yield decreased as the moisture content was reduced. The dried rhizome to 66.96% moisture content resulted in a yield of only 0.54% dw due to the length of drying time, which caused longer evaporation of turmeric oil. The high yield of turmeric oil obtained at 69% moisture content or 24 hours drying (1.89% dw) is in accordance with the literature, which states that drying for 24 hours will result in the extraction yield of essential oils from rhizome plants in the range of 1.6–2.2% [26]. Hence, a moisture content range of 68–71% was used in this study.

3.2. Effects of Fermentation Time on Starch Content of Biodegraded Rhizomes and Turmeric Oil

The test results on the content of turmeric rhizome starch fermented by the fungus *Aspergillus* sp. are shown in Fig. 2. The content of the control rhizome starch (day 0 of fermentation) was measured to be 7.8% wet weight (ww). The starch content in fermented rhizomes by all three species showed the same tendency. The content of rhizome starch continued to decrease along with the length of fermentation time. In the fermentation process using the *Aspergillus niger*, starch content decreased in the range of 14.7–30.6% ww to 6.6% ww on the 7th day, 5.8% ww on the 9th day, and 5.4% ww on the 11th day. Meanwhile, the decrease of starch content in the fermentation by *Aspergillus oryzae* was 11.8–59.3% ww to 6.9% ww on the 7th day, 4.2% ww on the 9th day, and 3.2% ww on the 11th day. Fermentation using *Aspergillus awamori* showed a better starch degradation activity. *Aspergillus awamori* successfully reduced starch in the range of 31.8–70.6% with the starch content to decrease to 5.4% ww on the 7th day, 3.1% ww on the 9th day, and 2.9% ww on the 11th day.

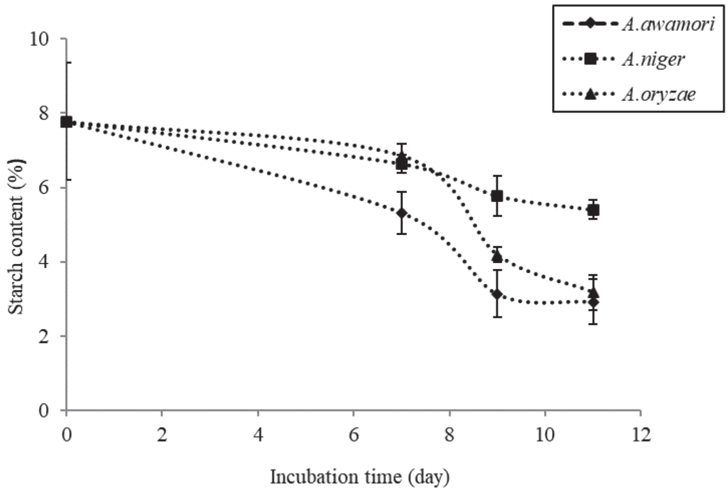

Fig. 2. Effects of fermentation on rhizome starch content.

The profile of turmeric oil obtained in this study is shown in Fig. 3. Turmeric oil yield for the control sample (day 0 of fermentation) was 1.06% dw. The fermentation process of each fungal species yielded an increase in turmeric oil with the increasing fermentation time. The *Aspergillus oryzae* showed a significant increase in the yield of turmeric oil compared to the other two fungal species. The 7th day fermentation resulted in the acquisition of turmeric oil by 2.17% dw and continued to increase to 2.60% dw on the 9th day and 3.17% dw on the 11th day. The fermentation process using *Aspergillus awamori* produced turmeric oil of 2.38% dw on the 7th day, 2.50% dw on the 9th day, and 2.62% dw on the 11th day. Meanwhile, fermentation using *Aspergillus niger* had the lowest yield of 1.44% dw on the 7th day, 1.82% dw on the 9th day, and 1.92% dw on the 11th day.

According to the study by de Castro [27], the amylase hydrolytic enzyme group stabilizes after 4 days of fermentation and reaches a maximum point after 6 days. The test results of the control rhizome starch content (Fig. 2) of 7.8% ww were similar to the research of Kusbiantoro and Purwaningrum [28], which obtained the value of turmeric rhizome starch content of 8% ww. A decrease in the starch content occurs with the ongoing fermentation process, owing to the growth and metabolic activity of the fungus *Aspergillus* sp.

Hydrolytic enzymes, especially amylase, are enzymes that correlate closely with growth [26]. *Aspergillus* spp. secrete enzymes as an effort to extract nutrients that support colony growth and regulation of metabolism [29]. The secretion of hydrolytic enzymes in the process of metabolic fungi results in the cutting of the glycosidic bonds of starch compounds on the cell wall, causing the breakdown of complex compounds into simpler ones, namely glucose, and a decrease in starch content [29-30]. It is known from the research of Reyes et al. [31] that the fermentation time of 3 days is sufficient to degrade starch granules in the material.

The previous study used pure starch whereas this study used turmeric rhizome as the substrate, which is a complex medium. In complex media, fungi consume simple sugars at the initial time to support their growth before finally degrading starch complexes. Therefore, they take longer to degrade than pure starch substrates [32].

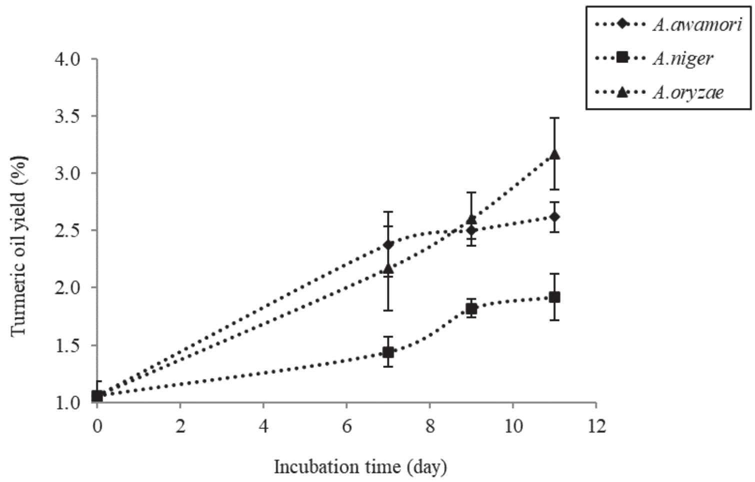

Fig. 3. Effect of fermentation on turmeric oil yield.

In this study, the growth of fungal hyphae was not seen until it reached the 2nd day. Aeration to the system was given after the emergence of hyphae, which was evenly distributed on the 2nd day of fermentation to allow the fungal hyphae to grow around the entire surface of the turmeric rhizome in the fermenter tray. More evenly distributed fungal growth was observed qualitatively on the 3rd to 9th day. After the 9th day, there was no mycelium growth observed owing to the absence of any remaining organic matter in the turmeric rhizome that *Aspergillus* could take as nutrition. In addition, the metabolic activity of the fungus allowed a decrease in pH on the substrate, so that the growing environment was no longer suitable for fungi [33]. In other words, fungal growth had entered a decreasing phase in which metabolic activity did not degrade starch [33].

The results of the starch content revealed that the *Aspergillus awamori* fungus showed the greatest reduction in starch content relative to the other two species, as shown in Fig. 2. This was predicted to occur because of the differences in the enzyme activity of the three species. The amylase enzyme activities measured in solid-state fermentation systems by *Aspergillus niger*, *Aspergillus oryzae*, and *Aspergillus awamori* were 467.8, 500, and 589.7 IU/g, respectively [34-35]. Greater enzyme activity in *Aspergillus awamori* causes the fungus to degrade more starch [36]. *Aspergillus awamori* can degrade starch in the range of 31.8–70.6%, with a maximum decrease occurring on the ninth day of 62.5%. This data is in accordance with the results of research by Umsza-Guez et al. [37], which states that *Aspergillus awamori* fungi can degrade up to 64% in a span of six days in solid-state fermentation systems.

The increase in turmeric oil yield was caused by the decreased presence of starch in the rhizome cell wall that had been degraded. The *Aspergillus* fungal metabolism results in secretory cells in the parenchyma tissue, that had been initially protected, to become more open. Changes in the structure around the secretory cells allow the turmeric oil to be more easily extracted [29, 38]. The results of fermented turmeric oil measurements in Fig. 3 show that the fermentation with *Aspergillus oryzae* produced the largest yield of turmeric oil. Even though the degradation of starch produced by *Aspergillus oryzae* was lower than *Aspergillus awamori*, the yield of oil produced was higher. During fungal metabolism, other hydrolytic enzymes are involved that can degrade complex compounds other than starch on cell walls, such as endo-1, 4-β-glucosidase, or β-glucosidase, which act as catalysts in degrading cellulose [39].

3.3. Characteristics and Composition of Turmeric Oil

The physical-chemical characteristics of turmeric oil obtained in this study are shown in Table 1. Turmeric oil from fermented rhizome was yellow in color with a density of 0.89 g/mL. The measured refractive index of turmeric oil was 1.45. The results are in accordance with the results of a previous study by Naibaho [40] and comply to the national standard in Indonesia. The composition of turmeric oil is shown in Table 2. This study found 30 components of constituent compounds of turmeric oil that comprise monoterpenoids and sesquiterpenoids. The main compounds found were ar-turmerone, α-turmerone, and β-turmerone. In general, the solid-state fermentation process caused some components of minor compounds not to be detected in turmeric oil. Fermentation by different *Aspergillus* sp. resulted in varied amounts of components of the main compounds in turmeric oil.

Table 1: Physical-chemical characteristics of turmeric oil

Characteristics	This study	SNI	Reference [40]
Color	Yellow	Yellow Orange	-
Density (g/mL)	0.89 ± 0,02	0.82-0.92	0.92
Refractive index	1.45 ± 0.07	1.46-1.47	1.47

The main compounds of fermented turmeric oil are ar-turmerone, 10.4%, α-turmerone, 16.2%, and β-turmerone, 33.8%. In the fermentation using *Aspergillus awamori*, there was a decrease in the ar-turmerone compound but an increase in α-turmerone and β-turmerone compounds. The ar-turmerone compound was measured in the range of 1.6–9.4%. The α-turmerone compound was measured in the range of 14.5–18.1%. The β-turmerone compound was measured in a larger range, 41.9–48.5%. The fermentation process using *Aspergillus niger* showed the same tendency. The ar-turmerone compound decreased to 0.98–9.88%. The α-turmerone and β-turmerone compounds were measured in the range of 11.59–15.29% and 20.97–45.36%, respectively. *Aspergillus oryzae* had a different influence on the content of the main compounds of turmeric oil. The fermented turmeric rhizome using *Aspergillus oryzae* did not have any detrimental effect on the content of the main compounds. Fermentation using *Aspergillus oryzae* increased ar-turmerone, α-turmerone, and β-turmerone compounds to the ranges of 10.09–13.50%, 14.47–16.38%, and 26.07–37.52%, respectively.

Turmeric oil from the biodegraded rhizomes of the three species generally had a relatively similar compound-content profile. β-turmerone was the highest concentration, followed by α-turmerone, then ar-turmerone. *Aspergillus niger* and *Aspergillus awamori* had relatively the same effect on changes in turmeric oil compound concentrations: decreasing the concentration of ar-turmerone on the seventh day, before an increase due to the transformation of α-turmerone and β-turmerone. However, the treatment using *Aspergillus oryzae* produced turmeric oil with decreases in ar-turmerone.

https://doi.org/10.31436/iiumej.v24i1.1629

Table 2: Composition of turmeric oil for fermented rhizome with *Aspergillus* sp.

Compounds	Percentage of Compounds (%)									
	Fermentation Day-7			Fermentation Day-9			Fermentation Day-11			Ref.
	AN	*AO*	*AA*	*AN*	*AO*	*AA*	*AN*	*AO*	*AA*	[3,4
α-turmerone	15.3	16.4	14.6	15.1	15.1	16.8	11.6	14.5	18.1	13
β-turmerone	45.4	37.5	48.5	34.1	36.2	41.8	21.0	26.1	46.2	7.1
ar-turmerone	1.0	13.5	1.6	9.9	10.2	9.4	6.3	10.9	2.8	17-
1-phellandrene	0.8	0.5	0.6	1.7	0.8	1.5	0.6	0.4	1.0	0.
α-terpinolene	0.2	-	0.2	0.4	0.2	0.3	0.2	-	0.3	0
trans-caryophyllene	0.8	0.8	0.8	0.8	1.1	0.6	0.6	0.4	0.6	2.
zingiberene	2.5	1.3	2.1	2.8	1.9	3.5	1.7	1.7	2.1	0.2-
α-bisabolene	0.6	-	-	0.6	0.3	-	0.4	-	-	0
β-bisabolene	0.8	0.3	0.7	0.7	0.6	0.5	0.5	0.4	0.5	0.
β-sesquiphellandrene	2.5	1.4	2.2	2.4	1.9	1.9	1.7	1.6	1.8	5.6
(-)-caryophyllene oxide	-	-	1.0	-	-	0.5	-	-	-	
β-myrcene	-	-	-	-	-	-	-	-	-	0
δ-3-carene	-	-	-	-	-	-	-	-	-	0
α-terpinene	-	-	-	-	-	-	-	-	-	1
1,8-cineole	-	-	-	0.2	-	0.1	-	-	-	0.9
γ-terpinene	-	-	-	0.1	-	-	-	-	-	
ar-curcumene	2.5	1.8	-	1,8	2.2	-	1.4	1.3	-	1.4
γ-curcumene	-	-	-	-	-	-	-	-	0.1	
α-santalol	0.3	-	-	0.3	0.5	3.7	0.2	1.2	-	0
β-santalol	-	-	-	-	-	-	-	-	-	
(-)-α-pinene	-	-	-	-	-	-	-	-	-	0
α-patchoulene	-	-	-	-	-	-	-	-	0.4	
(+)-α-atlantone	-	-	1.3	-	-	2.3	-	-	4.7	
β-himachalene	-	-	-	-	-	0.1	-	-	-	
farnesol	-	-	-	-	-	0.1	-	-	0.1	

AN: *A. niger*, AO: *A. oryzae*, AA: *A. awamori*

The concentration of each of the three main compounds in turmeric oil, as a result of the biodegradation of the three *Aspergillus* spp., increased and decreased on different fermentation days. The increase in the content of the antioxidant compounds can be due to starch degradation and other structural polymers that made antioxidant compounds more accessible during distillation [45]. However, in all samples with 11 days of fermentation time, there was no increase in the content of α-turmerone and β-turmerone compounds, owing to lower starch content, compared to the other timeframes.

With a higher concentration of ar-turmerone, a decrease in the content of α-turmerone and β-turmerone was found. α-turmerone and β-turmerone are unstable compounds that will turn into a more stable aromatic form (ar-turmerone) with continuous exposure to air. The content of ar-turmerone compounds decreased in turmeric oil by biodegradation treatment of the three *Aspergillus* spp., a genus that can carry out biotransformation of ar-turmerone to a more oxidized form [46]. This decrease was discovered on days 7 and 11 for *Aspergillus niger* and *Aspergillus oryzae* and day 9 for *Aspergillus awamori*. Previous studies reported that the largest compound in turmeric oil was ar-turmerone, followed by α-turmerone and β-turmerone in relatively equal amounts [3, 41]. Such results are slightly different with the findings obtained in this study and may be caused by several factors, such as geographical origins, microclimate conditions, soil content, and the differences of turmeric root age [41-47].

4. CONCLUSION

The treatment of biodegradation in turmeric rhizomes using fungi from the genus *Aspergillus* can reduce starch content in turmeric rhizomes, thereby increasing the yield of turmeric oil. *Aspergillus awamori* reduced starch content more than the other two species, reaching 2.9% ww. *Aspergillus oryzae* resulted in the highest turmeric oil yield compared to the other two species of 3.2% dw after 11 days of fermentation. Of the three *Aspergillus* spp., the greatest decrease in starch content and increase in the oil yield occurred on the 9th day. Incubation of turmeric rhizomes by *Aspergillus* reduced the content of ar-turmerone but increased the content of α-turmerone and β-turmerone compounds, which could be transformed into ar-turmerone. The use of *Aspergillus oryzae* as a biological agent for the biodegradation process showed the most positive influence on the extraction of turmeric oil compared to the other two species, with the maximum increase in oil yield and decrease in starch content on the 11th day.

REFERENCES

[1] Lertsutthiwong P, Rojsitthisak P. (2011) Chitosan-alginate nanocapsules for encapsulation of turmeric oil. Pharmazie, 66:911-915.
[2] Chopra D, Simon D. (2000) The Chopra Centre Handbook: Natural Prescriptions for Perfect Health. India, Rider.
[3] Awasthi P, Dixit S. (2009) Chemical composition of Curcuma longa leaves and rhizome oil from plants of Northern India. Journal of Young Pharmacists, 1(4):312.
[4] Parveen Z, Nawaz S, Siddique S, Shahzad K. (2013) Composition and antimicrobial activity of the essential oil from leaves of Curcuma longa L. Kasur variety. Indian J. Pharma Sci., 75(1):117-122.
[5] Statistika Tanaman Biofarmaka Indonesia. Available: https://www.bps.go.id/publication/2019/10/07/65ba24004819d2bbb96bdf63/statistik-tanaman-biofarmaka-indonesia-2018.html
[6] Diederich M, Noworyta K. (2012) Natural compounds as inducers of cell death. USA, Springer Science and Business Media.
[7] Manzan ACCM, Toniolo FS, Bredow E, Povh NP. (2003) Extraction of essential oil and pigments from Curcuma longa [L] by steam distillation and extraction with volatile solvents. Journal of Agricultural and Food Chemistry, 51(23):6802-6807.
[8] Kurmudle N, Bankar SB, Kagliwal LD, Singhal RS. (2013) Enzyme-assisted extraction for enhanced yields of turmeric oleoresin and its constituents. Food Bioscience, 3:36-41.
[9] Klein-Marcuschamer D, Oleskowicz-Popiel P, Simmons BA, Blanch HW. (2011) The challenge of enzyme cost in the production of lignocellulosic biofuels. Biotechnology and Bioengineering, 1-5.
[10] El-Gendi H, Saleh AK, Badierah R, Redwan EM, El-Maradny YA, El-Fakharany EM. (2022) A Comprehensive Insight into Fungal Enzymes: Structure, Classification, and Their Role in Mankind's Challenges. J Fungi (Basel), 8(1):23-33.
[11] Hakala TK. (2007) Characterization of the lignin-modifying enzymes of the selective white-rot fungus. PhD Thesis, University of Helsinki, Helsinki.
[12] Andersen MR, Giese M, de Vries RP, Nielsen J. (2012) Mapping the polysaccharide degradation potential of Aspergillus niger. BMC genomics, 13(1):313-319.
[13] Varga J, Frisvad JC, Samson RA. (2009) A reappraisal of fungi producing aflatoxin. World Mycotoxin Journal, 2:263-277.
[14] de Vries RP, Visser J. (2001) Aspergillus enzymes involved in degradation of plant cell wall polysaccharides. Microbiology and Molecular Biology Reviews, 65(4):497-552.
[15] Abduh MY, Zuliansyah W, Aprina L, Arazella N. (2019) Effect of pectin biodegradation with Aspergillus niger on total flavonoid content of Citrus limon L. J Biodjati, 4(2):194-203.
[16] Abduh MY, Nababan E, Ginting F, Juliati J, Nugrahapraja, H. (2020) Biodegradation of lemon peels using Aspergillus sp. to improve yield and composition of extracted lemon oil. IIUM Engineering Journal, 21(2):55-66.
[17] National Horticulture Board. Avalable: https://nhb.gov.in/model-project-reports/Horticulture%20Crops/Patchouli/Patchouli1.htm
[18] Zambare V. (2010) Solid state fermentation of Aspergillus oryzae for glucoamylase production on agro residues. International Journal of Life Sciences, 4:16-25.

[19] Diaz-Maroto MC, Perez-Coello MS, Gonzalez VMA, Cabezudo MD. (2003) Influence of drying on the flavor quality of spearmint (Mentha spicata L.) Journal of Agricultural and Food Chemistry, 51:1265-1269.
[20] Manzan ACCM, Toniolo FS, Bredow E, Povh NP. (2003) Extraction of essential oil and pigments from Curcuma longa [L.] by steam distillation and extraction with volatile solvents. Journal of Agricultural and Food Chemistry, 51:6802-6807.
[21] Inderaja BM, Pradhita O, Hanifa R, Manurung R, Abduh MY. (2018) Factors affecting biomass growth and production of essential oil from leaf and flower oil Salvia leucantha Cav. Journal of Essential Oil Bearing Plants, 21(4):1021-1029.
[22] Ahmad HN, Raba HE, Fadilla I, Fajar A, Manurung R, Abduh MY. (2018) Determination of yield and chemical composition of eucalyptus oil from different species and locations in Indonesia. Biological and Natural Resources Engineering Journal, 1(1):36-49.
[23] Abduh MY, Ibrahim IN, Atika U, Manurung R, Suheryadi D. (2020) Influence of water stress and plant age on the yield and chemical composition of essential oil from Cymbopogon winterianus Jowitt. BIOTROPIA, 27(1):80-87.
[24] Rahimmalek M, Goli SAH. (2013) Evaluation of six drying treatments with respect to essential oil yield, composition and color characteristics of Tymys daenensis subsp. daenensis, celak leaves. Industrial Crops and Products, 42:613-619.
[25] Hamrouni-Sellami I, Wannes WA, Bettaieb I, Berrima S, Chahed T, Marzouk B, Limam F. (2011) Drying sage (Salvia officinalis L.) plants and its effects on content, chemical composition, and radical scavenging activity of the essential oil. Food and Bioprocess Technology, 5(8):2978-2989.
[26] Sourestani MM, Malekzadeh M, Tava A. (2014). Influence of drying, storage, and distillation times on essential oil yield and composition of anise hyssop [Agastache foeniculum (Pursh.) Kuntze. Journal of Essential Oil Research, 26:177-184.
[27] de Castro AM, Carvalho DF, Freire DMG, Castilho LR. (2010) Economic analysis of the production of amylases and other hydrolases by Aspergillus awamori in solid-state fermentation of babassu cake. Enzyme Research, 1-9.
[28] Kusbiantoro D, Purwaningrum Y. (2018) Pemanfaatan kandungan metabolit sekunder pada tanaman kunyit dalam mendukung peningkatan pendapatan masyarakat. Jurnal Kultivasi, 17(1):544-549.
[29] de Soulza PM, Magalhaes PO. (2010) Application on microbial α-amylase in industry-a review. Brazillian Journal of Microbiology, 41(4):850-861.
[30] Nangin D, Sutrisno A. (2015) Enzim amilase pemecah pati mentah dari mikroba: kajian pustaka. Jurnal Pangan dan Agroindustri, 3(3):1032-1039.
[31] Reyes I, Cruz-Sosa F, Hernandez-Jaimes C, Venon-Carter EJ, Alvarez-Ramirez J. (2017) Effect of solid-state fermentation (Aspergillus oryzae var. oryzae) on the physcochemical properties of corn starch. Starch, 69:1-10.
[32] Standbury PF, Whitaker A, Hall SJ. (2003) Principles of Fermentation Technology. Oxford, Butterworth-Heinemann.
[33] Doughari JH, Santos BAQ, Ntwampe SKO. (2016) Application of Aspergillus awamori grown on citrus peel supplemented growth medium for cyanide bioremediation. Nigerian Journal of Microbiology, 30(1):3221-3224.
[34] Zambare V. (2010) Solid state fermentation of Aspergillus oryzae for glucoamylase production on agro residues. International Journal of Life Sciences, 4:16-25.
[35] Farid MAF, Shata HMAH. (2011) Amylase production from Aspergillus oryzae LS1 by solid-state fermentation and its use for the hydrolysis of wheat flour. Iranian Journal of Biotechnology, 9(4):267-274.
[36] Kalaiarasi K, Parvatham R. (2015) Optimization of process parameters for α-amylase production under solid-state fermentation by Aspergillus awamori MTCC 9997. Journal of Scientific & Industrial Research, 74:286-289.
[37] Umsza-Guez MA, Diaz AB, de Ory I, Blandino A, Gomes E, Carlo I. (2011) Xylanase production by Aspergillus awamori under solid state fermentation conditions on tomato pomace. Brazilian Journal of Microbiology, 42(4):1585-1597.

https://doi.org/10.31436/iiumej.v24i1.1629

[38] Kurmudle N, Bankar SB, Kagliwal LD, Singhal RS. (2013) Enzyme-assisted extraction for enhanced yields of turmeric oleoresin and its constituents. Food Bioscience, 3:36-41.

[39] Yamane Y, Fujita J, Izuwa S, Fukuchi K, Shimizu R, Hiyoshi A, Fukuda H, Mikami S. (2002) Properties of cellulose-degrading enzymes from Aspergillus oryzae and their contribution to material utilization and alcohol yield in sake mesh fermentation. Journal of Bioscience and Bioengineering, 93(5):479-484.

[40] Naibaho RA. (2018) Karakterisasi simplisia, isolasi dan analisis komponen minyak atsiri dari rimpang dan daun kunyit (Curcuma domestica Val.) kering secara GC-MS.

[41] Huong NTM, Cuc NTK, Dung TK, Ha TL, Cuong PV. (2013) Chemical composition and antifungal activity of Vietnamese turmeric aromatic products obtained from Curcuma longa (Zingiberaceae) by different methods. Food Science, Engineering, and Technology, 60:539-545.

[42] Chane-Ming J, Vera R, Chalchat JC, Cabassu P. (2002) Chemical composition of essential oils from rhizomes, leaves and flowers of Curcuma longa L. from Reunion Island. Journal of Essential Oil Research, 14(4):249-251.

[43] Naz S, Ilyas S, Parveen Z, Javed S. (2010) Chemical analysis of essential oils from turmeric (Curcuma longa) rhizome through GC-MS. Asian Journal of Chemistry, 22(4):3153-3160.

[44] Chowdhury JU, Nandi NC, Bhuiyan MNI, Mobarok MH. (2008) Essential oil constituents of the rhizomes of two types of Curcuma longa of Bangladesh. Bangladesh.

[45] Hur SJ, Lee SY, Kim YC, Choi I, Kim GB. (2014) Effect of fermentation on the antioxidant activity in plant-based foods. Food chemistry, 160:346-356.

[46] Fujiwara M, Marumoto S, Yagi N, Miyazawa M. (2010) Biotransformation of turmerones by Aspergillus niger. Journal of natural products, 74(1):86-89.

[47] Baser KHC, Buchbauer G. (2015) Handbook of essential oils: science, technology, and applications. CRC Press.

https://doi.org/10.31436/iiumej.v24i1.2400

EFFECT OF THE LIGNOCELLULOLYTIC SUBSTRATES AND FERMENTATION PROCESS PARAMETERS ON MYCO-COAGULANT PRODUCTION FOR WATER TREATMENT

MAROUA FELLAH[1], MD ZAHANGIR ALAM[1*], ABDULLAH AL MAMUN[2], NASSERLDEEN AHMED KHABBASHI[1], NURUL SAKINAH ENGLIMAN[1] AND SONIA HADJ ARAB[1]

[1]Department of Chemical Engineering and Sustainability,
[2]Department of Civil Engineering,
Kulliyyah of Engineering, International Islamic University Malaysia,
Jalan Gombak, 53100 Kuala Lumpur, Malaysia

[*]Corresponding author: zahangir@iium.edu.my

(Received: 21st April 2022; Accepted: 15th November 2022; Published on-line: 4th January 2023)

ABSTRACT: In the present research, a fungal strain was used to produce a myco-coagulant via solid-state bioconversion to reduce water turbidity. The production of myco-coagulant was achieved using several low-cost lignocellulolytic substrates, namely coco peat, sawdust, palm kernel cake, and rice bran as sources of carbon and nitrogen. This research involves the study of both the effect of lignocellulolytic substrates and the parameters involved in the fermentation process for myco-coagulant production. Coco peat was chosen as a suitable lignocellulolytic substrate to serve as a carbon source for producing myco-coagulant, potentially reducing the turbidity by 84.6% from the kaolin suspension. Sawdust, palm kernel cake, and rice bran showed 33.06%, 30.18, and 21.18 %, respectively. Furthermore, a statistical approach to the Plackett-Burman design was conducted to evaluate the significant parameters that affect the production of myco-coagulant. Eleven fermentation process parameters were selected: concentration of coco peat (2- 4 %), incubation time (5-9 days), temperature (25-35 °C), pH (5-9), glucose (0-2 %), malt extract (1-2 %), yeast extract (0-2%), wheat flour (0-2 %), ammonium sulfate (0-1 %), inoculum size (1-3 %) and potassium dihydrogen phosphate (0-0.5 %). The selected variables were assessed through statistical analysis (main effects) based on their significance. Based on the main effect of each variable on flocculation activity, three variables, namely glucose, malt extract, and pH influenced high levels. On the other hand, the remaining eight variables did not significantly affect the production of myco-coagulant. Furthermore, a deeper study was conducted to further optimize the three effective variables involved in the fermentation process to evaluate these factors' influence on flocculation activity.

ABSTRAK: Penyelidikan ini adalah berkenaan strain fungus yang digunakan bagi menghasilkan miko-koagulan melalui penukaran-bio berkeadaan pepejal bagi mengurangkan kekeruhan air. Miko-koagulan dihasilkan dengan menggunakan beberapa substrat lignoselulolitik berkos rendah, iaitu habuk kelapa, habuk papan, hampas kelapa sawit, dan dedak padi sebagai sumber karbon dan nitrogen. Penyelidikan ini mengkaji kesan substrat lignoselulolitik dan faktor-faktor yang terlibat dalam proses fermentasi bagi menghasilkan miko-koagulan. Habuk kelapa dipilih sebagai substrat lignoselulolitik yang sesuai berfungsi sebagai sumber karbon dalam menghasilkan miko-koagulan, berpotensi mengurangkan kekeruhan sebanyak 84.6% daripada ampaian kaolin. Sebaliknya, habuk papan, hampas kelapa sawit, dan dedak padi menunjukkan 33.06%, 30.18, dan 21.18 %, masing-masing. Tambahan pula, pendekatan statistik ke atas reka bentuk Plackett-Burman telah dijalankan bagi menilai parameter penting yang mempengaruhi penghasilan miko-koagulan. Sebelas parameter proses penapaian telah dipilih: kepekatan habuk kelapa (2- 4 %), masa pengeraman (5-9 hari), suhu (25-35 C), pH (5-9), glukosa (0-2 %), ekstrak malt (1-2), tepung gandum (0-2 %), ammonium sulfat (0-1%), saiz inokulum (1-3 %) dan Kalium dihidrogen fosfat (0-0.5 %). Pemboleh ubah yang dipilih dinilai melalui analisis statistik berdasarkan kepentingannya. Berdasarkan kesan utama setiap pemboleh ubah terhadap aktiviti penggumpalan, tiga pemboleh ubah ini adalah glukosa, ekstrak malt, dan pH yang memberi kesan tertinggi. Sebaliknya, lapan pemboleh ubah lain tidak mempengaruhi penghasilan miko-koagulan dengan ketara. Tambahan lagi, kajian yang lebih mendalam telah dijalankan bagi membaiki tiga pemboleh ubah utama yang terlibat dalam proses fermentasi bagi menilai kesan yang mempengaruhi aktiviti penggumpalan.

KEYWORDS: *Myco-coagulant, solid-state bioconversion, lignocellulolytic substrates, water treatment, turbidity removal, flocculation activity, PBD.*

1 INTRODUCTION

High turbidity and suspended solids (SS) are significant problems that affect rivers due to wastewater discharge, terrain conditions, land cover, rainfall, soil type, agriculture, stirred bottom sediments, algal blooms, and other development activities. These problems indicate the essential need to protect the aquatic environment and life by diminishing the turbidity and residual levels in the rivers using both conventional and advanced technologies in water: from treatment such as sedimentation and filtration to more complex methods, including ultrafiltration, ozonation, and reverse osmosis, to process raw water sources before supplying it to consumers and to ensure that the treated water can meet the effluent discharge requirement before it is discharged to water bodies [1,2].

The coagulation-flocculation process is considered one of the most straightforward approaches to accelerate the removal of suspended impurities in water efficiently. Even with advanced technologies, coagulation-flocculation remains one of the essential treatment processes for removing impurities (mainly suspended particles) in water treatment plants. This process requires adding components called coagulants/flocculants [3,4]. Coagulants/flocculants are commonly applied in many industrial processes, such as potable water purification and wastewater treatment. Generally, coagulants/flocculants are classified into three types: synthetic organic polymer flocculants like polyacrylamides, inorganic flocculants such as aluminium sulfate, iron sulfate, and iron chloride, and those that are naturally occurring, such as sodium alginate, chitosan, and microbial coagulants/flocculants [3,4]. Due to flocculating efficiency, chemical coagulants-flocculants are widely used in conventional water treatment processes [5,6,7]. However, using chemical coagulants/flocculants in water treatment has been limited due to several disadvantages [8,9]. As reported in many studies, its usage can cause several environmental problems and human health concerns [10,11,12].

Since the coagulants/flocculants play a significant role in the coagulation/flocculation process, developing highly efficient alternative coagulants/flocculants has always remained one of the most challenging research areas [13]. Biocoagulants/flocculants have piqued the interest of many researchers due to their numerous advantages: biodegradability, nontoxic properties, and potential as an alternative for conventional coagulants/flocculants [11,14]. Microbial coagulants/flocculants are extracellular biopolymers secreted by microorganisms such as bacteria, yeasts, fungi, and algae [2]. They contain mainly glycoproteins, polysaccharides, and proteins produced by microorganisms during active secretion [15]. However, the application of microbial coagulants/flocculants has been hindered by the challenge of producing them on a large scale. Currently, researchers produce microbial coagulants/flocculants by applying synthetic media which contain simple sugar (glucose, sucrose, lactose, fructose, maltose), alcohols, and organic acid as carbon sources through the liquid-state fermentation method. Despite the potential applications of microbial coagulants/flocculants, the high production costs still limit their use.

Interestingly, new strategies to produce microbial coagulants/flocculants have been identified. The preference for SSF is more economically attractive due to the usage of low-cost materials such as agricultural and industrial byproducts via solid-state fermentation to produce bioactive compounds. SSF is of interest as an alternative to other conventional fermentation methods that are more costly and mainly chemically driven [16]. These bioprocessing technologies are devoted to developing cost-effective measures by utilizing inexpensive fermentation substrates to meet the current market demand for bioproducts [16], which may reduce production costs on industrial scales. Thus, an appropriate, inexpensive, and abundant substitute for these substrates, such as byproducts and agricultural residues, should be utilized to replace the conventional substrates to solve this problem. Solid-state fermentation may be better for producing a microbial coagulant/flocculant using filamentous fungi [17,18]. Thus, this research will investigate a coagulant-produced fungus called myco-coagulant via solid-state fermentation using agricultural waste as a low-cost substrate.

The present study aims to select the best lignocellulolytic substrates via a solid-state fermentation (SSF) process to produce an efficient myco-coagulant to reduce the turbidity of the water. It was also designed to study the impact of various fermentation process parameters, namely concentration of coco peat, incubation time, temperature, pH, glucose, malt extract, wheat flour, ammonium sulfate, inoculum size, and potassium dihydrogen phosphate (KH_2PO_4) on the production of coagulants from a fungal strain using a Placket-Burman experimental design.

2 MATERIALS AND METHODS

2.1 Microorganisms

The microorganism used in the present study was a fungal strain collected from a supermarket in Kuala Lumpur, Malaysia. The fungal strain was maintained on potato dextrose agar (PDA), stored in the chiller at 4º C, and kept at room temperature (30±2º C) for further use.

2.2 Substrate collection and preparation

In this study, different lignocellulolytic (LC) substrates, namely coco peat, sawdust, palm kernel cake, and rice bran, were collected from the International Islamic University Malaysia, Kuala Lumpur. The substrates were used as the supplementary media throughout this study, which were ground and milled into a fine powder using a domestic blender. The fine powders passed through a 50 mm-mesh sieve and were stored at room temperature for solid-state fermentation (SSF). These substrates may be seen as an inexpensive and abundant agricultural waste model, making the entire SSF process feasible and low-cost.

2.3 Inoculum preparation (Mycelium suspension)

The mycelial suspension was prepared by fully grown plates of fungi cultures from the incubator after seven days of incubation. A wriggled L-shaped rod was gently scraped off each plate and washed carefully with 20 ml of sterilized distilled water. The suspended mycelial suspension was used as the main inoculum.

https://doi.org/10.31436/iiumej.v24i1.2400

2.4 Solid-state bioconversion (SSB)

The solid-state bioconversion was conducted by moistening 3 g of each substrate, namely coco peat, sawdust, palm kernel cake, and rice bran, with 1 ml of fungal mycelial suspension and 7 ml of production media in a petri dish, which was sealed with a parafilm to avoid contamination with unwanted microbes. The medium consisted of 20 g of malt extract dissolved into 1000 ml of distilled water (2% w/v), and its initial pH was adjusted to 7 using 1 M NaOH or 2 M HCl. The production medium was autoclaved at 120º C for 15 minutes. The inoculated plates were incubated at 30º C for seven days. The major activities involved in the research are shown in Fig. 1.

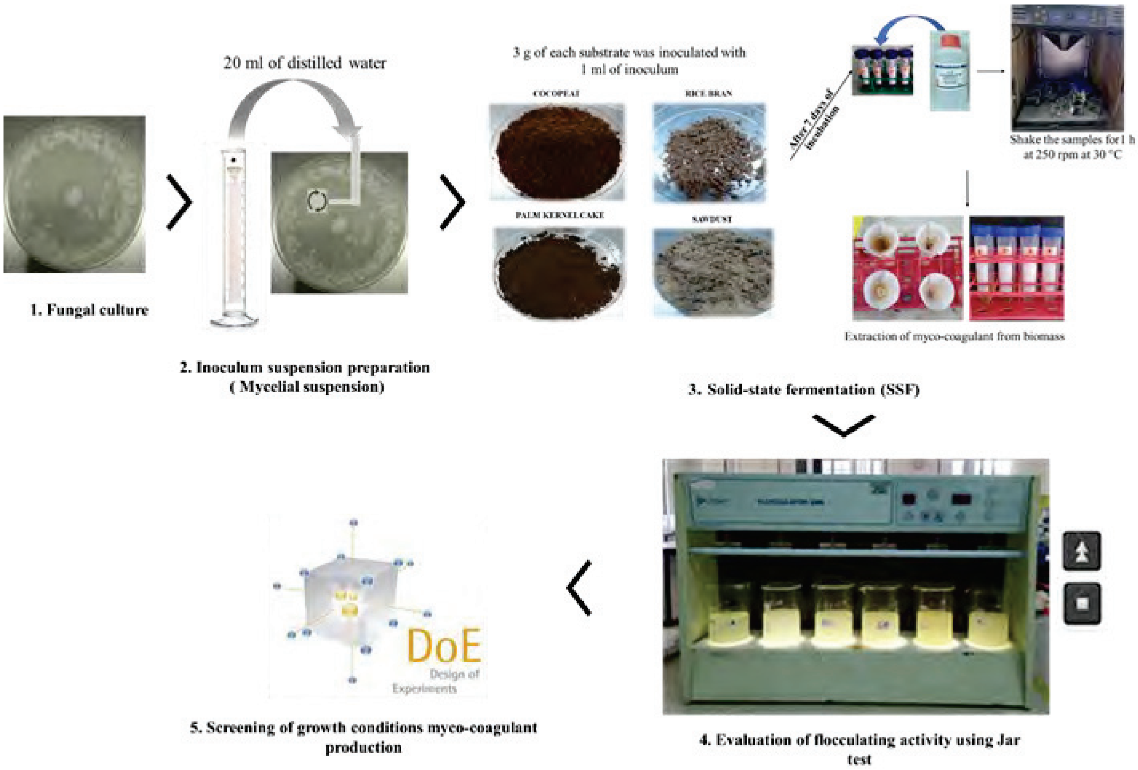

Fig. 1. Overall scheme of the major activity to produce myco-coagulant using solid-state fermentation.

2.5 Surface Morphology Analysis

Scanning electron microscopy (SEM) (SEM-Sipma-VP03-67, Zeiss, and P-Sigma, Munich, Germany) was used to observe the fungus's morphological surface and the mycelium formation in various lignocellulosic media.

2.6 Extraction of myco-coagulant

In this study, the extraction of the myco-coagulant from the biomass was conducted using an aqueous buffer solution at pH 7. After seven days of incubation, the fermented medium of SSF from each plate (2 g of the substrate) was mixed with 20 ml of aqueous buffered solution at pH 7. The mixture was kept in a shaker incubator for 1 hour at 250 rpm at 30º C. It was then filtered using muslin, followed by a Whatman paper. The clear supernatant was collected as

https://doi.org/10.31436/iiumej.v24i1.2400

the main myco-coagulant and used to determine their flocculating activity using the Jar apparatus method.

2.7 Determination of turbidity

The turbidity meter (Model 2100Q: HACH, Loveland, USA) was switched on before the data recording, and a blank sample of 10 mL distilled water was poured into the turbidity vial. 10 mL of the supernatant from each untreated water sample was poured into the turbidity vial. The outer vial was cleaned and placed into the turbidity meter before the 'read' button was pressed to get the turbidity reading in NTU. Finally, the average readings were calculated for record purposes.

2.8 Jar test experiment

The purpose of a jar test experiment was to observe the coagulation and flocculation processes of water treatment on the laboratory scale. The equipment needed in conducting jar tests was a Flocculator unit (SW6, UK) that consisted of six paddle mixers to which respective beakers were placed and a control panel to adjust the stirring speed and time. Four operating conditions of the jar test were set as the independent variables: the initial pH value, coagulant dosage of myco-coagulant, rapid mixing speed, and settlement time. After that, the required amount of myco-coagulant was added to synthetic turbid water and succeeded by rapid mixing to simulate the coagulation process. It was then followed by the slow mixing that demonstrated the flocculation process. Then, the beakers containing treated wastewater were left aside for one hour to allow flocs sedimentation. After the flocs had settled, the supernatant of the treated wastewater was taken and analyzed for its final turbidity.

2.9 Evaluation of flocculation activity via Jar test

The Kaolin suspension was used to determine the flocculation activity of the myco-coagulant in its capacity to reduce the turbidity level. First, 0.7 g/l kaolin clay was suspended in 1500 ml of distilled water and pH 7 using 1M NaOH or 2M HCl. Initial turbidity was recorded at 480 NTU. 10 ml of the supernatant (myco-coagulant) was added to each jar containing 300 ml kaolin suspension. Then, the jar was set up and operated at three stages: fast mixing at 250 rpm for 7 minutes, then 90 rpm for 22 minutes, and finally settling for one hour. Next, the top layer of the water in each jar was collected with a micropipette, and the flocculation activity was calculated based on the percentage removal of turbidity. All the experiments were conducted in triplicate. The flocculating activity was calculated according to Eq. (1).

$$\text{Turbidity removal efficiency (\%)} = \frac{A-B}{A} \times 100 \qquad (1)$$

where A is the initial turbidity of kaolin suspension directly after preparation (NTU) and B is the final turbidity of kaolin suspension after the settling period (NTU). A sartorius PB-10 pH meter was used to measure the pH value. The turbidity was measured by using a nephelometric turbidity unit (NTU) (standard method 2130 B) with a portable turbidimeter (2100Q HACH, USA).

2.10 Screening of growth conditions using Plackett-Burman design

Statistical experimental design plays an essential role in developing fermentation bioprocesses by screening for the main factors of interest and then further optimizing these to improve industrial process performance. Different nutritional and environmental variables were evaluated to determine the variables affecting flocculation activity by the production of the myco-coagulant. The Plackett–Burman statistical experimental design "Design Expert®

7.0.0" was used to identify the critical variables required to produce a myco-coagulant to reduce turbidity. The Plackett-Burman design (PBD) is an easy and fast method appropriate to screen multiple variables in a single experiment and is often used to evaluate the most significant variables affecting the culture requirements for fermentation and enzyme production.

Based on previous studies, several potential factors may affect the yield of the myco-coagulant. In this study, eleven factors were chosen. The eleven different independent variables are shown in Table 1, including the physical/chemical parameters (temperature, incubation time, inoculum size, cocopeat concentration, pH), and nutrients (malt extract, glucose, wheat flour, yeast, ammonium sulfate $(NH_4)_2SO_4$ and potassium dihydrogen phosphate (KH_2PO_4)). Each variable is represented at both high and low, denoted by (+) and (−). Flocculation activity was used as the response variable.

Table 1: Variables and their levels employed in Plackett–Burman design to screen culture conditions affecting myco-coagulant production by the fungus

Variables	Code	Low level (-)	High level (+)
Temperature (ºC)	A	25	35
Incubation time (Days)	B	5	9
pH	C	5	9
Cocopeat concentration (g)	D	2	4
Malt extract	E	1	2
Ammonium sulfate $(NH_4)_2SO_4$ (%)	F	0	1
Glucose (%)	G	0	2
Wheat flour (%)	H	0	2
Yeast extract (%)	J	0	2
Potassium dihydrogen phosphate KH_2PO_4 (%)	K	0	0.5
Inoculum size (ml)	L	1	3

3 RESULTS AND DISCUSSION

3.1 Estimation of biomass in solid-state fermentation

The fungal mycelium penetrates deep into solid-state fermentation and remains attached to the solid substrate particles. As a result, it is difficult to separate the microorganisms from the solid particles. The present study used standard methods to estimate the biomass in solid-state fermentation [19,20,21].

3.1.1 Prescreening test for estimation of fungal growth

Estimating biomass is a critical step in a variety of microbial fermentation processes. In the present study, a prescreening test was performed to monitor and compare the growth rate of fungal strains on four distinct lignocellulosic substrates. As shown in Fig. 2 on cocopeat substrates, the fungal strain grew swiftly and created intact homogenous and filamentous mycelium composite structures. In addition, sawdust showed slow growth during this time of incubation. On the other hand, the fungal strain grew on palm kernel cake and rice bran; you can barely see the growth.

Fig. 2. Culture of fungus on different substrates after seven days of incubation (a) culture of fungus on cocopeat; (b) culture of fungus on sawdust; (c) culture of fungus on PKC; (d) culture of fungus on rice bran.

3.1.2 Evaluation of fungal growth by scanning electron microscope (SEM)

A scanning electron microscope (SEM) was used to observe the fungus's morphological surface and the mycelium formation in various lignocellulosic media. Fig. 3 shows a significant variation in the density of the filamentous fibre of the fungus in various lignocellulosic media. On the other hand, the SEM indicates no change in the morphological surface due to the use of the same strains. Fig. 3 illustrates mycelium morphology observed in SEM with randomly arranged and oriented filaments on cocopeat, sawdust, palm cake, and rice bran substrates, respectively. The mean hyphae filament diameter was 0.6 ± 0.66 µm. In contrast, the other substrates show a hyphal density of less than coco peat with a diameter of filaments with a mean of 0.7 µm, 0.9 µm, and 1 µm for sawdust, palm kernel cake, and rice bran, respectively.

In general, there is no difference in the morphological structure, as shown in Fig.3, which refers to using the same fungal strain. However, the density and size of filaments differed from one substrate to another. The variation of the branching density can be explained by the environmental conditions here, where various lignocellulosic media were used. Fungal mycelial growth is aided by the substrate, which contains modest concentrations of carbohydrates, lipids, proteins, inorganic substances, and water [22]. Therefore, the physical characteristics of the substrate may reveal differences in mycelium growth [23,24].

https://doi.org/10.31436/iiumej.v24i1.2400

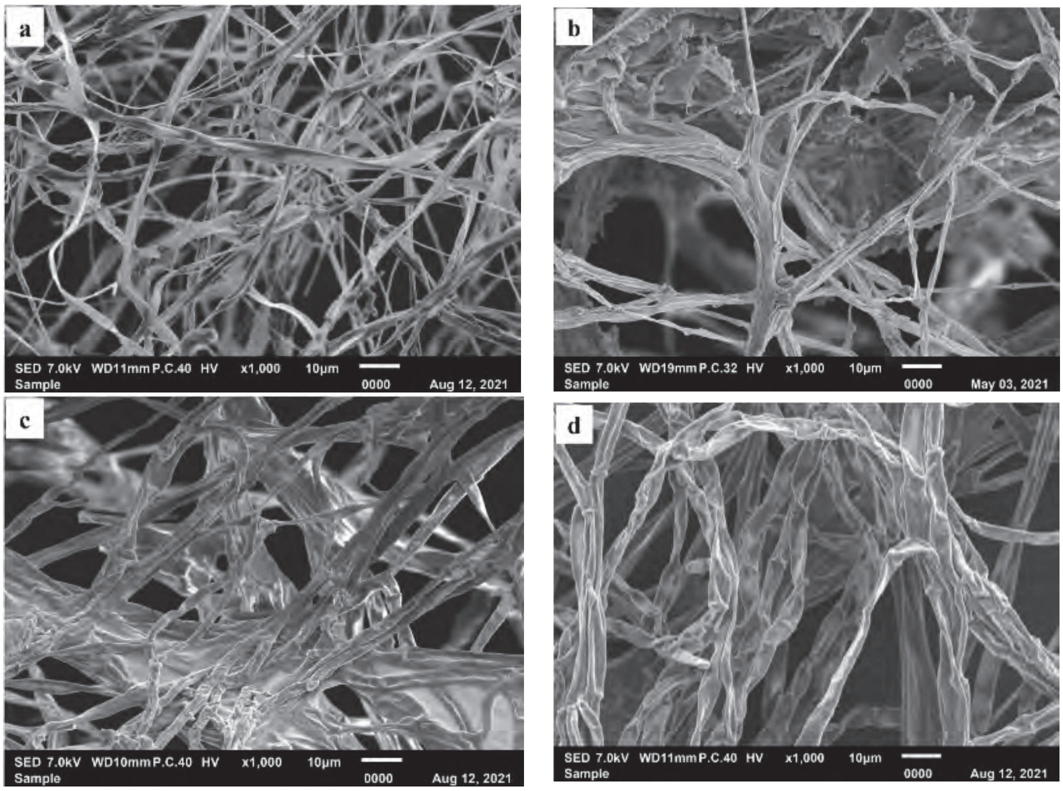

Fig. 3. Scanning Electron Microscopy (SEM) observations of fungal colonies on different substrates after seven days of incubation (a) culture of fungus on cocopeat; (b) culture of fungus on sawdust; (c) culture of fungus on PKC; (d) culture of fungus on rice bran magnification at X1000.

3.2 Analysis of myco-coagulant activity

Microbial secondary metabolites are regarded as valuable products due to their large number of biological activities. The secondary metabolites are synthesized in a fermentation medium during the growth of the microbes [19].

In this research, the desirable secondary metabolite was a myco-coagulant secreted during fungus growth on different lignocellulosic media. Fig. 4 shows the flocculation activity rate of the myco-coagulant using four lignocellulosic media. From the results, it can be clearly seen that coco peat recorded the highest flocculation rate at 84.59 % in removing suspended solids from kaolin suspension. On the other hand, the remaining LC substrates, namely sawdust, palm kernel cake, and rice bran, were recorded at 33.06 %, 23.91 %, and 21.18 %, respectively. Based on the results, coco peat was chosen as the best media to serve as an LC substrate for the fungal strain and produced an efficient myco-coagulant.

Selecting an appropriate substrate suitable for fungal growth and the target of myco-coagulant synthesis is crucial in developing an efficient technology for myco-coagulant production. Four substrates, namely coco peat, sawdust, palm kernel cake, and rice bran, were used in this study, which was collected from the biotechnology engineering laboratory of the International Islamic University Malaysia (IIUM). These solid substrates were considered to evaluate their ability to produce an efficient myco-coagulant to reduce the turbidity from water.

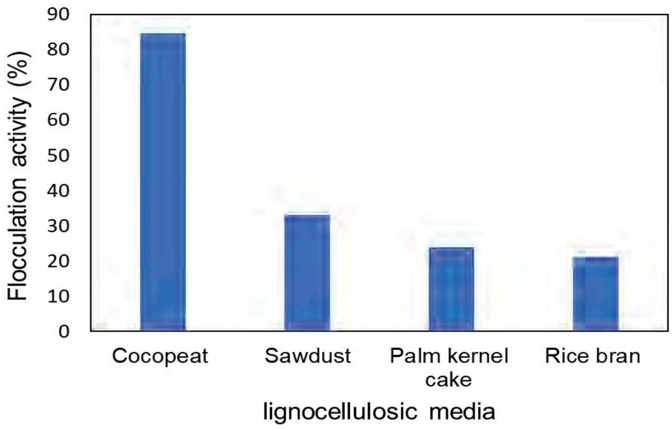

Fig. 4. Flocculation activity of the myco-coagulant in four different lignocellulosic media.

The supernatants of the used fungus extracted from biomass were tested to determine the flocculation ability in terms of turbidity reduction from synthetic turbid water (Kaolin suspension). The initial turbidity was recorded at 600 ± 30 NTU for kaolin suspension.

The flocculation activity rate of the treated synthetic turbid water by the fungal supernatants extracted from the biomass showed a wide variation in flocculation activity all over the fourth biomass ranging from 18.7 % to 89.19 %. Among the four fungal supernatants, the fungal supernatant extracted from coco peat from 623 to 96 NTU 84.59% showed the highest flocculation activity. On the other hand, sawdust, palm kernel cake, and rice bran showed 33.06%, 30.18, and 21.18 %, respectively.

The myco-coagulant was evaluated to test its ability to remove turbidity by flocculating the particles' kaolin suspension using the Jar apparatus. Based on the results, the fungal strain has proven its ability to produce an efficient myco-coagulant via solid-state using cocopeat as a substrate in reducing turbidity.

Coco peat was the best supplement that offered the best carbon source in yielding a myco-coagulant, with the highest FA (84.59 %) obtained with kaolin clay suspension. Therefore, the myco-coagulant extracted from coco peat that exhibited the best flocculating activity was chosen for further analysis, and the remaining substrates were eliminated from the remaining part of the study. As reported by Luthfi et al. [25], *Aspergillus niger* DWB showed a good flocculation activity rate of 60.5 % from oil palm empty fruit bunch (OPEFB) fiber. Qi et al. [26] reported that *Alcaligenes faecalis subsp. phenolicus* ZY-16 showed a good removal efficiency (90.05%) of citrus peel wastes as substrates.

3.3. Screening of process conditions for the SSF using PBD

The effects of different nutritional components on myco-coagulant production using coco peat were studied to develop a medium that requires minimal nutritional supplementation for enhanced enzyme production. A Plackett-Burman design (PBD) was applied in this study to determine which variables significantly affected the flocculation activity by producing a myco-coagulant using solid-state fermentation. The PB design is a simple and fast method suitable for screening multiple variables in a single experiment and is often used to evaluate the most significant variables affecting fermentation and enzyme production culture requirements.

The impacts of nutritional factors, including carbon and nitrogen sources and mineral salts, were studied using a PB design with 12 trials for 11 variables. As a first step, the corresponding responses in Table 2 were carried out to identify the significant variables on myco-coagulant production to reduce turbidity. PB experiments showed a wide variation in flocculation activity over all the different experiments, ranging from (18.7 to 89.19 %) presented in Table 2, highlighting the importance of further media optimization to attain a high yield of the interesting product myco-coagulant with high flocculation activity.

The effect of each nutrient component on flocculation activity is presented in Fig. 5. The main effect was estimated based on the difference between the sum of responses obtained at each component's high level (+1) and the low level (−1). Fig. 5 shows the main effect of each variable on the flocculation activity. Concerning the main effect of each variable, the results showed that three variables from the eleven different independent variables, which were malt extract, glucose, and wheat flour, affected the high flocculation activity at a high level. The level of the carbon source in the growth medium is an essential factor in the production of the myco-coagulant. In the present study, the carbon source, glucose, and wheat flour showed a significantly high effect on the production of the myco-coagulant. Previous studies reported that glucose positively affected the production of the myco-coagulant through liquid-state fermentation with *Lentinus squarrosulus* strain 7-4-2 [27].

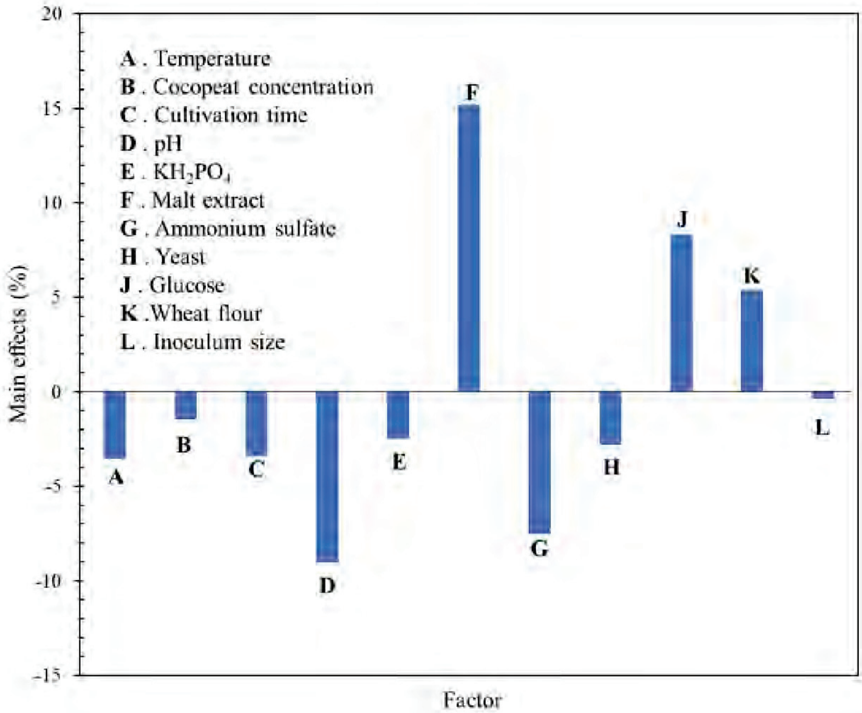

Fig. 5. Main effects of the nutritional components on Flocculation activity

Moreover, [28] reported that *B. agaradhaerens* C9 was cultured in a medium containing glucose, and yeast produced a coagulant with a flocculating activity of 91.9 %. Regarding the effect of pH a, similar results were reported by [15,29] which show the best initial pH of the medium was 6, which was in line with the best pH for bioflocculant production by *A. niger.* However, the remaining variables, temperature, coco peat concentration, cultivation time, KH_2PO_4, ammonium sulfate, pH, and inoculum size, affected the flocculation activity at a low level. The nitrogen source malt extract and ammonium sulfate showed a significant effect on the production of myco-coagulant. The most significant parameter at a low level on the main impact was pH and aluminium sulfate, whereby maintaining the fermentation at acidic pH enhanced the flocculating activity of the metabolite produced. Pu et al. [29] and Nurul et al. [30] have reported that the flocculating activity was not affected by the inoculum size, which supported our finding.

Table 2: Plackett–Burman experimental design and obtained responses

Variables	Temp. (°c)	Cocopeat concentration (%)	Cultivation time (day)	pH	KH_2PO_4 (%)	Malt extract (%)	Ammonium sulfate (%)	Yeast extract (%)	Glucose (%)	Wheat flour (%)	Inoculum size (ml)	Flocculation activity (%)
Code	**A**	**B**	**C**	**D**	**E**	**F**	**G**	**H**	**J**	**K**	**L**	
Run												
1	25	2.0	5	9.0	0.00	2.0	1.0	0.0	2.0	2.0	3.0	72.74
2	35	4.0	5	9.0	0.50	2.0	0.0	0.0	0.0	2.0	1.0	56.93
3	25	2.0	5	5.0	0.00	1.0	0.0	0.0	0.0	0.0	1.0	48.87
4	35	2.0	5	5.0	0.50	1.0	1.0	2.0	0.0	2.0	3.0	26.12
5	35	4.0	5	5.0	0.00	2.0	0.0	2.0	2.0	0.0	3.0	79.35
6	25	2.0	9	5.0	0.50	2.0	0.0	2.0	2.0	2.0	1.0	89.19
7	25	4.0	5	9.0	0.50	1.0	1.0	2.0	2.0	0.0	1.0	18.7
8	35	2.0	9	9.0	0.50	1.0	0.0	0.0	2.0	0.0	3.0	27.7
9	25	4.0	9	9.0	0.00	1.0	0.0	2.0	0.0	2.0	3.0	25.32
10	35	2.0	9	9.0	0.00	2.0	1.0	2.0	0.0	0.0	1.0	26.61
11	25	4.0	9	5.0	0.50	2.0	1.0	0.0	0.0	0.0	3.0	48.7
12	35	4.0	9	5.0	0.00	1.0	1.0	0.0	2.0	2.0	1.0	44.52

The use of coco peat as a low-cost nutrient composition was earlier not reported for the higher yield of myco-coagulant from fungal fermentation. Based on this study, it was determined that the designed lignocellulosic substrate was economically significant in producing the desired myco-coagulant.

To check the contribution of the selected factors affecting the flocculation activity of the produced myco-coagulant, Pareto analysis was performed. Analysis of the Pareto chart in Fig. 6 showed that malt extract, glucose, wheat flour, pH, and ammonium sulfate have the highest effect on flocculation activity.

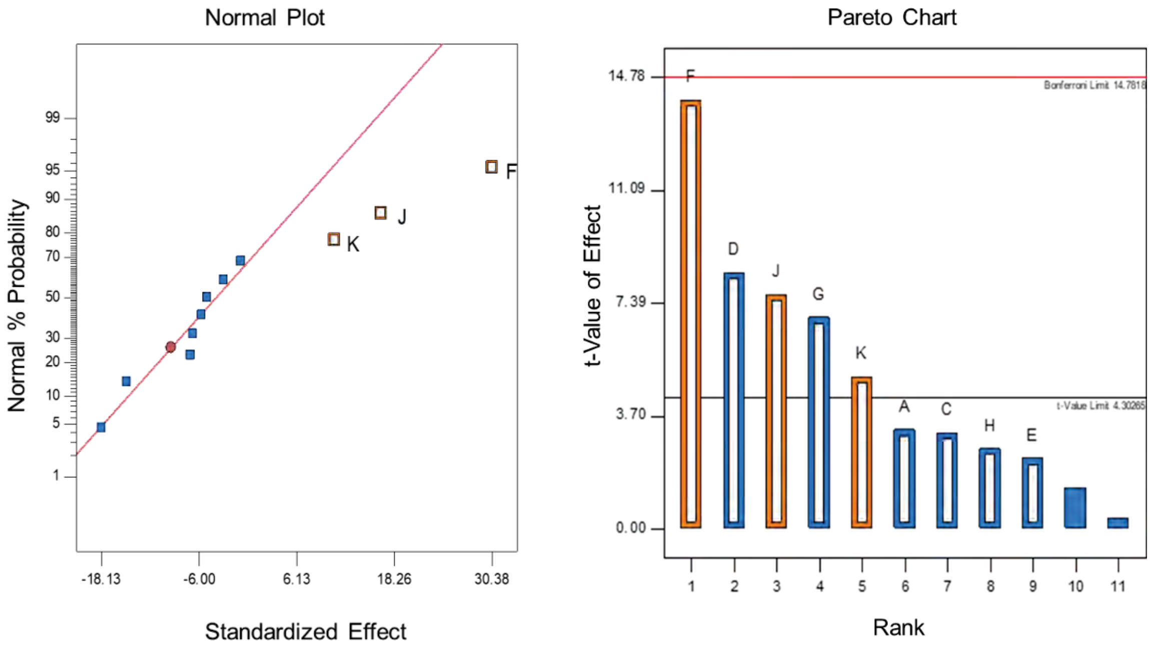

Fig. 6. Pareto chart illustrates the order and significance of the variables affecting flocculation activity using Plackett-Burman design (the blue color represents negative effects, and the orange color represent positive effects).

Plackett Burman's design does not provide a complete idea about the exact amount of each variable as well as the interaction between the variables. Thus, based on the calculations of the main effect and Pareto chart, the Plackett-Burman design selected three parameters: malt extract, pH, and glucose as the most significant factors to produce a myco-coagulant with optimum flocculation activity.

4 CONCLUSIONS

Since the cost of production of the myco-coagulant is among the challenges affecting its utilization, the results achieved in this study gave an insight into the utilization of different lignocellulosic substrates to produce an efficient myco-coagulant in reducing water turbidity as well as reduce the cost of experiments as we used abundant substrates.

In this study, among the used lignocellulosic substrate, cocopeat was identified as a suitable substrate that serves as a carbon and nitrogen source to produce the myco-coagulant using solid-state fermentation, which can potentially reduce the turbidity by 84.6% from the kaolin suspension. On the other hand, sawdust, palm kernel cake, and rice bran showed 33.06, 30.18, and 21.18 %, respectively. Coco peat, as an abundant raw material in Malaysia, may be utilized to meet this challenge and reduce the cost of production. The produced myco-coagulant may also contribute as a safe, low-cost, and environmentally friendly coagulant alternative to current chemical coagulants. The discovery of a safe and environmental-friendly microbial coagulant that possesses the ability for sustainable water treatment is in line with the global awareness towards creating a clean and healthy environment by using green technology employing solid-state fermentation.

ACKNOWLEDGEMENTS

The authors would like to acknowledge the ISDB Grant No SPI20-001-0001 for funding this research project. In addition, the authors would like to thank IIUM through the Research Management Center (RMC) for financial management and monitoring of project progress and the Biotechnology Engineering Department, IIUM for scientific equipment and facilities.

REFERENCES

[1] Ebeling JM, Sibrell PL, Ogden SR, Summerfelt ST. (2003). Evaluation of chemical coagulation-flocculation aids for the removal of suspended solids and phosphorus from intensive recirculating aquaculture effluent discharge. Aquacultural Engineering, 29(1-2): 23-42.

[2] Ang WL, Mohammad AW. (2020). State of the art and sustainability of natural coagulants in water and wastewater treatment. Journal of Cleaner Production, 262: 121267.

[3] Aljuboori AHR, Idris A, Abdullah N, Mohamad R. (2013). Production and characterization of a bioflocculant produced by *Aspergillus flavus*. Bioresource Technology, 127: 489-493.

[4] Bernard KNM, Sylvere NK, Patrice KG, Joseph KG. (2019). Coagulation and sedimentation of concentrated laterite suspensions: Comparison of hydrolyzing salts in presence of *Grewia* spp. biopolymer. Journal of Chemistry, 1-9.

[5] Ramavandi B. (2014). Treatment of water turbidity and bacteria by using a coagulant extracted from *Plantago ovata*. Water Resources and Industry, 6: 36-50.

[6] Moran S. (2018) An Applied Guide to Water and Effluent Treatment Plant Design. Butterworth-Heinemann.

[7] Lapointe M, Barbeau B. (2020). Understanding the roles and characterizing the intrinsic properties of synthetic vs. natural polymers to improve clarification through interparticle Bridging: A review. Separation and Purification Technology, 231: 115893.

[8] Flaten TP. (2001). Aluminium as a risk factor in Alzheimer's disease, with emphasis on drinking water. Brain Research Bulletin, 55(2): 187-196

[9] Ward RJ, McCrohan CR, White KN. (2006). Influence of aqueous aluminium on the immune system of the freshwater crayfish *Pacifasticus leniusculus*. Aquatic Toxicology, 77(2): 222-228.

[10] Mortula M, Bard SM, Walsh ME, Gagnon GA. (2009). Aluminum toxicity and ecological risk assessment of dried alum residual into surface water disposal. Canadian Journal of Civil Engineering, 36(1): 127-136.

[11] Tomljenovic L. (2011). Aluminum and Alzheimer's disease: after a century of controversy, is there a plausible link? Journal of Alzheimer's Disease, 23(4): 567-598

[12] Kluczka J, Zołotajkin M, Ciba J, Staroń M. (2017). Assessment of aluminum bioavailability in alum sludge for agricultural utilization. Environmental Monitoring and Assessment, 189(8): 1-8.

[13] Lee CS, Robinson J, Chong MF. (2014). A review on application of flocculants in wastewater treatment. Process Safety and Environmental Protection, 92(6): 489-508.

[14] Al-Mutairi NZ. (2006). Coagulant toxicity and effectiveness in a slaughterhouse wastewater treatment plant. Ecotoxicology and Environmental Safety, 65(1): 74-83.

[15] Aljuboori AHR, Uemura Y, Osman NB, Yusup S. (2014). Production of a bioflocculant from Aspergillus niger using palm oil mill effluent as carbon source. Bioresource Technology, 171: 66-70.

[16] Zulkeflee Z, Sánchez A. (2014). Solid-state fermentation of soybean residues for bioflocculant production in a pilot-scale bioreactor system. Water Science and Technology, 70(6): 1032-1039.

[17] Hölker U, Lenz J. (2005). Solid-state fermentation—are there any biotechnological advantages? Current Opinion in Microbiology, 8(3): 301-306.
[18] Gutarra MLE, de Godoy MG, Silva JDN, Guedes IA, Lins U, Castilho LDR, Freire DMG. (2009). Lipase production and *Penicillium simplicissimum* morphology in solid-state and submerged fermentations. Biotechnology Journal: Healthcare Nutrition Technology, 4(10): 1450-1459.
[19] Krishna C. (2005). Solid-state fermentation system – An overview. Critical Reviews in Biotechnology 25: 1-30.
[20] Pandey A, Larroche C, Soccol CR. (2008). General considerations about solid-state fermentation processes. In Current Developments in Solid-state Fermentation, Springer, New York, NY. pp. 13-25.
[21] Yingyi D, Lan W, Hongzhang C. (2012). Digital image analysis and fractal-based kinetic modelling for fungal biomass determination in solid-state fermentation. Biochemical Engineering Journal, 67: 60-67.
[22] Krishna S. (2005). Quantum dots-in-a-well infrared photodetectors. Journal of Physics D: Applied Physics, 38(13): 2142.
[23] Karimi S, Mahboobi Soofiani N, Mahboubi A, Taherzadeh MJ. (2018). Use of organic wastes and industrial byproducts to produce filamentous fungi with potential as aqua-feed ingredients. Sustainability, 10(9): 3296.
[24] Ross, M. (2015). Mechanical properties of sheets comprised of mycelium: A paper engineering perspective. Honours Theses. Paper 68. University of North Carolina, The USA.
[25] Luthfi WM, Alias H, Tay GS, Lee CK. (2020). Production and characterization of bioflocculant via solid state fermentation process using oil palm empty fruit bunch fibers as substrate. Biocatalysis and Agricultural Biotechnology, 23: 101454.
[26] Qi X, Zheng Y, Tang N, Zhou J, Sun S. (2020). Bioconversion of citrus peel wastes into bioflocculants and their application in the removal of microcystins. Science of the Total Environment, 715: 136885.
[27] Hamidah H. (2018). Study on myco-coagulant from *Lentinus squarrosulus* for water turbidity reduction. Master's thesis. Faculty of Engineering, International Islamic University Malaysia.
[28] Liu W, Hao Y, Jiang J, Zhu A, Zhu J, Dong, Z. (2016). Production of a bioflocculant from *Pseudomonas veronii* L918 using the hydrolyzate of peanut hull and its application in the treatment of ash-flushing wastewater generated from coal fired power plant. Bioresource Technology, 218: 318-325.
[29] Pu S, Ma H, Deng D, Xue S, Zhu R, Zhou Y, Xiong X. (2018). Isolation, identification, and characterization of an *Aspergillus niger* bioflocculant-producing strain using potato starch wastewater as nutrilite and its application. PloS one, 13(1): e0190236.
[30] Nurul-Adela B, Nasrin AB, Loh SK. (2016). Palm oil mill effluent as a low-cost substrate for bioflocculant production by *Bacillus marisflavi* NA8. Bioresources and Bioprocessing, 3(1): 1-8.

https://doi.org/10.31436/iiumej.v24i1.2447

THE OPTIMIZATION OF GROWTH CONDITION OF THE BACTERIA PRODUCING COLD-ACTIVE PROTEOLYTIC ENZYME FROM THE ANTARCTIC REGION

MUHAMMAD ASYRAF ABD LATIP[1,2], NOOR FAIZUL HADRY NORDIN[3*], SITI AISYAH ALIAS[4,7], JERZY SMYKLA[5], FARIDAH YUSOF[2], AND MOHD AZRUL NAIM MOHAMAD[6]

[1]Mariculture Research Division, Fisheries Research Institute Langkawi, Kompleks Perikanan Bukit Malut, 07000 Langkawi, Kedah, Malaysia
[2]Biotechnology Engineering Department, Kulliyyah of Engineering, International Islamic University Malaysia, Jalan Gombak, 53100 Kuala Lumpur
[3]International Institute for Halal Research and Training (INHART), Block A, Level 3, KICT Building, International Islamic University Malaysia, Jalan Gombak, 53100 Kuala Lumpur
[4]Institute of Ocean and Earth and Sciences, C308, Level 3, Block C, Institute for Advanced Studies Building, 50603 Kuala Lumpur, Malaysia
[5]Institute of Nature Conservation, Polish Academy of Sciences, al. A. Mickiewicza 33 PL-31-120 Krakow, Poland
[6]Department of Biotechnology, Kulliyyah of Science, International Islamic University Malaysia, Jalan Sultan Ahmad Shah, Bandar Indera Mahkota, 25200 Kuantan, Pahang, Malaysia
[7]National Antarctic Research Centre, B303, Level 3, Block C, Institute for Advanced Studies Building, 50603 Kuala Lumpur, Malaysia

[*]Corresponding author: faizul@iium.edu.my

(Received: 30th May 2022; Accepted: 9th September 2022; Published on-line: 4th January 2023)

ABSTRACT: The growth conditions of bacteria producing cold-active protease isolated from an Antarctic sample were screened using one-factor-at-time (OFAT). Then, crude protease of the strain was extracted during the late logarithmic phase for enzymatic assay. A strain that showed the highest enzyme activity was selected for optimization via response surface method (RSM). The parameters studied were incubation temperature (4 – 36 °C), pH media (4 – 10) and NaCl concentration (0 – 8%). Based on the OFAT results, all eight strains showed the highest growth rate at 20 °C, pH 7 and 4% (w/v) NaCl. The assay showed that the crude enzyme extracted from strain SC8 exhibited significantly higher activity (0.20 U and 0.37 U) than the positive control (0.11 U and 0.31 U) at -20 °C and 20 °C. RSM suggested that the optimized setting for growth of SC8 were at 20.5 °C, pH 6.83 and 2.05% (w/v) of NaCl with the results of the bacterial growth rate value was 3.70 ± 0.06 x 10^6 cells/hr. Optimal growth conditions of SC8 from this study are useful for the large-scale production of cold-active protease in future.

ABSTRAK: Keadaan pertumbuhan bakteria yang menghasilkan enzim protease aktif sejuk daripada sampel Antartika disaring menggunakan satu faktor pada masa (OFAT). Kemudian, enzim protease ini diekstrak pada lewat fasa logaritma untuk ujian enzimatik. Strain yang menunjukkan aktiviti enzim tertinggi telah dipilih untuk tujuan pengoptimuman melalui kaedah permukaan tindak balas (RSM). Parameter yang dikaji ialah suhu pengeraman (4 – 36 °C), pH media (4 – 10) dan kepekatan NaCl (0 – 8%). Berdasarkan OFAT, kesemua lapan bakteria menunjukkan kadar pertumbuhan tertinggi pada 20 °C, pH 7 dan 4% NaCl. Hasil ujian enzimatik menunjukkan bahawa enzim protease yang diekstrak daripada SC8 mempamerkan aktiviti yang jauh lebih tinggi (0.20 U dan 0.37 U) daripada kawalan positif (0.11 U dan 0.31 U) pada -20 °C dan 20 °C.

RSM mencadangkan tetapan optimum untuk pertumbuhan SC8 adalah pada 20.5 °C, pH 6.83 dan 2.05% NaCl dengan keputusan kadar pertumbuhan bakteria ialah 3.70 ± 0.06 x 10^6 sel/jam. Keadaan pertumbuhan optimum SC8 daripada kajian ini bermanfaat untuk menghasilkan produk protease aktif sejuk secara besar-besaran pada masa hadapan.

KEYWORDS: *cold-active protease; Antarctica; one factor at time; response surface method*

1. INTRODUCTION

Antarctica is located at the South Pole of the earth and acknowledged as one of the world's seven continents. This pristine place has recorded the lowest temperature on earth [1]. Compared to the Arctic, this continent encompasses solid land and is mostly covered with a thick snow layer. Roughly, the environment of the Antarctic is extremely cold and exposed to strong ultraviolet radiation [2]. Its sediment and soil contain a low level of carbon and nitrogen sources, contaminated with toxic metal compounds, fluctuating salt concentration, and exposure to low oxygen levels [3-5]. Although it looks like deserted terrain, a diverse microbial community has been discovered from its snows, soil, and sediment [6,7]. Recently, several novel environmental bacteria species have been identified such as *Paenisporosarcina antarctica* [8], *Labilibaculum antarcticum* [9] and *Pseudomonas fildesensis* [10].

Throughout history, many conventional methods used catalysts to speed up the process, either chemically or biologically. Nowadays, bio-catalyst-like enzymes have been accepted by communities. It has been widely used in daily life and industry. The discovery of novel enzymes has replaced the former catalyst and provides more convenient, eco-friendly and cost-effective processing. Several enzymes have been successfully extracted from microorganisms originated from the Antarctica regions [11-13]. One of the important enzymes is a protease. Generally, this enzyme breaks down proteins or polypeptides into smaller subunits or single amino acids. Microbial proteases have been widely used in many different industries including poultry, detergent, food and feed, leather, chemicals, waste management, medical, and research [14-16].

Cold-active protease is an extremozyme that enables a system to run at lower temperature where the majority of the commercial or industrial enzymes require higher temperatures for efficient catalytic activity and denaturation process. Consequently, introducing higher temperatures will always initiate an undesirable chemical reaction and loss of volatile compounds. Thus, cold-active protease has potential as an alternative to overcome these limitations. However, isolating and growing microorganisms in the laboratory directly from a sample is very challenging, especially samples from an extreme environment. A lot of factors must be considered, and the best idea is to mimic the sample environment to prepare the media conditions. In short, optimization of several parameters is important to provide ideal growing conditions for the isolated bacteria. The basic parameters used in this study was incubation temperature, pH media, and salt concentration. Based on previous studies, bacteria from the Antarctic region at 4 - 36 °C, pH 4 - 10 and 0 - 8% NaCl concentration was isolated [17]. Experimental design for optimization was conducted through response surface method (RSM). Initially, RSM was introduced by Box & Wilson [18] as a design of experiment for chemical processing and nowadays, the method has been widely applied in many areas. This system is supported by its regression analysis and allows us to investigate the effect and interaction of multiple variables on one or more responses [19]. In this study, we analyzed the growth conditions of isolated bacteria producing cold-active proteolytic enzymes from the Antarctic region.

2. MATERIALS AND METHODS

2.1 Determination of Bacteria Growth Phase

Previously, several bacteria that showed positive activity of cold-active extracellular protease on skim milk agar were isolated and stored in glycerol [20]. Samples BB and ROB were collected from moss communities, sample ROS was moist soil covered with alga and cyanobacterial mats, and sample SC was composed at an abandoned skua nest. The parameters to be characterized for bacteria growth rate were incubation temperature, pH media, and sodium chloride concentration. For every experiment, the bacteria were cultured in 10 mL of preferred LB broth with the initial OD_{600} set at 0.1 in a sterile 50 mL tube [21]. The culture was incubated for 24 hours with an orbital shake at 200 rpm. A preliminary experiment disclosed that the strain reached the late logarithmic phase after a 24-hour incubation period. Later, bacteria were harvested during this phase to be incubated in skim milk media for enzymatic assay. After 24 hours incubation period, the final OD_{600} of the culture bacteria was measured and the growth rate (cells x 10^6 /hr) was calculated based on the Eq. (1):

$$\text{Growth rate} = \frac{\text{OD (final)} - \text{OD(initial)}}{\text{24 hours}} \text{ x } 5{,}85 \text{ x } 10^7 \text{ cells} \quad (1)$$

2.1.1 Effect of Temperature

The first parameter to be characterized for bacteria growth rate was temperature while fixing the other parameters. The bacteria-producing cold-active proteolytic enzyme was incubated in LB broth at three different temperatures, 4 °C, 20 °C and 36 °C. The NaCl concentration and pH of the media were maintained at 1% (w/v) and 7, respectively.

2.1.2 Effect of pH

Different pH, i.e. 4, 7, and 10 of LB broth were prepared and autoclaved. The pH of the media was adjusted using HCl and KOH. Then, these media were used to characterize the growth rate of isolated strains. Based on temperature optimization results, these bacteria were incubated at 20 °C and the NaCl concentration of the media was kept constant at 1%.

2.1.3 Effect of NaCl Concentration

The last parameter to be characterized for bacteria growth rate was NaCl concentration. LB broth media with 0%, 4%, and 8% of NaCl concentration were prepared and autoclaved. The pH of this media was maintained at 7 and the bacteria culture was incubated at 20 °C.

2.2 Proteolytic Assay

Azo-casein (Sigma Aldrich) was used as a substrate to quantify the protease activity enzymatic assay as decribed by García-Cano et al. [22]. For the enzymatic assay, 250 μL of 1% azocasein, 250 μL of 0.5 M Tris and 250 μL of the crude enzyme from culture supernatant were added into 1.5 mL sterile tube and incubated at –20 °C, 20 °C, and 60 °C. Before adding the crude enzyme, the assay was pre-incubated at mentioned temperatures for 10 minutes. For positive control, 0.2 units/mL of protease from the bovine pancreas (optimum temperature at 37 °C) was used. After 20 minutes, 500 μL of 25% of trichloroacetic acid (TCA) was added to stop the reaction and centrifuged at 12,000 rpm for 30 minutes. This supernatant was transferred into a 1.5 mL cuvette and the absorbance was read at 340 nm. For blanks, only 250 mL of 1% azocasein and 250 μL of 0.5 M Tris were incubated before adding 500 μL of 25% TCA. Then, 5 % of skim milk media were added and centrifuged at 12,000 rpm for 30 minutes. The supernatant was transferred into a new cuvette and labelled as blank. The data represented as enzyme unit mean ± standard deviation (STDEV). Statistical analysis was calculated using one-way analysis of variance (ANOVA), SPSS 26.0. The results were considered significant differences if the p-value was < 0.05.

2.3 Response Surface Method (RSM)

The bacteria strain that showed the fastest shifting of clear skim milk media and highest protease activity were selected and preceded with an optimization process using response surface method (RSM) [23]. The experiment was designed based on three-level parameters of face centered central composite design (FCCCD) as in Table 1. The response variable was the growth rate of the bacteria. The initial and final OD_{600} of bacteria cultures were recorded and one unit of OD_{600} corresponded to 5.85 x 10^7 cells. The culture was incubated for 24 hours with an orbital shake at 200 rpm. A total of 20 experimental runs were generated by the software Design-Expert® Version 7.0.0 (State-Ease Inc., Minneapolis, MN) with six runs at center points included.

Table 1: Independent variables and their corresponding levels for FCCCD in a response to bacteria growth rate

Factor	Variables	Level		
		-1	0	1
A	Temperature [°C]	4	20	36
B	pH	4	7	10
C	Sodium chloride concentration [%, w/v]	0	4	8
Response	Growth Rate [A/hr] [cells x 10^6 cells/hr]			

3. RESULTS

From the previous study, the total amount of bacteria producing extracellular protease isolated from Antarctica's soils and sediments were 35 strains [20]. These strains were further tested on their capability to produce extracellular protease within 24 hours through halo zone formation around the colony on skim milk agar. Therefore, 8 bacteria strains consisting of BB1, DI25, ROB8, ROS7, ROS8, SC8, S10, and SC11 were selected for further analysis for their growth conditions. Experimental designs to analyze the growth rate conditions for each strain were carried out in a conventional one-factor-at-a-time (OFAT) approach. This approach was performed by altering one parameter at a time and maintaining the other parameters, so that the impact of the altering parameters can be accessed.

3.1 Effect of Temperature on Bacteria-producing Cold-active Proteolytic Enzyme

From the graph in Fig. 1, the optimum temperature for growth rates for all bacteria was 20 °C. There was a significant difference observed in all isolated strains at different temperatures. All bacteria grew faster at 20 °C compared to 4 °C and 36 °C.

3.2 Effect of pH on Bacteria-producing Cold-active Proteolytic Enzyme

The second factor, pH has been found as the important factor affecting the bacteria growth rate. Based on the graph in Fig. 2, all strains showed the highest growth rate at neutral pH 7. Besides, several strains can tolerate lower pH or acidic conditions such as BB1, ROB1, ROS7, ROS8, SC8, SC10 and SC11.

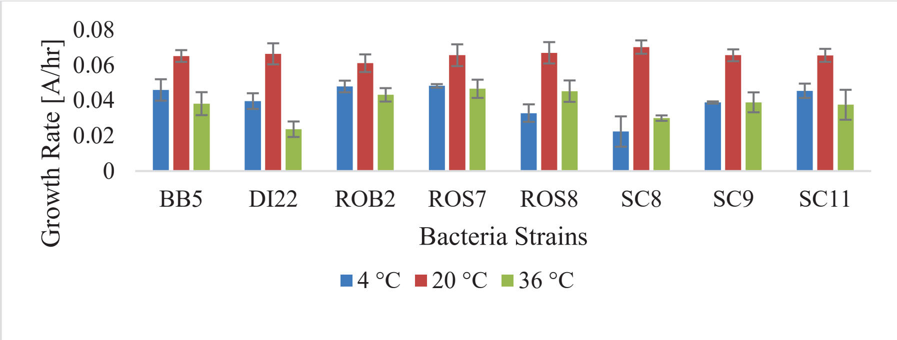

Fig. 1: Effect of different temperature levels to bacteria growth rate. The pH of the media and NaCl concentration were maintained at 7 and 1%, respectively.

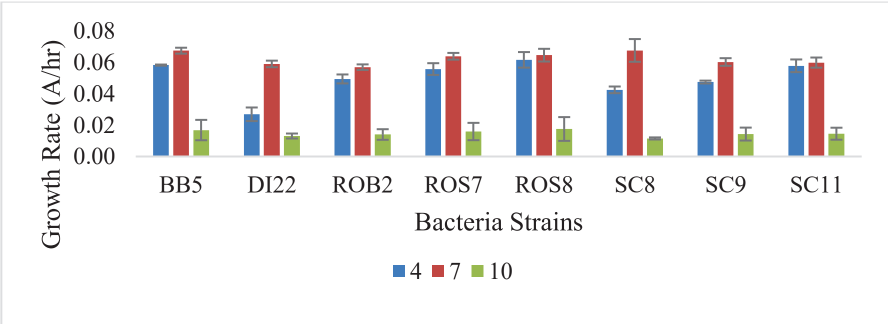

Fig. 2: Effect of different level of pH in a response to the bacteria growth rate. The incubation temperature and NaCl concentration were maintained at 20 °C and 1%, respectively.

3.3 Effect of NaCl Concentration on Bacteria-producing Cold-active Proteolytic Enzyme

The concentration of sodium chloride (NaCl) was considered an important factor as the coastal environment influenced the sample. All bacteria strains showed an optimum growth rate at 4% NaCl concentration as in Fig. 3. In the absence of NaCl, the slower growth rate of these bacteria compared to 4% NaCl was observed. However, with an increase in the concentration of NaCl from 4% to 8%, the growth rate of the bacteria was significantly reduced.

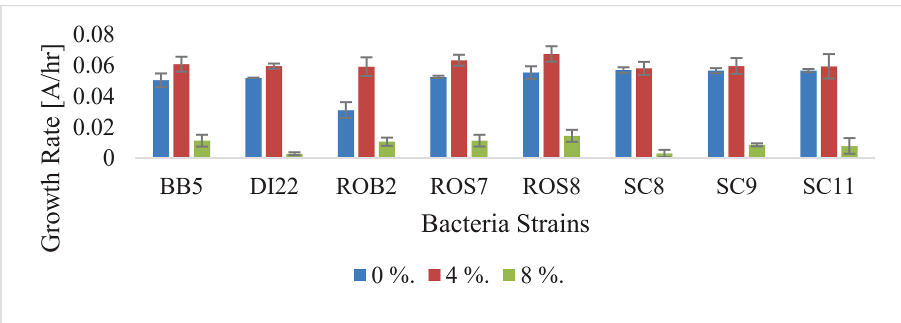

Fig. 3: Effect of NaCl at different levels to the bacteria growth rate. The incubation temperature and pH of the media were maintained at 20 °C and 7, respectively.

3.4 Proteolytic Assay

Change of white skim milk media to clear indicated that the bacteria produced extracellular protease to degrade the casein of milk. From the graph in Fig. 4, the crude enzyme extracted from strains SC8 and ROS8 showed higher proteolytic activity compared to other isolated bacteria. This indicates that the amount of protease produced was higher from both strains. In addition, both crude enzymes showed a significantly higher activity at -20 °C compared to the positive control.

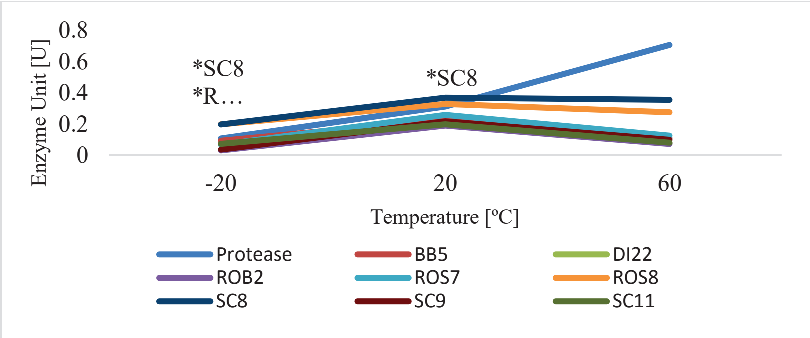

Fig. 4: Results of crude protease assay at three different temperatures. SC8 showed the highest proteolytic activity at the lowest temperature. * $p < 0.05$

3.5 Optimization of Growth Conditions of Bacteria Producing Cold-active Proteolytic Enzyme by Response Surface Methodology (RSM)

The growth rate of isolated bacteria SC8 was selected to be further optimized using Response Surface Method (RSM). This strain showed the fastest shifting of clear skim milk media and the highest proteolytic activity at the lowest temperature. The result of RSM is shown in Table 2. From the results, the bacteria growth rate was varied from 0.014 x 10^6 to 3.93 x 10^6 cells/hr.

Table 2: Experimental design and results of face centered central composite design (FCCCD). The experimental growth rate data represented as mean ± standard deviation (STDEV).

Treatment Number	NaCl [%, w/v]	pH	Temp. [ºC]	Response Growth Rate [A/hr]	Bacterial Growth Rate [cells x 10^6/hr]
1	0	4	4	0.0469 ± 0.0005	2.74 ± 0.03
2	8	4	4	0.0242 ± 0.0204	1.42 ± 1.19
3	0	10	4	0.0385 ± 0.0002	2.25 ± 0.01
4	8	10	4	0.0195 ± 0.0009	1.14 ± 0.05
5	0	4	36	0.0408 ± 0.0003	2.39 ± 0.02
6	8	4	36	0.0305 ± 0.0009	1.78 ± 0.05
7	0	10	36	0.0425 ± 0.0007	2.49 ± 0.04
8	8	10	36	0.0275 ± 0.0018	1.61 ± 0.12
9	0	7	20	0.0597 ± 0.0100	3.49 ± 0.59
10	8	7	20	0.0506 ± 0.0211	2.96 ± 1.23
11	4	4	20	0.0525 ± 0.0008	3.07 ± 0.05
12	4	10	20	0.0563 ± 0.0008	3.29 ± 0.05
13	4	7	4	0.0476 ± 0.0046	2.78 ± 0.27
14	4	7	36	0.0541 ± 0.0198	3.16 ± 1.16
15	4	7	20	0.0671 ± 0.0082	3.93 ± 0.48
16	4	7	20	0.0604 ± 0.0077	3.53 ± 0.46
17	4	7	20	0.0576 ± 0.0073	3.37 ± 0.43
18	4	7	20	0.0661 ± 0.0070	3.87 ± 0.41
19	4	7	20	0.0563 ± 0.0079	3.29 ± 0.46
20	4	7	20	0.0632 ± 0.0069	3.70 ± 0.40

Preliminary analysis showed that the highest growth rate was at the center of the design. Based on the fit summary, the model suggested was quadratic because the sequential model sum of squares (Type I) was significant and the lack of fit tests was insignificant. An insignificant lack of fit was good because the model should be fitted. The value of Prob > F less than 0.05 indicated that the model terms were significant. From the analysis of variance (ANOVA) in Table 3, for the response surface quadratic model, the model F-value of 45.87 implied the model was significant. In this experiment, the concentration of NaCl (A), temperature (C) and algebraic contribution (A2, B2, C2) were significant model terms. The multiple correlation coefficient of the model or R2 of 0.9574 meant that the regression prediction was capable of estimating 95 % fit to the actual data points. Besides, the predicted R-squared of 0.9191 was in reasonable agreement with the adjusted R-squared 0.8051 because the difference was less than 0.2. The adequate precision greater than 4 (14.948) indicated an adequate signal. The final equation in terms of coded factors was generated as Eq. (2):

$$\begin{aligned}\text{Growth rate} = {} & 0{,}0622 - 0{,}0076\,\text{A} - 0{,}0011\,\text{B} + 0{,}0019\,\text{C} - 0{,}0001\,\text{AB} \\ & + 0{,}0021\,\text{AC} + 0{,}0015\,\text{BC} - 0{,}0077\,\text{A2} - 0{,}008487\,\text{B2} \\ & - 0{,}0120\,\text{C2}\end{aligned} \tag{2}$$

Table 3: Analysis of variance (ANOVA) for response surface quadratic model.

Source	Sum of Squares	Degree of Freedom	F-Value	p-value
Model	2.096E-003	9	34.23	< 0.0001
A-NaCl	1.568E-004	1	23.05	0.0020
B-pH	6.300E-005	1	9.26	0.0188
C-Temp	2.704E-006	1	0.40	0.5484
AB	1.378E-005	1	2.03	0.1977
AC	1.513E-007	1	0.022	0.8857
BC	8.001E-005	1	11.76	0.0110
A^2	3.110E-005	1	4.57	0.0698
B^2	3.335E-004	1	49.02	0.0002
C^2	2.791E-004	1	41.02	0.0004
Residual	4.763E-005	7		
Lack of Fit	3.570E-005	5	1.20	0.5135
Pure Error	1.193E-005	2		
Cor Total	2.144E-003	16		

The graphs were constructed by plotting the response against any two independent variables while maintaining the other variable at the optimal level. For this experiment, as in Fig. 5, contour and the 3D surface graph showed the bacterial growth rate as a response was plotted at the z-axis, meanwhile, the x- and y-axis were assigned for two different variables. Higher growth rate was observed around 2% NaCl at pH 7 (Fig. 5A), 2% NaCl at 20 °C (Fig. 5B) and at pH 7 and 20 °C (Fig. 5C).

For optimization, the criteria were selected to maximize the bacterial growth rate while keeping all the variables in the range. The solution suggested by the design expert software to optimize the bacterial culture conditions were concentration of sodium chloride at 2.05% (w/v), pH of the solution at 6.83, and the incubation temperature at 20.5 °C. New experiments were conducted as post-analysis to validate these statistical models and regression equations. The experiments were run in triplicate under optimized variables as suggested previously. The predicted bacterial growth rate calculated by the software under these optimized variables was 3.75×10^6 cells/hr and the average observed experimental value was $3.70 \pm 0.06 \times 10^6$ cells/hr. From these validation results, it

https://doi.org/10.31436/iiumej.v24i1.2447

confirmed that the model was good enough because the error between predicted and actual value was only 1.2 %.

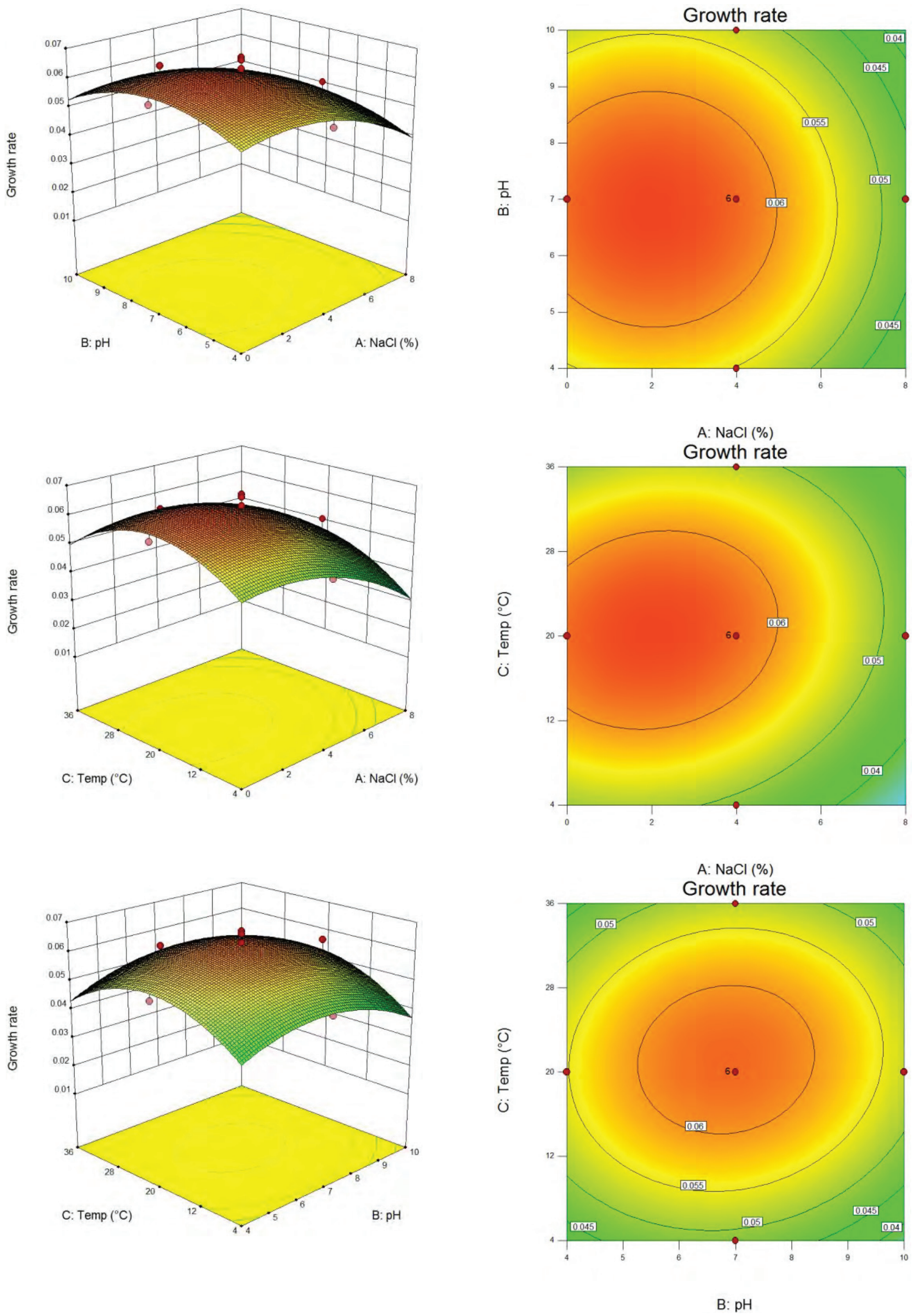

Fig. 5: 3D surface and contour graph showed the interaction of three independent variables with the response to the bacteria growth rate.

4. DISCUSSION

Generally, psychrophiles are microorganisms that can live under very low temperatures. The majority of these extremophilic organisms inhabit a permanently ice-covered environment on Earth. The word 'living' means that they can grow and reproduce under extremely low temperatures rather than hibernate. Some researchers characterized these psychrophiles into two groups: obligate psychrophiles and psychrotolerant organisms. Obligate psychrophiles referred to organisms with an optimum growth temperature of 15 ºC that cannot withstand higher temperatures of more than 20 ºC [24]. Psychrotolerants are organisms that can withstand a broader range of temperatures between 0 °C to approximately 36 °C [25]. Some researchers called them facultative psychrophiles or psychrotrophs and their maximal or optimal growth temperature was above 20 ºC [26,27]. Based on the OFAT, all isolated strains showed the fastest growth rate at 20 °C. These bacteria can be classified as psychrotolerant because they can live in a wide range of temperatures (4 – 36 °C). Besides, these bacteria can tolerate up to 4 % NaCl concentration indicating that their living environment was influenced by the coastal environment. On average, seawater contains a salt concentration of about 35 parts per thousand or about 3.5 % and the major sources of the salt are sodium and chloride [28]. Wind effect brought seawater onto the ice and during the summer season, the ice melted and the salt was concentrated in the soils and sediments [29]. Furthermore, the majority of the isolated strains can endure acidic conditions. This is possible because these strains were influenced by the surrounding environment at the collection point. Researchers have reported that lower pH on Antarctic soils and sediments from moss communities and wetlands were due to the accumulation of organic matter [30]. Besides, birds' nests and excrement created in situ unfavorable chemical reactions that led to acidic conditions of the soil and sediment [31].

An interesting aspect of these psychrophiles is their survivability is supported by the cold-adapted enzyme. They produce biocatalysts that are capable of working at very low temperatures. There were several theories on this unique characteristic of enzymes and the majority of the researchers claimed that flexibility of the protein structure is the main contributor [32]. Comparison studies between psychrophilic and mesophilic enzymes showed that structural modification and adaptation remain obscure although both active sites are preserved [30]. Some researchers claim that the amino acid composition affects the bonding between residues and the structural rigidity of the protein [22]. Besides, loop modification vicinity to active site matched to the induced fit model for enzymatic reaction [24]. These strategies were designated to consume less energy during enzymatic reactions when a smaller amount of heat is available at low temperatures. In this case, crude enzymes extracted from SC8 and ROS8 strains showed significantly higher protease activity than positive control at a lower temperature but gradually decreased at the higher temperature. This showed that increasing the flexibility of the enzyme adversely affected its thermostability [35]. Cold active proteases have been extracted from various species of psychrophiles and the majority showed optimal activity at a temperature range between 30–40 ºC [36-39]. A thorough search on cold-active protease yielded the lowest optimal temperature at only 15 ºC [40,41].

In this experiment, strain SC8 showed the capability to produce extracellular protease faster and higher compared to the other strains. It has a high potential for bioprospecting in future. Thus, we focused on this strain for growth rate optimization. Initially, the term optimization for the OFAT method was not accurate according to some scholars [42,43]. This is because changing one variable at a time could not estimate the interaction between variables and might miss the optimal setting for each variable [44]. Frequently, the OFAT technique was used in the experiment objectively to identify the maximal or minimal effect [45]. Maximal effect is the highest or greatest result's magnitude whereas, the optimal effect is the most desirable condition for the model. Yet, results from OFAT could be applied as a screening method to determine significant high and low levels for each variable [46,47]. Although the factorial method is best used as screening design in Design-Expert software before optimization using the response surface method, this OFAT technique is lower in cost and easier to conduct. In this experiment, based on the RSM result in Table 2, the fastest growth rate, 3.93 x 10^6 cells/hr, was treatment number 15 with variables set at 4% NaCl, pH 7, and 20 ºC. However, the optimized growth rate-setting suggested was slightly different from the fastest growth rate setting. Clarification on these results was RSM calculated the optimal setting for each variable or resource in the design to achieve maximized results. Based on the validation results, the optimum bacterial growth rate at 2.05% of NaCl, pH 6.83 and 20.5 °C was 3.70 x 10^6 cells/hr and it was only 5% to achieve the fastest result, 3.93 x 10^6 cells/hr. Therefore, this model could achieve a higher response and save the usage of NaCl by using the optimal setting recommended by RSM.

5. CONCLUSION

In conclusion, the isolated strains of bacteria-producing cold-active protease from the Antarctica region in this experiment could be categorized as psychrotolerants. Based on the crude enzymatic assay, the SC8 strain showed potential for bioprospecting as its protease activity was significantly higher than positive control and other strains at a lower temperature. Optimal growth conditions of SC8 strain from this study will be useful for the development of large-scale production of cold-active protease in future. In the food industry, this cold active protease may act as the commercial meat tenderizers (papain and bromelain) as it is applied to the meat during cold storage and export journey.

ACKNOWLEDGEMENT

The research leading to these results received funding from Yayasan Penyelidikan Antartika Sultan Mizan (2015) and International Islamic University Malaysia under grant number RIGS 16-332-0496. The field survey and sampling were made possible with funding to J. Smykla from the Polish National Science Center within grant number NN305376438.

REFERENCES

[1] Turner J, Anderson P, Lachlan-Cope T, Colwell S, Phillips T, Kirchgaessner A, et al. (2009) Record low surface air temperature at Vostok station, Antarctica. J Geophys Res Atmos., 114(24). https://doi.org/10.1029/2009JD012104

[2] Bornman JF, Barnes PW, Robson TM, Robinson SA, Jansen MAK, Ballare CL, et al. (2019) Linkages between stratospheric ozone, UV radiation and climate change and their implications for terrestrial ecosystems. Photochem Photobiol Sci., 18(3): 681-716. https://doi.org/10.1039/C8PP90061B

[3] Convey P, Peck LS. (2019) Antarctic environmental change and biological responses. Sci Adv., 5(11). https://doi.org/10.1126/sciadv.aaz0888

[4] Faucher B, Lacelle D, Davila A, Pollard W, Fisher D, McKay CP. (2017) Physicochemical and biological controls on carbon and nitrogen in permafrost from an ultraxerous environment, McMurdo Dry Valleys of Antarctica. J Geophys Res Biogeosciences, 122(10):

2593-2604. https://doi.org/10.1002/2017JG004006

[5] Pereira JL, Pereira P, Padeiro A, Gonçalves F, Amaro E, Leppe M, et al. (2017) Environmental hazard assessment of contaminated soils in Antarctica: Using a structured tier 1 approach to inform decision-making. Sci Total Environ., 574: 443-454. https://doi.org/10.1016/j.scitotenv.2016.09.091

[6] Pudasaini S, Wilson J, Ji M, van Dorst J, Snape I, Palmer AS, et al. (2017) Microbial diversity of browning Peninsula, Eastern Antarctica revealed using molecular and cultivation methods. Front Microbiol., 8(APR). https://doi.org/10.3389/fmicb.2017.00591

[7] Ji M, Van Dorst J, Bissett A, Brown M V., Palmer AS, Snape I, et al. (2016) Microbial diversity at Mitchell Peninsula, Eastern Antarctica: A potential biodiversity "hotspot." Polar Biol., 39(2): 237-249. https://doi.org/10.1007/s00300-015-1776-y

[8] Rong JC, Liu Y, Yu S, Xi L, Chi NY, Zhang QF. (2020) Complete genome sequence of *Paenisporosarcina antarctica* CGMCC 1.6503T, a marine psychrophilic bacterium isolated from Antarctica. Mar Genomics, 49. https://doi.org/10.1016/j.margen.2019.05.005

[9] Watanabe M, Kojima H, Fukui M. (2020) *Labilibaculum antarcticum* sp. nov., a novel facultative anaerobic, psychrotorelant bacterium isolated from marine sediment of Antarctica. Antonie van Leeuwenhoek, Int J Gen Mol Microbiol., 113(3): 349-355. https://doi.org/10.1007/s10482-019-01345-w

[10] Pavlov MS, Lira F, Martinez JL, Olivares-Pacheco J, Marshall SH. (2020) *Pseudomonas fildesensis* sp. Nov., a psychrotolerant bacterium isolated from Antarctic soil of King George Island, South Shetland Islands. Int J Syst Evol Microbiol., 70(5): 3255-3263. https://doi.org/10.1099/ijsem.0.004165

[11] Pereira JQ, Ambrosini A, Passaglia LMP, Brandelli A. (2017) A new cold-adapted serine peptidase from Antarctic Lysobacter sp. A03: Insights about enzyme activity at low temperatures. Int J Biol Macromol., 103: 854-862. https://doi.org/10.1016/j.ijbiomac.2017.05.142

[12] Vullo D, De Luca V, Del Prete S, Carginale V, Scozzafava A, Osman SM, et al. (2016) Sulfonamide inhibition studies of the γ-carbonic anhydrase from the Antarctic bacterium *Colwellia psychrerythraea*. Bioorganic Med Chem Lett., 26(4): 1253-1259. https://doi.org/10.1016/j.bmcl.2015.06.079

[13] Sanchez AC, Ravanal MC, Andrews BA, Asenjo JA. (2019) Heterologous expression and biochemical characterization of a novel cold-active α-amylase from the Antarctic bacteria *Pseudoalteromonas* sp. 2-3. Protein Expr Purif., 155: 78-85. https://doi.org/10.1016/j.pep.2018.11.009

[14] Razzaq A, Shamsi S, Ali A, Ali Q, Sajjad M, Malik A, et al. (2019) Microbial proteases applications. Front Bioeng Biotechnol., 7(JUN). https://doi.org/10.3389/fbioe.2019.00110

[15] Singh R, Mittal A, Kumar M, Mehta PK. (2016) Microbial proteases in commercial applications. J Pharm , Chem Biol Sci., 4: 365-374. http://www.jpcbs.info/2016_4_3_06_Rajendra.pdf

[16] Dos Santos Aguilar JG, Sato HH. (2018) Microbial proteases: Production and application in obtaining protein hydrolysates. Food Research International, 103: 253-262. https://doi.org/10.1016/j.foodres.2017.10.044

[17] Yu Y, Li HR, Zeng YX, Chen B. (2011) Bacterial diversity and bioprospecting for cold-active hydrolytic enzymes from culturable bacteria associated with sediment from Nella Fjord, Eastern Antarctica. Mar Drugs, 9(2): 184-195. https://doi.org/10.3390/md9020184

[18] Box GEP, Wilson KB. (1951) On the experimental attainment of optimum conditions. J R Stat Soc Ser B., 13(1):1-38. https://doi.org/10.1007/978-1-4612-4380-9_23

[19] Hamid NF, Said FM. (2018) Optimization of red pigment production by *Monascus purpureus* FTC 5356 using response surface methodology. IIUM Eng J., 19(1): 34-47. https://doi.org/10.31436/iiumej.v19i1.814

[20] Latip MAA, Alias SA, Smykla J, Yusof F, Mohamad MAN, Nordin NFH. (2020) Discovery of cold-active protease from psychrophilic bacteria isolated from Antarctic region for bio-prospecting. Malays Appl Biol., 49: 55-60. https://doi.org/10.55230/mabjournal.v49i1.1654

[21] Ram Y, Dellus-Gur E, Bibi M, Karkare K, Obolski U, Feldman MW, et al. (2019) Predicting microbial growth in a mixed culture from growth curve data. Proc Natl Acad Sci U S A.

https://doi.org/10.1073/pnas.1902217116
[22] García-Cano I, Rocha-Mendoza D, Ortega-Anaya J, Wang K, Kosmerl E, Jiménez-Flores R. (2019) Lactic acid bacteria isolated from dairy products as potential producers of lipolytic, proteolytic and antibacterial proteins. Appl Microbiol Biotechnol., 103(13): 5243-5257. https://doi.org/10.1007/s00253-019-09844-6
[23] Jimat DN, Firdamohamed IB, Azmi AS, Amid A. (2020) Statistical analysis of growth conditions of newly isolate *Bacillus* sp. producing L-asparaginase. IIUM Eng J. https://doi.org/10.31436/iiumej.v21i2.1351
[24] Sandle T. (2019) Selection and application of culture media. Biocontamination Control Pharm Healthc., 103-123. http://dx.doi.org/10.1016/B978-0-12-814911-9.00007-9
[25] Yadav AN, Verma P, Kumar V, Sangwan P, Mishra S, Panjiar N, et al. (2017) Biodiversity of the genus penicillium in different habitats. New Futur Dev Microb Biotechnol Bioeng Penicillium Syst Prop Appl., 3-18. https://doi.org/10.1016/B978-0-444-63501-3.00001-6
[26] Cavicchioli R. (2016) On the concept of a psychrophile. ISME J., 10(4): 793-795. https://doi.org/10.1038%2Fismej.2015.160
[27] Ramle Z, Abdul Rahim R. (2016) Psychrophilic lipase from Arctic bacterium. Trop Life Sci Res., 27: 151-157. https://doi.org/10.21315%2Ftlsr2016.27.3.21
[28] Li D, Liu S. (2018) Water quality monitoring and management: Basis, technology and case studies. 1st ed. Water Quality Monitoring and Management: Basis, Technology and Case Studies. Acedamic Press. 1-368. https://doi.org/10.1016/C2016-0-00573-9
[29] Bowman JS, Deming JW. (2017) Wind-driven distribution of bacteria in coastal Antarctica: Evidence from the Ross Sea region. Polar Biol., 40(1): 25-35. https://doi.org/10.1007/s00300-016-1921-2
[30] Smykla J, Drewnik M, Szarek-Gwiazda E, Hii YS, Knap W, Emslie SD. (2015) Variation in the characteristics and development of soils at Edmonson Point due to abiotic and biotic factors, northern Victoria Land, Antarctica. Catena., 132: 56-67. https://doi.org/10.1016/j.catena.2015.04.011
[31] Lambrechts S, Willems A, Tahon G. (2019) Uncovering the uncultivated majority in Antarctic soils: Toward a synergistic approach. Front Microbiol., 10(FEB). https://doi.org/10.3389/fmicb.2019.00242
[32] Siddiqui KS. (2017) Defying the activity–stability trade-off in enzymes: Taking advantage of entropy to enhance activity and thermostability. Crit Rev Biotechnol., 37(3): 309-322. https://doi.org/10.3109/07388551.2016.1144045
[33] Åqvist J, Isaksen GV, Brandsdal BO. (2017) Computation of enzyme cold adaptation. Nat Rev Chem., 1. https://doi.org/10.1038/s41570-017-0051
[34] Panja AS, Maiti S, Bandyopadhyay B. (2020) Protein stability governed by its structural plasticity is inferred by physicochemical factors and salt bridges. Sci Rep., 10(1): 1822. https://doi.org/10.1038/s41598-020-58825-7
[35] Latip MAA, Hamid AAM, Nordin NFH. (2019) Microbial hydrolytic enzymes: In silico studies between polar and tropical regions. Polar Sci., 20. https://doi.org/10.1016/j.polar.2019.04.003
[36] Damare S, Raghukumar C, Muraleedharan UD, Raghukumar S. (2006) Deep-sea fungi as a source of alkaline and cold-tolerant proteases. Enzyme Microb Technol., 39(2): 172-181. https://doi.org/10.1016/j.enzmictec.2006.03.032
[37] Wang QF, Miao JL, Hou YH, Ding Y, Wang GD, Li GY. (2005) Purification and characterization of an extracellular cold-active serine protease from the psychrophilic bacterium *Colwellia* sp. NJ341. Biotechnol Lett., 27(16): 1195 -1198. https://doi.org/10.1007/s10529-005-0016-x
[38] Turkiewicz M, Pazgier M, Kalinowska H, Bielecki S. (2003) A cold-adapted extracellular serine proteinase of the yeast *Leucosporidium antarcticum*. Extremophiles., 7(6): 435-442. https://doi.org/10.1007/s00792-003-0340-9
[39] Margesin R, Dieplinger H, Hofmann J, Sarg B, Lindner H. (2005) A cold-active extracellular metalloprotease from *Pedobacter cryoconitis* - Production and properties. Res Microbiol., 156(4): 499-505. https://doi.org/10.1016/j.resmic.2004.12.008
[40] Gao R, Zhou J, Leng W, Shi T, Jin W, Yuan L. (2020) Screening of a *Planococcus*

bacterium producing a cold-adapted protease and its application in low-salt fish sauce fermentation. J Food Process Preserv., 44(8). https://doi.org/10.1111/jfpp.14625

[41] Saba I, Qazi PH, Rather SA, Dar RA, Qadri QA, Ahmad N, et al. (2012) Purification and characterization of a cold active alkaline protease from *Stenotrophomonas* sp., isolated from Kashmir, India. World J Microbiol Biotechnol., 28(3): 1071-1079. https://doi.org/10.1007/s11274-011-0905-1

[42] Abou-Taleb KA, Galal GF. (2018) A comparative study between one-factor-at-a-time and minimum runs resolution-IV methods for enhancing the production of polysaccharide by *Stenotrophomonas daejeonensis* and *Pseudomonas geniculate*. Ann Agric Sci., 63(2): 173-180. https://doi.org/10.1016/j.aoas.2018.11.002

[43] Nor NM, Mohamed MS, Loh TC, Foo HL, Rahim RA, Tan JS, et al. (2017) Comparative analyses on medium optimization using one-factor-at-a-time, response surface methodology, and artificial neural network for lysine–methionine biosynthesis by *Pediococcus pentosaceus* RF-1. Biotechnol Biotechnol Equip., 31(5): 935-947. https://doi.org/10.1080/13102818.2017.1335177

[44] Czitrom V. (1999) One-factor-at-a-time versus designed experiments. Am Stat., 53(2): 126-131. https://doi.org/10.2307/2685731

[45] Biswas G, Kumari M, Adhikari K, Dutta S. (2017) Application of response surface methodology for optimization of biosorption of fluoride from groundwater using *Shorea robusta* flower petal. Appl Water Sci., 7(8): 4673-4690. https://doi.org/10.1007/s13201-017-0630-5

[46] Ahmed SA, Abdella MAA, El-Sherbiny GM, Ibrahim AM, El-Shamy AR, Atalla SMM. (2019) Application of one –factor- at-a-time and statistical designs to enhance α-amylase production by a newly isolate *Bacillus subtilis* strain-MK1. Biocatal Agric Biotechnol., 22. https://doi.org/10.1016/j.bcab.2019.101397

[47] Subara D, Jaswir I, Alkhatib MFR, Noorbatcha IA. (2018) Synthesis of fish gelatin nanoparticles and their application for the drug delivery based on response surface methodology. Adv Nat Sci Nanosci Nanotechnol., 9(4). https://doi.org/10.1088/2043-6254/aae988

https://doi.org/10.31436/iiumej.v24i1.2468

Rhodopseudomonas palustris COLLAGEN-LIKE RECOMBINANT PROTEIN PURIFICATION USING AN AQUEOUS TWO-PHASE SYSTEM

NURSYAHIDATUL AZWA AWANG[1], AZURA AMID[1*] AND ZATUL IFFAH ARSHAD[2]

[1]*International Institute for Halal Research and Training (INHART), International Islamic University of Malaysia, Jalan Gombak, 53100 Kuala Lumpur, Malaysia*
[2]*Faculty of Chemical Engineering and Natural Resources, Universiti Malaysia Pahang, Pekan, Pahang, Malaysia*

[*]*Corresponding author: azuraamid@iium.edu.my*

(Received: 7th June 2022; Accepted: 20th October 2022; Published on-line: 4th January 2023)

ABSTRACT: The potential use of recombinant collagen-like protein (recCLP) extracted from bacteria as disease-free collagen has been studied over the past decade. However, the complexity of the downstream processing generates high demand for an efficient and low-cost purification method. Aqueous two-phase system (ATPS) was adopted as a new approach to the recovery of biomolecules due to its simple, benign, and straightforward process. This study aimed to purify recombinant collagen-like protein from *Rhodopseudomonas palustris* using ATPS formed by a polymer/salt system. Recombinant collagen-like protein from *R. palustris* was partitioned in ATPS composed of polyethylene glycol (PEG) and potassium phosphate and several factors that influence the protein partitioning such as volume ratio, system pH, the concentration of polymer and salt were studied. Then, optimization of the selected ATPS conditions (PEG and salt concentration) were performed using response surface methodology (RSM). Results showed that the optimum conditions were found in ATPS with 24.80% (w/w) PEG 2000 and 29.23% (w/w) potassium phosphate with recCLP concentration of 3.23 ± 0.12 mg/mL with purification factor 7.48 ± 0.3. In comparison with the affinity chromatography method, ATPS was found to be low-cost, and time-saving with a higher protein recovery. Hence, this study demonstrated the potential application of ATPS in the recovery of recombinant CLPs for large-scale downstream processing.

ABSTRAK: Potensi penggunaan protein seperti kolagen rekombinan (recCLP) yang diekstrak daripada bakteria sebagai kolagen bebas penyakit telah dikaji sejak sedekad yang lalu. Walau bagaimanapun, kerumitan pemprosesan hiliran menjana permintaan yang tinggi untuk kaedah penulenan yang cekap dan berpatutan. Sistem akueus dua fasa (ATPS) telah diterima pakai sebagai pendekatan baharu dalam pemulihan biomolekul kerana prosesnya yang mudah. Tujuan utama kajian ini adalah untuk menyaring protein seperti kolagen rekombinan daripada *Rhodopseudomonas palustris* menggunakan ATPS yang dibentuk oleh sistem polimer/garam. Protein seperti kolagen rekombinan daripada *R. palustris* telah dibahagikan dalam ATPS yang terdiri daripada polietilena glikol (PEG) dan kalium fosfat dan beberapa faktor yang mempengaruhi pembahagian protein seperti nisbah isipadu, pH sistem, kepekatan polimer dan garam telah dikaji. Kemudian, keadaan ATPS terpilih (PEG dan kepekatan garam) telah dioptimumkan menggunakan metodologi permukaan tindak balas (RSM). Keputusan menunjukkan bahawa keadaan optimum dalam ATPS adalah 24.80% (b/b) PEG 2000 dan 29.23 % (b/w) kalium fosfat dengan kepekatan recCLP 3.23 ± 0.12 mg/mL dengan faktor penulenan 7.48 ± 0.3. Berbanding dengan kaedah kromatografi afiniti, ATPS didapati menjimatkan kos dan masa dengan pemulihan protein yang lebih tinggi. Oleh itu, kajian ini menunjukkan potensi aplikasi ATPS dalam pemulihan CLP rekombinan untuk pemprosesan hiliran berskala besar.

KEYWORDS: *recombinant collagen-like protein; R. palustri; aqueous two-phase system; purification; chromatography*

1. INTRODUCTION

Collagen is the main structural protein in the extracellular matrix of the animal kingdom comprised of specific amino acid compositions such as glycine (Gly), proline (Pro), and hydroxyproline that twisted together in the form of a triple-helix structure [1]. It strengthens the skin and benefits its elasticity and firmness besides helping in tissue and organ development. Widespread applications of collagen in cosmetic, biomedical, and pharmaceutical industries make collagen a major industrial component [2]. Furthermore, owing to its high biodegradability and biocompatibility thus making it is applicable as a biomaterial in the biomedical field [3].

Apart from mammalian and marine collagen, scientists have discovered collagen-like proteins (CLPs) annotated in bacteria, viruses, and archaea that shared the similar (Gly-Xaa-Yaa)n repetitive amino acid sequences of mammalian collagen but different in terms of amino acid content and distribution [4]. CLPs in bacteria can form triple helix structures similar to mammalian collagens with high thermal stabilities (Tm = 36.5-40 °C) despite the lack of hydroxyproline (Hyp), which is important in the stabilization of protein structure and promote self-association [5]. Furthermore, the result of calorimetric studies showed that high Hyp content increases the enthalpic contribution thus providing stability to the proteins [6].

It has been reported that some of the CLPs work as a virulence factor to evade the immune system of higher animals and thus promote host cell invasion [7]. Hence the availability of CLPs with similar features with mammalian collagen could benefit humans in establishing well-defined and novel collagen-based biomaterials [8,9]. Furthermore, using recombinant technology, these CLPs can be produced in large quantities [10]. Recombinant DNA technology is one of the recent advances in biotechnology that involve the joining together of DNA segments from different organisms and introduced into *E. coli* to produce a new genetic organism that is useful to science and industry [11]. This technology enables the production of disease-free products, uniform quality and abundance in quantity thus have been successfully exploited in various fields [12].

In recent years, downstream processing remains the major challenge in the production of recombinant protein. Conventional methods like precipitation, filtration, and chromatography need multiple stages to produce highly purified protein. These multi-step purification processes lead to high process cost, time consumption, low yield, and difficulty in scale up is viewed as a significant disadvantaged [13,14]. According to Warner and co-workers [15], nickel columns in affinity chromatography can give higher yield compared to other types of columns.

These difficulties are avoided using an aqueous two-phase system (ATPS) method, a liquid-liquid extraction technique formed when two incompatible water-soluble phase components are mixed at appropriate conditions resulting in the formation of two phases at equilibrium [16]. ATPS is more preferable due to its simplicity, low cost, ease of scale-up, higher biocompatibility, and shorter processing time [17]. Its high water content and low interfacial tensions provide the mild environment for sensitive biomolecules [18]. It has been documented to be an effective method for protein purification such as bromelain [19], protease [20], collagenase [21], lipase [22], papain [23], pepsinogen [24] and interferon [12]. However, there is still a lack of studies regarding the purification of recCLP using ATPS because of the complex process of protein partitioning that can be affected by many factors. The pH of the ATPS, concentration of salt, molecular weight, and concentration of polymers, are among the factors that can manipulate the distribution of protein molecules [12].

The potential factors that can affect the performance of ATPS such as volume ratio, pH, concentration of PEG, and salt were studied and optimized. In addition, affinity chromatography method was conducted to compare the purification effect of ATPS. The purpose of this study is to provide a simple yet effective method of purifying the recombinant collagen-like protein from *E. coli* crude extract. To date, recombinant collagen-like protein has been purified using the chromatography method [25,26] and no study has been attempted for purification of recombinant collagen-like protein from *E.coli* using the ATPS method, which could be promising in CLPs research.

2. MATERIALS AND METHOD

2.1 Materials

Polyethylene glycol with molecular weight of 2000 g/mol (PEG 2000), dipotassium hydrogen phosphate (K_2HPO_4), and potassium dihydrogen phosphate (KH_2PO_4) were purchased from Merck-Schuchardt (Munich, Germany). Vegitone Luria Bertani agar and Vegitone Luria Bertani Broth were obtained from Sigma-Aldrich (St. Louis, MO, USA) while Enzyfluo Collagen assay kit was procured from BioAssay Systems (Hayward, USA). All chemicals used in this paper are analytical grade.

2.2 Experimental Setup

2.2.1 Microorganism

The recombinant plasmid pColdII-CLP-*R. palustris* was prepared by subcloning the sequence of CLP-*R. palustris* from the source plasmid (PUC57, Genescipt, Hong Kong) to the target plasmid (pColdII TKR-3322, Takara, Japan). The recombinant plasmid was then transformed into *E. coli* B strain (BL21DE3) (New England BioLabs, USA) competent cell using cold shock expression method [20]. Ampicillin selection and colony PCR were performed to verify the successfully transformed pColdII-CLP into BL21 after overnight incubation at 37 °C on LB agar (unpublished data).

2.2.2 Protein Expression

The positive clone of *E. coli* BL21DE harboring collagen-like protein from *R. palustris* was cultured in 100 mL of M9 minimal medium at 37 °C, 250 rpm until OD600 nm reached 0.8-1.0 in an incubator shaker (Infors HT Ecotron, Switzerland). The recCLP culture was then induced at 15 °C by adding 1 mM isopropyl ß-D-1 thiogalactopyranoside. After 24 hours, cultures were centrifuged in a refrigerated centrifuge (Heraeus Multifuge X1R refrigerated centrifuge, Thermo Scientific, USA), at 4696 xg for 10 minutes at 4 °C, to remove the debris and tissue. The crude extract was stored at -20°C until further processing.

2.2.3 Cell Lysis

The cell pellets were resuspended in the lysis buffer (20 mM Na_2HPO_4, 0.5 M NaCl, pH 7.4) and sonicated at 40% amplitude, 10 seconds with 20 seconds interval between each sonication for 10 times using an ultrasonicator (LABSONIC®P, Sortarius, Germany) to break open the cell, therefore releasing the recCLP. Subsequently, the culture was then centrifuged using Eppendorf 580 4R refrigerated centrifuge (Eppendorf, Germany), at 12,000 rpm and 4 °C for 30 minutes to obtain a clear supernatant. The supernatant was considered as the soluble fraction whereas the pellet was known as the insoluble fraction.

2.2.4 Aqueous Two-phase System

ATPS was prepared on fixed mass basis in a 2.0 mL microcentrifuge tube by mixing predetermined quantities of PEG 2000, potassium phosphate buffer at pH 7.0 and 10% (w/w) of crude extract. Distilled water was added to the system to give a total weight of 2 g. The mixture was vortexed to mix for 1 minute and then centrifuged at 1000 x*g* (Heraeus Multifuge X1R, Thermo Scientific, USA), and 25 °C for 10 minutes to speed up phase separation. After that, top and bottom phases were carefully collected for further analysis. The volume of the phases was then used to estimate the volume ratio (VR). It was noted that the most potent ATPS could not be determined by monitoring the total protein in the phases. Thus, the total amount of recombinant collagen-like protein in both phases, partition coefficient (KE), as well as concentration of recCLP, were quantified using fluorometric collagen assay kit.

The binodal curves were referred elsewhere [28]. The strategy behind the selection of the experimental system is well described elsewhere [22]. According to Arshad and Amid [27], the tie-line length (TLL) was estimated graphically by using volume ratio and it can be calculated using the equation as follows,

$$TLL = \sqrt{[(\Delta x^2) + (\Delta y^2)]} \tag{1}$$

where ΔX and ΔY indicate the difference between salt and PEG concentration, respectively.

2.2.5 One-factor-at-a-time (OFAT)

OFAT (one-factor-at-a-time) method was designed and applied for ATPS separation. The tested parameters involved in this study were volume ratio, pH, and concentration of PEG and salt. The response was concentration of recombinant collagen-like protein and purification factor. Data from experiments were expressed as mean ± standard error. Analysis of variance (ANOVA) was performed on the data and statistical significance was defined at $p<0.05$.

2.2.6 Optimization

Response surface methodology (RSM) using Design of Expert 10.0.3 software (State-Ease Inc., Minneapolis MN, USA) was used for the optimization of ATPS conditions. A set of 11 experiments with two independent variables (concentration of polyethylene glycol and potassium phosphate) were coded using the face-centered central composite design with triplicate center point. The values of the center point were obtained based on previous ATPS separation by OFAT. The recCLP concentration and purification factor (PF) were chosen as the responses in each run.

2.2.7 Affinity Chromatography (Fast-Protein Liquid Chromatography)

Affinity chromatography was conducted using 1 mL HisTrap™ High Performance chromatography column (GE Healthcare, USA) prepacked with Ni Sepharose with an inner diameter of 7 mm connected to AKTA Prime Plus® (GE Healthcare, USA). The collected supernatant after cell lysis was filter-sterilized using 0.45 µm pore filter. Then, 2 ml of the solution was loaded into the packed column at a flow rate of 1 mL/min. The unbound proteins were washed with binding buffer and the target protein was eluted using elution buffer (20 mM Na_2HPO_4, 0.5 M NaCl, 0.5 M imidazole, pH 7.4). Collected fractions were analyzed by SDS-PAGE and fluorometric collagen assay.

2.2.8 Quantification of Recombinant collagen-like Proteins (recCLP)

The concentration and total recCLP in ATPS samples were measured using a commercially available collagen assay kit (BioAssay Systems, USA). Briefly, collagen in the sample was enzymatically digested into peptides by mixing equal amounts of samples with digest enzyme and incubated at 37°C for 1 hour. Then, dye reagent was added to react with the N-terminal glycine peptides in the solution, incubated at 37°C for 10 minutes, thus forming a fluorescent complex [26]. The sample was transferred to a 384-black flat bottom microplate reader (Corning, USA) and ready for fluorescence reading at $\lambda_{ex/em}$ 375/465 nm using a Spark® multimode microplate reader (Tecan, Switzerland). In this study, bovine collagen type I was used as a standard for collagen assay. The fluorescent intensity, measured at $\lambda_{ex/em}$ 375/465 was directly proportional to the collagen concentration in the sample.

2.2.9 Sodium Dodecyl Sulfate-Polyacrylamide Gel Electrophoresis (SDS-PAGE)

The protein sample from crude extract, top phase in ATPS and FPLC fractions were analyzed using SDS-PAGE method. The samples were diluted to 1:1 ratio prior to loading into 12% resolving gel and 4% stacking gel. Electrophoresis is run at 120 V, 400 mA for 60 min, the gels are stained using ReadyBlue™ Protein Gel Stain (Sigma, USA) or silver staining method.

2.3 Calculation

The volume ratio is defined as,

$$V_R = \frac{Volume\ in\ top\ phase}{Volume\ in\ bottom\ phase} \tag{2}$$

The partition coefficient (KE) of the recCLP was calculated as the ratio of total recCLP in two phases,

$$KE = \frac{Total\ collagen\ in\ top\ phase}{Total\ collagen\ in\ bottom\ phase} \tag{3}$$

The purification factor (PF) of the recCLP was calculated according to the equation below,

$$PF = \frac{Collagen\ amount\ in\ sample}{Collagen\ amount\ in\ crude\ lysate} \tag{4}$$

3. RESULTS AND DISCUSSION

3.1 Selection of ATPS

The result of system tie-line length (TLL) and partition coefficient (KE) for ATPS samples composed of PEG 2000/potassium phosphate with VR value of 1.0 are shown in Table 1. The selection of binodal curves was decided according elsewhere [28]. To identify the best combination of ATPS, a quantitative fluorometric collagen assay was done to both top and bottom phases. The highest partition coefficient (KE) was achieved by the system with 26% (w/w) PEG 2000 and 26% (w/w) potassium phosphate with tie-line length (TLL) of 54.78% (w/w), therefore proving that most of the protein of interest were favored in one phase which is PEG-rich top phase. The concentration of salt in the bottom phase increase as the TLL increase and this may drive recCLP towards the bottom phase as a consequence [12]. Therefore, this combination of ATPS was chosen for further analysis. The bottom phase of ATPS with 26% (w/w) PEG 2000 and 26 % (w/w) potassium phosphate showed a low concentration of recCLP in the quantitative assay (unpublished data). Therefore, in the further experiment, it was decided to conduct detection of recCLP in the top-phase only.

Table 1: The tie-line length (TLL) and partition coefficient (KE) of ATPS with VR of 1.0

% PEG 2000 (w/w)	% Potassium phosphate (w/w)	TLL	KE
25	25	50.51	1.33
26	26	54.78	4.03
27	27	60.26	1.55
28	28	64.42	1.28

3.2 Screening of ATPS Factors Using OFAT (one-factor-at-a-time)

3.2.1 Effect of VR on recCLP

The impact of different volume ratios along the same tie-line of a system consisting of 26% (w/w) potassium phosphate and 26% (w/w) of PEG 2000 at constant pH 7.0 was assessed and shown in Table 2. Five points indicate five different volume ratios (0.33, 0.8, 1.0, 1.57, 3.5) within the same tie-line. In defined ATPS, volume of top phase proportionally increases with the volume ratio resulting in more free volume available for the protein of interest to participate in the top phase. This situation caused a significant negative impact of free volume in the bottom phase [29]. On the other hand, an extremely low volume ratio may have limited free volume, thus limiting the partition of protein [12]. From the preceding result, either increasing or reducing the volume ratio did not cause any significant effect on recCLP concentration in the top phase. As a rule of thumb, researchers who are using ATPS method for the first time are advised to use volume ratio equal to 1, making it convenient to measure the volume of each phase during partition experiments [27].

Table 2: Influence of different volume ratios on recCLP in top-phase.
The data are presented as means ± standard error, $p<0.05$

Volume ratio	recCLP (mg/mL)	Purification factor (PF)
0.33	0.98 ± 0.004	2.77 ± 0.01
0.80	0.84 ± 0.003	5.78 ± 0.02
1.00	1.03 ± 0.006	8,84 ± 0.05

3.2.2 Effect of PEG 2000 % (w/w) on recCLP

The results of PF and concentration of recCLP in different PEG concentration were shown in Table 3. A higher concentration of recCLP with PF of 9.04 ± 0.25 was achieved in ATPS with 26% (w/w) PEG2000. Volume exclusion effect in top phase and salting-out effect in bottom phase are the crucial factors in partition behavior of biomolecules in the polymer-salt system [30]. Those effects are responsible for reducing the available space in the top phase and thus obstruct the partition of biomolecules in the top phase. This hypothesis was concurrent with the behavior of recCLP and PF when the PEG concentration was decreased from 26% (w/w) to 29% (w/w). Meanwhile, the trend with

PEG concentration from 20% (w/w) to 26% (w/w) and from 29% (w/w) to 32% (w/w) was parallel with the theory stated that an increase of polymer concentration caused the movement of biomolecules to PEG-rich phase due to the hydrophobic interactions between biomolecules and PEG [31]. Increasing PEG concentration leads to the increase of top phase volume, resulting in the rising of free volume available for the protein of interest to participate in the top phase [29,32]. Therefore, ATPS with 26% (w/w) of PEG 2000 was further employed for the next factor. However, the best concentration of PEG 2000 in the purification of recombinant recCLP cannot be corroborated with any studies due to a lack of references regarding the application of ATPS in the partition of recCLP.

Table 3: Influence on the concentration of PEG on recCLP concentration and purification factor. The data are presented as means ± standard error, $p<0.05$

%PEG 2000 (w/w)	recCLP (mg/mL)	Purification factor
20	0.944 ± 0.04	6.04 ± 0.27
23	1.08 ± 0.05	7.36 ± 0.33
26	1.18 ± 0.03	9.04 ± 0.25
29	0.95 ± 0.04	7.28 ± 0.33
32	1.10 ± 0.05	9.34 ± 0.39

3.2.3 Effect of Potassium Phosphate % (w/w) on recCLP

In this part, the effect of different potassium phosphate concentrations from 20 to 32% (w/w) at pH 7.0 on the concentration of recCLP was investigated and presented in Table 4. As shown in Table 4, the highest concentration of recCLP was shown in ATPS with 29% (w/w) potassium phosphate, with 0.97 ± 0.006 mg/mL recCLP and PF of 6.33 ± 0.04. The concentration of potassium phosphate % (w/w) is one of the factors which affect the partition behavior of the target protein. Theoretically, ionic strength will increase as the salt concentration in the system increases, thus pushing the proteins to the top phase. Besides, the ability of salt to capture water molecules will increase, hence moving biomolecules to the top phase [8,29]. However, a high concentration of salt also can lead to protein precipitation and denaturation thus reducing the amount of targeted protein in the phase [8,15]. This hypothesis supports the trend shown for concentration of recCLP when the concentration of salt decrease from 29% (w/w) to 32% (w/w). Meanwhile, due to the decreasing volume of top phase (20 to 32% (w/w)), PF decreased. When the free volume in the phase is preferred by protein of interest decreased, it will cause them to concentrate when the limits of protein solubility are exceeded [25]. Thus, the protein content in that phase will decline.

Table 4: Influence on the concentration of potassium phosphate on recCLP concentration and purification factor. The data are presented as means ± standard error, $p<0.05$

% Potassium phosphate (w/w)	recCLP (mg/mL)	Purification factor (PF)
20	0.78 ± 0.03	8.25 ± 0.28
23	0.93 ± 0.03	6.83 ± 0.22
26	0.92 ± 0.01	6.04 ± 0.06
29	0.97 ± 0.006	6.33 ± 0.04
32	0.95 ± 0.006	4.64 ± 0.03

3.2.4 Effect of pH on recCLP

The effect of different pH values on the partitioning of recCLP in ATPS was determined by varying the pH from 6.0-8.0 using different compositions of potassium phosphate salts (KH_2PO_4 and K_2HPO_4), ± 0.5 accuracy of pH. System pH affects the partitioning of proteins by altering the charge and surface properties of the solute. The partitioning behavior of recCLP is expected to be sensitive to the pH levels increased. This is due to the isoelectric point (pI) of the collagen (<7.0), which makes the protein become negatively charged and favors the PEG-rich top phase. According to [33], the zwitterion along collagen molecules are negatively charged, making the entire collagen is negative. Moreover, the pI glycine residues are 5.97 due to its acidic side chain, thus making the collagen-like protein carried a negative charge [34]. When the pH increases from 7.0 to 8.0, the protein of interest favored a partition in the bottom phase, which in turn decreased in protein concentration. Besides that, at higher pH, more contaminants become negatively charged and tend to partition to the top phase [17]. The presence of contaminants in the top phase lowered the concentration of collagen-like protein. Per the results shown in Table 5, the system of pH 7.0 exhibited the highest values for the responses, 1.37 ± 0.13 mg/ml of recCLP and PF of 6.44 ± 0.61. As a result, ATPS with pH 7.0 was chosen for further study.

Table 5: Influence of pH on recCLP concentration and purification factor.
The data are presented as means ± standard error, p<0.05

% Potassium phosphate (w/w)	recCLP (mg/mL)	Purification factor (PF)
6	0.76 ± 0.06	3.99 ± 0.32
7	1.37 ± 0.13	6.44 ± 0.61
8	1.22 ± 0.11	5.72 ± 0.51

3.3 Optimization of ATPS Experiment Using Design of Expert (DOE)

Response surface methodology with face-centered central composite design (FCCCD) was applied to determine the optimum condition of the ATPS purification method. The effect of two factors known as concentration of PEG 2000 and potassium phosphate on concentration of recCLP was studied. The temperature of phase separation and pH of the system was kept constant at 25 °C and 7.0 respectively. The design matrix and the result of optimization were summarized in Tables 6 and 7, respectively. For the successful development of ATPS purification method, the separation of recombinant collagen-like protein was optimized using a statistical experimental design involving the concentration of PEG 2000 (A) and concentration of potassium phosphate (B) at pH 7.0. Analysis of variance (ANOVA) of a quadratic model for the responses were employed to determine the significant variable and their interaction with the response variable (Tables 8-10). According to the analysis of variance, the F-value represents the accuracy of the model while the p-value indicates the interaction between the model terms. A significant model proved by the p-value that was less than 0.05 while a p-value greater than 0.10 is considered as an insignificant model. The coefficient of determination (R^2) and adjusted R^2 indicate the quality fit of the model equation [35].

It was found that the F-value of 7.65 and the p-value of 0.0217 (<0.05) indicate that the model is significant. Furthermore, a non-significant value of 0.2674 for lack of fit showed that the quadratic model was valid for this study. The model coefficient of determination (R^2) and adjusted R^2 value was 0.8843 and 0.7687, respectively. Both values represent the correlation between actual and predicted data. R^2 value obtained in this present study is acceptable as it exceeded 0.8 and the small difference between R^2 and adjusted R^2 is preferable and proved the good correlation for recCLP partitioning. The model contains many insignificant terms proved by the huge difference between R^2 and adjusted R^2 [20,23]. In this experiment, R^2 of 0.8843 indicates that the predicted model could explain 88.43 % of the variability in the response. As well, the adjusted R^2, 0.7687 is also good to demonstrate a good correlation between actual and predicted data [20], [23]. From the three-dimensional plot in Figs. 1 to 3, an increasing pattern showed when the concentration of PEG and salt increase to the intermediate values and decline as the concentrations of PEG and salt decrease. In summary, the maximum values of the response appeared near the center of the graph, indicating that the center point selected for this experiment is appropriate. The result from the software implied that optimized conditions for recCLP partitioning occurred when the concentration of PEG 2000 and potassium phosphate was set at 24.8% (w/w) and 29.23% (w/w) respectively with 3.026 mg/ml recCLP.

Table 6: Factors for face-centered central composite design (FCCCD) study

Symbols	Factor	Range and levels		
		-1	0	1
A	Concentration of PEG 2000 % (w/w)	20	25	30
B	Concentration of potassium phosphate % (w/w)	25	28.5	32

Table 7: Design of experiment for optimisation of ATPS of recCLP using FCCCD

% PEG 2000 (w/w)	% Potassium phosphate (w/w)	recCLP concentration (mg/mL)
20	25	1.913
30	25	1.450
20	32	2.351
30	32	1.794
20	28.5	2.151
30	28.5	2.178
20	25	1.913
25	25	1.874
25	32	2.945
25	28.5	2.974
25	28.5	3.271
25	28.5	2.904

Table 8: Analysis of variance (ANOVA) for the quadratic model for concentration of recombinant collagen-like protein

Sources	Sum of Squares	P-value Prob>F
Model	3.10	0.0217
A-PEG 2000 concentration	0.16	0.2142
B-Salt concentration	0.57	0.0450
AB	2.209E-003	0.8754
A^2	1.24	0.0113
B^2	0.52	0.0519
Lack of fit	0.33	0.2674 (not significant)
R^2	0.8843	
Adjusted R^2	0.7687	

https://doi.org/10.31436/iiumej.v24i1.2468

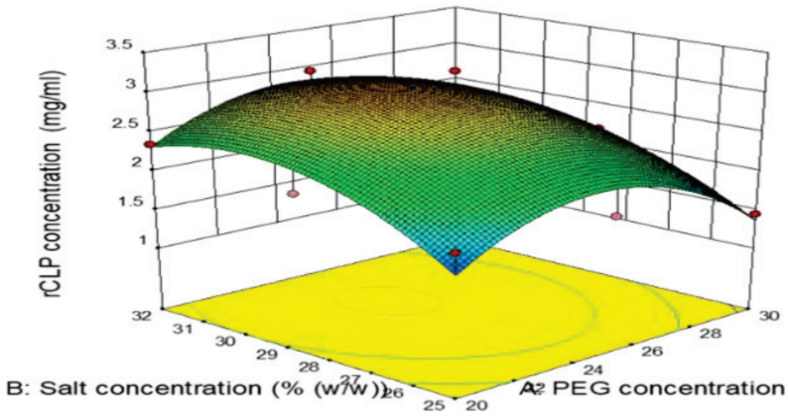

Fig. 1: Three-dimensional surface plot of response surface analysis showing the effect of the interaction of concentration of PEG 2000 and potassium phosphate on the recCLP.

Table 9: Analysis of variance (ANOVA) for the quadratic model for fluorescence intensity of recombinant collagen-like protein

Sources	Sum of Squares	P-value Prob>F
Model	1.610E+008	0.0238
A-PEG 2000 concentration	8.587E+006	0.221
B-Salt concentration	2.921E+007	0.050
AB	1.325E+005	0.869
A^2	6.482E+007	0.012
B^2	2.715E+007	0.056
Lack of fit	1.798E+007	0.024 (not significant)
R^2	0.8798	
Adjusted R^2	0.7596	

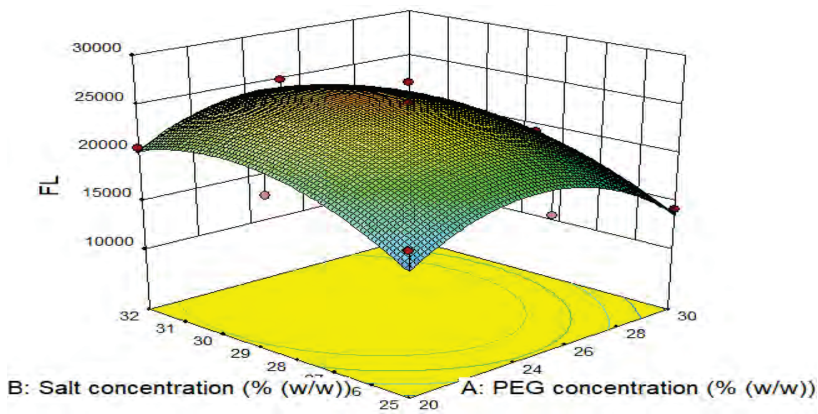

Fig. 2: Three-dimensional surface plot of response surface analysis showing the effect of the interaction of concentration of PEG 2000 and potassium phosphate on the fluorescence intensity.

Table 10: Analysis of variance (ANOVA) for the quadratic model for purification factor of recombinant collagen-like protein

Sources	Sum of Squares	P-value Prob>F
Model	17.96	0.0614
A-PEG 2000 concentration	0.62	0.417
B-Salt concentration	0.12	0.716
AB	0.033	0.847
A^2	6.65	0.034
B^2	5.96	0.041
Lack of fit	3.44	0.1905
R^2	0.8192	
Adjusted R^2	0.6383	

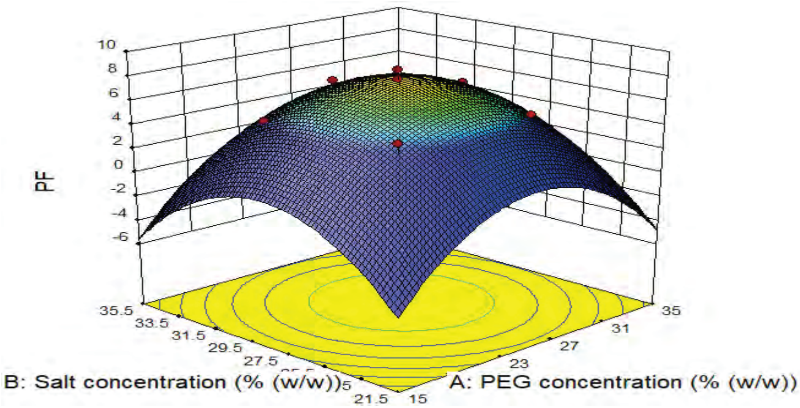

Fig. 3: Three-dimensional surface plot of response surface analysis showing the effect of the interaction of concentration of PEG 2000 and potassium phosphate on the purification factor.

The quadratic model for each response of fluorescence intensity, concentration of recCLP and purification factor coefficient were predicted from equations as follows:

$$\text{Fluorescence intensity (FL)} = 25175.95 - 1196.33C_{PEG2000} + 2206.50C_{PP} - 182.00C_{PEG2000}C_{PP} - 5058.37C_{PEG2000}^2 - 327.87C_{PP}^2 \quad (5)$$

$$\text{Concentration of recCLP} = 2.98 - 0.17C_{PEG2000} + 0.31C_{PP} - 0.023C_{PEG2000}.C_{PP} - 0.70_{PEG2000}^2 - 0.45C_{PP}^2 \quad (6)$$

$$\text{Purification factor (PF)} = 7.71 + 0.32C_{PEG2000} + 0.14C_{PP} + 0.091C_{PEG2000}.C_{PP} - 1.62C_{PEG2000}^2 - 1.53C_{PP}^2 \quad (7)$$

ATPS with only one polymer in the presence of salt (polymer/salt) is the better choice with cheaper cost, ease of handling, and low viscosity [13,36]. A similar finding, conducted by de Albuquerque Wanderley and co-workers [21], showed that the best condition for purification of collagenase by ATPS is 15% (w/w) PEG 3350 and 12.5% (w/w) phosphate salt.

3.4 Validation of Model

Validation of the model was conducted by carrying out three replicate experiments and the results were compared with the predicted results suggested by FCCCD of RSM as tabulated in Table 11. Under the optimized condition which composed of at 24.8% (w/w)

PEG 2000 and 29.23% (w/w) potassium phosphate at pH 7.0, the predicted recCLP and PF were 3.026 mg/mL and 7.654 respectively. The experiments for validation of the predicted model resulting recCLP of 3.233 ± 0.12 mg/mL. The minimal difference between predicted and experimental values proved RSM is a suitable tool for optimization of ATPS conditions for purification of recCLP.

Table 11: Validation of model. Experiments were conducted in triplicate with data were presented as means ± standard error, $p<0.05$

	Model predicted	**Experimental**	**Percentage Error (%)**
Concentration of recCLP (mg/mL)	3.026	3.233 ± 0.12	6.9
Purification factor	7.654	7.476 ± 0.29	2.3
	Model predicted	Experimental	Percentage Error (%)

3.5 Comparison of Purification by ATPS and Affinity Chromatography

As suggested by Xu and co-workers [10], pH of 7.4 was used for binding buffer containing 20 mM of Na_2HPO_4 and 0.5 M NaCl. Ni-NTA resin with pH between 7.0 and 8.0 is preferable for most of the his-tagged proteins to prevent non-specific binding [37]. In this present study, the elution buffer containing 20 mM of Na_2HPO_4, 0.5 M NaCl and 0.5 M imidazole, pH 7.4 eluted the target protein from the column at fractions 17 to 19 (Fig. 4.). Affinity chromatography was performed under native conditions since the protein of interest is in soluble form [38].

Based on the results, the sample at the peak of the chromatogram (fraction 18) was analyzed by collagen assay and SDS-PAGE and compared with purified recombinant recCLP from ATPS purification method. The purification efficiency of recombinant collagen-like protein purified by ATPS and chromatography is summarized in Table 12. Both methods were performed directly after cell lysis stage. In the present study, Ni Sepharose chromatography (affinity) resulted in concentration of recCLP of 2.036 mg/mL and with purification factor of 0.524. Meanwhile, sample from ATPS with (24.8% w/w) of PEG2000 and (29.20 % w/w) of potassium phosphate buffer at pH 7 recCLP exhibited favorable result with 3.23 mg/ml and 7.48 purification factor. The yield is defined as the amount of purified total proteins divided by the initial amount of total protein (defined as 100%).

Table 12: Purification efficiency of recombinant collagen-like protein by different purification methods.

Purification methods	**ATPS**	**Affinity chromatography**
Fluorescence Intensity	27069	18355
Concentration of recCLP (mg/mL)	3.233	2.036
Purification Factor	7.476	0.524
Total protein (mg)	0.233	0.172
Yield (100%)	19.74	17.28
Purification methods	ATPS	Affinity chromatography

Based on economic analysis point of view as presented in Table 13, ATPS exhibited shorter processing time with lower cost of operation compared to the chromatography method. Due to expensive prepacked column with resin and chemicals used for 1h processing time, affinity chromatography is considered an expensive downstream purification method, thus making it unsustainable for bigger scale and long-term production. Despite the high cost of operation, affinity chromatography is advantageous in terms of reusability. The chromatography resin can be re-used up to 100 times since the hydrophobic stationary phase is washable [39]. However, additional cost needs to be considered for the stripping and recharging chromatography columns [19]. In the case of ATPS, polymer and salt cannot be recycled as they were part of the final purified protein [19]. Such economic analysis lays out a better understanding for future study, and ATPS method is proven to be cost-effective, time-saving with higher recovery that may be considered for the scale-up process.

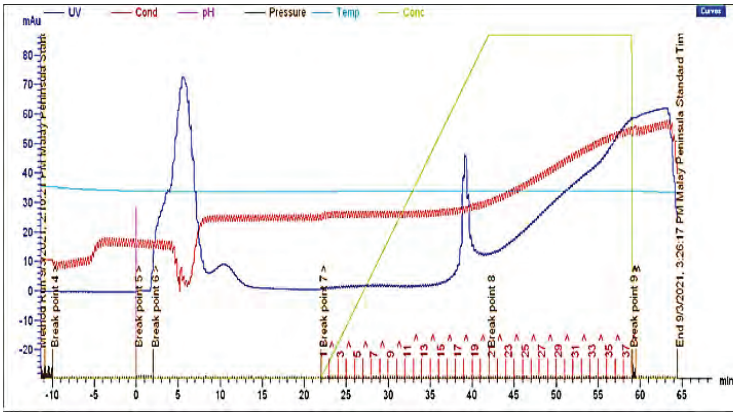

Fig. 4: Chromatogram of the purified samples from affinity chromatography of 2 mL loading volume of recombinant collagen-like protein lysates on Ni-Sepharose resin. Binding buffer contain 20 mM of Na_2HPO_4, 0. 5M NaCl at pH 7.4. Elution buffer contained 20 mM Na_2HPO_4, 0.5 M NaCl and 0.5 M imidazole, at pH 7.4. Fractions (1 mL/tube) were collected at flow rate of 1 mL/min.

Table 13: Direct comparison between chromatography and ATPS method for downstream processing of recombinant collagen-like protein

Purification methods	ATPS	Affinity chromatography (FPLC)
Processing time	30 minutes	1 hour
Cost prepacked column	-	228.36/5mL
Cost of chemicals (per kg)	K_2HPO_4: USD 235.4 KH_2PO_4: USD 163.98 PEG 2000: USD 91.6	Na_2HPO_4: USD 91.3 NaCl: USD 128.02 Imidazole: USD 543.88
Cost of operation per system	USD 490.86	USD 991.39

3.6 SDS-PAGE Analysis of Recombinant Collagen-like Protein

The presence of recombinant collagen-like protein purified by ATPS with optimized conditions of was analyzed by SDS-PAGE electrophoresis under reducing conditions and compared with purified samples from the chromatography method. Figure 5. shows the presence of a protein band with molecular weight of 36 kDa for ATPS sample, indicating the recCLP was successfully partitioned in the top phase. This was supported by the single band formed at the same size in samples from FPLC fractions. However, several bands were observed between 45 kDa and 60 kDa and above 75 kDa. This is explained by the fact that the bottom phase was unable to attract all of contaminants and unwanted proteins.

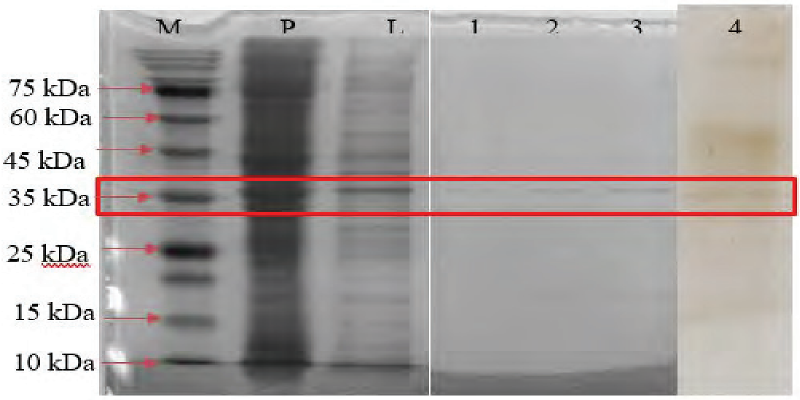

Fig. 5: SDS-PAGE analysis of purified sample of ATPS and affinity chromatography. Lane M: standard protein marker. Lane P: cell pellet. Lane L: crude cell lysate. Lane 1: FPLC fraction (17). Lane 2: FPLC fraction (18). Lane 3: FPLC fraction (19). Lane 4: ATPS top phase. Note: For SDS-PAGE analysis, 20 µl of sample with sample buffer was loaded into a 12% resolving and 4% stacking gel. Gel with FPLC fractions was stained with ReadyBlue™ Protein Gel Stain and the gel with ATPS sample was stained with silver staining after electrophoresis at 120 V, 400 mA for 60 minutes.

4. CONCLUSION

The present study had demonstrated the potential application of ATPS in purification of recCLP using PEG2000/potassium phosphate system. The optimum conditions of ATPS comprised of 24.8% (w/w) PEG 2000 and 29.20% (w/w) potassium phosphate at pH 7.0 which resulted in 27068 ± 900, 3.233 ± 0.12 mg/mL, 7.476 ± 0.29, for fluorescence intensity, concentration of recombinant collagen-like protein and purification factor, respectively. Moreover, sodium dodecyl sulfate-polyacrylamide gel electrophoresis (SDS-PAGE) confirmed the molecular weight of the recCLP, which is 36 kDa. This study clearly demonstrated ATPS was proven to be time-saving, cost-effective with higher recovery that may be considered for the scale-up process. The obtained results are pivotal for the design of a purification process and understanding the complex mechanisms controlling the phase behavior. Besides, due to the lack of application of ATPS in purification of CLPs specifically from *R. palustris*, this present study can be used as a reference and deliver new information for future studies.

ACKNOWLEDGEMENT

Special thanks are dedicated to Ministry of Higher Education (MOHE), Malaysia for financial support under Transdisciplinary Research Grant Scheme [TRGS/1/2018/UIAM/01/1/1]. The authors are grateful to INHART Laboratory for providing laboratory equipment and the Advanced Institute of Technology, UPM for helping with the collagen assay experiment.

REFERENCES

[1] Yamazaki CM, Kadoya Y, Hozumi K, Okano-Kosugi H, Asada S, Kitagawa K, Nomizu M, Koide T. (2010) Biomaterials A collagen-mimetic triple helical supramolecule that evokes integrin-dependent cell responses. Biomaterials., 31(7): 1925-1934. doi.org/10.1016/j.biomaterials.2009.10.014

[2] Awang NA, Amid A, Arshad ZI. (2020) Method for purification of collagen: A systematic review. Asia Pacific J. Mol. Biol. Biotechnol., 28(3): 99-112. doi: 10.35118/apjmbb.2020.028.3.10.

[3] Lim Y, Ok Y, Hwang S, Kwak J, and Yoon S. (2019) Marine Collagen as A Promising Biomaterial for Biomedical Applications. Mar. Drugs, 17(467):1-32.

[4] Ilamaran M, Janeena A, Valappil S, Ramudu KN, Shanmugam G, and Niraikulam A. (2019) Biomaterials Science A self-assembly and higher order structure biomaterial for cell proliferation. Biomateriasl Sci., doi: 10.1039/c9bm00186g.

[5] Gorres KL and Raines RT. (2010) Prolyl 4-hydroxylase. Crit. Rev. Biochem. Mol. Biol., 45(2): 106-124. doi: 10.3109/10409231003627991.

[6] Privalov PL. (1982) Stability of proteins. Proteins which do not present a single cooperative system. Adv. Protein Chem., 35: 1-104.

[7] An B, Kaplan DL, and Brodsky B. (2014) Engineered recombinant bacterial collagen as an alternative collagen-based biomaterial for tissue engineering, Front. Chem., 2: 1-5. doi: 10.3389/fchem.2014.00040.

[8] Pacak CA, MacKay AA, and Cowan DB. (2014) An improved method for the preparation of type I collagen from skin. J. Vis. Exp., 83(e51011). doi: 10.3791/51011.

[9] Mohs A. (2007) Mechanism of stabilization of a bacterial collagen triple helix in the absence of hydroxyproline. J. Biol. Chem., 282(41): 29757-29765. doi: 10.1074/jbc.M703991200.

[10] Xu C, Yu Z, Inouye M, Brodsky B, and Mirochnitchenko O. (2014) Bacterial collagen-like proteins that form triple-helical structures. J Struct Biol., 186(3): 451-461. doi: 10.1016/j.biotechadv.2011.08.021.Secreted.

[11] Purandarey H. (2018) Recombinant DNA Technology and its Applications. Int. J. MediPharm Res., 4(2): 98-98. doi: 10.5005/jp/books/10279_5.

[12] Khan S, Ullah MW, Siddique R, Nabi G, Manan S, Yousaf M, Hou H. (2016) Role of recombinant DNA technology to improve life. Int. J. Genomics., 2016: 1-14. doi: 10.1155/2016/2405954.

[13] Ratanapongleka K. (2013) Recovery of Biological Products in Aqueous Two Phase Systems. Int. J. Chem. Eng. Appl., 1(2): 191-198. doi: 10.7763/ijcea.2010.v1.33.

[14] Andrews BA, Nielsen S, and Asenjo JA. (1996) Partitioning and purification of monoclonal antibodies in aqueous two-phase systems. Bioseparation. 6(5): 303-313.

[15] Warner LR, Blasick CM, Brown RJ, and Oxford JT. (2007) Expression, purification, and refolding of recombinant collagen alpha1(XI) amino terminal domain splice variants. Protein Expr. Purif., 52(2):403-409. doi: 10.1016/j.pep.2006.10.016.

[16] Alberto M. (2018) Aqueous Two-Phase Systems: Properties, Functions and Advantages, May:1–14. doi: 10.13140/RG.2.2.20368.51209.

[17] Lin YK, Ooi CW, Tan JS, Show PL, Ariff A, and Ling TC. (2013) Recovery of human interferon alpha-2b from recombinant Escherichia coli using alcohol/salt-based aqueous two-phase systems. Sep. Purif. Technol., 120: 362-366. doi: 10.1016/j.seppur.2013.09.038.

[18] Singh S and Tavana H. (2018) Collagen Partition in Polymeric Aqueous Two-Phase Systems for Tissue Engineering. Front. Chem, 6: 4-10. doi: 10.3389/fchem.2018.00379.

[19] Arshad ZIM, Amid A, Yusof F, Sulaiman SZ, Mudalib SKA, Man RC, Shaarani SM. (2017) Perbandingan kaedah penulenan rekombinan bromelain daripada *Escherichia coli* BL21-A1. Malaysian J. Anal. Sci., 21(4): 958-971. doi: 10.17576/mjas-2017-2104-23.

[20] Samad A and Shukor A. (2017) Protease purification from Bacillus amyloliquefaciens B7 using Aqueous Two-Phase System (ATPS). Int. Food Res. J., 24: 292-297.

[21] de Albuquerque Wanderley MC, Wanderley Duarte Neto JM, Campos Albuquerque WW, de Araújo Viana Marques D, de Albuquerque Lima C, da Cruz Silvério SI, de Lima Filho JL, Couto Teixeira JA, Porto ALF. (2017) Purification and characterization of a collagenase from Penicillium sp. UCP 1286 by polyethylene glycol-phosphate aqueous two-phase system. Protein Expr. Purif., 33: 8-14. doi: 10.1016/j.pep.2017.02.010.

[22] Ooi CW, Tei BT, Hii SL, Ariff A, Wu HS, Lan JCW, Juang RS, Kamal SMM, Ling TC. (2009) Direct purification of Burkholderia Pseudomallei lipase from fermentation broth using aqueous two-phase systems. Biotechnol. Bioprocess Eng., 14(6): 811-818. doi: 10.1007/s12257-008-0306-y.

[23] Ling YQ, Nie HL, Su SN, Branford-White C, and Zhu LM. (2010) Optimization of affinity partitioning conditions of papain in aqueous two-phase system using response surface methodology. Sep. Purif. Technol., 73: 343-348. doi: 10.1016/j.seppur.2010.04.020.

[24] Zhao L, Budge SM, Ghaly AE, Brooks MS, and Dave D. (2013) Partition of Pepsinogen from the Stomach of Red Perch (Sebastes marinus) by Aqueous Two Phase Systems: Effects of PEG Molecular Weight and Concentration. Enzym. Eng., 2(1). doi: 10.4172/2329-6674.1000108.

[25] Lukomski S and Mcnitt DH. (2020) Expression and Purification of Collagen-Like Proteins of Group A *Streptococcus* in Methods in molecular biology. 163-179. doi: 10.1007/978-1-0716-0467-0_12.

[26] Xu C, Yu Z, Inouye M, Brodsky B, and Mirochnitchenko O. (2010) Expanding the Family of Collagen Proteins : Recombinant Bacterial Collagens of Varying Composition Form Triple-Helices of Similar Stability. Biomacromolecules., 11: 348-356.

[27] Arshad ZIM and Amid A. (2018). Procedure to develop binodal curve and phase diagram for aqueous two-phase system. In Multifaceted Protocol in Biotechnology. Edited by A. Amid, S. Sulaiman, and D. N. Jimat, Eds. Gateaway East, Singapore: Springer; pp. 75-85.

[28] Awang NA, Amid A, Arshad ZIM. (2021) Liquid-liquid Equilibrium in Aquesous Two Phase System (ATPS) and Their Application in Purification of Recombinant Collagen-like Protein From Rhodopseudomonas palustris Expressed In *E.coli* System. In proceedings of Virtual International Halal Science Conference '21, July 2021, pp 127.

[29] Rito-palomares M, Dale C, and Lyddiatt A. (2014) Aqueous two-phase fractionation of biological suspensions for protein recovery from bovine blood. Biotechnol. Tech., 12(9): 711-714. doi: 10.1023/A.

[30] Babu BR, Rastogi NK, and Raghavarao KSMS. (2008) Liquid-liquid extraction of bromelain and polyphenol oxidase using aqueous two-phase system. Chem. Eng. Process. Process Intensif., 47:83-89. doi: 10.1016/j.cep.2007.08.006.

[31] González-Tello P, Camacho F, and Blázquez G. (1994) Density and Viscosity of Concentrated Aqueous Solutions of Polyethylene Glycol. J. Chem. Eng. Data., 39(3): 611-614. doi: 10.1021/je00015a050.

[32] Benavides J and Rito-Palomares M. (2006) Simplified two-stage method to B-phycoerythrin recovery from Porphyridium cruentum. J. Chromatogr. B Anal. Technol. Biomed. Life Sci., 844: 39-44. doi: 10.1016/j.jchromb.2006.06.029.

[33] Thomas AW and Kelly MW. (1922) The iso-electric point of collagen. J. Am. Chem. Soc, 44(1): 195-201. doi: 10.1021/ja01422a025.

[34] Borsook H and MacFadyen DA. (1930) The Effect Of Isoelectric Amino Acids on the pH+ of a Phosphate Buffer Solution, J. Gen. Physiol., 13(5): 509-527. doi: 10.1085/jgp.13.5.509.

[35] Ma XX, Fan DD, Zhu CH, Shang ZF, and Mi Y. (2014) Optimization of fermentation medium for collagen production of recombinant Pichia pastoris during induction phase. J. Chem. Pharm. Res., 6(7): 1802-1809.

[36] Awang NA. (2022) Purification of recombinant collagen-like protein from *Rhodopseudomonas palustris* expressed in *Escherichia coli* using aqueous two-phase system. Master's thesis. International Islamic University of Malaysia, International Institute for Halal Research and Training.

[37] Zachariou M. (2008) Affinity CHromatography: Methods and Protocols. Humana Press.

[38] Bornhorst J.A. and Falke JJ. (2000) Purification of Proteins Using Polyhistidine Affinity Tags. Methods Enzymol., 326: 245-254. doi: 10.1038/jid.2014.371.

[39] Oscar A, Veronica A, Leobardo SC, and Rito-palomares M. (2006) Direct comparison between ion-exchange chromatography and aqueous two-phase processes for the partial purification of penicillin acylase produced by *E . coli.* J. Chromatogr. B., 835: 77-83. doi: 10.1016/j.jchromb.2006.03.016.

https://doi.org/10.31436/iiumej.v24i1.2435

BATTERY ENERGY STORAGE SYSTEM (BESS) MODELING FOR MICROGRID

ZAHIR ZULKIFLY, SITI HAJAR YUSOFF*, NOR LIZA TUMERAN AND NUR SYAZANA IZZATI RAZALI

Department of Electrical and Computer Engineering, Kulliyyah of Engineering, International Islamic University Malaysia, Jalan Gombak, 53100 Kuala Lumpur, Malaysia

**Corresponding author: sitiyusoff@iium.edu.my*

(Received: 12th May 2022; Accepted: 9th August 2022; Published on-line: 4th January 2023)

ABSTRACT: In the age of technology, microgrids have become well known because of their capability to back up the grid when an unpleasant event is about to occur or during power disruptions, at any time. However, the microgrid will not function well during power disruptions if the controller does not respond fast enough and the BESS will be affected. Many types of controllers can be used for microgrid systems. The controllers may take the form of Maximum Power Point Tracking (MPPT) Controller, Proportional Integral Derivative (PID) Controller, and Model Predictive Controller (MPC). Each of the controllers stated has its functions for the microgrid. However, two controllers that must be considered are PID and MPC. Both controllers will be compared based on their efficiency results which can be obtained through simulations by observing both graphs in charging and discharging states. Most researchers implied that MPC is better than PID because of several factors such as MPC is more robust and stable because of its complexity. Other than that, MPC can handle more inputs and outputs than PID which can cater to one input and output only. Although MPC has many benefits over the PID, still it is not ideal due to its complex algorithm. This work proposed an algorithm of simulations for the MPC to operate to get the best output for microgrid and BESS and compare the performance of MPC with PID. Using Simulink and MATLAB as the main simulation software is a very ideal way to simulate the dynamic performance of MPC. Furthermore, with Simulink, unpredictable variables such as Renewable Energy (RE) sources input and loads demands that are related to MPC can be measured easily. The algorithm of MPC is a cost function. Then the performance of the MPC is calculated using Fast-Fourier Transform (FFT) and Total Harmonic Distortion (THD). Lower THD means a higher power factor, this results in higher efficiency. This paper recorded THD of 9.57% and 12.77% in charging states and 16.51% and 18.15% in discharging states of MPC. Besides, PID recorded THD of 22.10% and 29.73% in charging states and 84.29% and 85.58% in discharging states. All of the recorded THD is below 25% in MPC and it shows a good efficiency while PID's THD is above 25% shows its inefficiency.

ABSTRAK: Pada zaman teknologi, mikrogrid menjadi terkenal kerana keupayaannya untuk menjana kuasa grid apabila kejadian yang tidak menyenangkan bakal berlaku atau ketika terjadinya gangguan kuasa, pada bila-bila masa. Walau bagaimanapun, mikrogrid tidak dapat berfungsi dengan baik semasa gangguan kuasa jika alat kawalan tidak bertindak balas dengan cukup pantas dan BESS akan terjejas. Banyak alat kawalan (pengawal) boleh digunakan bagi keseluruhan sistem mikrogrid. Setiap pengawal adalah berbeza seperti Pengawal Penjejakan Titik Kuasa Maksimum (MPPT), Pengawal Berkadar Terbitan Kamilan (PID) dan Pengawal Model Ramalan (MPC). Setiap pengawal yang dinyatakan mempunyai fungsinya yang tersendiri bagi mikrogrid. Walau bagaimanapun, dua pengawal yang perlu dipertimbangkan adalah PID dan MPC. Kedua-dua pengawal ini akan dibandingkan berdasarkan keputusan kecekapan yang boleh didapati melalui simulasi dengan memerhati kedua-dua graf pada keadaan pengecasan dan nyahcas. Ramai penyelidik menganggap bahawa MPC adalah lebih baik berbanding PID kerana beberapa faktor seperti MPC lebih teguh dan stabil kerana kerumitannya. Selain itu, MPC dapat mengendalikan lebih banyak input dan output berbanding PID yang hanya dapat menyediakan satu input dan output sahaja. Walaupun MPC mempunyai banyak faedah berbanding PID, ianya masih tidak sesuai kerana algoritma yang kompleks. Kajian ini mencadangkan algoritma simulasi bagi MPC beroperasi mendapatkan output terbaik untuk mikrogrid dan BESS dan membandingkan prestasi MPC dengan PID. Perisian simulasi utama yang sangat ideal bagi mensimulasi prestasi dinamik MPC adalah dengan menggunakan Simulink dan MATLAB. Tambahan, dengan Simulink, pembolehubah yang tidak terjangka seperti sumber Tenaga Boleh Diperbaharui (RE) dan permintaan beban yang berkaitan MPC boleh diukur dengan mudah. Algoritma MPC adalah satu fungsi kos. Kemudian prestasi MPC dikira menggunakan Penjelmaan Fourier Pantas (FFT) dan Total Pengherotan Harmonik (THD). THD yang lebih rendah bermakna faktor kuasa meningkat, ini menghasilkan kecekapan yang lebih tinggi. Kajian ini mencatatkan THD sebanyak 9.57% dan 12.77% dalam keadaan mengecas dan 16.51% dan 18.15% dalam keadaan nyahcas oleh MPC. Selain itu, PID mencatatkan THD sebanyak 22.10% dan 29.73% dalam keadaan mengecas dan 84.29% dan 85.58% dalam keadaan nyahcas. Semua THD yang direkodkan adalah di bawah 25% bagi MPC dan ia menunjukkan kecekapan yang baik manakala THD bagi PID adalah melebihi 25% menunjukkan ketidakcekapan.

KEYWORDS: *maximum power point tracker (MPPT) controller; proportional integral derivative (PID) controller; model predictive controller (MPC); battery energy storage system (BESS)*

1. INTRODUCTION

Today, many countries have been slowly exchanging the generation of electricity from non-renewable energy to renewable energy such as biomass, solar, and wind energy. In Malaysia, the government has announced to increase power generation using renewable resources to 20% from 2%. In [1], it stated that Malaysia has higher opportunities in solar power generation than other types of renewable energy. This is because Malaysia is located near the equator where the amount of sun irradiation is high [1]. The photovoltaic (PV) system is applied to harvest solar power.

The PV system is a power system that generates electricity directly from sunlight using PV cells. When sunlight strikes a PV cell's surface, it transforms light energy into electrical energy using the principle of forming a potential energy difference between photons and electrons. The combination of PV cells is called PV panel and the combination of PV panels is called PV module/array as can be seen in Fig. 1 [2], [3]. PV modules that are connected to the utility grid are called grid-connected PV (GCPV) systems. Other than that, a PV module that is not linked to the utility grid is called a stand-alone PV system. PV systems consist of several components to meet the goal of each system [4]. [3] said that GCPV and stand-alone PV have different components and configurations, thus both have different performances. GCPVs excess electricity generated from the solar module can be sold to the grid, hence it does not require a battery in the system. However, a stand-alone PV needs batteries to keep excess electricity generated by the solar panels, and this type of PV system is usually for the consumer that lives far from the city [3]. Figure 2 illustrates the types of PV systems in a hierarchy chart [4]. A single GCPV system usually consists of power conditioning units, inverters, solar panels, and grid connection equipment. Most GCPV systems are related to the microgrid.

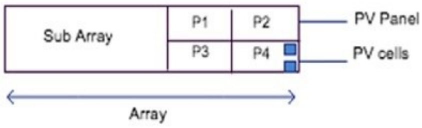

Fig. 1: The illustration of PV cell, PV panel, and PV array [3].

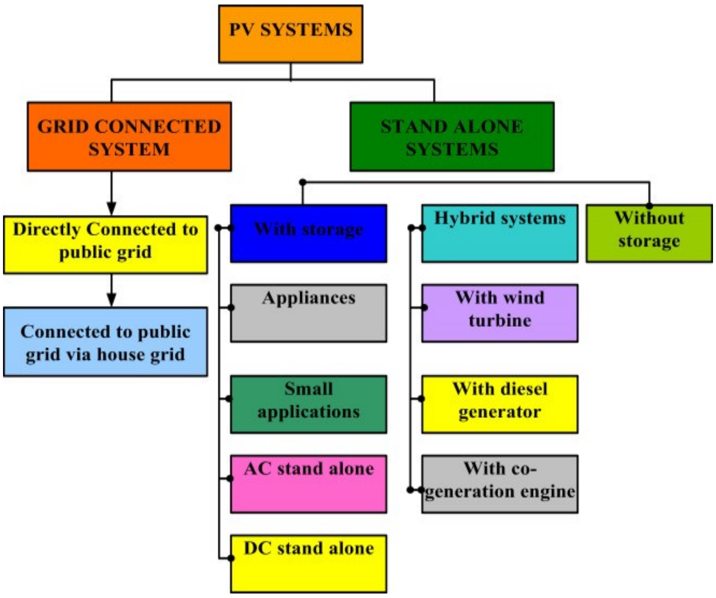

Fig. 2: The types of PV systems [4].

The microgrid is a type of electric power distribution system that consists of distributed energy resources (DER), interconnected loads, and various types of the consumer of electrical devices [5], [6]. Microgrids are not only able to supply small electrical devices but are also able to supply the full power needed by the consumer [7]. Moreover, the microgrid runs in a grid-connected mode through the subsidiary station transformer. When the grid is unable to operate, the microgrid will provide enough power to supply electricity to the end-user and remain operational as an autonomous (island-mode) entity [8]. However, for the microgrid to run smoothly, a high level of maintenance is needed. In this regard, a distributed energy storage system (ESS), distributed generation (DG) power, interlinking converter (IC), and controller are needed to develop system reliability [9]. A common microgrid structure including loads and distributed energy resource units is illustrated in Fig. 3 [10].

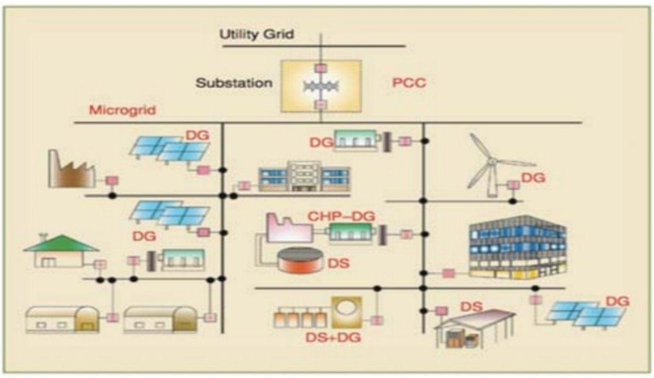

Fig. 3: Common microgrid structure integrating DERs and loads [10].

Nowadays, there are several common types of microgrids such as campus/institutional microgrids [11], military microgrids [12], and commercial and industrial microgrids [13] most of which have an architecture with AC-DC power systems or hybrid AC-DC microgrids [14] as shown in Fig. 4.

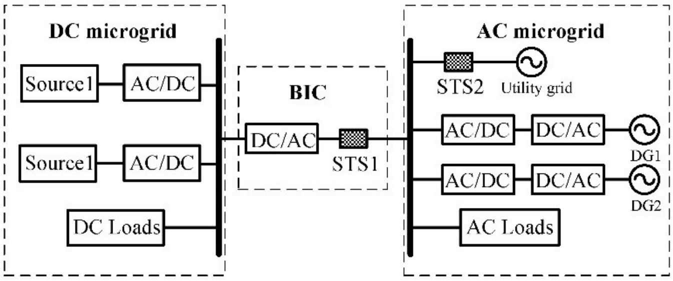

Fig. 4: Common microgrid structure integrating DERs and loads [14].

The hybrid microgrid is commercially used because of its efficiency that can easily change the architecture of the microgrid from islanded to grid-connected mode and reduce the conversion steps of AC power to DC power and vice versa [9]. Although it is a good power system, AC-DC architecture still has its drawback due to the interface power electronic converter [15]. This will disrupt the quality of power supply for both AC and DC networks.

The effect of the quality is majorly based on the controller and BESS. A microgrid controller is equipment that allows initializing of a microgrid by controlling DER and loads in an electrical system to maintain voltage and frequency in an optimized condition [16]. While BESS are rechargeable battery systems used for storing electric charges and providing them to homes or businesses. They are very efficient in handling difficult tasks, such as peak shaving and load shifting [17] and maintaining the reliability of the system (intake excess power generation or supply power to loads during power shortage) [18]. Both are important in the microgrid to maintain the quality of power which, if not handled properly, would create output power fluctuations [19], [20].

Several controllers are commonly used in microgrids such as the PID controller, the MPPT controller, and the MPC [21], [22]. However, the most used controller is the MPC. [23] states that the MPC has a better performance than the PID in terms of vehicle control and the enhanced MPC has the fastest response in the drone's movement control [24]. Besides, [25] remarks that the MPC is more robust and stable because of its complexity. Paper [26] explains that the MPC can handle more inputs whereas the PID can only cater to one input and output. MPC is a control technology that makes use of past information and model prediction to predict the process output which is the characteristic of a system's arbitrary number of sampling steps into a timeline view based on a set of the reference control signal and predicted variable [27], [28]. According to Panda and Arnab's [18] research, MPC is used to control the AC grid side inverters and DC grid side converters. This approach is to enhance the power quality and reliability of the grid. Other than that, MPC is used to improve cost optimization, single-period horizon prediction, and monitoring output voltage. Furthermore, the use of MPC has been increasing in the microgrid where it acts as the controller. MPC has also been applied to many other industrial-related applications due to its efficiency [28-30]. The reason why MPC is preferable to be implemented in a microgrid is that the microgrid depends on RES (solar and wind energy) and BESS which cause uncertainties in load demand during the day, night, and unpleasant weather [31]. Babayomi et al. [32] expressed that the MPC can cope with complex and dynamic systems with multiple inputs and outputs and systems with uncertainties and disturbances and even reduce the computational operation [33]. The microgrid is therefore an optimal control strategy [27], as shown in Fig. 5.

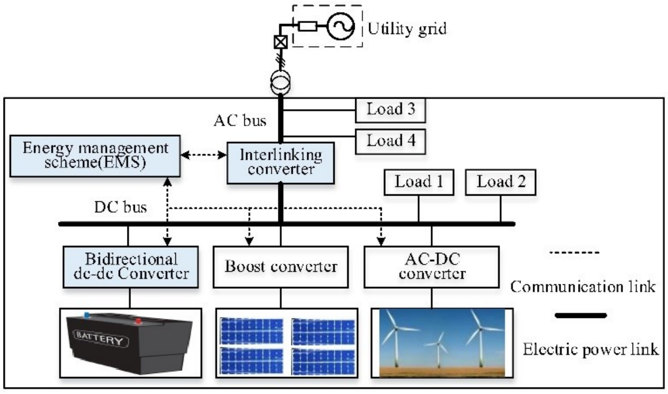

Fig. 5: Microgrid with multiple energy sources and converters [27].

Based on the figure described by Shan et al. [27], there are two parts critically involved: the AC sub-grid with AC loads and the DC sub-grid with DC loads. The AC and DC buses are connected to each other via bidirectional AC-DC IC. In this system, predictive voltage and power (MPVP) and model predictive current and power (MPCP) control models are both utilized. While MPVP is used to regulate the AC-DC IC., MPCP is employed to manage the bidirectional DC-DC converter in BESS. A DC-DC converter connects BESS to the DC bus. Both controls are applied to regulate the DC-DC converter and the AC-DC converter for reliable DC and AC bus voltage and smooth RE outputs.

Other than that, BESS, with good performance while charging and discharging, is needed for microgrid control. Yilmaz et al. [29] stated that the overall performance of BESS is solely dependent on control performance, MPC, which needs a predictive variable. With the aid of MPC, BESS's role in a microgrid is to make up for forecasting errors and lower operating costs brought on by RES and load demand. Additionally, MPC controls the power consumed or supplied by BESS, which is necessary to obtain the predictive variables. To maintain the power balance within microgrids, the BESS should discharge and charge accordingly [27].

In this paper, the simulation of MPC in a microgrid with BESS is done in MATLAB/SIMULINK. A model in the MATLAB/SIMULINK is made and the performance of MPC is tested using Fast-Fourier Transform (FFT).

2. ANALYSIS OF MICROGRID COMPONENT

Concerning BESS, one aspect that must be compliant before using it in any system is the state of charge (SoC). SoC is the proportion of a battery's nominal capacity to its capacity at a time. SoC detects the battery capacity, 100% denotes a full charge, while 0% denotes an empty battery [34]. Mu and Xiong [35] give the equation for the SoC ratio, as shown in Eq. (1):

$$SoC_t = SoC_0 - \int_0^t \eta_i I_L, \tau \, d\tau / C_a \quad (1)$$

where

SoC_t = present SoC

SoC_0 = SoC initial value

I_L = instantaneous load current

n_i = Coulomb efficiency

C_a = present maximum available capacity

The output of a PV generator is solely dependent on solar irradiance. If the weather is unpredictable with cloudy or rainy conditions, the PV output will surely fluctuate. Qian et al. [36] stated that, the result of the fluctuation will affect the power quality of the PV generator that is connected to BESS. The quality of the PV can be evaluated by the equation of Performance Ratio (PR) as informed in IEC 61724 as "Photovoltaic system performance monitoring: guidelines for measurement, data exchange, and analysis" [37]. The equation for PR is shown in Eq. (2):

$$PR = \frac{E_{AC}}{P^*_{MPP,NOM}\frac{G_{\Delta T}}{G^*}} \tag{2}$$

where

PR = Performance Ratio

E_{AC} = energy sent to the grid efficiently

$P^*_{MPP,NOM}$ = the product of the nameplate Standard Test Condition (STC) power and the quantity of PV modules in the system.

$G_{\Delta T}$ = annual in-plane irradiation in a certain period

G^* = in-plane effective irradiance

Noted that STC is also known as rated power PV generator.

In the meantime, managing SoC is very important for BESS effectiveness and BESS sizing capacity. Other than that, controlling SoC can reduce the violation of the BESS's SoC operating range during renewable integration continuously. SoC management of BESS is very important whenever PV and BESS are increasing rapidly. Other than that, the BESS that is connected to MPC needs predictive variables. The predictive variables of BESSs are set on the discrete-time model of converters.

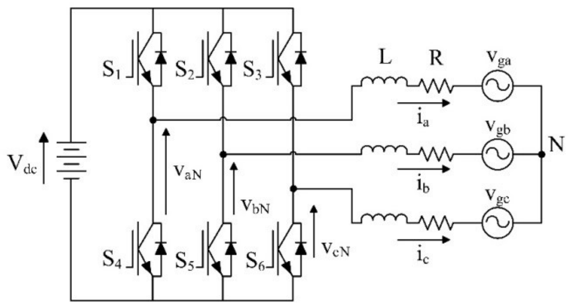

Fig. 6: Configuration of BESS.

From Fig. 6, [38] provided three equations that characterized the voltage Vg of a three-phase AC power supply, using filter inductance L and resistance R.

$$V_{aN} = L\frac{di_a}{dt} + Ri_a + V_{ga} \tag{3}$$

$$V_{bN} = L\frac{di_b}{dt} + Ri_b + V_{gb} \tag{4}$$

$$V_{cN} = L\frac{di_c}{dt} + Ri_c + V_{gc} \tag{5}$$

Table 1: Switching states and voltage vectors

x	*S_a*	*S_b*	*S_c*	*Voltage Vectors, v*
1	0	0	0	$v_0 = 0$
2	1	0	0	$v_1 = \frac{2}{3}V_{dc}$
3	1	1	0	$v_2 = \frac{1}{3}V_{dc} + j\frac{\sqrt{3}}{3}V_{dc}$
4	0	1	0	$v_3 = -\frac{1}{3}V_{dc} + j\frac{\sqrt{3}}{3}V_{dc}$
5	0	1	1	$v_4 = -\frac{2}{3}V_{dc}$
6	0	0	1	$v_5 = -\frac{1}{3}V_{dc} - j\frac{\sqrt{3}}{3}V_{dc}$
7	0	1	1	$v_6 = \frac{1}{3}V_{dc} - j\frac{\sqrt{3}}{3}V_{dc}$
8	1	1	1	$v_7 = 0$

$$s(t) = \begin{cases} 1, discharge\ mode \\ 0, charging\ mode \end{cases} \tag{6}$$

$$i^p(k+1) = \left(1 - \frac{RT_s}{L}\right)I(k) + \frac{T_s}{L}(v(k) - v_g(k)) \tag{7}$$

$$P^p(k+1) = 1.5Re\{i^{-p}(k+1)v_g^m(k)\} \tag{8}$$

$$Q^p(k+1) = 1.5Im\{i^{-p}(k+1)v_g^m(k)\} \tag{9}$$

The derivation of Eq. (3) to Eq. (5) through space vector, switching states and voltage vectors (Table1) will give Eq. (6) which is the future current at the sampling instant k + 1. From Eq. (6), i(k) and vg(k) are the three-phase currents, and voltage of BESS measured at sampling instant k with sampling time Ts. They [38] also assumed that the voltage at sampling instant k + 1 equals to measured grid voltage at kth sampling instant (vg(k + 1) = vg(k)). As a result, the predicted instantaneous real and predictive powers are Eq. (7) and Eq. (8). Eq. (6) to Eq. (8) show that the predictive current and power rely on the system model, converter, and filter parameters. In the conclusion, inaccuracy in predictive variables will occur if there are any changes in the model parameters.

Furthermore, according to Fig. 7, there are two states of BESS, which are charging and discharging. The illustration proposed by Shan et al. [27] demonstrates the current flow between BESS, RES and the rest of the microgrid (ROM).

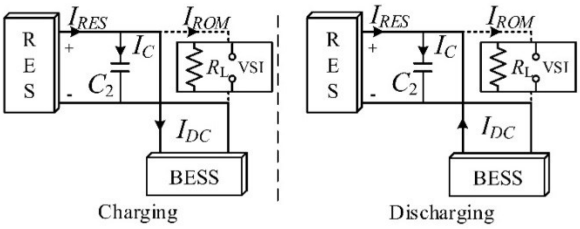

Fig. 7: Illustration of 2 states within the BESS system [27].

In order to charge or discharge the BESS, the cost function should be considered. So, they [27] proposed a cost function Eq. (9) to optimize BESS current.

$$J_c = |I_B^* - I_B(K+1)| \tag{10}$$

$$s.tSOC_{min} \leq SOC \leq SOC_{min}, I_B \leq |I_{B\_rated}|$$

$$i_L^* * I_B^* \frac{(v_{dc}{}^*)^2}{R*vb(k)} \tag{11}$$

- I_B = Battery current.
- I_B* = Battery current set with electricity price in grid-connected operation.

From Fig. 7, the relationship between the currents can be obtained using Kirchoff's current law (KCL) in the form of an equation.

$$I_{DC} = I_{RES} - I_C - I_{ROM} \tag{12}$$

- I_{DC} = current supplied/used by BESS.
- I_{RES} = current from RES.
- I_C = current flow of DC side capacitor.
- I_{ROM} = current flow into DC loads and inverter.

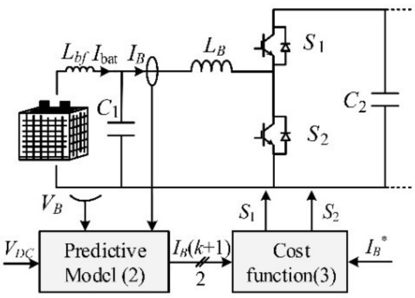

Fig. 8: Operation of BESS system in grid-connected microgrid [27].

In the meantime, proposed Fig. 8 by [27], showed the block diagram of the MPC strategy. They [27] said that, to control the charging and discharging current of BESS, the voltage V_B, current I_B and DC voltage V_{DC} are needed to predict the battery current $I_B(k+1)$.

A simple but effective MPC strategy for the Bidirectional converter is proposed, to improve its dynamic performance. The advantage of the presented strategy is that the problem is formulated in a way that only a one-step prediction horizon is needed to control

https://doi.org/10.31436/iiumej.v24i1.2435

the converter. Therefore, a proper cost function elaborated in terms of the inductor current is proposed. The MPC working principle applied to the Bidirectional converter under study is illustrated in Fig. 9. Tables 2 to 4 listed the required parameters for the simulations of model predictive control in Simulink.

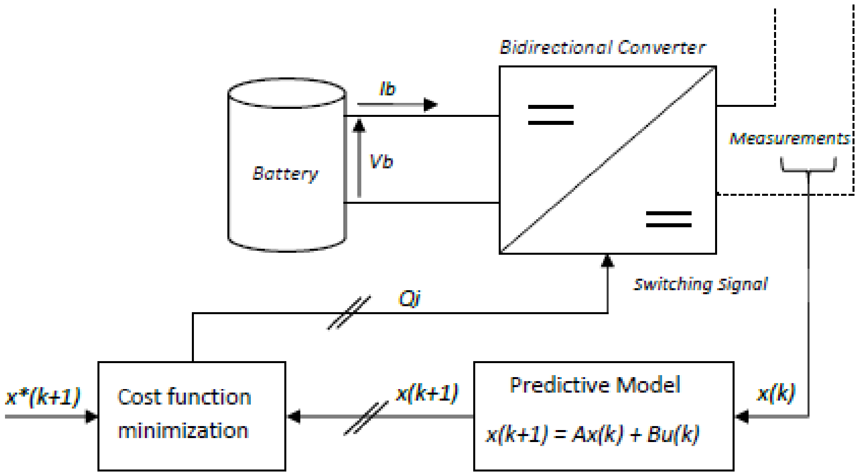

Fig. 9: Model Predictive Controller block diagram.

Table 2: Generic battery model parameters

Parameters	Formula	Value
Constant Battery Current, Ib		1.3 A
Rated Battery Capacity, Qo		6.5 Ah
Internal Resistance, Rb		2 $m\Omega$
Fully Charged Voltage, Vfull		1.39 V
Exponential Voltage, Vexp		1.28 V
Nominal Voltage, Vnom		1.18 V
Exponential Capacity, Qexp	$Qexp = Ib * 1$	1.3 A
Nominal Capacity, Qnom		6.25 Ah
Exponential Zone Amplitude, A	$A = Vfull - Vexp$	0.11
Exponential Zone Time Constant Inverse, B	$B = 3/Qexp$	2.3077
Polarization Voltage, K	$K = (Vfull - Vnom + A*(exp(-B*Qnom)-1))*(Qo - Qnom)/Qnom$	0.004
Battery Constant Voltage, Eo	$Eo = Vfull + K + Rb * Ib - A$	1.28

Table 3: Boost Converter Model parameters

Parameters	Value
PV Nominal Temperature	25℃
Irradiance	0 & 1000kW/m^2
Power GUI	Discrete
PV Capacitance, C_PV	100 µF
PV Inductance, L_PV	5mH
Boost Capacitance, C_Boost	3300 µF
Load	5Ω

https://doi.org/10.31436/iiumej.v24i1.2435

Table 4: Bidirectional Converter Model parameters

Parameters	Formula	Value
Battery Type		Nickel-Metal-Hydride (NiMH)
Battery Capacitance, C_Battery, Cb		700µF
Battery Inductance, L_Battery, Lb		33mH
Output Capacitance, C2		2mF
Load, R		5Ω
Measured Disturbance Signal, vb		6V
Steady State Duty Cycle, S		0.5
Steady State DC Bus Voltage, vdc	*vb/(1-S)*	12V
Steady State Inductor Current, iL	*vdc/((1-S) *R)*	4.8A
DC Reference Voltage, vdcref	*vb/(1-S)*	12V

3. RESULT AND DISCUSSION

The proposed MPC strategy was implemented in the MATLAB programming interface, together with the battery and the bidirectional models, to simulate the performance of the control unit. The bidirectional model is a model that flows in two directions, forward and backward, thus connecting the battery with the bidirectional converter. Figure 10 shows the microgrid model with MPC control in Simulink.

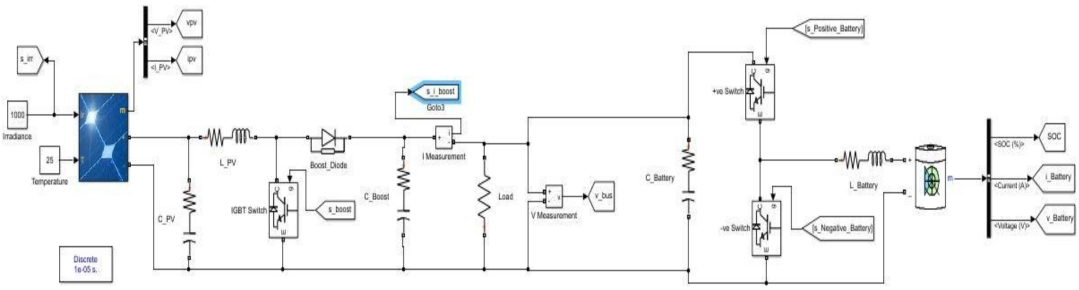

Fig. 10: The microgrid model with MPC in Simulink.

The simulation results for a start-up are shown in Fig. 9, using parameters given in Table 2 - 4. The purpose of the simulation is to simulate the performance of the control unit and optimize it by predicting the future behavior of controlled variables using MPC. However, the main purpose of using MPC is to reimburse the power difference between load and PV generation, during constant DC bus voltage [27].

Two states have been simulated, which are the charging state of battery and discharging state of battery. In Fig. 9, the output voltage (vdc) reaches its reference value in about 50 ms, the battery current (iL) is negative and below its nominal current and the DC bus voltage is constant at 6V (vb). This result is dependent and interconnected with Fig. 9, which shows the PV power generation is higher than the load demand while the battery is charged from it.

However, in Fig. 11, the results show the battery current is reaching its nominal current, while the output voltage results remain the same. For this scenario, it is shown that the load is powered by the battery, because in Fig. 14, the result shows the SoC of the battery is decreasing.

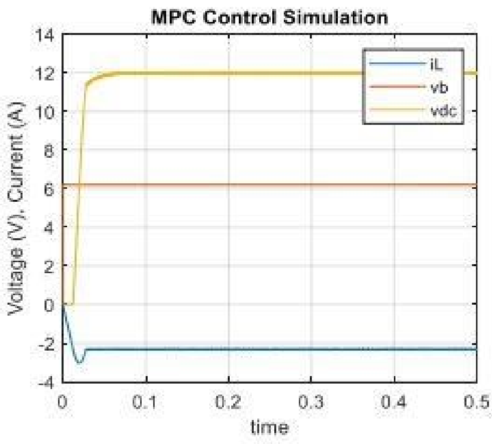

Fig. 11: MPC Control Simulation Results for Charging State.

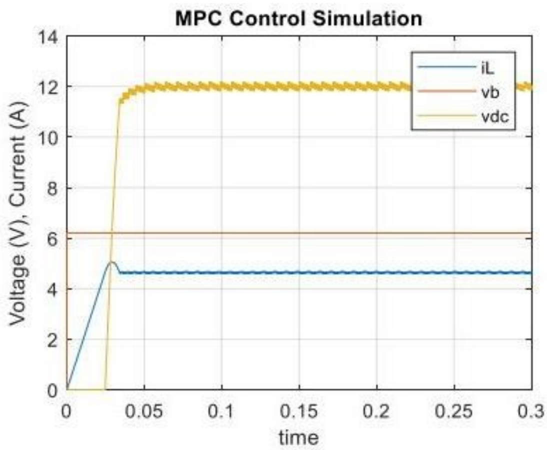

Fig. 12: MPC Control Simulation Results for Discharging State.

The performance of the suggested power management can be verified through simulation carried out using MATLAB programming interface based on Table 2 parameters. However, in this simulation, only charging and discharging will be considered as they are common situations for microgrids. Charging refers to daytime activity when the irradiance is high (1000 kW/m^2) while discharging refers to night-time activity when there is no irradiance (0 kW/m^2). The following figures illustrate the charging and discharging of the battery for different cases.

Figure 13 illustrates the charging state where there is excess power produced by the PV panel while the battery is not fully charged. This causes the power produced to charge the battery. For this case, SOC of the battery is initially at 60%, which then charges until 100% if there is irradiance for the time period. When the battery is fully charged, the MPPT controller will alert the PV to stop receiving power to avoid overcharge.

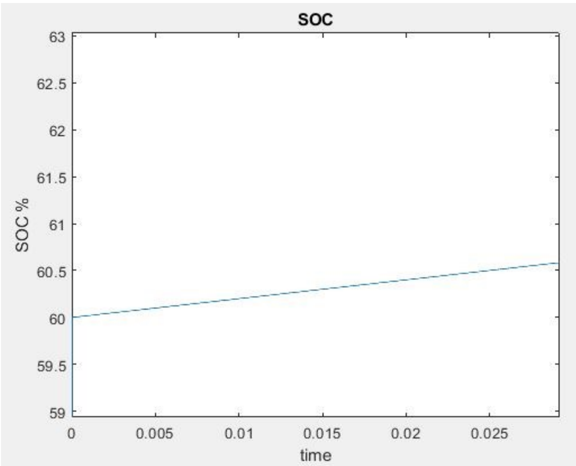

Fig. 13: MPC SOC Simulation Results for Charging State.

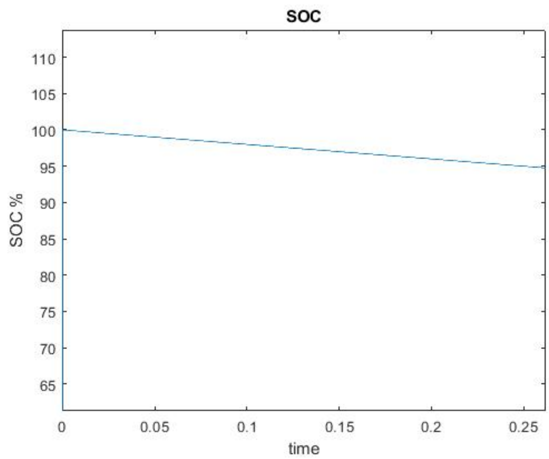

Fig. 14: MPC SOC Simulation Results for Discharging State.

Figure 14 illustrates the discharging state where there is no power produced from the PV panel and the load demand is supplied by the battery. For this case, the SOC of the battery is at 100% (fully charged) and it will continue to decrease until the load demand is supplied from the PV system.

The performance of the MPC can be shown and calculated by using FFT analysis. FFT analysis measures power supply or generator's output quality. The analysis aims to make sure the value of THD is maintained as low as possible. Lower THD means a higher power factor, which results in higher efficiency [39]. The acceptable THD value for generators is below 25%, while the best THD value for generators is below 10%.

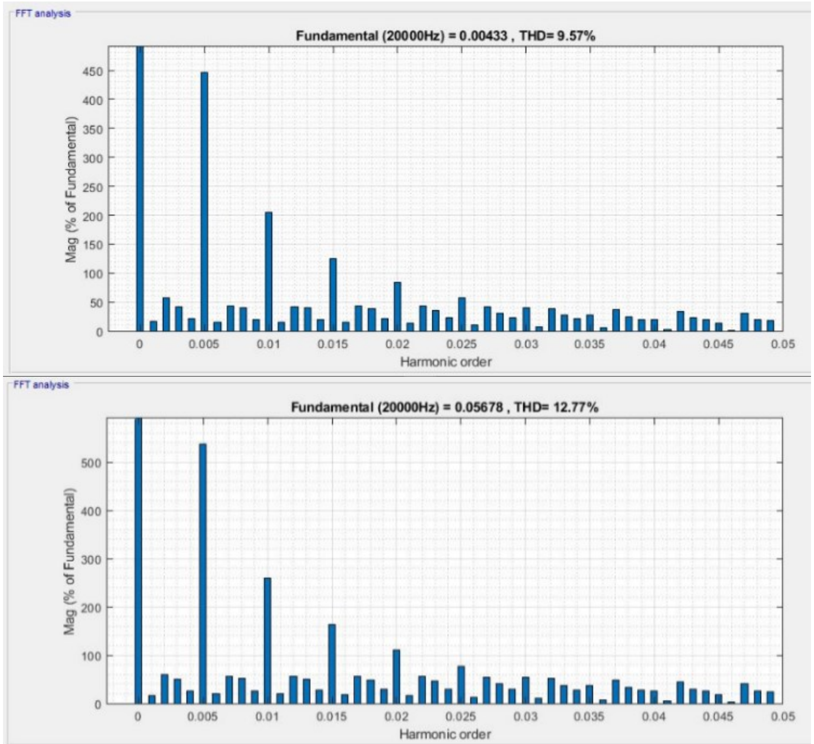

Fig. 15: MPC Charging voltage (above) and current (below) for FFT analysis.

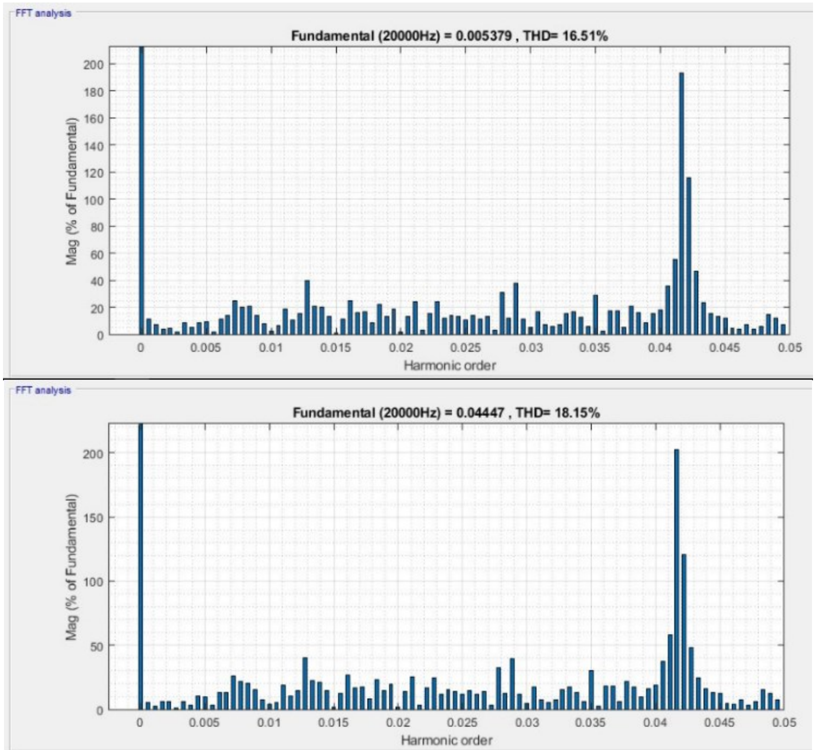

Fig. 16: MPC Discharging voltage (above) and current (below) for FFT analysis.

Based on Table 5 and according to [24], the THD value for both states are considered acceptable which is below 25% for the MPC. This proves that the generators are working efficiently when in a 20 kHz sampling rate.

Table 5: THD Value for Charging and Discharging States

Charging State	Output State	THD (MPC)
Charging	Voltage Output	9.57%
Charging	Current Output	12.77%
Discharging	Voltage Output	16.51%
Discharging	Current Output	18.15%

To compare the efficiency of MPC and PID, the simulation using PID has been done. Figures 17 and 18 show the charging and discharging voltage and current for FFT analysis. Table 6 compares the THD of MPC and PID. All of MPC's THD are acceptable, however, PID control is only stable when the control system is operating in charging state whereas in discharging state, the THD value is not acceptable and is above 25%. Thus, it can be seen that MPC is better in performance than PID.

Table 6: THD Value for Charging and Discharging States

Charging State	Output State	THD (MPC)	THD (PID)
Charging	Voltage Output	9.57%	22.10%
Charging	Current Output	12.77%	29.73%
Discharging	Voltage Output	16.51%	84.29%
Discharging	Current Output	18.15%	85.58%

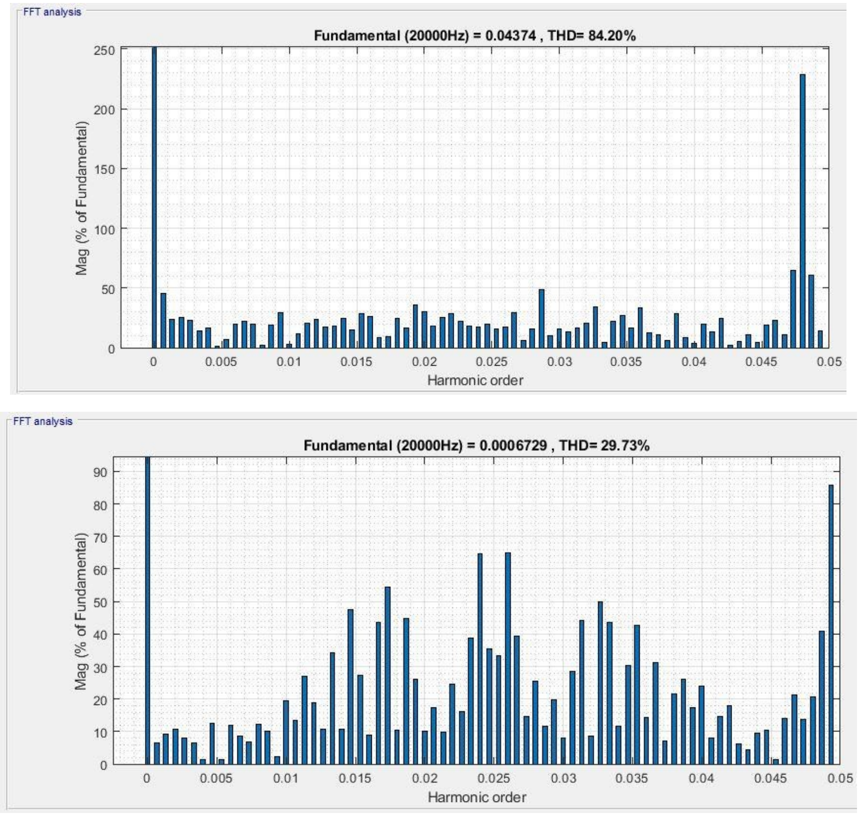

Fig. 17: PID Charging voltage (above) and current (below) for FFT analysis.

https://doi.org/10.31436/iiumej.v24i1.2435

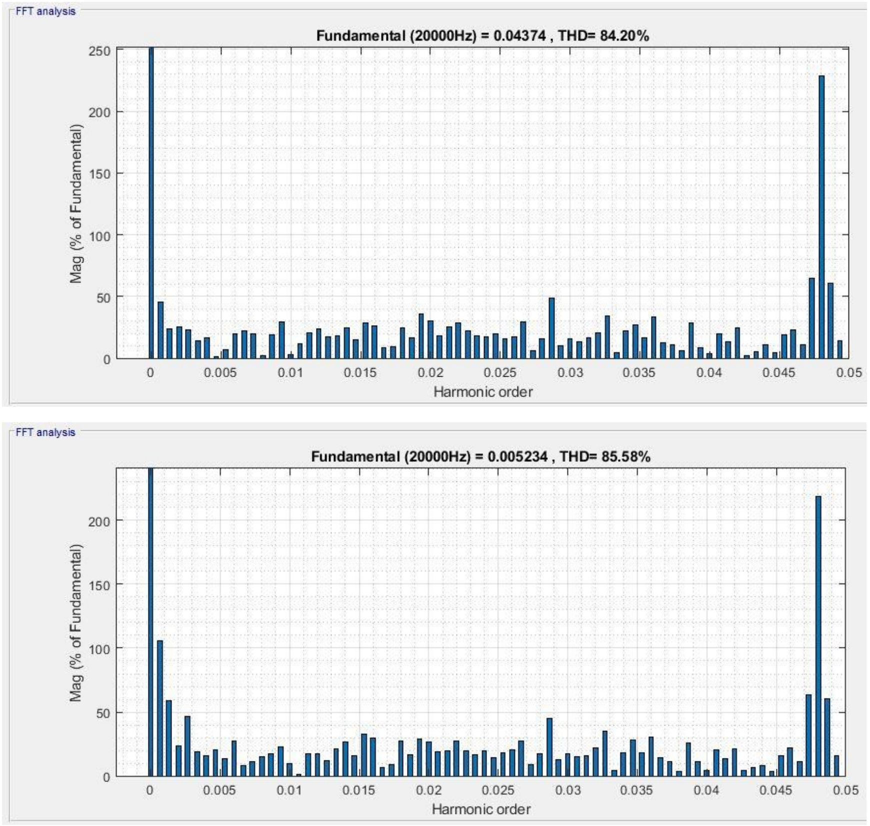

Fig. 18: PID Discharging voltage (above) and current (below) for FFT Analysis.

4. CONCLUSION

Microgrids have been used for many purposes every day. A microgrid is a self-sufficient energy system that consist of distributed generating units, loads, and control units. By using microgrids, one can save costs and reduce global warming. However, microgrids are not as simple as they seem. One of the basic elements of microgrids is its brain, aka its control unit(s). The control unit controls all the actions between the distributed generator and loads. Earlier, engineers used PID control as the control unit. However, PID control is not efficient in the case of unpredicted events that cause instantaneous disturbance to the microgrid. Later, when MPCs were introduced, they replaced all the PID control making MPCs the new brains in microgrids. MPCs gained favor because their algorithm can predict various outputs in the future with multiple inputs. This paper proposed an algorithm for the MPC using cost functions. To prove MPCs efficiency, this paper proposed to compare it with PID control. At the end of the experiment, it can be concluded that the MPC is better than PID control in terms of efficiency. In future work, other types of battery such as Li-ion and Li-Po, should be used. The battery type that was used in this simulation is nickel-metal hydride (Ni-MH) and its performance is not affected by changes in temperature. However, to get better MPC performance, batteries such as Li-ion and Li-Po are needed because the temperature will affect the performance of these batteries.

ACKNOWLEDGEMENT

This work was partially supported under IIUM-UMP-UITM Sustainable Research Collaboration Grant 2020 (SRCG) number SRCG20-049-0049.

REFERENCES

[1] Abdullah WSW, Osman M, Kadir MZAA, Verayiah R. (2019). The Potential and Status of Renewable Energy Development in Malaysia. Energies, 12: 2437. https://doi.org/10.3390/EN12122437

[2] Rakesh Tej Kumar K, Ramakrishna M, Durga Sukumar G. (2018). A review on PV cells and nanocomposite-coated PV systems. International Journal of Energy Research, 42(7): 2305-2319. https://doi.org/10.1002/ER.4002

[3] Usman Z, Tah J, Abanda H, Nche C. (2020). A Critical Appraisal of PV-Systems' Performance. Buildings, 10: 192. https://doi.org/10.3390/BUILDINGS10110192

[4] Koondhar MA, Laghari IA, Asfaw BM, Reji Kumar R, Lenin AH. (2022). Experimental and simulation-based comparative analysis of different parameters of PV module. Scientific African, 16: e01197. https://doi.org/10.1016/J.SCIAF.2022.E01197

[5] Kumar J, Agarwal A, Singh N. (2020). Design, operation and control of a vast DC microgrid for integration of renewable energy sources. Renewable Energy Focus, 34: 17-36. https://doi.org/10.1016/j.ref.2020.05.001.

[6] Badruhisham SH, Shahrin M, Hanifah A, Yusoff S H, Hasbullah NF, Yaacob M. (2021). Integration of Hybrid Biomass-Solar Photovoltaic- Wind turbine in Microgrid Application. 2021 8th International Conference on Computer and Communication Engineering (ICCCE), 87-92.

[7] Hirsch A, Parag Y, Guerrero J (2018). Microgrids: A review of technologies, key drivers, and outstanding issues. Renewable and Sustainable Energy Reviews, 90: 402-411. https://doi.org/10.1016/j.rser.2018.03.040

[8] Wu T, Ye F, Su Y, Wang Y, Riffat S. (2019). Coordinated control strategy of DC microgrid with hybrid energy storage system to smooth power output fluctuation. International Journal of Low-Carbon Technologies, 15: 46-54. https://doi.org/10.1093/ijlct/ctz056

[9] Ahmed M, Meegahapola L, Vahidnia A, Datta M. (2020). Stability and Control Aspects of Microgrid Architectures-A Comprehensive Review. IEEE Access, 8:144730-144766. https://doi.org/10.1109/ACCESS.2020.3014977

[10] Alhamrouni I, Hairullah MA, Omar NS, Salem M, Jusoh A, Sutikno T. (2019). Modelling and design of PID controller for voltage control of AC hybrid micro-grid. International Journal of Power Electronics and Drive Systems, 10: 151-159. https://doi.org/10.11591/ijpeds.v10n1.pp151-159

[11] Shahgholian G. (2021). A brief review on microgrids: Operation, applications, modeling, and control. https://doi.org/10.1002/2050-7038.12885

[12] Barry NG, Santoso S. (2021). Military Diesel Microgrids: Design, Operational Challenges, Energy Storage Integration. IEEE Power and Energy Society General Meeting, 2021-July. https://doi.org/10.1109/PESGM46819.2021.9637999

[13] Guarnieri M, Bovo A, Giovannelli A, Mattavelli P. (2018). A Real Multitechnology Microgrid in Venice: A Design Review. IEEE Industrial Electronics Magazine, 12(3) :19-31. https://doi.org/10.1109/MIE.2018.2855735

[14] Jiao J, Meng R, Guan Z, Ren C, Wang L, Zhang B. (2019). Grid-connected control strategy for bidirectional AC-DC interlinking converter in AC-DC hybrid microgrid. PEDG 2019 - 2019 IEEE 10th International Symposium on Power Electronics for Distributed Generation Systems. https://doi.org/10.1109/PEDG.2019.8807601

[15] Wei B, Han X, Wang P, Yu H, Li W, Guo L (2020). Temporally coordinated energy management for AC/DC hybrid microgrid considering dynamic conversion efficiency of bidirectional AC/DC converter. IEEE Access, 8: 70878–70889. https://doi.org/10.1109/ACCESS.2020.2985419

[16] Newaz S, Naiem-Ur-Rahman M (2020). Voltage Control of Single Phase Islanded Microgrid by Fuzzy Logic Controller for Different Loads. 2020 IEEE Region 10 Symposium, TENSYMP 2020, June, 1560-1563. https://doi.org/10.1109/TENSYMP50017.2020.9230686

[17] Alshehri J, Khalid M (2019). Power quality improvement in microgrids under critical disturbances using an intelligent decoupled control strategy based on battery energy storage system. IEEE Access, 7: 147314-147326. https://doi.org/10.1109/ACCESS.2019.2946265

[18] Kumar Panda S, Ghosh A. (n.d.). A Computational Analysis of Interfacing Converters with Advanced Control Methodologies for Microgrid Application. https://doi.org/10.1007/s40866-020-0077-x

[19] Chen X, Shi M, Zhou J, Chen Y, Zuo W, Wen J, He H. (2020). Distributed Cooperative Control of Multiple Hybrid Energy Storage Systems in a DC Microgrid Using Consensus Protocol. IEEE Transactions on Industrial Electronics, 67(3): 1968-1979. https://doi.org/10.1109/TIE.2019.2898606

[20] Hu J, Shan Y, Xu Y, Guerrero JM. (2019). A coordinated control of hybrid ac/dc microgrids with PV-wind-battery under variable generation and load conditions. International Journal of Electrical Power and Energy Systems, 104: 583-592. https://doi.org/10.1016/j.ijepes.2018.07.037

[21] Sarkar SK, Badal FR, Das SK. (2018). A comparative study of high performance robust PID controller for grid voltage control of islanded microgrid. International Journal of Dynamics and Control, 6(3):1207-1217. https://doi.org/10.1007/s40435-017-0364-0

[22] Sarkar SK, Badal FR, Das SK, Miao Y. (2018). Discrete time model predictive controller design for voltage control of an islanded microgrid. 3rd International Conference on Electrical Information and Communication Technology, EICT 2017, 2018-Janua (December), 1-6. https://doi.org/10.1109/EICT.2017.8275162

[23] Varma B, Swamy N, Mukherjee S. (2020). Trajectory Tracking of Autonomous Vehicles using Different Control Techniques (PID vs LQR vs MPC). Proceedings of the International Conference on Smart Technologies in Computing, Electrical and Electronics, ICSTCEE 2020, 84-89. https://doi.org/10.1109/ICSTCEE49637.2020.9276986

[24] Okulski M, Ławryńczuk M. (2022). How Much Energy Do We Need to Fly with Greater Agility? Energy Consumption and Performance of an Attitude Stabilization Controller in a Quadcopter Drone: A Modified MPC vs. PID. Energies, 15(4): 1380. https://doi.org/10.3390/EN15041380

[25] Haber R, Rossiter JA, Zabet K. (2016). An alternative for PID control: Predictive Functional Control - A tutorial. Proceedings of the American Control Conference, 2016-July, 6935-6940. https://doi.org/10.1109/ACC.2016.7526765

[26] Kozák Š. (2016). From PID to MPC: Control engineering methods development and applications. 2016 Cybernetics and Informatics, K and I 2016 - Proceedings of the 28th International Conference. https://doi.org/10.1109/CYBERI.2016.7438634

[27] Shan Y, Hu J, Chan KW, Fu Q, Guerrero JM (2019). Model Predictive Control of Bidirectional DC-DC Converters and AC/DC Interlinking Converters-A New Control Method for PV-Wind-Battery Microgrids. IEEE Transactions on Sustainable Energy, 10(4):1823-1833. https://doi.org/10.1109/TSTE.2018.2873390

[28] Chen M, Xu Z, Zhao J (2020). Triple-mode model predictive control using future target information. Processes, 8(1), 54. https://doi.org/10.3390/pr8010054

[29] Can Yilmaz U, Erdem Sezgin M, Gol M (n.d.). A Model Predictive Control for Microgrids Considering Battery Aging. https://doi.org/10.35833/MPCE.2018.000804.

[30] Yusoff SH, Midi NS, Khan S, Tohtayong M. (2017). Predictive control of AC/AC matrix converter. International Journal of Power Electronics and Drive Systems, 8(4): 1932-1942. https://doi.org/10.11591/ijpeds.v8i4.pp1932-1942

[31] Abbasi M, Dehkordi NM, Sadati N. (2020). Decentralized Model Predictive Voltage Control of Islanded DC Microgrids. 2020 11th Power Electronics, Drive Systems, and Technologies Conference, PEDSTC 2020. https://doi.org/10.1109/PEDSTC49159.2020.9088498

[32] Babayomi O, Li Y, Zhang Z, Kennel R, Kang J. (2020). Overview of Model Predictive Control of Converters for Islanded AC Microgrids. 2020 IEEE 9th International Power Electronics and Motion Control Conference, IPEMC 2020 ECCE Asia, 1023-1028.

https://doi.org/10.1109/IPEMC-ECCEAsia48364.2020.9368069

[33] Lee J, Chang HJ. (2018). Analysis of explicit model predictive control for path-following control. PLoS ONE, 13(3):1-19. https://doi.org/10.1371/journal.pone.0194110

[34] Zahid T, Xu K, Li W, Li C, Li H. (2018). State of charge estimation for electric vehicle power battery using advanced machine learning algorithm under diversified drive cycles. Energy, 162:871–882. https://doi.org/10.1016/J.ENERGY.2018.08.071

[35] Yao C, Ruan X, Wang X. (2010). Isolated buck-boost DC/DC converter for PV grid-connected system. IEEE International Symposium on Industrial Electronics, 889-894. https://doi.org/10.1109/ISIE.2010.5637196

[36] Long Q, Yu H, Xie F, Zeng W, Lukic S, Lu N, Lubkeman D. (2020). Microgrid power flow control with integrated battery management functions. IEEE Power and Energy Society General Meeting, August. https://doi.org/10.1109/PESGM41954.2020.9281437

[37] de la Parra I, Muñoz M, Lorenzo E, García M, Marcos J, Martínez-Moreno F. (2017). PV performance modelling: A review in the light of quality assurance for large PV plants. Renewable and Sustainable Energy Reviews, 78: 780-797. https://doi.org/10.1016/J.RSER.2017.04.080

[38] Nguyen T-T, Yoo H-J, Kim H-M. (2015). Application of Model Predictive Control to BESS for Microgrid Control. 8:8798-8813. https://doi.org/10.3390/en8088798

[39] Candidato Carnevale, G. (2019). Distributed model predictive control for power management in small-scale off-grid energy systems. http://webthesis.biblio.polito.it/id/eprint/11350

https://doi.org/10.31436/iiumej.v24i1.2435

Abbreviations

BESS	Battery energy storage system
MPPT	Maximum Power Point Tracker
PID	Proportional Integral Derivative
MPC	Model Predictive Controller
PV	Photovoltaic
GCPV	Grid-connected PV
ESS	Energy storage system
DG	Distributed generation
IC	Interlinking converter
DER	Distributed energy resources
AC-DC	Alternating current-direct current
RES	Renewable energy resources
MPCP	Model predictive current and power
MPVP	Model predictive voltage and power
FFT	Fast-Fourier Transform
THD	Total Harmonic Distortion
SoC	State of charge
PR	Performance ratio
STC	Standard Test Condition
KCL	Kirchoff's current law
Li-ion	Lithium-ion
Li-Po	Lithium polymer
Ni-MH	nickel-metal hydride

https://doi.org/10.31436/iiumej.v24i1.2508

ANALYTICAL MODEL OF SUBTHRESHOLD SWING FOR JUNCTIONLESS DOUBLE GATE MOSFET USING FERROELECTRIC NEGATIVE CAPACITANCE EFFECT

HAKKEE JUNG

Department of Electronic Engineering, College of Engineering, Kunsan National University, Gunsan, 54150 Republic of Korea

Corresponding author: hkjung@kunsan.ac.kr

(Received: 1st July 2022; Accepted: 10th November 2022; Published on-line: 4th January 2023)

ABSTRACT: An analytical Subthreshold Swing (SS) model is presented to observe the change in the SS when a stacked SiO_2-metal-ferroelectric structure is used as the oxide film of a JunctionLess Double Gate (JLDG) MOSFET. The SS of 60 mV/dec or less is essential to reduce power dissipation while maintaining transistor performance. If a ferroelectric material with Negative Capacitance (NC) effect is used, the SS can be reduced below 60 mV/dec. The analytical SS model of the ferroelectric NC FET presented to analyze this was in good agreement with the SS derived from the relation between the drain current and gate voltage, using 2D potential distribution. As results were derived from the analytical SS model, it was found that it is possible to obtain an SS of 60 mV/dec or less even at 15 nm channel length by adjusting the thicknesses of the silicon channel, SiO_2, and ferroelectric. In particular, the change in SS according to the ferroelectric thickness was saturated as the thickness of SiO_2 increased and was almost constant as the thickness of the silicon channel decreased.

ABSTRAK: Model Ayunan Subambang (SS) analitikal dibentangkan bagi melihat perubahan pada SS apabila struktur feroelektrik-logam-SiO_2 bertindan digunakan sebagai filem oksida bagi MOSFET Dua Get Tanpa Simpang (JLDG). SS 60 mV/dec atau kurang adalah penting bagi mengurangkan pelesapan kuasa sambil mengekalkan prestasi transistor. Jika bahan feroelektrik dengan kesan Kapasitans Negatif (NC) digunakan, SS dapat dikurangkan bawah 60 mV/dek. Model SS analitikal feroelektrik NC FET yang digunakan bagi kajian ini adalah sesuai dengan SS yang diperoleh daripada hubungan antara arus serapan dan voltan get, menggunakan edaran potensi 2D. Dapatan terbitan melalui model SS analitikal, mendapati bahawa adalah mungkin bagi mendapatkan SS pada 60 mV/dek atau kurang walaupun panjang laluan adalah 15 nm dengan melaraskan ketebalan saluran silikon, SiO_2, dan feroelektrik. Terutama apabila perubahan ketebalan feroelektrik SS adalah tepu ketika ketebalan SiO_2 meningkat, dan hampir malar apabila ketebalan saluran silikon berkurang.

KEYWORDS: *subthreshold swing; junctionless; ferroelectric; negative capacitance; double gate*

1. INTRODUCTION

In the competition for miniaturization of transistors, high-speed operation and low power consumption are essential. However, the recent scaling theory according to Moore's law is no longer followed by the power consumption generated during the switching process [1-3]. For low power consumption, the supply voltage must be reduced while maintaining high on-

https://doi.org/10.31436/iiumej.v24i1.2508

current. However, a decrease in the supply voltage requires a decrease in the threshold voltage, which causes an increase in parasitic current and static power dissipation [4]. A way to solve the trade-off relationship between power consumption and transistor performance is to reduce the Subthreshold Swing (SS). According to Boltzmann Tyranny [5], the body factor of conventional MOSFETs is greater than 1. A device developed to reduce the SS by making the body factor smaller than 1 is a Negative Capacitance (NC) FET [6-11]. NC FETs show the characteristics such as steep SS and high switching current ratio (I_{on}/I_{off}), and are known as good candidates for low power consumption [12-14]. The material used for the gate oxide film to fabricate the NC FET is a ferroelectric thin film. The NC effect occurs in the region where the ferroelectric polarization increases when the external electric field decreases. However, the NC effect is naturally unstable, and it is used in series with a general capacitor to solve this problem [15]. Therefore, instead of using only ferroelectric material as a gate oxide film, a stacked gate structure of a metal-ferroelectric-insulator-semiconductor (MFIS) structure and a metal-ferroelectric-metal-insulator-semiconductor (MFMIS) structure is used as shown in Fig. 1 [16-19]. Ultimately, controlling the charge in the channel of the FET using the ferroelectric polarization charge is the core of the NC FET. The organic-ferroelectric, lead (Pb) Zirconate titanate (PZT) of inorganic perovskite structure, $HfZrO_2$, etc. as ferroelectric materials, are used to show NC effect [20-23].

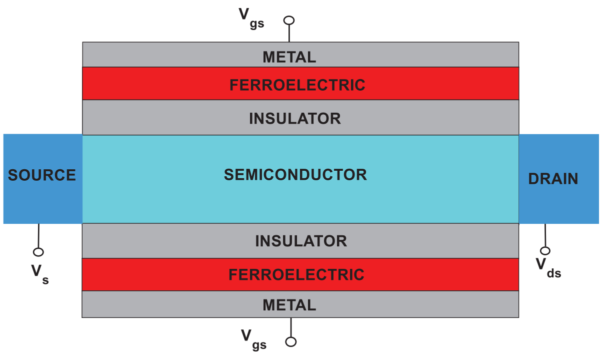

(a)

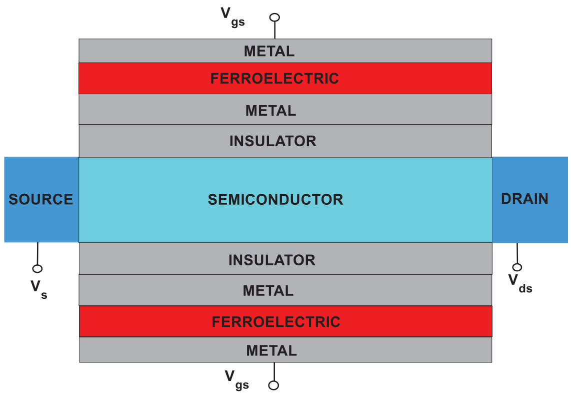

(b)

Fig. 1: (a) MFIS and (b) MFMIS structures of DG MOSFET.

In order to reduce the power consumption, the supply voltage must be reduced, but this obstacle must be overcome since the SS is limited to 60 mV/dec to room temperature. To this end, it is necessary to induce the necessary charge in the channel with a gate voltage as small as possible. This can be solved by NC voltage amplification occurring in NC FET using ferroelectric material, and at this time, a steep SS of 60 mV/dec or less can be induced. Rahi et al. [24] reviewed the advantage that the on-current of the NC FET is greater than that of the tunnel FET with a characteristic of 60 mV/dec or less. Alam et al. [25] only reviewed NC FETs with MFIS structure, and Tu et al. [26] presented ferroelectric NC FETs with SS <60 mV/dec. In this paper, we will use the MFMIS structure as the stacked gate structure.

This structure is widely used as a structure to solve the field nonuniformity problem that occurs in the MFIS structure, and Pahwa et al. [27] compared these two structures. In particular, we will observe the reduction effect of SS by using this structure for the gate oxide film of JunctionLess (JL) FET. The JLFET is a structure that can solve the difficulties of processing in the sub-10nm structure by configuring the doping of the source/drain and the channel with the same type and concentration [28-31]. Rassekh et al. [32] applied MFMIS structure to a JL Double-Gate (DG) FET and observed effects such as gate voltage amplification and DIBL, but did not present an analytical model of SS. Therefore, in this paper, we propose an analytical SS model of JLDG FET with MFMIS gate structure using the potential distribution model of JLDG FET and the relationship between the polarization and free energy of ferroelectric material according to Landau theory [33]. This result will be compared with the SS obtained from the current-voltage characteristic to prove the validity of this analytical SS model.

2. SUBTHRESHOLD SWING MODEL OF FERROELECTRIC NC FET

2.1 The Structure of Ferroelectric NC FET and I-V Characteristics

Figure 2 shows the cross-sectional view of the NC FET of the MFMIS structure used in this paper. The source/drain and channel were equally highly doped with N_d^+, and a symmetrical JL FET with the same upper and lower gates was used. In this paper, $N_d^+ = 10^{19}/cm^3$ was used. The voltage applied to METAL2, V_{gs2}, can be expressed as the sum of the voltage induced in METAL1, V_{gs1}, and the voltage across the ferroelectric material, V_f. The V_{gs2} is defined in Eq. (1)

$$V_{gs2} = V_{gs1} + V_f \ . \qquad (1)$$

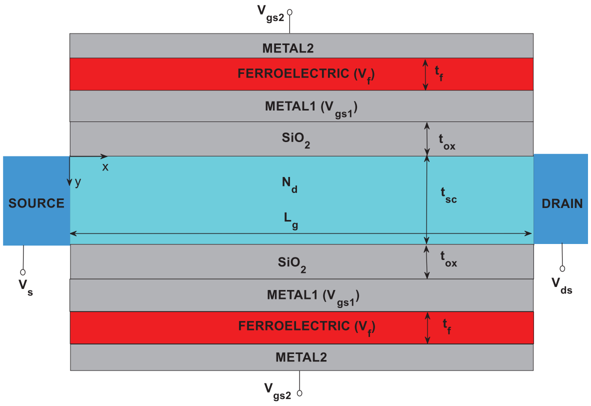

Fig. 2: Schematic diagram of a symmetric JLDG FET with ferroelectric material as the stacked gate oxides.

According to the ferroelectric charge density Q of [34], the voltage across the ferroelectric material, V_f can be expressed as in Eq. (2).

$$V_f = 2\alpha t_f Q + 4\beta t_f Q^3 + 6\gamma t_f Q^5 \qquad (2)$$

Here, the α, β, γ can be obtained from the *P-E* hysteresis curve between the ferroelectric Polarization, P and the Electric Field, E extracted from the ferroelectric capacitor. That is, using the Remanent Polarization, P_r and Coercive Field, E_c in the *P-E* hysteresis curve, it can be obtained as in Eq. (3) [35].

$$\alpha = -\frac{3\sqrt{3}}{2}\frac{E_c}{P_r}\ (m/F)$$
$$\beta = \frac{3\sqrt{3}}{2}\frac{E_c}{P_r^3}\ (m^5/F/C^2) \qquad (3)$$

In this paper, the α and β are found from $P_r = 17\,\mu C/cm^2$ and $E_c = 1.2\,MV/cm$, the experimental results of the HZO film, and $\gamma = 0$ [34]. In order to obtain V_f of Eq. (2), first the charge density of ferroelectric Q must be obtained. To find Q, the charge Q_{sc} in the channel by Rassekh's method [36] is as in Eq. (4).

$$Q_{sc} = -2C_{ox}(V_{gs1} - \Delta\phi_{ms} - \phi_s) \tag{4}$$

where $\Delta\phi_{ms}$ is the work function difference between the metal and the intrinsic semiconductor, ϕ_s is the surface potential, and C_{ox} is the capacitance according to the thickness of SiO_2 used as insulator. The following Poisson equation (5) is used to obtain ϕ_s in Eq. (4).

$$\partial^2\phi(x,y)/\partial x^2 + \partial^2\phi(x,y)/\partial y^2 = -qN_d/\varepsilon_{si} \tag{5}$$

In this case, the following four boundary conditions were used as shown in Eq. (6).

$$\begin{aligned}
&\phi(0,y) = V_s \\
&\phi(L_g,y) = V_s + V_d \\
&\phi(x,0) = V_{gs1} - V_{fb} + \frac{\varepsilon_{si}}{C_{ox}}\left.\frac{\partial\phi}{\partial y}\right|_{y=0} \\
&\phi(x,t_{si}) = V_{gs1} - V_{fb} + \frac{\varepsilon_{si}}{C_{ox}}\left.\frac{\partial\phi}{\partial y}\right|_{y=t_{sc}},
\end{aligned} \tag{6}$$

where ε_{si} is the dielectric constant of silicon, V_{fb} is the flat band voltage. Using Ding's expansion method [37], the potential distribution can be expressed as in Eq. (7).

$$\phi(x,y) = V_s + \frac{V_d x}{L_g} + \sum_{n=1}^{\infty} A_n(y)\sin\frac{n\pi x}{L_g}, \tag{7}$$

where

$$A_n(y) = C_n e^{k_n y} + D_n e^{-k_n y} - f_n/k_n$$

$$f_n = \begin{cases} -\dfrac{4qN_d}{n\pi\varepsilon_{si}}, & n = 1,3,5,\cdots \\ 0, & n = 2,4,6,\cdots \end{cases}$$

$$C_n = \frac{C_{ox}\left(f_n - G_n k_n^2\right)}{k_n^2\left[\left(C_{ox} + \varepsilon_{si}k_n\right)e^{k_n t_{sc}} + \left(C_{ox} - \varepsilon_{si}k_n\right)\right]}$$

$$D_n = C_n e^{k_n t_{sc}}$$

$$G_n = \begin{cases} \left(\dfrac{2}{n\pi}\right)\left[2\left(V_s - V_{gs1} + V_{fb}\right) + V_{ds}\right], & n = 1,3,5,\cdots \\ 0, & n = 2,4,6,\cdots \end{cases}$$

At this time, the surface potential at $y = 0$ is

$$\phi_s = \frac{V_{ds}}{L_g}x + \sum_{n=1}^{\infty}\left[C_n + D_n - f_n/k_n^2\right]\sin\frac{n\pi x}{L_g}\quad. \tag{8}$$

Substituting Eq. (8) into Eq. (4), the charge in the channel can be found as Eq. (9)

$$
\begin{aligned}
Q_{SC} &= -2C_{ox}(V_{gs1} - \Delta\phi_{ms} - \phi_s) \\
&= -2C_{ox}\left(V_{gs1} - \Delta\phi_{ms} - \frac{V_{ds}}{L_g}x - \sum_{n=1}^{\infty}\left[C_n + D_n - f_n / k_n^2 \right]\sin\frac{n\pi x}{L_g} \right)
\end{aligned} \tag{9}
$$

The charge Q in the ferroelectric can be obtained from Eq. (10) by calculating the integration of the total charge Q_{SC} existing in the channel over channel length.

$$
WL_g \times 2Q = -\int_0^{L_g} WQ_{SC}dx \tag{10}
$$

where W is the channel width. Then, the charge Q in ferroelectric is obtained as in Eq. (11).

$$
\begin{aligned}
Q &= -\frac{1}{2L_g}\int_0^{L_g} Q_{SC}dx \\
&= -\frac{1}{2L_g}\int_0^{L_g}\left\{ -2C_{ox}(V_{gs1} - \Delta\phi_{ms} - \frac{V_{ds}}{L_g}x - \sum_{n=1}^{\infty}\left[C_n + D_n - f_n / k_n^2 \right]\sin\frac{n\pi x}{L_g}) \right\}dx \\
&= \frac{C_{ox}}{L_g}\left[(V_{gs1} - \Delta\phi_{ms})L_g - \frac{V_{ds}}{2}L_g + \sum_{n=1}^{\infty}\left[C_n + D_n - f_n / k_n^2 \right]\left(\frac{L_g}{n\pi} \right)\cos\frac{n\pi x}{L_g}\Bigg|_0^{L_g} \right] . \\
&= C_{ox}\left[(V_{gs1} - \Delta\phi_{ms} - \frac{V_{ds}}{2}) + \sum_{n=1}^{\infty}\left[C_n + D_n - f_n / k_n^2 \right]\left(\frac{1}{n\pi} \right)\left[(-1)^n - 1 \right] \right]
\end{aligned} \tag{11}
$$

At this time, by substituting Eq. (11) into Eq. (2), V_f can be obtained.

In order to obtain the drain current for the corresponding gate voltage V_{gs2}, the drain current is obtained from the following Eq. (12) with Eq. (7).

$$
I_d = \frac{qn_i\mu_n WkT\left\{ 1 - \exp\left(\frac{-qV_d}{kT} \right) \right\}}{\int_0^{L_g}\frac{1}{\int_0^{t_{sc}}\exp\left(\frac{q\phi(x,y)}{kT} \right)dy}dx} \tag{12}
$$

where k, T , n_i , μ_n and W are Boltzmann's constant, absolute temperature, the intrinsic electron concentration, the electron mobility, and a channel width, respectively.

The relationship between drain current and gate voltage obtained using Eqs. (7) and (12) is shown with the thickness of the ferroelectric material, t_f as a parameter in Fig. 3. The red dotted line in Fig. 3 is the baseline where SS is 60 mV/dec. The SS represents the decrease in the gate voltage when the drain current decreases by one order. As shown in Fig. 3, when observing the change in drain current according to the gate voltage in the subthreshold region at $t_f = 0$ nm, SS shows a value of 60 mV/dec or higher. As the thickness of the ferroelectric material increases, the slope of the current-voltage curve increases in subthreshold, and it can be found that SS decreases below 60 mV/dec by the definition of SS as shown in Eq. (13). Therefore, the negative charge effect by the ferroelectric material can be observed. In addition, it was observed that the off current representing the drain current at 0 gate voltage also decreased significantly as the thickness of the ferroelectric material increased.

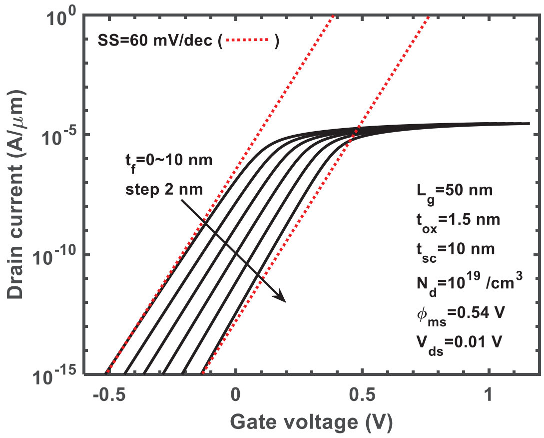

Fig. 3: Drain current vs. gate voltage curves with the thickness of ferroelectric material, t_f as a parameter.

Figure 4 shows the relationship between drain current and gate voltage obtained by using the gate channel length, L_g as a parameter when the thickness of the ferroelectric material, t_f is 10 nm. The red dotted line indicates SS=60 mV/dec in Fig. 4. It is known that there is a significant decrease in SS with increasing channel lengths. As can be seen from Fig. 4, it can be observed that the SS is 60 mV/dec value at about 25 nm of channel length under the conditions indicated inside Fig. 4, and decreases to 60 mV/dec or less as the channel length increases. Also note that the SS is saturated as the channel length increases. When the channel length is decreased to about 15 nm, it can be seen that SS significantly increases even at t_f=10 nm. Of course, as can be seen from Fig. 3, the SS will increase further as t_f decreases. As such, it was observed that a negative capacitance effect occurs due to the presence of ferroelectric thickness t_f, and a SS value of 60 mV/dec or less can be achieved.

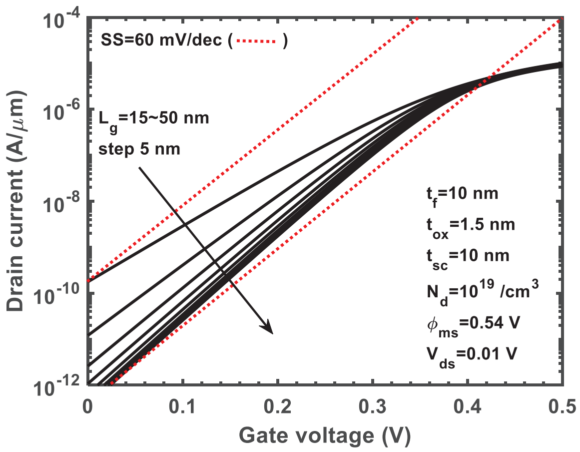

Fig. 4: Drain current vs. gate voltage curve with the channel length L_g as a parameter.

2.2 The Analytical SS Model of Ferroelectric NC FET

We want to derive an analytical model for the SS of ferroelectric NC FETs in this paper. By the definition of SS, the SS can be expressed as in Eq. (13).

$$SS = \frac{\partial V_{gs2}}{\partial \log I_{ds}} = \ln(10)\left(\frac{kT}{q}\right)\left(\frac{\partial \phi_{\min}}{\partial V_{gs2}}\right)^{-1} \tag{13}$$

https://doi.org/10.31436/iiumej.v24i1.2508

In particular, in the case of JLDG FET, most electrons will be conducted through the center, so using Eq. (7), the last parenthesis term of Eq. (13) can be expressed as in Eq. (14).

$$\frac{\partial\phi_{\min}}{\partial V_{gs2}} = \sum_{n=1}^{\infty}\frac{\partial A_n(y)}{\partial V_{gs2}}\sin\left(\frac{n\pi x}{L_g}\right)\Bigg|_{x=x_{\min},\,y=t_{sc}/2} = \sum_{n=1}^{\infty}\frac{\partial A_n(t_{sc}/2)}{\partial V_{gs2}}\sin\left(\frac{n\pi x_{\min}}{L_g}\right) \tag{14}$$

$$\begin{aligned}\frac{\partial A_n(t_{sc}/2)}{\partial V_{gs2}} &= e^{k_n t_{sc}/2}\frac{\partial C_n}{\partial V_{gs2}} + e^{-k_n t_{sc}/2}\frac{\partial D_n}{\partial V_{gs2}} \\ &= e^{k_n t_{sc}/2}\frac{\partial C_n}{\partial V_{gs2}} + e^{-k_n t_{sc}/2}\frac{\partial C_n}{\partial V_{gs2}}e^{k_n t_{sc}} \\ &= e^{k_n t_{sc}/2}\frac{\partial C_n}{\partial V_{gs2}} + e^{k_n t_{sc}/2}\frac{\partial C_n}{\partial V_{gs2}} = 2e^{k_n t_{sc}/2}\frac{\partial C_n}{\partial V_{gs2}}\end{aligned}$$

In Eq. (14), the derivative of C_n with respect to V_{gs2} must first be found. Since C_n is not a direct function of V_{gs2}, the following parametric differential method is used.

$$\frac{\partial C_n}{\partial V_{gs2}} = \frac{\partial C_n}{\partial V_{gs1}}\frac{\partial V_{gs1}}{\partial Q}\frac{\partial Q}{\partial V_{gs2}} \tag{15}$$

$$\frac{\partial C_n}{\partial V_{gs1}} = \frac{C_{ox}\left(\frac{2}{n\pi}[1-(-1)^n]k_n^2\right)}{k_n^2\left[e^{k_n t_{sc}}(C_{ox}+\varepsilon_{si}k_n)+(C_{ox}-\varepsilon_{si}k_n)\right]} = \frac{C_{ox}\left(\frac{2}{n\pi}[1-(-1)^n]\right)}{\left[e^{k_n t_{sc}}(C_{ox}+\varepsilon_{si}k_n)+(C_{ox}-\varepsilon_{si}k_n)\right]}$$

$$\frac{\partial V_{gs1}}{\partial Q} = \frac{1}{C_{ox}+\sum_{n=1}^{\infty}\frac{\partial C_n}{\partial V_{gs1}}\left(1+e^{k_n t_{sc}}\right)\left(\frac{1}{n\pi}\right)\left[(-1)^n-1\right]}$$

$$\frac{\partial Q}{\partial V_{gs2}} = \frac{1}{2\alpha t_f + 12\beta t_f Q^2 + 30\gamma t_f Q^4 + \frac{\partial V_{gs1}}{\partial Q}}$$

Substituting Eq. (15) into Eq. (14),

$$\begin{aligned}\frac{\partial A_n(t_{sc}/2)}{\partial V_{gs2}} &= 2e^{k_n t_{sc}/2}\frac{\partial C_n}{\partial V_{gs2}} = 2e^{k_n t_{sc}/2}\frac{\partial C_n}{\partial V_{gs1}}\frac{\partial V_{gs1}}{\partial Q}\frac{\partial Q}{\partial V_{gs2}} \\ &= \frac{2e^{k_n t_{sc}/2}C_{ox}\left(\frac{2}{n\pi}[1-(-1)^n]\right)}{\left[e^{k_n t_{sc}}(C_{ox}+\varepsilon_{si}k_n)+(C_{ox}-\varepsilon_{si}k_n)\right]}\frac{1}{C_{ox}\left\{1+\sum_{n=1}^{\infty}\frac{\partial C_n}{\partial V_{gs1}}\left(1+e^{k_n t_{sc}}\right)\left(\frac{1}{n\pi}\right)\left[(-1)^n-1\right]\right\}}\times \\ &\quad \frac{1}{2\alpha t_f + 12\beta t_f Q^2 + 30\gamma t_f Q^4 + \frac{\partial V_{gs1}}{\partial Q}}.\end{aligned}$$

The SS obtained using the presented model is compared with the SS obtained from the I-V curve using 2D potential. In this case, $x_{min}=L_g/2$ was used. The SSs derived from the I-V curve, this analytical model, and TCAD with the thickness of ferroelectric material, t_f as a parameter are compared under the conditions indicated inside Fig. 5. The dots denote SSs of TCAD in the case of t_f=0 nm in Fig. 5 [38]. Based on Fig. 5, the results are in good agreement.

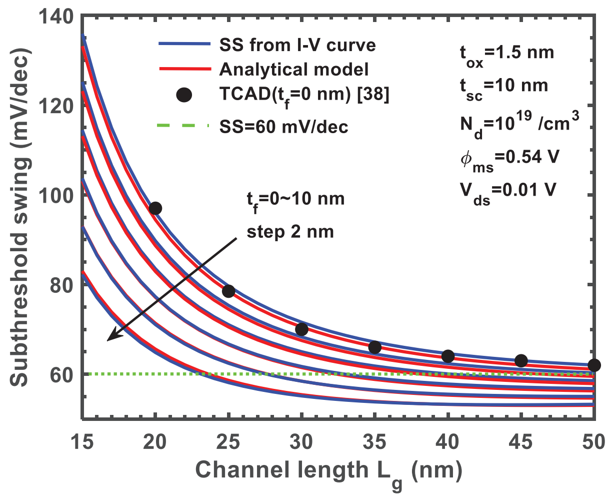

Fig. 5: Comparisons on SSs derived from I-V curve and this analytical model and TCAD [38].

Also, the analytical SS model in this paper shows good agreement with the TCAD result at t_f=0 nm, meaning it is valid. As mentioned in Figs. 2 and 3, as the thickness of the ferroelectric material increases, the SS decreases. In particular, when t_f = 10 nm under the conditions indicated inside Fig. 5, the SS values of 60 mv/dec or less were obtained even when the channel length was 28 nm. It was also observed that the size of the JLDG FET capable of observing SS of 60 mV/dec or less and the thickness of the ferroelectric material were correlated. Therefore, using the analytical SS model presented in this paper, we will analyze the SS with parameters such as the ferroelectric thickness t_f and channel length L_g. Table 1 summarizes the device parameters used in this paper.

Table 1: Device parameters for this analytical SS model

Device parameter	Symbol	Value
Channel length	L_g	15-50 nm
Channel width	W	1 μm
Channel thickness	t_{sc}	1-10 nm
SiO_2 thickness	t_{ox}	1-4 nm
Doping concentration	N_d	10^{19} /cm^3
Ferroelectric thickness	t_f	0-10 nm
Remanent polarization	P_r	17 μC/cm^2
Coercive field	E_c	1.2 MV/cm

3. ANALYSIS FOR SS OF JLDG FET WITH FERROELECTRIC

In order to observe the change of the SS with the change of the thickness of the ferroelectric material and channel length, Fig. 6 shows the change of the SS with respect to the ferroelectric thickness with the channel length as a parameter. It was observed that the SS decreased as the channel length and ferroelectric thickness increased. In particular, it can be seen that the region of SS < 60 mV/dec exists when the ferroelectric thickness, t_f is 10 nm or more and the channel length is 25 nm or more under conditions indicated in Fig. 6. It was also observed that the change in SS according to the channel length appeared smaller as the ferroelectric thickness increased. However, when the channel length was decreased, the SS showed a large value even though the change of SS according to the ferroelectric thickness was severe. When the channel length was increased to 50 nm, a region with SS<60 mV/dec appeared even when the ferroelectric thickness was about 1 nm. As such, ferroelectric thickness and channel length had a mutual effect on SS.

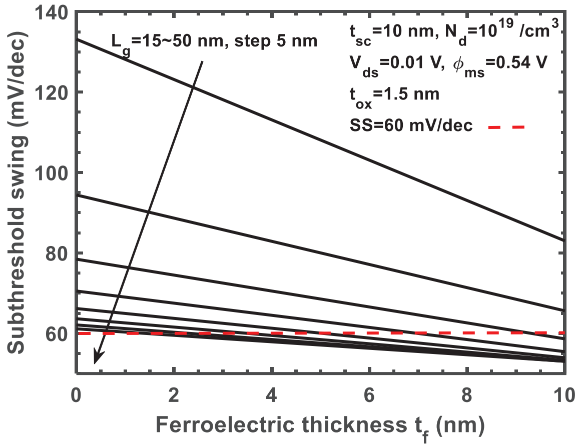

Fig. 6: The SSs for ferroelectric thickness t_f with the channel length L_g as a parameter.

The SS will vary not only with the ferroelectric thickness t_f and channel length L_g, but also with the thickness of SiO_2, t_{ox}. Figure 7 shows the contour line of SS=60 mV/dec for ferroelectric thickness and channel length with the thickness of SiO_2 as a parameter. The SS<60 mV/dec region is above the line. As can be seen in Fig. 7, the SS<60 mV/dec region changed significantly according to t_{ox}, and the SS<60 mV/dec region was observed in a wider area in the given simulation range as t_{ox} decreased. In particular, the SS=60 mV/dec line showed an inverse relationship between channel length and ferroelectric thickness. That is, if the channel length decreases, SS=60 mV/dec can be observed only when the ferroelectric thickness is increased. Figure 5 shows how ferroelectric thickness can be increased in order to decrease SS when decreasing the channel length.

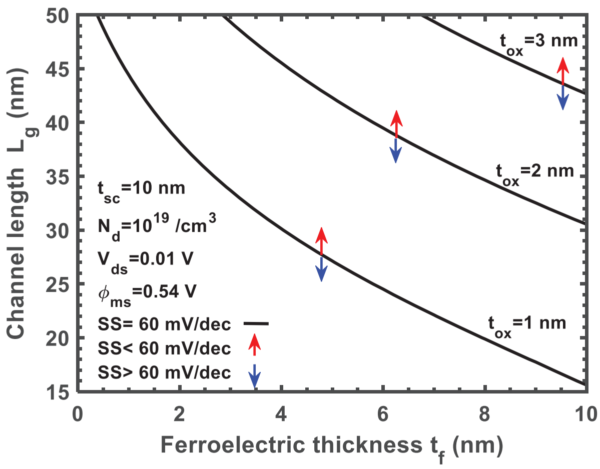

Fig. 7: Contours of SS=60 mV/dec with the thickness of SiO_2, t_{ox} as a parameter.

The SS also shows a large change according to the thickness of the silicon channel, t_{sc}. In Fig. 8, the contour of SS=60 mV/dec was plotted for channel length and ferroelectric thickness with silicon thickness t_{sc} as a parameter. In Fig. 8, it can be observed that the SS<60 mV/dec region (above the line as shown in Fig. 7) increases as silicon thickness t_{sc} decreases. Observing Fig. 8, if t_{sc}=5 nm, it can be seen that SS<60 mV/dec region exists when the ferroelectric thickness is 9 nm or more, even if the channel length is decreased to 15 nm. However, if t_{sc} =10 nm, it can be seen that SS > 60 mV/dec when the ferroelectric thickness is 2 nm or less even if the channel length is increased to 50 nm. As such, it was observed that the SS significantly decreased due to the presence of the ferroelectric material.

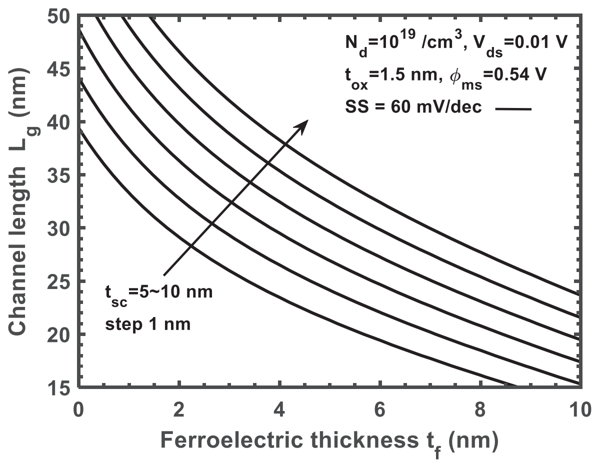

Fig. 8: Contours of SS=60 mV/dec with the thickness of silicon, t_{sc} as a parameter.

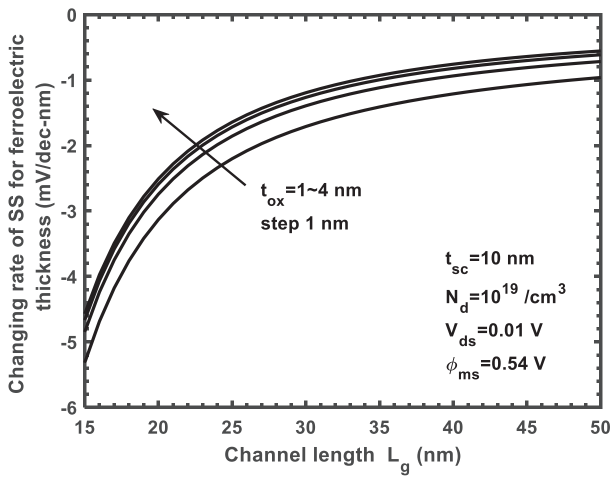

Fig. 9: Changing rate of SS for ferroelectric thickness with the thickness of SiO_2, t_{ox} as a parameter.

In order to examine the change in the SS according to the ferroelectric thickness t_f in more detail, Fig. 9 shows the change in SS ($\Delta SS/\Delta t_f$) with respect to the change in ferroelectric thickness according to the channel length with t_{ox} as a parameter. Fig. 9 illustrates how the change in SS varies with ferroelectric thickness very strongly when the channel length is as small as 15 nm. However, it was observed that the SS change with respect to the ferroelectric thickness became saturated and constant as the channel length increased. It can be seen that the change in ferroelectric thickness no longer has a significant effect on the change in SS when the channel length is increased. In other words, it can be seen that the negative capacitance effect caused by ferroelectric becomes larger as the channel length decreases. In addition, the change of the SS with respect to ferroelectric thickness was large as the t_{ox} decreased, and it was observed that the rate of change of SS with respect to ferroelectric thickness became almost constant when the t_{ox} increased and became more than 4 nm under the conditions indicated inside Fig. 9.

The change of the SS according to the ferroelectric thickness is shown in Fig. 10 with silicon thickness t_{sc} as a parameter. As can be seen from Fig. 10, the change of the SS according to the ferroelectric thickness does not change significantly with t_{sc} when the channel length increases, but it can be seen that it changes significantly with the t_{sc} when the channel length decreases. Also, the change rate of the SS according to the ferroelectric thickness was decreasing with the channel length when t_{sc} decreased, and if t_{sc} increased to 10 nm, it was found that the change rate of SS according to the ferroelectric thickness increased significantly with the channel length. From the results of Figs. 9 and 10, it was observed that the change rate of the SS according to the ferroelectric thickness decreased with the channel length as t_{ox} was larger and t_{sc} was smaller.

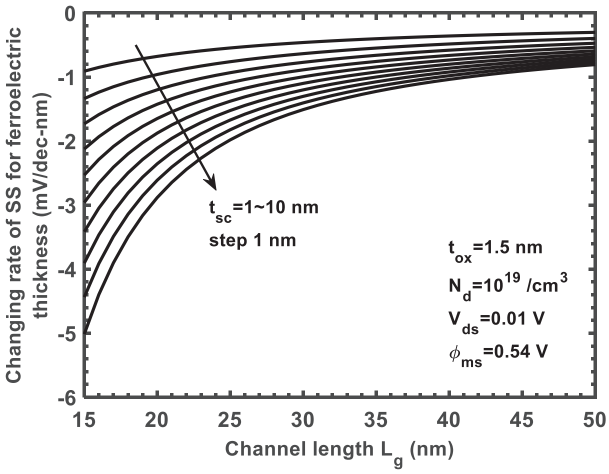

Fig. 10: Changing rate of SS for ferroelectric thickness t_f with silicon thickness t_{sc} as a parameter.

4. CONCLUSIONS

The analytical model of the SS for a JLDG FET using a gate oxide by stacking a ferroelectric material on SiO_2 is presented. If a ferroelectric material is used, a negative capacitance effect occurs due to the gate voltage amplification phenomenon, so that the SS can obtain a value of 60 mV/dec or less. The analytical SS model presented was in good agreement with the SS derived from the I-V curve obtained by 2D potential distribution. As a result of analysis using the analytical SS model, SS < 60 mV/dec was obtained when the ferroelectric thickness was 6 nm or more at a channel length of 25 nm, a silicon thickness of 10 nm, and a t_{ox} of 1 nm. In addition, the change rate of the SS according to the ferroelectric thickness was almost constant according to the channel length when the t_{sc} decreased to about 1 nm and the change of the SS according to the ferroelectric thickness was not affected by the thickness of SiO_2 when the t_{ox} increased to 4 nm or more. As can be seen from the above results, for the JLDG FET using ferroelectric, SS<60 mV/dec could be manufactured by adjusting the channel length, silicon thickness, thickness of SiO_2, and ferroelectric thickness. The analytical SS model presented in this paper can be used to analyze this phenomenon.

REFERENCES

[1] RK Cavin RK, Lugli P, Zhirnov VV. (2012) Science and Engineering Beyond Moore's Law. Proc. IEEE, 100: 1720-1749. doi:10.1109/JPROC.2012.2190155

[2] Mack CA. (2011) Fifty Years of Moore's Law. IEEE Trans. Semiconductor Manufacturing, 24(2): 202-207. doi:10.1109/TSM.2010.2096437

[3] Waldrop MM. (2016) The chips are down for Moore's law. Nature News, 530: 144-147.

[4] Taur Y, Ning TH. (2020) Fundamentals of Modern VLSi Devices. Cambridge University Press, 2nd Edn.

[5] Nadeem M, Bernardo ID, Wang X, Fuhrer MS, Culcer D. (2021) Overcoming Boltzmann's Tyranny in a Transistor vis the Topological Quantum Field Effect. Nano Lett. 21(7): 3155-3161. doi:10.1021/acs.nanolett.1c00378

[6] Hoffmann M, Slesazeck S, Mikolajick T. (2021) Progress and future prospects of negative capacitance electronics: A materials perspective. APL Materials, 9: 020902. doi:10.1063/5.0032954

[7] Iniguez J, Zubko P, Lukyanchuk I, Cano A. (2019) Ferroelectric negative capacitance. Nature Reviews Materials, 4: 243-256. doi:10.1038/s41578-019-0089-0

[8] Saha AK, Gupta SK. (2021) Negative capacitance effects in ferroelectric heterostructures: A theoretical perspective. J. Appl. Phys., 129: 080901. doi:10.1063/5.0038971

[9] Hoffmann M, Gui M, Slesazeck S, Fontanini R, Segatto M, Esseni D, Mikolajick T. (2022) Intrinsic Nature of Negative Capacitance in Multidomain $Hf_{0.5}Zr_{0.5}O_2$-Based Ferroelectric/Dielectric Heterostructures. Advanced Functional Materials, 32: 2108494. doi:10.1002/adfm. 202108494

[10] Hoffmann M, Fengler FPG, Max B, Schroeder U, Slesazeck S, Mikolajick T. (2019) Negative Capacitance for Electrostatic Supercapacitors. Advaced Energy Materials, 9: 1901154. doi:10. 1002/aenm.201901154

[11] Zhang S, Lui H, Zhou J, Liu Y. (2021) ZrOx Negative Capacitance Field-Effect Transistor with Sub-60 Subthreshold Swing Behavior. Nanoscale Research Letters, 16: 21. doi:10.1186/s11671-020-03468-w

[12] Deepa R, Devi MP, Vignesh NA, Kanithan S. (2022) Implementation and Performance Evaluation of Ferroelectric Negative Capacitance FET. Silicon, 14: 2409-2419. doi:10.1007/s12633-022-01722-7

[13] Cao W, Banerjee K. (2020) Is negative capacitance FET a steep-slope logic switch ?. nature communications, 11: 196. doi:10.1038/s41467-019-13797-9

[14] Guo S, Prentki RJ, Jin K, Chen C, Guo H. (2021) Negative-Capacitance FET With a Cold Source. IEEE Trans. Electron Devices, 68(2): 911-918. doi:10.1109/TED.2020.3041216

[15] Salahuddin S, Datta S. (2008) Use of negative capacitance to provide voltage amplification for low power nanoscale devices. Nano letters, 8(2): 405-410. doi:10.1021/nl071804g

[16] Yoon S, Min D, Moon S, Park KS, Won JI, Yoon S. (2020) Improvement in Long-Term and High-Temperature Retention Stability of Ferroelectric Field-Effect Memory Transistors With Metal-Ferrolectric-Metal-Insulator-Semiconductor Gate-Stacks Using Al-Doped HfO_2 Thin Films. IEEE Trans. Electron Devices, 67(2): 499-504. doi:10.1109/TED.2019.2961117

[17] Mulaosmanovic H, Breyer ET, Mikolajick T, Slesazeck S. (2019) Ferroelectric FETs with 20-nm- Thick HfO_2 Layer for Large Memory Window and High Performance. IEEE Trans. Electron Devices, 66(9): 3828-3833. doi:10.1109/TED.2019.2930749

[18] Pahwa G, Dutta T, Agarwal A, Chauhan YS, (2018) Physical Insights on Negative Capacitance Transistors in Nonhysteresis and Hysteresis Regimes: MFMIS versus MFIS Structures. IEEE Trans. Electron Devices, 65(3): 867-873. doi:10.1109/TED.2018.2794499

[19] Khan AI, Radhakrishna U, Chatterjee K, Salahuddin S, Antoniadis DA. (2016) Negative Capacitance Behavior in a Leaky Ferroelectric. IEEE Trans. Electron Devices, 63(11): 4416-4422. doi:10.1109/TED.2016.2612656

[20] Asadi K. (2021) Organic Ferroelectric Materials and Applications. Woodhead Publishing, 1st Edn.

[21] Frantti J. (2008) Notes of the Recent Structural Studies on Lead Zirconate Titanate. J. Phys.

Chem. B, 112(21): 6521-6535. doi:10.1021/jp711829t
[22] Kim T, Alamo JA, Antoniadis DA. (2020) Dynamics of $HfZrO_2$ Ferroelectric Structures : Experimentals and Models. 2020 IEEE International Electron Devices Meeting (IEDM), 12-18 Dec. 2020, San Francisco, CA, USA. doi:10.1109/IEDM13553.2020.9372013
[23] Saha AK, Gupta SK. (2020) Multi-Domain Negative Capacitance Effects in Metal-Ferroelectric-Insulator-Semiconductor/Metal Stacks: A phase-field Simulation Based Study. Scientific Reports, 10: 10207. doi:10.1038/s41598-020-66313-1
[24] Rahi SB, Tayal S, Upadhyay A K. (2021) A review on emerging negative capacitance field effect transistor for low power electrics. Microelectronics Journal, 116: 105242. doi:10.1016/j.mejo. 2021.105242
[25] Alam MA, Si M, Ye PD. (2019) A critical review of recent progress on negative capacitance field-effect transistors. Applied Physics Letters, 114: 090401. doi:10.1063/1.5092684
[26] Tu L, Wang X, Wang J, Meng X, Chu J. (2018) Ferroelectric Negative Capacitance Field Effect Transistor. Advanced Electronic Materials, 4: 1800231. doi:10.1002/aelm.201800231
[27] Pahwa G, Agarwal A, Chauhan YS. (2018) Numerical Investigation of Short-Channel Effects in Negative capacitance MFIS and MFMIS Transistors: Subthreshold Behavior. IEEE Trans. Electron Devices, 65(11): 5130-5136. doi:10.1109/TED.2018.2870519
[28] Jain AK, Kumar MJ. (2020) Sub-10 nm Scalability of Junctionless FETs Using a Ground Plane in High-K BOX: A Simulation Study. IEEE Access, 8: 137540-137548. doi:10.1109/ACCESS. 2020.3012579
[29] Sreenivasulu B, Vadthiya N. (2021) Design and Deep Insights into Sub-10 nm Spacer Engineering Junctionless FinFET for Nanoscale Application. ECS Journal of Solid State Science and Technology, 10(1): 013008. doi:10.1149/2162-8777/abddd4
[30] Nowbahari A, Roy A, Marchetti L. (2020) Junctionless Transistors: State-of-the-Art. Electronics, 9: 1174. doi:10.3390/electronics9071174
[31] Fu Y, Ma L, Duan Z, Han W. (2022) Effect of charge trapping on electrical characteristics of silicon junctionless nanowire transistor. Journal of Semiconductor, 43: 054101. doi:10.1088/1674-4926/43/5/054101
[32] Rassekh A, Sallese J, Jazaeri F, Fathipour M, Ionescu AM. (2020) Negative Capacitance Double-Gate Junctionless FETs: A Charge-Based Modeling Investigation of Swing, Overdrive and Short Channel Effect. J. of Electron Devices Society, 8: 939-947. doi:10.1109/JEDS.2020.3020976
[33] Reis M. (2013) Fundamentals of Magnetism, ACADEMIC PRESS. doi:10.1016/B978-0-12-405545-2.00011-4
[34] Rassekh A, Jazaeri F, Sallese J. (2022) Nonhysteresis Condition in Negative Capacitance Junctionless FETs. IEEE Trans. Electron Devices, 69(2): 820-826. doi:10.1109/TED.2021. 3133193
[35] Awadhiya B, Kondekar PN, Yadav S, Upadhyay P. (2021) Insight into Threshold Voltage and Drain Induced Barrier Lowering in Negative Capacitance Field Effect Transistor. Trans. Electrical and Electronic Materials, 22: 267-273. doi:10.1007/s42341-020-00230-y
[36] Rassekh A, Jazaeri F, Fathipour M, Sallese J. (2019) Modeling Interface Charge Trap in Junctionless FETs, Including Temperature Effects. IEEE Trans. Electron Devices, 66(11): 4653-4659. doi:10.1109/TED.2019.2944193
[37] Ding Z, Hu G, Gu J, Liu R, Wang L, Tang T. (2011) An analytical model for channel potential and subthreshold swing of the symmetric and asymmetric double-gate MOSFETs. Microelectronics Journal, 42: 515-519. doi:10.1016/j.mejo.2010.11.002
[38] Jazaeri F, Barbut L, Koukab A, Sallese JM. (2013) Analytical model for ultra-thin body junctionless symmetric double gate MOSFETs in subthreshold regime. Solid-State Electronics, 82: 103-110. doi:10.1016/j.sse.2013.02.001

ROBUST AND IMPERCEPTIBLE WATERMARKING ON MEDICAL IMAGES USING COEFFICIENT PAIR MODIFICATION

LEDYA NOVAMIZANTI[1,3*], ANDRIYAN BAYU SUKSMONO[2,4], DONNY DANUDIRDJO[2,4], AND GELAR BUDIMAN[3,4]

[1]Electrical Engineering and Informatics, School of Electrical Engineering and Informatics, Institut Teknologi Bandung, Bandung 40132, Indonesia
[2]School of Electrical Engineering and Informatics, Institut Teknologi Bandung, Bandung 40132, Indonesia
[3]School of Electrical Engineering, Telkom University, Bandung 40257, Indonesia
[4]Research Collaboration Center for Quantum Technology 2.0, Bandung 40132, Indonesia

[*]Corresponding author: ledyaldn@telkomuniversity.ac.id

(Received: 7th September 2022; Accepted: 3rd October 2022; Published on-line: 4th January 2023)

ABSTRACT: Sensitive data including medical images and electronic patient records (EPR) have potential value in the era of big data and telemedicine applications. Distribution of medical images and EPR over public networks requires a high level of privacy and security. Robust and imperceptible watermarking techniques are needed to provide copyright preservation for medical images and protect patient information security. This paper improves the technique of Coltuc et al. by modifying the discrete cosine transform (DCT) coefficient pairs in the watermark embedding formula. Our proposed formula ensures that the difference between the two coefficients is at least ζ. If the difference between the two coefficients is less than ζ, then the new pixels are modified so that the difference is equal to ζ. The proposed method was evaluated on a variety of medical images, including X-ray, CT, US, MRI, and Colonoscopy, and compared to numerous robust watermarking techniques of the recent time. The experimental results demonstrate that the suggested method outperforms contemporary robust watermarking techniques in terms of imperceptibility, robustness, and security. The peak signal noise ratio (PSNR) for all modalities of watermarked medical images exceeds 54 dB, and the average PSNR is approximately 56 dB. The proposed method is outstanding compared to Coltuc's method due to a 93% and 14% increase in bit error rate (BER) and normalized correlation (NC), respectively. Our work is superior to various state-of-the-art robust watermarking techniques, allowing it to be employed effectively in medical applications.

ABSTRAK: Data sensitif termasuk imej perubatan dan rekod pesakit elektronik (EPR) mempunyai potensi nilai dalam era aplikasi data besar dan teleperubatan. Pengedaran imej perubatan dan EPR melalui rangkaian awam memerlukan tahap privasi dan keselamatan yang tinggi. Teknik penanda air yang mantap dan tidak dapat dilihat diperlukan untuk menyediakan pemeliharaan hak cipta untuk imej perubatan dan melindungi keselamatan maklumat pesakit. Kertas kerja ini menambah baik teknik Coltuc et al. dengan mengubah suai pasangan pekali transformasi kosinus diskret (DCT) dalam formula pembenaman tera air. Formula yang dicadangkan kami memastikan bahawa perbezaan antara dua pekali adalah sekurang-kurangnya ζ. Jika perbezaan antara dua pekali kurang daripada ζ, maka piksel baharu diubah suai supaya perbezaannya sama dengan ζ. Kaedah yang dicadangkan telah dinilai pada pelbagai imej perubatan, termasuk X-ray, CT, US, MRI, dan Kolonoskopi, dan dibandingkan dengan banyak teknik penanda air yang mantap pada masa terkini. Keputusan eksperimen menunjukkan bahawa kaedah yang dicadangkan mengatasi teknik penanda air teguh kontemporari dari segi ketidakjelasan, keteguhan dan keselamatan. Nilai PSNR untuk semua modalitas imej perubatan bertanda air melebihi 54 dB, dan nilai purata PSNR adalah lebih kurang 56 dB. Kaedah yang dicadangkan adalah cemerlang daripada kaedah Coltuc kerana masing-masing peningkatan 93% dan 14% dalam BER dan NC. Kerja kami lebih unggul daripada pelbagai teknik penanda air teguh terkini, membolehkan ia digunakan dengan berkesan dalam aplikasi perubatan.

KEYWORDS: *DCT; imperceptible; medical image; robust; watermarking*

1. INTRODUCTION

Information and communication technology (ICT) is essential to all sectors of society, including government, banking, education, health, agriculture, and transportation. ICT integrates computer systems, digital data, communication devices, and the internet into one unified system. An important use of ICT for effective quality health care is the electronic storage of medical data. The information in the electronic medical data storage, including: patient identities, diagnosis reports, doctor's consultations, hospital information where the image was created, and other helpful information, can be used anywhere and anytime [1-3]. Medical data is susceptible and has great potential value in the era of big data because it is the most important basis for diagnosis in determining diagnostic methods and results [4,5]. Through public networks like the internet, medical professionals frequently exchange digitally created medical images of patients created using various modalities. Radiologists and doctors in the same field share these images for clinical interpretation [6].

Medical professionals use telemedicine applications to remotely diagnose, evaluate, and treat patients via electronic communications. The program facilitates the transmission of medical images between two healthcare providers for improved diagnosis. However, medical image and EPR delivery over public networks demand a high level of security [7]. Modified, manipulated, or distorted medical data can cause incorrect diagnoses and severe health issues for everyone. In addition, the destruction and theft of medical images and identities can give rise to various legal and ethical concerns, including image retention and fraud, piracy, and illegal handling [1]. In contrast to financial institutions, which have robust data protection methods through two-factor authentication, medical records in healthcare systems are poorly protected. Medical facilities must secure data from illegal actions such as hacking and virus intrusion, staff negligence, and the theft of medical records on purpose [3]. The transfer of data in an intelligent healthcare system while preserving privacy, integrity, authority, and security is a complex topic that requires additional consideration [4].

Digital watermarking is a common approach for concealing digital information by masking signals [8] due to its additional qualities of robustness and imperceptibility. Digital watermarking technology is becoming crucial for various fields since it offers a variety of compact solutions for numerous approaches and applications, such as cloud computing, electronic health, and the Internet of Things [2,11]. Watermarking of digital images is allowed in two domains, i.e., the spatial domain and the frequency domain. In the spatial domain of watermarking technology, personal information is integrated directly into the cover image by modifying the pixel values [3,9]. In frequency domain watermarking, the cover image is first translated into the frequency domain, and then the hidden data is embedded by modifying the frequency coefficient value [3,9]. Watermarking is also categorized based on the method of watermark extraction. Non-blind techniques require both the host and the watermark image to extract the watermark. A semi-blind watermark requires a secret key and a watermarked image to extract the watermark. If only the secret key is required to extract the watermark, the approach is known as blind watermarking [10]. Based on the application, watermarking techniques can be classified as either robust or fragile [1,5].

The robustness of confidential information, and how the encoded information can withstand attacks conducted by attackers during data transmission, is the primary goal of robust watermarking [9]. Robust watermarking is therefore widely used to preserve digital data's copyright. However, fragile watermarking [1] is used to identify the invader-damaged portions of the watermarked image, i.e., those regions of the image that were damaged during transmission. The integrity of digital data material is therefore verified using fragile watermarking. Processing time for spatial domain-based watermarking is lower than for methods that embed data in the transformation domain. However, compared to transformation-based strategies, spatial domain-based approaches are less resistant to attacks [7]. Two key requirements for creating effective watermarking methods are imperceptibility and robustness [6].

Compared to watermarking in the spatial domain, watermarking in the frequency domain offers additional benefits. That is why many researchers use frequency domain watermarking techniques. DCT is one of the widespread transformations and is often chosen in frequency domain watermarking techniques [6] because of its lower computational cost, high robustness and high compression [11]. In [12,13], the watermark was embedded by Coltuc and Chassery using the DCT domain watermarking method. The image is divided into 8×8 blocks. Next, DCT for each block is determined. One bit of information entered into each block depends on the difference between the two coefficients of the mid-band frequency. For example, bit "1" is encoded if the difference is negative, and a bit "0" otherwise. If the relative size of each coefficient does not match the bit to be encoded, the coefficients are swapped. The interchange of these coefficients does not considerably alter the watermarked image because the mid-frequency DCT coefficients have almost identical magnitudes. However, this method can cause errors due to the rounding case of DCT. As a result, not all watermarks can be extracted properly.

Coltuc's method is improved by modifying the DCT coefficient pairs in the watermark embedding formula. Our proposed formula ensures that the difference between the two coefficients is at least ζ. If the difference between the two coefficients is less than ζ, then the new pixels are modified so that the difference is ζ. The new watermarking system on medical images based on the modification of DCT coefficient pairs is proposed to achieve the following objectives: (1) to achieve good imperceptibility from watermarked images; (2) to provide intellectual property protection for medical images; (3) to preserve the safety of patient data [6].

2. RELATED WORKS

The discrete cosine transform (DCT), which has energy compaction features, is frequently employed in watermarking approaches. DCT can convert an image into a frequency band, which can be inverted to transform it back into the original image. Following the DCT process, the image pixels are turned into coefficients. Direct current (DC) is represented by the first coefficient DCT in the base array function's upper left corner, while the remaining coefficients represent alternating current (AC). Since the AC is so crucial to an image, any modifications to the AC can significantly affect the image. On the other hand, slight adjustments to the image have little impact on the AC.

Thanki et al. [14] developed a watermarking technique for medical images based on fast discrete curvelet transform (FDCuT) and DCT. The block-wise DCT is applied to the medical image's high-frequency curvelet coefficient. A white Gaussian noise (WGN) order is added to the original image's mid-band frequency coefficient in compliance with the watermark bit to create a watermarked medical image. Images from X-rays, ultrasounds, MRIs, and computed tomography (CT) scans were utilized to evaluate how the suggested watermarking technique worked. The study results show that watermarks are more invisible in all types of medical images with PSNR above 45 dB. However, two uncorrelated WGN sequences generated during the embedding process are required to recover the watermark. Therefore, only binary watermarks may be embedded using this technique; text-based EPR data cannot be. Another drawback is that the resulting watermark image always contains noise.

Novamizanti et al. [15] introduced the singular value decomposition (SVD) method to medical image watermarking techniques based on FDCuT and DCT. Watermark embedding by exchanging the singular value of the watermark and the host image result from the FDCuT and DCT transformations. The proposed algorithm has good imperceptibility with interval PSNR values 53 dB to 54 dB. However, this watermarking scheme is semi-blind, where it is necessary to output SVD results from the original watermark image at the extraction stage. This method is not resistant to blurring and geometry attacks.

Lei et al. [16] reported a robust image watermarking algorithm based on DCT domain and QIM. The host signal's medium and low-frequency DCT coefficient is divided into two regions. Then the watermark bit is embedded by quantizing the ratio of the two halves. According to experimental findings, this method is only superior against attacks of the common type. This algorithm has limited capacity, where a 512×512 image host can only accommodate a 128-bit watermark. Then, the optimal parameter for each image is obtained as PSNR of 41 dB.

Zhu et al. [17] presented a robust image steganography algorithm for JPEG compression. Firstly, a candidate DCT coefficient unaffected by JPEG compression is chosen. Second, the proposed distortion function gives each potential DCT coefficient a cost. The error correction code and the Syndrome Trellis Code help the method become even more robust and invisible. This algorithm's embedding capacity remains restricted to payloads between 0.01 and 0.1 bpnzAC. For 512×512 image hosts, the proposed algorithm only produces PSNR values with the interval 42 dB to 47 dB.

Rachmawanto et al. [18] designed an image watermarking algorithm using block-based DCT, where the DC coefficient is chosen to keep the watermark resistance included. The Beaufort cipher is used for the encryption process and the watermark distribution when inserted. The goal is to improve watermark security and imperceptibility aspects. Generally, the spread spectrum watermarking technique uses PN Sequence for watermark deployment. However, the proposed method is non-blind, where the cover image is still required for the watermark extraction process.

An image watermarking technique based on DCT was researched by Byun et al. [19]. First, the DCT coefficient for the specified location is determined. Next, the variation value is calculated to adjust the coefficient under the embedding bit and quantization step. Finally, the watermark bit is inserted directly into the pixel value without using a full-frame DCT. According to the findings, the suggested watermarking technology offers less computing complexity and ensures robustness. A color host image with a size of 512×512 can only accommodate a watermark of 1024 bits, indicating that the embedding capacity of this technique is still constrained. The proposed method's average PSNR is about 42 dB.

https://doi.org/10.31436/iiumej.v24i1.2597

Ko et al. [20] reported a watermarking method based on the correlation of DCT coefficients between blocks. The coefficient variance in the two blocks of DCT is calculated and changed depending on the watermark bits to adjust this difference to a specified range. The level of the DCT coefficient's modification is based on the DC coefficient and the median of the alternating current (AC) coefficient, which is ordered in zigzag order. The experimental findings demonstrate the robustness of the suggested technique against several single and combined attacks. For the Lena watermarked image, only a PSNR of 41.6 dB is obtained. In addition, the resistance is weak against types of noise attacks, including BER is 17.06 for salt-and-pepper noise and 9.98 for Gaussian noise.

A robust watermarking technique based on DCT, speeded up robust features (SURF), and perceptual hashing was proposed by Nawaz et al. [21]. The watermark image is preprocessed to enhance its security using affine transformation with feature matrix and chaotic encryption technology. SURF feature points are utilized to choose the DCT region and extract scalable watermarks after geometric rectification during the extraction process. Studies reveal that the algorithm efficiently defends against geometric and conventional attacks and can effectively maintain the security of images with an NC value higher than 90%. However, this paper does not report the PSNR results from the watermarked images without attack. This technique utilizes a correlation function to confirm the similarity of the derived watermarks. Hence scrambled data from the original watermark is still required at the watermark extraction stage.

Kumar et al. [22] presented a secure watermarking framework on medical images by applying IntDCT and SVD. The differential evolution technique was used to determine suitable scaling factors by randomizing the watermark with the step space fill curve. In addition to the watermarked image, the $U_W, S,$ and V_W values during insertion are also required for the watermark extraction process. The experimental findings demonstrate that the designed framework is robust to geometric attacks.

Fares et al. [23] introduced watermarking approaches based on DCT and Schur decomposition to protect medical images. Integration is performed at the intermediate frequencies. According to the findings, the designed algorithm produces acceptable imperceptibility with PSNR values at intervals 47 dB to 49 dB. However, capacity is limited, where a 1024×1024 image host can only accommodate a 1024-bit watermark. The suggested method is robust under some conventional attacks but, it is not resistant to geometric attacks, such as cropping and scaling.

3. PRELIMINARY

In this section, the DCT technique and the method of Coltuc are presented and used in the proposed watermarking method. The energy compaction and redundancy removal properties of DCT make this transformation popular in image processing, especially image watermarking. However, DCT-based watermarking is prone to rounding errors. When this DCT is applied to the Coltuc's method, which exchanges two DCT coefficients to embed a watermark into the host image, the watermarking method is challenging in developing watermarking techniques, especially in medical images.

3.1 Discrete Cosine Transform

As one of the prominent transformation techniques, DCT works by changing the image from the spatial to the frequency domain [13]. This technique has been used extensively in image processing. Some of the outstanding properties of DCT in image processing applications [24,25] include:

1. Decorrelation can eliminate redundancy between neighboring pixels.
2. DCT offers better energy compaction for correlated images.
3. Separability and symmetry: Transformation matrices can be computed offline, thus providing computational efficiency.
4. Orthogonality: This property makes some reduction in pre-computing complexity.

Generally, the image is segmented into 8×8 pixel blocks. Then, each of those blocks is subjected to a 2D-DCT. Mathematically, the 2D-DCT transformation and the 2D-DCT inverse for a block size of 8×8 can be seen in Eq. (1) and (2), respectively, as follows:

$$F(u,v) = \frac{1}{4} C(u)C(v) \sum_{x=0}^{7} \sum_{y=0}^{7} f(x,y)\ cos\left(\frac{(2x+1)u\pi}{16}\right) cos\left(\frac{(2y+1)v\pi}{16}\right) \quad (1)$$

$$f(x,y) = \frac{1}{4} C(u)C(v) \sum_{u=0}^{7} \sum_{v=0}^{7} F(u,v)\ cos\left(\frac{(2x+1)u\pi}{16}\right) cos\left(\frac{(2y+1)v\pi}{16}\right) \quad (2)$$

with $C(\omega) = \frac{1}{\sqrt{2}}$ for $\omega = 0$, and $C(\omega) = 1$, for otherwise ; $F(u,v)$ is the DCT coefficient; $f(x,y)$ is the pixel value in the spatial domain.

There are two ways to apply DCT to images: block-wise and without block-wise. DCT separates the image into three frequency sub-bands, i.e., low (LF), middle/ mid (MF), and high (HF), in a block-wise approach. Figure 1 shows the position of the DCT coefficient with blocks of size (8×8) pixels. The 8×8 pixel block transformation yields 64 DCT coefficients. The position of the upper left corner of the DCT coefficient, $F(0,0)$, is the DC component, and the other 63 coefficients are the AC component. The DC component represents the average color of the entire frequency-transformed region. Thus, embedding data in DC components can cause visual artifacts that are visible to the normal human eye. Embedding data is done in the MF coefficient region, because this region carries relatively less important image information than the HF and LF regions, and is less significant in perception. Thus, data embedding in the MF region does not significantly affect image quality or communication performance [14,26].

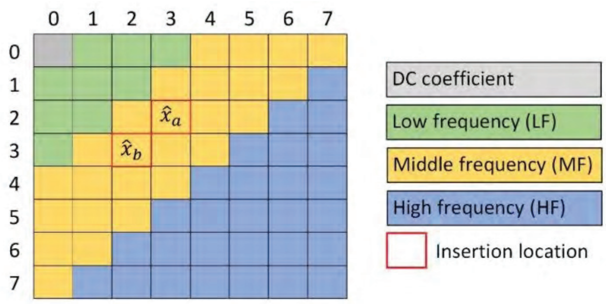

Fig. 1: The 2D discrete cosine transform (DCT) coefficients with blocks of size (8×8) pixels.

3.2 Coltuc's Method

Coltuc and Chassery [12,13] applied the DCT domain in the robust watermarking stage. Firstly, the cover image X is segmented into 8×8 blocks. Next, DCT is applied to each block. The two MF coefficients $\hat{x}_a$ and $\hat{x}_b$ in each DCT block are chosen to insert one watermark bit $w \epsilon \{0,1\}$, as follows [27]:

$$(\hat{x}'_a, \hat{x}'_b) = \begin{cases} (\hat{x}_a, \hat{x}_b), \ if \ \hat{x}_a - \hat{x}_b > 0 \text{ and } w = 1 \\ (\hat{x}_b, \hat{x}_a), \ if \ \hat{x}_a - \hat{x}_b \leq 0 \text{ and } w = 1 \\ (\hat{x}_a, \hat{x}_b), \ if \ \hat{x}_a - \hat{x}_b \leq 0 \text{ and } w = 0 \\ (\hat{x}_b, \hat{x}_a), \ if \ \hat{x}_a - \hat{x}_b > 0 \text{ and } w = 0 \end{cases} \quad (3)$$

with a and b being the two AC channel indexes. The index is the coordinates of the pixels. Thus, the AC channel index represents the coordinates of the DCT coefficients located in the AC component. For example, a=(2,3) and b=(3,2) are the selected AC channel indexes, so the two MF coefficients $\hat{x}_{(2,3)}$ and $\hat{x}_{(3,2)}$ are used to insert a watermark bit, as shown in Fig. 1.

By replacing $\hat{x}'_a$ and $\hat{x}'_b$ for the appropriate coefficients, the DCT coefficients for Y are obtained. The watermarked image Y is then created by applying the inverse DCT. For the decoding process, Y is segmented into 8×8 blocks. Next, each block is converted using the DCT technique. The embedded watermark for a coefficient pair of $\hat{y}_a$ and $\hat{y}_b$ is recovered as: if $\hat{y}_a - \hat{y}_b > 0$, then the bit watermark is 1, and 0 otherwise.

One bit of information is entered into each block depending on the difference between the two coefficients of MF. The new coefficient value does not change if the difference is positive and the bit is "1", or the difference is negative, and the bit is "0". However, for other conditions, the positions of the two MF coefficients are swapped. The exchange of these coefficients does not change the watermarked image significantly because the MF of DCT coefficients generally have almost the same magnitude. However, this condition is prone to extraction errors due to the rounding factor of DCT, as shown in Fig. 2(a). As a result, not all watermarks can be extracted properly. One solution is to select two MF coefficients $\hat{x}_a$ and $\hat{x}_b$ to embed a robust watermark. However, this method becomes impractical.

4. PROPOSED METHOD: WATERMARKING IMAGES VIA MODIFYING DCT COEFFICIENT PAIR

In this section, the modification of the insertion formula in Coltuc's method is described in subsection 4.1. The watermarking embedding step is presented in subsection 4.2, and the watermarking extraction step is presented in subsection 4.3. The watermarking framework for medical images is generally shown in Fig. 3. First, a watermark in the form of an EPR is hidden into a medical image, resulting in a Y watermarked image, and then sent through a communication channel. During transmission, the watermarked image undergoes various attacks, resulting in a medical image that is attacked as $\hat{Y}$. The attacks can be in the form of noise and intentional and unintentional modifications. In the extraction process, only Y (for noise-free channel) or Y (for noise channel) is needed to restore the original watermark. Thus, it can preserve medical images with copyright and maintain patient data security.

This paper enhances the robust watermarking method Coltuc et al. by modifying the DCT coefficient pairs in the watermark embedding formula. The proposed formula ensures that the difference between the two coefficients is at least as much as ζ. If the difference between the two coefficients is less than ζ, then the new pixels are modified so that the difference is equal to ζ. This new watermarking system on medical images based on modifying the DCT coefficient pair is suggested to obtain acceptable imperceptibility of watermarked images, impart data confidentiality of medical images, and preserve patient information privacy.

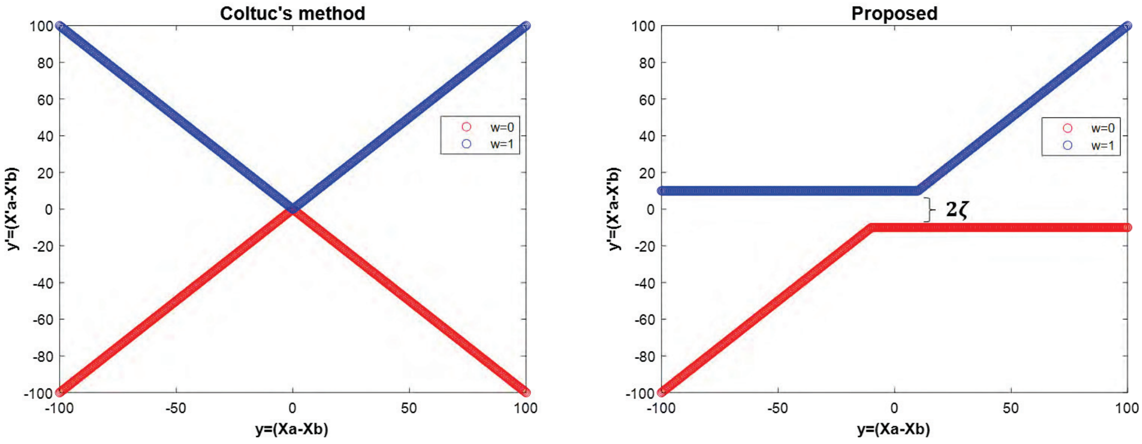

(a) (b)

Fig. 2: Illustration of watermark embedding formula (a) Coltuc's method, (b) Proposed.

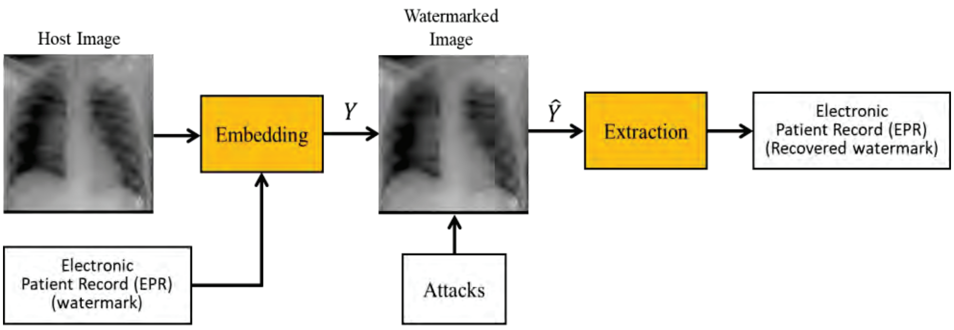

Fig. 3: The framework of medical image watermarking.

4.1 Modification of the Watermark Embedding Formula in Coltuc's Method

The value of the MF coefficient of the DCT generally has the same magnitude. After rounding operations to produce watermarked images and entering the decoding process, not all watermarks can be extracted correctly. We modified Eq. (3) so that the watermarked host image has high imperceptibility, protects the copyright (watermark) embedded in medical images, and maintains the privacy of patient information.

$$(\hat{x}'_a, \hat{x}'_b) = \begin{cases} (\hat{x}_a, \hat{x}_b), & if\ \hat{x}_a - \hat{x}_b > \zeta \text{ and } w = 1 \\ \left(\bar{x} + \frac{\zeta}{2}, \bar{x} - \frac{\zeta}{2}\right) & if\ |\hat{x}_a - \hat{x}_b| \leq \zeta \text{ and } w = 1 \\ \left(\bar{x} + \frac{\zeta}{2}, \bar{x} - \frac{\zeta}{2}\right) & if\ \hat{x}_a - \hat{x}_b < -\zeta \text{ and } w = 1 \\ (\hat{x}_a, \hat{x}_b), & if\ \hat{x}_a - \hat{x}_b < -\zeta \text{ and } w = 0 \\ \left(\bar{x} - \frac{\zeta}{2}, \bar{x} + \frac{\zeta}{2}\right), & if\ |\hat{x}_a - \hat{x}_b| \leq \zeta \text{ and } w = 0 \\ \left(\bar{x} - \frac{\zeta}{2}, \bar{x} + \frac{\zeta}{2}\right), & if\ \hat{x}_a - \hat{x}_b > \zeta \text{ and } w = 0 \end{cases} \tag{4}$$

The proposed formula ensures that the difference between the two MF coefficients, namely $\hat{x}_a$ and $\hat{x}_b$, is at least as much as ζ. If the distance between the two MF coefficients is less than ζ, then the new pixel is modified so that the difference in distance is as significant as ζ.

Modification of the insertion formula of Coltuc's method through the DCT coefficient pair can be seen in Eq. (4) and then simplified to Eq. (5). Figure 2(b) presents the illustration of the proposed formula

$$(\hat{x}'_a, \hat{x}'_b) = \begin{cases} (\hat{x}_a, \hat{x}_b), & \text{if } (\hat{x}_a - \hat{x}_b < -\zeta \text{ and } w = 0) \text{ or } (\hat{x}_a - \hat{x}_b > \zeta \text{ and } w = 1) \\ \left(\frac{\hat{x}_a + \hat{x}_b + (2w-1)\zeta}{2}, \frac{\hat{x}_a + \hat{x}_b - (2w-1)\zeta}{2}\right), & \text{otherwise} \end{cases} \quad (5)$$

with $\bar{x}$ is the average of the two MF coefficients of the DCT, namely $\hat{x}_a$ dan $\hat{x}_b$.

4.2 Embedding Stage

The input of the watermarking embedding stage is a medical image X as the host, and the output is a watermarked host image Y. The sizes of X and Y are M × M, while the size of W is N × N. Fig. 4(a) presents the watermarking embedding stage, and the detailed embedding steps are described as follows.

1. Split X into 8×8 non-overlapping blocks.
2. For each block, apply DCT using Eq. (1) so that it produces $\hat{X}$.
3. In each DCT block, the two MF coefficients $\hat{x}_a$ and $\hat{x}_b$ are decisive in embedding one-bit watermark $w \epsilon \{0,1\}$. The robust watermark embedding formula is expressed in Eq. (5).
4. The DCT coefficient of Y is done as follows:

$$\hat{y}_i = \begin{cases} \hat{x}'_i, & if\ i \in \{a, b\} \\ \hat{x}_i, & \text{otherwise} \end{cases} \quad (6)$$

5. Process the inverse DCT using Eq. (2), and a watermarked image is obtained.

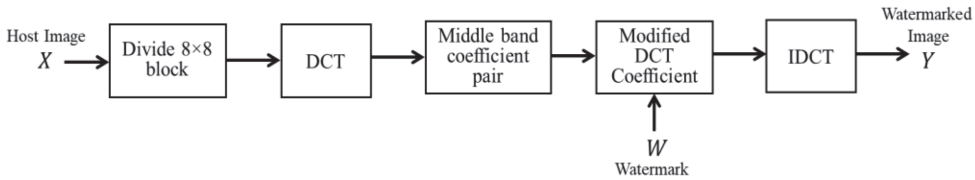

(a)

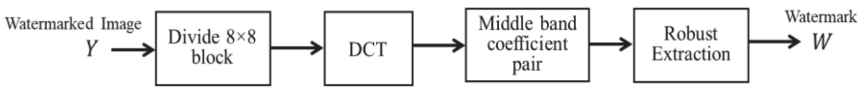

(b)

Fig. 4: The proposed watermarking method using DCT coefficient pair (a) embedding stage (b) extraction stage.

4.3 Extraction Stage

The input of the watermarking extraction stage is the Y watermarked host image, and the output is the extracted watermark W^*. While, Y and W^* sizes are M × M, and N × N, respectively. Figure 4(b) presents the watermarking extraction stage, and the extraction steps in detail are described as follows.

1. Split Y into 8×8 non-overlapping blocks.

2. Apply DCT to each block using Eq. (1) so that it produces $\hat{Y}$.
3. In each DCT block, the two MF coefficients $\hat{y}_a$ and $\hat{y}_b$ become determinants in extracting the one-bit watermark $w\epsilon\,\{0,1\}$. The robust watermark extraction formula is stated as follows.

$$W^* = \begin{cases} 1, & \text{if } \hat{y}_a - \hat{y}_b > 0 \\ 0, & \text{otherwise} \end{cases} \tag{7}$$

At the transmission is without noise, W^* equals W.

5. RESULTS AND DISCUSSION

This section evaluates the effectiveness of the suggested robust and imperceptible watermarking technique. Subjective visual observation and objective quantitative analysis are used to evaluate the proposed method. Numerous attacks with varying parameters were performed to assess robustness further. Finally, the proposed method's imperceptibility and robustness are compared to state-of-the-art works.

This experiment uses the grayscale format and image sizes 512×512 of the host medical image. A total of five medical images from different modality types were used as test data, including MRI, X-Ray, Computed Tomography (CT), ultrasound (US), and colonoscopy. Medical images were retrieved from the MedPixTM medical image database [26] and CVC-ClinicDB database [28]. The host medical image modality used in the experiment is shown in Fig. 5(a-e). Meanwhile, the watermark is a random binary image whose size depends on the block size discussed in the previous section. For an 8×8 block, the amount of watermarks embedded into the original host medical image is (512×512)/(8×8)=4096 bits. In other words, blocks measuring 8×8 yield a watermark of size 64×64.

The efficiency of the proposed method is thoroughly evaluated on two watermarking criteria, including imperceptibility and robustness. The performance metric for imperceptibility criteria uses peak signal noise ratio (PSNR) [9]. The watermarked host image must be invisible to humans to guarantee information security. Therefore, imperceptibility/ invisibility criteria are essential metrics in watermarking techniques. The PSNR measures how visually similar the watermarked image and the original host are. Both images should look the same, so there is no significant difference between the two. The similarity between the two images increases with increasing PSNR values and vice versa. Generally, the watermarked image is acceptable if the PSNR is more than 37 dB and the watermark is not discernible to the human visual system [29]. Here, X is the original host image, Y is the watermarked host image, and M×M is the host image size. Mathematically, PSNR (in dB) is formulated as follows [11,15].

$$PSNR = 10 \times \log \frac{255^2 \times \mathrm{M} \times \mathrm{M}}{\sum_{i=1}^{\mathrm{M}} \sum_{j=1}^{\mathrm{M}} (X_{i,j} - Y_{i,j})^2} \tag{8}$$

The bit error rate (BER) and normalized correlation (NC) are the performance metric to evaluate a watermarking technique's robustness criteria. Technically, BER measures the erroneous bit rate after the watermark extraction process. If the BER value is close to 0, then a few messages are lost, and vice versa. Ideally, the value of BER should be 0. If EB is the amount of incorrectly decoded bits, and TB is the number of watermark bits, then BER can be calculated [14], [27] as EB/TB.

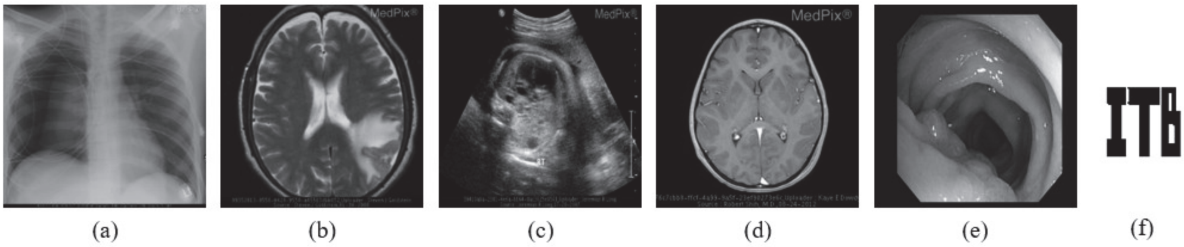

Fig. 5: Five modalities of original medical image and a watermark (a) X-ray , (b) CT, (c) US, (d) MRI, (e) Colonoscopy, (f) watermark.

Principally, the NC measures the similarity between the original and extracted watermark images. The NC can be described mathematically by Eq. (9). If the NC value is near 1, then the watermarking method is very robust.

$$NC = \frac{\sum_{i=1}^{N}\sum_{i-1}^{N} W_{i,j}\, W_{i,j}^{*}}{\sum_{i=1}^{N}\sum_{i-1}^{N} W_{i,j}^{2}} \quad (9)$$

where W and W^* are the original watermark and extracted watermark images, respectively. N×N is the watermark image's size [14]. After applying the embedding and extraction processes, the proposed scheme's imperceptibility and robustness tests are carried out for varied medical images.

5.1 ζ Parameter Evaluation

The proposed watermark embedding formula ensures that the difference between the two MF coefficients, namely $\hat{x}_a$ and $\hat{x}_b$, is at least ζ. If the distance between the two MF coefficients is less than ζ, then the new pixels are modified so that the distance difference is ζ. We changed the value of the ζ parameter in the watermark embedding formula to get the PSNR and expected robustness level. Experiments were carried out on five types of medical images, i.e., X-ray, CT, US, MRI, and Colonoscopy. Figure 6 presents the effect of the ζ parameter on PSNR and BER. Figure 6(a) shows the relationship between ζ and BER.

Higher ζ results in lower BER. The criterion BER is 0 when $\zeta \geq 3$. It means that the extracted watermark can be recovered very well. BER of 0 means there are no bit errors in watermark extraction. While Fig. 6(b) shows the relationship between BER and PSNR over ζ, which corresponds to Fig. 6(a). The higher the ζ value, the higher the resistance, but the lower the PSNR. When the resistance condition is ideal, namely BER is 0, the PSNR value ranges around 48 dB to 59 dB for the range of ζ is 3 to 10. Thus, ζ determines the imperceptibility and robustness of the watermark embedding into the host medical image.

5.2 Imperceptibility Analysis

For integrity and ensuring information security, watermarked host medical images must be imperceptible/ invisible to humans. Figure 7 shows a watermarked host X-ray image when not under attack and the extracted watermark. The experiment was carried out when $\zeta = 3$. The PSNR, BER, and NC results of each corresponding image are also shown in Fig. 7. The watermarked image is acceptable because the PSNR is more than 37 dB, and the watermark is not discernible to the human visual system [30].

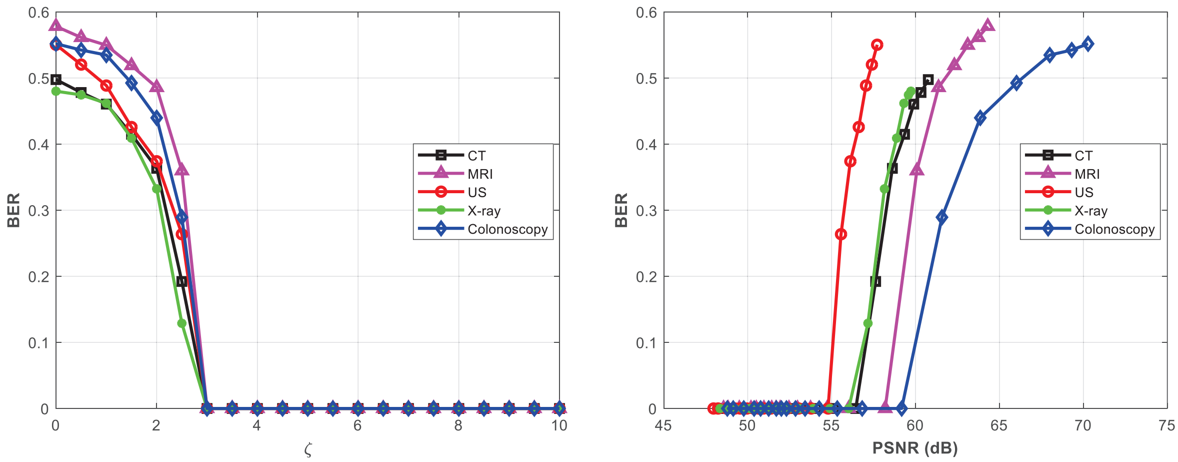

(a) (b)

Fig. 6: Evaluation of ζ (a) The BER of extracted watermark
(b) The trade-off between PSNR and BER.

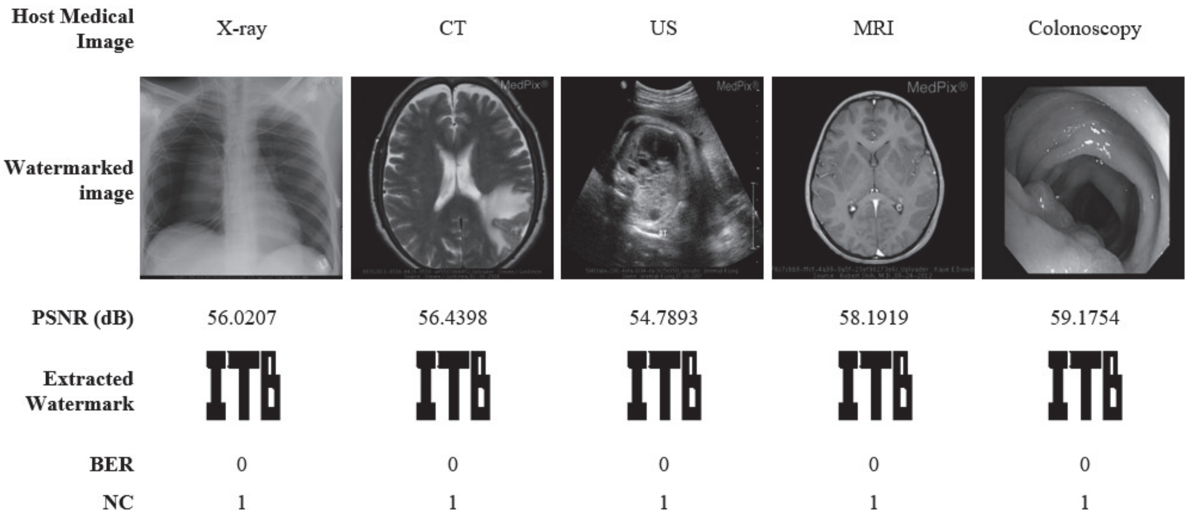

Fig. 7: Imperceptibility and robustness performance. Rows represent the extracted watermarked image and watermark along with their corresponding PSNR, NC, and BER. Columns represent type medical images, i.e., X-ray, CT, US, MRI, and Colonoscopy.

Based on Fig. 7, the imperceptibility criterion of the suggested method is that all PSNR of each watermarked medical image is greater than 54 dB. The average PSNR generated for the five watermarked medical image modalities is 56.3604 dB. Then, all extracted watermarks yielded BER is 0 and NC is 1 when the watermarked host image was not subjected to attack. It demonstrates that the method of watermarking is imperceptible. Furthermore, the suggested approach satisfies both the subjective and objective standards for watermarking invisibility. When the watermarked host image is not subjected to an assault, extracted watermarks have a BER of 0 and an NC of 1. Therefore, the process of watermarking has a high level of imperceptibility. Thus, the suggested method satisfies both the subjective and objective requirements for watermarking invisibility.

5.3 Robustness Analysis

Various watermarking attacks were applied to watermarked medical images to examine the robustness criteria of the proposed method. Table 1 represents different attacks with parameter specifications used in the experiment. These attacks include compression, filtering, noise, histogram equalization, sharpening, and motion blur. In particular, compression attacks include JPEG and JPEG2000. JPEG compression parameters with quality factor (QF) 80 and JPEG2000 compression with compression ratio (CR) = 4 and 8. Filter attacks consist of median, Gaussian, average, and lowpass filters. The parameters in the filtering attack use a filter with a window size of 3×3. Noise attacks include Gaussian, salt & pepper, and speckle. The parameters in the noise addition attack are set by the variance or noise density of 0.001. Parameters of motion blur attack with linear motion of the camera with pixels Len = 7, with angle degrees Theta = 4. At the same time, histogram equalization and sharpening use default parameters.

Table 1: Various Attacks with Parameter Specifications in Experiments

Attack	Parameter Specifications
JPEG compression (JC)	QF = 80, 90
JPEG2000 compression (J2k)	CR = 8, 12
Median filter (MF)	3×3
Gaussian filter (GF)	3×3
Average filter (AF)	3×3
LPF	3×3
Gaussian noise (GN)	Mean = 0, Variance = 0.001
Salt & peppers noise (SP)	Noise density = 0.001
Speckle noise (SN)	Mean = 0, Variance = 0.001
Histogram equalization (HE)	-
Sharpening (SH)	-
Motion blur (MB)	Len = 7, Theta = 4

In the extraction stage, if the extracted watermark can recover from damaged watermarked images, then the watermarking method is said to be robust and secure. Here, BER and NC performance metrics examine the robustness of the proposed method under various watermarking attacks. In addition, the result of the suggested scheme is compared with the existing techniques [15,17] for the same medical image dataset. The BER of extracted watermark on numerous watermarked medical images is shown in Fig. 8. Meanwhile, Figure 9 presents the results of the extracted watermark from the attacked watermarked X-ray along with corresponding BER and NC.

Various attacks are rendered on watermarked medical images. These medical images include X-ray, CT, US, MRI, and Colonoscopy. On the extraction side, the extracted watermark image is expected to be recovered from the damaged watermarked medical image. Based on Fig. 8, JPEG compresses images without significantly altering their appearance. Medical images with watermarks are compressed with JPEG using varying quality factors. Then, the proposed method is used to extract the watermarked image. The experiments indicated that the proposed method performs well for all the medical images we tested on JPEG compression with QF > 80 and JPEG2000 compression with CR < 12. The extracted watermark can still be interpreted visually if BER < 0.3 [30]. On X-ray, CT, and Colonoscopy images, watermarks can be extracted well even at JPEG compression with QF = 90 and JPEG2000 compression with CR = 12. Remarkably, watermarks can be best extracted, with BER is 0 for all compression parameters given in watermarked Colonoscopy image. Based on Fig. 9, watermarks can be extracted well with BER of 0 and NC of 1 for JPEG compression attacks with QF = 90 and JPEG2000 with CR = 8, and 12 given to the attacked watermarked X-ray images.

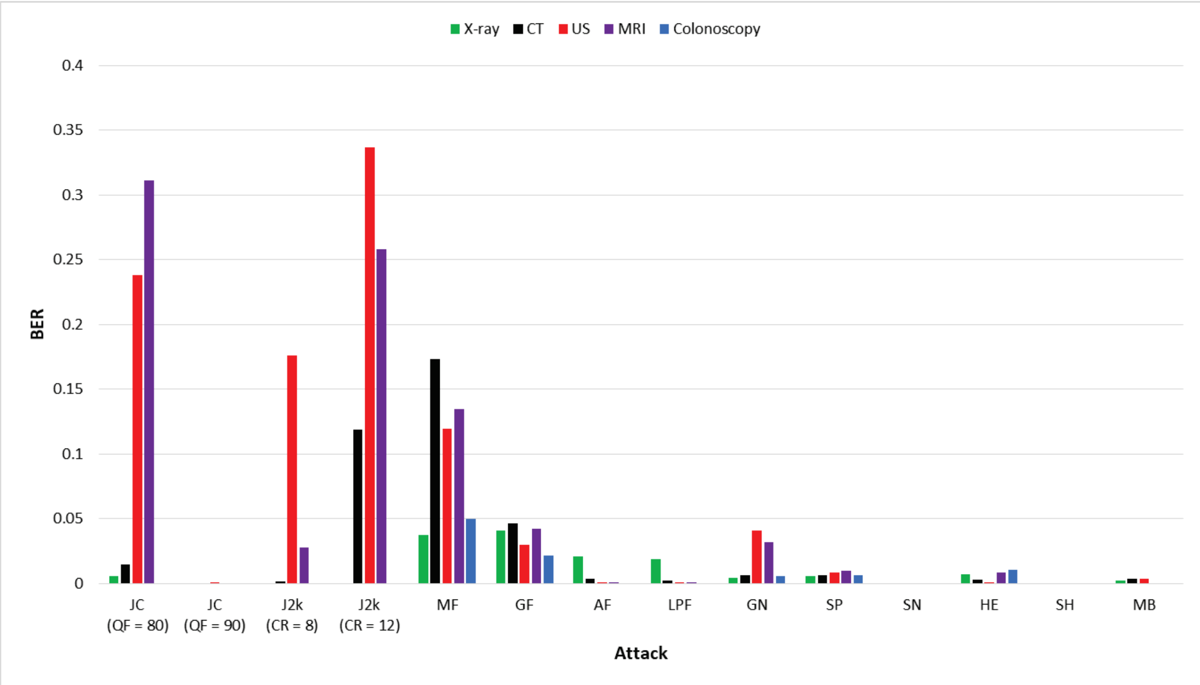

Fig. 8: The BER of extracted watermarks when condition with attack.

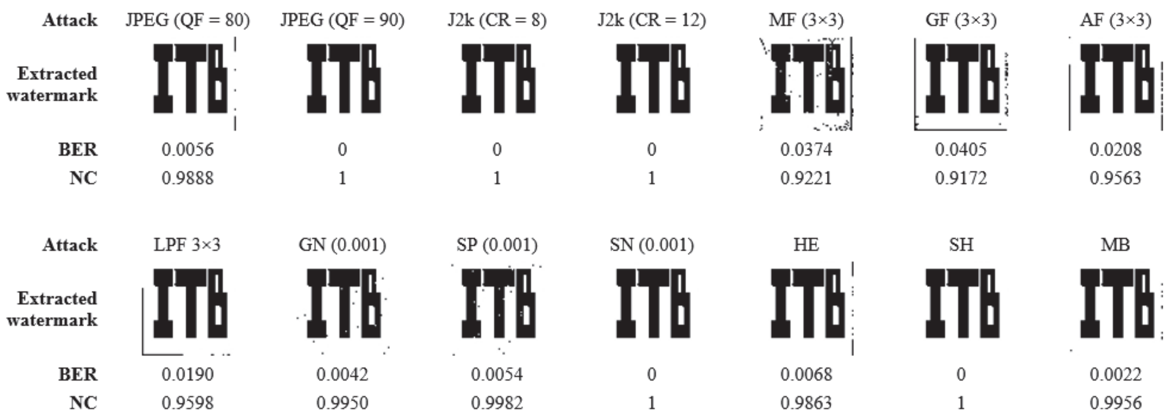

Fig. 9: The BERs and NCs of extracted watermarks from watermarked X-rays attacked.

Four filters, including the median, Gaussian, average, and low pass, and three different noises, such as Gaussian, salt & pepper, and speckle, are applied to watermarked medical images. Afterward, the watermark image is extracted using the proposed method. The experiment results (Fig. 8 and Fig. 9) prove that the proposed method performs well for all medical images provided a filtering attack. Remarkably, watermarks can be extracted very well with BER 0 for watermarked Colonoscopy medical images subjected to average filter and LPF attacks. The experiment results also prove that the proposed scheme performs well for all medical images under the noise attack. Remarkably, watermarks can be successfully extracted with a BER of 0 for all watermarked medical images subjected to speckle noise attacks.

https://doi.org/10.31436/iiumej.v24i1.2597

A series of other attacks, such as histogram equalization, sharpening, and motion blur are also applied to watermarked medical images for endurance testing. Based on the experiment results (Fig. 8 and Fig. 9), the proposed scheme performs well for all medical images given the three attacks. Impressively, watermarks can be well extracted with a BER of 0 for all watermarked medical images given a sharpening attack. Watermarks can also be extracted with a BER of 0 for motion blur attacks rendered in watermarked MRI and Colonoscopy images.

5.4 Comparison of the Proposed Method with State-of-the-Art Work

In Fig. 10, the imperceptibility performance of the proposed method is compared with Coltuc's method [13] and the recently developed watermarking method [14,15] for medical image identity protection. The watermark payload under the same conditions, which is 1 bit for every 64 pixels of the host medical image. The PSNR value of the proposed method is compared with the related work. The methods are compared using ζ = 3 and without watermarking attacks. The proposed scheme offers superior performance to the three existing schemes [13-15]. In the proposed method, the average PSNR value of watermarked medical images is 56.3604 dB. Meanwhile, the mean of PSNR for watermarked medical images from the [13-15] scheme are 50.5647 dB, 48.3150 dB, and 53.6184 dB, respectively. It means that the insertion of watermark bits does not influence the watermarked medical image of the proposed method. The proposed method produces high imperceptibility over the the state-of-the-art works [13-15].

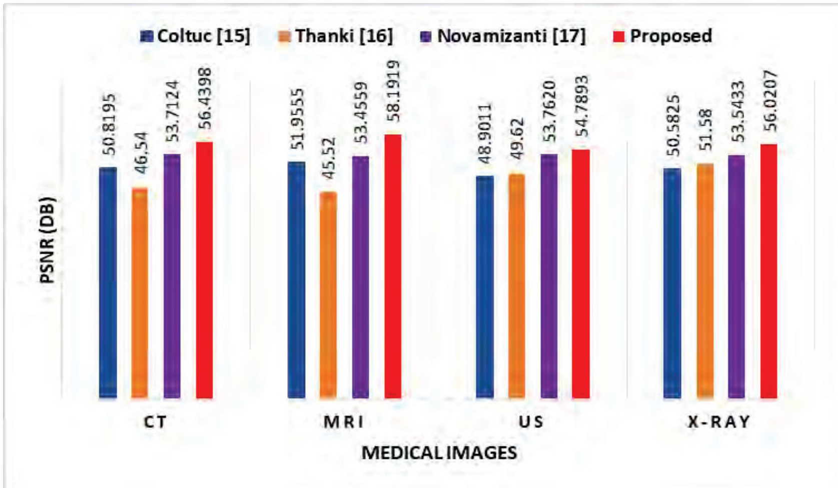

Fig. 10: Comparison under different medical images and methods.

Specifically, Table 2 summarizes the robustness performance of the proposed method compared to Coltuc's method [13] to evaluate how much contribution the proposed watermarking method makes. The host image used as test data is an X-ray. The suggested method performs well compared to the previous method against all types of watermarking attacks. In fact, the watermark can be extracted perfectly in a JPEG compression attack with QF = 90, JPEG2000 with CR = 8 and 12, speckle noise, and sharpening. The proposed method is outstanding from Coltuc's method [13], with the increase in BER and NC being 93% and 14%, respectively.

Table 2: Comparison of BERs and NCs of the Proposed Method to the Coltuc's Method [13] in Attacked Watermarked X-Ray

Attack	BER	NC

	[13]	Proposed	[13]	Proposed
JPEG (QF=80)	0.2488	**0.0056**	0.8491	**0.9888**
JPEG (QF=90)	0.2493	**0**	0.8523	**1**
J2k (CR=8)	0.1177	**0**	0.9605	**1**
J2k (CR=12)	0.1626	**0**	0.9337	**1**
MF [3×3]	0.2842	**0.0374**	0.4059	**0.9221**
GF [3×3]	0.1492	**0.0405**	0.6942	**0.9172**
AF [3×3]	0.0615	**0.0208**	0.8693	**0.9563**
LPF [3×3]	0.0625	**0.0190**	0.8673	**0.9598**
GN (0.001)	0.2261	**0.0042**	0.8644	**0.9950**
SP (0.001)	0.0173	**0.0054**	0.9877	**0.9982**
SN (0.001)	0.2146	**0**	0.8652	**1**
HE	0.1060	**0.0068**	0.9237	**0.9863**
SH	0.0225	**0**	0.9843	**1**
MB	0.0603	**0.0022**	0.9706	**0.9956**

Table 3: NCs Comparison of the Proposed Method to the State-of-the-Art [14,15] in Attacked Watermarked X-Ray

Attack	Thanki [14]	Novamizanti [15]	Proposed
JPEG (QF=80)	0.9282	0.8769	**0.9888**
JPEG (QF=90)	0.9806	0.8973	1
GN (0.001)	0.6377	0.9970	0.9950
SP (0.001)	0.7532	0.9473	**0.9982**
HE	0.9708	0.8909	**0.9863**
SH	0.9674	0.9890	**1**

The proposed method is also compared with the recently developed watermarking methods [14,15] to maintain the privacy and protection of the EPR as a watermark. Host X-ray images were used as test data for all compared methods. Watermarking in both techniques [14,15] was performed in the FDCuT and DCT domains. The extraction process of both methods is semi-blind. The difference is the insertion of the watermarking technique [14] using the correlation sequence method. While in [15], the watermarking embedding technique uses the SVD method. Compared with the state-of-the-art works [14,15], the proposed method is superior in terms of resistance to JPEG compression attacks, sharpening, histogram equalization, and sharpening. In addition, on a JPEG compression attack with QF = 90 and sharpening, the watermark can be extracted perfectly. The proposed method modifies the DCT coefficient pairs to embed a robust watermark. Thus, the average result demonstrates that the suggested method outperforms the present scheme regarding imperceptibility, robustness, and security. The proposed approach can be part of a robust reversible watermarking scheme [31] due to the blind extraction stage of the proposed watermarking method.

3. CONCLUSION

This paper proposes a modification of the DCT coefficient pair in the watermark embedding process. The proposed formula ensures that the difference between the two coefficients is at least as ζ. If the difference between the two coefficients is less than ζ, then the new pixels are modified so that the difference is equal to ζ. This simple watermarking technique based on modifying DCT coefficient pairs is offered to achieve high imperceptibility, provide intellectual property protection for medical images, and ensure patient data security. The suggested method was evaluated on different types of medical images, including X-ray, CT, US, MRI, and Colonoscopy, and compared to numerous robust watermarking techniques of the current work. The experimental results indicate that the suggested method outperforms various contemporary watermarking techniques regarding imperceptibility, robustness, and security. The PSNR value for all categories of watermarked medical images exceeds 54 dB, and the average PSNR value is approximately 56 dB. In terms of resistance to JPEG compression attacks, histogram equalization, and sharpening, the suggested method is superior to numerous state-of-the-art robust watermarking methods. Future research could apply the presented technology to a robust reversible watermarking strategy and medical image protection for telemedicine applications.

ACKNOWLEDGEMENT

This research is part of L. Novamizanti's dissertation research funded by the Doctoral Dissertation Research Grant from the Ministry of Research and Technology of the Republic of Indonesia, file numbers: 083/E5/PG.02.00.PT/2022 and 343/IT1.B07.1/SPP- LPPM/V/2022. The Indonesian Endowment Fund for Education (LPDP) Scholarship and Telkom University also partially funded this research.

REFERENCES

[1] Memon, NA. Alzahrani A. (2020) Prediction-based reversible watermarking of CT scan images for content authentication and copyright protection. IEEE Access, 8: 75448-75462. doi: 10.1109/ACCESS.2020.2989175.

[2] Sajedi H, Rahbar S. (2020) Information hiding methods for E –Healthcare. Smart Health, 15: 100104. doi: 10.1016/j.smhl.2019.100104.

[3] Ahmad GI, Singla J, Giri KJ. (2021). Security and Privacy of E-health Data. In Multimedia Security, Springer Singapore, pp. 199-214.

[4] Lanxiang C, Wutong BAI, Zhiqiang YAO. (2020) A Secure and Privacy-Preserving Watermark Based Medical Image Sharing Method. Chinese J. Electron., 29(5): 819-825. doi: 10.1049/cje.2020.07.003.

[5] Magdy M, Hosny KM. (2022) Security of medical images for telemedicine : a systematic review. Multimed. Tools Appl., 81: 25101-25145. doi: 10.1007/s11042-022-11956-7

[6] Alzahrani A, Memon NA. (2021) Blind and Robust Watermarking Scheme in Hybrid Domain for Copyright Protection of Medical Images. IEEE Access, 9: 113714-113734. doi: 10.1109/ACCESS.2021.3104985.

[7] Thakur S, Singh AK, Ghrera SP, Mohan A. (2020) Chaotic based secure watermarking approach for medical images. Multimed. Tools Appl., 79: 4263-4276. doi: 10.1007/s11042-018-6691-0

[8] Hassan B, Ahmed R, Li BO, Hassan O. (2019) An Imperceptible Medical Image Watermarking Framework for Automated Diagnosis of Retinal Pathologies in an eHealth Arrangement. IEEE Access, 7: 69758-69775. doi: 10.1109/ACCESS.2019.2919381.

[9] Anand A, Singh AK. (2021) Watermarking techniques for medical data authentication : a survey. Multimed. Tools Appl., 80: 30165-30197. doi: 10.1007/s11042-020-08801-0

[10] Evsutin O, Dzhanashia K. (2022) Watermarking schemes for digital images : Robustness overview. Signal Process. Image Commun., 100: 116523. doi: 10.1016/j.image.2021.116523.

[11] Saini D, Ali M. (2020) A robust medical image watermarking framework based on SVD and DE In Integer DCT domain (Workshop Paper), pp. 373-378. doi: 10.1109/BigMM50055.2020.00064.

[12] Coltuc D, Chassery JM. (2007) Distortion-free robust watermarking: a case study. Secur. Steganography, Watermarking Multimed. Contents IX, 6505: 65051N, doi: 10.1117/12.702445.

[13] Coltuc D. (2007) Towards distortion-free robust image authentication. J. Phys. Conf. Ser., 77: 012005. doi: 10.1088/1742-6596/77/1/012005.
[14] Thanki R, Borra S, Dwivedi V, Borisagar K. (2017) An efficient medical image watermarking scheme based on FDCuT–DCT. Eng. Sci. Technol. an Int. J., 20(4): 1366-1379. doi: 10.1016/j.jestch.2017.06.001.
[15] Novamizanti L, Wahidah I, Wardana NPDP. (2020) A Robust Medical Images Watermarking Using FDCuT-DCT-SVD. Int. J. Intell. Eng. Syst., 13(6): 266-278. doi: 10.22266/ijies2020.1231.24
[16] Lei M, Liu X, Wang M, Yang Y, Qu Z. (2018) Robust image watermarking based on quantization index modulation in the DCT domain. J. Internet Technol., 19(2): 507-514. doi: 10.3966/160792642018031902019.
[17] Zhu Z, Zheng N, Qiao T, Xu M. (2019) Robust steganography by modifying sign of DCT coefficients. IEEE Access, 7: 168613-168628. doi: 10.1109/ACCESS.2019.2953504.
[18] Rachmawanto EH, Setiadi DRIM, Sari CA, Rijati N. (2019) Imperceptible and secure image watermarking using DCT and random spread technique. Telkomnika (Telecommunication Comput. Electron. Control., 17(4): 1750-1757. doi: 10.12928/TELKOMNIKA.v17i4.9227.
[19] Byun SW, Son HS, Lee SP. (2019) Fast and Robust Watermarking Method Based on DCT Specific Location. IEEE Access, 7: 100706-100718. doi: 10.1109/ACCESS.2019.2931039.
[20] Ko HJ, Huang CT, Horng G, WANG SJ. (2020) Robust and blind image watermarking in DCT domain using inter-block coefficient correlation. Inf. Sci. (NY)., 517: 128-147. doi: 10.1016/j.ins.2019.11.005.
[21] Nawaz SA, Li J, Bhatti UA, Mehmood A, Shoukat MU, Bhatti MA (2020) Advance hybrid medical watermarking algorithm using speeded up robust features and discrete cosine transform. PLoS One, 15(6): 1-21. doi: 10.1371/journal.pone.0232902.
[22] Kumar S, Jha RK. (2019) FD-based detector for medical image watermarking. IET Image Processing, 13(10): 1773-1782 2019. doi: 10.1049/iet-ipr.2018.5485.
[23] Fares K, Khaldi A, Redouane K, Salah E. (2021) DCT & DWT based watermarking scheme for medical information security. Biomed. Signal Process. Control, 66: 102403. doi: 10.1016/j.bspc.2020.102403.
[24] Khayam SA. (2003) The Discrete Cosine Transform (DCT): Theory and Application. In Information Theory and Coding, Michigan State University, pp. 1-13.
[25] Hamidi M, Haziti ME, Cherifi H, Hassouni ME. (2018) Hybrid blind robust image watermarking technique based on DFT-DCT and Arnold transform. Multimed. Tools Appl., 77(20): 27181-27214. doi: 10.1007/s11042-018-5913-9.
[26] Hernandez JR, Amado M, Perez-Gonzalez F. (2000) DCT-domain watermarking techniques for still images: detector performance analysis and a new structure. IEEE Trans. Image Process.,9(1): 55-68. doi: 10.1109/83.817598.
[27] Wang X, Li X, Pei Q. (2020) Independent Embedding Domain Based Two-Stage Robust Reversible Watermarking. IEEE Trans. Circuits Syst. Video Technol., 30(8): 2406-2417. doi: 10.1109/TCSVT.2019.2915116.
[28] Rahim T, Novamizanti L, Ramatryana INA, Shin SY. (2021) Compressed medical imaging based on average sparsity model and reweighted analysis of multiple basis pursuit. Comput. Med. Imaging Graph., 90: 101927. doi: 10.1016/j.compmedimag.2021.101927.
[29] Guo Y, Li BZ., Goel N (2017) Optimised blind image watermarking method based on firefly algorithm in DWT-QR transform domain. IET Image Process, 11(6): 406-415. doi: 10.1049/iet-ipr.2016.0515
[30] Budiman G, Suksmono AB, Danudirdjo D. (2020) Compressive Sampling with Multiple Bit Spread Spectrum-Based Data Hiding. Appl. Sci., 10(12): 1-21. doi: 10.3390/app10124338.
[31] Novamizanti L, Suksmono AB, Danudirdjo D, Budiman G. (2022) Robust Reversible Watermarking using Stationary Wavelet Transform and Multibit Spread Spectrum in Medical Images. Int. J. Intell. Eng. Syst., 15(3): 343-354. doi: 10.22266/ijies2022.0630.29.

https://doi.org/10.31436/iiumej.v24i1.2625

MULTI-OBJECTIVE MAYFLY OPTIMIZATION IN PHASE OPTIMIZATION OF OFDM

ABDUL AZEEZ*AND SURAIYA TARANNUM

Department of Electronics and Communication Engineering, HKBK College of Engineering, Bangalore, 560045, India

**Corresponding author: abdulazeez.ec@hkbk.edu.in*

(Received: 10th October 2022; Accepted: 8th November 2022; Published on-line: 4th January 2023)

ABSTRACT: Communication systems have been used tremendously in recent years which results in the need for high data transmission rates. Orthogonal Frequency Division Multiplexing (OFDM) provides robust performance in frequency selective fading due to high bandwidth efficiency and inter-symbol interference. Various optimization techniques were applied in existing research to increase the efficiency of OFDM in a communication system. The existing research has a limitation of considering a single objective to improve the efficiency of OFDM and also has a local optima trap. This research proposes a Multi-Objective Mayfly algorithm (MOMF) to consider multi-objective and provides a proper trade-off between exploration and exploitation. The Partial Transmit Sequence (PTS) is applied in the model to test the performance. The FFT sizes and modulation orders are varied to evaluate the performance of the MOMF technique in phase optimization. The MOMF technique effectively increases the performance of the model than other existing optimization techniques. The MOMF technique provides a non-dominated solution to escape from local optima trap. The MOMF model considers PAPR, BER, and SER in MIMO-OFDM system to increase the efficiency of the system. The exploration-exploitation trade-off helps to improve the convergence and overcome local optima trap. The MOMF in OFDM phase optimization was evaluated using BER, SER, and Peak-to-Average Power Ratio (PAPR) metrics. The MOMF method has PAPR of 3.95 dB and PSO-GWO method has 4.92 dB of PAPR.

ABSTRAK: Sistem komunikasi telah digunakan secara meluas sejak beberapa tahun ini dan dapatan kajian menunjukkan keperluan pada kadar transmisi data yang tinggi. Pemultipleksan Bahagian Frekuensi Ortogon (OFDM) menyediakan prestasi berkesan dalam pemilihan pemudaran frekuensi berdasarkan keberkesanan lebar jalur tinggi dan gangguan antara-simbol. Pelbagai teknik optimum digunakan pada kajian sebelum ini bagi meningkatkan keberkesanan OFDM dalam sistem komunikasi. Kajian tersebut mempunyai kekurangan dalam memilih satu objektif bagi membaiki keberkesanan OFDM dan juga mempunyai perangkap optima setempat. Kajian ini mencadangkan algoritma Mayfly Objektif-Pelbagai (MOMF) bagi memilih objektif-pelbagai dan menyediakan keseimbangan yang wajar antara eksplorasi dan eksploitasi. Urutan Pancar Separa (PTS) telah digunakan dalam model ini bagi menguji prestasi. Saiz FFT dan turutan modulasi dipelbagaikan bagi menguji keberkesanan teknik MOMF pada fasa pengoptimuman. Teknik MOMF dengan berkesan menaikkan prestasi model ini berbanding teknik-teknik sedia ada yang lain. Teknik MOMF menyediakan solusi kepada teknik bukan-dominasi bagi mengelak perangkap optima setempat. Model MOMF ini mengambil kira PAPR, BER, dan SER dalam sistem MIMO-OFDM bagi meningkatkan kecekapan sistem. Keseimbangan yang wajar antara eksplorasi-eksploitasi membantu dalam membaiki penumpuan dan mengatasi perangkap optima setempat. MOMF dalam fasa optimanisasi OFDM telah dinilai menggunakan BER, SER, dan matrik Nisbah Kuasa Puncak-kepada-Purata (PAPR). Kaedah MOMF mempunyai nilai PAPR sebanyak 3.95 dB dan kaedah PSO-GWO mempunyai PAPR 4.92 dB.

KEYWORDS: *exploration; multi-objective mayfly algorithm; OFDM phase optimization; partial transmit sequence*

1. INTRODUCTION

Smart grid systems, Digital Audio Broadcasting (DAB), LTE, 3GPP, Wi-MAX, Wireless LAN, and Terrestrial Digital Video Broadcasting (DVB-T) of various wireless broadband communication systems are applied with the OFDM technique to improve their efficiency. OFDM systems have superior qualities and have a limitation of high PAPR for RF signals. OFDM has amplitude variation in the time domain due to its multicarrier nature and also has a large dynamic range or PAPR [1]. The OFDM signal is clipped when applied to a non-linear High-Power Amplifier (HPA) if high PAPR degrades the in-band distortion and out-of-band radiation. A wide dynamic range of expensive linear HPA is required in OFDM transmitters for efficient performance [2]. The many PAPR reduction methods of OFDM systems include Selective Mapping (SLM), PTS, tone reservation and tone injection, non-linear companding, coding, and clipping [3]. The PTS and SLM are popular distortionless techniques that received substantial attention due to decrease in PAPR without BER degradation. High computation complexity and Side Information (SI) are major limitations in these techniques. The complexities of the PTS and SLM PAPR reduction methods are compared, in which the comparison shows that the PTS method has lower complexity and the SLM method has high PAPR reduction [4,5].

Less search complexity of several optimization methods has been recently developed to optimize the PTS method for CM reduction and PAPR reduction in OFDM systems. Some of the optimization methods are Grey Wolf Optimization (GWO), Tabu Search (TS), Harmony Search (HS), Adaptive Particle Swarm Optimization (APSO), and Hybrid Genetic Algorithm (HGA) [6,7]. OFDM of Multiple-Input Multiple-Output (MIMO) has received wide attention due to its advantages such as channel fading robustness, fading environment diversity, spectral efficiency and high data rate. However, the OFDM-MIMO also suffers from disadvantages such as high envelope fluctuations in a transmitted signal called PAPR that decreases the HPA efficiency, increases complexity of non-linear elements and Bit Error Rate (BER) degradation occurs from out-of-band radiation [8-10]. The contribution of this research is discussed below.

- The MOMF method is proposed to consider PAPR, BER, and SER in the MIMO-OFDM system to increase the efficiency of the model. The MOMF method provides a proper exploration-exploitation trade-off that improves the efficiency of the optimization.
- The exploration-exploitation trade-off process improves the convergence rate of the method and escapes from local optima trap. The MOMF method has higher efficiency compared to existing methods in optimization of MIMO-OFDM systems.

2. LITERATURE REVIEW

OFDM is a reliable and robust multicarrier modulation method that is sufficient for broadband communication. Various methods applied in OFDM for phase optimization are discussed in this section.

Lavanya et al. [11] applied Improved Monarch Butterfly Optimization (IMBO) method for PAPR reduction in the OFDM framework. The IMBO method was efficient for optimal character fusion of phase rotation factor for minimizing computation. The IMBO method provides efficient search optimization, and using optimum phase factor and phase weighting

https://doi.org/10.31436/iiumej.v24i1.2625

method with less complexity. The IMBO method significantly reduces the PAPR and computational complexity. Sorting was carried out twice with the Monarch Butterfly Optimization method during every generation. The IMBO method applies Random Local Perturbation (RLP) and Opposition-Based Learning (OBL) to solve the sorting problem.

Ali and Hamza [12] applied Teaching Learning Based Optimization (TLBO) for PAPR reduction in OFDM optimization. The TLBO method has the advantage of less computational effort and no algorithm-specific parameter requirement. The TLBO consists of two-phases, teacher and learner phases, for learning the input data. The interaction between teacher and student is the teaching phase, and the interaction between the learners is the learning phase. The TLBO based method was applied to obtain the phase factor of optimum rotation in the SLM method for PAPR reduction. The TLBO-SLM method achieved considerably better performance in PAPR reduction.

Sharif and Emami [13] proposed the Improved Flower Pollination (IFP) algorithm to reduce the search complexity of Partial Transmit Sequence (PTS). The ACO-OFDM method was applied with PTS technique to reduce high PAPR in the system. The IFP method was derived from flower pollination behaviors and an asymmetrical clipped optical OFDM system was applied in IFP. The IFP method increased the optimization capability of standard flower pollination using a local pollination operator to increase exploitation ability and the global pollination phase was applied to increase exploration. The IFP method balanced the exploitation and exploration capacity of the optimization method. The IFP method had less computational complexity than the existing method in OFDM optimization.

Emami and Sharif [14] applied a Tree Growth Optimization (TGO) method to reduce the computational complexity for the selection of optimal phase factors in PTS. The TGO method was efficient in reducing the high PAPR of optical OFDM signals. The TGO consists of three operators: seed scattering, root spreading, and competition. The solution population was updated by these operators to find near-optimal solutions for optimization problems. The TGO-PTS method dramatically decreased the PAPR of the OFDM signal and had higher performance than existing methods in terms of convergence rate and solution quality.

Emami and Sharif [15] applied a Chaotic Differential Search Algorithm (CDSA) with an efficient and fast convergence optimizer for OFDM optimization. The CDSA method was an optimization technique to solve non-linear, largescale, and complex problems. The CSA method was compared with several optimization methods in terms of mitigation performance and search complexities. The CDSA and PTS were combined to solve the search complexity problem in the conventional method and to control a few parameters for exploring phase factors for the optimal set. The CDSA method had considerable performance in phase optimization than existing methods.

An improved Adaptive Simplified Optimized Iterative Clipping and Filtering (ASOICF) technique has been shown by Padarti and Nandhanavanam [16] to lower PAPR in OFDM systems. Due to its ease of application in the PAPR minimization in OFDM, ICF, between these PAPR reduction techniques, drew a lot of interest. The approach uses Lagrange Multiplier Optimization (LMO), which has the benefit of reducing the number of iterations in a specific way. It was discovered that the PAPR in OFDM signals was greatly reduced by the adaptive technique. The results clearly showed that the suggested approach performed better in terms of computational complexity. The peak of the clipped OFDM affected the noise overhead, therefore, it decreased the BER.

A Regularization Optimization Based Flexible Hybrid Companding and Clipping technique (ROFHCC) employed for PAPR reduction in OFDM systems was developed by Xing et al. [17]. The companding function comprised two components to lessen the complexity of the design. In order to achieve both peak power reduction and small power compensation, it limited the signal samples whose amplitudes exceeded a certain value to a constant value. Signals were extended using a linear companding function for samples below a specified amplitude. In order to jointly optimize the companding distortion and the continuity of the companding function, a regularization optimization model was developed. Nonetheless, the proposed method could not confirm the average power as constant.

3. RESEARCH METHOD

The input signal is applied to LDPC encoding to encode the signal and apply for its modulation. The pilot insertion of the signal is transformed with IFFT and the pilot insertion information is provided as input to the proposed MOMF optimization to find optimal parameter settings. The optimal parameter settings of the MOMF optimization method are applied in the STBC encoder as well as in the AWGN noise channel. The STBC decoding is carried out and cyclic prefix removal is applied. The FFT is applied in the signal and pilot removal is carried out to process the output signal. The block diagram of the MOMF method in phase optimization of OFDM is shown in Fig. 1 and Fig. 2.

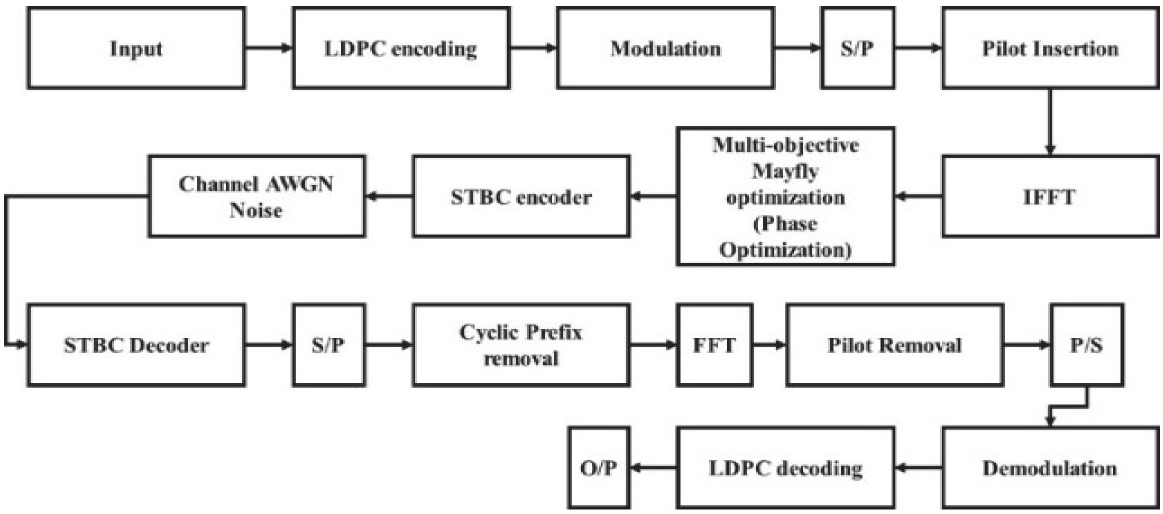

Fig. 1: The MOMF optimization in pilot insertion.

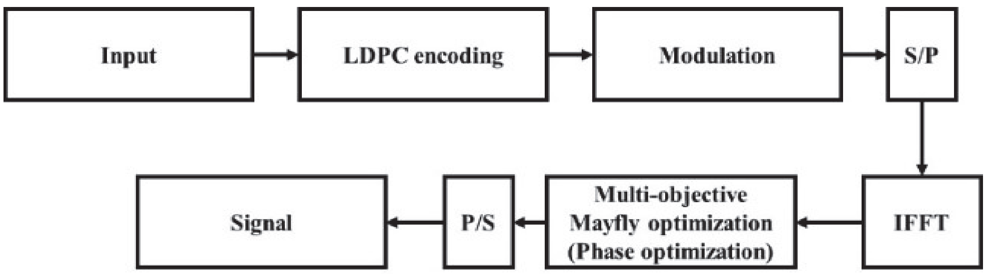

Fig. 2: The MOMF optimization in phase factor of OFDM.

3.1 PAPR in MIMO-OFDM

The subcarriers arrangement of relating subcarriers are adjusted to each signal surrounding the subcarriers M of OFDM data [13], [18], [19]. The MIMO-OFD structure of Orthogonal M subcarriers is over the period of $0 \le p \le G$ where the primary data signal period is denoted as G and the near sub-carriers repeat partitioning is denoted as $T0 = 1/G$. The OFDM movement of complex baseband in M subcarriers is given in Eq. (1).

$$s(p) = \frac{1}{\sqrt{M}} \sum_{n=0}^{M-1} A_n e^{j2\pi n T_o p}, 0 \le p \le G \tag{1}$$

The discrete time adaptation is mentioned as $G_c = G/M$ and substitutes $p = mG_c$ which is expressed in Eq. (2),

$$s(m) = \frac{1}{\sqrt{M}} \sum_{n=0}^{M-1} A_n e^{\frac{j2\pi mn}{DM}}, \quad m = 0,1,\ldots,MD-1 \tag{2}$$

Wherein, the oversampling element is denoted as D.

Spikes are not found in the inspection of the signal; therefore, it provides optimistic results for PAPR. Fourier change in the OFDM transmits the ordinary power and quick power of PAPR which is given as (p), as in Eq. (3).

$$PAPR = \frac{max_{0 \le p \le G} |a(p)|^2}{E\left[\left|a(p)^2\right|\right]} \tag{3}$$

Wherein, the desire expectation is $E[.]$.

The consistent time of PAPR is not unquestionably registered in the Nyquist inspecting rate which completely depends on OFDM signal. The OFDM signals of PAPR in the Complementary Cumulative Distribution Function (CCDF) are used to improve PAPR reduction accurately. The CCDF probability outperforms the edge of PAPR and is represented in Eq. (4).

$$CCDF\left(PAPR\left(a(t)\right)\right) = p_q\left(PAPR\left(a(t)\right)\right) > PAPR_0 \tag{4}$$

3.2 Partial Transmit Sequences (PTS)

The PAPR diminish technique based on fractional transmit arrangement is PTS. This is based on the original OFDM sequence which is divided into sub-grouping experts and each sub-progression weight is varied until the expert is in optimal value [13,20-22].

Random space of data information is separated into W sub-pieces of non-covering and has comparable size S of each sub-square. The S/W non-zero segments are present in each sub piece and the real part is zero. The sub-squares are given in Eq. (5).

$$\hat{A} = \sum_{W=1}^{W} c_w a_w \tag{5}$$

Here, $c_w = e^{r\partial_w}\left(\partial_w \in [0, 2\pi]\right)\{w = 1, 2, \ldots, w\}$.

Stage pivot of weighting part is denoted as c_w and time range of the signal is applied using IFFT operation on a_w.

A proper part mix $c = [c_1,\ c_2 \ldots c_w]$ is applied to measure the optimal value for PAPR reduction, as in Eq. (6).

$$c = arg \underset{(c_1, c_2, \ldots, c_w)}{min} \left(\underset{1 \le m \le M}{max} \left| \sum_{W=1}^{W} c_w, a_w \right|^2 \right) \tag{6}$$

Wherein, best estimation is found using the condition of $arg\ min(*)$ and by remembering the ultimate objective of c for PAPR execution redesign. Most of the complication arises on the downside and IFFT operations are performed for an extra $W-1$ times.

3.3 Multi-objective Mayfly Algorithm

In Mayfly, the nuptial dance and random flight operations help an algorithm escape local optimums and improve the harmony between its exploitation and exploration features. In this way, Mayfly efficiently identifies the space of each and every sequence of a given phase factor set. While considering the PSO in high-dimensional space, it falls into local optimum and attains a lower convergence rate in the iterative process. Therefore, the proposed MOMF optimization method is applied in the phase factor of OFDM to improve the efficiency of the model, BER, and PAPR. Mayfly group behavior is mimicked to develop the Mayfly algorithm with mating behavior [23-30]. Female and male mayflies are randomly divided from the population at the initial stage of algorithm. All mayflies are randomly scattered in d-dimensional space and $\xi = (\xi_1,\ \xi_2,\ \cdots,\ \xi_d)$ expression is considered for the selection of candidate solutions. The position change $\varpi = (\varpi_1,\ \varpi_2,\ \cdots,\ \varpi_d)$ is represented by the velocity vector.

1) Male mayflies' movement: i^{th} male Mayfly with the position of ξ_i^t at time t and velocity is denoted as ξ_i^t to change ith individual position. Male mayflies $\xi(t+1)$ of position $t+1$ is expressed in Eq. (7).

$$\xi_i^{t+1} = \xi_i^t + \varpi_{i,male}^{t+1} \tag{7}$$

The velocity for j^{th} dimension of i^{th} mayfly is denoted in Eq. (8).

$$\begin{aligned} \varpi_{ij,male}^{t+1} = \varpi_{ij,male}^{t} + a_1 \exp\left(-\beta\rho_p^2\right) \times \left(pbest_{ij} - \xi_{ij}^t\right) + \\ a_2 \exp\left(-\beta\rho_g^2\right) \times \left(gbets_j - \xi_{ij}^t\right) \end{aligned} \tag{8}$$

The position and velocity of j^{th} dimension of i^{th} mayfly are denoted as ξ_{ij}^t and $\varpi_{ij,male}^t$, respectively. The positive attraction constants are denoted as $a_i\ (i = 1,2)$ that respond based on social components and cognitive rules. The global optimal and local optimal positions are $gbest_j$ and $pbest_{ij}$, respectively. A fixed visibility coefficient is denoted as β, that controls individual visibility to other individuals. Cartesian distance is denoted as ρ_p and ρ_g from i^{th} mayfly, respectively for local and global optimal solutions. The global optimal value $gbest_j$ and local optimal value $pbest_{ij}$ are calculated using Eq. (9 & 10).

$$pbest_i = \begin{cases} \xi_i^{t+1} & , \quad if\ \{\phi_{1,\ldots,c}\left(\xi_i^{t+1}\right) < \{\phi_{1,\ldots,c}\left(pbest_i\right)\}\} \\ kept\ the\ same\ , & \quad otherwise \end{cases} \tag{9}$$

$$gbest \in \left\{ pbest_1, pbest_2, \ldots, pbest_N | \phi_{1,\ldots,c}\left(cbest\right) \right\} = dominate\left\{ \left\{ \phi_{1,\ldots,c}\left(pbest_1\right) \right\}, \left\{ \phi_{1,\ldots,c}\left(pbest_2\right) \right\}, \ldots, \left\{ \phi_{1,\ldots,c}\left(pbest_N\right) \right\} \right\} \quad (10)$$

Wherein, objective functions are represented as $\phi_{1,\ldots,c} : R^n \to R$. To ensure effective operation of the algorithm, the population of optimal mayflies constantly perform the up and down nuptial dance. The optimal mayflies' velocities are changed in the following Eq. (11).

$$\varpi_{ij,male}^{t+1} = \varpi_{ij,male}^{t} + d \times \rho \quad (11)$$

Wherein, the position for j^{th} dimension of i^{th} male mayfly is denoted as $\varpi_{ij,male}^{t}$, a random number of ρ is in the range of [-1, 1], and the nuptial dance coefficient is denoted as d.

2) Movement of female mayflies: For breeding, female individuals move toward males and male mayflies gather in swarms. The corresponding velocity and current position at time t of i^{th} female mayfly are denoted as $\varpi_{i,female}^{t+1}$ and ψ_i^t, respectively. The female mayflies of $(t+1)^{th}$ positions are given in Eq. (12).

$$\psi_i^{t+1} = \psi_i^t + \varpi_{i,female}^{t+1} \quad (12)$$

A deterministic scheme is used to define the attraction process in the Mayfly Algorithm optimization process. The fitness function is used by an optimal female and sub-optimal females to provide a tendency toward male individuals and sub-optimal male individuals. The j^{th} dimension of i^{th} female mayfly velocity is used for a minimization problem, as in Eq. (13).

$$\varpi_{ij,female}^{t+1} = \begin{cases} \varpi_{ij,female}^{t} + a_2 \exp\left(-\beta\rho_{mf}^2\right) \times \left(\xi_{ij}^t - \psi_{ij}^t\right), & if\, \phi\left(\psi_i\right) > \phi\left(\xi\right) \\ \varpi_{ij,female}^{t} + fl \times \rho \quad , & if\, \phi\left(\psi_i\right) \le \phi\left(\xi_i\right) \end{cases} \quad (13)$$

Wherein, the position and velocity for j^{th} dimension of i^{th} female mayfly are denoted as $\varpi_{ij,female}^{t}$ and ψ_{ij}^{t} respectively. The Cartesian distance of i^{th} male mayfly to i^{th} female mayfly is denoted as ρ_{mf}. The random walk coefficient is denoted as fl.

3) Mating of mayflies: Female and male populations are selected as two parents. As per the mating principle, the best male mates with the best female, that creates two offspring as shown in Eq. (14) and Eq. (15).

$$offspring1 = \mu \times male + \left(1-\mu\right) \times female \quad (14)$$

$$offspring2 = \mu \times female + \left(1-\mu\right) \times male \quad (15)$$

Wherein, the random value of male and female individuals in the previous generation is represented as $\mu \in (0,1)$. Initial individual velocities in the current generation are 0.

4) Multi-objective Mayfly Algorithm: The MOMF is a multi-objective variant of the Mayfly Algorithm based on roulette wheel selection, the strategy of non-dominated sorting, and the archive mechanism. Non-dominated Pareto optimal solution is applied to generate the present iteration and to archive the upper limit. Once a non-dominated solution is achieved, it is compared with the present solution. The least values are eliminated and a better solution is archived. Most populated neighborhoods are eliminated using $Pro_i = N_i / \chi,\ \chi > 1$ and when the archive is full, i^{th} individual number of members is denoted as N_i and χ is a constant. The roulette wheel method is used to develop solutions that are added to MOMF. The probability of the roulette wheel is set in Eq. (16).

$$Pro_i = \chi / N_i \tag{16}$$

A solution is selected from a set of non-dominated solutions using a multiple-criteria selection method. Fitness function values are normalized for male and female mayflies in Eq. (17).

$$Fitness_j^{i} = \frac{\left\lfloor Fitness_j^i - \underset{i \le j \le N}{min} \right\rfloor}{\left\lceil \underset{l \le j \le N}{max}\left(Fitness^i\right) - \underset{l \le j \le N}{min} \right\rceil} \tag{17}$$

The i^{th} fitness function of normalized value is denoted as $Fitness_j^i$ measured from j^{th} female or male mayfly and population size is denoted as N.

The j^{th} female or male mayfly is computed using multiple-criteria (Mc), as in Eq. (18).

$$Mc_j = \sum_{i=1}^{m} Fitness_j^i \tag{18}$$

The Mc values are used to sort male and female mayflies in MOMF; the lowest Mc values of mayfly's optimal male and female are obtained from individuals and non-dominated solution.

4. RESULTS AND DISCUSSION

This research applies the MOMF algorithm in phase optimization of OFDM to improve its efficiency. The OFDM parameters are given in Table 1 and parameter settings of MOMF are given in Table 2. Various FFT sizes of 64, 128, 256, 512, and 1024 were used to evaluate MOMF algorithm in OFDM phase optimization.

Table 1: OFDM parameters

FFT size	64, 128, 256, 512, 1024
User carriers	52, 104, 156, 208, 260
Pilot carriers	12, 24, 48, 60, 72
Antenna	2X2, 2X4, 4X2, 4X4
Cyclic prefix or guard time	0 to 2e-6s
Modulation	8 QAM, 16 QAM, 32 QAM, 64 QAM, 256 QAM
Oversampling factor	1e6 HZ
Channel type	Rayleigh Channel
Noise	AWGN

Table 2: MOMF Algorithm

Number of iteration	100
Population Size (males and females)	25 & 25
nPareto (Repository Size)	30
LowerBound	-3
UpperBound	6
g (Inertia Weight)	1
gdamp (Inertia Weight Damping Ratio)	1
a1 (Personal Learning Coefficient)	1.5
a2 & a3 (Global Learning Coefficient)	1.5 & 1.5
beta (Distance sight Coefficient)	0.99
dance (Mutation Coefficient)	0.77
dance_damp (Mutation Coefficient Damping Ratio)	0.77
f1 (Random flight)	0.77
f1_damp (Random flight Damping Ratio)	0.99
% Mating Parameters	-
nCrossover (Number of Parnets (Offsprings))	4
nMutation (Number of Mutants)	round (0.4*nPop)
mu (Mutation Rate)	0.001

The MOMF optimization method is applied in the phase factor of OFDM to improve the efficiency of the model and BER is shown in Fig. 3. The DCT and FFT techniques have higher efficiency in MOMF methods. The DWT has lower efficiency in the phase optimization of OFDM.

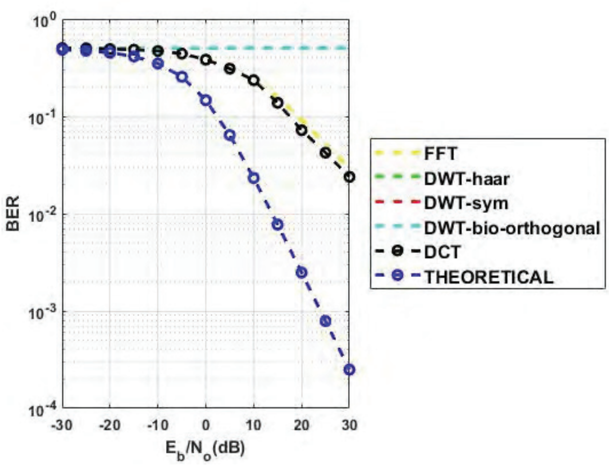

Fig. 3: The BER of MOMF optimization with various techniques.

Figures 4, 5 and 6 show BER, SER and PAPR of MOMF in FFT 128 M8 modulation of OFDM phase optimization. The MOMF has a higher convergence rate and overcomes local optima trap. The existing GWO method has a trap in local optima and PSO has lower convergence in optimization. The MOMF method reduces the PAPR compared to existing methods in OFDM phase optimization.

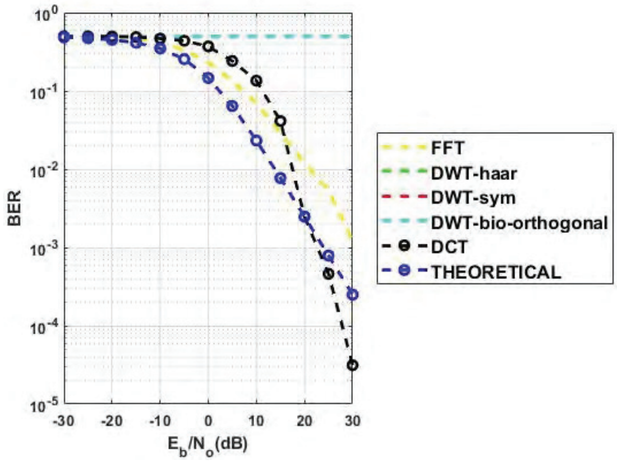

Fig. 4: BER of FFT 128 M8 modulation.

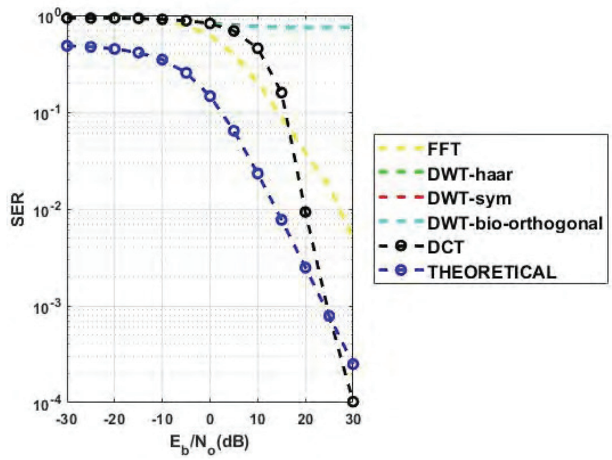

Fig. 5: Symbol error rate of FFT 128 M8 modulation.

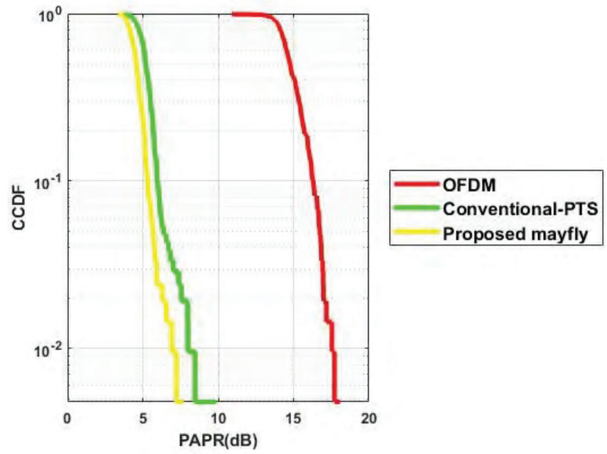

Fig. 6: MOMF PAPR of FFT 128 M8 modulation.

Table 3 shows the difference in PAPR reduction achieved by various methods including PTS, PSO, GWO, PSO-GWO and Proposed MOMF. Table 3 clearly shows that the PAPR reduction of proposed MOMF achieved a value of 3.9537 dB which is much better when compared to specified methods.

Table 3: Results of PAPR on FFT 64 M16 modulation

Methods	PAPR (dB)
MIMO-OFDM	7.8345
PTS	5.0140
PSO	5.0168
GWO	5.1163
PSO-GWO	4.9222
Proposed MOMF	3.9537

The MOMF optimization method is measured with BER and PAPR in FFT 128 M256 modulation, as in Fig. 7 and Fig. 8. The MOMF method provides higher efficiency in FFT 128 compared to existing methods. The MOMF method has the advantages of high convergence and overcoming local optima trap.

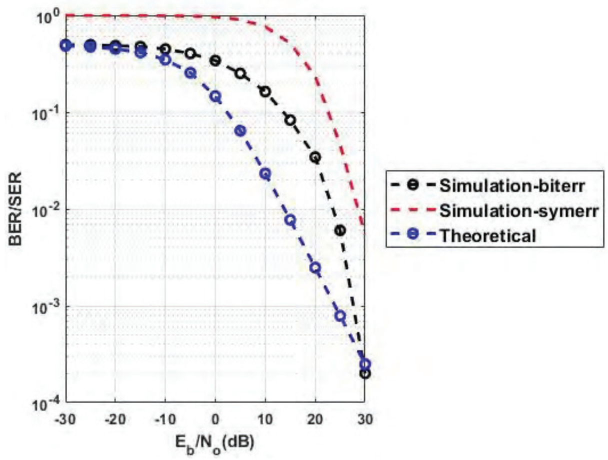

Fig. 7: MOMF BER of FFT 128 M256 modulation.

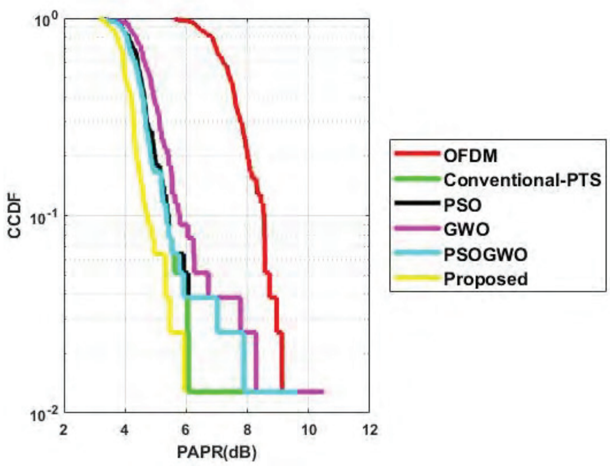

Fig. 8: MOMF PAPR of FFT 128 M256 modulation.

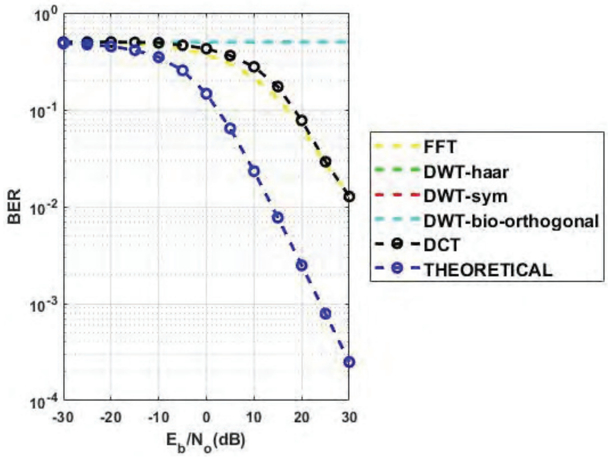

Fig. 9: MOMF BER of FFT 512.

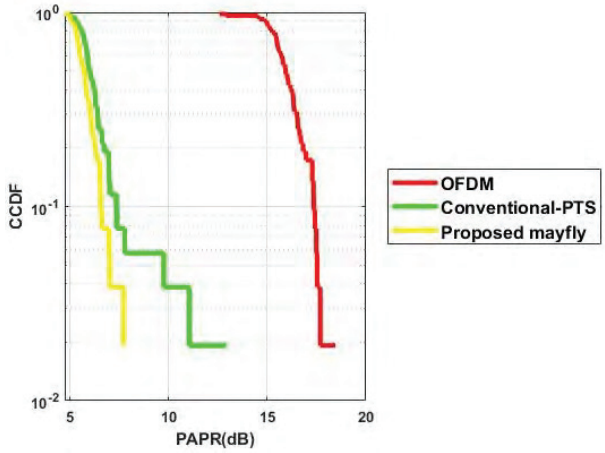

Fig. 10: MOMF PAPR of FFT 512.

The MOMF BER and PAPR in FFT 512 in OFDM phase optimization are given in Fig. 9 and Fig. 10. The MOMF method has the advantages of higher convergence and overcoming local optima trap. The GWO method is easily trapped into local optima and PSO method has lower convergence.

The MOMF method in OFDM phase optimization for M8 and M64 modulation are shown in Fig. 11 and Fig. 12. The MOMF method provides a higher efficiency in both modulations than existing methods.

The MOMF BER and PAPR of FFT 1024 in OFDM phase optimization are shown in Fig. 13 and Fig. 14. The MOMF method considers various parameters in OFDM to reduce BER, SER and PAPR. The existing methods consider a single objective and have a limitation of local optima trap.

The MOMF BER of FFT 1024 M128 modulation in OFDM phase optimization is given in Fig. 15. The MOMF method has lower BER due to the consideration of multi-objective optimization and has higher convergence.

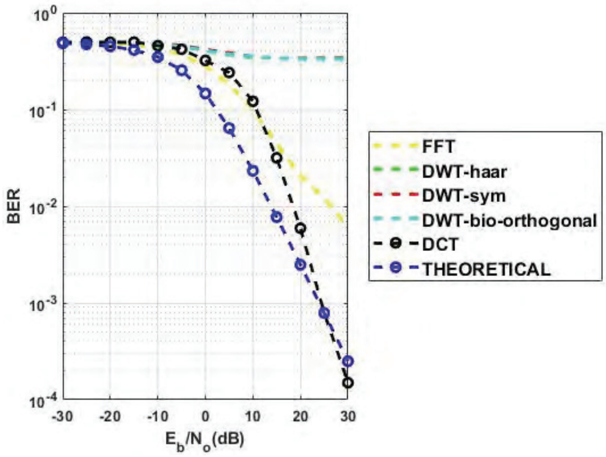

Fig. 11: MOMF BER of FFT 512 M8 modulation.

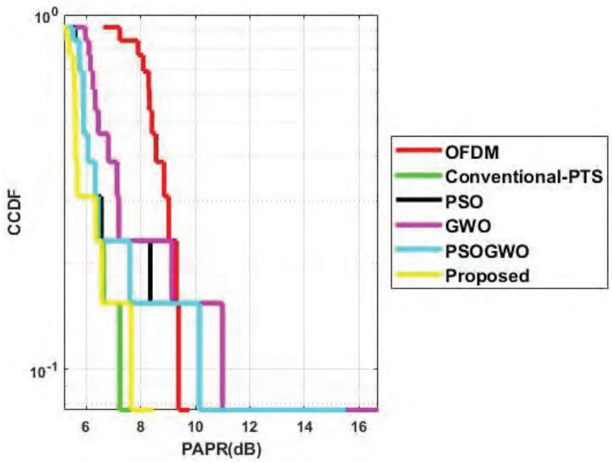

Fig. 12: MOMF PAPR of FFT 512 M64.

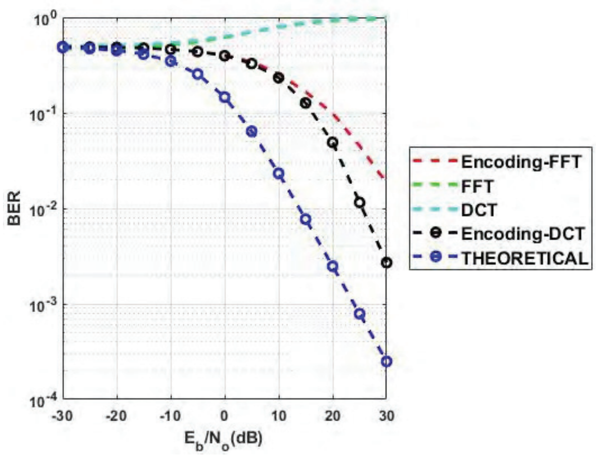

Fig. 13: MOMF BER of FFT 1024.

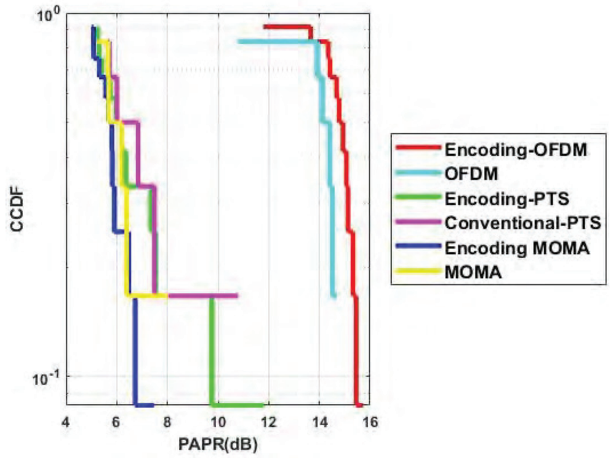

Fig. 14: MOMF PAPR of FFT 1024.

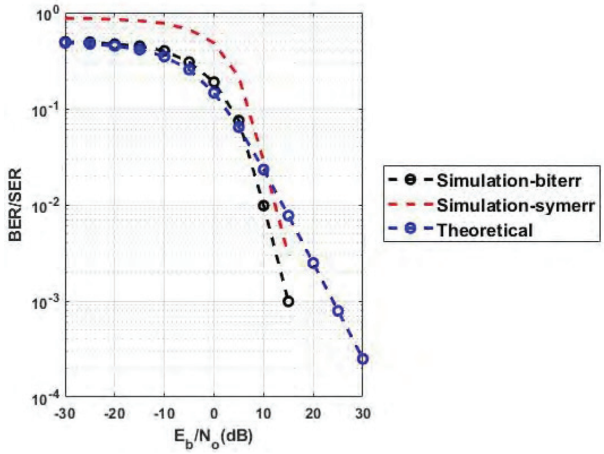

Fig. 15: MOMF BER of FFT 1024 M128.

In order to properly balance exploration and exploitation, this research suggests using the Multi-Objective Mayfly algorithm (MOMF), which takes many objectives into account. The model applies the Partial Transmit Sequence (PTS) to test performance. To assess the effectiveness of the MOMF technique in phase optimization, several FFT widths and modulation orders are used. When compared to other optimization strategies, the proposed MOMF technique significantly improves model performance. From the result analysis, it clearly shows that various FFT sizes of 64, 128, 256, 512, and 1024 are used to evaluate MOMF algorithm in terms of BER and PAPR. The proposed strategy is a better way to achieve a better trade-off between PAPR reduction and computing complexity, according to simulation results.

5. CONCLUSION

The existing methods in OFDM apply optimization methods to improve the efficiency of the OFDM. The existing methods have limitations of considering a single objective in optimization and also have a local optima trap. This research proposes the MOMF algorithm to increase the efficiency of OFDM phase optimization by considering multiple objectives. The MOMF method balances the exploration and exploitation in the search process of optimization. The MOMF method considers three objectives for OFDM phase optimization: BER, SER, and

PAPR. The MOMF method is evaluated in various FFT and modulations in the OFDM. The MOMF method provides higher performance in the OFDM phase optimization than existing methods. The GWO method has the limitation of a local optima trap and the PSO method has lower convergence. The MOMF method balances the trade-off between exploration and exploitation that increases the convergence and overcomes the local optima trap. The future work of this research involves applying the enhanced Artificial Bee Colony method to improve the efficiency of the MIMO-OFDM system.

REFERENCES

[1] Singh M, Patra SK. (2018) On the PTS optimization using the firefly algorithm for PAPR reduction in OFDM systems. IETE Tech. Rev., 35(5): 441-455. https://doi.org/10.1080/02564602.2018.1505563.

[2] Aghdam MH, Sharifi AA. (2019) PAPR reduction in OFDM systems: An efficient PTS approach based on particle swarm optimization. ICT Express, 5(3): 178-181. https://doi.org/10.1016/j.icte.2018.10.003.

[3] Wu W, Cao Y, Wang S, Wang Y. (2018) Joint optimization of PAPR reduction based on modified TR scheme for MIMO-OFDM radar. Digital Signal Process., 80: 27-36. https://doi.org/10.1016/j.dsp.2018.05.008.

[4] Ahmed MS, Boussakta S, Al-Dweik A, Sharif B, Tsimenidis CC. (2019) Efficient design of selective mapping and partial transmit sequence using T-OFDM. IEEE Trans. Veh. Technol., 69(3): 2636-2648. doi: 10.1109/TVT.2019.2928361.

[5] Hu W, Li F, Jiang Y. (2021) Phase Rotations of SVD-Based Precoders in MIMO-OFDM for Improved Channel Estimation. IEEE Wireless Commun. Lett., 10(8): 1805-1809. DOI: 10.1109/LWC.2021.3081583.

[6] Emami H, Sharifi AA. (2020) An improved backtracking search optimization algorithm for cubic metric reduction of OFDM signals. ICT Express, 6(3): 258-261. https://doi.org/10.1016/j.icte.2020.03.001.

[7] Sarkar M, Kumar A, Maji B. (2021) PAPR reduction using twin symbol hybrid optimization-based PTS and multi-chaotic-DFT sequence-based encryption in CP-OFDM system. Photonic Network Communications, 41(2): 148-162. https://doi.org/10.1007/s11107-020-00923-7.

[8] Amhaimar L, Ahyoud S, Elyaakoubi A, Kaabal A, Attari K, Asselman A. (2018) PAPR reduction using fireworks search optimization algorithm in MIMO-OFDM systems. J. Electr. Comput. Eng., 2018: 3075890. https://doi.org/10.1155/2018/3075890.

[9] Geetha MN, Mahadevaswamy UB. (2020) Performance evaluation and analysis of peak to average power reduction in OFDM signal. Wireless Personal Communications, 112(4): 2071-2089. https://doi.org/10.1007/s11277-020-07140-5.

[10] Du J, Xu W, Zhao C, Vandendorpe, L. (2019) Weighted spectral efficiency optimization for hybrid beamforming in multiuser massive MIMO-OFDM systems. IEEE Trans. Veh. Technol., 68(10): 9698-9712. DOI: 10.1109/TVT.2019.2932128.

[11] Lavanya P, Satyanarayana P, Mohatram M. (2022) Peak to average power ratio reduction of ZT DFT-s-OFDM signals using improved monarch butterfly optimization-PTS scheme. J. Ambient Intell. Hum. Comput. https://doi.org/10.1007/s12652-022-03954-2.

[12] Ali TH, Hamza A. (2021) Low-complexity PAPR reduction method based on the TLBO algorithm for an OFDM signal. Ann. Telecommun., 76(1): 19-26. https://doi.org/10.1007/s12243-020-00777-0.

[13] Sharifi AA, Emami H. (2020) PAPR reduction of asymmetrically clipped optical OFDM signals: Optimizing PTS technique using improved flower pollination algorithm. Opt. Commun., 474: 126057. https://doi.org/10.1016/j.optcom.2020.126057.

[14] Emami H, Sharifi AA. (2020) A novel bio-inspired optimization algorithm for solving peak-to-average power ratio problem in DC-biased optical systems. Opt. Fiber Technol., 60: 102383. https://doi.org/10.1016/j.yofte.2020.102383.

[15] Emami H, Sharifi AA. (2020) Optimizing cubic metric in orthogonal frequency division multiplexing systems using chaotic differential search algorithm. Phys. Commun., 43: 101231. https://doi.org/10.1016/j.phycom.2020.101231.
[16] Padarti VK, Nandhanavanam VR. (2021) An improved ASOICF algorithm for PAPR reduction in OFDM systems. Int. J Intell. Eng. Syst., 14: 352-360. https://doi.org/10.22266/ijies2021.0430.32
[17] Xing Z, Liu K, Rajasekaran AS, Yanikomeroglu H, Liu Y. (2021) A hybrid companding and clipping scheme for PAPR reduction in OFDM systems. IEEE Access, 9: 61565-61576. https://doi.org/10.1109/ACCESS.2021.3074009
[18] Yuan Y, Wei S, Luo X, Xu Z, Guan X. (2022) Adaptive PTS scheme based on fuzzy neural network for PAPR reduction in OFDM system. Digital Signal Process., 126: 103492. https://doi.org/10.1016/j.dsp.2022.103492.
[19] Carcangiu S, Fanni A, Montisci A. (2022) A Closed Form Selected Mapping Algorithm for PAPR Reduction in OFDM Multicarrier Transmission. Energies, 15(5): 1938. https://doi.org/10.3390/en15051938.
[20] Murad M, Tasadduq IA, Otero P. (2022) Ciphered BCH Codes for PAPR Reduction in the OFDM in Underwater Acoustic Channels. J. Mar. Sci. Eng., 10(1): 91. https:// doi.org/10.3390/jmse10010091.
[21] Aghdam MH, Sharifi AA. (2021) A novel ant colony optimization algorithm for PAPR reduction of OFDM signals. Int. J. Commun. Syst., 34(1): e4648. https://doi.org/10.1002/dac.4648.
[22] Wu Y, Hu Y, Wan Z, Wang T, Sun Y, Zhang Q. (2022) Joint security enhancement and PAPR mitigation for OFDM-NOMA VLC systems. Opt. Commun., 508: 127719. https://doi.org/10.1016/j.optcom.2021.127719.
[23] Kumar C, Karpurapu A, Singh YP. (2022) Reduction of PAPR for FBMC-OQAM system using Ant Colony Optimisation technique. Soft Comput., 26(9): 4295-4302. https://doi.org/10.1007/s00500-021-06503-9.
[24] Elaziz MA, Senthilraja S, Zayed ME, Elsheikh AH, Mostafa RR, Lu S. (2021) A new random vector functional link integrated with mayfly optimization algorithm for performance prediction of solar photovoltaic thermal collector combined with electrolytic hydrogen production system. Appl. Therm. Eng., 193: 117055. https://doi.org/10.1016/j.applthermaleng.2021.117055.
[25] Shaheen MAM, Hasanien HM, El Moursi MS, El Fergany AA. (2021) Precise modeling of PEM fuel cell using improved chaotic MayFly optimization algorithm. Int. J. Energy Res., 45(13): 18754-18769. https://doi.org/10.1002/er.6987.
[26] Liu Z, Jiang P, Wang J, Zhang L. (2021) Ensemble forecasting system for short-term wind speed forecasting based on optimal sub-model selection and multi-objective version of mayfly optimization algorithm. Expert Syst. Appl., 177: 114974. https://doi.org/10.1016/j.eswa.2021.114974
[27] Adnan RM, Kisi O, Mostafa RR, Ahmed AN, El-Shafie A. (2022) The potential of a novel support vector machine trained with modified mayfly optimization algorithm for streamflow prediction. Hydrol. Sci. J., 67(2): 161-174. https://doi.org/10.1080/02626667.2021.2012182
[28] Wei D, Ji J, Fang J, Yousefi N. (2021) Evaluation and optimization of PEM Fuel Cell-based CCHP system based on Modified Mayfly Optimization Algorithm. Energy Rep., 7: 7663-7674. https://doi.org/10.1016/j.egyr.2021.10.118
[29] Liu Y, Chai Y, Liu B, Wang Y. (2021) Bearing Fault Diagnosis Based on Energy Spectrum Statistics and Modified Mayfly Optimization Algorithm. Sensors, 21(6): 2245. Doi: 10.3390/s21062245
[30] Tamilmani G, Devi VB, Sujithra T, Shajin FH, Rajesh P. (2022) Cancer MiRNA biomarker classification based on Improved Generative Adversarial Network optimized with Mayfly Optimization Algorithm. Biomed. Signal Process. Control, 75: 103545. https://doi.org/10.1016/j.bspc.2022.103545

https://doi.org/10.31436/iiumej.v24i1.2505

DESIGN OF MINIATURIZED ANTENNA FOR IOT APPLICATIONS USING METAMATERIAL

AHMAD ZAMANI JUSOH, NUR FATIHAH HUSAIN*, NORUN FARIHAH ABDUL MALEK, FARAH NADIA MOHD ISA, AND SARAH YASMIN MOHAMAD

Department of Electrical and Computer Engineering, Kulliyyah of Engineering International Islamic University Malaysia, Jalan Gombak, 53100 Kuala Lumpur, Malaysia

**Corresponding author: tihah0704@gmail.com*

(Received: 30th June 2022; Accepted: 5th November 2022; Published on-line: 4th January 2023)

ABSTRACT: With the accelerated development of wireless technology, miniaturized antennae have become outstandingly favored due to the growing demand of Internet of Things (IoT) devices that are essential to accommodate low power, high data rates, and long-range communication. When an antenna operates at lower frequencies, the size of the antenna becomes bulky, which has raised an issue in the integration of the antennae within IoT devices due to their size constraints. Hence, in this paper, a miniaturized ring-monopole antenna incorporated with Rectangular Complementary Split Ring Resonator (RCSRR) and slotted ground plane, was designed at 2.4 GHz and 5.8 GHz frequency bands. The antenna was miniaturized by 46.8 % with overall size of 30 mm x 24.8 mm x 1.6 mm, and it was printed on FR-4 substrate with dielectric constant of 4.3. Design optimization was carried out by modifying the antenna structure, optimizing the dimensions, and using a low loss Rogers RT5880 substrate with a dielectric constant of 2.2, and thickness of 1.575 mm. The width of the antenna was also reduced to 20 mm which furthered the size reduction to 57.8 %. From the simulation results, the antenna was operated at 2.448 GHz, 2.864 GHz, and 5.8 GHz frequency bands with good return loss at -13.872 dB, -33.491 dB, and -19.3 dB respectively. The antenna fabrication and measurement were also implemented to the best simulated design using different substrates to validate its performance by comparing the simulated results with the measured results.

ABSTRAK: Dengan perkembangan pesat teknologi tanpa wayar, antena miniatur telah menjadi sangat digemari kerana permintaan yang semakin meningkat bagi peranti Internet Benda (IoT), iaitu mempunyai kuasa rendah, kadar data yang tinggi dan berkomunikasi jarak jauh. Apabila antena beroperasi pada frekuensi rendah, saiz antena menjadi besar, ini menimbulkan isu kekangan saiz pada antena ketika berada dalam peranti IoT. Oleh itu, kajian ini adalah berkenaan antena ekakutub-gelang kecil yang digabungkan dengan Resonator Gelang Pemisah Pelengkap Segiempat Tepat (RCSRR) dan satah tanah berslot, telah direka bentuk pada jalur frekuensi 2.4 GHz dan 5.8 GHz. Antena telah dikecilkan sebanyak 46.8 % dengan saiz keseluruhan 30 mm x 24.8 mm x 1.6 mm, dan ia dicetak pada substrat FR-4 dengan pemalar dielektrik 4.3. Reka bentuk optimum telah dilakukan dengan mengubah suai struktur antena, berdimensi optimum, menggunakan substrat Rogers RT5880 rendah kuasa dengan pemalar dielektrik 2.2, dan berketebalan 1.575 mm. Lebar antena juga dikurangkan sebanyak 20 mm, ini bermakna pengurangan saiz berjaya ditingkatkan kepada 57.8%. Dapatan simulasi menunjukkan antena telah beroperasi pada jalur frekuensi 2.448 GHz, 2.864 GHz dan 5.8 GHz dengan pengurangan kehilangan pulangan kuasa yang baik iaitu pada -13.872 dB, -33.491 dB dan -19.3 dB masing-masing. Fabrikasi dan pengukuran antena juga telah dilaksanakan pada reka bentuk simulasi terbaik menggunakan substrat yang berbeza bagi mengesahkan kemampuannya dengan membandingkan dapatan simulasi dengan hasil yang diukur.

KEYWORDS: *miniaturized antenna; IoT application; metamaterial; complementary split ring resonator (CSSR).*

1. INTRODUCTION

Internet of Things (IoT) has been widely used in wireless applications such as wireless sensor networks, smart homes, and wearable technology [1]. This wireless technology requires persistent connectivity with the devices within its network to stay connected and to preserve its communication. To fulfil this need, Wi-Fi is attested to be the key requirement for IoT systems by providing numerous antennas for network connection. In 2019, the Wi-Fi Alliance launched the Wi-Fi CERTIFIED 6 based on IEEE 802.11ax standard to accommodate with IoT demand for low power, high data rates, and long-range communication [2]. However, Wi-Fi CERTIFIED 6 requires antennas that can operate at dual frequency bands of 2.4 GHz and 5 GHz which has created an issue in antenna integration within the devices due to its large size. Hence, various research has been conducted by scholars to develop diverse antenna miniaturization techniques to design compact antennae of distinct types such as patches, dipoles, loops, and slots that can satisfy the size constraints without degrading the performance of the antenna [3]. The many miniaturization techniques include adding slots [4], truncated and defected ground plane [5-8], meandered line [9], fractals [10] and metamaterial [11].

Metamaterial structure is a type of unnatural compound structure with physical characteristics that are distinct and novel from genuine elements and thus frequently used in designing a miniaturized antenna [12]. SNG metamaterial is a single negative material where either the value of permittivity, ε or permeability, μ is negative. Split Ring Resonator (SRR) is Mu-negative (MNG) metamaterial structure that consists of two metallic rings that can be designed in various shapes, such as square and circular, that are separated by a gap on opposite sides [12]. SRR unit cell is also equivalent to a circuit composed of inductor and capacitor which are represented by the rings and the gap between rings respectively [13].

Moreover, metamaterial structures can enhance the operation of the antenna on some parameters. In [14], DNG structure was constructed by making a 4 x 3 layer of metamaterial unit cells where it had 15 mm backlash space between the unit cells sheet and the substrate. This design of unit cells metamaterial improved the gain of the antenna from 1.48 dBi to 1.8 dBi and has good impedance matching with return loss of -52 dB. In [15], Complementary Split Ring Resonator (CSRR) form of metamaterial or the reciprocal split ring resonator, was designed at the front side of the patch antenna while at the back side, modified split ring resonator structure was designed. This enhanced the gain to 3.23 dBi, improved the bandwidth to 574 MHz, and reduced its size. Moreover, a square split ring resonator consisting of four metallic rings in [16], was able to exhibit resonant frequencies of different bands, making it especially useful in various applications. In this project, a miniaturized antenna incorporated with Rectangular Complementary Split Ring Resonator (RCSRR) and slotted ground plane, is designed, which accommodate a compact size of $0.2\lambda_0$ in term of its electrical length, and multi-band operation at 2.4 GHz and 5.8 GHz.

2. SLOTTED METAMATERIAL ANTENNA DESIGN

2.1 Preliminary Designs

Designing a miniaturized multi-band antenna requires the selection of a suitable miniaturization technique able to accommodate the required antenna characteristics while maintaining a good performance. Hence, metamaterial structure and slotted techniques are incorporated in the antenna design based on work by [17], where three design development steps were used to analyze its performance from each implementation of miniaturization techniques. A ring monopole antenna was initially designed with a size of 40 mm x 35 mm x 1.6 mm using the resonance frequency based on equation (1) [17].

$$f_r = \frac{c}{\pi C_1 \sqrt{\varepsilon_{eff}}} \tag{1}$$

where c refers to speed of light, c=3x10^{8}m/s, C_1 is the outer diameter of the ring monopole ($C_1 = 2r_2$) and ε_{eff} is the equivalent dielectric constant. For FR4, $\sqrt{\varepsilon_{eff}} = 1.99, C_1 = 2r_2 = 18.9\ mm,$ then $f_r = 2.54$ GHz. For Rogers Duroid 5880, $\sqrt{\varepsilon_{eff}} = 1.48, C_1 = 2r_2 = 18.9\ mm,$ then $f_r = 3.4$ GHz.

First, antenna 1 was designed with the above parameters using CST Microwave Studio software [18]. The antenna was printed on FR-4 substrate with dielectric constant of 4.3 and loss tangent of 0.025. It was chosen as the substrate due to its easy accessibility. Then, the design was further developed by integrating Rectangular Complementary Split Ring Resonator (RCSSR) metamaterial structure as the radiating element. This development miniaturized the antenna to 30 mm x 24.8 mm x 1.6 mm which was approximately 46.8 % size reduction compared to conventional ring monopole. The changes in the near-field boundary conditions of the design had downsized the antenna to the targeted electrical length of $0.2\lambda_0$. The structure of the ground plane was kept similar as the previous design. This design produced a resonant frequency at 2.4 GHz which is the targeted operating frequency for Wi-Fi applications [19-22]. However, multi-band operation was not achieved from this design. Hence, L-shaped slots and a T-shaped slot were etched from the ground plane of the design to ensure multi-band operation. The addition of the slots altered the surface current distribution path to be longer, which made the antenna resonate at 2.32 GHz, 4.408 GHz, 6.34 GHz respectively. Nevertheless, the antenna had not yet achieved the targeted resonant frequencies at 2.4 GHz and 5.8 GHz. The illustration of the design development is depicted in Fig. 1 while the comparison of return loss characteristics of design development is shown in Fig. 2. The performance comparison of all preliminary designs (Antenna 1, Antenna 2, and Antenna 3) is summarized in Table 1.

2.2 RCSRR Metamaterial Design and Characteristic Verification

RCSRR, as depicted in Fig. 3, is the metamaterial structure consisting of two metallic rings as the radiating element with gaps between the rings and the split width on the opposite side of the rings. The split width of the rings was designed following the shape of capacitor to control its resonant frequency as it possesses the capacitance characteristics while the metallic rings possess inductance characteristics [17]. As a result of the applied outward H-field, an EMF is created around the RCSRR metamaterial structure, resulting in the coupling of the two rings. This happens due to the current travelling from outer ring to inner ring corresponding to the disperse capacitance by the split width of the rings Hence, RCSRR metamaterial structure behaves as an LC circuit [17]. RCSRR was positioned into the waveguide as illustrated in Fig. 4 where perfect electric conductor (PEC) and perfect magnetic conductor (PMC) boundary conditions were provided on the y-axis and z-axis respectively to verify its characteristics. The boundary condition at the x-axis was set to open boundary to provide waveguides for both ports. The resonant frequency of RCSRR metamaterial structure can be ascertained using equation (2) where L_{tot} is the total inductance while C_{tot} is the total capacitance [17].

$$\omega_{r} = \frac{1}{\sqrt{L_{tot}C_{tot}}} \tag{2}$$

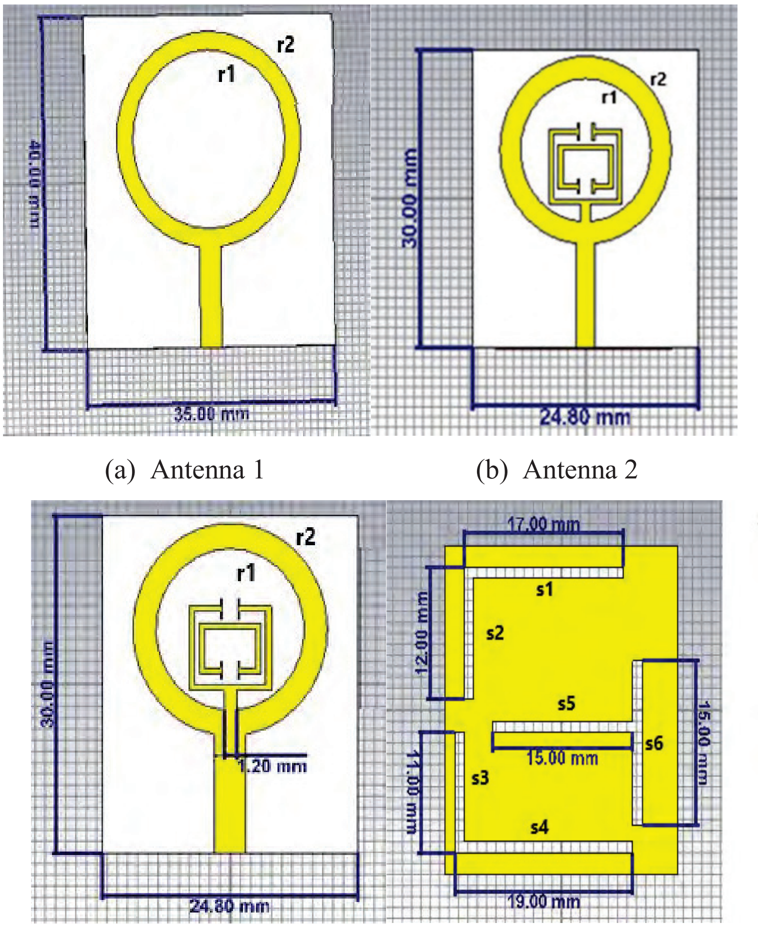

(a) Antenna 1 (b) Antenna 2

(c) Antenna 3

Fig. 1: Antenna design development.

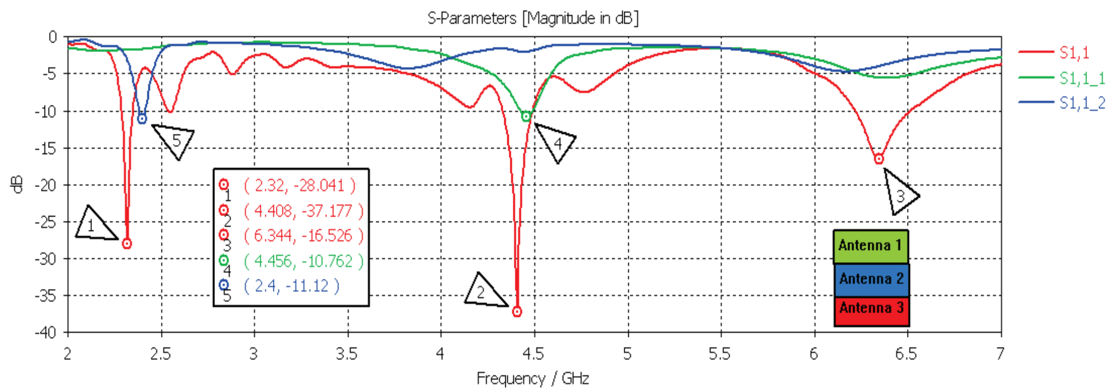

Fig. 2: Return loss characteristics of design development.

Table 1: Comparison of preliminary antenna designs

Antenna	Resonant frequency [GHz]	Size [mm^3]	Return loss [dB]
1	4.456	40 x 35 x 1.6	-10.762
2	2.4	30 x 24.8 x 1.6	-11.12
3	2.32, 4.408, 6.344	30 x 24.8 x 1.5	-28.041, -37.177, -16.526

From Fig. 5, it can be observed that the RCSRR unit cell that was positioned inside the waveguide medium had shown a stop band characteristic at 2.714 GHz. This is because, at this frequency, the value for S21or the transmission coefficient was below -10 dB and the value for the reflection coefficient or S11 was approaching 0 dB. Hence, a band notch was observed in the configuration of the return loss. Metamaterial structure is characterized by its negative value of permittivity or permeability depending on its type and RCSRR is categorized in Mu-negative metamaterial which indicates negative value of permeability as can be observed in Fig. 6, where the real value of permeability was negative at 2.714 GHz due to stop band characteristic of RCSRR. Therefore, negative permeability of RCSRR exhibits new resonance for the antenna. The dimensions of the RCSRR unit cell are: - a = 8 mm, b = 7.5 mm, c = 6 mm, d = 4.5 mm, s = 1.5 mm, g1 = 1 mm, and g2 = 0.5 mm.

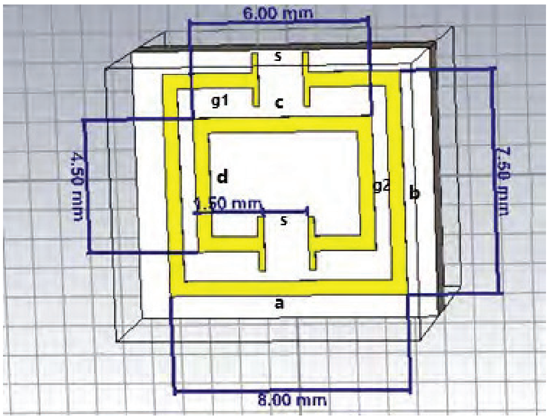

Fig. 3: RCSRR metamaterial structure.

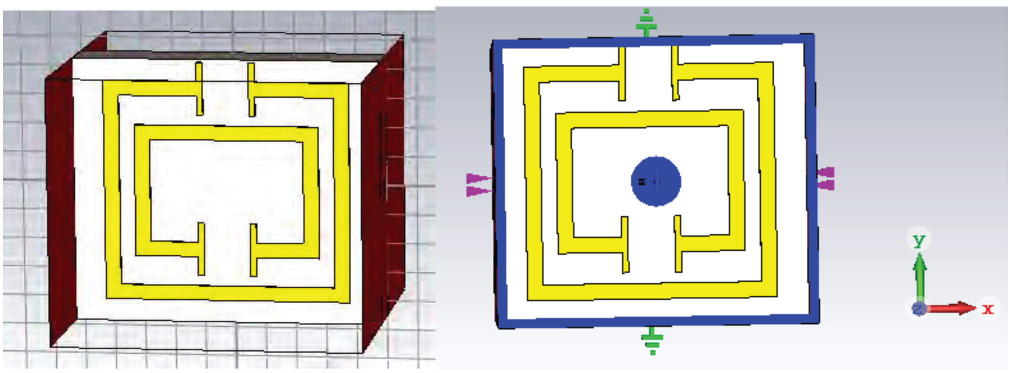

Fig. 4: RCSRR unit cell in waveguide medium with boundary conditions.

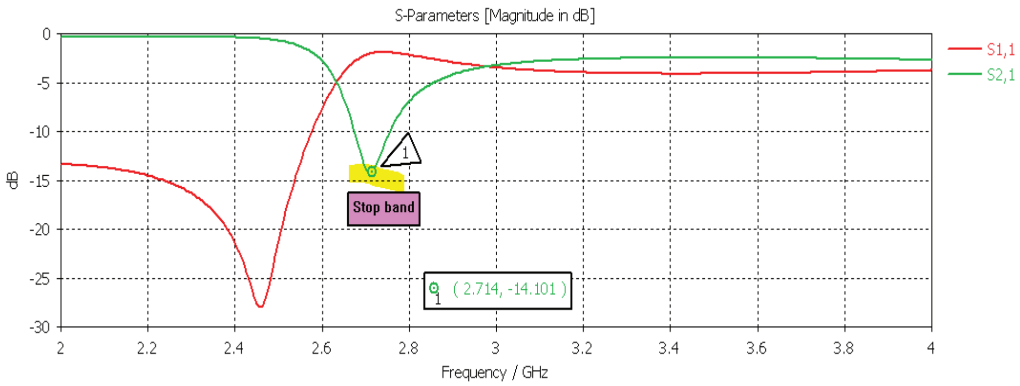

Fig. 5: Return loss of RCSRR unit cell.

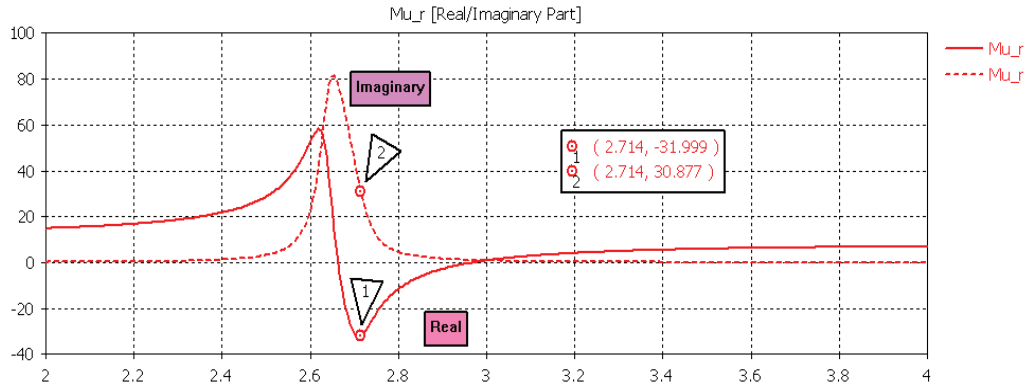

Fig. 6: Permeability of RCSRR unit cell.

2.3 Optimized Design

The preliminary antenna designs did not fulfill the targeted operating frequencies for Wi-Fi application to resonate at 2.4 GHz and 5.8 GHz. Thus, the design was optimized to ensure the best performance of the antenna. For antenna optimization, it is necessary to review its structure for performance enhancement by observing the effects of each addition of the slots to the ground plane. Hence, the T-shaped slot on the ground plane of Antenna 3 was eliminated from the design due to its effect in shifting the frequency to be greater than 2.4 GHz. After the modification to the ground plane structure, only two L-shaped slots were left for optimum radiation of the antenna.

Besides, parametric analysis was also carried out to some antenna dimensions to attain the best dimensions for the optimized design. The inner radius of the ring monopole, x was varied by a step of 0.05 mm as illustrated in Fig. 7. A value of x equal to 7.15 mm was chosen as the inner radius because it had good impedance matching at -19.487 dB compared to others. Then, the width of the connector between the ring monopole and RCSRR metamaterial structure, c was diversified by a step of 0.6 mm as depicted in Fig. 8. A value of c equal to 2.4 mm was selected as the best dimension because it had good return loss at -30.841 dB and its resonant frequency approached the targeted frequency of 2.4 GHz. Moreover, the length of the upper L-shaped slot, p was varied by a step of 0.5 mm as shown in Fig. 9. A value of p equal to 14.5 mm was used in the design as it had good impedance matching at -19.465 dB compared to others and it was able to resonate at approximately the targeted frequencies of 5.8 GHz. Other than that, the length of the lower L-shaped slot on the ground plane, q was altered by a step variation of 0.5 mm as depicted in Fig. 10. A value of q equal to 19.5 was selected as the best dimension for q because it had good return loss at -21.777 dB compared to other dimensions. The complete optimized antenna design is illustrated in Fig. 11. The dimensions for optimized antenna design using FR-4 substrate (Antenna 4) are shown in Table 2.

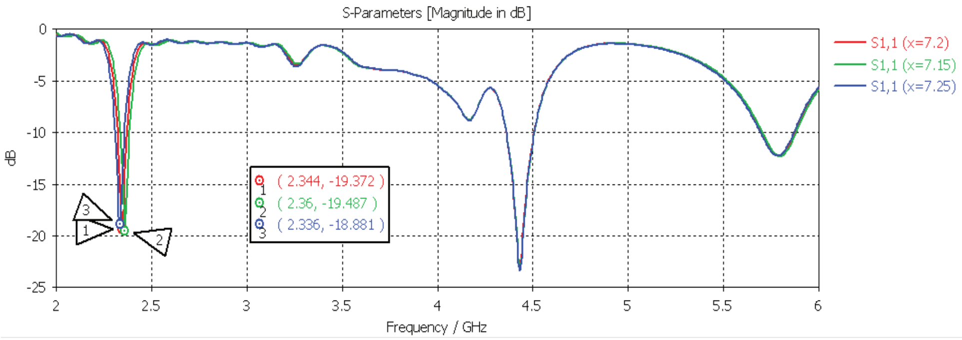

Fig. 7: Parametric analysis of the inner radius of ring monopole, x.

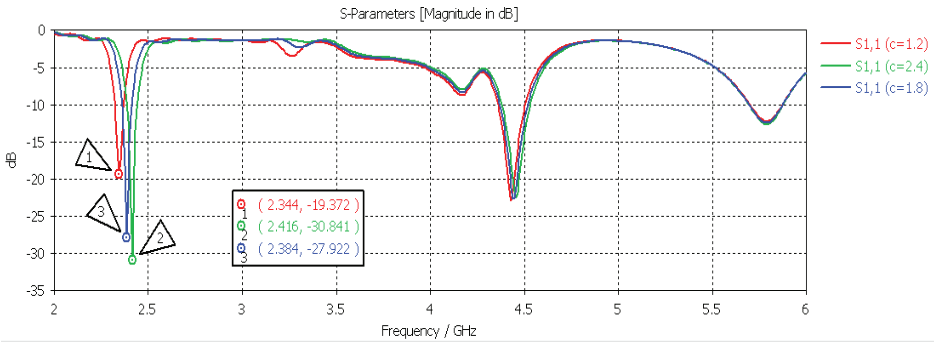

Fig. 8: Parametric analysis of the connector of feedline and RCSRR, c.

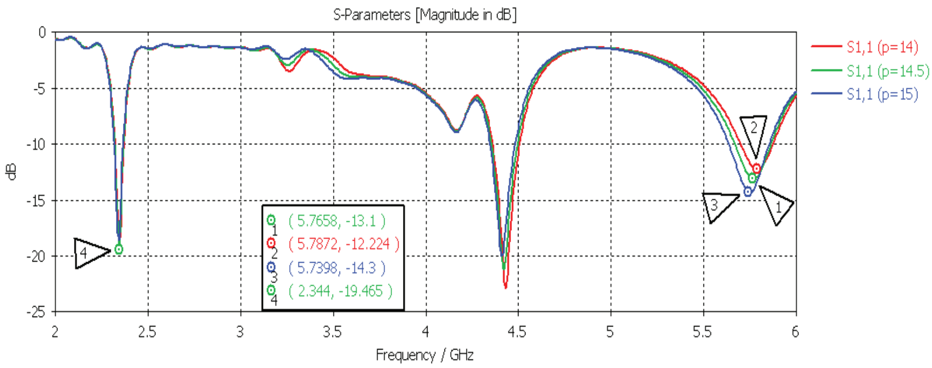

Fig. 9: Parametric analysis of the length of upper L-shaped slot, p.

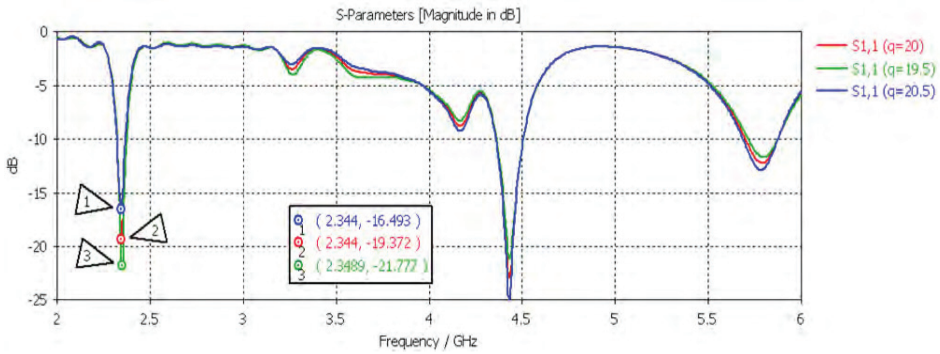

Fig. 10: Parametric analysis of the length of lower L-shaped slot, q.

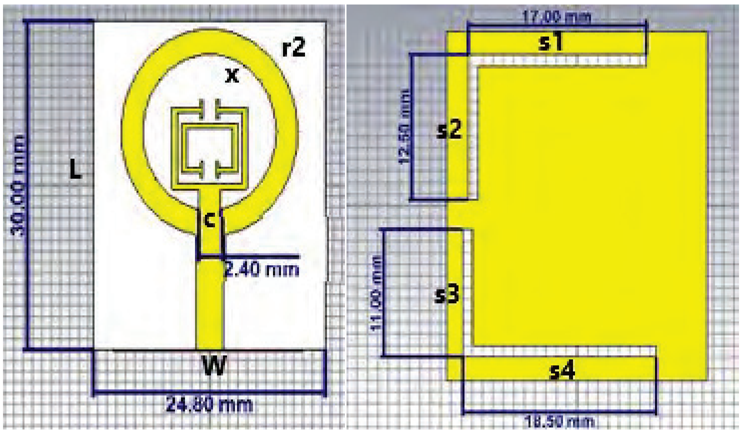

Fig. 11: Complete optimized antenna design using FR-4 substrate (Antenna 4).

Table 2: Dimensions of Antenna 4

Parameters	Unit (mm)
L	30
W	24.8
c	2.4
x (inner radius)	7.15
r2 (outer radius)	9.45
s1	17
s2	12.5
s3	11
s4	18.5

The dielectric material used in the design also affects the performance of the antenna. Hence, low loss dielectric material was considered in boosting the antenna performance. The antenna was designed on Rogers RT5880 substrate (Antenna 5), to replace FR-4. It has low dielectric constant equal to 2.2 compared to FR-4 that has high dielectric constant of 4.3 [17]. Moreover, the loss tangent of Rogers RT5880 substrate is 0.0009, which is also smaller than FR-4 with a loss tangent of 0.025 [17]. The complete optimized design of Antenna 5 is illustrated in Fig. 12 while its optimized dimensions are shown in Table 3. The optimized dimensions for RCSRR metamaterial structure incorporated in Antenna 5 is depicted in Fig. 13 where a = 9.5 mm, b = 8 mm, c = 6.5 mm, d = 5 mm, s = 1.5 mm, g1 = 1 mm, and g2 = 0.5 mm.

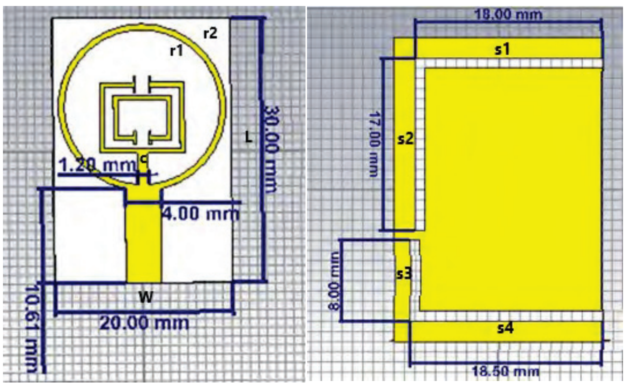

Fig. 12: Complete optimized antenna design using Rogers RT5880 substrate (Antenna 5).

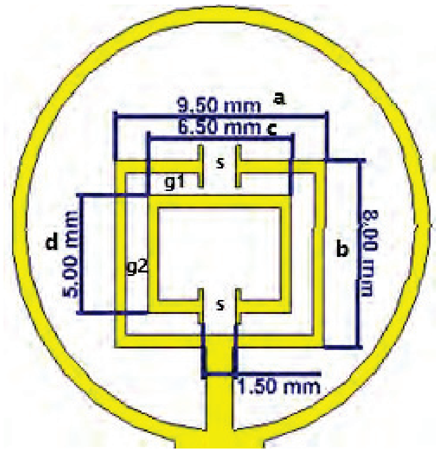

Fig. 13: RCSRR metamaterial structure optimized dimensions.

Table 3: Dimensions of Antenna 5

Parameters	Unit (mm)
L	30
W	20
c	1.2
r1 (inner radius)	8.8
r2 (outer radius)	9.45
s1	18
s2	17
s3	8
s4	18.5
Thickness	1.575

2.4 Antenna Fabrication and Measurement

The optimized antenna design printed on two different substrates, which are FR-4 and Rogers RT5880, were fabricated to validate the antenna performance by comparing the simulated result with the measured result. The fabrication was done at Mechatronics Workshop, Kulliyyah of Engineering, IIUM, where it involved six important steps: drilling the board to the required size, laminating the board using film, UV exposure, developing the required antenna design, etching the excess copper, and stripping the film residue [23]. An SMA connector was soldered on the antenna feedline for performance measurement. The complete fabricated antenna using two different substrates is depicted in Fig. 14. The measurement process was done at Microwave Lab using Vector Network Analyzer (VNA) as illustrated in Fig. 15.

3. OPTIMIZED DESIGN RESULTS AND DISCUSSION

Simulation of the design was conducted using CST Microwave Studio software. The optimized design using two different substrates of FR-4 (Antenna 4) and Rogers RT5880 (Antenna 5), were simulated. Some performance parameters were observed such as return loss, bandwidth, radiation pattern, directivity, and the gain to ascertain the best antenna performance for Wi-Fi application.

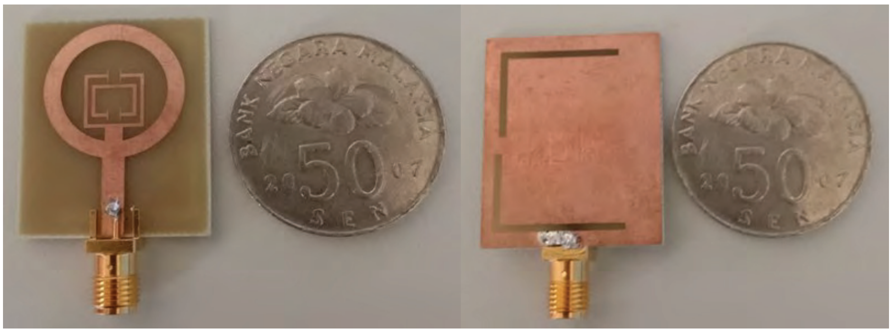

(a)

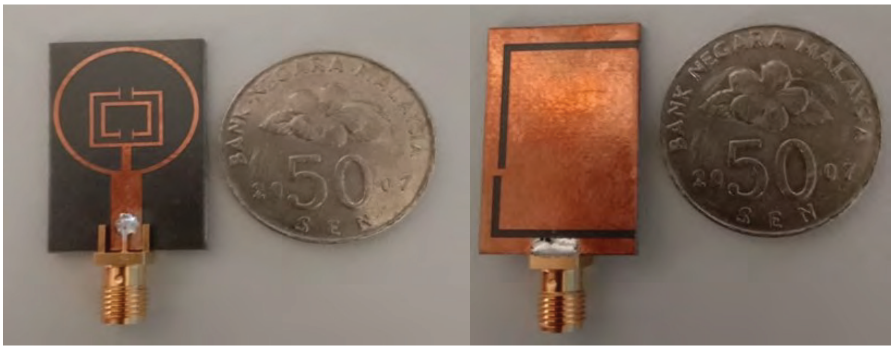

(b)

Fig. 14: Complete fabricated antenna using (a) FR4 substrate, (b) Rogers RT5880.

Fig. 15: Measurement of miniaturized antenna using Vector Network Analyzer.

3.1 Return Loss and Bandwidth

The important simulation data to be observed is the return loss (S11) or reflection coefficient. It is because it indicates the resonant frequency of the antenna and to evaluate whether the designed antenna will be able to operate at the targeted frequencies of both 2.4 GHz and 5.8 GHz. The acceptable value for S11 is below -10 dB which specified that 90 % power is transmitted to the antenna while 10 % of the power is being reflected. Bandwidth is the difference between the upper frequency and the lower frequency where it defined the frequency range covered for the operation of an antenna. It can be calculated using Eq. (3) where f_{upper} is the upper frequency, f_{lower} is the lower frequency, and f_0 is the centre frequency [1]. The -10dB bandwidth is considered in determining the bandwidth. The optimized design of slotted metamaterial ring monopole antenna using FR-4 substrate (Antenna 4) has good return losses of -27.102 dB, -20.864 dB, -13.517 dB at operating frequencies of 2.4 GHz, 4.44 GHz, and 5.8 GHz as depicted in Fig.16 with -10 dB bandwidth of 54.5 MHz or 2.27 %, 144.1 MHz or 3.25%, and 204.9 MHz or 3.53

%. Fig.17 shows the return losses of the optimized antenna design printed on Rogers RT5880 substrate (Antenna 5) which were -13.872 dB, -33.491 dB, and -19.3 dB at resonant frequencies of 2.448 GHz, 2.864 GHz, and 5.8 GHz respectively. It has -10 dB bandwidth of 137.2 MHz or 5.6 %, 350.9 MHz or 12.3 %, and 551.2 MHz or 9.5 % at respective resonant frequencies. The comparison between the return losses for antenna printed on two different substrates are depicted in Fig. 18 where both antennas achieved targeted resonant frequencies and had good impedance matching.

$$\text{Bandwidth} = \frac{f_{upper} - f_{lower}}{f_0} \tag{3}$$

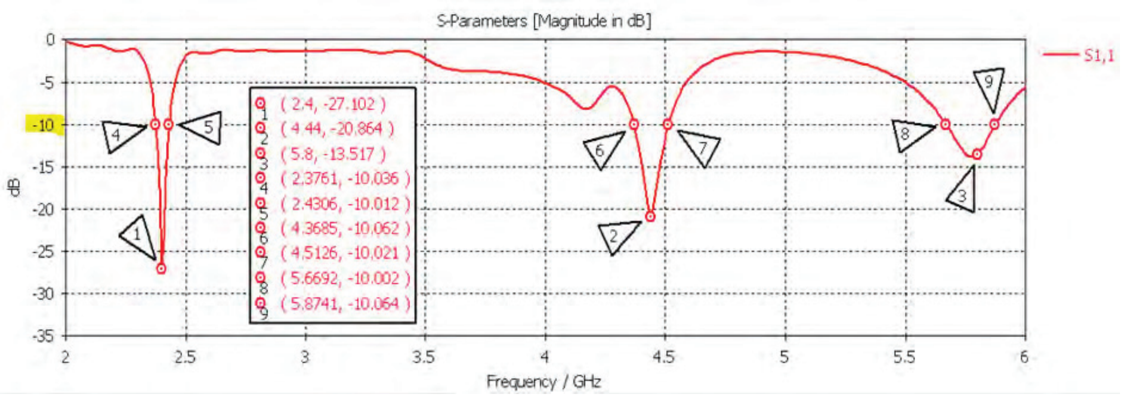

Fig. 16: Return loss of Antenna 4.

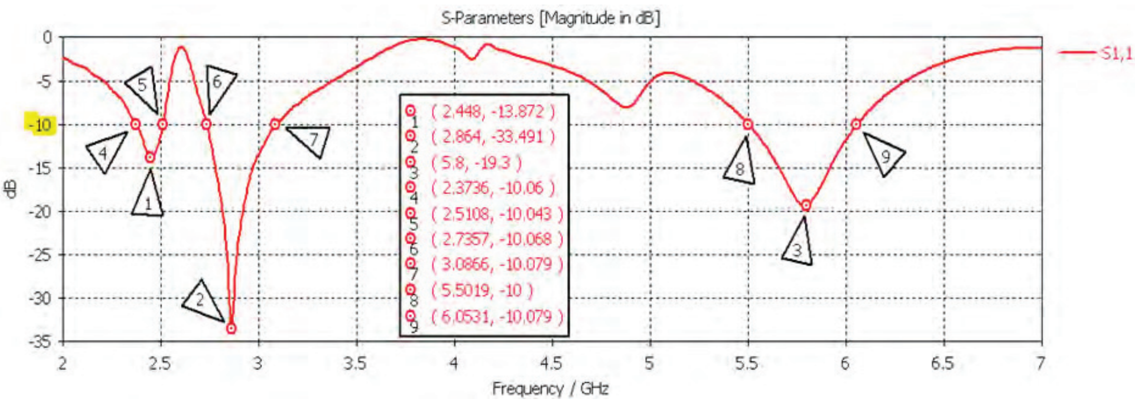

Fig. 17: Return loss of Antenna 5.

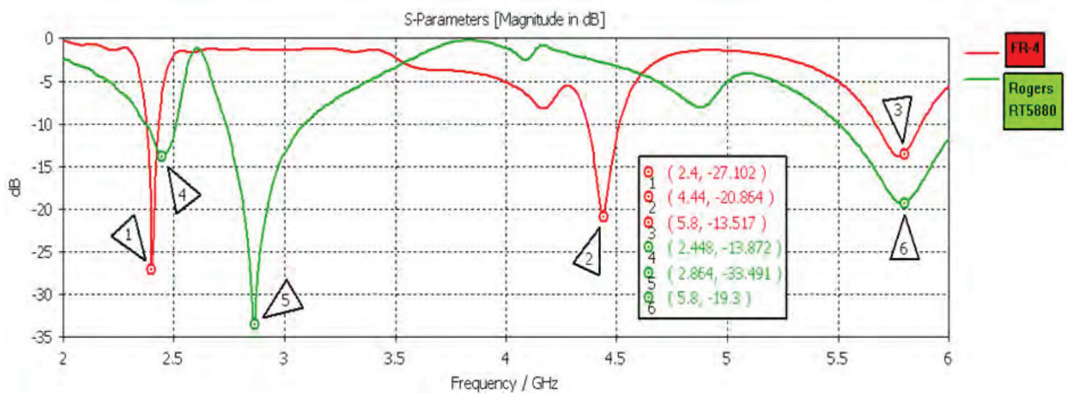

Fig. 18: Return loss comparison of antenna using different substrates.

3.2 Radiation Pattern

The 3D radiation patterns of Antenna 4 are illustrated in Fig. 19 where the patterns were directional at the respective operating frequencies. However, Antenna 5 had 3D radiation patterns that were almost omnidirectional patterns at resonant frequencies of 2.448 GHz and 2.864 GHz while at operating frequency of 5.8 GHz, the directional pattern, as depicted in Fig. 20, was seen. Hence, Antenna 5 is suitable for use in IoT applications since they require omnidirectional antennae and wider bandwidth for wireless connectivity [19-22]. The pattern considered was a far-field type and each pattern of all designs had different efficiencies and realized gains.

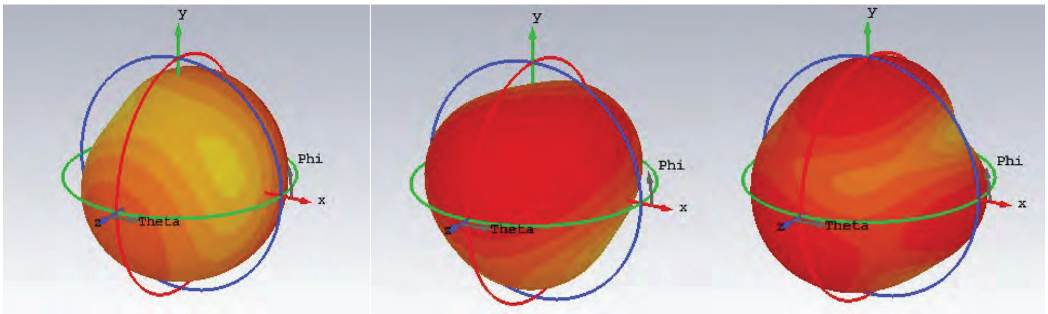

(a) (b) (c)

Fig. 19: 3D radiation pattern of Antenna 4 at (a) 2.4 GHz, (b) 4.44 GHz, (c) 5.8 GHz.

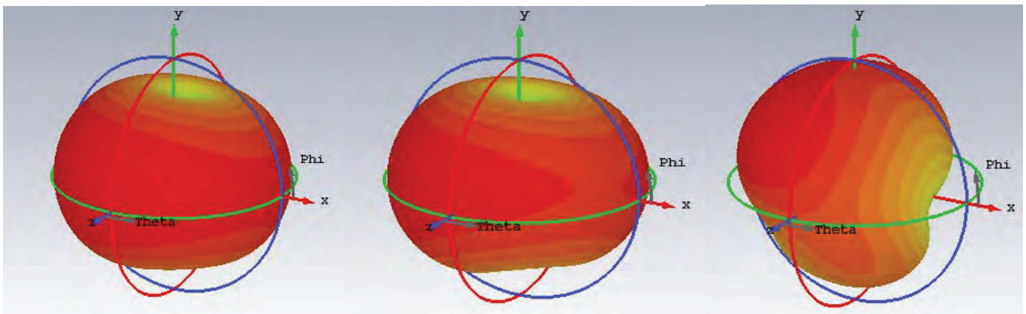

(a) (b) (c)

Fig. 20: 3D radiation pattern of Antenna 5 at (a) 2.448 GHz, (b) 2.864 GHz, (c) 5.8 GHz.

3.3 Gain and Directivity

The gain for both designs were determined based on the realized gain where it is the actual gain that considers the total efficiency of the antenna [1]. The realized gains of Antenna 4 were -12.38 dBi, -1.272 dBi, and -4.065 dBi at 2.4 GHz, 4.44 GHz, and 5.8 GHz, while Antenna 5 had realized gains of 1.110 dBi, 1.382 dBi, and 2.829 dBi at 2.448 GHz, 2.864 GHz, and 5.8 GHz. It can be inferred that Antenna 5, at resonant frequency of 5.8 GHz, had the most gain from the radiation at the main lobe and all gains of Antenna 5 were positive.

The directivity of the antenna indicates the ratio of maximum radiation intensity to the average radiation intensity in a specified direction [1]. Antenna 4 had a main lobe directivity of 2.183 dBi, 2.563 dBi, and 1.005 dBi at respective resonant frequencies of 2.4 GHz, 4.44 GHz, and 5.8 GHz. As for Antenna 5, that operated as multi-band antenna at 2.448 GHz, 2.864 GHz, and 5.8 GHz, it had main lobe directivity of 2.462 dBi, 2.765 dBi, and 4.231 dBi respectively. Hence, Antenna 5 had the highest directivity in the main lobe direction compared to Antenna 4.

Based on the simulation results, Antenna 5 had better performance compared to Antenna 4 because it had good impedance matching, greater gain, wider bandwidth, and had an omnidirectional pattern.

3.4 Comparison of Simulated and Measured Result

The fabricated Antenna 4 had three operating bands at 2.326 GHz, 4.408 GHz, and 5.806 GHz with good return loss below -10 dB where it indicates that this antenna only manages to resonate at targeted frequency of 5.8 GHz, as illustrated in Fig. 21. Moreover, the measured resonant frequencies of the antenna were shifted to smaller frequency than the simulated resonant frequencies due to the loss from the SMA connector that affects its performance. Figure 23 illustrates the comparison between the simulated and measured result of Antenna 4 where they almost correspond to each other.

Figure 22 illustrates the measured return loss of Antenna 5 where the fabricated antenna resonated at 3.388 GHz, 5.848 GHz, and 6.058 GHz with a good return loss below -10 dB. However, it was not fully correlated with the simulated return loss as depicted in Fig.24. This is due to the defective structure of the antenna produced during the chemical etching process that affects the antenna performance. Besides, multiple soldering attempts between the SMA connector and the antenna also caused excess heat to be applied to the board, which also had an impact on its performance. Therefore, it can be inferred that the measured results for both fabricated Antenna 4 and Antenna 5 were partially agreed with the simulated result.

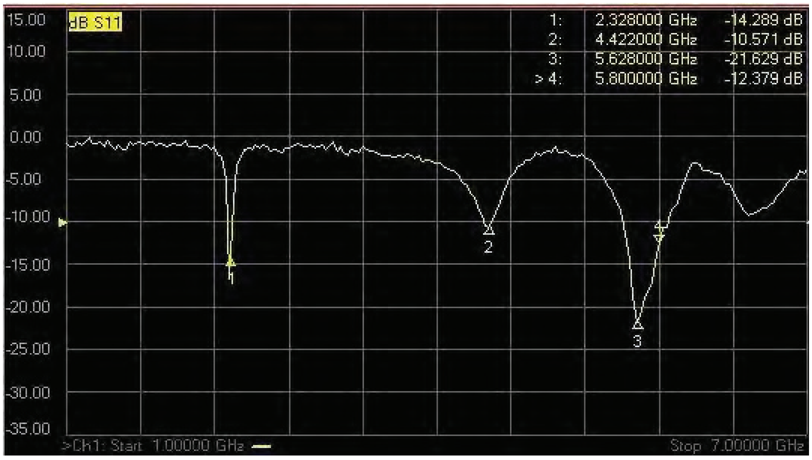

Fig. 21: Measured return loss of Antenna 4.

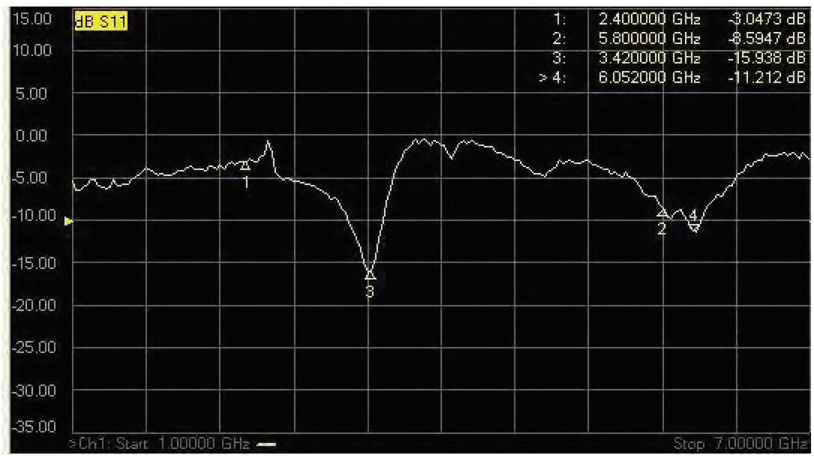

Fig. 22: Measured return loss of Antenna 5.

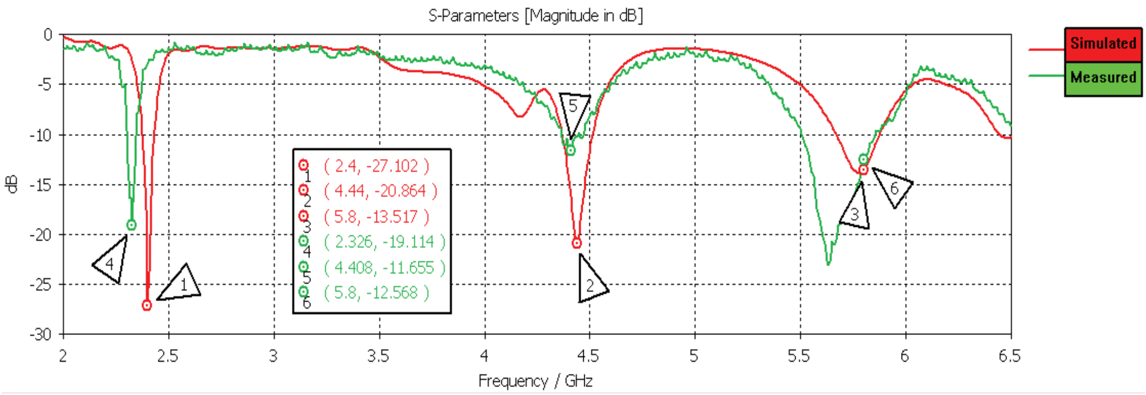

Fig. 23: Return loss comparison of simulated and measured Antenna 4.

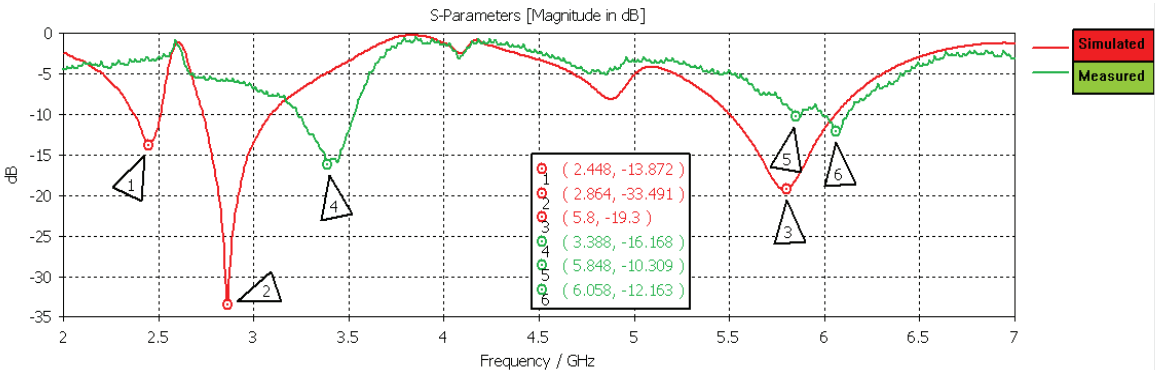

Fig. 24: Return loss comparison of simulated and measured Antenna 5.

Table 4 shows the comparison of the proposed designs (Antenna 4 and Antenna 5) to related works. It can be observed that all the works resonated at 2.4 GHz, which is the ISM band frequency that is commonly used by IoT applications. The proposed antenna designs in this paper had bigger size compared to work by [14]. However, the work by [14] only had one operating band which indicates that the proposed antenna designs had better performance with multi-band operation despite its size. Work by [15] had higher gain compared to the proposed antenna designs, but it only had one resonant frequency with bigger size. Moreover, work by [16] had the smallest antenna size and tri-band operation which is similar to the proposed antenna designs with three resonant frequencies. However, it did not resonate at 5.8 GHz, which is the required frequency for Wi-Fi application. Moreover, work by [17] had more bands of operation at five resonant frequencies, but its bandwidth is narrower and is of bigger size compared to proposed antenna design 2 that had wider bandwidth and smaller size.

Table 4: Comparison of proposed designs with related works

Ref.	Resonant frequency [GHz]	Size [mm^3]	Gain [dBi]	Bandwidth [MHz]
[14]	2.4	16 x 32.5 x 1.6	1.8	0.132
[15]	2.4	40 x 30 x 1.6	3.23	574
[16]	2.4, 3.5, 6.7	20 x 20 x 1.5	-	-
[17]	2.4, 2.7, 4.7, 5.6, 8.8	30 x 24.8 x 1.6	-	100, 130, 480, 350,210
Proposed 1	2.4, 4.44, 5.8	30 x 24.8 x 1.6	-12.38, -1.272, -4.065	54.5, 144.1, 204.9
Proposed 2	2.448, 2.864, 5.8	30 x 20 x 1.575	1.110, 1.382, 2.829	137.2, 350.9, 551.2

4. CONCLUSION

A miniaturized multi-band ring monopole antenna incorporated with RCSRR metamaterial structure as the radiating element and L-slotted ground plane, was successfully designed, simulated, measured, and analyzed. The antenna that resonated at 2.448 GHz, 2.864 GHz, and 5.8 GHz, and designed on Rogers RT5880 substrate, had a compact size with dimensions of 30 mm x 20 mm x 1.575 mm which indicates 57.8 % size reduction from conventional ring monopole antenna. The antenna had good impedance matching at -13.8 dB, -33.491 dB, and -19.3 dB, greater gain of 1.110 dBi, 1.382 dBi, and 2.829 dBi, wider bandwidth of 137.2 MHz, 250.9 MHz, and 551.2 MHz compared to the antenna that was designed on FR-4 substrate. It also had omnidirectional pattern which is suitable for use in the wireless connectivity that is essential for IoT applications. However, the measured result partially agreed with the simulation result where the fabricated antennas were unable to resonate at 2.4 GHz due to the defective antenna structure and the loss from the SMA connector and soldering process that affect its performance. Hence, the measured result was unable to fully validate the simulated result of the antenna. For future work, it is suggested to fabricate the miniaturized antenna with a laser etching method to ensure that a good antenna structure is produced. Besides, the antennas can also be miniaturized by incorporating different metamaterial structure such as electromagnetic bandgap (EGB) to broaden the research on miniaturized antenna using metamaterials.

ACKNOWLEDGEMENT

This paper was part of works conducted under the IIUM-UMP-UITM Sustainable Research Collaboration 2020 grant (SRCG20-041-0041). The authors would also like to acknowledge all supports given by the IIUM Research Management Centre through the grant.

REFERENCES

[1] Balanis CA. (2016) Antenna Theory: Analysis and Design. 4th Edition. New York, Wiley.
[2] Wi-Fi certified 6 [https://www.wi-fi.org/discover-wi-fi/wi-fi-certified-6].
[3] Rothwell EJ, Ouedraogo RO. (2014) Antenna miniaturization: definitions, concepts, and a review with emphasis on metamaterials. Journal of Electromagnetic Waves and Application, 28(17): 2089-2123.
[4] Cheng K, Liang Z, Hu B. (2021) Design of Miniaturized Microstrip Antenna for Smart Home Wireless Sensor. In Proceedings of the 2021 IEEE 4th International Conference on Electronic Information and Communication Technology (ICEICT): 18-20 Aug 2021; , pp. 234-236, Xi'an, China. pp 234-236. doi: 10.1109/ICEICT53123.2021.953 1163.
[5] Chandan K. (2020) Truncated ground plane multiband monopole antenna for WLAN and WiMAX applications. IETE Journal of Research. 68(4): 2416-2421. https://doi.org/10.1080/03772063.2019.1709568
[6] Bhatia SS, Sharma N. (2020) A Compact Wideband Antenna Using Partial Ground Plane with Truncated Corners, L–Shaped Stubs and Inverted T–Shaped Slots. Progress In Electromagnetics Research M. 97: 133-144. doi:10.2528/pierm20072503
[7] Chandan, Barthi G, Srivastava T, Rai BS. (2018) Dual band monopole antenna for WLAN 2.4/5.2/5.8 with truncated ground. In Proceedings of AIP, 1952(1). AIP Publishing LLC, https://doi.org/10.1063/1.5031998
[8] Baudha S, Basak A, Manocha M, Yadav MV. (2020) A compact planar antenna with extended patch and truncated ground plane for ultra-wide band application. Microwave and Optical Technology Letters 62(1): 200-209. https://doi.org/10.1002/mop.31988

[9] Rahardi R, Rizqi M, Lukito WD, Wibowo R, Oktafiani F, Munir A. (2020) Reduced Size Meander Line-based 433MHz Printed Dipole Antenna for UAV Telemetry Application. In Proceedings of International Conference on Radar, Antenna, Microwave, Electronics, and Telecommunications (ICRAMET), pp. 176-179. doi: 10.1109/ICRAMET51080.2020.9298675

[10] Ezhumalai A, Ganesan N, Balasubramaniyan S. (2021) An extensive survey on fractal structures using iterated function system in patch antennas. International Journal of Communication Systems. 34(15): e4932. https://doi.org/10.1002/dac.4932

[11] Chourasia S, Sharma SK, Goswami DP. (2020) Review on miniaturization techniques of microstrip patch antenna. In Proceedings of the 4th International Conference: Innovative Advancement in Engineering & Technology (IAET). http://dx.doi.org/10.2139/ssrn.3550995

[12] Manage PS, Naik U, Nargundkar S, Rayar V. (2020) A Survey on applications of Metamaterials in Antenna Design. In Proceedings of Third International Conference on Smart Systems and Inventive Technology: 20-22 August 2020; Tirunelveli, India. IEEE; pp. 153-158. doi: 10.1109/ICSSIT48917.2020.9214088

[13] Mishra RN, Arora A, Singh S, Bhattacharyya S. (2017) A split ring resonator (SRR) based metamaterial structure for bandstop filter applications. In Proceedings of IEEE Applied Electromagnetics Conference (AEMC): 19-22 December 2017; Aurangabad, India. IEEE; pp. 1-2. doi: 10.1109/AEMC.2017.8325685.

[14] Al-Bawri SS, Jamlos MF. (2018) Design of Low-Profile Patch Antenna Incorporated with Double Negative Metamaterial Structure. In Proceedings of International RF and Microwave Conference (RFM): 17-19 December 2018; Penang, Malaysia, IEEE; pp. 45-48. doi: 10.1109/RFM.2018.8846501

[15] Geetharamani G, Aathmanesan T. (2020) Design of Metamaterial Antenna for 2.4 GHz WiFi Applications. Wireless Personal Communication 113: 2289-2300. https://doi.org/10.1007/s11277-020-07324-z

[16] Lou R, Mohammad K, Naser-Moghadasi M, Sadeghzadeh RA. (2017) Compact multi-band circularly polarized CPW fed antenna based on metamaterial resonator. Wireless Personal Communications 94(4): 2853-2863. https://doi.org/10.1007/s11277-016-3722-x

[17] Ali T, Mohammad Saadh AW, Biradar RC, Anguera J, Andújar A. (2017) A miniaturized metamaterial slot antenna for wireless applications. AEU - International Journal of Electronics and Communications, 82: 368-382. https://doi.org/10.1016/j.aeue.2017.10.005

[18] CST Studio Suite 3D EM simulation and analysis software [https://www.3ds.com/products-services/simulia/products/cst-studio-suite]

[19] Muneer B, Shaikh FK, Zhu Q. (2020) Antennas for IoT application: An RF and microwave aspect of IoT. In IoT Architectures, Models, and Platforms for Smart City Applications. Hershey, PA: IGI Global, 2020: 180-192. doi: 10.4018/978-1-7998-1253-1.ch009

[20] Lizzi L, Ferrero F, Monin P, Danchesi D, Boudaud S. (2016) Design of miniature antennas for IoT applications. In Proceedings of Sixth International Conference on Communications and Electronics (ICCE): 27-29 July 2016; Ha-Dong, Vietnam, IEEE, pp. 234-237. doi: 10.1109/CCE.2016.7562642.

[21] Elijah AA, Mokayef M. (2020) Miniature microstrip antenna for IoT application. In Proceedings of Materials Today, 29: 43-47. https://doi.org/10.1016/j.matpr.2020.05.678

[22] Al-Sehemi A, Al-Ghamdi A, Dishovsky N, Atanasova G, Atanasov N. (2020) A flexible broadband antenna for IoT applications. International Journal of Microwave and Wireless Technologies: 12(6): 531-540. https://doi.org/10.1017/S1759078720000161

[23] Palhade SM, Yawale SP. (2015) Design and Photo-Lithographic Fabrication of Microstrip Patch Antenna. International Journal of Science and Research (IJSR), 4(2): 2021-2024. https://www.ijsr.net/get_abstract.php?paper_id=SUB151708

https://doi.org/10.31436/iiumej.v24i1.2611

COMPARATIVE ASSESSMENT OF NUMERICAL TECHNIQUES FOR WEIBULL PARAMETERS' ESTIMATION AND THE PERFORMANCE OF WIND ENERGY CONVERSION SYSTEMS IN NIGERIA

IGNATIUS K. OKAKWU[1], DANIEL O. AKINYELE[1], OLAKUNLE E. OLABODE[2], TITUS O. AJEWOLE[2], EMMANUEL S. OLUWASOGO[3] AND AJIBOLA O. OYEDEJI[4*]

[1]*Department of Electrical and Electronics Engineering, Olabisi Onabanjo University, Ago-Iwoye, Nigeria*
[2]*Department of Electrical and Electronics Engineering, Osun State University, Osogbo, Nigeria*
[3]*School of Energy Engineering, Kyungpook, National University, Daegu, South Korea.*
[4] *Department of Computer Engineering, Olabisi Onabanjo University, Ago-Iwoye, Nigeria.*

**Corresponding author: oyedeji.ajibola@oouagoiwoye.edu.ng*

(Received: 24th September 2022; Accepted: 14th December 2022; Published on-line: 4th January 2023)

ABSTRACT: The wind speed of a location is a critical parameter for analyzing wind energy conversion systems. Background knowledge has revealed that the two-parameter Weibull distribution is commonly used for fitting wind speed data because of its simplicity, flexibility and suitability. This research study examines wind speed data from five locations in Nigeria (Kano, Maiduguri, Jos, Abuja and Akure). It employs five numerical techniques, namely the maximum likelihood method, method of moment, power density method, empirical method and the logarithmic moment method, to estimate the Weibull parameters based on the locations' data. The goodness of fit test is used to determine which numerical method best fits the distribution. The paper also considers the techno-economic design of wind electricity of five 25 kW pitch-controlled wind turbines with dissimilar characteristics. The test result presents the method of moment and empirical method as the best methods for calculating the Weibull parameters. Results also show that wind turbine-3 has the least cost of energy and wind turbine-5 has the highest cost of energy.

ABSTRAK: Kelajuan angin sesuatu lokasi adalah parameter kritikal bagi menganalisa sistem penukaran tenaga angin. Latar belakang berkaitan telah mendedahkan 2-parameter taburan Weibull (Wbl) lazimnya digunakan bagi memadan data kelajuan angin berdasarkan kesederhanaan, fleksibiliti dan kesesuaian. Kajian penyelidikan ini adalah berkaitan ujian data kelajuan angin pada lima lokasi di Nigeria (Kano, Maiduguri, Jos, Abuja dan Akure). Ia menggunakan lima teknik berangka iaitu kaedah kemungkinan maksimum, kaedah momen, kaedah ketumpatan kuasa, kaedah empirikal dan kaedah momen logaritma bagi menganggar parameter Weibull berdasarkan lokasi data. Ujian kesesuaian digunakan bagi memastikan kaedah berangka adalah padanan paling sesuai bagi taburan. Kajian ini juga turut menimbang reka bentuk tekno-ekonomi elektrik angin bagi lima turbin angin 25 kW kawalan anggul dengan ciri berbeza. Dapatan kajian menunjukkan momen dan kaedah empirikal adalah kaedah terbaik bagi mengira parameter Weibull. Ini menunjukkan bahawa turbin angin-3 mempunyai kos tenaga paling rendah dan turbin angin-5 mempunyai kos tenaga tertinggi.

KEY WORDS: *Wind Speed, Numerical Method, Weibull Distribution, Energy Cost*

1. INTRODUCTION

The term "energy" is considered one of the most crucial human needs and is also identified as one of the essential indicating factors for measuring a country's level of development and the human development index (HDI) [1]. Although conventional energy sources, i.e., fossil fuels, play a critical role in meeting the world's energy demand requirements, its utilization has continued to raise environmental concerns [2]. Therefore, the quest to reduce the usage of fossil fuels due to its negative environmental effects, depletion, unstable price and the issue of energy consumption growth has driven the need for cleaner alternative energy resources [3].

Despite the global cry for the energy transition to green energy, burning of fossil fuel still occupy the larger percentage of Nigeria's electricity generation both at the utility and the energy users' levels [4]. The present electricity generation capacity of the country is less than 5000 MW for all sources (thermal, gas and hydro) as at March 2022. This is inadequate considering the country's population of over 200 million. The gap in generation and the citizens' demand has resulted in energy poverty and low standard of living [5]. In order to address this problem, it is necessary to grow the country's energy mix by harnessing the available renewable energy (RE) sources, one of which is the wind energy resource.

Wind energy is naturally-occurring and can be deployed for on-grid and off-grid generation applications [6]. However, in order to utilize wind energy, the probability density function (PDF) related to wind speed must be well assessed or evaluated for the supply of reliable electricity at an affordable cost. Such parameter provides crucial information in wind energy planning and implementation and also helps to ascertain a location's wind power potential. Various PDFs have been proposed in the literature to describe the distribution of wind speed, but the 2-parameter Weibull (Wbl) distribution is widely employed because of its simplicity, flexibility and suitability for fitting recorded wind data [7]. In analyzing wind speed data, the distribution that fits the data statistically needs to be firstly determined, and then the estimations of the relevant parameters concerning this distribution can be calculated. Some studies have been presented on wind energy generation in Nigeria. Some of these scholarly works will be presented in this section for the purpose of laying useful background for this present study.

Oyedepo et al., [8] presented the wind characteristics and the potential for selected locations in Nigeria utilizing data that spans 24 to 27 years, measured at the height of 10 m. The central concern of the paper includes the determination of the annual output power and capacity factor (CFw). Adaramola et al., [9] presented wind turbines' performance for electricity production in seven different areas within the Niger-Delta region of Nigeria based on wind data that spans 9 to 37 years, using the 2-parameter Wbl distribution functions. Observation showed that 35 kW wind turbine discussed in their work has the highest CFw irrespective of the locations.

Ajayi et al., [10] presented a Techno-economic (TE) evaluation of wind turbines for electricity supply to 10 locations in Nigeria. The 2-parameter method WPD was used to assess the wind potential for the locations. The turbine matching results reveal that the cut-in and rated wind speeds range from 2.0 to 3.0 m/s, and 10 to 12.0 m/s, respectively. Sulaiman et al., [11] also discussed the assessment of the wind potential of 4 different locations in Nigeria, emphasizing wind power potentials and wind speed characteristics using the 2-parameter WDF technique. The paper used the CFw calculation to determine the most suitable turbine for the specified locations and reported monthly mean wind speed of 4.50, 3.72, 4.77 and 5.34 m/s with corresponding wind power densities of 67.74, 40.87, 79.52 and 107.49 Wm-2 for the sites.

https://doi.org/10.31436/iiumej.v24i1.2611

Okakwu et al., [12] discussed the TE evaluation of wind resources for power generation in Nigeria. The study used a 2-parameter WDF for analyzing the wind potential of four different locations based on the average wind speeds/day measured at the anemometer positioned at 10 m over a period of 11 years. It employed the power density and the CFw to classify the sites and select the most suitable turbine for these locations. It also used the present-value cost to the COE by the WECS at various h/hs.

Mohammadi et al., [13] considered the TE analysis of large-scale wind electricity systems in Iran. The paper employed the 2-parameter WDF for analyzing the measured wind data between 2008 and 2009 at the height of 40 m height. However, the authors examined the TE analysis of four large-scale wind turbine systems at a height of 70 m height. Ajayi et al. [14] discussed the wind profile and turbine system performance assessment in Kano, Nigeria. The authors also presented the wind energy analysis using the 2-parameter WDF method based on the wind data that spans between 1987 and 2007 at 10 m. The study also employed wind rose to describe the direction of the wind energy in different seasons.

Alkhalidi et al., [15] evaluated wind potential at coastal and offshore locations in Kuwait. This work explores ten coastal and offshore locations for the analysis and then considered the potential at different heights of 50, 80, 100, and 120 m. The authors employed a 2-parameter Wbl distribution method to analyze the wind resource and calculate wind energy density. In addition, the study calculated the Wbl distribution parameters by using the maximum likelihood method. Mostafaeipour et al., [16] analyzed the wind potential and the WECSs cost for Zahedan, Iran using 5-year wind resource data. The wind power density and the energy output have also been determined by using the WDF. The study considered the comparative analyses of the 3 different PDF models such as Wbl, Rayleigh, and lognormal, to analyze the location's wind profile.

Soulouknga et al. [18] evaluated the cost of generating wind-generated electricity in Chad. The work used the Wbl distribution for assessing the wind resource data obtained at an anemometer height of 10 m. The work also determined the Wbl statistical parameters (k and c) at different heights of 10, 30, 50, and 70 m. Belabes et al., [19] evaluated the wind potential and the cost of electricity by the WECSs for 6 different areas of the north of Algeria. The data recorded for over 10 years were used; the authors also obtained the Wbl parameters k and c for all months at different heights of 30, 50 and 70 m by extrapolating the 10 m data at the locations.

The reviewed studies have contributed substantially to the body of knowledge in the research direction of wind potential and cost analysis for different locations, all of which are based on the 2-parameter WDF at the height of 10 m. It is also found that [15] used the maximum likelihood method, while some others used the empirical method to calculate Wbl distribution parameters. The work in [20] compared the Wbl, Rayleigh, and lognormal models to assess the locations' wind resources and profiles. The main focus of the aforementioned studies includes the identification of suitable locations and the selection of WTs and COE, which are useful background contributions for understanding wind potential analysis and WECS design and planning.

However, this present study will first identify the best fit for the probability density function (PDF) of wind speed data and then ascertain suitable sites for wind power generation. It will also calculate the impact of varying the h/hs on the COE to provide useful insights into decision-making for a sound investment model for wind energy production in Nigeria. Importantly, this study uses five different techniques, namely the maximum likelihood, method of moment, power density, empirical and logarithmic moment methods, to characterize the wind resource data of 5 different locations in Nigeria and then determine the respective Wbl parameters (i.e., k and c). The comparative analysis is employed to understand the performance of different numerical methods mentioned given the locations' resource data, which also takes this paper a step further than the analysis presented in some previous studies discussed earlier.

In addition, the research study examines the TE performances of five 25 kW pitch-controlled wind turbines (WT1 – WT5) from different manufacturers with dissimilar design characteristics at varying h/hs. The results of this paper are expected to demonstrate a detailed TE analysis, which may be useful for designing, planning and assessing WECSs for local energy and agricultural applications, e.g. water-pumping.

The remaining part of this research article is arranged as follows: section 2 is on materials and methods, section 3 focuses on the results and discussion, while section 4 presents the conclusion of the paper.

2. MATERIALS AND METHOD

2.1 Study Area

This study considered five locations in Nigeria, namely Kano, Maiduguri, Jos, Abuja and Akure, in the northern and southern parts of the country. The wind speed data used in this work was obtained from the Nigeria Meteorological Agency (NIMET), Lagos State, Nigeria. The wind resource was measured by NIMET at a h/h of 10 m by an anemometer cup-generator. Table 1 presents the case study areas.

Table 1: The case study areas [24]

Locations	Latitude (^{0}N)	Longitude (^{0}E)	Data Period
Kano	12.05	8.52	2002-2012
Maiduguri	11.85	13.08	2002-2012
Jos	9.64	8.88	2002-2012
Abuja	9.00	7.27	2002-2012
Akure	7.25	5.20	2002-2012

2.2 Simulation Software

The implementation of the proposed approaches in terms of modelling, simulation and analysis was achieved using MATLAB version (2013a) and Microsoft Excel software.

2.3 Numerical Approaches to Weibull Parameters' Estimation

Background knowledge of wind resources and systems modelling and analysis shows that several methods can be employed for calculating the Wbl parameters k and c. However, five different methods are employed in this paper to characterize the wind speed data under review.

2.3.1. Maximum Likelihood Approach

Using the maximum likelihood method (MLM), k and c parameters are calculated by Eqs. (1) and (2) [21-23]:

$$k = \left[\frac{\sum_{i=1}^{n} V_i^k \ln V_i}{\sum_{i=1}^{n} V_i^k} - \frac{\sum_{i=1}^{n} \ln(V_i)}{n}\right]^{-1} \tag{1}$$

$$c = \left[\frac{1}{n}\sum_{i=1}^{n} V_i^k\right]^{\frac{1}{k}} \tag{2}$$

where V_i and n are the wind speed in time step i, and the number of 'non-zero' wind speed data points. In the MLM, numerical iterations are required to determine the Wbl parameters.

2.3.2. Method of Moment

In the method of moment (MOM), the k and c parameters are given by Eqs. (3) and (4) [21-23]:

$$k = \left[\frac{0.9874}{\frac{\sigma}{\overline{V}}}\right]^{1.0983} \tag{3}$$

$$c = \frac{\overline{V}}{\Gamma\left(1+\frac{1}{k}\right)} \tag{4}$$

where; σ and $\overline{V}$ in this case, are the standard deviation and the mean wind speed.

2.3.3. Power Density Method

In employing the power density method (PDM) for wind resource analysis, the value of k parameter is calculated by Eqs. (5) and (6) [21-23]:

$$k = 1 + \frac{3.69}{E_{pf}^2} \tag{5}$$

The scale parameter (c) in the case of PDM is estimated using Eq. (4).

$$E_{pf} = \frac{\overline{V^3}}{(\overline{V})^3} = \frac{\frac{1}{n}\sum_{i=1}^{n} V_i^3}{\left(\frac{1}{n}\sum_{i=1}^{n} V_i\right)^3} \tag{6}$$

2.3.4. Empirical Method

In the empirical method (EPM), the k parameter is estimated by Eq. (7), while c parameter is calculated by employing Eq. (4) [22-24]:

$$k = \left[\frac{\sigma}{\overline{V}}\right]^{-1.086} \tag{7}$$

In which case σ and $\overline{V}$ represent the standard deviation and the mean wind speed, respectively.

2.3.5. Logarithmic Moment Method

In the logarithmic moment method (LMM), the values of k and c parameters are estimated by Eqs. (8) and (9) [21-23]:

$$k = \left[\frac{1.645}{\sigma^2}\right]^{\frac{1}{2}} \tag{8}$$

$$c = exp\left[\frac{k\overline{V}+0.5772}{k}\right] \tag{9}$$

2.4 Numerical Method Accuracy Assessments

In order to test the accuracy of the presented numerical methods for estimating the Wbl parameters, two different approaches are employed, which are the root mean square error (RMSE) and the coefficient of determination (R^2). The value of RMSE is given by Eq. (10) [21-23]:

$$RMSE = \left[\frac{1}{n}\sum_{i=1}^{n}(y_i - x_i)^2\right]^{\frac{1}{2}} \tag{10}$$

The coefficient of determination is then given by Eq. (11) [21-23]:

$$R^2 = \frac{\sum_{i=1}^{N}\left(f(V_i)-\overline{f(V)}\right)^2 - \sum_{i=1}^{N}\left(f(V_i)-\hat{f}(V_i)\right)^2}{\sum_{i=1}^{N}\left(f(V_i)-\overline{f(V)}\right)^2} \quad (11)$$

2.5 Wind Speed Analysis

The daily mean wind speed, $\overline{V}$ and the standard deviation, σ of the wind resource data can be calculated by Eqs. (12) and (13), respectively [12]:

$$\overline{V} = \frac{1}{n}\left(\sum_{i=1}^{n} V_i\right) \quad (12)$$

$$\sigma = \sqrt{\frac{1}{n} \sum_{i=1}^{n}\left(V_i - \overline{V}\right)} \quad (13)$$

where V_i and n represent the daily wind speed in time step of i and the number of wind speed data points.

The WPD function ($f_w(v)$) and the cumulative distribution function ($f_w(V)$) are given by Eqs. (14) and (15) [20]:

$$f_w(v) = \left(\frac{k}{c}\right)\left(\frac{v}{c}\right)^{k-1} exp\left[-\frac{v}{c}\right]^k \quad (14)$$

$$f_w(V) = 1 - exp\left[-\frac{v}{c}\right]^k \quad (15)$$

where; v, k and c represent the wind speed (m/s), shape parameter (dimensionless) and the scale parameter (m/s), respectively. In addition, the most probable wind speed (V_{mps}) and the wind speed at the maximum energy (V_{emax}) are given by Eqs. (16) and (17) [24]:

$$\mathrm{V_{mps}} = \mathrm{c}\left(\frac{\mathrm{k}-1}{\mathrm{k}}\right)^{\frac{1}{\mathrm{k}}} \quad (16)$$

$$V_{emax} = c\left(\frac{k+2}{k}\right)^{\frac{1}{k}} \quad (17)$$

At times, wind speeds are measured at a reference h/h (h_0) but needs to be adjusted to the relevant wind turbine h/h (h). The new wind speed (V_h), scale factor (c_h) and shape factor (k_h) are given by Eqs. (18) to (20) by using a relevant power law equation, while Eq. (21) is employed to estimate the value of n [25]:

$$V_h = V_0\left(\frac{h}{h_0}\right)^{\propto} \quad (18)$$

$$c_h = c_0\left(\frac{h}{h_0}\right)^{n} \quad (19)$$

$$k_h = k_0\left\{\frac{\left[1-0.088\ln\frac{h_0}{10}\right]}{\left[1-0.088\ln\frac{h}{10}\right]}\right\} \quad (20)$$

$$n = \frac{\left[0.37-0.088\ln c_0\right]}{\left[1-0.088\ln\frac{h}{10}\right]} \quad (21)$$

where $\propto$ represents the site surface roughness coefficient and assumed in this work to be 0.143 [11].

2.6 Wind Power Estimation

The wind power density, P_{WPD} is a measure of the capacity of the wind resource of a particular location per unit swept area of the blades. Eq. (22a) is employed to estimate the wind power density, while the wind power capacity, P_{WPC} is estimated by Eq. (22b) [10]:

$$P_{WPD} = \frac{1}{2}\rho c^3 \Gamma\left(1 + \frac{3}{k}\right) \tag{22a}$$

$$P_{WPC} = \frac{1}{2} A\rho V_{ms}^3 \tag{22b}$$

where ρ and A stand for the air density (i.e., 1.225 kg/m^3) and the swept area of the rotor blades (m^2). The P_{WPD} and P_{WPC} parameters are measured in (W/m^2) and (W), respectively.

To extend the performance of the WECS further, in terms of the available power in the wind, this study considers the contribution made by Albert Betz (a German Physicist). This scientist made bold in 1919 as part of his contributions to knowledge that there is no wind turbine system that can convert above $\frac{16}{27}$ (i.e., 0.593) of the wind's kinetic energy to mechanical energy for turning the wind turbine rotor [26, 27]. In wind power system engineering, this factor 0.593 is referred to as the Betz limit. It is translated as the theoretical maximum power efficiency or (the aerodynamic efficiency of the rotor [28] of a wind turbine system design, i.e., 0.59), implying that not more than 59% of energy can be obtained from the wind by the WT system. It is then referred to as the power coefficient, $C_{p(max)}$ and is added to Eqs. (22b) leading to Eq. (22c) describes the maximum power obtainable from the WT:

$$P_{(WPC)max} = \frac{1}{2} A\rho C_{p(max)} V_{ms}^3 \tag{22c}$$

It is important to state that the value of the power coefficient in real life limit is practically lower than the Betz limit [26, 28]. Typical values of the Betz limit range from 0.35 to 0.45 even for best wind turbine systems; therefore, after making realistic design considerations for the gearbox, bearings, generator, etc., only around 0.1 to 0.3 fraction of the power of in the wind that is in reality converted into usable electrical energy [26].

2.7 Estimation of WECS' Output Power and Cf_w

The wind turbine output power is of a significant benefit, as it presents a good economic indicator compared to its rated capacity. The wind turbine output power, i.e., the power curve, is modelled via four parameters: the cut-in wind speed (V_{ci}), the cut-off wind speed (V_{co}), the rated wind speed (V_r) and the rated power capacity of the WT (P_r). For a pitch-controlled WT, the power curve model can be approximated by a parabolic law, given by Eq. (23) [11-12]:

$$P = P_r \begin{cases} \frac{V_{ms}^2 - V_{ci}^2}{V_r^2 - V_{ci}^2} & V_{ci} \le V_{ms} \le V_r \\ 1 & V_r \le V_{ms} \le V_{co} \\ 0 & V_r \le V_{ci} \text{ and } V_{ms} \ge V_{co} \end{cases} \tag{23}$$

The average power output (P_{ave}) of a WT is given by Eq. (24) [13-14]:

$$P_{ave} = P_r \left[\frac{e^{-\left[\frac{V_{ci}}{c}\right]^k} - e^{-\left[\frac{V_r}{c}\right]^k}}{\left[\frac{V_r}{c}\right]^k - \left[\frac{V_{ci}}{c}\right]^k} - e^{-\left[\frac{V_{co}}{c}\right]^k} \right] \tag{24}$$

Technically, CF_w of a WT is the ratio of P_{ave} to P_r and is given by Eq. (25) [11-12]:

$$CF_w = \frac{P_{avr}}{P_r} = \left[\frac{e^{-\left[\frac{V_{ci}}{c}\right]^k} - e^{-\left[\frac{V_r}{c}\right]^k}}{\left[\frac{V_r}{c}\right]^k - \left[\frac{V_{ci}}{c}\right]^k} - e^{-\left[\frac{V_{co}}{c}\right]^k} \right] \quad (25)$$

In addition, the yearly energy produced by the WT is given by Eq. (26):

$$E_{ae} = CF_w \times P_r \times t \quad (26)$$

where *t* represents the total hours in a year, i.e., 8760 hours.

2.8 Economic Cost Analysis

Estimating the unit cost of energy, COE, is a way of knowing the most viable wind turbine to select for this study. The economic aspect of this work focuses on calculating the cost of the individual components of the system, which include the investment, operation and maintenance (O and M) and the replacement costs. The WECSs life-cycle cost can be calculated by Eq. (27) [11]:

$$C_{LCC} = C_{inv} + C_{opm}\left(\frac{1+i_r}{d-i_r}\right)\left(1-\left(\frac{1+i_r}{1+d}\right)^p\right) \quad (27)$$

where; C_{opm}, i_r, d, r and p in this case represent the operation and maintenance cost, inflation rate, discount rate, interest rate and the project lifetime, respectively, and the corresponding values of these are assumed to be 0.1 % of investment cost C_{inv}, 8.4 %, 11%, 15% and 20 years.

The annualized life-cycle cost (C_{ALCC}) is given by Eq. (28):

$$C_{ALCC} = C_{LCC} \times CRF \quad (28)$$

where CRF is regarded as the capital recovery factor and is given by Eq. (29) [10]:

$$CRF = \frac{i_r\,(1+i_r)^n}{(1+i_r)^n - 1} \quad (29)$$

The unit cost of energy is then given by Eq. (30) [33]:

$$COE = \frac{C_{ALCC}}{8760 \times P_r \times CF_w} \quad (30)$$

In this study, five different turbines from different manufacturers were considered and are represented by WT1, WT2, WT3, WT4 and WT5, respectively, with their characteristics shown in Table 2.

Table 2: Characteristics of the selected WTs [16, 34]

Characteristics	WT1	WT2	WT3	WT4	WT5
Rated power P_r (kW)	25	25	25	25	25
Rotor diameter (m)	15	15	15	15	15
Cut-in wind speed V_{ci} (m/s)	2.0	2.5	3.0	3.5	4.0
Rated wind speed V_r (m/s)	16	18	15	17	19
Cut-off wind speed V_{co} (m/s)	25	27	23	28	30
Investment cost $\$/kW$	1300	1300	1300	1300	1300

3. RESULTS AND DISCUSSION

3.1 Comparison of Wind Speed Distributions of Estimated Wbl PDF

Figures 1 to 5 show the comparison of the wind speed histogram with the calculated Wbl PDFs for the five numerical approaches for the specified locations under study. The Wbl density function gets narrower and becomes peaked as k becomes larger, meaning that wind speeds tend to stay within a narrow range. The peak also moves in the higher wind speed direction as the value of c increases. For instance, in Kano, Maiduguri, Abuja and Akure, as shown in Figures 1, 2, 4 and 5, respectively, since the calculated value of k from the LMM is greater than those obtained from the other methods, the peaks of the probability density curves were larger compared to the others. However, in Jos as shown in Figure 3, the calculated k using MOM was greater than the value obtained using the other methods; hence, the peak of its probability density curve is observed to be larger. Therefore, Figures 1 to 5 demonstrates that lower shape parameters correspond to broader probability density curves (i.e., higher scale parameters), which implies that winds vary over a wide range of wind speeds.

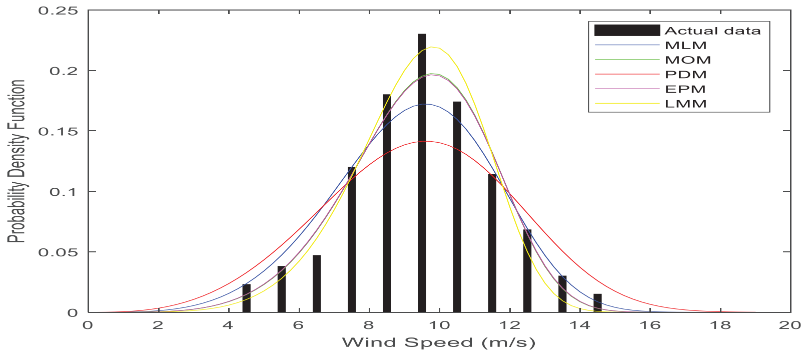

Fig. 1. Comparison of the PDFs for Kano

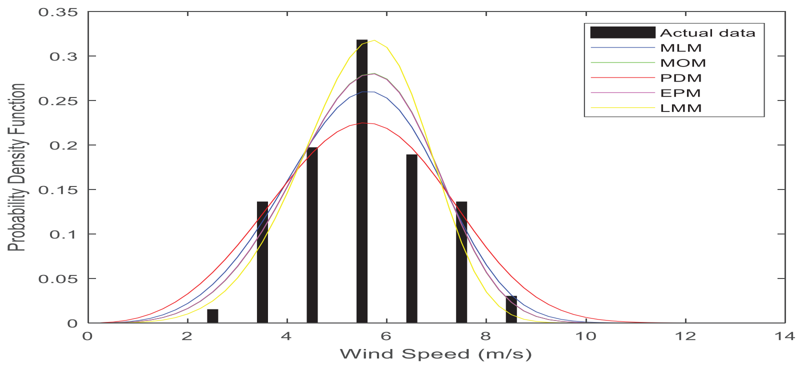

Fig. 2. Comparison of the PDFs for Maiduguri

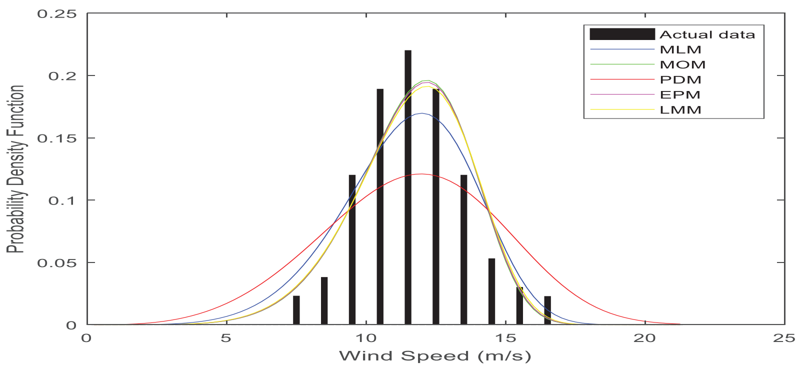

Fig. 3. Comparison of the PDFs for Jos

The Wbl parameters in the locations based on minimum $RMSE$ and maximum R^2 are presented in Tables 3 to 7, respectively. It is obvious from these results that the values of k range from 2.90 in Akure to 7.01 in Abuja, while those of c range from 3.86 in Akure to 12.82 in Jos. In the cases under study, $RMSE$ varies from 0.0584 to 0.1474, R^2 varies from 0.9611 to 0.9988. Therefore, Tables 3 to 7 summarize the fitness errors between the estimated PDFs and the histogram of the observed wind speed data at the height of 10 m. Results of calculated Weibull parameters from all the five NEMs (MLM, MOM, PDM, EPM and LMM) and two statistical methods (RMSE and R^2) for measuring the efficiency of these NEMs in all the five locations considered are presented in Table 3-7, respectively. For a robust comparison purpose of all NEMs, the statistical values for measuring efficiency have been listed up to 9 decimal points. From these tables, it is observed that out of the five NEMs of estimating Weibull parameters, MOM and EPM have estimated the same values for k and c respectively in Kano (Table 7), hence, have the same efficiency of estimation. Each NEMs have been ranked against its performance on a scale from 1-5 (with 1 being the best efficient and 5 as the worst efficient). From Table 3, it is observed that MOM is the best and PDM is the worst with respect to RMSE and R^2 respectively. From Table 4, EPM has been found to be the most efficient and PDM the worst efficient with respect to RMSE and R^2 respectively. Furthermore, in Table 5, it is

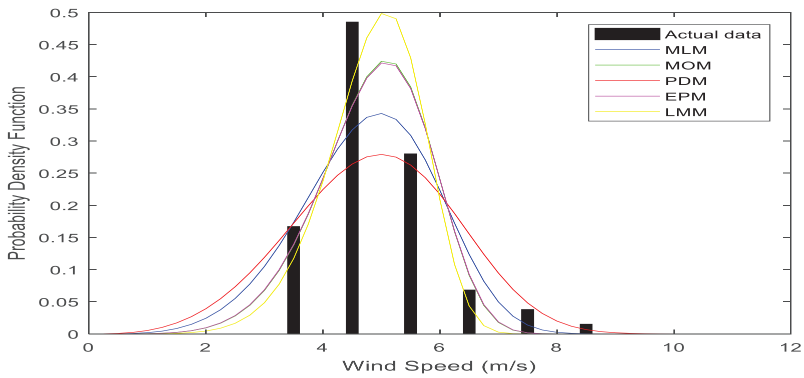

Fig. 4. Comparison of the PDFs for Abuja

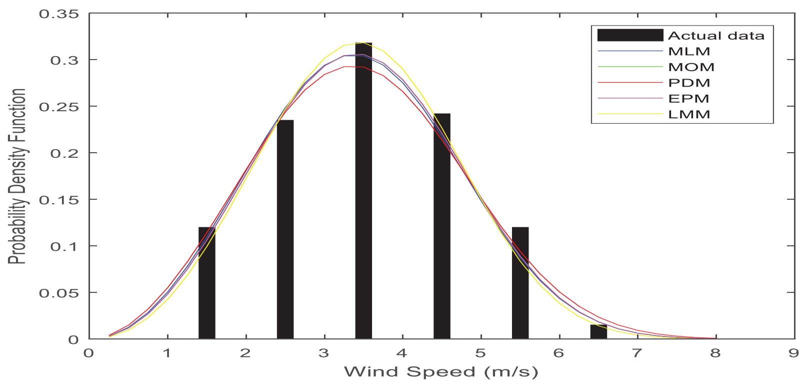

Fig. 5. Comparison of the PDFs for Akure

observed that MOM depicts the best performance and PDM still retains its worst efficient performance with respect to RMSE and R^2 respectively. In Table 6, EPM shows the best performance and PDM still shows the worst performance with respect to RMSE and R^2 respectively. However, in Table 7, MOM and EPM were found to be the most efficient, while PDM still retains its worst position. The results shown in Tables 3-7 demonstrate that the EPM and MOM are the best fit across all five locations due to their minimum $RMSE$ value and maximum R^2 value. The results also reveal that PDM was the worst-performing NEM across all five locations.

3.2 Wind Characteristics of Location

The wind speed characteristics of the locations are shown in Table 8. It can be seen that V_{ms} varies from 3.47m/s in Akure site to 11.63m/s in Jos; k varies from 2.90 in Akure to

4.08 in Jos, while c varies from 3.89 m/s in Akure to 12.82 m/s in Jos. Also, V_{mps} varies from 3.36 m/s in Akure to 11.97 m/s in Jos; V_{emax} varies from 4.66 m/s in Akure to 14.14 m/s in Jos; P_{WPD} varies from 36 W/m^2 in Akure to 1182.12 W/m^2 in Jos, all at a h/h of 10 m. The results further show that Kano and Jos study locations are viable sites for grid integration because the wind power density at the h/h of 10 m is > 400 W/m^2. In addition, Abuja and Akure study locations are not viable for wind electricity production because the wind power density in these locations is < 100 W/m^2, while Maiduguri is only applicable for a stand-alone application because the wind power density is > 100 W/m^2 [11].

Table 3. Wbl parameters and goodness of fit estimation for Kano

	Numerical Methods	Wbl parameters		Statistical criteria		Rank
		k	c	RMSE	R^2	
Kano	MLM	4.62	10.12	0.022298950	0.999994120	4
	MOM	5.37	10.19	0.015769237	0.999997059	1
	PDM	3.83	10.39	0.035938398	0.999984726	5
	EPM	5.34	10.19	0.015880219	0.999997018	2
	LMM	5.95	10.12	0.015976125	0.999996982	3

Table 4. Wbl parameters and goodness of fit estimation for Maiduguri

	Numerical Methods	Wbl parameters		Statistical criteria		Rank
		k	c	RMSE	R^2	
Maiduguri	MLM	4.12	6.01	0.029812308	0.999968890	3
	MOM	4.47	6.02	0.029509497	0.999969519	2
	PDM	3.57	6.10	0.040316395	0.999943106	5
	EPM	4.46	6.02	0.029456943	0.999969628	1
	LMM	5.05	5.97	0.036872000	0.999952412	4

Table 5. Wbl parameters and goodness of fit estimation for Jos

	Numerical Methods	Wbl parameters		Statistical criteria		Rank
		k	c	RMSE	R^2	
Jos	MLM	5.63	12.41	0.029395252	0.999993500	4
	MOM	6.57	12.47	0.024726277	0.999995401	1
	PDM	4.08	12.82	0.052023787	0.999979641	5
	EPM	6.52	12.48	0.025154590	0.999995240	2
	LMM	6.42	12.50	0.026047047	0.999994896	3

Table 6. Wbl parameters and goodness of fit estimation for Abuja

	Numerical Methods	Wbl parameters		Statistical criteria		Rank
		k	c	RMSE	R^2	
Abuja	MLM	4.76	5.23	0.074049683	0.999751495	3
	MOM	5.99	5.25	0.071313582	0.999769520	2
	PDM	3.94	5.38	0.097370552	0.999570320	5
	EPM	5.95	5.25	0.071065282	0.999771122	1
	LMM	7.01	5.20	0.076836985	0.999732435	4

Table 7. Wbl parameters and goodness of fit estimation for Akure

	Numerical Methods	Wbl parameters		Statistical criteria		Rank
		k	c	RMSE	R^2	
Akure	MLM	3.01	3.86	0.019045125	0.999966622	3
	MOM	3.04	3.88	0.017679962	0.999971235	1
	PDM	2.90	3.89	0.019662755	0.999964422	4
	EPM	3.04	3.88	0.017679962	0.999971235	1
	LMM	3.17	3.87	0.018876644	0.999967210	2

Table 8. Wind speed characteristics of the locations

Location	V_{ms}	k	c	V_{mps}	V_{emax}	P_{WPD} (W/m^2)
Kano	9.39	3.83	10.39	9.60	11.59	636.84
Maiduguri	5.49	3.57	6.10	5.56	6.91	131.60
Jos	11.63	4.08	12.82	11.97	14.14	1182.12
Abuja	4.87	3.94	5.38	4.99	5.97	87.94
Akure	3.47	2.90	3.89	3.36	4.66	36.59

3.3 Estimation of CF_w of WTs

Although designing a wind turbine that will match a particular site's wind characteristics is the best practice; however, this can be time-consuming and frustrating [23], hence, the need to utilize available wind turbines in the market (W1 – W5). For this study, the CF_w method is used for the WT selection. Table 2 shows the characteristics of the WT used for this study. Wind turbines with a high value of CF_w is usually considered suitable for selection. Table 9 presents the results of CF_w of each turbine with respect to the specified locations. WT1, WT2, WT3, WT4 and WT5 have CF_w values of 0.0134 to 0.3705, 0.0083 to 0.2456, 0.0126 to 0.4471, 0.0067 to 0.3017, and 0.0034 to 0.1981, respectively.

Table 9. CF_w of the wind turbines in different locations

	CF_w				
Location	WT1	WT2	WT3	WT4	WT5
Kano	0.1901	0.1214	0.2393	0.1495	0.0968
Maiduguri	0.0314	0.0202	0.0373	0.0225	0.0139
Jos	0.3705	0.2456	0.4471	0.3017	0.1981
Abuja	0.0134	0.0082	0.0160	0.0090	0.0051
Akure	0.0144	0.0089	0.0126	0.0067	0.0034

Table 9 demonstrates that WT3 has the highest CF_w followed by WT1, WT4, WT2 and WT5, respectively. For uniformity of comparison, all the turbines considered have the same rated capacity of 25 kW. However, they have different cut-in and rated wind speeds as the machines are from different manufacturers.

3.4 Estimation of COE

Table 10 presents theCOE for the selected WTs at a h/h of 10 m. WT3 has the least cost performance for all the locations considered in this study. The values of COE for WT3 range from \$ 0.041/kWh in Jos to \$ 1.457/kWh in Akure. However, WT5 has the highest cost performance of all the systems. Its *COE* values range from $ 0.093/kWh in Jos to $5.331/kWh in Akure. In Nigeria, electricity tariff in the country for residential "Band A" customers with daily minimum of 20 hours of electricity availability is $ 0.13. This translates to ₦ 52 at an official exchange rate of $1 to ₦ 400. Hence, generation of electricity using wind turbines, WT1 – WT5 is suitable for Jos and WT1 – WT4 is suitable for Kano, while other locations are not economically viable for wind power generation compared with the national grid supply.

Table 10. COE of the WECSs

	COE ($/kWh)				
Location	WT1	WT2	WT3	WT4	WT5
Kano	0.096	0.151	0.077	0.123	0.189
Maiduguri	0.584	0.909	0.491	0.814	1.316
Jos	0.049	0.075	0.041	0.061	0.093
Abuja	1.370	2.243	1.149	2.046	3.601
Akure	1.278	2.050	1.457	2.728	5.331

3.5 Sensitivity Analysis Cases

The sensitivity analysis introduced in this study showcases the dependency of the WECSs variable on certain defined input variables. In this study, the variable considered is the effect of change in the h/hs on the probability density curve and the values of k, c, P_{WPD}, CF_w and *COE*. The results are shown in Figures 6 to 11.

The results in Figures 6 and 7 show that the Wbl parameters are directly proportional to the h/h; this is because the air mass flow appears to be smoother at a higher height. This is as a result of less impact of land topography obstructions to the flow of moving air. As shown in Figures 6 and 7, increasing h/h will lead to an increase in k and c. Also, an increase in k and c will make the shape of the PDF narrower (i.e., peaked) and broader by the right side of the graph (i.e., higher wind speeds). This peaked shape is not noticeable because of the little increase in the value of k as a result of higher h/hs, while an increase in the value of c will make the PDF move to the direction of higher wind speeds as can be seen in Figure 8. Figure 8 presents the effect of increasing h/hs on the probability density curve.

The values of k for Kano, Maiduguri, Jos, Abuja and Akure range from 3.83 to 5.09, 3.57 to 4.75, 4.08 to 5.43, 3.94 to 5.24 and 2.90 to 3.86, respectively, for corresponding h/hs of 10 to 50 m. Similarly, the values of c for these locations range from 10.39 to 14.13, 6.10 to 9.06, 12.82 to 16.84, 3.89 to 8.16 and 3.89 to 6.22, respectively, for the h/hs ranging from 10 to 50 m.

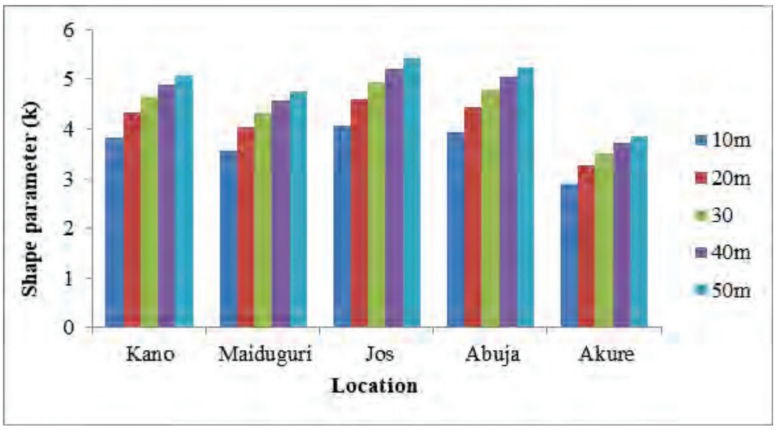

Fig. 6. Sensitivity analysis relating k with h/h

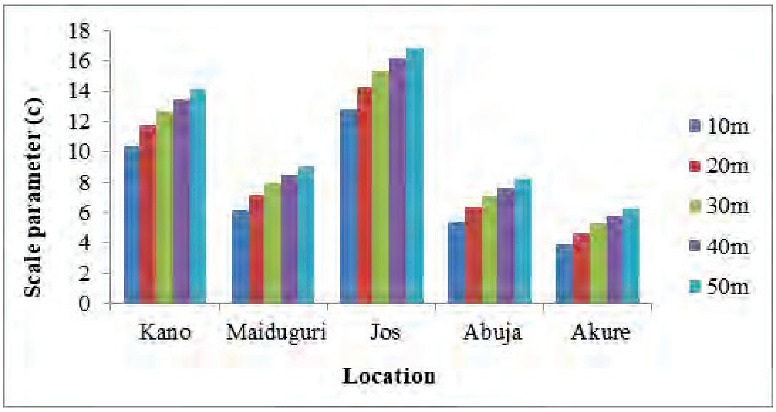

Fig. 7. Sensitivity analysis relating *c* with h/h

Fig. 9 shows the impact of varying h/h on the wind power density of the locations. Increasing h/hs leads to an increase in wind power density. The values of P_{WPD} for Kano, Maiduguri, Jos, Abuja and Akure range from 636.84 to 1541.34 W, 131.06 to 408.81 W, 1182.13 to 2600.36 W, 87.94 to 296.52 W and 36.59 to 136.41 W, respectively, for corresponding h/hs of 10 to 50 m.

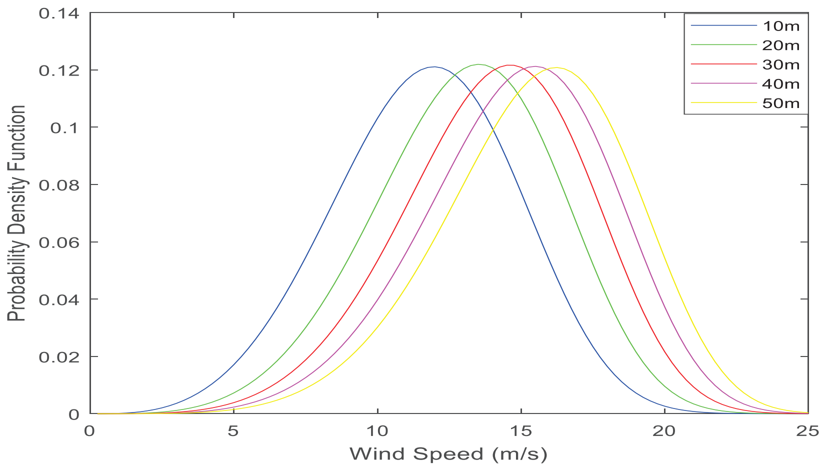

Fig. 8. Sensitivity analysis relating PDFs with h/hs

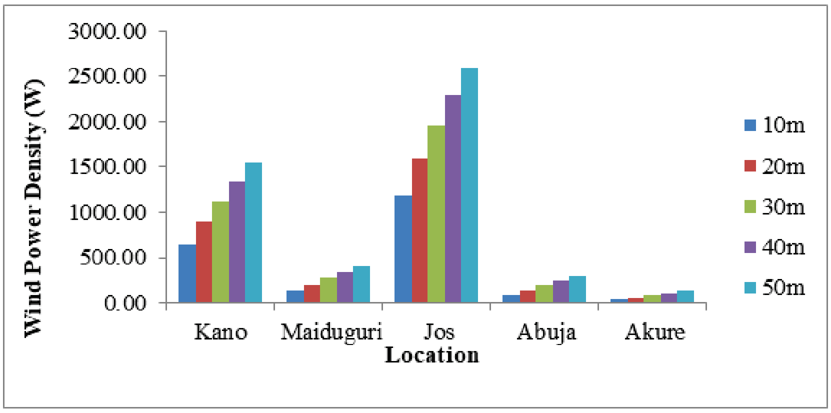

Fig. 9. Sensitivity analysis relating wind power density with h/h

Table 9 presents the results of the CF_w for the WTs in the specified locations. The results show that the CF_w of the WTs range from 0.0968 to 0.2393, 0.0139 to 0.0373, 0.1981 to 0.4471, 0.0051 to 0.0160 and 0.0034 to 0.0126 for Kano, Maiduguri, Jos, Abuja and Akure, respectively. It is also obvious from Table 9 that the value of CF_w of $WT3$ is the highest in all the five locations, and this is selected for utilization for all the locations under consideration as the most suitable turbine. According to [30], WTs with a value of $CF_w \leq 0.25$ is not suitable for grid integration applications. However, those with higher CF_w in excess of 0.25 are considered the best option any given location.

The response of CF_w of the WTs with respect to different h/hs of 10 to 50 m is shown in Figure 10. The results show that the h/h is directly proportional to CF_w, hence, the need to operate wind turbines at a reasonable height in order to achieve a value of CF_w that is ≥ 0.25. From Figure 10, Jos is suitable for grid integration at all the h/hs; Kano is suitable for grid integration at a h/h of $\geq 20m$; while Maiduguri, Abuja and Akure are not suitable for grid integration at these hub-heights.

Figure 11 shows the relationship between the COE and the turbine h/h. The results clearly demonstrate that COE decreases with increasing h/hs; this is because the wind turbine harness more energy at a higher height due to an increase in wind speed. Therefore, the values of COE obtained for Kano, Maiduguri, Jos, Abuja and Akure were reduced from$0.077\ to\ 0.033$, $0.491\ to\ 0.202$,$0.041\ to\ 0.024$, $1.149\ to\ 0.449$ and $1.457\ to\ 0.579$, respectively, for the specified heights of 10 to 50 m.

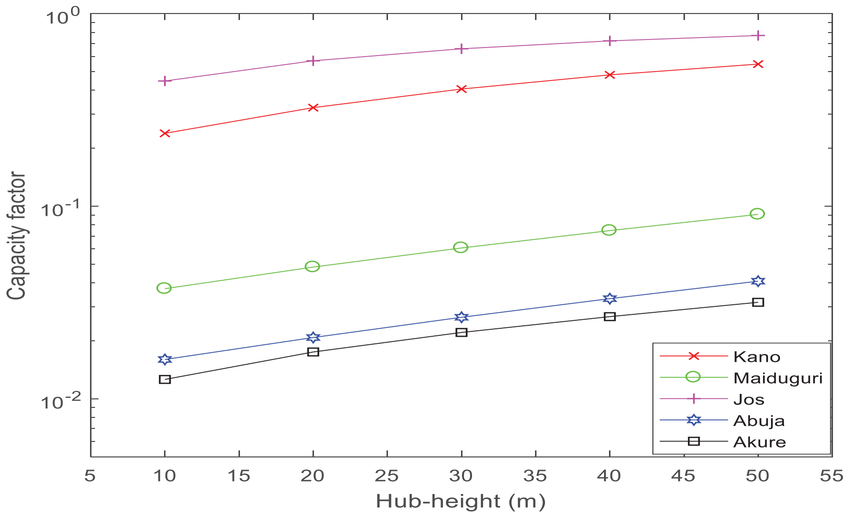

Fig. 10. Sensitivity analysis relating CF_w with h/h

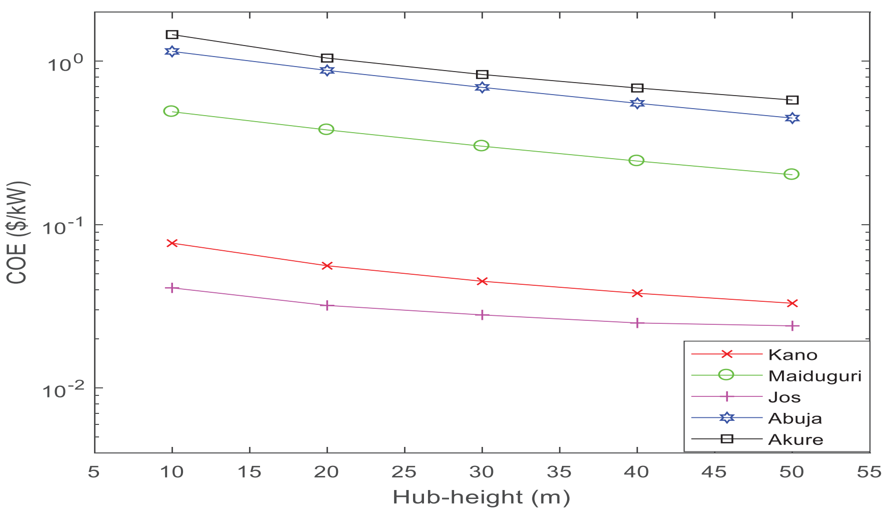

Fig. 11. Sensitivity analysis relating COE with h/h

3.6 Environmental analysis

Wind energy systems are renewable energy-based power generation technology. The environmental performance of the WECSs in the specified locations is realized by quantifying the amount of carbon emissions saved by utilizing the WECSs in the specified locations - Kano, Maiduguri, Jos, Abuja and Akure, using the emission factor approach. An emission factor of 1.27×10^3 kg CO_2 per MWh of electricity generated by a diesel generator [30, 31] is used to estimate the amount of CO_2 avoided by the wind energy generating systems in the five locations.

The environmental aspect, as presented in this study, is a function of the technical performance of the wind power system, which is based on wind energy resources of the locations. It is on this basis that the emission factor is multiplied by Eq. (26) to obtained the amount of emissions saved suppose that WECSs are employed as alternatives to fossil fuel system (i.e., diesel power systems) in the locations.

The values of the annual energy generated by the wind power systems, E_{ae}, are presented in Figure 12 for different heights - 10 to 50 m considered. The energy delivered at these heights for Kano, Maiduguri, Jos, Abuja and Akure range from 52,341 to 119,793 kWh/yr; 8,168.7 to 19,863.3 kWh/yr; 97,893 to 168,630 kWh/yr; 3,504 to 8,935.2 kWh/yr, and 2,759.4 to 6,942.3 kWh/yr, respectively. The results clearly ranks the WECSs in Jos, Kano, Maiduguri, Abuja and Akure as 1st, 2nd, 3rd, 4th and 5th positions, respectively, in terms of the amount of electricity they generate in a year, or simply the wind energy potential. These align with the results presented in Figure 13, which demonstrate that the wind speed determines the wind power as presented by Eqs. (22b) and (22c). Therefore, the wind speed of a location is a critical parameter that determines what the wind power and the energy output will be.

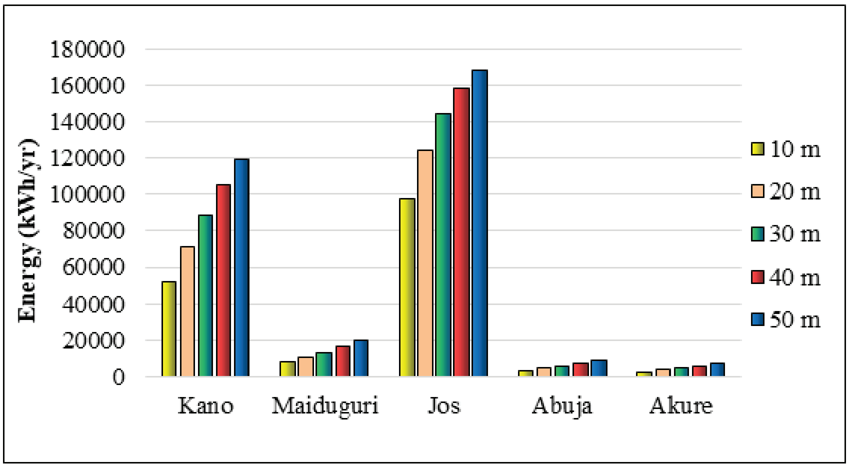

Fig. 12. The annual energy produced by the WECSs in the locations

Figure 14 presents the amount of carbon dioxide emissions assumed to be avoided when the wind energy systems are used in the location instead of diesel generating systems at hub heights of 10 to 50 m. The CO_2 emissions at the specified heights for Kano, Maiduguri, Jos, Abuja and Akure range from 66,473 to 152,137 kg/yr; 10,374 to 25,226 kg/yr; 124,324 to 214,160 kg/yr; 4,450 to 11,348 kg/yr, and 3,504 to 8,817 kg/yr, respectively. Again, the results show a similar trend with those presented in Figure 12 and Figure 13. This is so because the higher the wind speed, the higher the power and the energy produced and the higher the quantity of emissions saved by the WECSs.

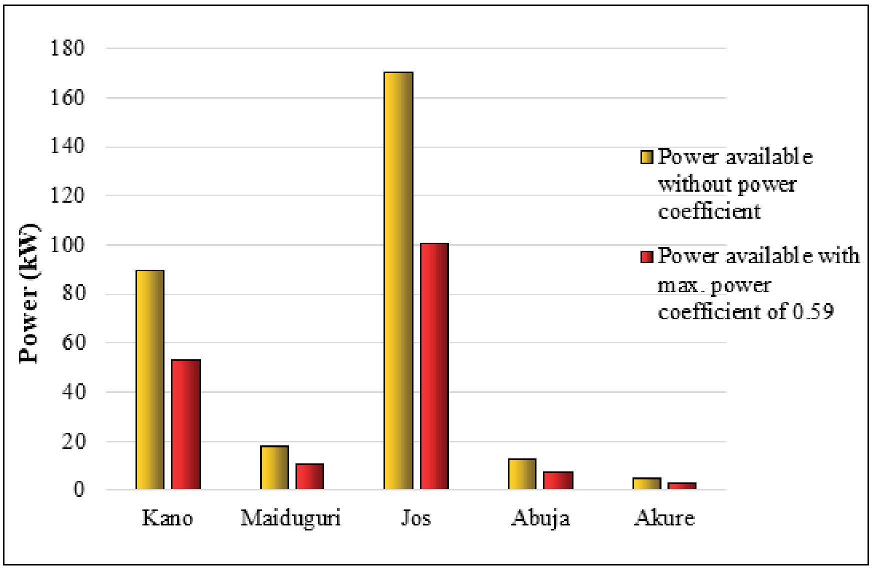

Fig. 13. Power available in the wind at the locations

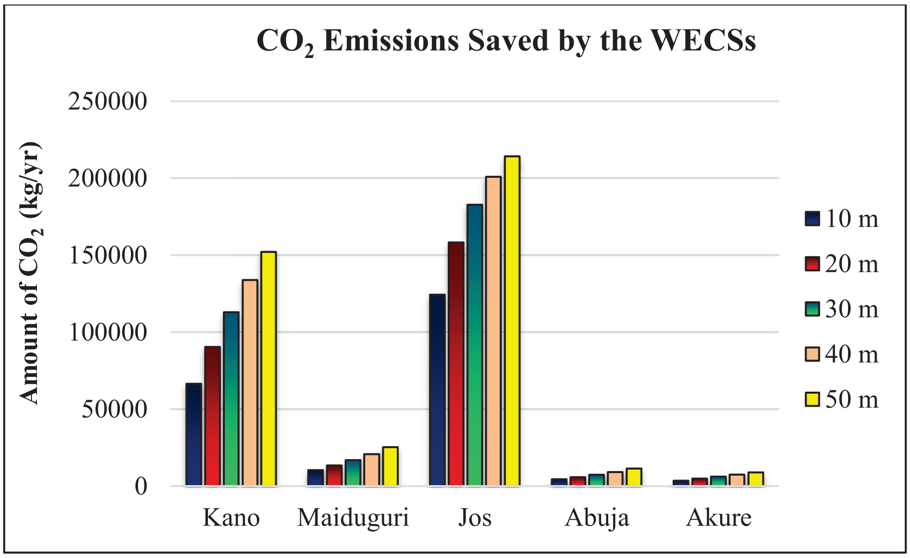

Fig. 14. Quantity of CO_2 emissions saved by the WECSs

4. CONCLUSIONS

This study has presented a detailed comparative evaluation of numerical methods for estimating Wbl parameters. It then discussed the TE analysis of wind electricity production in five different locations in Nigeria, such as Kano. Maiduguri, Jos, Abuja and Akure. The study utilized average daily wind speeds for 10 years, which have been obtained from Nigerian Meteorological Agency (NIMET). The paper examined five different numerical approaches for assessing the Wbl parameters and employed wind turbines of the same rating of 25kW for WECSs in those locations. The study reveals the following as useful conclusions to this paper:

i. The study reveals MOM as suitable for Kano and Jos, while EPM is suitable for Maiduguri and Abuja. With both NEMs suitable for Akure.
ii. The study also shows that PDM was the worst numerical approach for assessing the Wbl parameters.

iii. WECSs in Jos and Kano are viable for grid integration of wind energy, with Jos being the most viable for wind energy generation applications.
iv. WT3 has the highest CF_w in all the locations, which is a major determinant in selecting turbines.
v. WT3 has the least COE in all the selected locations, hence, it was selected among other wind turbines.
vi. WT5 has the highest COE in all the locations considered.
vii. It is more efficient to utilize WTs at a suitable h/h in order to maximize the location's wind resources. This is demonstrated in the study that COE decreases with increasing turbine hub-heights.
viii. The WECSs have the potential to avoid significant carbon footprints when implemented as an alternative to fossil fuel systems.

REFERENCES

[1] Oyedepo SO. (2012) Energy and sustainable development in Nigeria: the way forward. Energy. Sustainability and Society, 2(15):1-17.
[2] Mohammadi K, Mostafaeipour A, Dinpashoh Y, Pouya N. (2014) Electricity generation and energy cost estimation of large-scale wind turbines in Jarandagh, Iran. Journal of Energy, 1-8.
[3] Zheng L, Peng G, Ruihua H, Hexu S. (2019) Current status and development trend of wind power generation-based hydrogen production technology. Journal of Energy Exploration and Exploitation, 37:5-25.
[4] Norbert E. (2016) On the path to sustainability: Key issues on Nigeria's sustainable development. Energy Report, 2:28-34.
[5] Njiru CW, Letema SC. (2018) Energy poverty and its implication on standard of living in Kenya. Journal of Energy, 1-12.
[6] Cory B, Deanna S, Heather T, Leon M, Dana E, Willett K. (2013) Cost-minimized combinations of wind power, solar power and electrochemical storage, powering the grid up to 99.9% of the time. Journal of Power Sources, 225:60-74.
[7] Badawi ASA, Hasbullaha NF, Yusoff SH, Khan S, Hashim A, Zyoud A, Elamassie M. (2019) Weibull probability distribution of wind speed for Gaza strip for 10 years. Applied Mechanics and Materials, 892:284-291.
[8] Oyedepo SO, Adaramola MS, Paul SS. (2012) Analysis of wind speed data and wind energy potential in three selected locations in South-east Nigeria. International Journal of energy and environment engineering, 3:1-11.
[9] Adaramola MS, Oyewola OM, Ohunakin OS, Akinnawonu OO. (2014) Performance evaluation of wind turbines for energy generation in Niger Delta, Nigeria. Sustainable Energy Technologies and Assessments, 6:75-85.
[10] Ajayi OO, Fagbenle RO, Katende J, Ndambuki JM, Omole DO, Badejo AA. (2014) Wind energy study and energy cost of wind electricity generation in Nigeria: Past and recent results and a case study for south west Nigeria. Energies, 7(12):8508-8534.
[11] Sulaiman MA, Okakwu IK, Alayande AS, Olabode OE, Ibhaze AE. (2020) Wind energy evaluation and turbine identification for power generation in some selected areas in Nigeria. Journal of Engineering Studies and Research, 26:67-76.
[12] Okakwu IK, Olabode OE, Alayande AS, Somefun TE, Ajewole TO. (2021) Techno-economic assessment of wind turbines in Nigeria. International Journal of Energy Economics and Policy, 11:240-246.
[13] Mohammadi K, Mostafaeipour A, Dinpashoh Y, Pouya N. (2014) Electricity generation and energy cost estimation of large-scale wind turbines in Jarandagh, Iran. Journal of Energy, 613681:1-8.

https://doi.org/10.31436/iiumej.v24i1.2611

[14] Ajayi OO, Fagbenle RO, Katende J, Aasa SA, Okeniyi JO. (2013) Wind profile characteristics and turbine performance analysis in Kano, north-western Nigeria. International Journal of Energy and Environmental Engineering, 4(27).
[15] Alkhalidi MA, Al-Dabbous S, Neelamani S, Aldashti HA. (2019) Wind energy potential at coastal and offshore locations in the state of Kuwait. Renewable Energy, 135:529-539.
[16] Mostafaeipour A, Jadidi M, Mohammadi K, Sedaghat A. (2014) An analysis of wind energy potential and economic evaluation in Zahedan, Iran. Renewable and Sustainable Energy Reviews, 30:641-650.
[17] Ayodele TR, Jimoh AA, Munda JL, Agee JT. (2013) A statistical analysis of wind distribution and wind power potential in the coastal region of South Africa. International Journal of Green Energy, 10:814-834.
[18] Soulouknga M, Oyedepo SO, Doka SY, Kofane TC. (2020) Evaluation of the cost of producing wind-generated electricity in Chad. International Journal of Energy and Environmental Engineering, 11:275-287.
[19] Belabes B, Youcefi A, Guerri O, Djamai M, Kaabeche A. (2015) Evaluation of wind energy potential and estimation of cost using wind energy turbines for electricity generation on north of Algeria. Renewable and Sustainable Energy Reviews, 51:1245-1255.
[20] Ayodele TR, Ogunjuyigbe ASO, Amusan TO. (2016) Wind power utilization assessment and economic analysis of wind turbines across fifteen locations in the six geographical zones of Nigeria. Journal of Cleaner Production, 1-32.
[21] Kang D, Ko K, Huh J. (2018) Comparative study of different methods for estimating Weibull parameters: A case study on Jeju Island, South Korea. Energies, 11:1-19.
[22] Kaplan YA. (2017) Determination of the best Weibull methods for wind power assessment in the southern region of Turkey. IET Renewable Power Generation, 11:175-182.
[23] Okakwu IK, Oluwasogo ES, Ibhaze AE, Imoize AL. (2019) A comparative study of time series analysis for forecasting energy demand in Nigeria. Nigerian Journal of Technology, 38:465-469.
[24] Rehman S, Alam AMM, Meyer JP, Al-Hadhrami LM. (2012) Wind speed characteristics and resource assessment using Weibull parameters. International Journal of Green Energy, 9:800-814.
[25] Dalabeeh ASK. (2017) Techno-economic analysis of wind power generation for selected locations in Jordan. Renewable Energy, 101:1369-1378.
[26] Wind turbine power calculations. RWE npower renewables, Mechanical and Electrical Engineering, UK.
[27] Akinyele DO, Rayudu RK, Nair NKC. (2015) Grid-independent renewable energy solutions for residential use: The case of an offgrid house in Wellington, New Zealand. In Proceedings of IEEE PES Asia-Pacific Power and Energy Engineering Conference (APPEEC), pp 1-5.
[28] Freris L, Infield D. (2008) Renewable energy in power systems. 1st Ed., Wiley and Sons, UK.
[29] Olatomiwa L, Mekhilef S, Ohunakin OS. (2016) Hybrid renewable power supply for rural health clinic (RHC) in six geo-political zones of Nigeria. Sustainable Energy Technology and Assessment, 13:1-12.
[30] Alsema E. (2000) Environmental life cycle assessment of solar home systems. Department of Science Technology and Society, Utrecht University, Utrecht, The Netherlands, Report NWS-E-15:1-89.
[31] Jakhrani AQ, Othman AK, Rigit ARH, Samo SR. (2012) Estimation of carbon footprints from diesel generator emissions. In Conference on Green and Ubiquitous Technology, pp 78-81.

https://doi.org/10.31436/iiumej.v24i1.2611

Nomenclature Table

COE: Cost of energy	E_{pf} = Energy pattern factor
EPM: Empirical method	$\overline{V^3}$ = Average of wind speed cubes
HDI: Human development index	$(\overline{V})^3$ = Cube of average wind speed
MLM: Maximum likelihood method	y_i = actual data frequency;
MOM: Method of moment,	x_i = frequency of Wbl parameter;
NIMET: Nigeria Meteorological Agency	N = number of intervals;
PDM: Power density method	$f(V_i)$ = observed PDF value at bin i;
TE: Techno-economic	$\overline{f(V)}$ = observed average PDF value
Wbl: Weibull	$\hat{f}(V_i)$ = estimated PDF value of the computed Wbl method at the same bin.
WECSs: Wind energy conversion systems	C_{opm}= operation and maintenance cost
k = Shape Parameter	i_r= inflation rate
c = Scale Parameter (m/s)	$d = discount\ rate$,
V_i = Wind speed in time step i	r= Interest rate
n= number of non-zero	p = project lifetime
σ = standard deviation	
$\overline{V}$ = mean wind speed	

HIGHER DERIVATIVE BLOCK METHOD WITH GENERALISED STEP LENGTH FOR SOLVING FIRST-ORDER FUZZY INITIAL VALUE PROBLEMS

KASHIF HUSSAIN, OLUWASEUN ADEYEYE* AND NAZIHAH AHMAD

School of Quantitative Sciences, Universiti Utara Malaysia, Kedah, Malaysia

**Corresponding author: adeyeye@uum.edu.my*

(Received: 30th March 2022; Accepted: 10th August 2022; Published on-line: 4th January 2023)

ABSTRACT: Block methods have been adopted in studies for solving first and higher order differential equations due to its impressive accuracy property. Taking a step further to improve this accuracy, researchers have considered the inclusion of higher-derivative terms in the block method, although this has been limited to the presence of one higher-derivative term in previous studies. Hence, this article aims at better accuracy by introducing two higher-derivative terms in the block method. In addition, this article presents a scheme with generalised step length such that there is flexibility on the choice of step length when developing the block method. The generalised step length scheme is adopted to develop a three-step block method for solving first-order fuzzy initial value problems. Its properties to ensure convergence and to show the region of absolute stability is investigated, and problems relating to charging and discharging of capacitor are considered. The absolute error shows the impressive accuracy of the three-step block method including obtaining the same values as the exact solution. Therefore, in addition to the new generalised algorithm presented in this article, a new three-step method for solving linear and nonlinear first order fuzzy initial value problems is presented.

ABSTRAK: Kaedah blok digunakan dalam banyak kajian untuk menyelesaikan persamaan pembezaan peringkat pertama dan peringkat tinggi kerana sifat ketepatannya yang baik. Bagi meningkatkan ketepatan ini, penyelidik telah mengambil kira dengan memasukkan terbitan peringkat tinggi dalam kaedah blok, walaupun ini terhad pada satu sebutan terbitan peringkat tinggi dalam kajian sebelum. Oleh itu, kajian ini bertujuan bagi mendapatkan ketepatan yang lebih baik dengan memperkenalkan dua sebutan terbitan peringkat tinggi dalam kaedah blok. Tambahan, kajian ini memperkenalkan skema dengan panjang-langkah kaki biasa supaya terdapat kebolehlenturan pada pilihan langkah semasa membangunkan kaedah blok. Skema ini diadaptasi bagi membangunkan kaedah blok tiga-langkah bagi menyelesai masalah nilai awal peringkat pertama secara rawak. Ciri-ciri terperinci dikaji bagi memastikan penumpuan lingkungan kestabilan mutlak, dan masalah berkaitan pengecasan dan nyahcas kapasitor juga turut diambil kira. Ralat mutlak menunjukkan ketepatan yang mengkagumkan pada kaedah blok tiga-langkah termasuk mendapatkan nilai yang sama seperti penyelesaian. Oleh itu, tambahan pada algoritma ini, kaedah tiga-langkah bagi menyelesaikan linear dan tidak linear pada masalah nilai awal peringat pertama secara rawak diperkenalkan.

KEYWORDS: *fuzzy initial value problem; generalised steplength; block method; higher derivative; charging and discharging of capacitor*

https://doi.org/10.31436/iiumej.v24i1.2380

1. INTRODUCTION

The primary focus of numerical methods for solving fuzzy differential equations has been on presenting numerical methods with a higher level of accuracy. This includes providing a more accurate numerical solution for first order fuzzy initial value problems (FIVPs) of the form

$$y'(x) = f(x, y(x)), y(x_0) = y_0, x \in [x_0, X]. \tag{1}$$

Numerous researchers have developed different numerical methods [1-6] to solve problems in the form of Equation (1), however, the major problem encountered is that these existing numerical methods give a low level of accuracy in terms of absolute error due to order of the method used. Specifically, researchers considered the use of linear multistep methods implemented in predictor-corrector mode (a non-self-starting approach with low accuracy) as seen in studies [7,8]. To improve the accuracy, block methods were introduced in [9-11] and better accuracy was observed than linear multistep methods. However, there is still a need for an improvement in the solution accuracy in terms of absolute error. Hence, the motivation to develop block methods in this article with the presence of two higher derivative terms with the aim of obtaining better accuracy. In comparison to existing methods, the proposed method has the advantage of better accuracy, being self-starting, and flexibility in development and implementation of the block method.

2. PRELIMINARIES

This section recalls some basic definitions which will be adopted in this article.

Triangular Fuzzy Number [12]. Consider that $(u,v,w) \in \mathbb{R}^3$, $u \le v \le w$. Then the triangular fuzzy number, $M(x)$ is given as

$$M(x,u,v,w) = \begin{cases} 0, x < u \\ \dfrac{x-u}{v-u}, u \le x \le v \\ \dfrac{w-x}{w-v}, v < x \le w \\ 0, x > w \end{cases}. \tag{2}$$

The corresponding *r*-level set of the triangular fuzzy number is denoted as

$$M_r = \left[u + r(v-u), w - r(w-v)\right],\ r \in [0,1]. \tag{3}$$

Trapezoidal Fuzzy Numbers [12]. Consider that $(u,v,w,\delta) \in \mathbb{R}^4$, $u \le v \le w \le \delta$. Then the trapezoidal fuzzy number $M(x)$ is given as

$$M(x,u,v,w,\delta)=\begin{cases}0, x<u\\ \dfrac{x-u}{v-u}, u\le x<v\\ 1, v\le x\le w\\ \dfrac{w-x}{w-v}, w<x\le\delta\\ 0, x>\delta\end{cases}. \tag{4}$$

The corresponding r-level set of the trapezoidal fuzzy number is denoted as

$$M_r=\left[u+r\left(v-u\right),\delta-r(\delta-w)\right],\ r\in[0,1] \tag{5}$$

Some of the basic fuzzy definitions and notions that are not included in this Section 2 are widely known. Notions of fuzzy sets, functions and their operations, fuzzy derivatives, and Zadeh's extension theory can be retrieved from literature such as [13-16].

3. METHODOLOGY

Given that the first-order FIVP of the form defined in Eq. (1) be a mapping, $f:\mathbb{R}_f\to\mathbb{R}_f$ and $y_0\in\mathbb{R}_f$, with r-level set $y_0\in\left(\underline{y}(0,r),\overline{y}(0,r)\right)_{\underline{r}}^{\overline{r}}$, $r\in[0,1]$. Also, denote the approximation solution as $\left(\mathrm{y}(\mathrm{x}_n,\alpha)\right)_{\underline{r}}^{\overline{r}}=\left(\underline{y}(\mathrm{x}_n,\mathrm{r}),\overline{y}(\mathrm{x}_n,\mathrm{r})\right)_{\underline{r}}^{\overline{r}}$ at points $x_n=x_0+nh$, where $0\le n\le N$ and $h=\dfrac{X-x_0}{n}$.

The generalized k-step block method with presence of second and third derivative in first-order form is stated below as,

$$\left(y_{n+\eta}\right)_{\underline{r}}^{\overline{r}}=\left(y_n+\sum_{d=0}^{2}\left[\sum_{v=0}^{k}\psi_{dv\eta}f_{n+v}^{(d)}\right]\right)_{\underline{r}}^{\overline{r}},\eta=1,2,3,...,k. \tag{6}$$

Expanding Eq. (6) gives the expression

$$\left(y_{n+\eta}\right)_{\underline{r}}^{\overline{r}}=\left(y_n+\begin{bmatrix}\psi_{00\eta}f_n+\psi_{01v}f_{n+1}+,...,+\psi_{0k\eta}f_{n+k}\\ +\psi_{10\eta}f'_n+\psi_{11\eta}f'_{n+1}+,...,+\psi_{1k\eta}f'_{n+k}\\ +\psi_{20\eta}f''_n+\psi_{21\eta}f''_{n+1}+,...,+\psi_{2k\eta}f''_{n+k}\end{bmatrix}\right)_{\underline{r}}^{\overline{r}}. \tag{7}$$

Consider the Taylor series expansions defined by [17]:

$$\left(\mathrm{y}(x_n+jh;\mathrm{r})\right)_{\underline{r}}^{\overline{r}}=\left(\sum_{i=0}^{n}\frac{(jh)^i}{i!}f^i(x_n;\mathrm{r})\right)_{r}^{\overline{r}},j=0,1,...,\mathrm{k}, \tag{8}$$

$$\left(y_{n+j}\right)_{\underline{r}}^{\overline{r}}=\left(\mathrm{y}(x_n;\mathrm{r})+jhy'(x_n;\mathrm{r})+\frac{(jh)^2}{2!}\mathrm{y}''(x_n;\mathrm{r})+\frac{(jh)^3}{3!}\mathrm{y}'''(x_n;\mathrm{r})+....+\frac{(jh)^n}{\mathrm{n}!}\mathrm{y}''(x_n;\mathrm{r})\right)_{\underline{r}}^{\overline{r}}. \tag{9}$$

Applying these expansions in Eqs. (8) and (9) to expand each term in Eq. (7) results in obtaining the unknown coefficients $\psi_{dv\eta}$ from $\psi_{dv\eta} = A^{-1}B$, where

$$A = \begin{pmatrix} 1 & 1 & \dots & 1 & 0 & 0 & \dots & 0 & 0 & 0 & \dots & 0 \\ 0 & h & \dots & kh & 1 & 1 & \dots & 1 & 0 & 0 & \dots & 0 \\ 0 & \frac{h^2}{2!} & \dots & \frac{(kh)^2}{2!} & 0 & h & \dots & kh & 1 & 1 & \dots & 1 \\ 0 & \frac{h^3}{3!} & \dots & \frac{(kh)^3}{3!} & 0 & \frac{h^2}{2!} & \dots & \frac{(kh)^2}{2!} & 0 & h & \dots & kh \\ . & . & \dots & . & . & . & \dots & . & . & . & \dots & . \\ . & . & \dots & . & . & . & \dots & . & . & . & \dots & . \\ . & . & \dots & . & . & . & \dots & . & . & . & \dots & . \\ 0 & \frac{h^{3k+2}}{(3k+2)!} & \dots & \frac{(kh)^{3k+2}}{(3k+2)!} & 0 & \frac{h^{3k+1}}{(3k+1)!} & \dots & \frac{(kh)^{3k+1}}{(3k+1)!} & 0 & \frac{(h)^{3k}}{3k!} & \dots & \frac{(kh)^{3k}}{3k!} \end{pmatrix}^{\bar{r}}_{\underline{r}}, \text{ and } B = \begin{pmatrix} \eta h \\ \frac{(\eta h)^2}{2!} \\ \frac{(\eta h)^3}{3!} \\ \frac{(\eta h)^4}{4!} \\ . \\ . \\ . \\ \frac{(\eta h)^{3k+3}}{(3k+3)!} \end{pmatrix}^{\bar{r}}_{\underline{r}}.$$

The resultant values are substituted in Eq. (7) to get the desired generalized *k*-step block method with the presence of second and third derivatives for solving first-order FIVPs. A more detailed explanation is given in the following subsection, where the generalised step length (*k*-step) block method scheme with presence of second and third derivatives is adopted to develop a three-step ($k = 3$) block method for first order FIVPs.

3.1 Development of Three-Step Block Method

To develop a three-step block method with second and third derivatives for first order FODEs requires substituting $k = 3$ in Eq. (7) and then applying Taylor series expansions in Eqs. (8), (9). The unknown coefficients $\psi_{dv\eta}$ are obtained as follows:

$$\begin{pmatrix} \psi_{001} \\ \psi_{011} \\ \psi_{021} \\ \psi_{031} \\ \psi_{101} \\ \psi_{111} \\ \psi_{121} \\ \psi_{131} \\ \psi_{201} \\ \psi_{211} \\ \psi_{221} \\ \psi_{231} \end{pmatrix}^{\bar{r}}_{\underline{r}} = \begin{pmatrix} \frac{912523}{2395008} \\ \frac{23717}{29568} \\ \frac{-5851}{29568} \\ \frac{35339}{2395008} \\ \frac{214943}{3991680} \\ \frac{-10657}{147840} \\ \frac{10657}{147840} \\ \frac{-5941}{1330560} \\ \frac{11369}{3991680} \\ \frac{4423}{88704} \\ \frac{-7453}{443520} \\ \frac{1513}{3991680} \end{pmatrix}, \begin{pmatrix} \psi_{002} \\ \psi_{012} \\ \psi_{022} \\ \psi_{032} \\ \psi_{102} \\ \psi_{112} \\ \psi_{122} \\ \psi_{132} \\ \psi_{202} \\ \psi_{212} \\ \psi_{222} \\ \psi_{232} \end{pmatrix}^{\bar{r}}_{\underline{r}} = \begin{pmatrix} \frac{7031}{18711} \\ \frac{302}{231} \\ \frac{71}{231} \\ \frac{178}{18711} \\ \frac{544}{10395} \\ \frac{32}{1155} \\ \frac{-32}{1155} \\ \frac{92}{31185} \\ \frac{17}{6237} \\ \frac{212}{3465} \\ \frac{-19}{3465} \\ \frac{8}{31185} \end{pmatrix}, \begin{pmatrix} \psi_{003} \\ \psi_{013} \\ \psi_{023} \\ \psi_{033} \\ \psi_{103} \\ \psi_{113} \\ \psi_{123} \\ \psi_{133} \\ \psi_{203} \\ \psi_{213} \\ \psi_{223} \\ \psi_{233} \end{pmatrix}^{\bar{r}}_{\underline{r}} = \begin{pmatrix} \frac{3849}{9856} \\ \frac{10935}{9856} \\ \frac{10935}{9856} \\ \frac{3849}{9856} \\ \frac{2799}{49280} \\ \frac{-2187}{49280} \\ \frac{2187}{49280} \\ \frac{-2799}{49280} \\ \frac{153}{49280} \\ \frac{2187}{49280} \\ \frac{2187}{49280} \\ \frac{153}{49280} \end{pmatrix}.$$

Substituting the obtained coefficients in Eq. (7) for $k = 3$, the three-step block scheme is derived as

$$\left(y_{n+1} = y_n + \left[\begin{array}{l} h\left(\frac{912523}{2395008} f_n + \frac{23717}{29568} f_{n+1} - \frac{5851}{29568} f_{n+2} + \frac{35339}{2395008} f_{n+3} \right) + \\ h^2 \left(\frac{214943}{3991680} g_n - \frac{10657}{147840} g_{n+1} + \frac{10657}{147840} g_{n+2} - \frac{5941}{1330560} g_{n+3} \right) + \\ h^3 \left(\frac{11369}{3991680} m_n + \frac{4423}{88704} m_{n+1} - \frac{7453}{443523} m_{n+2} + \frac{1513}{3991680} m_{n+3} \right) \end{array} \right] \right)_{\underline{r}}^{\bar{r}},$$

$$\left(y_{n+2} = y_n + \left[\begin{array}{l} h\left(\frac{7031}{18711} f_n + \frac{302}{231} f_{n+1} + \frac{71}{231} f_{n+2} + \frac{178}{18711} f_{n+3} \right) + \\ h^2 \left(\frac{544}{10395} g_n + \frac{32}{1155} g_{n+1} - \frac{32}{1155} g_{n+2} - \frac{92}{31185} g_{n+3} \right) + \\ h^3 \left(\frac{17}{6237} m_n + \frac{212}{3465} m_{n+1} - \frac{19}{3465} m_{n+2} + \frac{8}{31185} m_{n+3} \right) \end{array} \right] \right)_{\underline{r}}^{\bar{r}}, \tag{10}$$

$$\left(y_{n+3} = y_n + \left[\begin{array}{l} h\left(\frac{3849}{9856} f_n + \frac{10935}{9856} f_{n+1} + \frac{10935}{9856} f_{n+2} + \frac{3849}{9856} f_{n+3} \right) + \\ h^2 \left(\frac{2799}{49280} g_n - \frac{2187}{49280} g_{n+1} + \frac{2187}{49280} g_{n+2} - \frac{2799}{49280} g_{n+3} \right) + \\ h^3 \left(\frac{153}{49280} m_n + \frac{2187}{49280} m_{n+1} + \frac{2187}{49280} m_{n+2} + \frac{153}{49280} m_{n+3} \right) \end{array} \right] \right)_{\underline{r}}^{\bar{r}}$$

The block method in Eq. (10) has corrector form

$$\left(A^0 Y_{n+k}\right)_{\underline{r}}^{\bar{r}} = \left(A^1 Y_{n-k}\right)_{\underline{r}}^{\bar{r}} + h\left(B^0\, \mathrm{Y}'_{n+k} + B^1\, \mathrm{Y}'_{n-k}\right)_{\underline{r}}^{\bar{r}} + h^2\left(C^0\, \mathrm{Y}''_{n+k} + C^1\, \mathrm{Y}''_{n-k}\right)_{\underline{r}}^{\bar{r}} +$$
$$h^3\left(D^0\, \mathrm{Y}''_{n+k} + D^1\, \mathrm{Y}'''_{n-k}\right)_{\underline{r}}^{\bar{r}}$$

where

$$A^0 = \begin{pmatrix} 1 & 0 & 0 \\ 0 & 1 & 0 \\ 0 & 0 & 1 \end{pmatrix}_{\underline{r}}^{\bar{r}}, A^1 = \begin{pmatrix} 0 & 0 & 1 \\ 0 & 0 & 1 \\ 0 & 0 & 1 \end{pmatrix}_{\underline{r}}^{\bar{r}}, B^0 = \begin{pmatrix} \frac{23717}{29568} & \frac{-5851}{29568} & \frac{35339}{2395008} \\ \frac{302}{231} & \frac{71}{231} & \frac{178}{18711} \\ \frac{10935}{9856} & \frac{10935w}{9856} & \frac{3849}{9856} \end{pmatrix}_{\underline{r}}^{\bar{r}},$$

$$C^0 = \begin{pmatrix} \frac{-10657}{147840} & \frac{10657}{147840} & \frac{-5941}{1330560} \\ \frac{32}{1155} & \frac{-32}{1155} & \frac{-92}{31185} \\ \frac{-2187}{49280} & \frac{2187}{49280} & \frac{-2799}{49280} \end{pmatrix}_{\underline{r}}^{\bar{r}}, B^1 = \begin{pmatrix} 0 & 0 & \frac{912523}{2395008} \\ 0 & 0 & \frac{7031}{18711} \\ 0 & 0 & \frac{3849}{9856} \end{pmatrix}_{\underline{r}}^{\bar{r}}, C^1 = \begin{pmatrix} 0 & 0 & \frac{214943}{3991680} \\ 0 & 0 & \frac{544}{10395} \\ 0 & 0 & \frac{2799}{49280} \end{pmatrix}_{\underline{r}}^{\bar{r}},$$

$$D^0 = \begin{pmatrix} \frac{4423}{88704} & \frac{-7453}{443520} & \frac{1513}{3991680} \\ \frac{212}{3465} & \frac{-19}{3465} & \frac{8}{31185} \\ \frac{2187}{49280} & \frac{2187}{49280} & \frac{153}{49280} \end{pmatrix}_{\underline{r}}^{\bar{r}}, Y_{n-k} = \begin{pmatrix} y_{n-2} \\ y_{n-1} \\ y_n \end{pmatrix}_{\underline{r}}^{\bar{r}}, D^1 = \begin{pmatrix} 0 & 0 & \frac{11369}{3991680} \\ 0 & 0 & \frac{17}{6237} \\ 0 & 0 & \frac{153}{49280} \end{pmatrix}_{\underline{r}}^{\bar{r}}, Y'_{n-k} = \begin{pmatrix} f_{n-2} \\ f_{n-1} \\ f_n \end{pmatrix}_{\underline{r}}^{\bar{r}},$$

$$Y''_{n+k} = \begin{pmatrix} g_{n+1} \\ g_{n+2} \\ g_{n+3} \end{pmatrix}_{\underline{r}}^{\bar{r}}, Y''_{n-k} = \begin{pmatrix} g_{n-2} \\ g_{n-1} \\ g_{n} \end{pmatrix}_{\underline{r}}^{\bar{r}}, Y'''_{n+k} = \begin{pmatrix} m_{n+1} \\ m_{n+2} \\ m_{n+3} \end{pmatrix}_{\underline{r}}^{\bar{r}}, Y'''_{n-k} = \begin{pmatrix} m_{n-2} \\ m_{n-1} \\ m_{n} \end{pmatrix}_{\underline{r}}^{\bar{r}}, Y_{n+k} = \begin{pmatrix} y_{n+1} \\ y_{n+2} \\ y_{n+3} \end{pmatrix}_{\underline{r}}^{\bar{r}}, Y'_{n+k} = \begin{pmatrix} f_{n+1} \\ f_{n+2} \\ f_{n+3} \end{pmatrix}_{\underline{r}}^{\bar{r}}.$$

4. CONVERGENCE PROPERTIES

This section will detail the convergence properties of the developed three-step second-third derivative scheme. The following definitions are used: consistency, zero-stability, and region of absolute stability from [18]. These definitions for block methods in crisp form are adopted to the proposed method for fuzzy initial value problems to prove the convergence properties for the proposed method.

4.1 Order and Error Constant

The linear operator which is associated with Equation (6) for the three-step block method is defined as:

$$L(y(x),h) = \left(y_{n+\eta} - y_n - \sum_{d=0}^{2}\left[\sum_{v=0}^{3} \psi_{dv\eta} f_{n+v}^{(d)} \right] \right)_{\underline{r}}^{\bar{r}} \tag{13}$$

$$L(y(x),h) = \left(\mathbb{N}_0\, y(x_n) + \mathbb{N}_1 h y'(x_n) + \mathbb{N}_2 h^2\, y''(x_n) +,...,+ \mathbb{N}_z h^z y^z(x_n) + \mathbb{N}_{z+1} h^{z+1} y^{z+1}(x_n) \right)_{\underline{r}}^{\bar{r}}.$$

The order of this method is z if $\mathbb{N}_0 = \mathbb{N}_1 = \mathbb{N}_2 =,....,= \mathbb{N}_z = 0$ and $\mathbb{N}_{z+1}$ is the error constant. By using the definition of order and error constant, the developed block method has order $z = 12$ with error constant $\left[\frac{-29609}{28768836096000}, \frac{23}{32108076000}, \frac{9}{5637632000}\right]$. So, the developed block method is consistent.

4.2 Zero-stability

The zero-stability of the proposed method is computed from

$$p(\psi) = \left| \psi \begin{pmatrix} 1 & 0 & 0 \\ 0 & 1 & 0 \\ 0 & 0 & 1 \end{pmatrix} - \begin{pmatrix} 0 & 0 & 1 \\ 0 & 0 & 1 \\ 0 & 0 & 1 \end{pmatrix} \right|_{\underline{r}}^{\bar{r}} = \psi^2(\psi - 1) = 0.$$

The obtained roots satisfy the condition in [18]. Hence, the proposed three-step block method is zero-stable. Since the proposed method satisfies the properties of consistency and zero-stability for block methods, this implies that the method is convergent.

4.3 Region of Absolute Stability

The characteristic polynomial used to obtain the region of absolute stability of the developed block method is obtained as

$$\left(\det\left[-(w)^k + A^1 + q\left[\sum_{j=0}^{k} B^j w^{k-j} \right] + q^2\left[\sum_{j=0}^{k} C^j w^{k-j} \right] + q^3\left[\sum_{j=0}^{k} D^j w^{k-j} \right] + q^4\left[\sum_{j=0}^{k} E^j w^{k-j} \right] \right] \right)_{\underline{r}}^{\bar{r}},$$

$$q = \lambda h.$$

https://doi.org/10.31436/iiumej.v24i1.2380

$$R(w) == \left(\begin{array}{l} \left[\frac{q^9}{369600} - \frac{52183q^8}{910694400} + \frac{388873q^7}{546416649} - \frac{231359q^6}{40981248} + \frac{1549771q^5}{45534720} - \frac{10104397q4}{68302080} + \frac{5805453q^3}{12142592} - \frac{47q^2}{44} - \frac{3q}{2} - 1 \right] w^6 \\ \left[\frac{q^9}{369600} + \frac{q^8}{16800} + \frac{157q^7}{221760} + \frac{109q^6}{19008} + \frac{179q^5}{5280} + \frac{589q4}{3960} + \frac{21q^3}{44} + \frac{47q^2}{44} + \frac{3q}{2} + 1 \right] w^3 \end{array} \right).$$

The region of absolute stability is determined by plotting the roots of the polynomial using a boundary locus approach, as shown in Fig. 1.

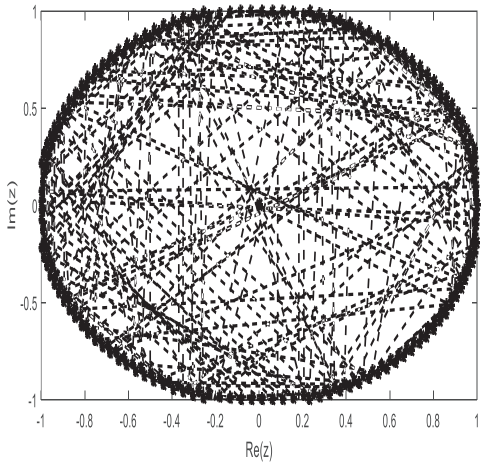

Fig. 1: Absolute stability region of three-step second-third derivative block method.

5. RESULTS AND DISCUSSION

This section details using the three-step block method to solve first-order linear and nonlinear FIVPs numerically and comparing the results to the exact solution. Tables and graphs are being used to compare exact and approximate solutions. The following notations are utilised in this section.

x-axis shows the value of approximation solution

y-axis shows the value of r-level set

$\underline{Y}, \overline{Y}$ are the exact solution of lower and upper bound respectively

$\underline{y}, \overline{y}$ are the approximation solution of lower and upper bound respectively

$\left|\underline{Y} - \underline{y}\right|$ absolute error of lower bound approximation

$\left|\vec{Y} - \overline{y}\right|$ absolute error of upper bound approximation

h is the stepsize

Example 1 [19].

Consider the following crisp capacitor model

$$\frac{d(U_c(x))}{dx} = -\frac{1}{RC}U_c(x) + \frac{1}{RC}U_G(x) \tag{14}$$

with exact solution

$$U_c(x) = K.e^{-\int \frac{dx}{RC}} + \left[\int \left(\frac{U_G(x)}{RC} .e^{-\int \frac{dx}{RC}} \right) dx \right] .e^{-\int \frac{dx}{RC}} . \tag{15}$$

For the initial condition charging of the capacitor

$$U_C(x) = U_B.[1 - e^{\frac{x}{RC}}] , \tag{16}$$

while for the initial condition discharging of the capacitor

$$U_C(x) = U_{c,0}.e^{\frac{x}{RC}} . \tag{17}$$

According to [4], the crisp equation can be modelled in a fuzzy form using the definition of fuzzy theory, which is given in Section 2. The uncertain behaviour of a capacitor using the voltage, capacitance, or resistance of the circuit current is defined as triangular fuzzy numbers.

5.1 Charging of a Capacitor

The exact and approximate solutions are presented at $x = 4s$. Table 1 presents the accuracy for the lower and upper solutions of charging capacitor under DC condition with triangular fuzzy number. The corresponding graphs are shown in Fig. 2. The specifications adopted are battery voltage $= 12V$, $C = 0.25F$ (farads), $U_c(0) = 0$, and resistance with triangular fuzzy number is $R = (2 + r, 4 - r)$.

5.2 Discharging of a Capacitor

The exact and approximate solutions are presented at $x = 4s$. Table 2 presents the accuracy for the lower and upper solutions of the discharging capacitor under DC condition with triangular fuzzy number. The corresponding graphs are shown in Fig. 3. The specifications adopted as same as the charging of a capacitor scenario.

Table 1: Lower and Upper Solutions for Charging of Capacitor Problem in Example 1

r	$\underline{y}$	$\lvert\underline{Y} - \underline{y}\rvert$	$\overline{y}$	$\lvert\overline{Y} - \overline{y}\rvert$
0	11.995974448465169	0.0e+00	11.780212333335189	0.0e+00
0.2	11.991669406884018	0.0e+00	11.821937321808754	0.0e+00
0.4	11.984728394383922	0.0e+00	11.859076458515744	0.0e+00
0.6	11.974496498029186	0.0e+00	11.905917027388661	0.0e+00
0.8	11.960417930928731	0.0e+00	11.931188450176629	0.0e+00
1	11.942064600074023	0.0e+00	11.942064600074023	0.0e+00

Table 2: Lower and Upper Solutions for Discharging of Capacitor Problem in Example 1

r	$\underline{y}$	$\lvert\underline{Y} - \underline{y}\rvert$	$\overline{y}$	$\lvert\overline{Y} - \overline{y}\rvert$
0	0.00402555153483014	4.336e-18	0.21978766666481017	8.3266e-17
0.2	0.00833059311598270	7.806e-18	0.17806267819124583	8.3266e-17
0.4	0.01527160561607770	8.673e-18	0.14092354148425637	1.9428e-16
0.6	0.02550350197081452	1.737e-18	0.10850319025595753	2.2204e-16
0.8	0.03958206907126909	1.008e-17	0.08085536398902561	8.3266e-17
1	0.05793539992597728	1.048e-17	0.05793539992597728	1.5265e-16

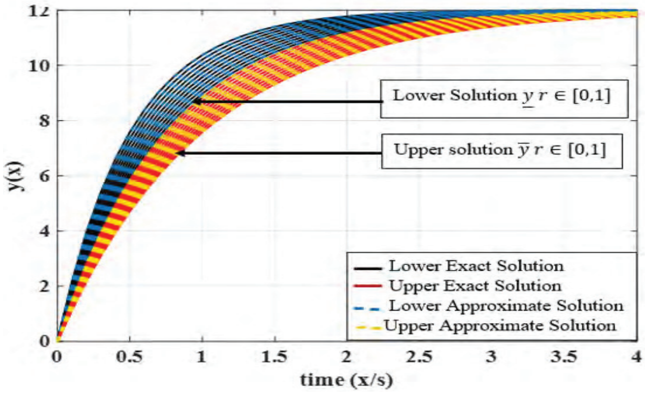

Fig. 2: Example 1 at h=0.1, $x \in [0,4], r \in [0,1]$

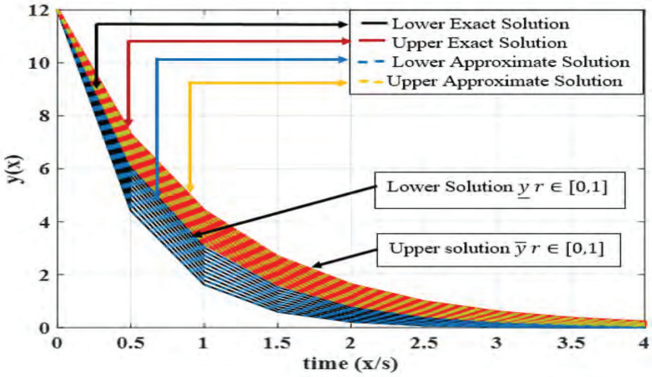

Fig. 3: Example 1 at h=0.1, $x \in [0,4], r \in [0,1]$

In subsequent examples (Examples 2 and 3), since the exact solution cannot be obtained analytically, the proposed method in this study is used to obtain the approximate solution. It is seen that the approximate solution shows a non-monotone behaviour as time increases. The approximate solution in Tables 3 and 4 shows the lower and upper solutions using triangular fuzzy numbers.

Example 2. [20].

Consider the following nonlinear FIVP

$$y'(x) = \cos(xy), y(0,r) = (\tfrac{\pi}{2}r, \pi - \tfrac{\pi}{2}r).$$

Table 3: Lower and Upper Solution for Example 2

r	$\underline{y}$	$\overline{y}$
0	0.61513329423446	2.81437834172917
0.2	0.62072922853453	1.31086566147775
0.4	0.62648141558304	0.74700523547913
0.6	0.63281743366655	0.68810151091971
0.8	0.64032241288569	0.66399579330793
1	0.6500044930335	0.65000449303352

Example 3. [21].

Consider the following nonlinear FIVP

$$y'(x) = x^2 + y^2, y(0,r) = (0.1r - 0.1, 0.1 - 0.1r) .$$

Table 4: Lower and Upper Solution for Example 3

r	$\underline{y}$	$\overline{y}$
0	0.24913567333881	0.48255938900528
0.2	0.26259107127145	0.45370358499704
0.4	0.28321967366284	0.42612209786584
0.6	0.30466869011884	0.39973233756115
0.8	0.32698805629646	0.37445870012445
1	0.35023184431536	0.35023184431536

In Example 1, a crisp capacitor model was successfully solved using the proposed method with a fuzzy initial value, and the results were compared to the exact solution. The results are seen in Table 1 and 2 with charging and discharging of the capacitor. These tables, showing the comparison between exact and approximate solution, indicate that the accuracy of the solution in terms of absolute error is quite impressive. The nonlinear Examples 2 and 3, which cannot be solved exactly, are solved numerically by the proposed method. The obtained results are demonstrated in Tables 3 and 4. Although, Example 3 was solved by [21] with homotopy perturbation method, where the authors solved crisp Riccati equation with two defuzzification for FIVPs, their obtained results lie in the short time interval [0,0.5] which indicate that their proposed method is limited to the specific points with large amounts of mathematical complexity.

6. CONCLUSION

The major objective of this research is to enhance the solution accuracy in terms of absolute error for first order FIVPs. As a result, this article developed a generalised step length block method for first order fuzzy ordinary differential equations with the presence of second and third derivatives. Because the algorithm can simultaneously construct block methods of step length k for solving first order FIVPs, the generalised technique is considered as extremely flexible. The sample block method with second and third derivatives scheme has proven to be a viable strategy with increased accuracy for solving both linear and nonlinear FIVPs. The method was developed using a linear block approach with low computational complexity, while also satisfying all convergence conditions for the block methods. The solution of the FIVPS as seen in the tables and graphs demonstrates the applicability of the three-step implicit block method for first order FIVPs. So, this generalised approach is suitable for developing block methods for first order FIVPs.

REFERENCES

[1] Ahmady N, Allahviranloo T, Ahmady E. (2020) A modified Euler method for solving fuzzy differential equations under generalized differentiability. Computational and Applied Mathematics, 39(2):1-21. Doi: https://doi.org/10.1007/s40314-020-1112-1

[2] Kodal Sevindir H, Cetinkaya S, Tabak G. (2018) On numerical solutions of fuzzy differential equations. International Journal of Development Research, 8(9): 22971- 22979. Doi: https://www.researchgate.net/publication/329737810
[3] Ahmadian A, Salahshour S, Chan CS, Baleanu D. (2018) Numerical solutions of fuzzy differential equations by an efficient Runge–Kutta method with generalized differentiability. Fuzzy Sets and Systems, 331: 47-67. Doi: https://doi.org/10.1016/j.fss.2016.11.013
[4] Jameel AF, Saleh HH, Azmi A, Alomari AK, Anakira NR, Man NH. (2022) Efficient approximate analytical methods for nonlinear fuzzy boundary value problem. International Journal of Electrical & Computer Engineering, 12(2): 1916-1928. Doi: https://doi.org/10.11591/ijece.v12i2.pp1916-1928
[5] Maghool FH, Radhy ZH, Mehdi HA, Abass HM. (2019) Simpson's rule to solve fuzzy differential equations. International Journal of Advanced Research in Science, Engineering and Technology, 6(10): 11306-11315. Doi: https://www.researchgate.net/publication/337941473
[6] Fariborzi Araghi MA, Barzegar Kelishami H. (2021) Numerical accuracy of the predictor-corrector method to solve fuzzy differential equations based on the stochastic arithmetic. Fuzzy Information and Engineering, 12(3): 335-354. Doi: https://doi.org/10.1080/16168658.2021.1880134
[7] Shang D, Guo X. (2013) Adams predictor-corrector systems for solving fuzzy differential equations. Mathematical Problems in Engineering, 2013(1): 1-12. Doi: https://doi.org/10.1155/2013/312328
[8] Allahviranloo T, Abbasbandy S, Ahmady N, Ahmady E. (2009) Improved predictor–corrector method for solving fuzzy initial value problems. Information Sciences, 179(7): 945-55. Doi: https://doi.org/10.1016/j.ins.2008.11.030
[9] Isa S, Abdul Majid Z, Ismail F, Rabiei F. (2018) Diagonally implicit multistep block method of order four for solving fuzzy differential equations using Seikkala derivatives. Symmetry, 10(2): 42-53. Doi: https://doi.org/10.3390/sym10020042
[10] Ramli A, Abdul Majid Z. (2016) Fourth order diagonally implicit multistep block method for solving fuzzy differential equations. International Journal of Pure and Applied Mathematics, 107(3): 635-660. Doi: https://doi.org/10.12732/ijpam.v107i3.12
[11] Mohd Zawawi IS, Ibrahim ZB, Suleiman M. (2013) Diagonally implicit block backward differentiation formulas for solving fuzzy differential equations. In AIP Conference Proceedings, 1522(1), 681-687. Doi: https://doi.org/10.1063/1.4801191
[12] Barnabas B. (2013) Fuzzy sets. In Mathematics of Fuzzy Sets and Fuzzy Logic, pp. 1-12: Springer. Doi: https://doi.org/10.1007/978-3-642-35221-8_1
[13] Zimmermann HJ. (2010) Fuzzy set theory. Wiley Interdisciplinary Reviews: Computational Statistics, 2,(3): 317-320. Doi: https://doi.org/10.1002/wics.82
[14] Madan PL, Ralescu DA. (1983) Differentials of fuzzy functions. Journal of Mathematical Analysis and Applications, 91(2): 552-558. Doi: https://doi.org/10.1016/0022-247X(83)90169-5
[15] Babakordi F, Allahviranloo T. (2021) A new method for solving fuzzy Bernoulli differential equation. Journal of Mathematical Extension, 15(4): 1-20. Doi: https://doi.org/10.30495/JME.2021.1704
[16] Hashim HA, Shather A., Jameel AF, Saaban A. (2019) Numerical solution of first order nonlinear fuzzy initial value problems by six-stage fifth-order Runge-Kutta method. International Journal of Innovative Technology and Exploring Engineering, 8(5): 166-170. Doi: https://www..net/2/publication/332141468
[17] Sindu DS, Ganesan K. (2017) An approximate solution by fuzzy Taylor's method. International Journal of Pure and Applied Mathematics, 113(13): 236-44. Doi: https://acadpubl.eu/jsi/2017-113-pp/articles/13/26.pdf
[18] Adeyeye O, Omar Z. (2019) Direct solution of initial and boundary value problems of third order ODEs using maximal order fourth-derivative block method. In AIP Conference Proceedings, 2138: 030002_1-030002_6. Doi: https://doi.org/10.1063/1.5121039

[19] Hohenauer W. (2018) Hohenauer-Physical Modelling Based on First Order Odes. Doi: https://simiode.org/resources/4448

[20] Ahmad MZ, Hasan MK, De Baets B. (2013) Analytical and numerical solutions of fuzzy differential equations. Information Sciences, 236: 156-167. Doi: https://doi.org/10.1016/j.ins.2013.02.026

[21] Jameel AF, Ismail AIM. (2015) Approximate solution of first order nonlinear fuzzy initial value problem with two different fuzzifications. Journal of Uncertain Systems, 9(3): 221-229. Doi: http://www.worldacademicunion.com/journal/jus/jusVol09No3paper06.pdf

https://doi.org/10.31436/iiumej.v24i1.2382

A QUICK AND FACILE SOLUTION-PROCESSED METHOD FOR PEDOT:PSS TRANSPARENT CONDUCTIVE THIN FILM

MEI BAO LEE[1*], CHIEW TIN LEE[1], WILLIAM WOEI FONG CHONG[1,2] AND SUHAILA MOHD SANIP[3]

[1]*Faculty of Mechanical Engineering, Universiti Teknologi Malaysia, 81310 Johor Bahru, Johor, Malaysia.*
[2]*Automotive Development Centre (ADC), Institute for Vehicle Systems and Engineering (IVeSE), Universiti Teknologi Malaysia, 81310 Johor Bahru, Johor, Malaysia.*
[3]*Faculty of Engineering and Physical Sciences, University of Southampton Malaysia (UoSM), Kota Ilmu Educity@Iskandar, 79200 Iskandar Puteri, Johor, Malaysia.*

[*]*Corresponding author: mblee2@graduate.utm.my*

(Received: 31st March 2022; Accepted: 2nd September 2022; Published on-line: 4th January 2023)

ABSTRACT: PEDOT:PSS is a conducting organic polymer widely studied for a transparent conductive electrode. The conventional method to fabricate PEDOT:PSS thin film involves a post-treatment process entailing dipping into strong and toxic saturated acid to enhance the film's conductivity. Eliminating the post-treatment process reduces excess strong saturated acid or solvent waste, shortening the fabricating time by half. Therefore, this study presents a quick and facile solution-processed method for fabricating the PEDOT:PSS transparent conductive thin film (without a post-treatment process) while still achieving the requirements for a transparent conductive electrode (TCE). A parametric study was conducted by adding 5 wt% to 80 wt% of benzene sulfonic acid (BA) to PEDOT:PSS during the formulation stage before being dried at elevated temperatures from 80 °C to 200 °C. The optimum sheet resistance and transmittance value could be achieved for a thin film fabricated from PEDOT:PSS added with 40 wt% of BA, and dried at 120 °C. The sheet resistance and transmittance values are 80 Ω/sq and 93.6%, respectively. The generated figure of merit (FOM) value is 70.1, indicating an improvement of almost five times compared to the FOM value of 14.6 generated using the conventional method, requiring a post-treatment process.

ABSTRAK: PEDOT:PSS adalah bahan polimer organik yang mengkonduksi arus dan dikaji secara meluas bagi digunakan sebagai elektrod konduktif telus. Kaedah konvensional untuk menghasilkan filem nipis PEDOT:PSS melibatkan proses pasca rawatan iaitu dengan mencelupkan filem nipis PEDOT:PSS ke dalam asid pekat bertoksik bagi meningkatkan konduksi filem tersebut. Tanpa proses pasca rawatan ini dapat mengurangkan penghasilan sisa lebihan seperti asid pekat bertoksik atau pelarut buangan, memendekkan masa fabrikasi sebanyak separuh. Oleh itu, kajian ini menghasilkan kaedah proses-penyelesaian yang cepat dan mudah bagi fabrikasi filem nipis PEDOT:PSS (tanpa proses pasca rawatan) disamping masih mencapai keperluan sebagai elektrod konduktif telus (TCE). Kajian parametrik telah dijalankan dengan menambah 5 wt% hingga 80 wt% asid sulfonik benzena (BA) ke dalam PEDOT:PSS pada peringkat percampuran kimia sebelum dikeringkan pada kenaikan suhu secara berperingkat dari 80 °C sehingga 200 °C. Nilai optimum bagi rintangan lapisan dan nilai ketelusan bagi filem nipis PEDOT:PSS yang difabrikasi dapat dicapai melalui penambahan sebanyak 40 wt% BA dan dikeringkan pada suhu 120 °C. Rintangan lapisan dan nilai ketelusan telah dicapai sebanyak 80 Ω/sq dan 93.6%, masing-masing. Nilai gambaran merit (FOM) yang terhasil adalah 70.1, menunjukkan peningkatan hampir lima kali ganda berbanding nilai FOM 14.6 yang terhasil menggunakan kaedah konvensional yang memerlukan proses pasca-rawatan.

KEYWORDS: *PEDOT:PSS; thin film; sheet resistance; transmittance; figure of merit*

1. INTRODUCTION

The need for optoelectronic devices in the 21st century has increased daily. The optoelectronic devices developed nowadays, for example; solar cells [1], light-emitting diodes [2], liquid crystal displays [3], touch screens [4], and photodetectors [5], consist of one essential and common component, namely the transparent conductive electrode (TCE) or the transparent conductive thin film. TCE plays a role in electrical contact in the devices, and at the same time, it needs to allow light to pass through it. This type of electrode must provide low sheet resistance and high transmittance level. Indium tin oxide (ITO) has been the most applied TCE in the last decade. However, ITO has several serious drawbacks. For instance, ITO can be depleted as it is a rare material [6]. The cost of fabricating ITO into TCE is rapidly increasing due to shortage and complex production processes [7]. In addition, ITO is also brittle [8] and susceptible to corrosion [9].

Recently, poly(3,4-ethylenedioxythiophene) polystyrene sulfonate (PEDOT:PSS) conducting polymer has emerged as a popular and widely studied organic material for replacing conventional ITO. PEDOT:PSS consists of “PEDOT” grains that are hydrophobic and conducting. The “PEDOT” grains are encapsulated by “PSS” shells that are hydrophilic and insulating [10, 11]. PEDOT:PSS has desirable advantages, such as its solution-processed method, which could support low-cost and large-scale fabrication [6]. Other than that, PEDOT:PSS also offers high flexibility [12] and high transparency in the visible light range [6]. Despite all the attractive factors, it cannot be denied that the limitation of PEDOT:PSS organic material remains its low electrical conductivity below 350 S cm^{-1} [10]. Many studies [13,14] focused on removing the insulating “PSS,” commonly through an acid post-treatment, to overcome such deficiency. Generally, the post-treatment process often involves dropping, rinsing, dipping, soaking, or fumigating the fabricated PEDOT:PSS thin film with various acids or solvents (sulphuric acid, H_2SO_4 often gives the best results) [15-17]. Using these various acids and solvents in the post-treatment process to increase the conductivity of the PEDOT:PSS thin film is referred to as the "conventional method" in the present work.

The conventional method discussed above has the drawback of high preparation cost due to the large consumption of volume in strong saturated acids [18]. The harsh acidic post-treatment process would lead to a large amount of strong acid waste after the process and also cause acid residuals to be left on the PEDOT:PSS film surfaces. The residuals could cause corrosion to any attached materials on the PEDOT:PSS surfaces or the underlying substrate. Besides that, the conventional method also prolongs the fabrication processing time because additional steps such as washing, rinsing, and drying must be repeated when each acid treatment is done. Thus, an alternative method is required to improve the conductivity of the PEDOT:PSS thin film by replacing this conventional method. Therefore, this paper proposes a quick and facile solution-processed method (without any post-treatment) to fabricate PEDOT:PSS thin film by adding diluted benzene sulfonic acid (BA). It is expected that a PEDOT:PSS thin film with desirable conductivity and transmittance can be fabricated by introducing an optimised volume of BA into the PEDOT:PSS solution.

2. EXPERIMENTAL APPROACH

2.1 Materials Preparation

For the present study, PEDOT:PSS solution (Heraeus Clevios^{TM} PH1000 with solid content 1.0-1.3 wt% in water and PEDOT:PSS ratio of 1:2.5) was procured from Ossila Ltd. isopropyl alcohol (IPA), benzene sulfonic acid (BA), sulfuric acid (H_2SO_4), ethylene glycol (EG), dimethyl sulfoxide (DMSO) were procured from Sigma-Aldrich. Graphene nanopowder (1.6 nm flakes) was procured from Graphene Supermarket. The as-received PEDOT:PSS solution (PH1000) was diluted by adding IPA to improve the solution's wettability [19] on a quartz substrate. Then, the solution was filtered through a 0.45 μm syringe filter to remove large-sized particles.

2.2 Fabrication of PEDOT:PSS Thin Film

In Fig. 1, process A presents the essential fabricating process involving the chemical formulation of the PEDOT:PSS solution, followed by spin-coating the formulated PEDOT:PSS solution onto the desired substrate before finally drying the PEDOT:PSS thin film. Process B is the post-treatment process, where the dried PEDOT:PSS thin film is dipped into an acid (e.g., sulfuric acid, H_2SO_4). After being immersed for a set time, the sample is rinsed with alcohol or deionised water to wash away the dipping acids before another drying process. The conventional method involves both processes A and B. The present study attempts to fabricate the PEDOT:PSS thin film with only process A and without involving any process B, as given in Fig. 1.

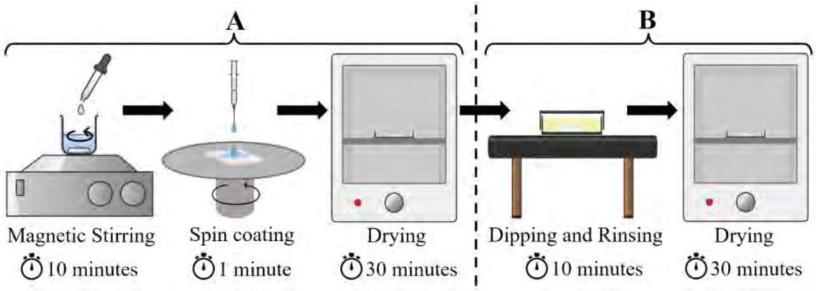

Fig. 1: Conventional method used to fabricate and improve the conductivity of PEDOT:PSS thin film.

Firstly, the IPA-diluted PEDOT:PSS solution was added with BA from 5 wt% to 80 wt%. BA is considered because of its conjugated structure, which can establish π–π interactions between benzene rings, making intermolecular charge transfer easier, thus, enhancing electrical conductivity [20]. Then, the PEDOT:PSS and BA mixture was spin-coated on a pre-cleaned quartz substrate with spin speed and time fixed at 1500 rpm for 50 s, followed by 3000 rpm for a further 10 s. After spin coating, the thin film sample was dried in an oven for 30 mins. The present study also investigated the drying temperature effect (between 80 °C and 200 °C). Note that the drying temperature has been reported to influence the conductivity of fabricated PEDOT:PSS thin film [21]. The drying temperature for PEDOT:PSS thin film is typically not recommended to be over 200 °C because this is the temperature where the chains' degradation and the deterioration of the crystallinity PEDOT:PSS film start to occur [22]. For comparative study, the samples with the post-treatment process were immediately immersed in a saturated H_2SO_4 for 10 mins after being taken out from the oven. Subsequently, the sample was rinsed with IPA and deionised water to remove the excess acid on the surface before being dried in the oven at the same drying temperature and time.

2.3 Characterisation

The PEDOT:PSS thin film fabricated was characterised for sheet resistance (R_s) and transmittance (T). The relationship between these two properties is represented by the following equation [22, 23]:

$$T = \left(1 + \frac{Z_o}{2R_s}\frac{\sigma_{op}}{\sigma_{dc}}\right)^{-2} \quad (1)$$

where Z_o is the impedance of free space (377 ohm), and σ_{op}, σ_{dc} indicate the optical and dc conductivities, respectively. The term σ_{dc}/σ_{op} refers to the figure of merit (FOM) and acts as an indicator to quantify the quality of thin film sample as TCE. The sheet resistance and transmittance of the PEDOT:PSS thin film were measured using a four-point probe (DMR-1C square resistivity tester, Nanjing Damien Instrument Co., Ltd.) and ultraviolet-visible light spectrometer (model PC2000, Shanghai Wenyi Optoelectronics Technology Co., Ltd.), respectively. The transmittance values were measured at the wavelength of 550 nm, excluding the absorption of the quartz substrate. The thickness of the thin film layer was measured by Atomic force microscopy (AFM, Bruker JPK Instruments) in non-contact mode. Lastly, the water contact angle of the PEDOT:PSS solution on quartz sample was measured using an in house built goniometer, operated following ASTM D7334.

3. RESULTS AND DISCUSSIONS

3.1 IPA-diluted PH1000 for Improving Wettability

The wettability of PEDOT:PSS solution as a function of IPA volumes percentage is shown in Figure 2. It is observed that the solutions' wettability on a quartz substrate increased when the IPA volume percentage increased from 0% to 50%. The contact angle measured for 0%, 12.5%, 25%, and 50% of IPA diluted-PH1000 on quartz substrate were 68.9°, 56°, 43°, and 28°, respectively. A reduced contact angle value indicates a better wetting of solutions on the surface.

The PEDOT:PSS solutions were then spin-coated onto pre-cleaned quartz substrates. Figure 3 shows the effect of the volume percentage of IPA dilution on the uniformity of the spin coating process. Dilution of PH1000 with 25% IPA or more can achieve a good uniform spin coat of PEDOT:PSS thin film. Even though a more uniform spin-coated film can be achieved with better wettability, the resistance of 50% IPA-diluted PH1000 thin film was measured at 745.8 kΩ, which is higher than the one measured for 25% IPA-diluted PH1000 thin film at 645.0 kΩ. Thus, a 25% IPA-diluted PH1000 solution was adopted for the subsequent analysis and is referred to as the pristine PEDOT:PSS.

3.2 Pristine PEDOT:PSS + Benzene Sulfonic Acid (BA)

The R_s and T values for PEDOT:PSS solutions added with different concentrations of BA (from 5 wt% to 80 wt%) are given in Fig. 4(a). The R_s values at 5 wt% and 10 wt% BA concentration are not plotted in Fig. 4(a) because of their excessively high values (over 10,000 Ω/sq). With such high R_s values and T of around 88%, the figure of merit (FOM), calculated using equation (1), is approximately 0.3, which is considered poor (near zero). After adding at least 20 wt% of BA, the R_s value is shown to drastically reduce to 120 Ω/sq with a T of 92.7%. The R_s is the lowest when added with 40 wt% of BA (80 Ω/sq), while T is the highest when added with 40 wt% of BA (93.6%). Figure 4(b) plots the FOM versus BA concentration, indicating that 40 wt% of BA concentration results in the highest FOM value of 70.1.

https://doi.org/10.31436/iiumej.v24i1.2382

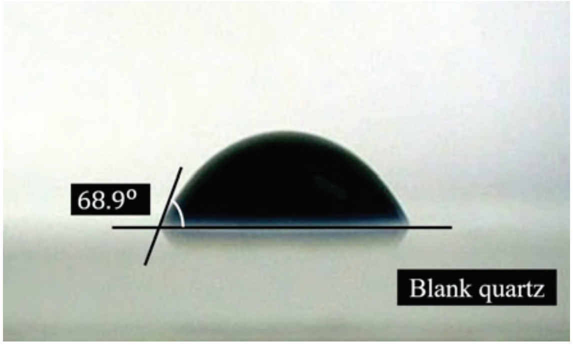

(a) 0% IPA

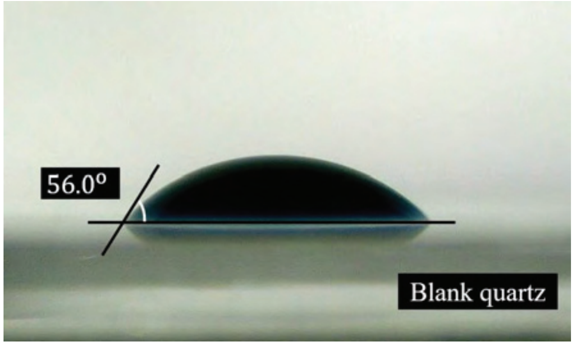

(b) 12.5% IPA

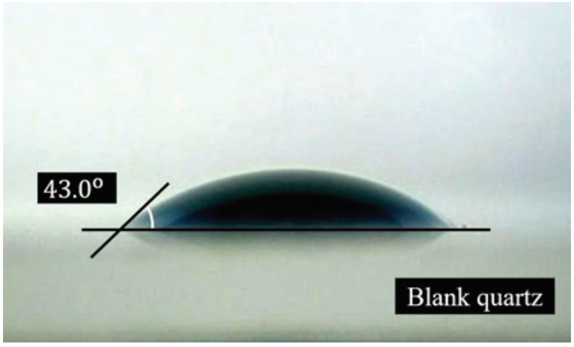

(c) 25% IPA

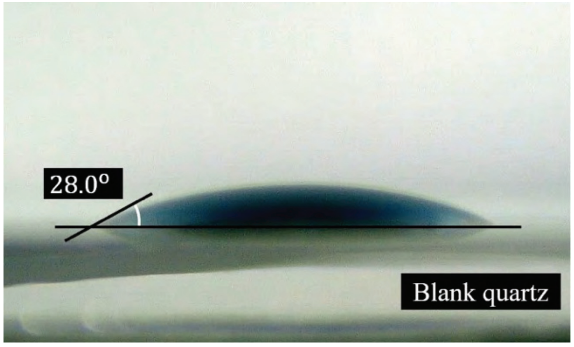

(d) 50% IPA

Fig. 2: Wettability of PEDOT:PSS solutions on quartz substrate with the increase of IPA volume percentage.

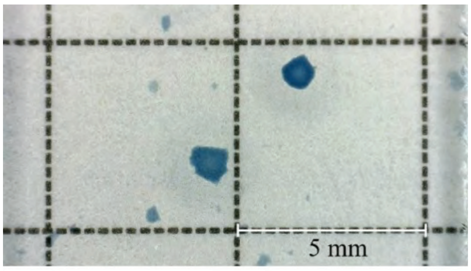

(a) 0% IPA

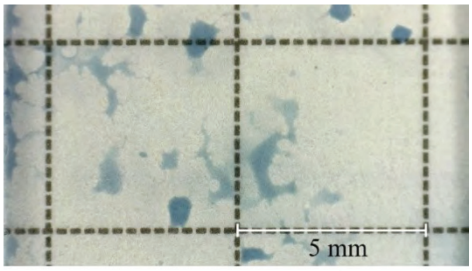

(b) 12.5% IPA

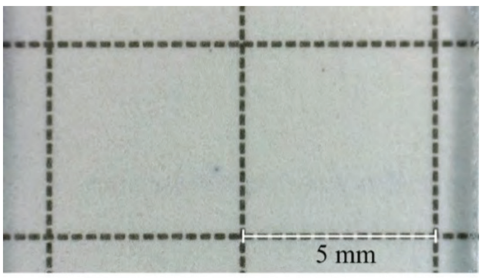

(c) 25% IPA

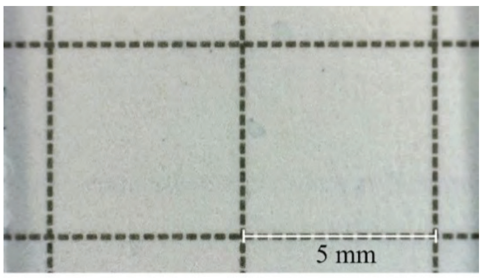

(d) 50% IPA

Fig. 3: Effect of volume percentage of IPA dilution towards the uniformity of spin coating.

https://doi.org/10.31436/iiumej.v24i1.2382

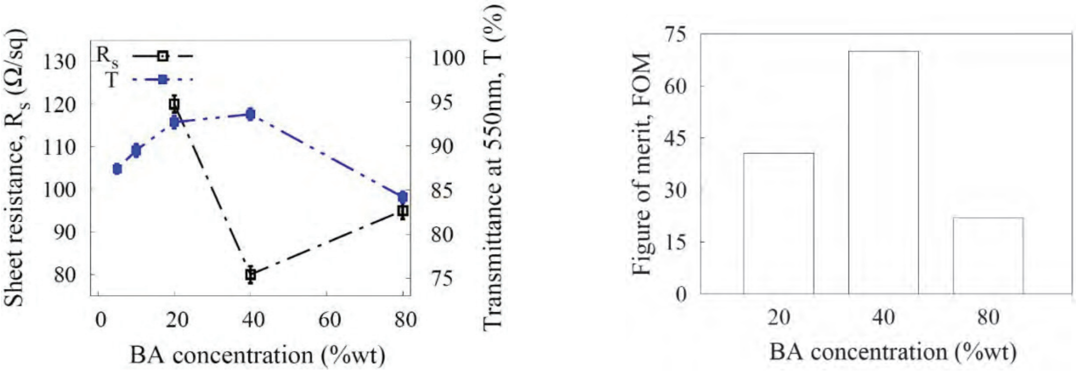

(a) R_s, T (b) FOM

Fig. 4: Effect of benzene sulfonic acid (BA) concentration towards the R_s, T and FOM of PEDOT:PSS transparent conductive thin film dried at 120 °C.

The second fabricating condition tested was the drying temperature. The PEDOT:PSS thin film fabricated with 40 wt% BA was dried under temperatures varying from 80 °C to 200 °C. From Fig. 5(a), it is observed that the lowest R_s and highest T remain at the drying temperature of 120 °C. The PEDOT:PSS thin film drying at temperatures other than 120 °C showed an increase in R_s and a decrease in T. This is related to the water, BA, and IPA (solvents) that exist in the PEDOT:PSS solutions. If such solutions dried at excessively high temperatures (160 °C and 200 °C), the solvents would evaporate before the PEDOT grains could form into a crystal. However, with a much lower drying temperature (80 °C), the solvents will remain between the PEDOT grains molecules and hinder the crystal structure formation [24]. Thus, 120 °C drying temperature is observed as the optimum drying temperature.

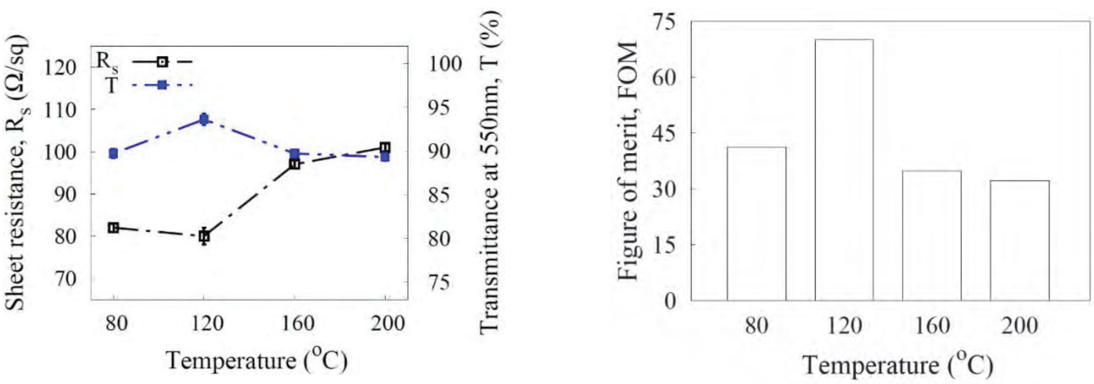

(a) R_s, T (b) FOM

Fig. 5: Effect of drying temperatures towards the R_s, T and FOM of PEDOT:PSS transparent conductive thin film.

In addition, numerous studies [6] have focused on enhancing the electrical conductivity of PEDOT:PSS thin film through layer-by-layer structure coating. Thus, the present study also investigated the effect of the number of coating layers on the FOM value of PEDOT:PSS thin film. Using the optimised fabricating conditions (40 wt% BA and 120 °C drying temperature), the PEDOT:PSS thin film was fabricated (repeated spin coating after each drying process) to achieve one to four layers of film. As shown in Fig. 6(a), although the R_s

and T values of one layer (1 L) and two layers (2 L) are different, it was determined that both cases resulted in similar FOM values of 70.1 and 70.3, as given in Fig. 6(b). However, after more than two layers of spin coating, the third (3 L) and fourth (4 L) layers of spin coating reduced the FOM value to 47.7 and 31.3, respectively.

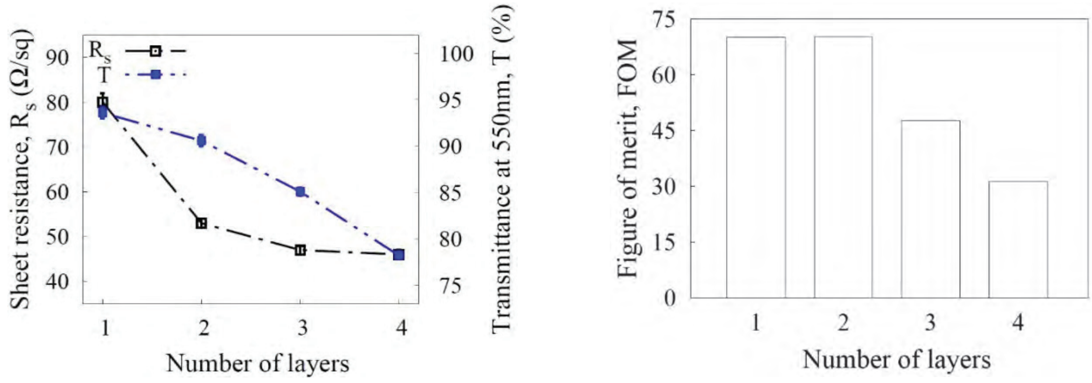

(a) R_s, T

(b) FOM

Fig. 6: Effect of number of coating layers towards the R_s, T and FOM of PEDOT:PSS transparent conductive thin film.

3.3 Comparative Study with Different Solution-processed Methods

Four other solution-processed methods were selected for comparison with the method proposed in the present study (named as method-4). It is to note that methods 1 and 2 were selected as baseline comparisons. The methods are summarised below:

- Method-1: process A (pristine PEDOT:PSS) + process B (dipping saturated H_2SO_4)
- Method-2: process A (pristine PEDOT:PSS) + process B (dipping saturated BA)
- Method-3: process A (pristine PEDOT:PSS added with 40 wt% H_2SO_4)
- Method-4: process A (pristine PEDOT:PSS added with 40 wt% BA)
- Method-5: process A (pristine PEDOT:PSS added with 40 wt% BA) + process B (dipping saturated H_2SO_4)

Figure 7 shows the (a) R_s, (b) T, and (c) FOM values of PEDOT:PSS transparent conductive thin film fabricated with different solution-processed methods. Method-1 and method-5 fabricated PEDOT:PSS thin films resulted in higher R_s of 215 and 176 Ω/sq, respectively, while method-4 resulted in the lowest R_s value of 80 Ω/sq. It is found that PEDOT:PSS thin film undergoing the conventional post-treatment process (process B) tends to generate lower levels of transmittance. For example, method-4 fabricated PEDOT:PSS thin film resulted in a transmittance of 93.6%. However, when subjected to the addition process B (method-5), the T value reduced 8.9% to 84.7%. Similarly, method-1 and method-2, subjected to process B, also resulted in a lower T value than method-4. Hence, through the calculation from equation (1), only the method-4 fabricated PEDOT:PSS thin film gives a FOM value of 70.1, which is over 35.0 (minimum industrial standard of TCE [22, 23]). Note that method-3 is not shown in Fig. 7 because the PEDOT:PSS solution was solidified during the chemical formulation process and could not get a uniform spin coating.

Method-1 (baseline), method-4 (1 L), and method-4 (2 L) PEDOT:PSS thin film samples' thicknesses were measured using atomic force microscopy (AFM). Figure 8 shows the film thickness of samples from method-1, method-4 (1 L), and method-4 (2 L), measured at 43 nm, 85 nm, and 154 nm, respectively. With the thickness (nm) and (Ω/sq) data

https://doi.org/10.31436/iiumej.v24i1.2382

available, the conductivity of the thin film samples can then be determined. Thus, the conductivity of method-1 thin film is approximately 1081.7 Scm^{-1}, method-4 (1 L) thin film is 1470.6 Scm^{-1}, and method-4 (2 L) is 1225.2 Scm^{-1}.

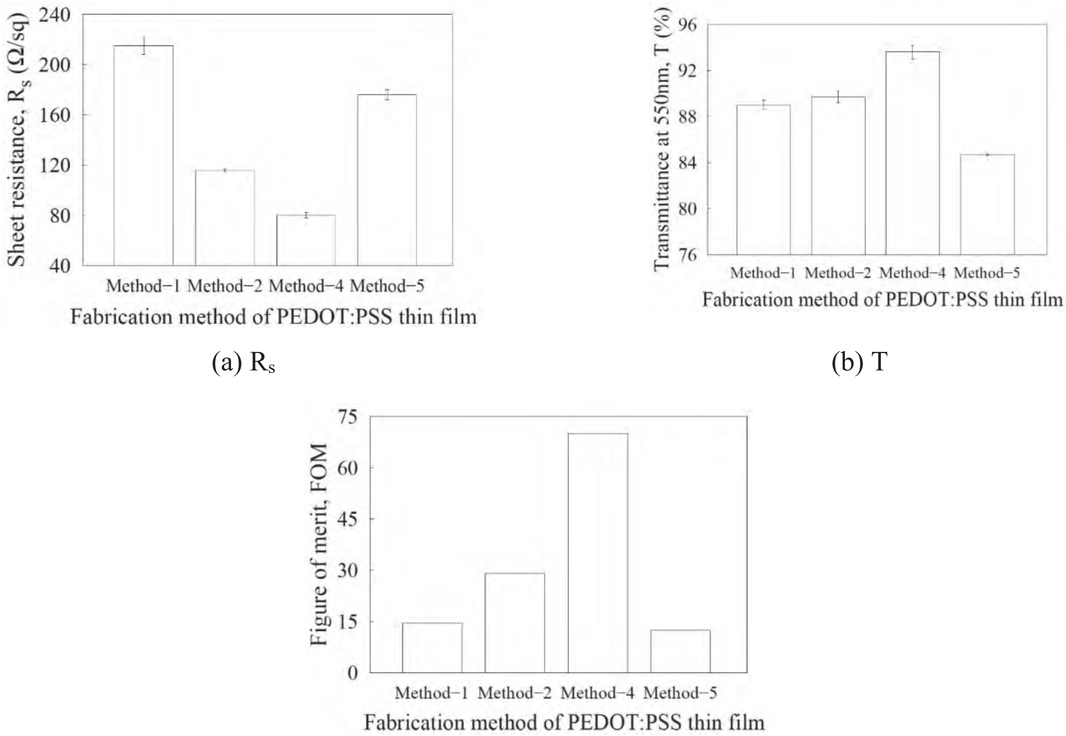

(a) R_s (b) T

(c) FOM

Fig. 7: Effect of different solution-processed methods towards (a) R_s, (b) T and (c) FOM of PEDOT:PSS transparent conductive thin film.

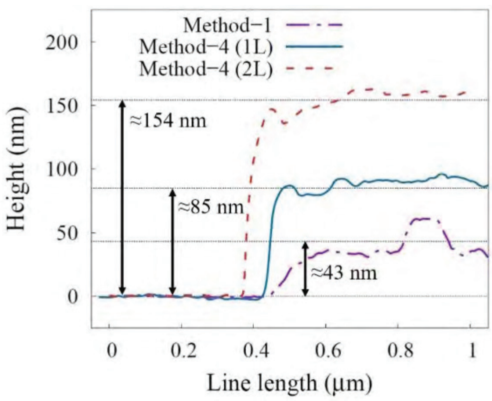

Fig. 8: PEDOT:PSS film thickness from method-1, method-4 (1 L) and method-4 (2 L).

The results obtained from this study were also compared to the recent papers published in the same field. Table 1 compares the properties of PEDOT:PSS transparent conductive film fabricated with or without the post-treatment process. The present study's conventional method (method-1) yielded a FOM value of 14.6, which is comparable to the FOM value of 17.5 obtained by Bießmann et al. [15]. The slightly lower FOM value produced in this study using the same processing procedure as Bießmann et al. [15] can be attributed to the IPA dilution in the PH1000 solution adopted in this research. Wen et al. [18] demonstrated that mixing PH1000 with dimethyl sulfoxide (DMSO) solvent and undergoing a post-treatment process with trifluoromethanesulfonic acid (TA) can produce PEDOT:PSS film with a much higher FOM value, which is 116.5. Nevertheless, the result of this study still demonstrates a reasonably high FOM value (70.1) compared to all other studies in the literature in which the fabrication method is completed without any post-treatment process.

Table 1: A comparison of properties of PEDOT:PSS transparent conductive thin film fabricated.

Type of PEDOT :PSS	Additional mixing materials	W/Wo post-treatment (solvent/acid)	t [nm]	C [S cm^{-1}]	T at 550nm [%]	R_s [Ωsq^{-1}]	FOM	Ref
PH 1000	none	Wo	103.0	1.1	-	88261.3	-	[17]
		H_2SO_4	92.0	1167.0	-	93.1	-	
PH 500	none	Wo	43.2	0.2	-	1500000.0	-	[16]
		H_2SO_4	12.9	596.3	-	1300.0	-	
	MCNT	Wo	150.0	5.1	-	13000.0	-	
		H_2SO_4	150.0	78.4	-	850.0	-	
PH 1000	Zonyl and EG	DMSO	-	-	93.7	124.5	45.6	[25]
		MA	-	-	93.5	111.0	50.0	
		DMSO and MA	-	-	94.9	110.0	64.4	
PH 1000	none	Wo	165.0	7.0	90.0	8658.0	0.4	[15]
		EG	138.0	1128.0	86.0	64.2	37.5	
		HCL	169.0	392.0	84.6	150.9	14.3	
		FA	108.0	1289.0	84.6	71.8	30.1	
		HNO_3	66.0	2099.0	85.7	72.2	32.6	
		H_2SO_4	80.0	2938.0	88.5	42.5	70.3	
		H_2SO_4 (washed)	65.5	1293.0	84.0	118.1	17.5	
PH 1000	SCNT, SDBS and TX100	Wo	-	-	88.0	400.0	7.1	[26]
		Methanol	-	-	89.0	290.0	10.8	
		Methanol and HNO_3	-	-	90.1	100.3	35.1	
PH 1000	DMSO	Wo	-	-	90.5	170.0	21.7	[18]
		TA	-	-	92.0	38.0	116.5	
AI-4083	Sorbitol and Martitol	Wo	173.9	0.4	87.9	150000.0	0	[21]
		FA	129.6	847.9	87.8	91.0	30.8	
PH 1000	IPA	Wo	-	-	88.0	645000.0	0	Present study
		H_2SO_4	43.0	1081.7	89.0	215.0	14.6	
	IPA and BA (1 L)	Wo	85.0	1470.6	93.6	80.0	70.1	
	IPA and BA (2 L)	Wo	154.0	1225.2	90.6	53.0	70.3	

W/Wo = with or without; t = thickness; C = conductivity; T = transmittance; R_s = sheet resistance; FOM = Figure of Merit; EG = ethylene glycol; DMSO = dimethyl sulfoxide; SCNT = single-walled carbon nanotubes; SDBS = sodium dodecyl benzene sulfonate; TX100 = Triton X-100; MCNT = multiwall carbon nanotubes; IPA = isopropyl alcohol; BA = benzene sulfonic acid; MA = methane sulfonic acid; TA = trifluoromethanesulfonic acid; HCl = hydrochloric acid; FA = formic acid; HNO_3 = nitric acid; H_2SO_4 = sulfuric acid

3.4 Effect of Additives

The effect of common additives, namely ethylene glycol (EG), dimethyl sulfoxide (DMSO), and graphene (Gr) nanopowder, on the FOM value for the PEDOT:PSS film produced using method-4 (1L) was further investigated. Figure 9 (a) shows that the R_s value starts to increase with an increase of wt% additives added to the chemical formulation of PEDOT:PSS solution. Figure 9 (b) shows that with an increase in wt% of EG additive, the T value drops at first and rises back. The T value drops 5.4% when added with 10 wt% of EG and rises 2.4% when added with 20 wt% EG. For DMSO additive, adding 5 wt% does not change the T value of the thin film, while adding 10 wt% and 20 wt% of DMSO increases the T value by 8.0% and 12.0%, respectively. For Gr nano powder additive, adding 5 wt% also does not change the T value, but adding 10 wt% decreases the T value of thin film by 11%. Although adding 20 wt% of Gr powder only reduces the T value by 0.2%, it still resulted in an extensive error bar of 14%. Hence, with the FOM calculated as shown in Figure 9 (c), the effect of additive to further enhance the FOM of PEDOT:PSS thin film can be concluded to be not adequate when coupled with method-4. The PEDOT:PSS with 40 wt% of BA concentration remains the best-optimised formulation in this study.

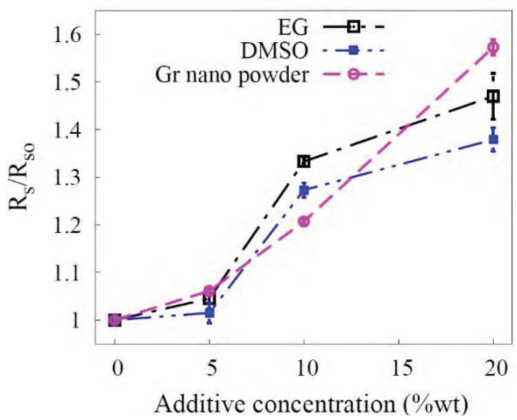

(a) R_s

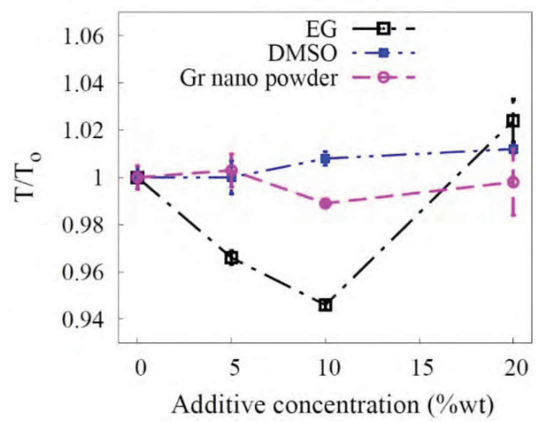

(b) T

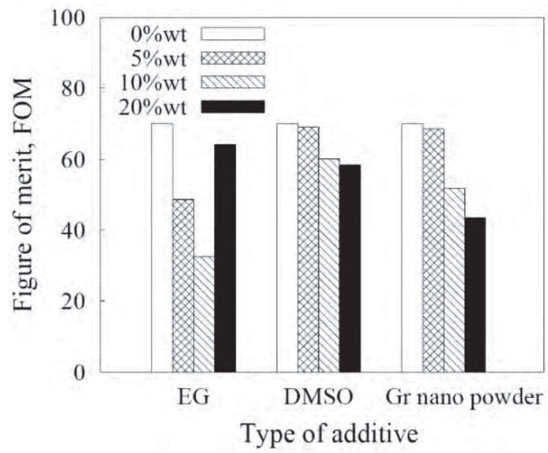

(c) FOM

Fig. 9: Effect of adding different concentration of different type additives (EG, DMSO, Gr nano powder) towards the changes of (a) R_s, (b) T and (c) FOM of PEDOT:PSS transparent conductive thin film.

https://doi.org/10.31436/iiumej.v24i1.2382

4. CONCLUSION

This study presents a quick and facile solution-processed method for fabricating PEDOT:PSS thin film without a post-treatment process, capable of achieving requirements to be adopted as a transparent conductive electrode (TCE). The sheet resistance, transmittance, and FOM properties are enhanced by optimising the fabricating conditions with 40 wt% of added benzene sulfonic acid BA, drying at 120 °C, and one layer of spin coating. The lowest sheet resistance and highest transmittance achieved were 80 Ω/sq and 93.6%, respectively, producing a FOM value of 70.1. The FOM value improved almost five times compared to the FOM value of 14.6 for the conventional method of fabricating PEDOT:PSS film. The conductivity of PEDOT:PSS thin film fabricated using the proposed method reached 1470.6 Scm^{-1}, improving by 36% compared to the conductivity of 1081.7 Scm^{-1} achieved using the conventional method.

The PEDOT:PSS film produced in this study delivers properties that are either on-par or better than those reported in the literature, which mostly requires a post-treatment with various acids or solvents. Thus, this study concluded that the proposed quick and facile solution-processed method could produce PEDOT:PSS thin films with much-improved sheet resistance, transmittance, and FOM properties. In future studies to validate the potential of the thin film, it will be used as TCE in fabricating photovoltaic devices, allowing for the proof of concept in adopting PEDOT:PSS as an alternative TCE to ITO.

ACKNOWLEDGEMENT

The authors would like to acknowledge the support provided by the Ministry of Higher Education, Malaysia through the Fundamental Research Grant Scheme (FRGS/1/2018/TK10/USMC/02/1) awarded to the University of Southampton Malaysia and Research University Grant (RUG) of Universiti Teknologi Malaysia through the Transdisciplinary Research Program (TDR) of “Innovative Materials for Resilient Contact Systems” (Q.J1300 00.3551.05G56).

REFERENCES

[1] Tan Z, Zhang W, Zhang Z, Qian D, Huang Y, Hou J, Li Y. (2012) High performance inverted polymer solar cells with solution processed titanium chelate as electron collecting layer on ITO electrode. Advanced Materials, 24(11): 1476-81. https://doi.org/10.1002/adma.201104863

[2] Osada T, Kugler T, Bröms P, Salaneck W. (1998) Polymer-based light-emitting devices: investigations on the role of the indium—tin oxide (ITO) electrode. Synthetic Metals, 96(1): 77-80. https://doi.org/10.1016/S0379-6779(98)00069-1

[3] Oh B-Y, Jeong M-C, Moon T-H, Lee W, Myoung J-M, Hwang J-Y, Seo D-S. (2006) Transparent conductive Al-doped ZnO films for liquid crystal displays. Journal of Applied Physics, 99(12): 124505. https://doi.org/10.1063/1.2206417

[4] Mochizuki T, Takigami Y, Kondo T, Okuzaki H. (2018) Fabrication of flexible transparent electrodes using PEDOT: PSS and application to resistive touch screen panels. Journal of Applied Polymer Science, 135(10): 45972. https://doi.org/10.1002/app.45972

[5] Liu Z, Parvez K, Li R, Dong R, Feng X, Müllen K. (2015) Transparent conductive electrodes from graphene/PEDOT: PSS hybrid inks for ultrathin organic photodetectors. Advanced Materials, 27(4): 669-675. https://doi.org/10.1002/adma.201403826

[6] Kim Y, Kim Y, Kim JH. (2020) Highly Conductive PEDOT: PSS Thin Films with Two-Dimensional Lamellar Stacked Multi-Layers. Nanomaterials, 10(11): 2211. https://doi.org/10.3390/nano10112211

[7] Na SI, Kim SS, Jo J, Kim DY. (2008) Efficient and flexible ITO free organic solar cells using highly conductive polymer anodes. Advanced Materials, 20(21): 4061-4067. https://doi.org/10.1002/adma.200800338
[8] Alzoubi K, Hamasha MM, Lu S, Sammakia B. (2011) Bending fatigue study of sputtered ITO on flexible substrate. Journal of Display Technology, 7(11): 593-600. https://doi.org/10.1109/JDT.2011.2151830
[9] Galagan Y, Mescheloff A, Veenstra SC, Andriessen R, Katz EA. (2015) Reversible degradation in ITO-containing organic photovoltaics under concentrated sunlight. Physical Chemistry Chemical Physics, 17(5):3891-3897. https://doi.org/10.1039/C4CP05571C
[10] Liu Z, Wang N. (2018) Effects of highly conductive PH1000 anode in combination with ethylene glycol additive and H_2SO_4 immersion treatments on photovoltaic performance and photostability of polymer solar cells. Journal of Materials Chemistry C, 6(36): 9734-9741. https://doi.org/10.1039/C8TC02467G
[11] Benoudjit A, Guthoos HFA, Arris FA, Salim WWAW. (2017) PEDOT:PSS–modified platinum microelectrodes for measurements in aqueous media: effect of polymer surface area on long-term anodic peak current stability. IIUM Engineering Journal, 18(2): 11-15. https://doi.org/10.31436/iiumej.v18i2.715
[12] Kim Y, Cho W, Kim Y, Cho H, Kim JH. (2018) Electrical characteristics of heterogeneous polymer layers in PEDOT: PSS films. Journal of Materials Chemistry C, 6(33): 8906-8913. https://doi.org/10.1039/C8TC02598C
[13] Kim N, Kee S, Lee SH, Lee BH, Kahng YH, Jo YR, Kim BJ, Lee K. (2014) Highly conductive PEDOT: PSS nanofibrils induced by solution processed crystallization. Advanced Materials, 26(14):2268-2272. https://doi.org/10.1002/adma.201304611
[14] Vigna L, Verna A, Marasso S, Sangermano M, D'Angelo P, Pirri F, Cocuzza M. (2021) The effects of secondary doping on ink-jet printed PEDOT: PSS gas sensors for VOCs and NO_2 detection. Sensors and Actuators B: Chemical, 345: 130381. https://doi.org/10.1016/j.snb.2021.130381
[15] Bießmann L, Saxena N, Hohn N, Hossain MA, Veinot JG, Müller Buschbaum P. (2019) Highly conducting, transparent PEDOT: PSS polymer electrodes from post treatment with weak and strong acids. Advanced Electronic Materials, 5(2): 1800654. https://doi.org/10.1002/aelm.201800654
[16] Yun D-J, Ra H, Kim J-M, Lee J-H, Park SH, Hwang J, Chung J, Kim S-H, Kim Y-S, Jeong YJ. (2019) A study on distinctive transition mechanism of sulfuric acid treatment on performance enhancement of poly (3, 4-ethylenedioxythiophene): Polystyrene based electrodes depending on multiwall carbon nanotube dose. Applied Surface Science, 487: 480-487. https://doi.org/10.1016/j.apsusc.2019.05.125
[17] Kim J, Jang JG, Hong J-I, Kim SH, Kwak J. (2016) Sulfuric acid vapor treatment for enhancing the thermoelectric properties of PEDOT: PSS thin-films. Journal of Materials Science: Materials in Electronics, 27(6): 6122-6127. https://doi.org/10.1007/s10854-016-4538-x
[18] Wen R, Huang H, Wan J, Wen S, Wang J, Fan X. (2021) High Efficiency Stable Flexible Organic Solar Cells with PEDOT: PSS Electrodes via Superacid Fumigation Treatment. Energy Technology, 9(11): 2100595. https://doi.org/10.1002/ente.202100595
[19] Montanino M, De Girolamo Del Mauro A, Tesoro M, Ricciardi R, Diana R, Morvillo P, Nobile G, Imparato A, Sico G, Minarini C. (2015) Gravure-printed PEDOT: PSS on flexible PEN substrate as ITO-free anode for polymer solar cells. Polymer Composites, 36(6): 1104-1109. https://doi.org/10.1002/pc.23486
[20] Wang C, Sun K, Fu J, Chen R, Li M, Zang Z, Liu X, Li B, Gong H, Ouyang J. (2018) Enhancement of conductivity and thermoelectric property of PEDOT: PSS via acid doping and single post-treatment for flexible power generator. Advanced Sustainable Systems, 2(12): 1800085. https://doi.org/10.1002/adsu.201800085
[21] Lien S-Y, Lin P-C, Chen W-R, Liu C-H, Sze P-W, Wang N-F, Huang C-J. (2022) Improving Optoelectrical Properties of PEDOT: PSS by Organic Additive and Acid Treatment. Crystals, 12(4): 537. https://doi.org/10.3390/cryst12040537

[22] Kim YH, Sachse C, Machala ML, May C, Müller Meskamp L, Leo K. (2011) Highly conductive PEDOT: PSS electrode with optimized solvent and thermal post-treatment for ITO-free organic solar cells. Advanced Functional Materials, 21(6): 1076-1081. https://doi.org/10.1002/adfm.201002290

[23] Scardaci V, Coull R, Coleman JN. (2010) Very thin transparent, conductive carbon nanotube films on flexible substrates. Applied Physics Letters, 97(2): 023114. https://doi.org/10.1063/1.3462317

[24] Lee K, Lee S-H, Nara K, Seyoung K. (2016) PEDOT:PSS based electrode and method for manufacturing the same. Google Patents. Oct 25. US Patent 9,478,743. https://patents.google.com/patent/US9478743B2/en

[25] Cui H, Song W, Fanady B, Peng R, Zhang J, Huang J, Ge Z. (2019) Flexible ITO-free organic solar cells over 10% by employing drop-coated conductive PEDOT: PSS transparent anodes. Science China Chemistry, 62(4):500-505. https://doi.org/10.1007/s11426-018-9426-2

[26] Tian Y, Wang T, Zhu Q, Zhang X, Ethiraj AS, Geng W-M, Geng H-Z. (2021) High-performance transparent PEDOT: Pss/CNT films for OLEDs. Nanomaterials, 11(8): 2067. https://doi.org/10.3390/nano11082067

https://doi.org/10.31436/iiumej.v24i1.2426

A HYBRID OF KANSEI ENGINEERING (KE) AND ANALYTICAL HIERARCHY PROCESS (AHP) TO DEVELOP CONCEPTUAL DESIGNS OF PORTABLE OIL SPILL SKIMMER

RPRAKASH RAMANATHAN, LOKMAN ABDULLAH*, MUHAMMAD HAFIDZ FAZLI MD FAUADI, MUHAMMAD SYAFIQ SYED MOHAMED AND KHAIRUN NAJMI KAMALUDIN

Faculty of Manufacturing Engineering, Universiti Teknikal Malaysia Melaka, 76100 Durian Tunggal, Melaka, Malaysia

**Corresponding author: lokman@utem.edu.my*

(Received: 9th May 2022; Accepted: 24th August 2022; Published on-line: 4th January 2023)

ABSTRACT: Currently, there are huge demands on developing a design that fulfils the characteristics of performance, cost, safety, and aesthetics. However, the conceptual design stages in industrial products lack the involvement of user requirements as it is typically focused on the product's performance. Consequently, specific criteria such as the product's ease of use, safety, and robustness cannot be compared and measured when designing industrial products. Owing to this reason, this research proposes a new technique that integrates Kansei Engineering with Analytical Hierarchy Process (AHP) to address the issue. The research objective is to investigate an oil spill skimmer's user and technical requirements by incorporating the Kansei Engineering method. The approach to carry out this research is to incorporate the Kansei and the basic AHP methods. Kansei Engineering will suggest the required design elements that must be included to design and fabricate a portable oil spill skimmer. At the same time, the AHP method is used to select the best design based on the developed conceptual design. The effectiveness of the proposed method was verified by comparing it with other established methods, such as TOPSIS (Technique of Order Preference by Similarity to Ideal Solution). Moreover, sensitivity analysis was used to investigate the robustness of the AHP result. There are 5 conceptual designs in total, assessed in this research. The result showed that out of the 5 conceptual designs, design number 3 has the highest ranking (priority ranking = 0.2603). Thus, the most suitable conceptual design for the portable oil spill skimmer to be fabricated is design 3. The finding also shows that the result from AHP was valid and robust.

ABSTRAK: Pada masa kini, terdapat permintaan besar bagi membangunkan reka bentuk yang memenuhi ciri-ciri prestasi, kos, keselamatan dan estetika. Walau bagaimanapun, industri kurang melibatkan keperluan pengguna pada peringkat reka bentuk konsep produk industri, kerana ia biasanya tertumpu pada prestasi produk. Ini menyebabkan kriteria khusus seperti kemudahan menggunakan produk, keselamatan dan keteguhan produk tidak dapat dibandingkan dan diukur semasa mereka bentuk produk industri. Disebabkan faktor berkenaan, kajian ini mencadangkan teknik baharu yang mengintegrasikan Kejuruteraan Kansei bersama Proses Hierarki Analitik (AHP) bagi menangani isu tersebut. Objektif kajian adalah bagi menyiasat keperluan pengguna dan keperluan teknikal menyaring tumpahan minyak dengan menggabungkan kaedah Kejuruteraan Kansei. Pendekatan kajian ini adalah dengan menggabungkan Kansei dan kaedah asas AHP. Kejuruteraan Kansei mencadangkan elemen reka bentuk yang diperlukan yang mesti disertakan bagi mereka bentuk dan menyaring tumpahan minyak mudah alih. Pada masa sama, kaedah AHP digunakan bagi memilih reka bentuk terbaik berdasarkan reka bentuk konsep yang dibangunkan. Keberkesanan kaedah yang dicadangkan telah disahkan dengan membandingkannya dengan kaedah lain yang telah terbukti, seperti TOPSIS (Teknik Aturan Kehendak Berdasarkan Persamaan dengan Solusi Ideal). Selain itu, analisis sensitiviti digunakan bagi mengkaji keteguhan keputusan AHP. Terdapat 5 reka bentuk konseptual yang dinilai dalam kajian ini. Dapatan kajian menunjukkan bahawa reka bentuk nombor 3 mempunyai keputusan tertinggi (keutamaan kedudukan = 0.2603) daripada 5 reka bentuk konseptual ini. Oleh itu, reka bentuk konsep yang paling sesuai bagi saringan tumpahan minyak mudah alih yang akan dibina adalah reka bentuk 3. Dapatan kajian juga menunjukkan bahawa hasil daripada AHP adalah sah dan kukuh.

KEYWORDS: *Kansei Engineering; analytical hierarchy process (AHP); product development process; oil spill skimmer*

1. INTRODUCTION

Industrial equipment sales often face tough challenges in maintaining their sales volume and customer loyalty since many manufacturers compete with one another for customers. Therefore, manufacturers often spend their time and resources studying customers' purchasing behaviour and preferences, such as function, appearance, and usability. Of all these requirements, visual appeal plays a vital role in influencing customer purchasing decisions. Customer impressions are influenced by various elements, including the brand of the product, its purpose, look, and usefulness. However, the product look is the one that creates the most visual engagement to the client and product compared to other aspects [1]. The application of AHP has been utilised in the area of the machine tools industry and the textile industry

Consumer products, such as household appliances, are typically regarded as attractive and inexpensive, but industrial items, such as heavy machinery, should be of high quality but not necessarily attractive. Any industrial product's development usually focuses on technical standards, including objectives and well-defined metrics such as speed, power, and many others that could be compared and tested. While meeting technical criteria is essential, it is not always enough for a product to succeed [2]. Several elements are difficult to quantify yet influence machine design and selection. Users' impressions of different machine tools have received minimal attention in terms of strategies for selecting, analysing, and comparing machine tools. Thus, there is a need to incorporate both customer and technical requirements in the industrial product development process.

A study done by Marini investigated the use of AHP and Analytical Network Process (ANP) together with Quality Function Deployment (QFD) in concept design and material selection for making better decisions to improve product success [3]. However, the involvement of customer requirements is still lacking when developing a design concept [4]. Therefore, research was done to propose a method based on TOPSIS and fuzzy AHP, which could be used in concept design evaluation [5]. Renzi researched using AHP and ANP together with other multi-criteria decision methods for design evaluation in the automotive industry, trying to transfer knowledge on decision-making methods to the industrial context [6]. Moreover, Rosli investigated a systematic product design model that assists decision-makers or design engineers in improving current design through the idea generation method of Theory of Inventive Problem Solving (TRIZ) and utilising the analytical hierarchy process (AHP) to perform the selection of best-generated idea [7].

A study was conducted to show that the proposed (House of Quality) HOQ and Fuzzy-AHP provided a novel alternative to existing methods to perform design concept evaluations in the early stages of product development, with the capability to accommodate uncertainties and vagueness using the optimum number of pairwise comparisons [8]. Furthermore, a research was conducted by Turan, proposing a rough number to be used by VIKOR and AHP methods to develop a systematic framework for the concept evaluation process [9]. Nevertheless, the proposed best design concept might be biased toward designers' expectations rather than the customers' expectations.

It is well known that previous researchers have investigated and reported on several modified AHP. To the best of the author's knowledge, however, the implementation of Kansei Engineering as a tool for optimisation paired with AHP in the development of industrial products such as oil spill skimmer is still inadequate and uncommon. Furthermore, although several researchers have researched the fabrication of oil spill skimmers, there is no proof that KE and AHP were utilised in the design and fabrication process [10]–[15]. Therefore, this study aims to employ Kansei Engineering to investigate the user and technical requirements to generate multiple conceptual designs for an oil spill skimmer, which will be analysed using Analytical Hierarchy Process (AHP) to choose the ideal oil spill skimmer conceptual design.

2. METHODOLOGY

2.1 Research Framework

The development and selection of the best conceptual design for a portable oil spill skimmer are split into two sections in this study. First, Kansei Engineering is employed to build an overall design aspect of the oil spill skimmer in phase one. This methodology has five layers: Kansei word selection, product sample collection, questionnaire distribution, reliability testing, data interpretation, and design idea creation. The AHP is then utilised in part 2 to determine the relative weight of each factor at each level to arrive at the overall product assessment system. This is done to determine which design idea produced by Kansei Engineering is the best. Finally, to evaluate the robustness of the AHP, the results are compared and analysed using TOPSIS and sensitivity analysis.

2.2 Kansei Engineering and Reliability Testing

Kansei Engineering (KE) uses seven primary stages to categorise the customer's needs and technical requirements. Kansei Engineering type 1 is employed in this study. This method transforms a single product concept into a more complex concept, which is then developed to numerous levels and interpreted in terms of the physical characteristics of the product design. Category categorisation is a breakdown strategy from a targeted concept of a new product to the corresponding subjective Kansei to the objective design requirements. Mazda's design of the Miata, the world's most successful sports automobile, is a well-known example of this category application [16]. A previous research can be referred to identify the step-by-step procedure of Kansei Engineering methodology [17].

Reliability testing aims to evaluate the reliability or internal consistency by utilising Cronbach's alpha to measure the strength of the consistency. Cronbach's alpha analysis determines whether the multiple-question Likert scale survey is reliable. Higher values of Cronbach's Alpha signify more reliability of the survey or questionnaire; it has a range of 0 to 1. The minimal number of questions and weak interconnection between objects result in a low alpha score in the reliability test. The alpha value achieved, for example, will be pretty low due to a lack of correlation between the variables and items, resulting in the questionnaire being rejected and requiring modification. On the other hand, the items may be redundant if the alpha is too high since the questions are the same but in a different format. The formula of Cronbach's Alpha and the rule of thumb is shown below in Eq. (1) [18].

$$a = \frac{N.\bar{c}}{\bar{v}+(N-1).\bar{c}} \quad (1)$$

where,

N= the number of items

$\bar{c}$ = average covariance between items-pairs

$\bar{v}$ = average variance

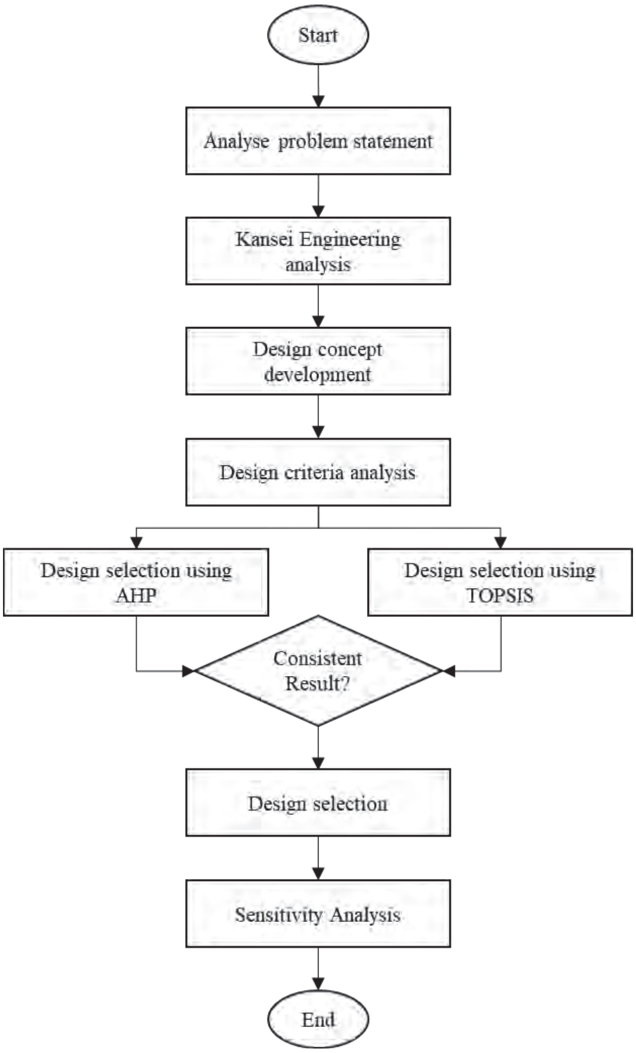

Fig. 1: Research framework.

2.3 Analytical Hierarchy Process (AHP)

In the next step, the research will focus on establishing the Analytical Hierarchy Process (AHP) in determining the most proper rank of the design options. Elements related to the goals, criteria, and relevant alternatives are synthesised from the Kansei Engineering method. Table 1 shows the linguistic variables and the pairwise matrix value.

Table 1: Linguistic variables and values for pairwise matrix for basic AHP [19].

Linguistic variables	AHP Scale
Important	9
Very strongly important	7
Strongly important	5
Weakly important	3
Equally important	1
Intermediate	2,4,6,8

AHP technique is a process that consists of the following steps with the help of a few equations as narrated by [20]:

Step 1: First, decide what needs to be achieved, then narrow down the options. Selecting criteria, a quantifiable aspect that aids in illustrating and specifying options, necessitates practical judgment.

Step 2: Paired comparisons are needed in two segments as follows:

1. Between criteria
2. Between alternatives using each criterion.

The matrices of pairwise comparisons are on a fundamental scale from 1 to 9. The application of AHP is based on expert judgment. One of the major advantages of AHP is that the analysis does not always require statistically significant sample size as reported by [21]. Furthermore, it is obvious that conducting such huge numbers of real expert examinations requires too much effort, time, and financial resources. Thus, an evaluation from a single qualified expert is adequate [22]. As the input data in AHP analysis are based on an expert's perceived judgement, a single input from an expert is sufficient as a representative in the pairwise evaluation of AHP [23]. However, AHP may also be ineffective in research with a high sample size since "cold-called" experts are prone to give arbitrary responses, severely altering the consistency of the assessments [24]. Data is gathered through questionnaires and interviews. The comparison matrix determines which criteria and sub-criteria are more critical than others. Therefore, expert input is critical. An oil skimmer expert was selected as the respondent in this research. The respondent was chosen based on years of expertise and knowledge in the oil skimmer sector. The comparison matrix (n x n), where n is the number of criteria.

Step 3: Let Xij denote the order of preference of the ith factor compared to the jth factor. Then Eq. (2):

$$\text{Xij} = \frac{1}{X_{ij}} \tag{2}$$

Step 4: A normalised pairwise comparison matrix is obtained by adopting the following procedure:

1. Sum of every column.
2. Divide all the numbers in the matrix respectively by the obtained column sum.
3. Average the rows to obtain relative weights.

Step 5: Calculate Eigenvector, maximum Eigenvalue, and Consistency Index (CI). Refer to Eq. (3).

$$CI = \frac{\lambda_{\max} - n}{n-1} \tag{3}$$

Here, λmax is the Eigenvalue corresponding to the matrix of pairwise comparisons, and n is the number of criteria.

Consistency ratio (CR) is defined by referring to Eq. (4):

$$CR = \frac{CI}{RCI} \tag{4}$$

Where (RCI) is a random consistency index.

Generally, a CR value of less than 0.1 is acceptable; otherwise, the pairwise comparisons should be altered to eliminate incoherence. The TOPSIS and sensitivity analysis methods are used to validate the AHP results. First, the TOPSIS analysis is used to confirm the AHP ranking result. The AHP and TOPSIS parameters are the same, but the mathematical computations are different, allowing the TOPSIS ranking result to confirm the AHP ranking result. In terms of sensitivity analysis, the AHP result is examined to determine the result's robustness in relation to the weighted criteria. When modifications in criterion weightage are applied, a complete sensitivity analysis is done to detect the variance in the behaviour of the ranking alternatives.

2.4 Technique of Order Preference by Similarity to Ideal Solution (TOPSIS)

TOPSIS technique is a process that consists of the following steps with the help of equations [25]:

Step 1: Form the decision matrix. Refer to Eq. (5).

$$DM = \begin{matrix} x_{11} & \cdots & x_{1n} \\ \vdots & \ddots & \vdots \\ x_{m1} & \cdots & x_{mn} \end{matrix} \tag{5}$$

Step 2: The normalised decision matrix is done. Refer to Eq. (6)

$$NDM = r_{ij} = \frac{x_{ij}}{\sqrt{(\Sigma_{i=1}^{m} x_{ij}^2)}} \tag{6}$$

Step 3: The weighted normalised decision matrix refers to Eq. (7) (skipped as the weightage is obtained from AHP).

$$V = v_{ij} = w_j . r_{ij} \tag{7}$$

Step 4: The positive and negative ideal solutions for each criterion refer to Eq. (8) and Eq. (9), respectively

$$PIS = V_j^+ = MAX_i(V_{ij}) \tag{8}$$

$$NIS = V_j^- = MIN_i(V_{ij}) \tag{9}$$

Step 5: The geometry distance of each alternative from positive and negative ideal solution is calculated refer to Eq. (10) and Eq. (11), respectively.

$$S_i^* = \sqrt{\Sigma_{j=1}^{n}(V_{ij} - V_j^+)^2} \tag{10}$$

$$S_i^* = \sqrt{\Sigma_{j=1}^{n}(V_{ij} - V_j^-)^2} \tag{11}$$

2.5 Sensitivity Analysis

Validation is a crucial method to be incorporated into any type of research to identify the credibility and validation of results. The application can be widely seen in the domain of renewable energy [26], controller design [27], CNC machining process [28], decision making [29] and others. Moreover, in engineering domains such as structural analysis and optimisation challenges, sensitivity analysis is used to analyse uncertainty. The goal of MCDM sensitivity analysis is to evaluate how changing the weights assigned to the criteria affects the ranking of the options. It also assures the robustness of the offered technique [29]. In addition, a sensitivity analysis is performed to confirm the final ranking recommendation. The sensitivity analysis results in several scenarios show that the best option could change depending on how the assessment criteria are weighted.

3. RESULTS AND DISCUSSION

3.1 Kansei Engineering

To conclude, the design aspects of the oil spill skimmer were identified using (PLS) analysis, which could be referred from [17]. The technique and analysis provide the coefficient plot values, illustrating whether or not that design aspect is essential for designing a portable oil spill skimmer. Certain design aspects have many high positive scores based on the table below. Therefore, certain design factors will be prioritised when developing the oil spill skimmer. On the other hand, several design aspects negatively associate with the Kansei terms. As a result, several design features will be neglected when developing the oil spill skimmer. These design components must be introduced into the design process and those that should be ignored while designing the portable oil spill skimmer (Table 2).

Table 2: List of positive and negative design elements

Positive design elements	Negative design elements
• Compact body appearance	• More than a pair of floating support
• Medium body size	• External oil tank location
• 41-100 kg weight	• Non-oleophilic skimmer material
• Medium-size oil tank	• Bulky body appearance
• A pair of floating support aid	• Round body shape
• Outrigger floating support shape	• Vacuum type skimmer
• Square/rectangular body shape	• Small body size
• Oleophilic skimmer material	• Cylindrical body shape
• Water extraction below 10%	
• Brush type skimmer	
• Internal oil tank storage	
• Less than 5 m/s speed	

3.1.1 Reliability Testing

The acquired data is subjected to reliability testing using a questionnaire to assess whether the data is trustworthy. As a result, Cronbach's Alpha is used to assess the data's dependability. Cronbach's alpha is an internal consistency measurement that depicts the interaction of a group of items in collective data reliability, as represented by the coefficient figures. In contrast, homogeneity refers to one-dimensionality and falls under the Reliability Internal Consistency component, which measures the phenomenon that provides stable and consistent data collection. The questionnaire was conducted for 30 respondents in this research, calculated in Eq. 1. The Cronbach's Alpha calculated using the SPSS programme (Statistical Package for Social Science) is 0.912, indicating that the questionnaire set has a excellent Reliability Coefficient, as shown in Table 3 below. This result demonstrates that the questionnaires fit in, exhibiting the homogeneity of each question. However, originating from various parts demonstrates the dimensionality in measuring every response received, resulting in a more stable and complete analysis for this study.

Table 3: The Cronbach's Alpha Value and Reliability Coefficient [30].

Cronbach's Alpha Value	Reliability Coefficient
$\alpha > 0.9$	Excellent
$\alpha > 0.8$	Good
$\alpha > 0.7$	Acceptable
$\alpha > 0.6$	Questionable
$\alpha \geq 0.5$	Poor

3.1.2 Conceptual Design

The design concept of a portable oil spill skimmer is based on the results obtained from the Kansei Engineering analysis. Figure 2 shows the conceptual designs of the portable oil spill skimmer. Furthermore, the strengths and weaknesses of each design are elaborated in the AHP analysis, where it is compared using pairwise comparison with several sub-criteria.

(a) (b) (c) (d) (e)

Fig. 2: Developed conceptual design of portable oil spill skimmer:
(a) Design 1, (b) Design 2, (c) Design 3, (d) Design 4, (e) Design 5.

3.1.3 Specifications of Each Design

The specification of each design is shown in Table 4.

3.2 Analytical Hierarchy Process (AHP)

The pairwise comparison matrix is created using the hierarchy model from Fig. 3. The number in the pairwise matrix is decided by an expert such as oil and gas or OSRR engineers. This is done to improve the result accuracy of the AHP. The pairwise comparison in this research has three stages: design alternatives, sub-criteria and overall analysis of the criteria, sub-criteria, and design alternatives analysis. Finally, a matrix with regards to the plan will be determined. AHP is used to implement a hierarchy paradigm for structuring product principal decisions. Figure 3 depicts a four-level hierarchy decision mechanism.

Table 4: The specification of each conceptual design

Specification	Design 1	Design 2	Design 3	Design 4	Design 5
Weight	5 – 40 kg	41 – 100 kg	5 – 40 kg	41 – 100 kg	41 – 100 kg
Speed	Less than 1 m/s	Less than 1 m/s	Less than 5 m/s	Less than 1 m/s	Less than 1 m/s
Oil Tank Capacity	Large	Large	Medium	Large	Medium
Oil Suction Capacity	Below 51 L/h	Below 51 L/h	Below 51 L/h	Below 51 L/h	Below 51 L/h
Self-Propelling Capacity	No	Yes	Yes	Yes	Yes
Size	Big	Big	Medium	Medium	Large
Oil Tank Location	External	Internal	Internal	External	Internal
Water extracted with oil	20%	20%	10%	10%	20%
Body shape	Square/Rectangular	Square/Rectangular	Square/Rectangular	Square/Rectangular	Square/Rectangular
Body appearance	Bulky	Bulky	Bulky	Compact	Compact
Portability	Carried by 2 person	Carried by more than 2 person	Carried by 2 person	Carried by more than 2 person	Carried by 2 person
Skimmer type	Brush	Brush	Roller	Roller	Brush
Material	Oleophilic	Oleophilic	Oleophilic	Oleophilic	Oleophilic
Floating support aid shape	Round	Cylindrical	Outrigger	Outrigger	Outrigger
Number of floating support aid	4	2	2	4	4
Support aid type	Polyvinyl chloride (PVC)	Polyvinyl chloride (PVC)	Fibreglass	PVC	Fibreglass

The criteria are labelled as follows: Performance (P), Safety (S), Maintenance (M) and Portability (P). The sub-criteria are labelled as follows: Oil Suction (OS), Manoeuvrability (MA), Strong Body Frame (SBF), Stability (SA), Enclosed Components (EC), Easy to Repair (ER), Easy to Disassemble (ED), Easy to Relocate (ETR) and Lightweight (L). The stability of the design is evaluated according to the number of floating support (closely influenced by the shape of floating support) and floating support shapes (bow-ship shapes are recommended). Furthermore, the oil suction is evaluated according to the types of skimmer material.

This research does not consider the cost as main or sub-criteria since the criteria is not a concerning factor and also was inconsiderate in the previous research as well. The research in the oil and gas field that presents this scenario [31,32]. Moreover, the product will be focusing on specific customers as it is characterised as high variety, low volume production. The basic characteristics of high variety, low volume is the manufacturing of one or few numbers of products designed and produced as per the requirement of customers within pre decided time, with a drawback of high cost of production [33]. Thus, cost is not taken as one of the influencing factor as cost criteria will not affect the pairwise evaluation.

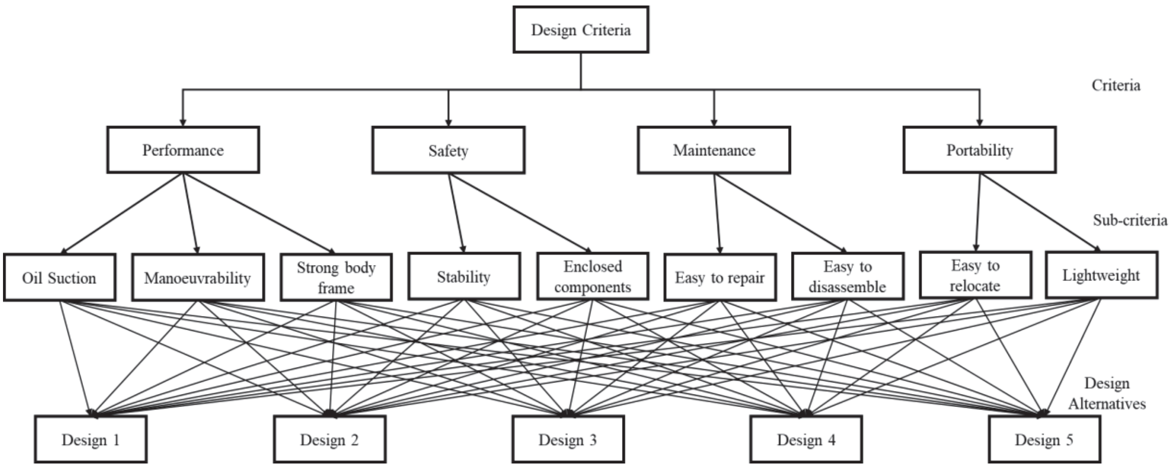

Fig. 3: A hierarchy model for the selection of design concept.

The following table is the pairwise comparison matrix of the design alternatives in each sub-criterion. The table below shows the step-by-step process of the pairwise comparison matrix for the oil suction sub-criteria. This process is done through all the nine sub-criteria. Note that the CR value needs to be less than 0.1. The expert decides the value inside the matrix. All the calculations were done following the steps explained in the methodology. Table 4 shows the pairwise comparison matrix of each design in the oil suction sub-criteria.

Table 5: Pairwise comparison matrix of each design in oil suction sub-criteria

Weight	D1	D2	D3	D4	D5
D1	1	4	3	4	4
D2	0.25	1	2	3	3
D3	0.33	0.5	1	0.5	0.5
D4	0.25	0.33	2	1	1
D5	0.25	0.33	2	1	1

Next, the synthesised matrix and consistency testing were done in Table 5. The same calculation applies to each of the sub-criteria. It is observed that the consistency ratio (CR) is below 0.1; thus, the pairwise comparison evaluation is accepted.

All the sub-criteria are analysed as shown in Tables 4 and 5. In the following analysis, the pairwise comparison of Oil Suction (OS), Manoeuvrability (MA), and Strong Body Frame (SBF) was made to calculate which sub-criteria in the performance criteria has higher weightage. Table 6 shows the pairwise comparison matrix of performance criteria. Table 7 shows the process of averaging the normalised columns. First, the eigenvector was calculated by multiplying to obtain the new vector. As the consistency ratio (CR) value is less than 0.1, thus the pairwise comparison evaluation is accepted.

Table 6: Synthesised matrix for the design alternatives

Wt	D1	D2	D3	D4	D5	SUM	PV	NV	NV/PV	CI	RI	CR
D1	0.4800	0.6480	0.3000	0.4210	0.4210	2.271	0.4542	2.5483	5.6111	0.08	1.12	0.07
D2	0.1200	0.1620	0.2000	0.3150	0.3150	1.1137	0.2227	1.2163	5.4605			
D3	0.1600	0.0810	0.1000	0.0520	0.0520	0.4463	0.0893	0.4689	5.2531			
D4	0.1200	0.0540	0.2000	0.1050	0.1050	0.5846	0.1169	0.6002	5.1332			
D5	0.1200	0.0540	0.2000	0.1050	0.1050	0.5846	0.1169	0.6002	5.1332			
								Total	26.59			
								λ max	5.3182			

Table 7: Pairwise comparison matrix of performance criteria

Wt	OS	MA	SBF
OS	1.0000	3.0000	5.0000
MA	0.3333	1.0000	2.0000
SBF	0.2000	0.5000	1.0000

Table 8: Synthesised matrix for the sub-criteria

Wt	OS	MA	SBF	PV	NV	NV/PV	CI	RI	CR
OS	0.6522	0.6667	0.6250	0.6479	1.9485	3.0071	0.00	0.58	0.0032
MA	0.2174	0.2222	0.2500	0.2299	0.6902	3.0026			
SBF	0.1304	0.1111	0.1250	0.1222	0.3667	3.0013			
					Total	9.01			
					λ max	5.3182			

Table 9: Overall priority vector for the alternatives

Alternatives	Overall PV			
D1	0.3098	0.0587	0.0588	0.1347
D2	0.1800	0.1359	0.1367	0.0531
D3	0.2055	0.2375	0.4580	0.3928
D4	0.1451	0.2840	0.2474	0.1691
D5	0.1596	0.2840	0.0991	0.2503

Table 9 reveals that design 3 (D3) has the most significant value (0.2603 or 26.03 per cent) among the various design concepts suitable for further development. Design 4 (D4) is the second highest, with a value of 0.2356 (23.6 per cent), while design 1 (D1) is the lowest, with a value of just 0.1323 per cent (13.23 per cent). As a result, D3 has been chosen as the preferred design idea, as it provides the most value among the five options.

Table 10: Oil spill skimmer design concept ranking

Alternatives	Priority Vector	Rank
D1	0.1323	5
D2	0.1440	4
D3	0.2603	1
D4	0.2356	2
D5	0.2278	3

3.3 Technique for Order Preference by Similarity to Ideal Solution (TOPSIS)

The TOPSIS multi-criteria decision matrix is utilised in this paper to compare the ranking result with AHP for verification purposes. The step-by-step calculations are explained earlier in the paper. The weights of the criteria were obtained from AHP. The weightage of the criteria and sub-criteria was calculated to identify the global weight of each sub-criteria. The calculation example of the criteria and sub-criteria are as follows. Table 11 shows the global weight of the priority vector obtained from AHP.

Table 11: Global weight of the priority vector obtained from AHP

Criteria	Priority Vector	Sub-criteria	Priority Vector	Global Weight
Performance	0.2776	(OS)	0.6479	0.1799
		(M)	0.2299	0.0638
		(SBF)	0.1222	0.0339
Safety	0.5635	(S)	0.7500	0.4226
		(EC)	0.2500	0.1409
Maintenance	0.1077	(ER)	0.6667	0.0718
		(ED)	0.3333	0.0359
Portability	0.0512	(ETR)	0.2500	0.0128
		(L)	0.7500	0.0384

Table 12 shows the pairwise comparison matrix of the TOPSIS analysis showing the Beneficial (B) and Non-Beneficial (NB) criteria. The value of the Positive Ideal Solution (PIS) is the highest, and the lowest value for the Negative Ideal Solution (NIS) is the beneficial (B) criteria. As for the non-beneficial (NB), it is contrariwise.

Table 12: Pairwise comparison matrix

	B	B	NB	B	NB	B	NB	NB	B
	OS	**M**	**SBF**	**S**	**EC**	**ETR**	**ETD**	**ER**	**L**
D1	5	2	3	3	2	2	2	4	4
D2	3	3	2	3	4	3	3	2	2
D3	4	5	4	4	4	5	5	4	4
D4	3	4	3	4	4	4	4	4	4
D5	3	4	5	4	4	2	2	4	4

The ranking is based on the Ci score, with a more excellent value of Ci indicating the best option among the five options (D1, D2, D3, D4, and D5). After calculating relative closeness (Ci), the value of Ci is used to rank the candidates. Because the D3 alternative has a better value than the other alternatives, it is rated first. D3 >D2 >D4 >D5 >D1 are the outcomes of all alternatives based on better scores, and their ordering preferences are shown in Table 13.

Table 13: The ranking of the best design concept for oil spill skimmer

Alternatives	Si+	Si-	Ci	Rank
D1	0.1199	0.3024	0.7160	5
D2	0.0946	0.2524	0.7274	2
D3	0.1146	0.3078	0.7287	1
D4	0.1206	0.3113	0.7208	3
D5	0.1232	0.3154	0.7192	4

Table 14 shows the ranking result from AHP and TOPSIS. The analysis between AHP and TOPSIS shows that design 3 is chosen as the best conceptual design for a portable oil spill skimmer. This result shows that the ranking from AHP is verified through the TOPSIS analysis.

Table 14: The comparison ranking of AHP and TOPSIS result

Alternatives	AHP Rank	TOPSIS Rank
D1	5	5
D2	4	2
D3	1	1
D4	2	3
D5	3	4

3.4 Sensitivity Analysis

The weighting of the primary criteria significantly impacts the final priority alternatives. As a result, even slight adjustments in the weighting of the criteria might have a significant impact on the final ranking. Furthermore, when extra criterion weights are applied, the ranking's stability must be reviewed because these weights are typically based on highly subjective viewpoints. Consequently, sensitivity analysis was used to test the AHP finding's robustness.

Super Decision software was used to conduct the sensitivity analysis. The performance graph depicts how the alternatives perform when the situation of all parameter's changes. D1 red, D2 blue, D3 black, D4 green, and D5 yellow are the colours of the design choices. In figure 1, the first ranking changes from design idea 3 to design concept 1 when the performance priority vector increases by 65 per cent. Figure 2 shows that when the priority is increased by 75%, design 4 gets the top position, followed by design 5 and design 1. In addition, when maintenance priority is increased by 70%, the ranking in design 2 to rank 3 and design 5 to rank 4 is shown in Fig. 3. Finally, there are ranking modifications for designs 2, 3, 4 and 5 for the portable criteria in Fig. 4, at 15%, although design 3 remains at the top of the ranking.

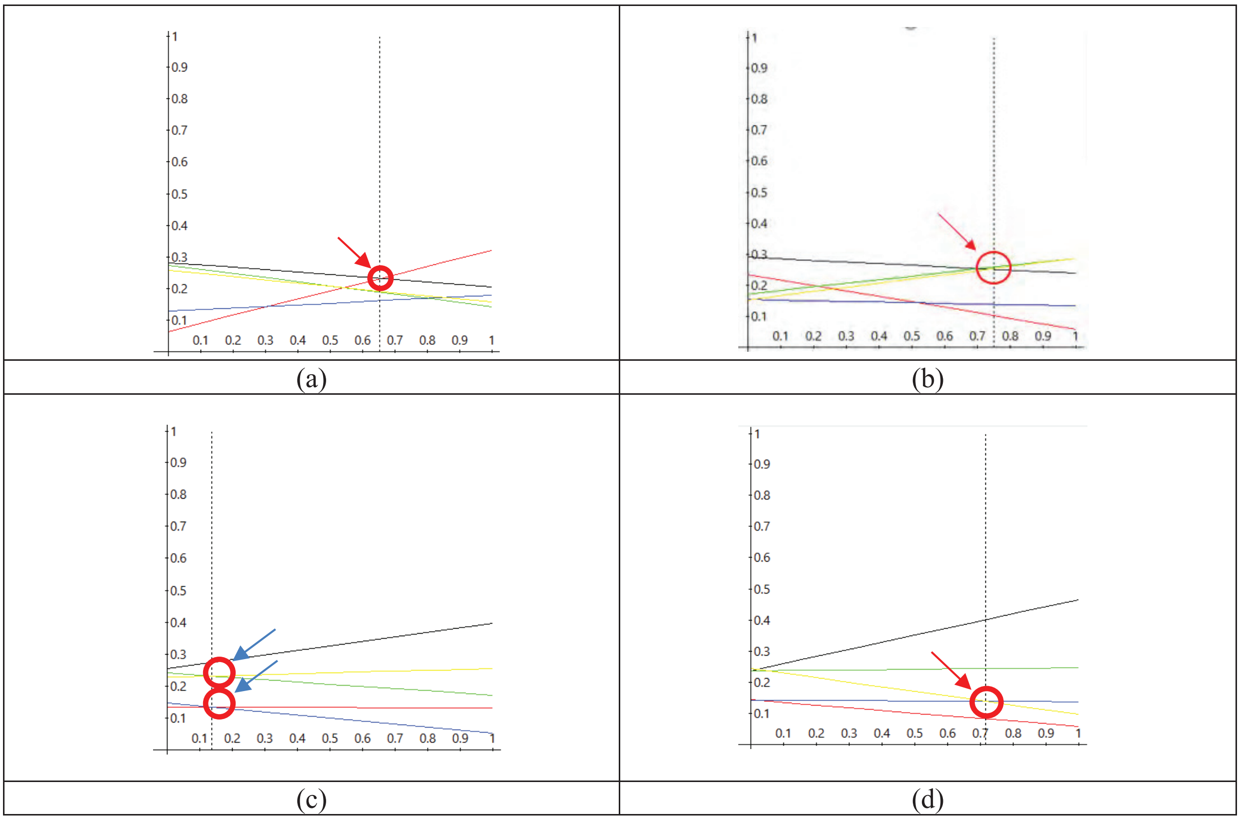

Fig. 4: The sensitivity analysis graph of the criteria; (a) performance, (b) safety, (c) maintenance, (d) portable.

4. CONCLUSION

Extensive studies on product development trends and customer demands, as well as the study on design techniques and methodologies, are required for product design. Designers should be able to see flaws in the design process, sum up the design experience regularly, and think about the meaning of the design from the perspectives of businesses, consumers, and social culture. The correct balance of perceptual inventiveness and rational assessment is required to develop exceptional design works. By combining Kansei Engineering and the Analytical Hierarchy Process, this study extracts the approach of analysing an oil spill skimmer's user demand and technical specification at the early design stage and proposes a technique for assessing and choosing the most appropriate design concepts during the conceptual design stage. TOPSIS and the sensitivity analysis approach were used to verify the AHP results. Design 3 was the best design concept for a portable oil spill skimmer because it has the highest value (26% or 0.26). AHP can help design engineers analyse and choose the optimal design concept based on the criteria and sub-criteria for a decision. Other forms of MCDM methods might be integrated with Kansei Engineering in the future as a recommendation since the findings would be valuable in determining whether other decision methods could be integrated to obtain more precise conclusions. In addition, the number of criteria and sub-criteria could be increased to produce more accurate result.

ACKNOWLEDGMENT

This paper and its research would not have been possible without the exceptional support from the UTeM Short Term Grant no (PJP/2020/FKP/PP/S01775). Furthermore, we are eternally grateful for the generous support from the Center of Research Innovation Management (CRIM) Universiti Teknikal Malaysia Melaka for the publication of this paper.

REFERENCES

[1] Gan Y, Ji Y, Jiang S, Liu X, Feng Z, Li Y, Liu Y. (2021) Integrating aesthetic and emotional preferences in social robot design: An affective design approach with Kansei Engineering and Deep Convolutional Generative Adversarial Network. Int J Ind Ergon. https://doi.org/10.1016/j.ergon.2021.103128

[2] Mondragón S, Company P, Vergara M. (2005) Semantic Differential applied to the evaluation of machine tool design. Int J Ind Ergon. https://doi.org/10.1016/j.ergon.2005.05.001.

[3] Marini CD, Fatchurrohman N, Azhari A, Suraya S. (2016) Product Development using QFD, MCDM and the Combination of these Two Methods. IOP Conference Series: Materials Science and Engineering. http://dx.doi.org/10.1088/1757-899X/114/1/012089.

[4] Azammi AN, Sapuan SM, Ishak MR, Sultan MT. (2018) Conceptual design of automobile engine rubber mounting composite using TRIZ-Morphological chart-analytic network process technique. Defence Technology, 14(4): 268-277. https://doi.org/10.1016/j.dt.2018.05.009.

[5] Zhu GN, Hu J, Ren H. (2020) A fuzzy rough number-based AHP-TOPSIS for design concept evaluation under uncertain environments. Applied Soft Computing Journal, 91: 106228. https://doi.org/10.1016/j.asoc.2020.106228.

[6] Renzi C, Leali F, Di Angelo L. (2017) A review on decision-making methods in engineering design for the automotive industry. Journal of Engineering Design, 28(2): 118-143. https://doi.org/10.1080/09544828.2016.1274720.

[7] Rosli MU, Ariffin MKA, Sapuan SM, Sulaiman S. (2013) Integrating TRIZ and AHP: A MPV's Utility Compartment Improvement Design Concepts. International Journal of Materials, Mechanics and Manufacturing, 1(1): 32-35. https://doi.org/10.7763/IJMMM.2013.V1.7.

[8] Turan FM, Omar B. (2013) The integration of HOQ and fuzzy-AHP for design concept evaluation. Applied Mechanics and Materials, 315: 25-29. https://doi.org/10.4028/www.scientific.net/AMM.315.25.

[9] Tiwari V, Jain PK, Tandon P. (2016) Product design concept evaluation using rough sets and VIKOR method. Advanced Engineering Informatics, 30(1): 16-25. https://doi.org/10.1016/j.aei.2015.11.005.

[10] Song J, Lu Y, Luo J, Huang S, Wang L, Xu W, Parkin IP. (2015) Barrel-shaped oil skimmer designed for collection of oil from spills. Advanced materials interfaces, 2(15): 1-8. https://doi.org/10.1002/admi.201500350.

[11] Kumar SA, Pawar SH, Vishu A, Yashodhan P, Mayuresh P. (2020) Design and fabrication of Oil Collector. International Journal of Progressive Research in Science and Engineering, 1(3): 167-185.

[12] Patil P, Shinde P, Shetty A, Lodha S, Vaidya N. (2017) Design and Fabrication of Oil Skimmer. International Research Journal of Engineering and Technology, 4(5): 2282-2284.

[13] Rahman MA, Manojkumar S, Seenivasan M, Sivaa GM, Vignesh R. (2018) Design and Fabrication of Oil Skimmer. International Research Journal of Engineering and Technology, 6(4): 4-6.

[14] Siva S, Praveen P. (2017) Design and Fabrication of Belt Type Oil Skimmer. International Journal of Engineering Research & Technology (IJERT), 5(7): 1-5.

[15] Abidli A, Huang Y, Cherukupally P, Bilton AM, Park CB. (2020) Novel separator skimmer for oil spill cleanup and oily wastewater treatment: From conceptual system design to the first pilot-scale prototype development. Environ Technol Innov, 18: 100598. https://doi.org/10.1016/j.eti.2019.100598.

[16] Nagamachi M. (2008) Perspectives and the new trend of Kansei/affective engineering. The TQM Journal, 20(4): 290-298. https://doi.org/10.1108/17542730810881285.
[17] Ramanathan R, Abdullah L, Mohamed MS. (2021) The Utilisation of Kansei Engineering in Designing Conceptual Design of Oil Spill Skimmer. In Symposium on Intelligent Manufacturing and Mechatronics, 25: 434-447. https://doi.org/10.1007/978-981-16-8954-3_41.
[18] Ekolu SO, Quainoo H. (2019) Reliability of assessments in engineering education using Cronbach's alpha, KR and split-half methods. Journal of Engineering Education, 21(1): 24-29.
[19] Waris M, Panigrahi S, Mengal A, Soomro MI, Mirjat NH, Ullah M, Azlan ZS, Khan A. (2019) An application of analytic hierarchy process (AHP) for sustainable procurement of construction equipment: Multicriteria-based decision framework for Malaysia. Journal of Mathematical Problem in Engineering. https://doi.org/10.1155/2019/6391431.
[20] Sindhu S, Nehra V, Luthra S. (2017) Investigation of feasibility study of solar farms deployment using hybrid AHP-TOPSIS analysis: Case study of India. Renewable and Sustainable Energy Reviews, (73): 496-511. https://doi.org/10.1016/j.rser.2017.01.135.
[21] Darko A, Chan APC, Ameyaw EE, Owusu EK, Pärn E, Edwards DJ. (2019) Review of application of analytic hierarchy process (AHP) in construction. International Journal of Construction Management, 19: 436-452. https://doi.org/10.1080/15623599.2018.1452098.
[22] Doloi H. (2008) Application of AHP in improving construction productivity from a management perspective. Construction Management and Economics, 26(8): 841-854. https://doi.org/10.1080/01446190802244789.
[23] Schot J, Fischer K. (1993) Introduction: The Greening of the Industrial Firm, Volume 3. Island Press; pp 3-33.
[24] Cheng EW, Li H, Ho DC. (2002) Analytic hierarchy process (AHP):A defective tool when used improperly. Measuring Business Excellence, 6(4): 33-37. https://doi.org/10.1108/13683040210451697.
[25] Jain V, Sangaiah AK, Sakhuja S, Thoduka N, Aggarwal R. (2018) Supplier selection using fuzzy AHP and TOPSIS: a case study in the Indian automotive industry. Neural Computing Applications, 29: 555-564. https://doi.org/10.1007/s00521-016-2533-z.
[26] Parameshwaran MA, Sivaraj S, Venkataram N. (2019) Numerical Simulation and Experimental Validation of Planetary gearbox System Design to Govern Constant Generator Speed in Hydro Power Plant. In IOP Conference Series: Materials Science and Engineering, https://doi.org/10.1088/1757-899X/624/1/012008.
[27] Abdullah L, Jamaludin Z, Chiew TH, Rafan NA, Mohamed MS. (2012) System identification of XY table ballscrew drive using parametric and non parametric frequency domain estimation via deterministic approach. Procedia Engineering, 41: 567-574. https://doi.org/10.1016/j.proeng.2012.07.213.
[28] Escudero GG, Bo P, González-Barrio H, Calleja-Ochoa A, Bartoň M, de Lacalle LNL. (2022) 5-axis double-flank CNC machining of spiral bevel gears via custom-shaped tools—Part II: physical validations and experiments. International Journal of Advanced Manufacturing Technology, 119(3-4): 1647-1658. https://doi.org/10.1007/s00170-021-08166-0
[29] Haddad M, Sanders D. (2018) Selection of discrete multiple criteria decision making methods in the presence of risk and uncertainty. Operations Research Perspectives, 5: 357-370. https://doi.org/10.1016/j.orp.2018.10.003.
[30] Vaske JJ, Beaman J, Sponarski CC. (2016) Rethinking Internal Consistency in Cronbach's Alpha. Leisure Science, 39: 163-173. https://doi.org/10.1080/01490400.2015.1127189.
[31] Dey PK. (2004) Analytic hierarchy process helps evaluate project in Indian oil pipelines industry. International Journal of Operations and Production Management, 24: 588-604. https://doi.org/10.1108/01443570410538122.
[32] Al-Marri AN, Nechi S, Ben-Ayed O, Charfeddine L. (2020) Analysis of the performance of TAM in oil and gas industry: Factors and solutions for improvement. Energy Reports, 6: 2276–2287. https://doi.org/10.1016/j.egyr.2020.08.012.
[33] Bandyopadhyay S. (2019) Introduction to production and operations concept. Production and Operations Analysis: Traditional, Latest, and Smart Views. 1st edition CRC Press; pp 1-8.

https://doi.org/10.31436/iiumej.v24i1.2223

TERMINAL CONTROL AREA COMPLEXITY MEASUREMENT USING SIMULATION MODEL

RULLY MEDIANTO[1,2*], NAFLAH MUTIARA ADINDA[1], YAZDI IBRAHIM JENIE[1], HISAR MANONGAM PASARIBU[1] AND HARI MUHAMMAD[1]

[1]*Faculty of Mechanical and Aerospace Engineering, Bandung Insitute of Technology, Bandung, Indonesia*
[2]*Faculty of Aerospace Technology, Institut Teknologi Dirgantara Adisutjipto, Yogyakarta, Indonesia*

[*]*Corresponding author: hmpasaribu@itb.ac.id*

(Received: 9th November 2021; Accepted: 18th June 2022; Published on-line 4th January 2023)

ABSTRACT: Traffic density in the terminal control area will increase flight safety risks. One effort to reduce the risk is to minimize the controller's workload when affected by air traffic complexity. This research uses a simulation model to measure air traffic complexity in terminal control areas. The aircraft performance model has been constructed from ADS-B data and represents the aircraft movement in the terminal control area of Soekarno-Hatta International Airport. The simulation model can detect and resolve conflicts to keep separations between aircraft at a specified minimum separation limit. Air traffic complexity measurement uses several indicators, i.e., aircraft density, number of climbing and descending aircraft, aircraft type mixing, conflict control, aircraft speed difference, and controller communication. The weighting factor for each indicator has been obtained from Jakarta Air Traffic Service Center (JATSC) controller perception using an analytic hierarchy process. The simulation results show that the variation of resolution type affects the complexity level significantly. The results of this study can be used as consideration for improving air traffic control procedures and air space structures.

ABSTRAK: Kepadatan trafik di kawasan terminal kawalan bakal menyebabkan peningkatan risiko keselamatan penerbangan. Salah satu cara bagi mengurangkan risiko adalah dengan meminimumkan beban kerja pengawal yang terlibat dengan kesesakan trafik udara. Kajian ini menggunakan model simulasi bagi mengukur kesesakan trafik udara di kawasan terminal kawalan. Model pretasi pesawat telah dibina menggunakan data ADS-B dan ini mewakili pergerakan pesawat di terminal kawalan lapangan terbang antarabangsa Soekarno-Hatta. Model simulasi ini dapat mengesan konflik dan membuat resolusi bagi mengekalkan penjarakan antara pesawat mengikut had penjarakan minimum yang ditetapkan. Beberapa indikator telah digunakan bagi mengukur kerumitan trafik udara, iaitu: ketumpatan pesawat, bilangan pesawat mendaki dan menurun, jenis pesawat, kawalan konflik, perbezaan kelajuan pesawat dan pengawal komunikasi. Faktor pemberat bagi setiap indikator telah diperoleh daripada pengawal persepsi Pusat Servis Trafik Udara Jakarta (JATSC) menggunakan proses analisis hierarki. Keputusan simulasi menunjukkan pelbagai jenis resolusi mempengaruhi tahap kerumitan dengan ketara. Hasil kajian ini boleh digunakan bagi menambah baik prosedur kawalan trafik udara dan struktur ruang udara.

KEYWORDS: *terminal control; air traffic complexity; simulation model; analytic hierarchy process*

1. INTRODUCTION

The Terminal Control Area (TCA) is airspace with the most complex and dense system compared to other airspace sectors. Three modes of flight operations run simultaneously: arrival, departure, and cross-flight [1]. TCA is highly sensitive to changes in traffic, weather, flight procedures, runway used, and other unusual events. The assessment of the system's performance is important and is affected by the system's complexity [2].

The air traffic complexity rate can be very high due to the traffic intensity and patterns in mutual interactions between different traffic flows and individual aircraft in the TCA. The increasing complexity of the TCA will increase the complexity of controller tasks and result in increased workload [3]. The management of traffic flow and airspace can be carried out correctly to avoid excessive controller workload if the measurement and prediction of air traffic complexity can be carried out accurately [4].

Table 1: Air traffic complexity indicators summary

Air Traffic Complexity Indicators	Arad [8]	Grossberg [9]	Mogford et al. [10]	Pawlak et al. [11]	Laudeman et al. [12]	Majumdar et al. [13]	Chatterji et al. [14]	Koros et al. [15]	Diaconu et al. [4]
Sector design/geometry	√		√			√			
Aircraft density/volume	√	√		√		√	√	√	
Aircraft speed difference				√	√	√	√		√
Emergency operations								√	
Altitude change	√			√	√	√	√		
The horizontal distance between aircraft	√		√	√	√		√		
The vertical distance between aircraft	√			√		√	√		
Aircraft type mixing	√	√	√	√				√	√
Frequency of ATCo's communication		√	√	√					
Flight entering and exiting the sector						√			
Potential conflict control	√		√		√		√		
Number of cruising aircraft						√	√		√
Number of climbing/descending aircraft	√	√	√	√		√	√		√
Weather condition			√	√					√
Aircraft heading change/difference				√	√				
Special flight	√		√	√				√	
Radiofrequency congestion	√		√						
Number of intersecting airways	√								
Restricted airspace	√		√						
The proximity of sector boundary	√			√					
ATC's procedure			√					√	

It is necessary to consider the interactions between individual aircraft and their flight characteristics to determine complexity more precisely. The interactions involve possible conflicts and the tendency for aircraft movement to converge at one point. [5]. There are at least nine references from Mogford et al., Diaconu et al. and Dervic and Rank (2 that mention various indicators of complexity [4,6,7]. Table 1 shows the summary of some complexity indicators.

Air traffic complexity can be measured by experts, who have experience controlling air traffic under various conditions, or by the complexity indicator obtained from air traffic data and the number of interactions between aircraft in a particular sector [16]. Another method to determine air traffic complexity is using a dynamic weighted network model. The nodes represent aircraft, waypoints, and airways in the network model. The total weights of all network edges represent air traffic complexity [17]. Andrasi et al. used an artificial neural networks model to estimate air traffic complexity. The best configuration of artificial neural networks was determined by a genetic algorithm [18].

This research developed an ATM model simulation in the TCA using MATLAB to reflect aircraft movements and the air traffic control process. The simulation model is then used to analyze air traffic complexity in the TCA, specifically at Soekarno-Hatta International Airport, Jakarta. The simulation model has several advantages in describing the air traffic system and its complexity, i.e. the movement of the aircraft can be visualized to analyze and validate it [19]. The simulation parameters also can be modified easily to obtain various scenarios.

2. MODELLING

2.1 System Description

The ATM system model represents arrival and departure operations for Runway 25R and 25L on Soekarno-Hatta International Airport - Jakarta (JAKARTA). The arriving aircraft will enter the TCA from the en-route airspace through the transition points. The aircraft then fly towards the runway following a specific trajectory profile defined by some waypoints. The arrival trajectory profile refers to Standard Terminal Arrival Routes (STAR). The departing aircraft enter the TCA from the aerodrome control area and fly to the airway following the Standard Instrument Departure trajectory profile (SID). The information about STAR and SID can be accessed in the Aeronautical Information Regulation and Control (AIRAC) as a supplement to the Aeronautical Information Publication (AIP) published by the Directorate General of Civil Aviation (DGCA) of Indonesia [20].

With Flight Management Computer (FMC) support, aircraft can automatically fly along with these profiles. Under certain circumstances, the aircraft must follow the instruction from the air traffic controller containing the aircraft's direction (heading), altitude, and speed changes, often referred to as vectoring. Arrival operations have more significant conflict potential than departures because aircraft have trajectories that converge, especially when entering a merging point. Aircraft speed on arrival will also experience a reduction so that the aircraft in front tends to be overtaken by the aircraft behind it. The departure model has a smaller potential for conflict than the arrival because the trajectory tends to be diverging. Potential conflicts with arriving aircraft are also minimal due to differences in altitude and flight path.

There are six TCA sectors related to Runway 25R and 25L are modeled in this study: Jakarta Lower Control North (LN), Jakarta Lower Control Center (LC), Jakarta Lower Control East (LE), Jakarta Terminal West (TW), Jakarta Terminal East (TE), and Jakarta Terminal South (TS). Each sector has boundaries described by latitude-longitude, altitude/flight level, and radius from ATC head radar. Information about the boundaries can be accessed in Standard Operating Procedures Air Traffic Services Approach Control Service published by Airnav Indonesia Branch of Jakarta Air Traffic Service Center (JATSC) [21]. The arrival traffic model has six trajectory profiles, and the departure traffic model has ten. Complete trajectory profiles and TCA sectors related to the Runway 25R and 25L air traffic model are shown in Fig . 1.

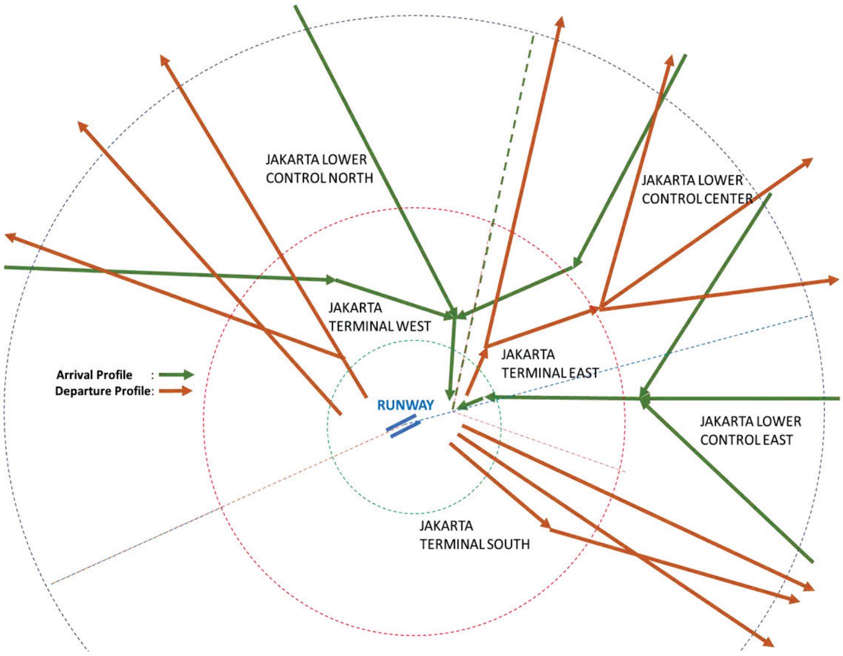

Fig. 1: Trajectory profiles and TCA sectors related to Runway 25R and 25L.

2.2 Air Traffic Model

The air traffic model was built using MATLAB software by combining discrete-event and agent-based models. The wind speed model was added as an environmental element influencing the system. The wind speed consists of wind velocity and direction represents the weather condition. Each aircraft has a fixed parameter that will not change during simulation: aircraft type and trajectory profile based on SID/STAR. There are also dynamic parameters that will change during simulation; these parameters are:

- Position: In the form of local NED (North, East, Down) coordinates with a reference point at the NOKTA waypoint (X, Y, Z);
- Airspeed: Airspeed in the local NED direction (Vx, Vy, and Vz);
- Waypoint: present the waypoint to which the aircraft is headed;
- Heading: Heading aircraft relative to local north;
- Distance to waypoint: the distance of the aircraft to the next waypoint;
- Right of Way: priority of aircraft when heading/being on the same track;
- Conflict status: free from conflict or not;
- Resolution: selected conflict resolution mode (vectoring, speed control, or altitude control);
- TAS and GS: aircraft true airspeed and ground speed;
- Vertical speed: vertical aircraft speed when climbing (+) or descent (-); and
- RADAR radius: radius from RADAR.

Each trajectory has a unique profile based on STAR and SID published in Aeronautical Information Publication (AIP) [20]. Each aircraft will move along the trajectory with the waypoint as profile guidance. The aircraft distance relative to the waypoint is obtained by the equation [22]:

$$dx_t = X_{wp} - X_t \tag{1}$$

$$dy_t = Y_{wp} - Y_t \tag{2}$$

$$dz_t = Z_{wp} - Z_t \tag{3}$$

$$d_{s,t} = \sqrt{(dx_t)^2 + (dy_t)^2 + (dz_t)^2} \tag{4}$$

With,

X_t, Y_t, Z_t: aircraft coordinates on each coordinate axis;
X_{wp}, Y_{wp}, Z_{wp}: waypoint coordinates on each coordinate axis;
dx_t, dy_t, dz_t: distance to the waypoint on each coordinate axis;
$d_{s,t}$: aircraft distance relative to the waypoint.

After getting the distance relative to the waypoint using the above equation, then the heading angle can be calculated relative to the waypoint (θ_t) apply the equation:

$$\theta_t = \tan^{-1}\frac{dx_t}{dy_t} \tag{5}$$

The aircraft heading angle relative to the waypoint is used to calculate the relative aircraft speed on each axis (Vx, Vy, Vz) using the equation below:

$$Vx_t = \begin{cases} = V_t \cos\theta_t\,, & dz_t = 0 \\ \neq \left(\sqrt{{V_t}^2 - {Vz_t}^2}\right)\cos\theta_t & dz_t \neq 0 \end{cases} \tag{6}$$

$$Vy_t = \begin{cases} = V_t \sin\theta_t\,, & dz_t = 0 \\ \neq \left(\sqrt{{V_t}^2 - {Vz_t}^2}\right)\sin\theta_t & dz_t \neq 0 \end{cases} \tag{7}$$

$$Vz_t = \begin{cases} = 0, & dz_t = 0 \\ \neq 0 & dz_t \neq 0 \end{cases} \tag{8}$$

Furthermore, it can be determined the position of the aircraft for each axis at a time (t + 1) through the equation:

$$X_{t+1} = (Vx_t * \delta t) + X_t \tag{9}$$

$$Y_{t+1} = (Vy_t * \delta t) + Y_t \tag{10}$$

$$Z_{t+1} = (Vz_t * \delta t) + Z_t \tag{11}$$

The separation between aircraft is maintained by using conflict detection and resolution models. It is necessary to calculate horizontal (d_{hor}) and vertical (d_{ver}) separations between aircraft (a and b) to check whether the separation between aircraft is still safe (does not exceed the minimum limit) using the following equation:

$$d_{hor} = \sqrt{(X^a - X^b)^2 + (Y^a - Y^b)^2} \tag{12}$$

$$d_{ver} = \sqrt{(Z^b - X^a)^2} \tag{13}$$

X, Y, and Z are the aircraft coordinates a and b on each coordinate axis.

After the separation between aircraft is known, whether the separation is still safe or if there has been a potential conflict (smaller than the specified minimum separation buffer) can be checked. Conflicts at TCA more often occur when the plane is heading to the merging point. If several aircraft experience conflict, it will be determined which aircraft gets the Right of Way (ROW) based on the closest distance to the merging point. The aircraft that gets the first ROW continues to fly following the specific trajectory without resolving conflict. The other aircraft should make specific maneuvers as part of conflict resolution.

The flowchart of the aircraft's movement in the simulation model is shown in Fig. 2. The model has three conflict resolution modes: vectoring, airspeed control, and altitude control.

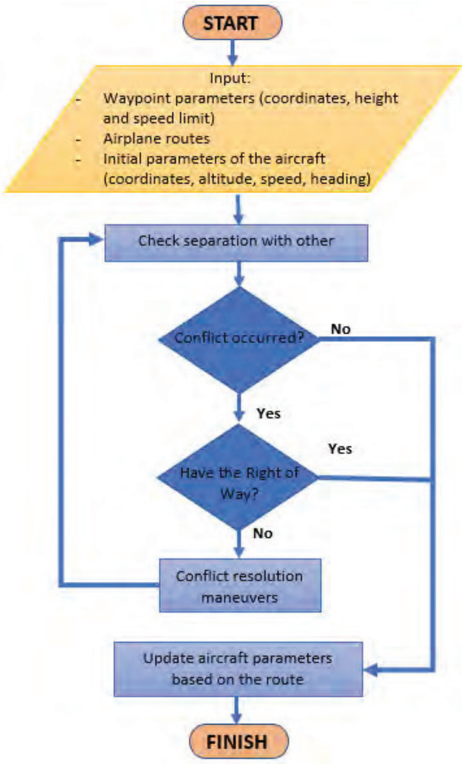

Fig. 2: Flow chart of aircraft movements in the simulation model.

2.3 Flight Parameter Model

Flight parameter models were extracted from ADS-B data provided by FlightRadar24. The ADS-B data was collected from more than 38800 flights that departed and landed at Soekarno-Hatta International Airport, Jakarta [23]. The models included five aircraft flight parameters: Airbus A320, Boeing B737, Airbus A330, Boeing B777, and Boeing B787. Machine learning was used to handle a large quantity of ADS-B data to identify the phase of the flight and the time when the aircraft flew across specific waypoints. One advantage of this technique is that ADS-B data can be efficiently and cost-effectively gathered over the internet. ADS-B data was combined with weather data from Aviation Meteorological Information System in Meteorological, Climatology, and Geophysical Agency (BMKG) to develop the flight parameter model [24].

The waypoints used for analysis were the waypoints flown by aircraft using Runway 25R and 25L for departing and arriving. The waypoint information was obtained from the Soekarno Hatta International Airport Terminal Chart published by the Indonesia DGCA [20]. The K-Nearest Neighbor algorithms processed flight parameters from ADS-B data when the aircraft had the nearest position to specific waypoints within a radius of 1 NM. The altitude and the vertical speed were processed straight from the ADS-Data. The true airspeed was generated from the ground speed and wind speed data from weather data.

Three probability distribution functions (Normal Distribution, Beta Distribution, and Gamma Distribution) approached flight parameter models using maximum likelihood estimation. The best distribution was determined using Kolmogorov-Smirnov Test. The flight parameters for this research used the mean value from the models. Validation was carried out on previous research by comparing the estimated parameters with flight parameters from the Eurocontrol Aircraft Performance Database [25] and the reference parameter from the JAKARTA (WIII) Terminal Chart issued by the Indonesia Directorate General of Civil Aviation [26]. Table 2 shows some of the aircraft's flight parameter models when flying by specific waypoints.

Table 2: Flight parameter models for each type of aircraft when flying by waypoints

Waypoint	Altitude (feet)					True Airspeed (knot)					Vertical Speed (m/s)				
	A320	B737	A330	B777	B787	A320	B737	A330	B777	B787	A320	B737	A330	B777	B787
ABILO	35834	35834	35834	35834	35834	436	436	436	436	436	836	836	836	836	836
AJUNA	7758	7339	7131	6492	7208	287	283	279	285	278	2524	2473	2484	2115	2283
ALAMO	38228	38228	38306	38228	38228	450	450	450	477	477	425	425	425	524	524
ARKAP	2227	2215	2368	2350	2300	190	180	187	190	183	216	239	263	366	305
BUNIK	22799	22771	21798	22370	22788	395	373	389	389	391	1838	1630	1619	1543	1562
CA	10107	10929	11161	11161	11161	455	454	454	455	455	777	696	1193	1193	1193
CARTA	14032	14032	14032	13618	14101	314	336	335	330	326	1558	1789	1465	1396	1407
CORIL	8482	9483	9483	9483	9483	464	458	458	458	16	890	1096	1096	1096	1096
DAPIK	1262	1310	1320	1381	1291	217	214	208	212	207	371	560	384	601	397
DENDY	24419	24419	24124	23850	24169	378	378	390	392	393	1259	1259	1389	1554	1511
DOLTA	27591	29814	28087	26436	32599	446	453	443	470	473	1007	1171	1377	1479	1918
ESALA	3316	3317	3371	3627	3489	288	286	285	286	282	1271	1256	1227	1141	1251
FRIDA	32125	33409	33409	33409	33409	463	456	463	463	463	776	731	776	776	776
GAPRI	6909	6682	6912	7103	7335	375	365	378	375	362	1699	1538	1494	1105	1119
GASPA	9155	9335	8314	9020	9056	449	384	430	429	431	1180	775	1714	1750	992
HLM	4093	4203	4363	4620	4620	354	361	20	361	374	1987	2263	2093	3375	3375
IMU	8813	8765	8964	9254	9254	425	423	424	438	438	1350	1450	1554	1823	1823
KURUS	9418	8932	9079	9273	9273	447	432	460	469	469	2046	1715	1961	2338	2338
LARAS	21015	21015	19140	22357	19524	397	397	402	434	405	1778	1778	1578	1968	1856
LEPAS	29868	29868	29868	34739	31644	457	457	457	480	483	874	874	874	211	1040
NABIL	4425	4217	4121	4298	4298	356	346	350	350	367	2111	2259	1924	2338	2338
NADIN	7942	7670	7944	8185	8185	405	394	401	399	399	1731	1554	1591	1362	1362
NOKTA	11931	12443	12207	12385	13008	290	284	290	295	295	1403	1185	1185	1136	1132
PRIOK	3537	3712	3395	3425	3309	218	216	215	212	211	643	802	582	648	663
PW	7538	7847	9144	9144	9144	433	423	423	437	437	1235	966	1738	1738	1738
RAMAL	17531	17660	16867	17489	17576	342	329	338	343	345	1636	1426	1543	1535	1559
RAMBU	6905	6998	6768	7241	7202	255	256	259	262	262	1050	1112	1005	1088	1186
RATIH	15998	15998	16475	18685	16634	377	377	373	400	379	2034	2034	1737	2071	1870
SIKAD	18000	17300	17675	17675	17675	358	362	414	414	414	2100	2300	2800	2800	2800
TEGAR	2122	2146	2110	2115	2031	247	249	245	247	246	902	1027	813	899	857
WETES	5062	4967	5088	5284	5043	331	327	333	330	320	1596	1511	1604	1453	1335
WINAR	6157	5757	5409	5016	5271	278	274	264	273	271	2635	2595	2535	2144	2429

2.4 Air Traffic Complexity

The calculation of air traffic complexity at TCA begins by determining the indicators affecting the complexity and relevance of the airspace sector. After that, the weight of each indicator needs to be determined using the analytic hierarchy process (AHP) method.

The most mentioned indicators relevant to the TCA airspace sector can be selected based on Table 1. Hence, air traffic complexity measurement in this paper uses seven indicators: air traffic density (N_{in}), number of climbing (N_{clb}) and descending (N_{des}) aircraft, aircraft type mixing (T_{typ}), potential conflict control (crossing and overtaking conflict, T_{trf}), aircraft speed difference (T_{spd}), and frequency of controller's coordination or communication (T_{com}). The weight of each indicator was obtained using an analytic hierarchy process (AHP) method.

The first step in the AHP method was to collect input data with pairwise comparisons of the indicators. Complexity indicators were paired with a rating that determined which indicator was more critical. This data was collected by a survey involving respondents from experts and practitioners. The questionnaire was created to assess the relative importance (weight value) of the target respondents, experts, and air traffic controllers from Airnav Indonesia, notably the Jakarta Air Traffic Services Center (JATSC). The questionnaire was filled out by respondents using online media. The second step was to average the input comparison values using the Row Geometric Mean Method (RGMM). The average r_i value was determined using the following equation.

$$r_i = exp\left[\frac{1}{N}\sum_{j=1}^{N} ln(a_{ij})\right] = \left(\prod_{i=1}^{N} a_{ij}\right)^{\frac{1}{N}} \tag{14}$$

The comparison matrix A = a_{ij} with dimensions of N×N, N = 7 (number of indicators). The third step was calculating the first eigenvector of matrix A (Eigen 1 in the E1 matrix). The fourth step was calculating the second eigenvector (Eigen 2 in the E2 matrix). Then proceed to the fifth step, calculating the difference between E1 and E2. The sixth step was to assess the consistency of the respondent's answers in the following way.

a. Calculate the Weighted Sum Vector (WSV) by multiplying the rows of matrix A by matrix E1.
b. Divide each element of the WSV matrix by each element of the E1 matrix to obtain the Consistency Vector (CV).
c. Calculate the lambda (λ) by averaging CV and calculating the Consistency Index (CI) using the following equation.

$$CI = \frac{\lambda - N}{N-1} \tag{15}$$

d. Divide CI by the Random Consistency Index to get the Consistency Ratio (CR) (RI).

$$CR = \frac{CI}{RI} \tag{16}$$

Table 3 shows the RI value for a given N value.

Table 3: Random consistency index [4].

N	1	2	3	4	5	6	7	8	9	10
RI	0	0	0,58	0,9	1,12	1,24	1,32	1,41	1,45	1,49

After knowing the value of each indicator and its weight of importance, the general equation for the function of air traffic complexity at TCA can be calculated.

$$\begin{aligned} F_c = (W_{in} \times N_{in}) + (W_{clb} \times N_{clb}) + (W_{des} \times N_{des}) + \left(W_{typ} \times T_{typ}\right) \\ + \left(W_{rtf} \times T_{rtf}\right) + \left(W_{spd} \times T_{spd}\right) + (W_{com} \times T_{com}) \end{aligned} \tag{17}$$

Air traffic complexity values were calculated for several scenarios. The scenarios were varied on the inter-arrival time (IAT) and the percentage of possible resolution types (speed control, altitude control, and vectoring).

3. RESULTS AND DISCUSSION

The simulation animation is used to validate the model by observing the model's behavior while the simulation is running [27]. Some entities (aircraft) are observed moving from the time they enter the system to the time they leave the system to determine whether the aircraft moves correctly according to the predetermined modeling concept and whether the conflict detection and resolution have been applied.

The animation observations show that the entity followed its arrival and departure trajectory according to the predetermined trajectory route. The data validation and operational graphics results also show that the model correctly implemented the applied conflict detection and resolution. No aircraft violated the minimum separation rules when the simulation ran in normal conditions.

The waypoint modeling for Soekarno-Hatta International Airport is based on local coordinates of NED with NOKTA as a reference point. The model is used to simulate the air traffic in the TCA, especially at JAKARTA TCA for Runway 25R and 25L. The model visualized 2-dimensional forms that moved for each unit of time. Flight parameters were estimated from ADS-B data for specific waypoints.

The movement of the aircraft in the simulation were repreented by a green dot when there was no conflict, a yellow dot when there was a potential conflict, and a red dot when there was a conflict with other aircraft. The simulation had twelve entry points and ran for 7200 units or the equivalent of 7200 seconds. There were three scenarios, each was running for just one resolution mode choice to solve the traffic conflict. Air traffic complexity was measured by calculating seven complexity indicators recorded during the simulation. Visualization of the simulation model is shown in Fig. 3.

A total of 119 questionnaire respondents from the JATSC controller provided information to determine which complexity indicator was more critical among the indicators that have been paired. The questionnaire results were then processed by AHP to obtain the weighting value for each indicator, as shown in Table 4.

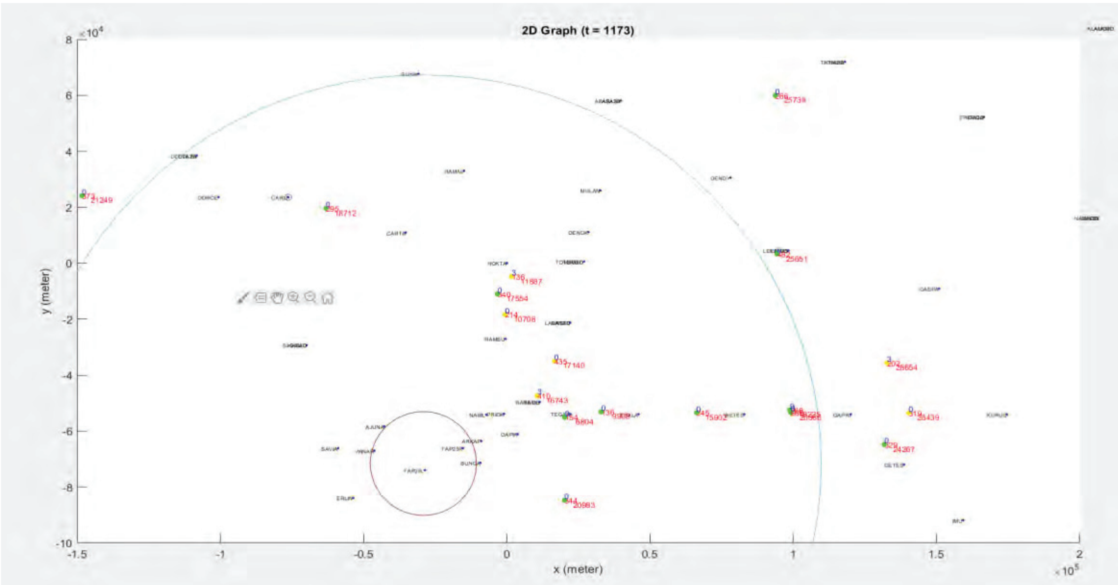

Fig. 3: Visualization of the simulation model with aircraft movement representation.

The level of consistency (Consistency Ratio) of the AHP was 0.72% which means that the answers were consistent (CR < 10%). This CR value indicated that the weighting values that were obtained could be used in the simulation. As shown in the table, the indicator that most influences complexity is the potential conflict control for crossing and overtaking conflict, with a weighting value of 38.87%. The indicator with the smallest weighting value is the number of climbing aircraft (8.99%). Thus, the general function for air traffic complexity at JAKARTA TCA can be written as follows.

$$F_c = (0.1218 \times N_{in}) + (0.0899 \times N_{clb}) + (0.1078 \times N_{des}) + \left(0.1015 \times T_{typ}\right) + \left(0.3887 \times T_{rtf}\right) + \left(0.0924 \times T_{spd}\right) + (0.0980 \times T_{com}) \quad (18)$$

Table 4: Weighting value of each complexity indicator

Complexity Indicators	Weighting Value
Air Traffic Density (N_{in})	12.18%
Number of Climbing Aircraft (N_{clb})	8.99%
Number of Descending Aircraft (N_{des})	10.78%
Aircraft Types Mixing (T_{typ})	10.15%
Potential Conflict Control (T_{rtf})	38.87%
Aircraft Speed Difference (T_{spd})	9.24%
Frequency of Air Traffic Controller's Coordination or Communication (T_{com})	9.80%

Function (18) shows that the number of descending aircraft is more critical than the number of climbing aircraft in influencing air traffic complexity. It is also shown that the aircraft type mix is more important than the aircraft speed difference. This result is different from Diaconu et al. (2014) in which the climbing was more important than the descent, and the aircraft speed difference was more important than the aircraft type mix [4]. The controller's significant preference with the same indicator may vary for different air traffic service units. So it is necessary to analyze the weighting value of the complexity indicator for related air traffic service units before measuring the air traffic complexity in specific airspace sectors.

Controller task load is represented by controller communication time in the function through the frequency of the controller's coordination or communication (T_{com}). The complexity rate will increase the more frequently the controller coordinates or communicates with the pilot and another controller. The weighting of communication time in the complexity function is more critical than the number of climbing aircraft (N_{clb}) and Aircraft Types Mixing (T_{typ}). In addition to task load, other factors such as equipment capability, individual preferences, and cognitive controller strategies are required to obtain a complete picture of the correlation between complexity and workload [28].

The simulation run for ten repetitions with aircraft type mix is a 9:1 ratio for Medium type (Boeing B737 and Airbus A330) and Heavy type (Airbus A330, Boeing B777, and Boeing B787). When entering the arrival point, time separation is set to 4 minutes, and departure is about 6 minutes. This gives high traffic density to the model. The minimum separation is 5 NM with a buffer of 15 NM to solve the potential conflict. A graphic of complexity measurement from a simulation (altitude control mode only) for each TCA sector is shown in Fig. 4.

From Fig. 4, Jakarta Lower Control North and Jakarta Terminal West have a high rate of complexity relative to the other sectors. Jakarta Terminal East has the lowest complexity rate compared with the others on Runway 25R and 25L operation. The model can show the complexity rate comparison between sectors. It can be used to assess what sector has a higher rate of complexity for a particular runway operation, and the management should take some action to balance it.

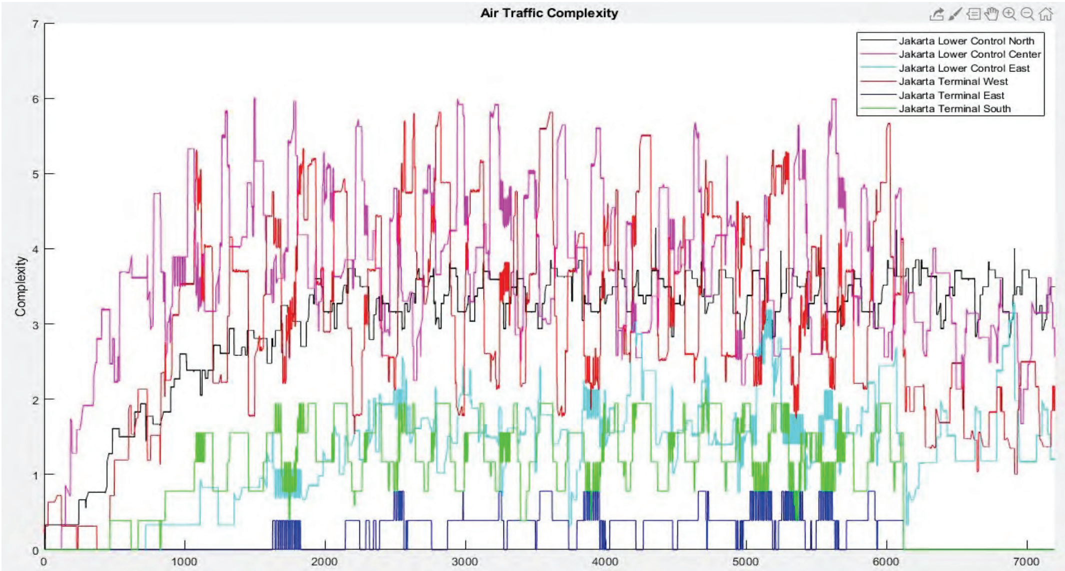

Fig. 4: Result of complexity measurement (altitude control mode only).

Simulation results of air traffic complexity measurement and the number of potential conflicts for specific resolution mode scenarios in each sector are shown in Fig. 5 and 6.

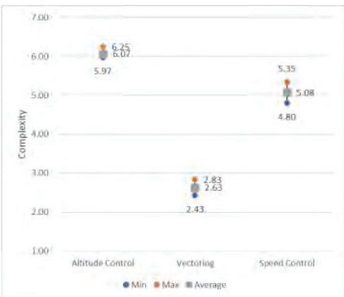

(a) Jakarta Lower Control North

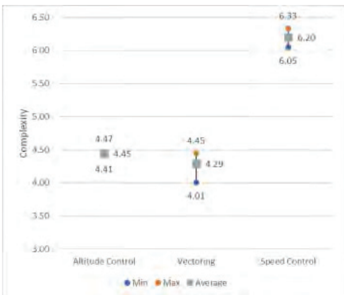

(b) Jakarta Lower Control Center

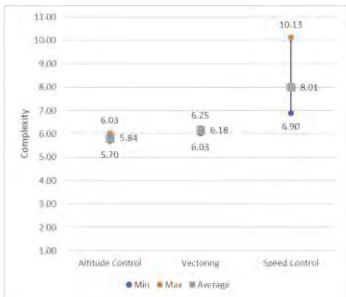

(c) Jakarta Lower Control East

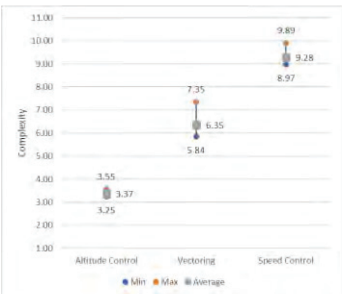

(d) Jakarta Terminal West

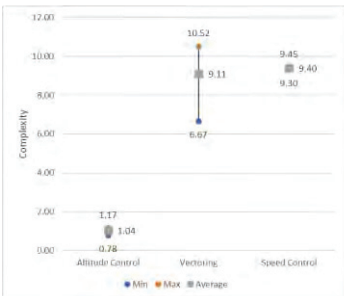

(e) Jakarta Terminal East

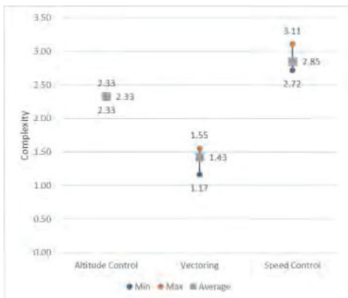

(f) Jakarta Terminal South

Fig. 5: Values of air traffic complexity on sectors for specific resolution mode's scenario.

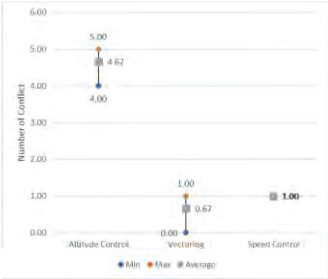

(g) Jakarta Lower Control North

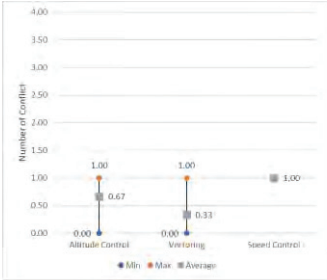

(h) Jakarta Lower Control Center

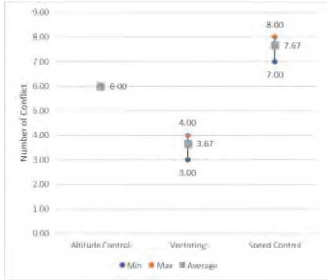

(h) Jakarta Lower Control East

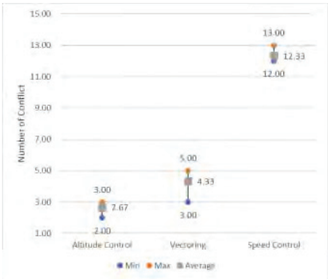

(i) Jakarta Terminal West

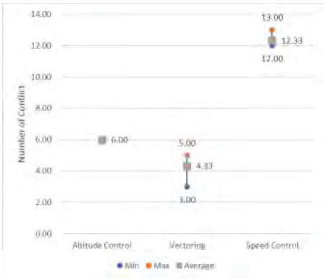

(j) Jakarta Terminal East

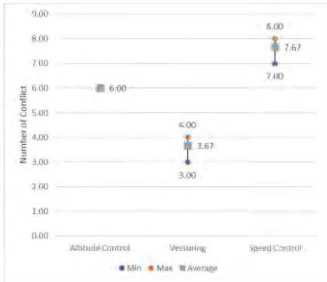

(k) Jakarta Terminal South

Fig. 6: Number of potential conflicts on sectors for specific resolution mode's scenario.

Figure 5 shows that the speed control mode assigns a higher complexity rate for all sectors except Jakarta Lower Control North. For lower rate complexity, vectoring mode gives the lowest complexity than the other resolution mode, as seen in Jakarta Lower Control North, Jakarta Lower Control Centre, and Jakarta Terminal South. Altitude control mode gives a higher rate of complexity and more potential conflict if applied to the sector with many departure trajectories like Jakarta Lower Control North. Fig. 5 and 6 elaborate that speed control to solve the conflict increases complexity and creates more potential conflict for almost all sectors. Vectoring mode gives the least potential conflict than the other modes except on Jakarta terminal West.

The simulation result can compare the complexity between sectors in a TCA and its effect on potential conflicts. However, the model cannot yet determine how this complexity affects aviation safety risks. As we know, complexity will affect the controller's workload level [5]. Representation of the human factor is needed to measure the controller workload, and its effect on safety risk factors can be observed. Future research needs methods to represent the human factor in a simulation model, including adding a controller to the simulation (human in the loop simulation) [16] or developing a controller workload model [29].

4. CONCLUSION

The weighting value of seven air traffic complexity indicators has been calculated using the AHP method in this study. The indicator that most significantly affects the air traffic complexity is the potential conflict control. The consistency of respondents' answers is less than 10%, indicating that these results are consistent. It can determine the air traffic complexity rate in the JAKARTA TCA model.

The simulation has been run to measure the air traffic complexity of JAKARTA TCA in a high-density situation. The simulation result explains that the resolution mode selection influences the complexity rate and potential conflicts. The simulation model requires further development by representing the human factor in the model so the model can be used to analyze safety risks.

ACKNOWLEDGEMENT

The authors would like to acknowledge Jakarta Air Traffic Services Center (JATSC), AirNav Indonesia, for providing information and the Indonesian Endowment Fund for Education (LPDP Scholarship) for the financial support.

REFERENCES

[1] Bouarfa S. (2015) Agent-Based Modelling and Simulation of Safety and Resilience in Air Transportation. Doctoral Dissertation, Delft University of Technology. https://doi.org/10.4233/uuid:b676db6c-ed86-4b42-9940-9b90b94651f1

[2] Netjasov F, Janic M, Tosic V. (2009) The Future Air Transport System: Looking for Generic Metrics of Complexity for Terminal Airspace. 88th Transportation Research Board (TRB) Annual Meeting, Washington DC, USA.

[3] Netjasov F, Janic M, Tosic V. (2011) Developing a Generic Metric of Terminal Airspace Traffic Complexity. Transportmetrica 7(5), 369-394. https://doi.org/10.1080/18128602.2010.505590

[4] Diaconu AG, Stanciu V, Pleter OT. (2014) Air Traffic Complexity Metric for En-Route and Terminal Areas. U.P.B. Sci. Bull., Series D, Vol. 76, Iss. 1.

[5] Djokic J, Lorenz B, Fricke H. (2010) Air Traffic Control Complexity as Workload Driver. Transportation Research Part C Emerging Technologies 18(6):930-936. https://doi.org/10.1016/j.trc.2010.03.005

[6] Mogford RH, Guttman JA, Morrow SL, Kopardekar P. (1995) The Complexity Construct in Air Traffic Control: A Review and Synthesis of the Literature. Report N0. DOT/FAA/CT-TN95/22. U.S. Department of Transportation, Federal Aviation Administration, Office of Aviation Research, Washington, D.C.

[7] Dervic A, Rank A. (2015) ATC complexity measures: Formulas measuring workload and complexity at Stockholm TMA. Department of Science and Technology, Linköping University, Sweden.

[8] Arad BA, Golden BT, Grambart JE, Mayfield CE, Van Saun HR. (1963) Control Load, Control Capacity, and Optimal Sector Design (Report No. RD64-16). Federal Aviation Administration, Atlantic City, NJ.

[9] Grossberg M. (1989) Relation of Sector Complexity to Operational Errors. Quarterly Report of the FAA Office of Air Traffic Evaluations and Analysis.

[10] Mogford RH, Murphy ED, Yastrop G, Guttman JA, Roske-Hofstrand R. (1993) The Application of Research Techniques for Documenting Cognitive Processes in Air Traffic Control (Report No. DOT/FAA/CT-TN93/39). Federal Aviation Administration, Atlantic City, NJ.

[11] Pawlak WS, Brinton CR, Crouch K, Lancaster KM. (1996) A Framework for the Evaluation of Air Traffic Control Complexity. American Institute of Aeronautics and Astronautics, Inc.

[12] Laudeman I, Shelden S, Brannstrom R, Brasil C. (1998) Dynamic Density: An Air Traffic Management Metric. Ames Research Center.

[13] Majumdar A, Ochieng WY. (2000) The Factor Affecting Air Traffic Controller Workload: A Multivariate Analysis Based upon Simulation Modelling of Controller Workload. Center for Transport Studies.

[14] Chatterji GB, Sridhar B. (2001) Measures for Air Traffic Controller Workload Prediction. First AIAA Aircraft Technology, Integration and Operations Forum. https://doi.org/10.2514/6.2001-5242

[15] Koros A, Della Rocco PS, Panjwani G, Ingurgio V, D'Arcy JF. (2003) Complexity in Air Traffic Control Towers: A Field Study. Part 1: Complexity Factors. DOT/FAA/CT-TN03/14. Federal Aviation Agency, Atlantic City, NJ.

[16] Radišić T, Andraši P, Novak D, Juričić B, Antulov-Fantulin B. (2020) Risk Assessment in Air Traffic Management. Edited by P. Castán and J. Alberto. IntechOpen, London. pp 56-83.

[17] Wang H, Song Z, Wen R. (2018) Modeling Air Traffic Situation Complexity with a Dynamic Weighted Network Approach. Journal of Advanced Transportation, vol. 2018 vol. 2018, Article ID 5254289, 15 pages. https://doi.org/10.1155/2018/5254289

[18] Andraši P, Radišić T, D. Novak, and B. Juričić (2019) Subjective Air Traffic Complexity Estimation Using Artificial Neural Networks. Traffic & Transportation, 31(4): 377-386. https://doi.org/10.7307/ptt.v31i4.3018

[19] Medianto R, Pasaribu HM, Muhammad H. (2019) Development of Hybrid Simulation Model of Air Traffic Management in the Terminal Control Area. IOP Conf. Series: Materials Science and Engineering, 645: 012003. https://doi.org/10.1088/1757-899x/645/1/012003

[20] Directorate General of Civil Aviation (2019) Nr: The Establishment And Revision of Instrument Flight Procedures at Soekarno Hatta International Airport – Jakarta, AIRAC AIP Supplement 14/19 25 APR 19. Directorate of Air Navigation, Directorate General of Civil Aviation, Republic Of Indonesia. FlightRadar24 Data/History Flights.

[21] Airnav Indonesia (2020) Standard Operating Procedures Air Traffic Services Approach Control Service. Airnav Indonesia Branch of Jakarta Air Traffic Service Center.

[22] Horasio K. (2019) Air Traffic Conflict Resolution Modelling and Analysis in Controlled Airspace. Master's Thesis. Bandung Institute of Technology, Aerospace Engineering Department.

[23] FlightRadar24 Flight Database [https://www.flightradar24.com/data/flights]

[24] METAR/SPECI & Trend Forecast, Aviation Meteorological Information System in Meteorological, Climatology, and Geophysical Agency (BMKG) [http://aviation.bmkg.go.id/web/metar_speci.php]

[25] Pasaribu HM, Medianto R, Jusuf J, Oktafianto R, Atiqah R (2021) ADS-B data processing to develop aircraft kinematics model parameters. AIP Conference Proceedings, 2366: 02001. https://doi.org/10.1063/5.0060611

[26] Medianto R, Jusuf J, Oktafianto R, Atiqah R, Sembiring J, Pasaribu HM, Jenie YI, Muhammad H. (2021) Stochastic modelling of aircraft flight parameters in terminal control area based on automatic dependent surveillance-broadcast (ADS-B) data. IOP Conference Series: Materials Science and Engineering, 1173: 012053. https://doi.org/10.1088/1757-899X/1173/1/012053

[27] Sargent RG. (2005) Verification and Validation of Simulation Models, Proceedings of the 2005 Winter Simulation Conference, 130-143. https://doi.org/10.1109/wsc.1994.717077

[28] Mogford R, Guttman J, Morrow S, and Kopardekar P. (1995) The Complexity Construct in Air Traffic Control: A Review and Synthesis of the Literature, Federal Aviation Administration.

[29] Li-na S, Li Z, Lei Z. (2015) The Sector Capacity Evaluation Considering the Controller's Workloads. International Journal of Control and Automation, 8: 307-324. https://doi.org/10.14257/ijca.2015.8.7.31

https://doi.org/10.31436/iiumej.v24i1.2341

PERFORMANCE ANALYSIS OF PREDICTIVE FUNCTIONAL CONTROL FOR AUTOMOBILE ADAPTIVE CRUISE CONTROL SYSTEM

MOHAMED AL-SIDEQUE ZAINUDDIN[1,2], MUHAMMAD ABDULLAH[1*], SALMIAH AHMAD[1], MOHD SUHAIMI UZAIR[3] AND ZAID MUJAIYID PUTRA AHMAD BAIDOWI[4]

[1]Department of Mechanical and Aerospace Engineering, International Islamic University Malaysia, Jalan Gombak, 53100, Kuala Lumpur, Malaysia
[2]Department of Automotive Engineering Technology, Kolej Kemahiran Tinggi MARA, Masjid Tanah, Melaka, Malaysia
[3]Testing & Development, Engine Development, Powertrain R&D, Powertrain Division, Proton Holdings Berhad, Shah Alam, Malaysia
[4]Centre of Foundation Studies, Universiti Teknologi MARA, Cawangan Selangor, Kampus Dengkil, 43800 Dengkil, Selangor, Malaysia

[*]Corresponding author: mohd_abdl@iium.edu.my

(Received: 28th February 2022; Accepted: 21st June 2022; Published on-line: 4th January 2023)

ABSTRACT: This paper presents the performance analysis of Predictive Functional Control (PFC) for Adaptive Cruise Control (ACC) application. To cope with multiple driving objectives of modern ACC systems such as passenger comfort, safe distancing, and fast time response, an advanced optimal controller such as Model Predictive Control (MPC) is often used. Nevertheless, MPC requires a high computation load due to its complex formulation and may overload the processing power of a microcontroller. Thus, the prime objective of this work is to propose a PFC algorithm as an alternative controller, while providing a formal comparison between MPC and the traditional Proportional Integral (PI) controller. A standard kinematic model for vehicle longitudinal dynamics was modelled and used to derive the control law of PFC. Since the open-loop dynamic of the derived transfer function is not stable, the second objective is to propose a pre-stabilized loop or cascade PFC structure for the system. A complete tuning procedure and analysis were presented. The simulation result shows that although MPC performance is the best for the ACC application with Root Mean Square Error (RMSE) of 1.4873, PFC has shown a promising response with RMSE of 1.5501, which is better compared to the PI controller with RMSE of 1.6219. All the imposed driving constraints such as maximum acceleration, maximum deceleration and safe distance were satisfied in the car following application. Thus, the findings from this work can become a good initial motivation to further explore the capability of the PFC algorithm for future ACC development.

ABSTRAK: Kajian ini adalah berkenaan analisis prestasi Kawalan Fungsi Ramalan (PFC) aplikasi Kawalan Mudah Suai (ACC). Bagi memenuhi pelbagai keperluan objektif sistem pemanduan moden ACC seperti keselesaan penumpang, penjarakan selamat dan tindak balas pantas, kawalan optimum terbaru seperti Model Kawalan Ramalan (MPC) sering digunakan. Walau bagaimanapun, MPC memerlukan beban pengiraan tinggi kerana rumusnya yang kompleks dan mungkin mengakibatkan beban berlebihan kuasa pemprosesan mikrokawalan. Oleh itu, matlamat utama kajian ini adalah bagi mencadangkan algoritma PFC yang mempunyai pengiraan mudah sebagai kawalan alternatif, sementara menyediakan perbandingan formal antara MPC dan kawalan

https://doi.org/10.31436/iiumej.v24i1.2341

tradisional Berkadar Keseluruhan (PI). Oleh kerana model ini tidak stabil, objektif kedua adalah mencadangkan penggunaan struktur PFC berlapis bagi menstabilkan sistem terlebih dahulu sebelum algorithma kawalan digunakan atau dengan menggunakan struktur PFC secara berturut pada sistem. Prosedur lengkap dan terperinci untuk analisis PFC dibentangkan. Dapatan simulasi kajian menunjukkan walaupun prestasi MPC adalah baik bagi aplikasi ACC dengan Ralat Punca Min Kuasa Dua (RMSE) bernilai 1.4873, namun PFC menunjukkan tindak balas baik dengan RMSE bernilai 1.5501 berbanding kawalan PI yang mempunyai RMSE sebanyak 1.6219. Kesemua kekangan seperti pecutan dan nyahpecutan maksima, dan penjarakan selamat bertepatan dengan aplikasi kenderaan ini. Dengan itu, penemuan ini adalah motivasi awal yang baik bagi meneroka lebih jauh keupayaan algoritma PFC bagi membangun ACC pada masa hadapan.

KEY WORDS: *predictive functional control; model predictive control; PID; adaptive cruise control*

1. INTRODUCTION

Adaptive Cruise Control (ACC) is one of the basic features for an Advanced Driving Assistant System (ADAS), where its function is to regulate the speed of a vehicle while retaining a safe following distance. Compared to the conventional Cruise Control system, ACC has two modes of operation: speed control and space control. With the advancement of sensor and microprocessor technologies, an energy efficient ACC system which can satisfy multiple driving objectives such as passengers' comfort, fuel efficiency, and safe distancing with acceptable time response are currently being developed. This type of ACC system requires a more sophisticated control algorithm and structure as each of the driving objective functions needs to be optimized to get the optimum control action. It is also well noted that the vehicle longitudinal dynamics for full range operation is highly nonlinear and thus a hierarchal control structure is required where the upper-level system is controlled to provide a desired signal for the lower-level system to track [1]. At the same time the switching between space and speed control also needs to be considered to ensure the safety and comfort of the passenger.

With a traditional PI controller, a special switching algorithm is used to ensure a smooth transition between the two modes to avoid jerking [2]. This operation can be done with the help of a look up table. Nevertheless, the control performance is not robust since the decision making is solely based on the current measurement. To improve the robustness, a proper tuning strategy can be implemented, as demonstrated by [3]. However, the control structure has become more complicated and there is no systematic tuning approach for this type of modification leaving only trial and error or use of some optimal algorithm tuning scheme. Several works also have proposed the use of Fuzzy Logic Controller (FLC) for an ACC system. Using a common logic rule, the switching strategy is developed based on the relative distance with the lead vehicle. The strategy is quite straightforward and implantable, yet as reported by [4], in the presence of unmeasured disturbance, the control performance will be deteriorated. Indeed, there are several options to overcome these issues such as improving the accuracy of the fuzzy rule by using a different logic function or combining it with other advanced controllers [5]. However, there is no systematic rule that can be implemented as there are many parameters that need to be tuned and most of the modifications are system dependent.

A predictive controller is another suitable option to control the upper level of an ACC system. A representative kinematic mathematical model is used to predict the future velocity and the input acceleration will be optimized to get the desired response while satisfying other driving constraints such as passenger's comfort, fuel efficiency, and safe distancing. As reported in the literature, various authors have managed to prove that this algorithm can effectively control the vehicle speed in satisfying the multiple driving objectives either in simulation or real-time implementation [6-8]. The main reason behind this is the prediction capability where the controller can anticipate what will happen in the future and try to provide the best solution. Hence, no special switching strategy is required and it can be replaced by a more systematic optimization problem. Indeed, there are also several limitations such as a proper selection of the tuning parameters of prediction and control horizons based on certain applications. However, even with suitable parameters, the computation burden will still be heavy to implement in existing vehicle microprocessors. In a short sampling time i.e., 0.1 *s*, the algorithm needs to compute several heavy mathematical operations such as prediction, optimization, and constraints handling using a standard quadratic cost function. Of course, there are several options to reduce the computation such as offline implementation [9] and changing the prediction structures using a special function [7,10], yet still the basic microprocessor in existing vehicles needs to be upgraded. This requirement will increase the cost and, in the future, full implementation of autonomous vehicles would further lead to a greater computation demands.

Due to the above reasons, this work intended to propose an alternative low computation predictive controller known as Predictive Functional Control (PFC), which is novel in the ACC application. In general, the algorithm principle is the same, but the optimization process is simplified without the use of the quadratic cost function. In return, the computation time can be reduced significantly [11]. The PFC algorithm has also been implemented in other engineering fields ranging from chemical, mechanical, and electrical industries [12,13]. However, there is a tradeoff in using PFC, where the optimality of the control solution will be reduced. This is a well-known tradeoff but for a Single Input Single Output (SISO) application such as an ACC system, it may become a good alternative strategy. Besides, there are also a number of works that have improved the existing algorithm such as [14,15]. Thus, the main objective of this work is to investigate and provide a formal performance comparison of PFC with MPC and a traditional PI controller to assess its capability in a vehicle following application.

Another important issue that needs to be highlighted is the application of PFC for marginally stable processes or type 1 processes where there will be an independent integrator in the transfer function's denominator. Since the input to the ACC system is acceleration and the output is speed, if a step input is given, the output will not converge to a steady state value. Thus, when a conventional PFC algorithm is implemented, the control solution will be ill-posed, where the prediction and actual control performance will differ [16]. To cope with this issue, a cascade PFC with feedback compensator will be used where the prediction structure is pre-stabilized before implementing the conventional algorithm [17]. A proper analysis on the tuning process will be discussed and denoted as one of the contributions of this works.

2. METHODOLOGY

2.1 Vehicle Longitudinal Dynamics Modelling

The mathematical model is the most important part of predictive control formulation. In general, the inputs to the system will be the pedal pressure from the throttle and brake, while the output of interest will be velocity. In a traditional cruise control system, the braking effect is not considered, thus the standard kinetic vehicle longitudinal model can be used straight away to derive the control law of PFC as presented in [18]. However, the ACC system needs braking input as well to keep the safe distancing with a lead vehicle. If a full kinetic modelling is used to derive the control law as in [18], the constraint implementation will be quite complicated especially if it is designed for full range dynamic operation where the nonlinearities will be very high due to the changing gear ratio and coefficient of friction between road and tire [2]. Thus, a hierarchal control strategy is often proposed in the literature [5,6] as shown in Fig. 1.

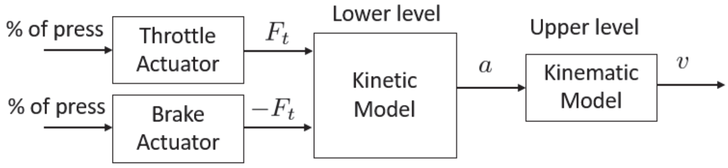

Fig. 1: Hierarchical structure for vehicle longitudinal dynamics.

In the hierarchal structure, the throttle and brake actuator correspond to powertrain and brake line dynamics respectively. As for the lower-level dynamic, it is responsible for the relationship between traction force F_t and acceleration, a, by Newton's second law. The details of these models are available in many references including academic textbooks [2]. Since the lower-level model is nonlinear in nature, the PFC controller will be derived based on the upper-level system that represents the kinematic dynamic between acceleration and velocity where the transfer function is given as:

$$v(s) = \frac{1}{s(\tau s+1)} a(s) \tag{1}$$

The additional time constant τ in Eq. (1) corresponds to the estimation of the first order lag of the lower-level controller [2]. In this case, it is expected that the car will track the velocity imperfectly and thus the nominal time constant τ is approximately equal to 0.5 s [2]. In this work, it is assumed that the lower-level controller can retain the nominal value in every operating speed, although in reality, it will be changed due to nonlinearities, especially for low-speed operation where the gear ratio is not constant. The investigation of the impact of nonlinearities on the overall control performance of an ACC system and the possibility of using other robust control methods will denote future work.

2.2 Cascade PFC Prediction

Since the PFC algorithm works in the digital domain, the transfer function in Eq. (1) needs to be discretized a with sampling time of 0.1 s [6]. From here on, a standard symbol for input u will be used for acceleration a and output y for velocity v. The discrete transfer function can be represented as:

$$G(z) = \frac{y(z)}{u(z)} = \frac{0.009365z^{-1}+0.008762z^{-2}}{1-1.819z^{-1}+0.819z^{-2}} \tag{2}$$

Another important part that needs to be considered is the nature of the transfer function in Eq. (1) and Eq. (2), where it is a type 1 system with independent integrator in the denominator. Since the output response will not converge when given a bounded input, it needs to be pre-stabilized before deriving the control law. If not, it will lead to an ill-posed solution as reported in the literature [14]. There are two ways to overcome this issue [14,17], one is by splitting Eq. (2) into two separate transfer functions that run in parallel, one using partial fractions and the other using a proportional gain, K, to stabilize the system as shown in Fig. 2. This work utilizes the second option since only a minor modification in the computed input is required when implementing the control law.

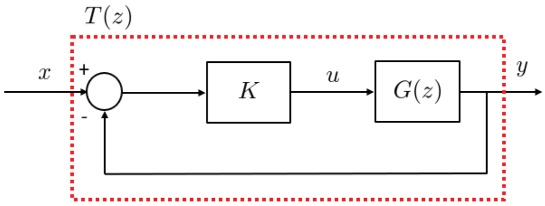

Fig. 2: Proportional feedback loop for plant pre-stabilization.

The inner loop $T(z)$ will be used as a prediction model instead of $G(z)$ as in Eq. (2) to get a stable response and it is computed as:

$$T(z) = \frac{y(z)}{x(z)} = \frac{G(z)K}{1+G(z)K} \tag{3}$$

where, $x(z)$ is the modified controlled input. A suitable value of proportional gain K can be selected based on trial and error or by using a more systematic approach as presented in [17]. As in this work, the MATLAB PID tuner is utilized. Using the function *pidtune(sys,type),* it provides the proportional value of $K = 1.147$. According to the function description in MATLAB help desk, the given value is computed based on the balance performance between response time and robustness.

A linear prediction structure based on the superimposed principle for transfer function in Eq. (3) can be formed, and since the derivation is standard [23-26], only the final form is presented. The i-step ahead prediction at the k sampling is presented as:

$$y(k+i|k) = HX + PX_0 + QY + d \tag{4}$$

The dimension of matrix H, P, and Q depends on the model parameters, and for a standard second order transfer function, the parameters X, X_0 and Y are:

$$X = \begin{bmatrix} x(k) \\ x(k+1) \\ \vdots \\ x(k+i) \end{bmatrix}, X_0 = x(k-1), Y = \begin{bmatrix} y(k) \\ y(k-1) \end{bmatrix}$$

The term d in Eq. (4) corresponds the correction term to get an unbiased prediction using an independent model structure as shown in Fig. 3. Technically, it is the difference between the actual measured output form a plant y_p and the calculated output y from $T(z)$ in Fig. 2.

$$d = y_p - y \tag{5}$$

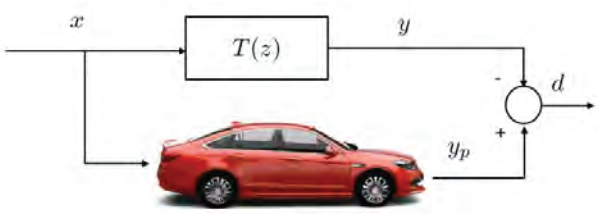

Fig. 3: Independent model structure for PFC prediction.

2.3 Cascade PFC Control Law

To compute the control input, the prediction in Eq. (4) at n-step ahead is forced to coincide with a first order setpoint trajectory r, which is given as [11]:

$$r(k+n|k) = (1-\lambda^n)R + \lambda^n y_p(k) \tag{6}$$

where R is the desired set point speed. In this stage, there are two tuning parameters that need to be specified. The first one is the coincidence horizon $n,$ where the prediction in Eq. (4) is forced to match with the target trajectory in Eq. (6). The second one is λ, which corresponds to the desired Closed-loop Time Response (time taken to reach 95 % form the steady state value):

$$\lambda = e^{-3T_s/CLTR} \tag{7}$$

The term T_s in Eq. (7) denotes the sampling time. For a second order system, the selection of n has a general tuning guideline as presented in [17]. It should be selected between 40% and 80% of the response to avoid prediction mismatch. Once all the tuning parameters have been selected, the general control law of PFC can be derived. Using its standard assumption that the future modified control input will be constant i.e., $x(k) = x(k+1) = \cdots . x(k+n)$ [25], the n-th row of matrix H_n will reduce to a single value in the form of:

$$h_n = H_n \begin{bmatrix} 1 \\ 1 \\ \vdots \\ 1 \end{bmatrix} \tag{8}$$

Extracting the n-th prediction form each matrix and equating the predictions in Eq. (4) and Eq. (6) gives:

$$h_n x(k) + P_n X_0 + Q_n Y + d = (1-\lambda^n)R + \lambda^n y_p(k) \tag{9}$$

The compensated input x can be computed as:

$$x(k) = h_n^{-1}\left[(1-\lambda^n)R + \lambda^n y_p(k) - P_n X_0 - Q_n Y - d\right] \tag{10}$$

It should be noted that since a cascade structure is used to pre-stabilized the response as explained in Section 2.2. By referring to Fig. 4, the actual input that will be sent to the plant is computed as:

$$u(k) = K\left[x(k) - y_p(k)\right] \tag{11}$$

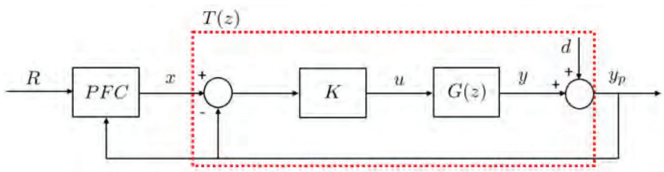

Fig. 4: Cascade PFC structure.

2.4 Constraint Handling for Passenger Comfort and Safe Distancing

For the predictive controller framework, the conventional switching strategy from speed mode to space mode can be implemented by formulating a constraint control problem. Fig. 5 shows the schematic diagram for vehicle following application and how the ACC controller is implemented.

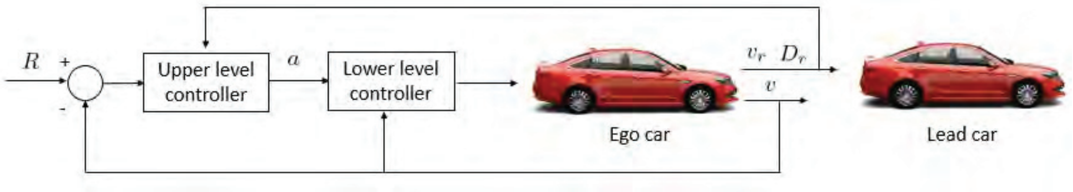

Fig. 5: ACC schematic diagram for vehicle following application.

With the help of a distance sensor such as LIDAR, a relative distance D_r or relative velocity v_r with a lead vehicle can be measured. These two parameters can be used to regulate the acceleration to retain a safe following distance if necessary. A standard safe following distance equation as recommended in [2] is used, where:

$$D_{safe}(k) = D_{default} + T_{gap}v(k) \tag{12}$$

The default distance $D_{default}$ is set to 10 m, it means that if the velocity of vehicle is 0 *m/s* (both lead and ego vehicle are not moving or approaching a complete stop), the relative distance should not be less than $D_{default}$. The safe time gap T_{gap} between the vehicle is set to 1.4 s. Based on Eq. (12), the higher the velocity of a vehicle, the larger the safe distance needed to be maintained because it will take more time to slow down the car. Based on the output velocity prediction in Eq. (4), the future relative position between the car D_r can be estimated by assuming the future velocity of the lead car is constant at the instantaneous sampling

$$D_r(k+1) = [v_l - v(k)]T_s + D_r(k) \tag{13}$$

Using superposition, at each sampling time, the maximum velocity to keep the safe distance can be formed as:

$$v_{max} = \left(v_l T_s + D_r(k) - D_{default}\right)/\left(T_{gap} + T_s\right) \tag{14}$$

Then a normal PFC output constraints formulation can be implemented by selecting a suitable validation horizon n_i. The algorithm is given as below:

Algorithm (A). *At each sample time*:

(1) Compute the unconstrained compensated input x *as in Eq. (10).*

(2) A simple 'for' loop is used to check the constraint violation while updating Eq. (13) and Eq. (14)

(3) If $v > v_{max}$*, then:*

$$x(k) = HL_i^{-1}[v_{max}(i) - P_iU_0 - Q_iY - d] \tag{15}$$

(4) Else, the value of x *is retained.*

For taking care of passenger comfort and fuel efficiency, the input acceleration is constrained in between u_{min}= -3 to u_{max}= 2 m/s^2. As discussed in many PFC papers [16-17] a simple clipping strategy is enough to cater for input constraint such that if $x < y(k) + u_{min}/K$, then:

$$x(k) = y(k) + u_{min}/K \tag{16}$$

Similarly, if $x > y(k) + u_{max}/K$, then:

$$x(k) = y(k) + u_{max}/K \tag{17}$$

3. SIMULATION RESULT

3.1 Analysis of Tuning Parameter of PFC

The first step in tuning the PFC is to select a suitable compensator gain to stabilize the open-loop behavior of the vehicle dynamics. Since the open-loop transfer function is type 1 (with one integrator in the denominator), a single proportional gain is enough to stabilize the system. As discussed in Section 2.2, an autotune PI controller in MATLAB is used to find an optimum proportional gain K = 1.147 that will provide a balanced performance between response time and robustness [17]. Figure 5 shows the open-loop response of the pre-stabilized system output y against the desired output trajectory R with CLTR of 5s (λ = 0.9418).

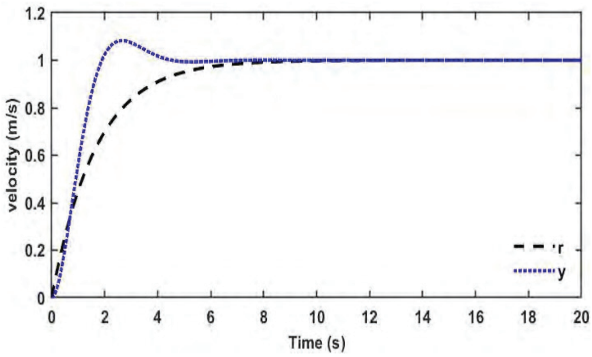

Fig. 5: Pre-stabilized open-loop response compared to the desired trajectory.

The objective of the PFC is to force the system to match the desired target trajectory at a specific coincidence horizon, n. In this stage, a proper coincidence horizon needs to be selected carefully. In general, a smaller coincidence horizon will provide more aggressive response and input, while higher coincidence horizon will be less aggressive and slow. The effect of coincidence horizon may be varied for different systems since the dynamics are different. Several coincidence horizons are simulated to track a desired velocity of 5 m/s with 0.1 s sampling time, as shown in Fig. 6.

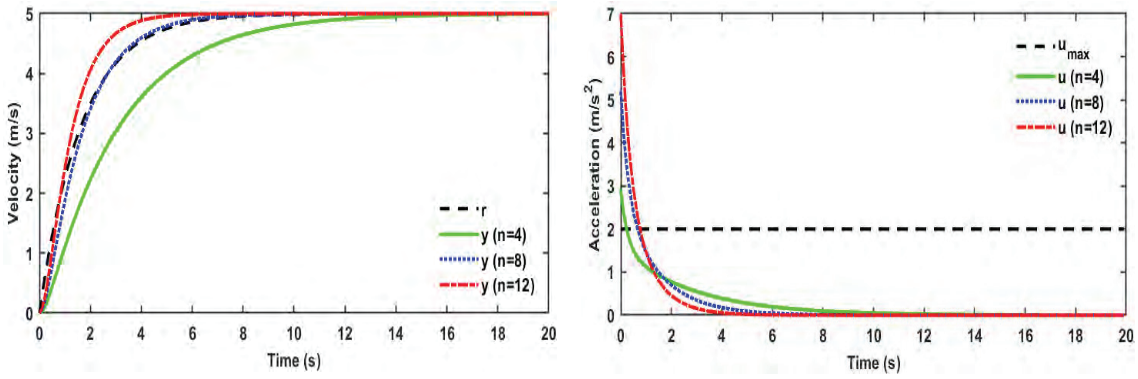

Fig. 6: Closed-loop response with varying coincidence horizon (n).

It can be observed that a smaller horizon will lead to slower response and a larger value will lead to faster response than the desired one (black dashed line). Based on the tuning guide proposed by [17], a suitable value should be selected between 40% and 80% rise of step response to its steady state value. In this case n=8 provides the closest response compared to the desired trajectory. A similar effect can be seen in the control effort where large horizon will need larger over actuation compared to the smaller horizon value. Nevertheless, all the control efforts violate the maximum allowable input acceleration, which is 2 m/s^2.

To satisfy the driving constraint, the algorithm (A) in section 2.4 is implemented. As expected, Fig. 7 shows the response where the implied constraint is satisfied systematically, yet with a slower response in tracking the desired target trajectory.

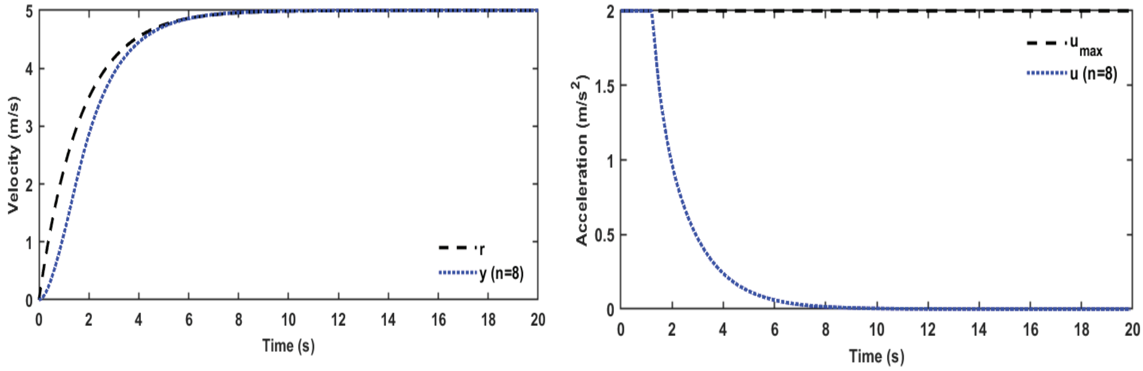

Fig. 7: Closed-loop response when input constraint is activated.

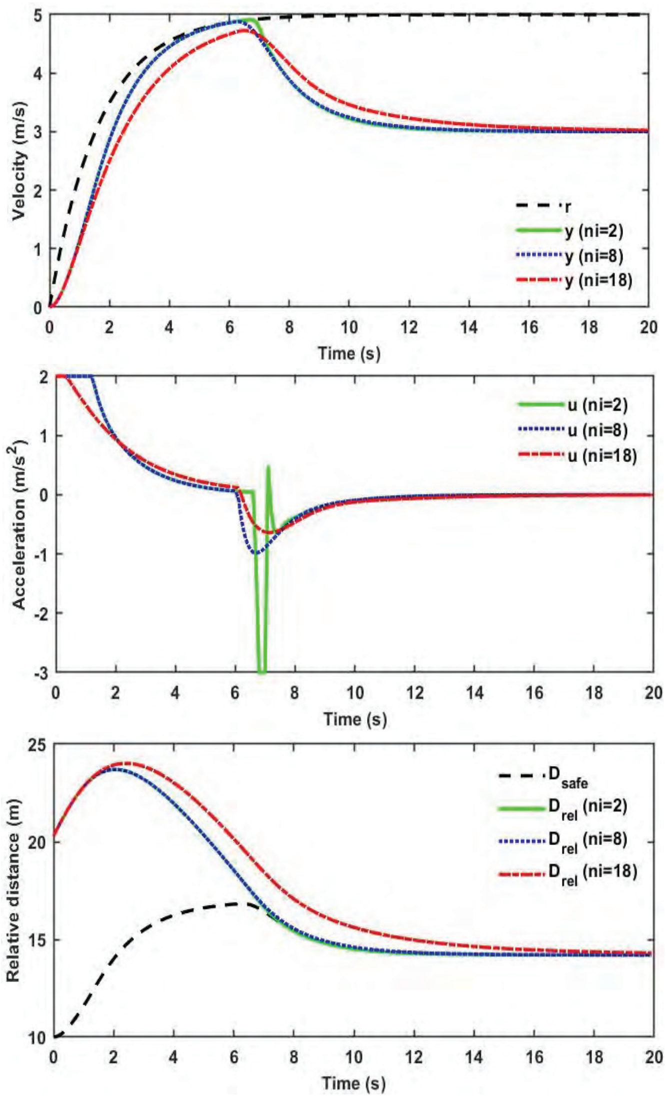

Fig. 8: Closed-loop response for vehicle following application.

For the *car following application*, the output velocity also needs to be constrained to ensure that the safe following distance is always respected. With the prediction capability of PFC, it can anticipate the future relative distance and change the input accordingly. Nevertheless, a suitable validation horizon (how far ahead the constraint is implemented) needs to be selected. Figure 8 overlays different selections of validation horizons when following a lead vehicle with a constant velocity of 3 *m/s* and initial relative distance of 21 *m*. As can be observed, all three responses managed to prevent the relative distance from going lower than the safe following distance and respecting all the input constraints. Nevertheless, there is a clear tradeoff in the selection of validation horizon, if it is too short (n_i=2 green solid line), an aggressive control effort is needed. Nevertheless, if it is too large (n_i=18, red dash dotted line), the response may be too conservative, and the computation burden of the controller will increase as it needs to compute more mathematical operation. For this case, a validation of n_i=8 (blue dotted line), which is equal to the coincidence horizon, is selected since it respects all the constraints with optimum control effort. This feature is very important to ensure the safety and comfort of the passengers.

3.2 Performance Comparison with PI and MPC

To analyze the control performance of PFC, its closed-loop response is compared with two benchmark controllers: PI and MPC. The reason the PI controller is used instead of the PID is because it is a type 1 system. Figure 9 shows the comparison of the input acceleration, output velocity and relative distance of the three controllers. The lead vehicle (black-dashed line) is assumed to operate with sinusoidal acceleration signal with amplitude of 0.35 m/s^2 and frequency of 0.1 *rad/s*. The ego vehicle (the controlled vehicle) is set to track a desired velocity of 30 *m/s* while respecting the safe following distance. For predictive controllers (PFC and MPC), the safe following distance is treated as a constraint, while for PI controller, a simple switching strategy is used to change between speed and space mode. The gains are selected based on an auto tune function in MATLAB with P = 0.8, I = 0.001. At the same time, input acceleration is constrained between -3 m/s^2 to 2 m/s^2 for passenger comfort.

As expected, it can be observed that from the result in Fig. 9, MPC (green dashed-dotted line) provides the most optimal response with less aggressive input acceleration followed by PFC (blue dotted line) and PI (red solid line). The difference in output velocity is not quite significant except that a large spike response is generated by the PI controller at 10 *s* when the ego car is trying to adjust its speed to match the leading vehicle. As for the safe distancing, both PFC and MPC managed to retain it, while PI needs to violate the safe distancing to satisfy input acceleration constraints at 60 *s*, 120 *s* and 180 *s*.

Besides the qualitative results, some quantitative values are shown in Table 1 for each controller to numerically demonstrate their output velocity performance in terms of rise time τ_r, settling time τ_s and Root Mean Square Error (RMSE). These quantitative values are measured over the duration of 40 *s* for tracking 30 *m/s* from rest and will be the performance indices of the controllers. It can be observed from Fig. 9 and Table 1 that the PI controller for the constrained closed-loop response requires longer settling times (199.5386 *s*) as compared to others although it has the fastest rise time (2.7213 *s*). Another observation is that all the controllers do not produce an overshoot. However, the MPC and PFC provide the best fit response curve to the desired speed of 30 *m/s* with lower RMSE of (1.5501) and (1.4873) respectively compared to PI controller RMSE of (1.6219).

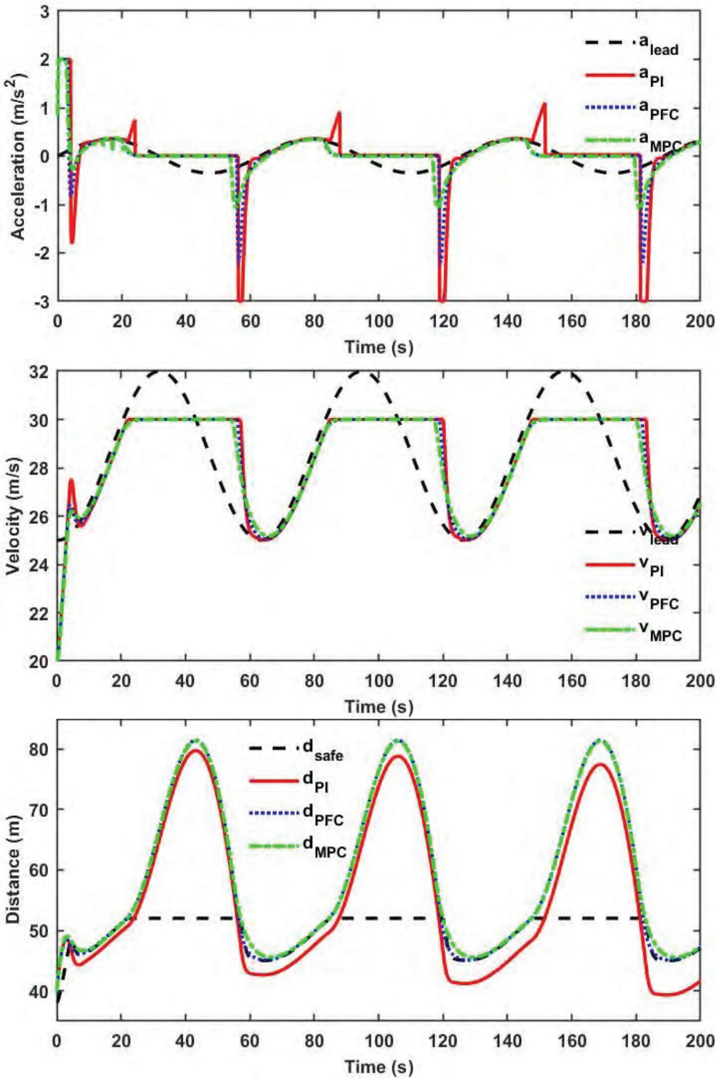

Fig. 9: Closed-loop performance comparison between PI, PFC, and MPC for vehicle following application.

Table 1: Performance indices for all controllers.

Performance Criteria	PI	PFC	MPC
Rise time, τ_r	2.7213	2.7348	2.9551
Settling time, τ_s	199.5386	199.5348	199.5295
RMSE	1.6219	1.5501	1.4873

Based on the analysis, it can be explained that the prediction capability is very important in an ACC system to provide optimal response. By estimating a future behavior, a better control input can be generated while satisfying the constraints systematically. Nevertheless, there is an obvious difference between PFC and MPC because the optimization algorithm is simplified to reduce the computation burden. However, it worth pointing out that PFC performance is better compared to PID. The main reason is because the PI computes the control action based on the current measurement rather than prediction. Indeed, one may argue that if it is tuned properly or a suitable special switching strategy is used, a better performance can be obtained. Nevertheless, it also should be noted that the tuning procedure is not as straightforward as expected since many trial-and-error procedures need to be implemented.

4. CONCLUSION

In summary, this paper describes a design that proposes the use of PFC in controlling the ACC system of a vehicle. Based on the simulation results, it is found that although the PFC performance with RMSE of 1.4873 is not comparable with the more advanced MPC algorithm with RMSE of 1.5501, it gives a better performance compared to the PI controller with RMSE of 1.6219. Besides, the PFC algorithm is also simple and straightforward to implement and requires less calculation compared to the MPC while retaining its predictive advantage compared to other traditional controllers. The tuning process is also intuitive, being based on the desired time constant and coincidence horizon selection. Indeed, there is a lot of room for improvement and future work will provide a more systematic analysis of the computation requirement of both MPC and PFC controllers and their robustness properties. Hence, it can be concluded that PFC can become a good alternative to MPC and PI by trading off some of the optimality properties for a lower computation burden.

ACKNOWLEDGEMENT

The authors would like to acknowledge the Ministry of Higher Education, Malaysia for funding this work under the Fundamental Research Grant Scheme FRGS/1/2021/TK02/UIAM/02/2 (FRGS21-240-0849). The first author would like to acknowledge Majlis Amanah Rakyat (MARA) for his tuition fee waiver.

REFERENCES

[1] Jiang Y, Deng W, He R, Yang S, Wang S, Bian N. (2017) Hierarchical framework for adaptive cruise control with model predictive control method (No. 2017-01-1963). SAE Technical Paper.
[2] Rajamani R. (2011) Vehicle dynamics and control. Springer Science & Business Media.
[3] Haroon Z, Khan B, Farid U, Ali SM, Mehmood CA. (2019). Switching control paradigms for adaptive cruise control system with stop-and-go scenario. Arabian Journal for Science and Engineering, 44(3): 2103-2113.
[4] Alomari K, Mendoza RC, Sundermann S, Goehring D, Rojas R. (2020). Fuzzy Logic-based Adaptive Cruise Control for Autonomous Model Car. In ROBOVIS (pp. 121-130).
[5] Phan D, Amani AM, Mola M, Rezaei AA, Fayyazi M, Jalili M., ... Khayyam H. (2021). Cascade Adaptive MPC with Type 2 Fuzzy System for Safety and Energy Management in Autonomous Vehicles: A Sustainable Approach for Future of Transportation. Sustainability, 13(18): 10113.
[6] Takahama T, Akasaka D. (2018). Model predictive control approach to design practical adaptive cruise control for traffic jam. International Journal of Automotive Engineering, 9(3): 99-104.
[7] Li SE, Jia Z, Li K, Cheng B. (2014). Fast online computation of a model predictive controller and its application to fuel economy–oriented adaptive cruise control. IEEE Transactions on Intelligent Transportation Systems, 16(3): 1199-1209.
[8] Guo L, Ge P, Sun D, Qiao Y. (2020). Adaptive cruise control based on model predictive control with constraints softening. Applied Sciences, 10(5): 1635.
[9] Borek J, Groelke B, Earnhardt C, Vermillion C. (2019, July). Optimal control of heavy-duty trucks in urban environments through fused model predictive control and adaptive cruise control. In 2019 American Control Conference (ACC) (pp. 4602-4607). IEEE.
[10] Awad N, Lasheen A, Elnggar M, Kamel A. (2022). Model predictive control with fuzzy logic switching for path tracking of autonomous vehicles. ISA transactions, 129: 193-205.
[11] Rossiter JA. (2018). A first course in predictive control. CRC press.

[12] Nasiri Soloklo H. (2018). Predictive Functional Control for Tracking of Core Power Variations in Pressurized Water Reactor based on Laguerre functions and Reduced-Order Model. Modares Mechanical Engineering, 18(1): 299-306.
[13] Li MY, Lu KD, Dai YX, Zeng GQ. (2020). Fractional-Order Predictive Functional Control of Industrial Processes with Partial Actuator Failures. Hindawi Complexity, 2020: 1-25.
[14] Abdullah M, Rossiter JA. (2018). Input shaping predictive functional control for different types of challenging dynamics processes. Processes, 6(8): 118.
[15] Abdullah M, Rossiter JA, Ghaffar AFA. (2021). Improved constraint handling approach for predictive functional control using an implied closed-loop prediction. IIUM Engineering Journal, 22(1): 323-338.
[16] Abdullah M, Rossiter JA. (2021). Using Laguerre functions to improve the tuning and performance of predictive functional control. International Journal of Control, 94(1): 202-214.
[17] Rossiter JA, Aftab MS. (2021). A Comparison of Tuning Methods for Predictive Functional Control. Processes, 9(7): 1140.
[18] Zainuddin MAS, Abdullah M, Ahmad S, Tofrowaih KA. (2022). Performance Comparison Between Predictive Functional Control and PID Algorithms for Automobile Cruise Control System. International Journal of Automotive and Mechanical Engineering, 19(1): 9460-9468.

https://doi.org/10.31436/iiumej.v24i1.2448

RICOCHET OF SPINNING SPHERES OFF WATER

RIYAH NAJIM KITER[1], MAZIN YASEEN ABBOOD[1] AND OMAR HASHIM HASSOON[2*]

[1]*Department of Mechanical Engineering, College of Engineering, University of Anbar, Iraq*
[2]*Department of Production Engineering and Metallurgy, University of Technology, Baghdad, Iraq*

[*]*Corresponding author: omar.h.hassoon@uotechnology.edu.iq*

(Received: 17th May 2022; Accepted: 5th October 2022; Published on-line: 4th January 2023)

ABSTRACT: Liquid impact and ricochet is still attracting researchers interested in the field of hydrodynamics and naval engineering. The ricochet from a water surface experienced by spinning spheres was examined both analytically and numerically. A theoretical analysis was made to quantify the enhancement attained by imparting backspin to the sphere. Numerical simulation of the process was conducted by implementing ABAQUS software. The mathematical analysis and the simulation were built on the assumption that the effects of cavitation, splash, and two phase flow are negligible compared to hydro-dynamical forces of lift and drag. It was proven that both mathematical analysis and simulation were capable of predicting the trajectory of a spinning sphere during its course of entry into the water. Aspects like the critical angle of ricochet and the maximum depth of immersion were extracted from these trajectories and compared with available data. It was found that the analytical and numerical results were generally validated with respect to each other as well as to existing findings. Aluminum ($\sigma = 2.7$) spinning spheres, of radius 10 mm and speed of 10 m/sec, were examined. It was found that a 300 rad/sec backspin improves the critical angle of ricochet from 10.43 to 12.5 deg and increases the maximum depth of immersion from 1.52 to 1.83. "Magnus Effect" usually acting on a fully immersed spinning sphere, was described and relations estimating the hydrodynamic forces were deduced.

ABSTRAK: Keadaan pertumbuhan bakteria penghasil enzim protease aktif-sejuk terasing daripada sampel Antartika disaring menggunakan satu-faktor-satu-masa (OFAT). Kemudian, enzim protease ini diekstrak pada lewat fasa logaritma untuk ujian enzimatik. Strain yang menunjukkan aktiviti enzim tertinggi telah dipilih bagi tujuan pengoptimuman melalui Kaedah Permukaan Tindak Balas (RSM). Parameter yang dikaji adalah pada suhu pengeraman (4 - 36 °C), media pH (4 – 10) dan kepekatan NaCl (0 - 8 %). Berdasarkan dapatan OFAT, kesemua lapan bakteria menunjukkan kadar pertumbuhan tertinggi pada 20 °C, pH 7 dan 4% NaCl (w/v). Hasil ujian enzimatik menunjukkan enzim protease mentah yang diekstrak daripada SC8 menunjukkan aktiviti yang jauh lebih tinggi (0.20 U dan 0.37 U) daripada kawalan positif (0.11 U dan 0.31 U) pada -20 °C dan 20 °C. RSM ini menunjukkan kadar optimum bagi pertumbuhan SC8 adalah pada 20.5 °C, pH 6.83 dan 2.05% NaCl (w/v) dengan dapatan kadar pertumbuhan bakteria pada $3.70 \pm 0.06 \times 10^6$ sel/jam. Keadaan pertumbuhan optimum SC8 melalui kajian ini bermanfaat bagi menghasilkan produk protease aktif-sejuk secara besar-besaran pada masa hadapan.

KEYWORDS: *Magnus; water-entry bodies; Ricochet behavior; bouncing rigid body*

https://doi.org/10.31436/iiumej.v24i1.2448

1. INTRODUCTION

The phenomenon of liquid impact and ricochet is still attracting researchers interested in the field of hydrodynamics and naval engineering. It also fascinates the layman, as evidenced by attempting to achieve skipping of stones across the water's surface. The interaction between liquids and solids in many modern applications has stimulated engineers and scholars to conduct more research towards comprehensive understanding of the phenomenon. These applications include – but are not limited to - ships, offshore structures, missiles, torpedoes, underwater vehicles, watercrafts, and oceanographic measuring devices. Interest in the liquid-solid impact may well stem from the historical technique of ricocheting cannonballs to attack ships in the past two centuries. In this context, the famous bomb used in World War II and known as the Barnes Wallis's bouncing bomb, is particularly recognized. Barnes Wallis proposed an attack on German dams which were protected against normal high-level air attacks. A torpedo attack was also excluded for the defenders of those dams had arranged a web of heavy anti-torpedo netting. He thus proposed spherical bombs dropped from low-level flying aircraft; being too low and too speedy, the bombs would ricochet and skip over the nets. In addition, Wallis succeeded to impart back-spin to the flying bomb for more stability during flight and the ability to ricochet; for more details about this fascinating device, the reader is referred to Johnson [1].

During this period, the water-entry of solid bodies was experimentally investigated by Richardson [2]. A movie camera of 200 frames per second was used to record the trajectories of Duralumin, Steel, and ebonite spheres during their impacts onto water at different combinations of speed and angle, see Fig. 1. Measurements of the entry and exit speeds and angles were also made.

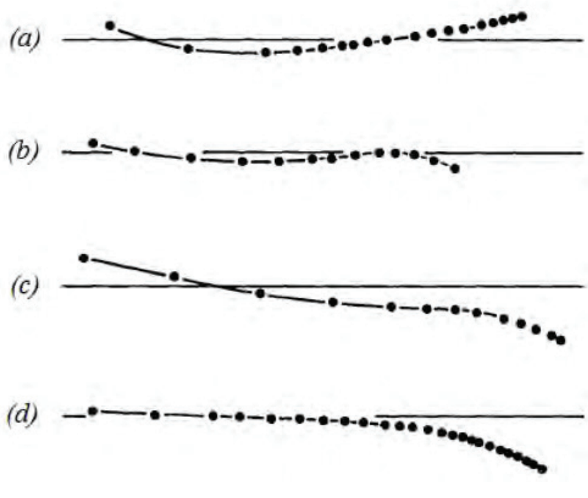

Fig. 1: Depiction of sphere trajectories [2].

It has also been noted that the sphere was always followed by a cavity due to the separation which occurs immediately after contact. In addition, the critical angle of ricochet was found to be 60, 90, and 150 for Steel ($\sigma = 7.8$), Duralumin ($\sigma = 2.7$), and Ebonite ($\sigma = 1.1$), respectively. Finally, the submergence of ricocheting spheres falls in the range of one radius to two.

The first formula appeared in the literature which governs the critical angle of entry of a spherical object for ricochet is due to Birkhoff et al. [3], i.e.:

https://doi.org/10.31436/iiumej.v24i1.2448

$$\vartheta_c = \frac{18}{\sqrt{\sigma}}(degrees) \tag{1}$$

In reproducing Eq. (1), Johnson & Reid [4] adopted the assumptions made in [3] which were: i. the pressure on a surface element is $0.5\rho(Vcos\beta)^2$, ii. the pressure of splash above the undisturbed surface of water is discounted, and iii. the limiting condition for ricochet is that the sphere moves horizontally at the instance of full immersion. No attempt was made to justify these assumptions. Thus, Johnson & Reid [4] concluded that:

$$\vartheta_c = \frac{17.5}{\sqrt{\sigma}}(degrees) \tag{2}$$

Trajectories for the sphere having different combinations of (V_0, θ_0) were also calculated by applying the equations of motion in both x and y directions.

The effect of spin on the critical angle of ricochet of a cylinder was firstly examined by Hutchings [5]. To this end, and realizing the infeasibility of using the pressure formula $0.5\rho(Vcos\beta)^2$, he adopted the Rayleigh pressure formula, namely:

$$p = \frac{\pi cos\beta}{4 + \pi cos\beta}\rho V^2 \tag{3}$$

In addition, Hutchings [5] assumed that: i. the angular extent of the wetted area is twice that used by Johnson & Reid [4] due to splash of water ahead of the sphere, and thus, ii. the limiting condition for ricochet is that the sphere moves horizontally at the instance of the centroid of sphere just reaches the undisturbed surface of water. In this way, Hutchings [5] reported that for a non-spinning sphere:

$$\vartheta_c = \frac{17.3}{\sqrt{\sigma}}(degrees) \tag{4}$$

So far, the weight of the spherical projectile was assumed negligible in comparison with the hydrodynamic forces at high speeds. At relatively low speeds, however, the effect of projectile weight has to be considered. Following the procedure of Johnson & Reid [4], the weight and hence the speed of sphere has been accounted for by Soliman et al. [6] as:

$${\vartheta_g}^2 = {\vartheta_c}^2 - \frac{4}{\bar{\bar{F}}} \tag{5}$$

where ϑ_c is that of Eq. (2) and ϑ_g is the new one modified for the speed of sphere. Soliman et al. [6] also carried out tests on the ricochet of Steel and Duralumin spheres from shallow depths of water. Different values of the speed of sphere and the angle of attack were employed. A minimum value of 30 ft/sec was required for Steel spheres in order to achieve ricochet. The effect of spin, albeit uncontrolled, was furthermore explored; only forward spin has been achieved due to which smaller angle was observed for ricochet.

Miloh & Shukron [7] strongly criticized the assumptions made in [3-6], describing it as lack in physical rigor. They formulated the Kelvin-Kirchoff-Lagrange equations of motion based on the energy method assuming large impact velocity. The formulation was performed in terms of time-dependent added-mass coefficients and their time derivatives. No pressure distribution over the sphere surface is prescribed since the method temporarily evaluates the added-mass coefficients and their time-derivatives in the high-frequency limit where the spray energy is ignored with respect to the total kinetic energy of water. Moreover, the limiting condition for ricochet is that the sphere is just above the undisturbed surface and has zero normal velocity. It was found that the submergence of ricocheting sphere in no time exceeds 1.4 times its radius, even for infinite speed and density of the sphere. Also, the value of critical angle for ricochet predicted by Eq. (1) was found by Miloh & Shukron [7] to represent the infinite Froude number asymptote of their analytic solution. Finally, they predicted a threshold value of Froude number below which a ricochet is not possible, no matter how small the angle. This number is directly proportional with the density of the sphere.

Numerical methods have also been employed for the solution of the ricochet problem, like the source panel method [8] where impact forces and ricochet behavior of the arbitrary-shaped solid bodies can be computed. A disk cylinder and two tangent ogives were tested for validation of the method.

The effect of spin on the characteristics of skipping of thin flat disks was addressed by Rosellini et al. [9]. Experiments revealed a positive effect on the ricochet occurrence through enhancing the aerodynamic stability due to gyroscopic effects. No effect of the spin was noted on the angle of attack. In addition, the number of skips was found to be in direct proportionality with the linear velocity of disk.

An interesting extensive work by Truscot & Techet [10] investigated the effect of spin on the aspects of normal water-entry of a sphere. Controlled spin about the horizontal axis was imparted to standard billiard balls and projected normally onto water surface. Different values of spin and linear speed were attempted to explore their influence on the sphere trajectory and the splash and cavity dynamics. Figure 2 includes images of the cavity and splash as well as the trajectory of non-spinning (left) and spinning (right) spheres.

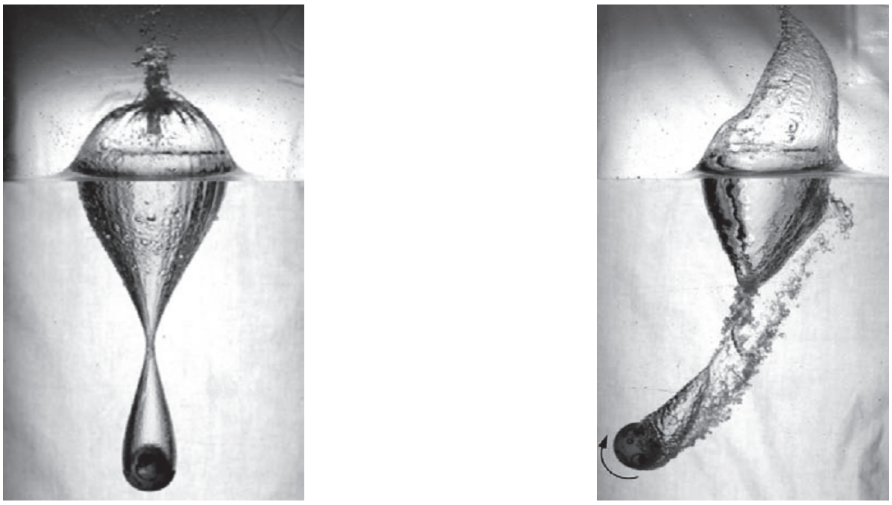

(a) (b)

Fig. 2: Images of the cavity and splash as well as the trajectory of 57 mm diameter spheres. (a) non-spinning: V= 5.95 m/s. (b) spinning V=5.45 m/s, spin=251 rad/s. Both images were taken at the same time after impact (t=102 ms). [10]

The apparent curvature in the trajectory of the spinning sphere was attributed to the lift widely known as "Magnus effect"; the lift force increased with spin increase.

The oblique impact of a torpedo onto water was studied theoretically, numerically, and experimentally by Wei et al. [11]. The linear and angular motions of a torpedo were formulated and solved for the trajectory. MSC DYTRAN was used to simulate the water entry, and the wind tunnel experimentation was based on the similarity principle.

Moxnes et al. [12] used AUTODYN code with the Smooth Particle Hydrodynamics (SPH) method to simulate the ricochet of a spherical steel projectile from the water surface. The simulation with AUTODYN showed too large a drag coefficient but the critical angle of ricochet was consistent with Eq. (1).

Numerical solution of the ricochet of solid non-spinning cylinders from water surface was investigated by Omidvar et al. [13] where fixed ghost boundary conditions were added to Smooth Particle Hydrodynamics (SPH) open source code. It was concluded that the Smoothed Particle Hydrodynamics is a suitable method to investigate the water impact of solid objects.

Recently, Nguyen et al. [14] extended and applied a two-phase three-equation model to simulate the ricochet of circular cylinders from water surface. The numerical method was solved for a cylinder with different densities, and comparisons of predicted and experimental data showed fairly good agreement, which confirmed the capability and robustness of the model for accurate simulation of free surface and water impact flows.

Nguyen et al. [15] presented an efficient free surface solver to simulate the three dimensional modeling of the ricochet problems for solid bodies entries to the water. A dynamic numerical scheme was implemented of grid to facilitate the flow simulation of the complex geometries entered to water.

Lyu et al. [16] experimentally studied the impact of a bouncing sphere to the water surface. The effect of impact velocity and initial impact angle and the energy dissipation on the ricochet of spheres were evaluated. Also the cavitation effect on ricochet were conducted. The study showed that more than half of the initial energy was dissipated at low impact angles.

The authors believe that the ricochet of solids off liquid surfaces is far from exhaustive, particularly in the cases where spinning is involved. In the absence of available theoretical estimate of the critical angle of ricochet associated with spinning spheres, it is hoped that this work will fill some the blanks.

2. THEORETICAL ANALYSIS

Most of the criticisms cited regarding theoretical analyses are focused on the assumptions made prior to, or throughout the analysis, especially those made not on a physical- but on ad hoc- basis. Approximations are another source of precision loss too. In this work, only necessary assumptions, pertaining to the physics of the problem and leading to feasible and reasonable results, will be made. Moreover, the oft-neglected terms (based on their insignificance) will be retained or at least partly sacrificed. The present analysis is based on the following:

1. The hydrodynamic pressure on an elemental surface whose normal makes an angle $\beta \leq \frac{\pi}{2}$ with oncoming stream of non-viscous fluid is that due to Rayleigh - Eq.(3). As stated in the preceding section, Hutchings [5] used this formula in order that the spin effect can be accounted for.

2. The effects of cavitation, splash and two phase flow are negligible compared to the hydro-dynamic forces of lift and drag. Thus, the pressure is primarily due to the equipotential undisturbed surface of the water.

3. The limiting condition for ricochet is that the whole sphere is just above the undisturbed surface and has zero normal velocity.

4. Gravitational forces are introduced in order that the speed and radius of the sphere can be accounted for.

Referring to Fig. 3(A), a backwards spinning sphere enters a calm plane surface of water at an intermediate stage where the sphere has entered a distance y, attained a current speed V in the direction inclined at angle. The wetted portion of the sphere (shown shaded in the figure) extends from $\varphi = 0$, or $y' - axis$ to $\varphi = \varphi_0$.

The hydrodynamic force normal to a surface element of area dS is:

$$dF_n = pdS \tag{6}$$

where, after Hutchings [5]:

$$p = \frac{\pi cos\beta}{4 + \pi cos\beta}\rho V'^2 \cong \frac{\pi}{5}\rho V'^2 cos\beta \tag{7}$$

The elemental area can be calculated as:

$$dS = a^2 sin\varphi . d\varphi d\psi \tag{8}$$

The resultant velocity $V'$of a point on the element relative to oncoming water is given by:

$$V'^2 = V^2 + 2r\omega V cos\alpha + r^2\omega^2 \tag{9}$$

From Fig. 3(B), it is shown that:

$$rcos\alpha = acos\varphi \tag{10}$$

$$rsin\alpha = asin\varphi . cos\psi \tag{11}$$

It can easily be shown that:

$$V' cos\beta = Vsin\varphi . cos\psi \tag{12}$$

As a result:

$$dF_n = \frac{\pi}{5}\rho VV' a^2 sin^2\varphi . cos\psi . d\varphi d\psi \tag{13}$$

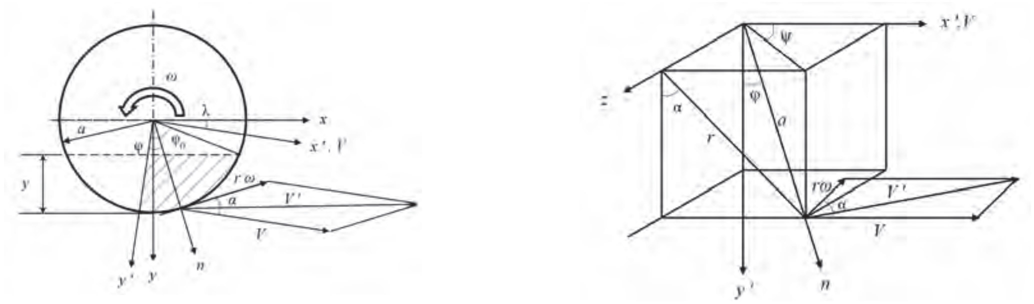

(a) (b)

Fig. 3: (a) Velocity vectors on spinning sphere and (b) Relation between the radius of sphere and radius of rotation.

It is noteworthy to distinguish between two intervals in terms of depth of submergence: the first interval, shown in Fig. 4, in which $0 \le y \le a(1 - cos\lambda)$, and the second interval is which $y > a(1 - cos\lambda)$, see Fig. 3(A). These intervals are differentiated through the parameter, δ, where:

$$\delta = \begin{Bmatrix} \lambda - \gamma \ , & 0 \le \gamma \le \lambda \\ 0 \ , & \gamma > \lambda \end{Bmatrix} \tag{14}$$

$$\gamma = cos^{-1}\frac{a - y}{a} \tag{15}$$

$$\varphi_0 = \lambda + \gamma \tag{16}$$

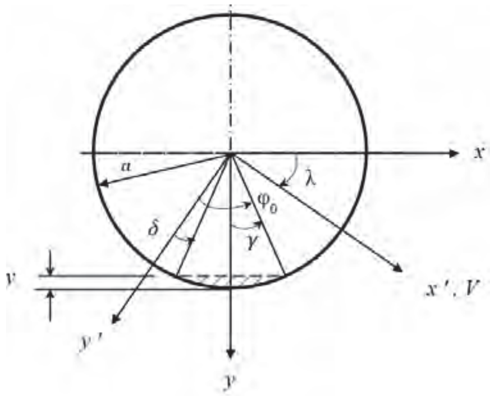

Fig. 4: First stage of wetted portion is shown shaded.

The drag force, D, along x '- axis is given by:

$$D = \int_{S}^{\varphi_0} dF_n . sin\varphi . cos\psi \tag{17}$$

or:

$$D = \frac{\pi}{5}\rho a^2 \int_{\delta}^{\varphi_0} 2\int_{0}^{\frac{\pi}{2}} \sqrt{V^2 + 2r\omega V cos\alpha + r^2\omega^2} . V sin^3\varphi . cos^2\psi . d\varphi d\psi \tag{18}$$

The integration is performed over the leading half of the sphere below the undisturbed surface of water. At this stage, one may neglect the $r^2\omega^2$ term and still seek a numerical solution or retain a part of it while rendering the above integral totally tractable. So, let $r^2\omega^2 \cong r^2\omega^2 cos^2\alpha$, then:

$$D = \frac{\pi}{5}\rho a^2 \int_{\delta}^{\varphi_0} 2\int_{0}^{\frac{\pi}{2}} (V + a\omega cos\varphi) . V sin^3\varphi . cos^2\psi . d\varphi d\psi \tag{19}$$

Thus:

$$D = \frac{\pi^2 \rho a^2 V^2}{240}[F_1(\varphi_0) - F_1(\delta)] \tag{20}$$

where:

$$F_1(\varphi) = 8cos^3\varphi - 24cos\varphi + \frac{6a\omega}{V} sin^4\varphi \tag{21}$$

Following the same procedure, the lift, L, acting upwards along the y- axis, is given by:

$$L = \int_{S}^{\varphi_0} dF_n . cos\varphi \tag{22}$$

or:

$$L = \frac{\pi}{5}\rho a^2 \int_{\delta}^{\varphi_0} 2\int_{0}^{\frac{\pi}{2}} \sqrt{V^2 + 2r\omega V cos\alpha + r^2\omega^2} . V sin^2\varphi . cos\psi . cos\varphi d\varphi d\psi \tag{23}$$

Finally:

$$L = \frac{\pi\rho a^2 V^2}{240}[F_2(\varphi_0) - F_2(\delta)] \tag{24}$$

where:

$$F_2(\varphi) = 32sin^3\varphi + \frac{3a\omega}{V}(4\varphi - sin4\varphi) \tag{25}$$

The two components of the hydrodynamic force are used in the equations of motion of the sphere to calculate the horizontal and vertical displacements and velocities of the sphere whereby the trajectory of the sphere can be determined.

Hence:

$$m\frac{dV_x}{dt} = -F_x = -(D.cos\lambda - L.sin\lambda) \tag{26}$$

Using Equations. (20 and 24):

$$\frac{4}{3}\pi a^3 \rho_s \frac{dV_x}{dt} = -\frac{\pi a^2 V^2}{240}\rho[\pi cos\lambda\{F_1(\varphi_0) - F_1(\delta)\} - sin\lambda\{F_2(\varphi_0) - F_2(\delta)\}] \tag{27}$$

$$\frac{dV_x}{dt} = -\frac{V^2}{320a\sigma}[\pi cos\lambda\{F_1(\varphi_0) - F_1(\delta)\} - sin\lambda\{F_2(\varphi_0) - F_2(\delta)\}] \tag{28}$$

Moreover:

$$m\frac{dV_y}{dt} = mg - F_y = mg - (D.sin\lambda + L.cos\lambda) \tag{29}$$

Thus:

$$\frac{4}{3}\pi a^3 \rho_s \frac{dV_y}{dt} = mg - \frac{\pi\rho a^2 V^2}{240}[\pi sin\lambda\{F_1(\varphi_0) - F_1(\delta)\} + cos\lambda\{F_2(\varphi_0) - F_2(\delta)\}] \tag{30}$$

or:

$$\frac{dV_y}{dt} = g - \frac{V^2}{320a\sigma}[\pi sin\lambda\{F_1(\varphi_0) - F_1(\delta)\} + cos\lambda\{F_2(\varphi_0) - F_2(\delta)\}] \tag{31}$$

It should be noted that:

$$tan\lambda = \frac{V_y}{V_x} = \frac{dy/dt}{dx/dt} = \frac{dy}{dx} \tag{32}$$

$$V^2 = {V_x}^2 + {V_y}^2 \tag{33}$$

Equations (28) and (31) were solved using MATLAB, with the following initial conditions: At t=0, x=y=0, $V_x = V_0 cos\theta_0$, $V_y = V_0 sin\theta_0$. A flowchart of the MATLAB code is given in Fig. 5.

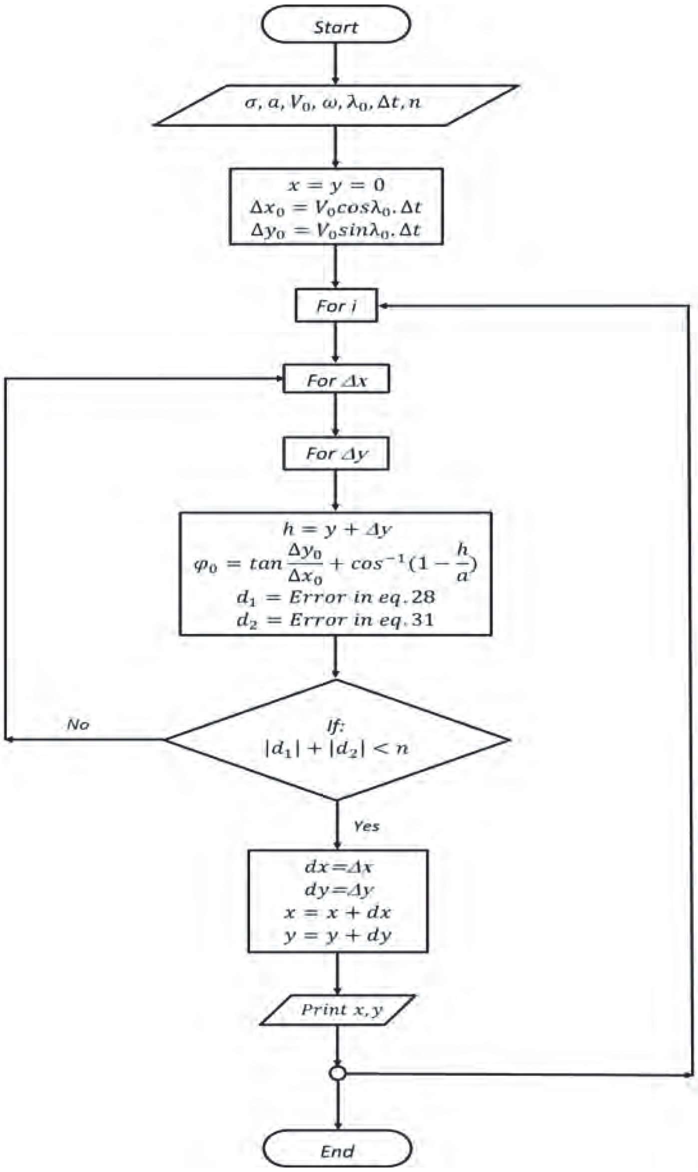

Fig. 5: MATLAB code flowchart.

3. NUMERICAL MODEL

In order to be able to judge the accuracy of the present analysis, extensive experimentations are usually recommended. However, due to the vast difficulties encountered during a single experiment, the simulation of the problem would be far more suitable in this respect. The effects of cavitation, splash, and two phase flow are negligible compared to the hydro-dynamic forces of lift and drag. ABAQUS 17-1 version was utilized to model the oblique entry of a solid sphere into water with both rotational and translational velocities. As shown in Fig. 6, the model consists of two entities, namely "water box" and "Aluminum sphere". The water box dimensions are 600, 120, and 70 mm and the radius of the ball is invariably 10 mm. The length of the water box was chosen such that the sphere has enough water space during the expected course of travel of the sphere. Other sides of the water box were selected as non-reflecting edges to neglect the effect of reflecting waves. The initial translational velocity is fixed at 10 m/sec while the rotational speeds considered are 0, 100, 200, and 300 rad/sec.

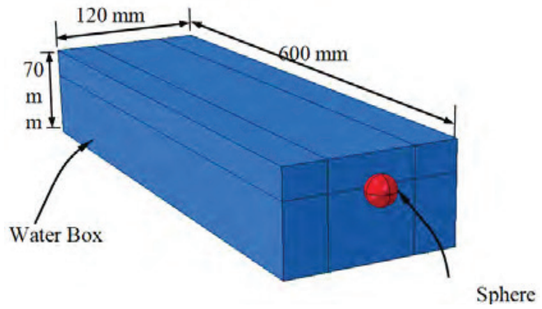

Fig. 6: Schematic drawing of the assembled model.

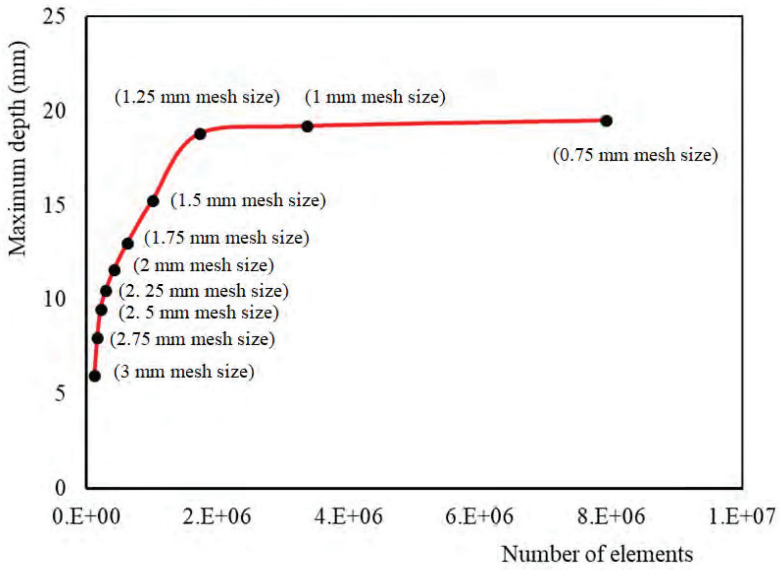

Fig. 7: Mesh convergence, λ_0=11 deg.

Referring to Fig. 7, the maximum depth was selected according to the mesh size. It remained almost stable beyond the 1.25 mm mesh size (1720320 elements). For reasonably accurate results with possible run times, the 1.25 mm element size was selected. The type selected for mesh elements of the water box was EC3D8R (An 8-node linear Eulerian brick, reduced integration, hourglass control), while C3D10M (A 10-node modified quadratic tetrahedron) was assigned for the aluminum ball. This model was capable of capturing the effect of the attack angle of the aluminum sphere upon ricochet against the water surface.

4. RESULTS AND DISCUSSION

The oblique entry of aluminum ($\sigma = 2.7$) spinning spheres of radius 10 mm and speed of 10 m/sec (Fr = 32) was determined analytically and simulated as well. As a benchmark, the non-spinning case was also considered.

The present analysis proposes two differential equations of motion of the sphere, Equations (28) and (31), in x- and y- directions respectively. An algorithm was built to solve these equations for different values of angle between the sphere flight and the water surface. Critical angles of ricochet were sought for a non-spinning sphere as well as for spheres spinning at 100, 200, and 300 rad/sec, as shown in Figs. 8, 9, 10 and 11, respectively.

In these figures, positions of the sphere were determined from the moment of initial contact with water (at origin of graph) to the moment of either total emergence from the water (i.e. ricochet) or eventual sinking. According to the definition of the limiting condition of ricochet, the whole sphere emerges with just a horizontal speed. This implies that the trajectory of the sphere in this case has a local maximum point located right on the water surface. As seen in Figs. 8(A), 9(A), 10(A) and 11(A) the trajectories of ricocheting spheres almost exhibit local maxima at the water surface; exact determination of these maxima was dictated by effort and time of computation. On the other hand, a non-spinning sphere eventually sinks (or non-ricochet) if it is fully submerged, see Fig. 8(B). This, of course, is attributed to the fact that the sphere in this case has no more hydrodynamic lift to overcome the gravity. Another explanation is also provided by Equations (24) and (25) for ω=0 and $\varphi_0 = \pi$. Since the spinning spheres are continually experiencing lift, even when they are totally submerged, the sphere is said to be in a state of non-ricochet only if it reaches the local maximum point without total emergence from the water surface, see Figures 9(B), 10(B) and 11(B).

Compared with the experimental findings of Richardson [2], the trajectories of ricochet in Figs. 8-11(A) resemble that depicted in Fig. 1(b), while those of non-ricochet resemble that of Fig. 1(c).

Of special interest is the uniform motion of the sphere at the end of its course of entry, see Fig.9(B). This suggests that the lift is just counteracted by gravity by the time the drag ceases to exist.

The values of the critical angle of ricochet and non-dimensional maximum depth of submergence at critical ricochet, for non-spinning sphere drawn from the above mentioned figures, are listed in Table 1 together with available published data.

Table 1: Comparison of the critical angle of ricochet λ_c and the non-dimensional maximum depth of submergence at critical ricochet, y_{max}/a for non-spinning sphere with published data.

Ref.	Present work	Exp.[2]	Eq.(1).[3]	Eq.(2).[4]	Eq.(4).[5]	Analytic [7]
λc , deg.	10.43	9	10.95	10.65	10.53	10
y_{max}/a	1.56	-----	-----	2.00	1.00	1.16

Except for λc = 90, the present analysis prediction is favorably in agreement with the available data. The experimental value reported by Richardson [2], λc = 90, was previously discussed by Johnson & Reid [4] who attributed this variation to the extremely low Froude number.

The non-dimensional maximum depth of submergence at critical ricochet, y_{max}/a, is determined from the trajectory of the sphere. As apparently seen in Table 1, the present analysis falls within the previously assumed values in References [4,5] and the numerically computed value in Ref. [7]. In the absence of extensive experimental work, the discrepancies shown in Table 1 cannot be presently resolved.

A similar presentation of results was addressed to the effect of spin in order to assess the desired benefits, if any, when a back spin is imparted to a solid sphere entering the water. Table 2 is a summary of the results drawn from Figs. 9, 10, and 11.

Table 2: Analytical values of critical ricochet angle and max. immersion depth.

Backspin, ω (rad/s)	**0**	**100**	**200**	**300**
Critical ricochet angle, λc (deg.)	10.43	11.1	11.7	12.5
Max. immersion depth, y_{max}/a	1.56	1.64	1.74	1.86

It is clear that the backspin enhances the tendency of the sphere towards ricocheting off the water surface and that the enhancement is higher at higher values of spin. Moreover, the sphere experiences higher depths of submergence at higher values of spin. No relevant previous works are available with which a comparison of these findings could be made, since the effect of spin, on the characteristics of sphere impact with water, is only presently investigated.

Data from Figs. 8 through 11 were rearranged to display the influence of spin on the range of contact of the sphere with water for the cases of critical angles of ricochet, as displayed in Fig. 12. It is obvious that the increase in maximum depth of immersion due to spin is accompanied by a shortening in the range of contact, and the effect is nonlinear. This can be returned to the direct proportionality of the lift force with the spin.

"Magnus effect", widely known in spinning solids of revolution in air, is especially addressed in this work. For this purpose, the experimental finding of Truscot & Techet [10], shown in Fig. 2(b), was chosen. In this experiment, a ball enters the water pool normally with translational as well as rotational speeds. The same data of the experiment were used in the present analysis, whereby the trajectory of the spinning sphere was computed and plotted as shown in Fig. 13. The comparison is merely qualitative in that the present analysis is capable of predicting the evident curvature in the path of sphere motion which manifests considerable lift forces induced by spin. Nevertheless, the comparison is reasonable in terms of vertical and lateral displacements of the sphere. The drag and lift forces acting on a submerged sphere can be estimated by means of Equations (20), (21), (24) and (25) in conjunction with $\varphi_0 = \pi$ and $\delta = 0$. Hence:

$$D = \frac{\pi \rho a^2 V^2}{12} \tag{34}$$

$$L = \frac{\pi \rho a^3 \omega V}{16} \tag{35}$$

Numerical analysis was presently performed using ABAQUS 17-1 version to simulate the process of oblique impact of spheres with the water surface. A typical example of the simulation of the ricochet process is displayed in Fig. 14. The critical angle of ricochet for the same four cases, namely non spin and 100, 200, and 300 rad/s-spins, were sought. The trajectories for these critical cases are gathered as shown in Fig. 15. Similar trends to those found analytically in Fig. 12, were observed. This suggests that the ricochet process can well be simulated and used in extensive studies of similar processes. The process of simulation is highly sensitive to the mesh size and hence the number of elements. The optimum size was governed by the conditions prevailing in such an event on one hand and in the other hand by the inevitable limitations of time and effort. In Fig. 15, the range of sphere trip of ricochet differs slightly from the analytical results of Fig. 12, in value as well as in the nature of dependence with spin. The difference, however, lies within the range of scatter cited in the available data. The critical angle of ricochet as well as the non-dimensional maximum depth of immersion were extracted from the trajectories and listed in Table 3. For purpose of comparison between the analytical and numerical findings, Table 4 is constructed by collecting the data of Tables 3 and 4.

Table 3: Numerical values of critical ricochet angle and max. immersion depth

Backspin, ω (rad/s)	**0**	**100**	**200**	**300**
Critical ricochet angle, λc (deg.)	10.75	11.35	12	12.8
Max. immersion depth, y_{max}/a	1.52	1.62	1.71	1.83

Table 4: Analytical and numerical values of critical ricochet angle and max. immersion depth

Backspin, ω (rad/s)	**Critical ricochet angle, λc (deg.)**		**Max. immersion depth, y_{max}/a**	
	Analytical	**Numerical**	**Analytical**	**Numerical**
0	10.43	10.75	1.56	1.52
100	11.1	11.35	1.64	1.62
200	11.7	12	1.74	1.71
300	12.5	12.8	1.86	1.83

As revealed by Table 4, the simulation results in higher values for the critical angle of ricochet than that found by the analysis. On the contrary, the simulation predicts lower values regarding the maximum depth of immersion. This suggests that the hydrodynamic forces in the simulation were higher than those assumed in the analysis. The variation in analytical with numerical results can be reduced either by increasing the constant ($\pi/5$) in the pressure formula, Eq. (7), or selecting moderate pressures in the simulation process. Either way is only possible or favorable in the presence of extensive experimentation as the actual and realistic datum.

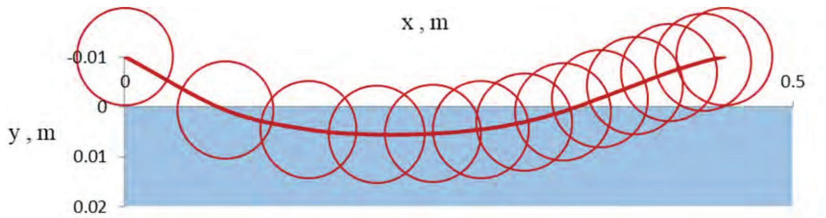

(a) Ricochet, $\lambda_0 = 10.43\ deg$

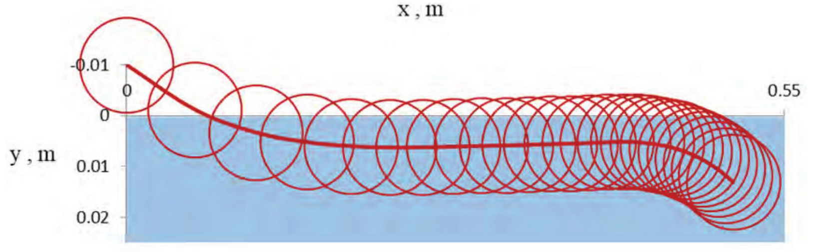

(b) Non ricochet, $\lambda_0 = 10.45\ deg$

Fig. 8: Trajectories of non-spinning sphere at different angles of attack.

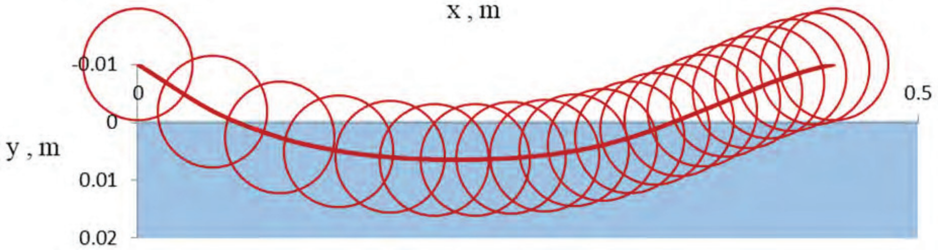

(a) Ricochet, $\lambda_0 = 11.1\ deg$

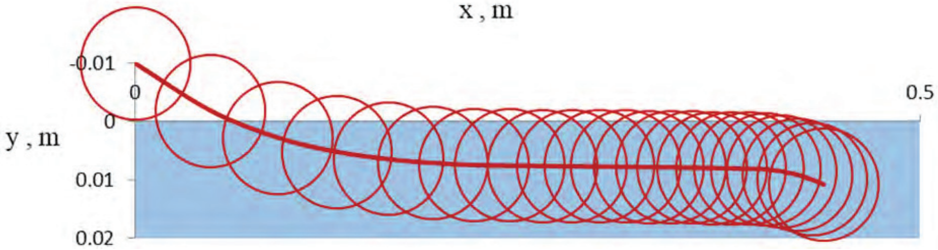

(b) Non ricochet, $\lambda_0 = 11.2\ deg$

Fig. 9: Trajectories of sphere spinning at ω=100 rad/sec at critical angles of attack.

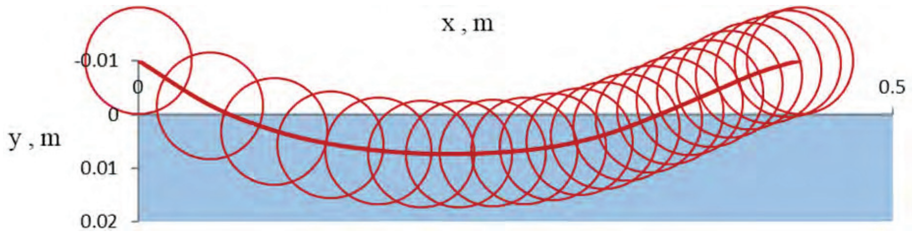

(a) Ricochet, $\lambda_0 = 11.7\ deg$

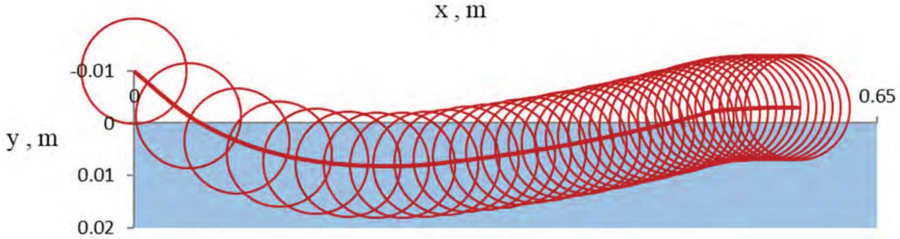

(b) Non ricochet, $\lambda_0 = 11.8\ deg$

Fig. 10: Trajectories of sphere spinning at ω=200 rad/sec at critical angles of attack.

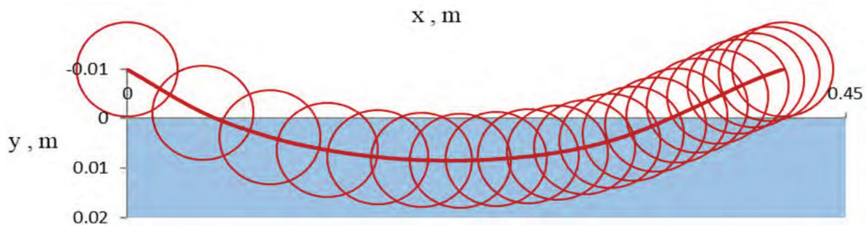

(a) Ricochet, $\lambda_0 = 12.5\ deg$

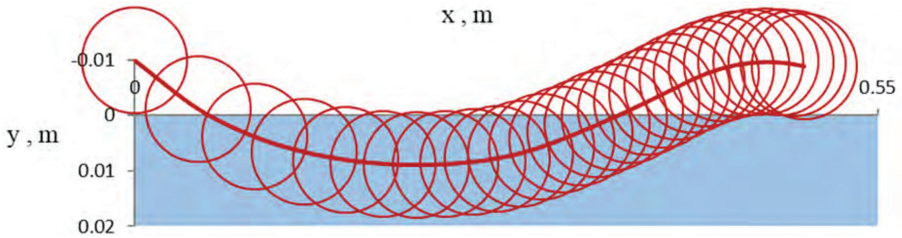

(b) Non ricochet, $\lambda_0 = 12.55\ deg$

Fig. 11: Trajectories of sphere spinning at ω=300 rad/sec at critical angles of attack.

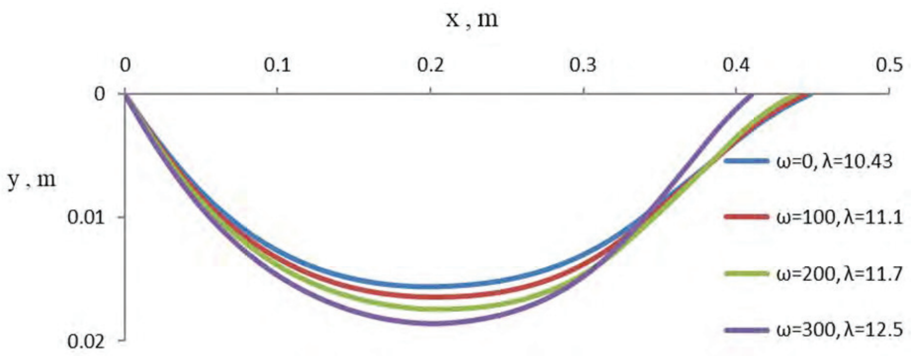

Fig. 12: Analytical trajectories of ricocheting sphere spinning at different values of spin and critical angles of attack.

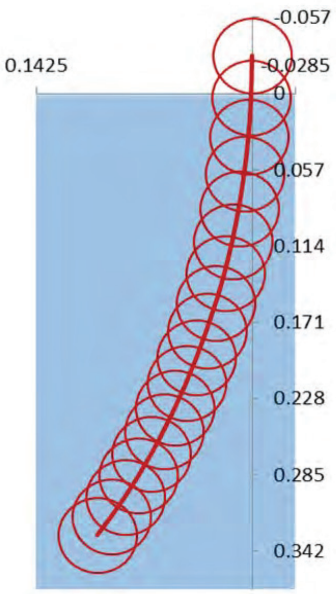

(a)

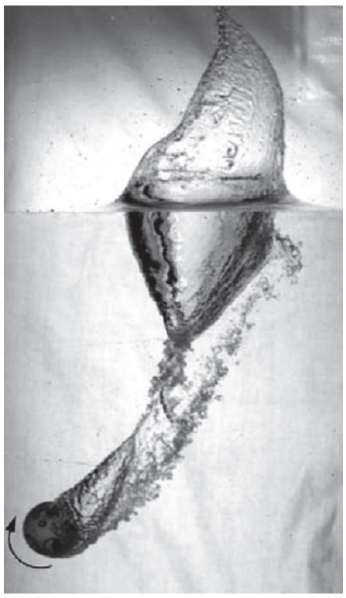

(b)

Fig. 13: Qualitative comparison between the trajectories of spinning spheres: (a) Present analysis, (b) Experiment [10].

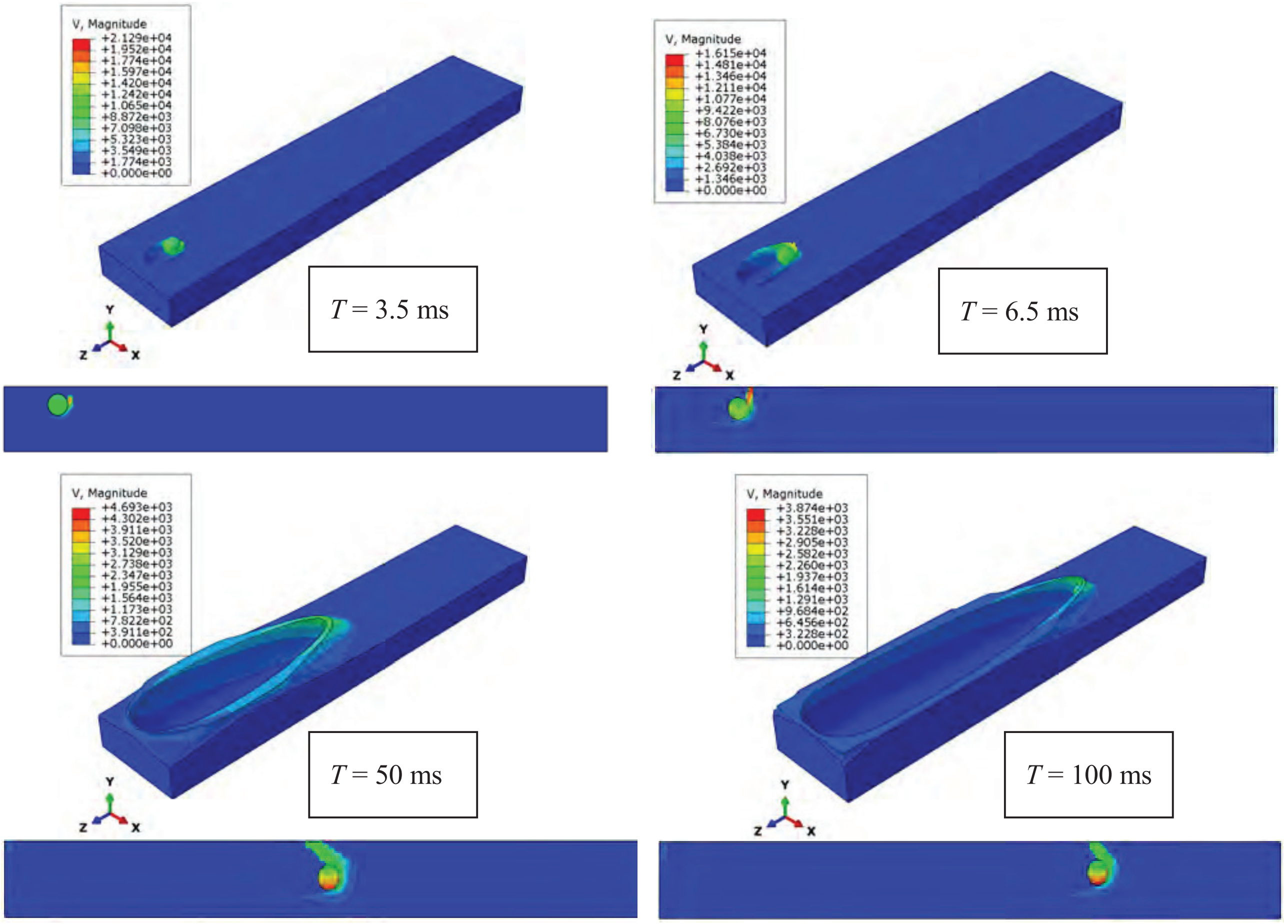

Fig. 14: Simulation of the ricochet process.

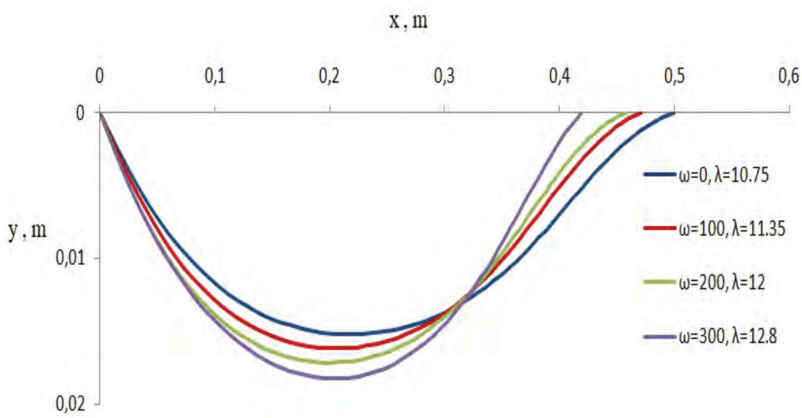

Fig. 15: Numerical trajectories of ricocheting sphere spinning at different values of spin and critical angles of attack.

5. CONCLUSIONS

Liquid-solid interaction phenomena are still receiving the attention of engineers and scholars in view of the rapid advances in technology. The research in the field of ricochet of solid spheres from water surfaces, though seemingly exhausted, is yet far from being well established. A consensus now exists related to the tendency of a sphere to ricochet from water, i.e. ricochet is more likely with high translational and backspin speeds, low density, large diameter, and low angle of impact.

Although the process is highly complex and no single work can handle all the parameters and their effects, the present work assumes that the effects of cavitation, splash, and two phase flow are negligible compared to hydro-dynamical forces of lift and drag. The main contributing conclusions are:

1. A theoretical analysis, based on a previous one and modified for the spin, is made.
2. The maximum critical angle of ricochet increases with backspin of the sphere. A backspin of 300 rad/sec improves the angle from 10.43^0 to 12.5^0.
3. The non-dimensional maximum depth also increases with backspin. A backspin of 300 rad/sec increases the depth from 1.56 to 1.86.
4. The theoretical analysis was found capable of describing previous experimental work, as well as matching other analytical and numerical works.
5. A numerical model simulation of fluid-structure and ricochet of spinning spheres was also made using ABAQUS 17-1 version.
6. The implementation of ABAQUS was efficient in simulating the ricochet process.
7. The analytical and numerical results were consistent in that the backspin enhances the capability of a sphere in performing ricochet.
8. Magnus effect in liquids was presently described and relations predicting the drag and lift forces were deduced.
9. The analytical and numerical results vary to the same extent of variation of hydrodynamic forces.
10. A detailed and extensive experimental work is highly recommended to end the widely cited debate among other works.

REFERENCES

[1] Johnson W. (1997) The ricochet of spinning and non-spinning spherical projectiles, mainly from water. Part II: An outline of theory and warlike applications. Int. J. Impact Engineering, 21: 25-34. https://doi.org/10.1016/S0734-743X(97)00033-X.

[2] Richardson EG. (1948) The impact of a solid on a liquid surface. Proc. Phy. Soc., 61: 352-367. https://doi.org/10.1088/0959-5309/61/4/308.

[3] Birkhoff G, Birkhoff GD, Bleick WE, Handler EH, Murnaghan FD, Smith TL. (1944) Ricochet off water. App.Math. Panel, National Defense Research committee, Memo. 42, 4M, AMG-C.

[4] Johnson W, Reid SR. (1975) Ricochet of spheres off water. J. Mech. Engineering. Sci., 17: 71-81. https://doi.org/10.1243/JMES_JOUR_1975_017_013.

[5] Hutchings IA. (1976) The ricochet of spheres and cylinders from the surface of water. Int. J. Mech. Sci., 18: 243-247. https://doi.org/10.1016/0020-7403(76)90006-0.

[6] Soliman AS, Reid SR, Johnson W. (1976) The effect of spherical projectiles speed in ricochet off water and sand. Int. J. Mech. Sci., 18: 279-284. https://doi.org/10.1016/0020-7403(76)90029-1.

[7] Miloh T, Shukron Y. (1991) Ricochet off water of spherical projectiles. J. Ship Research, 35: 91-100. https://doi.org/10.5957/jsr.1991.35.2.91.

[8] Park MS, Jung YR, Park WG. (2003) Numerical study of impact force and ricochet behavior ofhigh speed water-entry bodies. Computers & Fluids, 32: 939-951. https://doi.org/10.1016/S0045-7930(02)00087-7.

[9] Rosellini L, Hersen F, Clanet C, Bocquet L. (2005) Skipping stones. J. Fluid Mech, 543: 137-146. https://doi.org/10.1017/S0022112005006373.
[10] Truscott TT, Techet AH. (2009) Water entry of spinning spheres. J. Fluid Mech. , 625: 1-31. https://doi.org/10.1017/S0022112008005533.
[11] Wei Z, Shi X , Wang Y. (2012) The oblique water entry impact of a torpedo and its ballistic trajectory simulation. Int. J. Numerical Analysis and Modeling, 9: 312–325. https://doi.org/10.1007/978-3-642-11842-5_62.
[12] Moxnes JF, Frøyland Ø, Skriudalen S, Prytz AK, Teland JA, Friis E. (2016) On the study of ricochet and penetration in sand, water and gelatin by spheres, 7.62 mm APM2, and 25 mm projectiles. Defence Technology, 12: 159-70. https://doi.org/10.1016/j.dt.2015.12.004.
[13] Omidvar P, Farghadani O, Nikeghbali P. (2017) SPH for impact force and ricochet behavior of water-entry bodies. Int. J. Modern Physics C., 28: 1750119. https://doi.org/10.1142/S0129183117501194.
[14] Nguyen VT, Phan TH, Park WG. (2020) Modeling and numerical simulation ofricochet and penetration of water entry bodiesusing an efficient free surface model. Int. J. Mech. Sci., 182: 105726. https://doi.org/10.1016/j.ijmecsci.2020.105726.
[15] Nguyen VT, Phan TH, Duy TN , Park WG. (2021) 3D simulation of water entry of an oblique cylinder with six-degree-of-freedom motions using an efficient free surface flow model. Ocean Engineering, 220: 108409. https://doi.org/10.1016/j.oceaneng.2020.108409.
[16] Lyu X , Yun H, Wei Z (2021) Experimental Study of a Sphere Bouncing on the Water. Journal of Marine Science and Application, 20: 714-722. https://doi.org/10.1007/s11804-021-00236-9.

Nomenclature			
a	Radius of sphere	x, y, z	Coordinate axes
D	Drag force	ω	Angular velocity of sphere
F_n	Hydrodynamic force normal to solid surface	σ	Specific density of sphere
F_x	Horizontal component of hydrodynamic force	β	Angle of obliquity of plane relative to liquid flow
F_y	Vertical component of hydrodynamic force	ρ, ρ_s	Density of liquid and sphere
$\bar{F}$	Froude number $= \bar{V}/\sqrt{ag}$	θ	Angle of rotation
L	Lift force	ϑ_c	Critical angle of ricochet
m	Mass of solid	φ	Longitude angle
n	Error allowance	Ψ	Latitude angle
p	Hydrodynamic pressure of liquid	λ	Current angle of travel of sphere
r	Radius of rotation	λ_0	Initial angle of travel of sphere
S	Area of sphere surface	φ_0	Angular extent of wetted area
V', V	Velocity of liquid flow relative to sphere surface	θ_0	Angle of entry
V_0	Speed of entry	Δt	Time interval

https://doi.org/10.31436/iiumej.v24i1.2366

PLC-BASED PID CONTROLLER FOR REAL-TIME pH NEUTRALIZATION PROCESS USING PALM OIL MILL EFFLUENT

AZAVITRA ZAINAL[1,2], NORHALIZA ABDUL WAHAB[1*] AND MOHD ISMAIL YUSOF[2]

[1]*Control and Mechatronics Engineering, Faculty of Electrical Engineering, Universiti Teknologi Malaysia, Johor, Malaysia*
[2]*Instrumentation and Control Engineering Section, Malaysian Institute of Industrial Technology, Universiti Kuala Lumpur, Johor, Malaysia*

[*]*Corresponding author: aliza@fke.utm.my*

(Received: 21st March 2022; Accepted: 3rd November 2022; Published on-line: 4th January 2023)

ABSTRACT: The pH neutralization process is a highly non-linear process and time delay system that is difficult to control and to accurately model mathematically. Therefore, the empirical method, which needs reliable experimental data to represent the process dynamics, is often used. In this paper, the performance of the PLC-based PID controller was studied using a different adjustment of the acid dosing pump stroke rate in the pH neutralization process. The pH neutralization process is a single-input, single-output system where the manipulated variable is the alkali dosing pump stroke rate, the controlled variable is pH, and the acid dosing pump stroke rate is set as a constant. The acid dosing pump stroke rate was adjusted to 10%, 15% and 25%. The results showed that the best performance of the PID controller was based on setpoint tracking when the setting of the acid dosing pump stroke rate was set at 10%, which could be used as experimental data in the empirical method. In addition, the real-time control system was integrated between PLC and MATLAB using National Instruments OPC server to access the experimental data in real-time, conduct simulation, and to develop the advanced control in the future.

ABSTRAK: Peneutralan pH adalah proses tidak linear yang sukar dikawal dan sukar mendapat model matematik yang tepat. Oleh itu, kaedah empirikal memerlukan data eksperimen masa nyata bagi mewakili proses dinamik untuk mengatasi masalah ini. Kajian ini adalah berkaitan kajian prestasi pengawal PLC-berdasarkan PID menggunakan pelbagai perubahan kadar strok pam dos asid dalam proses peneutralan pH. Proses peneutralan pH ini adalah sistem satu input/output, di mana pemboleh ubah yang dimanipulasi adalah kadar peratusan strok pam dos alkali menggunakan pam peristaltik, pemboleh ubah kawalan ialah pH dan pemboleh ubah malar ialah peratusan dos asid.Kadar strok pam dos asid dilaraskan pada 10%, 15% dan 25%. Dapatan kajian menunjukkan prestasi terbaik kawalan PID adalah berdasarkan pengesan titik-set apabila kadar strok pam dos asid dilaraskan pada 10%, di mana ianya berkesan apabila digunakan sebagai data eksperimen dalam kaedah empirikal. Tambahan, kajian ini telah berjaya membentuk sistem kawalan masa nyata bagi proses penutralan pH menggunakan PLC dan MATLAB melalui pelayan National Instruments OPC bagi membolehkan pertukaran data eksperimen secara masa nyata yang cekap, menjalankan simulasi dan pembangunan kawalan termaju pada masa hadapan.

KEYWORDS: *OPC DA server; PLC; PID controller; pH neutralization; POME*

1. INTRODUCTION

The palm oil plantation and processing industry is dominated by countries such as Malaysia, Indonesia, and Thailand. Treating palm oil mill effluent (POME) in accordance with regulations and standards from environmental agencies is a major problem in the palm oil industry [1,2]. The discharge POME in Malaysia must meet the standard requirements of Standards A and B of the Environmental Quality (Industrial Effluents) Regulations 2009. The direct discharge of POME has an impact on the environment.

Fresh POME from the palm oil mills is acidic (pH 4-5), hot (80-90 ºC), non-toxic, with high organic content (chemical oxygen demand, COD 50,000 mg/L, biochemical oxygen demand, BOD 25,000 mg/L) and contains significant amounts of plant nutrients [3]. In addition, the discharge of dark brown colored POME into rivers inhibits the growth of aquatic organisms by reducing the penetration of sunlight and impairing photosynthetic activity. The ponding system is a common conventional method of treating POME. Most palm oil mills use anaerobic digestion as their primary treatment for POME. In Malaysia, more than 85% of the palm oil mills use the ponding system for POME treatment, and others use an open digestion tank [4]. Anaerobic digestion is the process of breaking down complex organic substances without oxygen. The process takes longer as the bacterial consortia must adapt to the new environment before using the organic matter to grow [5].

The major factors that affect the performance of the POME treatment digester are pH, mixing process, operating temperature, and organic loading rates into the digester. Operating temperature and pH are important to maximize microbial community performance in an aerobic digester [6]. In Malaysia, the pH of the POME discharge standard according to Standard B of the Environmental Quality (Industrial Effluents) Regulations 2009 is 5.5-9.0 [7]. However, pH control is a highly non-linear process and time delay system that is difficult to control. The dynamics of the pH neutralization process led to the difficulty of obtaining an accurate mathematical model [8]. Therefore, the empirical model of the pH process is the most suitable method to use for solving this problem [9,10]. Reliable experimental data are required to represent the dynamics of process, which only can be obtained with correct experimental setup.

PC-based supervisory control and data acquisition systems (SCADA) are typically used in POME treatment plants to collect, store, and analyze the process data. The system uses a controller, usually a PLC system with embedded PID controller algorithm, to adjust the parameters. The pH neutralization is one of the non-linear processes that requires advanced process control. In this study, the pH neutralization plant system is built from a SIMATIC S7-1200 controller with CPU firmware V4.0 and used TIA Portal V13 software with PLC PID compact block V2.2 for the PID controller control system. However, this system architecture does not support the performance of any simulation with SIMATIC PLCSIM software [11]. In addition, the challenges of the PLC system are that the PLC does not allow for real-time simulation or changes unless the system is under maintenance, and it is difficult to implement the mathematical model and advanced control algorithm in the PLC system. Therefore, the MATLAB platform can be used to design advanced process control, run simulations, and test the controller. The results obtained in MATLAB through simulation can be directly applied to the process plant through the PLC. In industrial automation, this requires a standard method for communicating and exchanging data with multiple types of data tags. The limitation of MATLAB is the difficulty of connecting to the rest of the real-time application system. To overcome this limitation, OPC Data Access (DA) servers can be implemented for real-time data exchange between

PLC and MATLAB using the MATLAB OPC Toolbox [12]. OPC DA server provides specification for the transfer of real-time data from the data acquisition device [13,14].

Several studies have successfully integrated the PLC with MATLAB using the OPC server. A study by Bagal et al. [15] shows a method for implementing a real-time DC motor speed control PLC based on SCADA and MATLAB. With this method, the authors integrated a Mitsubishi FX2N 32MR PLC with OPC DA server KEPServerEx.V4 for data acquisition between the DC motor, SCADA application (Citect SCADA 7.2), and MATLAB. Gajjar et al. [16] developed a water heating tank system for temperature control with VIPA 315-SB PLC using the OPC DA Server KEPServerEx as communication protocol with MATLAB. In this study, a PID controller and a model predictive controller (MPC) were developed to control the temperature for different treatment zones for bottle washing machines. In addition, Bhaskarwar et al. [17] developed the cascade control application for level process plants with a PLC-OPC-MATLAB configuration with the additional function that it can monitor by remote monitoring with the ThingSpeak server. The RSLinx OPCserver is used for the communication protocol between PLC and MATLAB. A recent study by Ahmad et al. [18] using the PLC-OPC server MATLAB communication system was carried out to compare the performance of a traditional PID controller with a neural network controller for PLC-based water flow process control.

The contribution of this paper is described as follows: (1) Developing the real-time system integration between the PLC with MATLAB software through NI OPC servers to ensure data exchange and ability to develop advanced controller in the future. (2) Determining the performance of the PID controller with PLC PID_compact using different settings of the acid pump dosing stroke rate.

2. STRUCTURE OF THE PROCESS PLANT FOR pH NEUTRALIZATION

2.1 The pH Neutralization Pilot Plant

The pilot plant for pH neutralization is installed in the Industrial Process Control Warehouse D1 of the Malaysian Institute of Industrial Technology, Universiti Kuala Lumpur. Figure 1 shows the schematic representation of the pH neutralization plant.

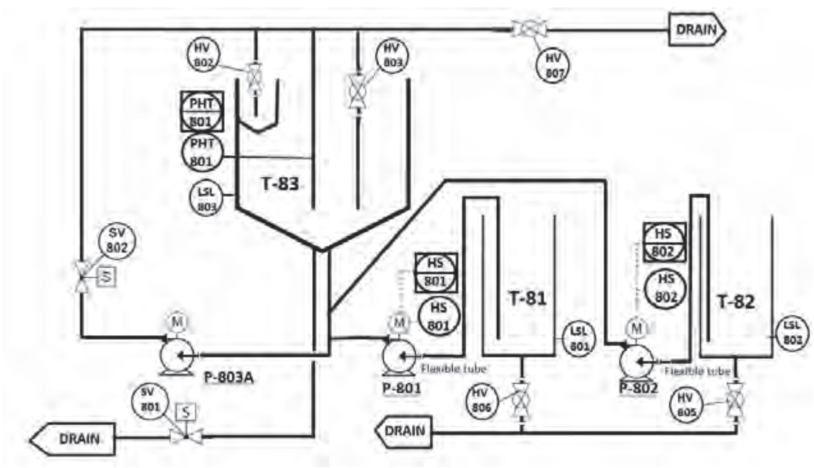

Fig. 1: The pH neutralization pilot plant, MPC318.

The plant consists of three main tanks, namely the acid tank (T-81), alkali tank (T-82), and analysis tank (T-83). The tank volume of the analysis tank is regulated to 30 liters. The volume of the acid and alkali tanks are 40 liters each. The dosing pumps P-801 and P-802 are used to provide the required amount of acid and alkali for the pH neutralization process. The P-803A pump is used to circulate the liquid and mix it with the acid and alkali. Table 1 shows the list of instruments used in the pilot plant development.

Table 1: List of instruments

Tag no.	Descriptions	Measurement Range	Signal range [mA]	Manufacturer
PHT801	pH sensor	0 - 14	4 - 20	Hana Instruments HI61008
P-801	Acid dosing pump	0 – 100 [%]	4 - 20	ProMinent Gamma/L D-69123
P-802	Alkali dosing pump	0 – 100 [%]	4 - 20	ProMinent Gamma/L D-69123

2.2 Development of the PLC Based Process Application

The pilot plant design for pH neutralization consists of hardware and software components. The Siemens Simatic S7-1200 controller is used as the system hardware. Rack 1 is the PLC CPU module which is CPU 1214C DC/DC/Rly. Rack 2 is for the analog input/output module (AI 4x13BIT/AQ 2x14BIT_1). Rack 3 and 4 house the digital output module (DQ 8xRelay_1). The pH transmitter is connected to the analog output module channel 0. The acid and base dosing pumps are connected to the analog input module channel 0 and 1, respectively. The PLC controller is programmed with the Totally Integrated Automation Portal (TIA Portal) software from Siemens. The PLC receives the input signals from the sensor and controls the output device by sending an output signal to achieve the desired operation in a system. Table 2 shows the relationships between the PLC input/output types of tag name - data type.

Table 2: The relationship between the PLC input/output tag name with data type

Field device		PLC-CPU		Data Acquisition	
Tag no.	**Descriptions**	**Tag name**	**Integer value (Analog value)**	**Tag name**	**Measurement value**
PHT801	pH sensor	%IW96	0-27648	%MD200	0 - 14
P-801	Acid dosing pump	%QW96	0-27648	%MD236	0 – 100 [%]
P-802	Alkali dosing pump	%QW98	0-27648	%MD228	0 – 100 [%]

The pH sensor supplies electrical signals in the range from 4 to 20 mA to the analog input module. The analog input module converts 4 to 20 mA electrical signals to 0 to 27648 decimal values (digital signal), which can be read by the PLC. The acid and alkali dosing pumps receive electrical signals in the range of 4 to 20 mA from the analog output module. The analog output module converts 0 to 27648 decimal values (digital signal) into 4 to 20 mA electrical signals. Therefore, the tag with the data type integer is required to save the values from the analog input/output devices.

Figure 2 shows the PLC ladder diagram for scaling analog values for a pH sensor. The electrical signal from the pH sensor memory address %IW96 is normalized to an integer value with the NORM_X Normalize block and then stored in the temporary memory #TEMP1. Then the integer value is scaled to the physical value (pH value 0 - 14) with the SCALE_X Scale block and saved in % MD200 memory address. The same method is used to program the PLC ladder diagram to scale analog values for an analog outputs, acid, and alkali dosing pump. The physical value of the memory address %MD236 is normalized to an integer value with the NORM_X Normalize block and held in the temporary memory #TEMP2. Then, the physical value is scaled to the integer value with the SCALE_X Scale block and sent to the memory address % QW96 or %QW98 of the acid and alkali metering pump.

Fig. 2: The ladder diagram for scaling analog values for the pH sensor (analog input).

Figure 3 shows the built-in PID function in the PLC PID_compact function block, which provides a continuous PID controller. The PLC PID_compact continuously acquires the measured process value within a control loop and compares it with the required setpoint. The technology object PLC PID_compact has the function of tuning, whereby the P, I and D parameters can be calculated automatically depending on the control system.

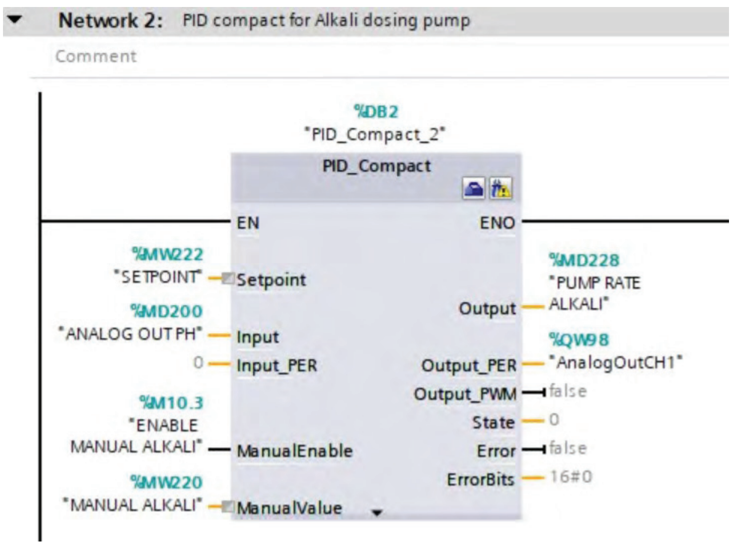

Fig. 3: The PLC PID_compact block used for universal PID controller with integrated tuning.

3. OPC COMMUNICATION STRUCTURE FOR DATA ACQUISITION

3.1 NI OPC Server

A robust and established system is required to ensure the data acquisition between the device and the system. Automation devices that come from different manufacturers require a common communication platform for integration into the overall system. Object Linking and Embedding for process control technology (OPC) can thus be used as a solution that can offer interoperability between the various device manufacturers for safe and efficient data acquisition. Fig. 4 shows the components of the network diagram for PLC based real-time pH neutralization process control with MATLAB Simulink.

Fig. 4: The network diagram of pH neutralization plant.

The PLC is connected to the OPC DA server via OPC Server 2016 from National Instruments. By configuring the OPC server software, the input and output parameters of the PLC can be recorded in real time in the OPC server. The MATLAB OPC Toolbox is used to connect the MATLAB Simulink to the OPC server. The toolbox consists of OPC Configuration, OPC Read, and OPC Write blocks that are used to receive and transfer the data from the OPC DA Server to MATLAB Simulink. MATLAB Simulink acts as a client for the OPC DA Server. The communication between PLC and OPC DA server takes place via PROFINET/Industrial Ethernet (PN/IE) with specific IP address configuration. The NI OPC server is configured and defines the channel, the group and the tags with the appropriate data type as shown in Table 2. The OPC Quick Client is used to read/write data, run a structured text suite, and test the server performance. It can generate error reports that contain detailed feedback on all OPC errors from the server and help to diagnose problems from common OPC clients/servers.

3.2 LABVIEW Configuration

The next step is the configuration to set up the data acquisition between the NI OPC Server with LABVIEW. The purpose is that MATLAB cannot directly detect the communication with the NI OPC server. First, the new project must be created in LABVIEW. Then it finds the new I/O server. The NI OPC server is successfully registered when the OPC1 icon is displayed. Next, it selects National Instrument NIOPC Servers V5 option under Registered OPC Server in the OPC Client. In the next step, it clicks Create Bound Variables to find the registered variables in NI OPC Server. The variables are important for data acquisition and must be added to the LABVIEW program to establish communication. Then the variables can be used in the LABVIEW program.

3.3 MATLAB Simulink Configuration

The final step is to configure the MATLAB OPC Toolbox in Simulink. The MATLAB OPC Toolbox is the source of real-time and historical OPC data that was accessed directly from MATLAB. It can also read, write, and log OPC data from field devices via the PLC. The blocks named OPC Configuration, OPC Read, and OPC Write are used in the model. The OPC configuration block is used to configure pseudo real-time options, OPC clients for use in the model, and behavior in response to OPC errors and events. The required server National Instruments.Variable Engine.1 must be selected under the OPC Configuration block to set up the data acquisition from the pH neutralization plant via the NI OPC Server. Fig. 5 shows the Simulink model of a pH neutralization plant. The value of the stroke rate of the acid and alkali dosing pumps can be set directly with this model. The real-time data is stored in the MATLAB workspace. The next step is the configuration for the OPC Read block, which is used to read data from the OPC Server. In this project, the controlled variable pH value is read synchronously by the pH sensor in a pH neutralization plant. The function of the OPC Write block is to write data to the OPC server. The manipulated variables for this project are acid and alkali dosing pumps, which send an appropriate signal to the field device.

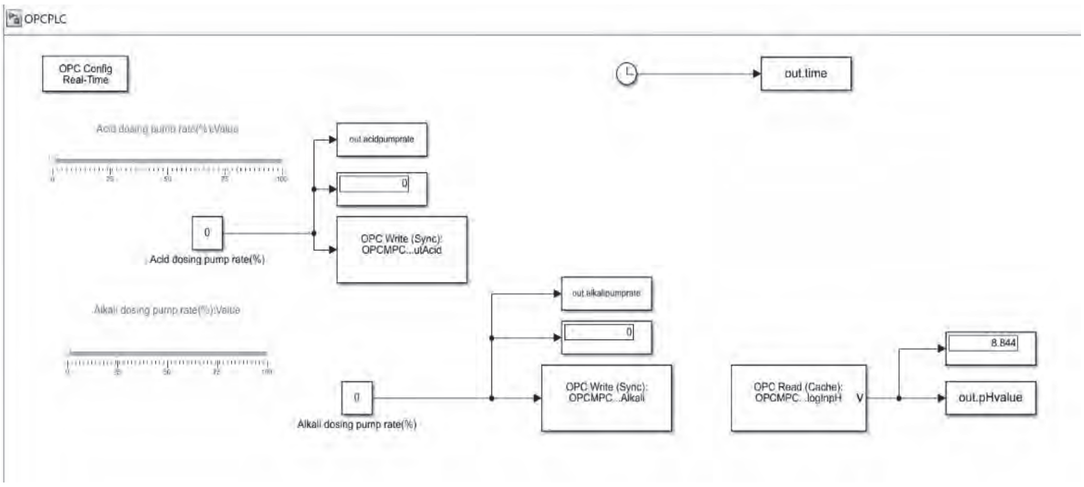

Fig. 5: The Simulink model of pH neutralization plant.

4. PID CLOSED-LOOP CONTROL SYSTEM

4.1 Experimental setup

In this study, the controlled value is pH, and the manipulated variable is the alkali dosing pump stroke rate while the acid dosing pump stroke rate is set constant. The aim of the experiment is to determine the most suitable setting for the acid dosing pump stroke rate, at which the PID controller can work at an optimum level. The experiment was divided into three data sets with the acid dosing pump stroke rate set at 10% (Set A), 15% (Set B) and 25% (Set C). The hydrochloric acid, 0.1M HCl and sodium hydroxide, 0.1M NaOH as acid and alkali are prepared. 1 liter of POME is diluted with 29 liters of 0.1M HCl, and then poured into analysis tank, T-83. The initial value of POME after dilution is 3.8. The POME is supplied by Sedenak Palm Oil Mill Sdn. Bhd. in Johor, Malaysia. The final discharged standard of the POME pH value under the Environmental Quality Act 1974 (Department of Environment, Malaysia) must be in the range of 5.5 to 9.0 [19].

The closed-loop experiment was performed using the built-in PID function in the S7-1200 PLC controller. The PLC PID_Compact function block (refer to Fig. 3) is used, which was specially developed for the control of proportional actuators.

$$y = K_p\left[(bw - x) + \frac{1}{T_i s}(w - x) + \frac{T_d s}{aT_d s+1}(cw - x)\right] \tag{1}$$

Eq. (1) describes the PID algorithm for the PID_Compact [11], where y is the output value of the PID algorithm, w is the set point, T_d is the derivative action time, T_i is the integral action time and K_p is the proportional gain. For the parameters, a is the derivative delay coefficient, which delays the effect of the derivative action, b is the proportional action weighting which represents the proportional action with setpoint changes, and c is the derivative action weighting which represents the derivative action with setpoint changes.

The PLC PID_compact auto tuning is divided into two stages, where the proportional, integral and derivative parameters are calculated during pre-tuning and the parameters are tuned further during fine tuning. However, for this process, the initial pH value is 3.8 and the setpoint is 7. Pre-tuning is therefore not required since the difference between the set point and the pH value is less than 30% of the difference between the pH value minimum and maximum limit, which is 0 and 14. For the requirements of the fine tuning, the setpoint and the pH value must be within the configured limits. During fine tuning, the PLC PID_compact generates an oscillation of the pH value with periodic changes in the manipulated value and alkali dosing stroke rate and calculates the PID parameters for the pH neutralization process. After the fine tuning is complete, the pH setpoint is changed with a positive step from 7.0 to 8.0 at t = 200 s.

4.2 Results and Discussion

With PLC PID_compact pH value fine tuning, an attempt was made to reach the setpoint with the minimum or maximum of alkali dosing stroke rate, which can lead to increased overshoot. Fine tuning begins when the setpoint is reached. The PLC PID_compact is switched to automatic mode and uses the tuned parameters when the fine tuning is completed. Table 3 shows the fine tuning parameters of the PID controller. For set A, the value of the derivative delay coefficient is greater than 1.0, which means the effect of the derivative action is delayed longer. However, for set B and set C, the derivative delay coefficient value is approximately 0, which means that the derivative action is effective for only one cycle and therefore almost not effective. Although the acid dosing stroke rate is set to constant, the amount of acid dosing on the process will affect the fine tuning performance of the PID controller. The fine tuning results show that set A performs well compared to set B and set C.

Table 3: The fine tuning parameter of the PLC PID_Compact

Fine tuning parameter	**The acid dosing stroke rate (%)**		
	SET A: 10%	**SET B: 15%**	**SET C: 25%**
Proportional gain, K_p	3.030118	0.861554	5.138405
Integral action time, T_i	52.58616	0.5780812	1.999941
Derivative action time, T_d	14.1015	0.0709655	0.4994175
Derivative delay coefficient, a	0.1	0.1	0.1
Proportional action weighting, b	0.5276183	1.0	0.7926073
Derivative action weighting, c	0.0	0.0	0.0
Derivative delay $=a \times T_d$	1.4015	0.007096554	0.0499475

Figures 6 to 8 show the corresponding responses of the closed-loop systems to a step reference signal, where the setpoint is changed from 7 to 8. The wavelet transform is used for data preprocessing to remove the disturbance signals. The disturbance signals are due to the on-and-off state of the SV801, which was used to maintain the liquid level in the analysis tank. The total duration of the collected data for each set is 1426 s with a sampling time of 1 s. The acid dosing pump starts dosing according to the setting, and the unit step is changed at t=200 sec. For set A, the alkali dosing pump stroke rate is gradually increased based on the pH value, and then after the setpoint changes, increases to 20% and gradually decreases the value until the setpoint is reached.

The performance indexes of the PID controller are given in Table 4, where t_r, t_p and t_s denote the rise time, peak time and 5% settling time, respectively and the overshoot percentage of the control signal. In Fig. 6 for set A, although the step response of the closed loop system has a high percentage of overshoot, it is able to reach the steady state at 1423.5 sec. Note that in Fig. 7 for set B and 8 for set C, the step response of the closed

https://doi.org/10.31436/iiumej.v24i1.2366

loop system is more oscillatory, has a higher percent overshoot and is unable to reach and remain stable within the specified range of 5% of its setpoint.

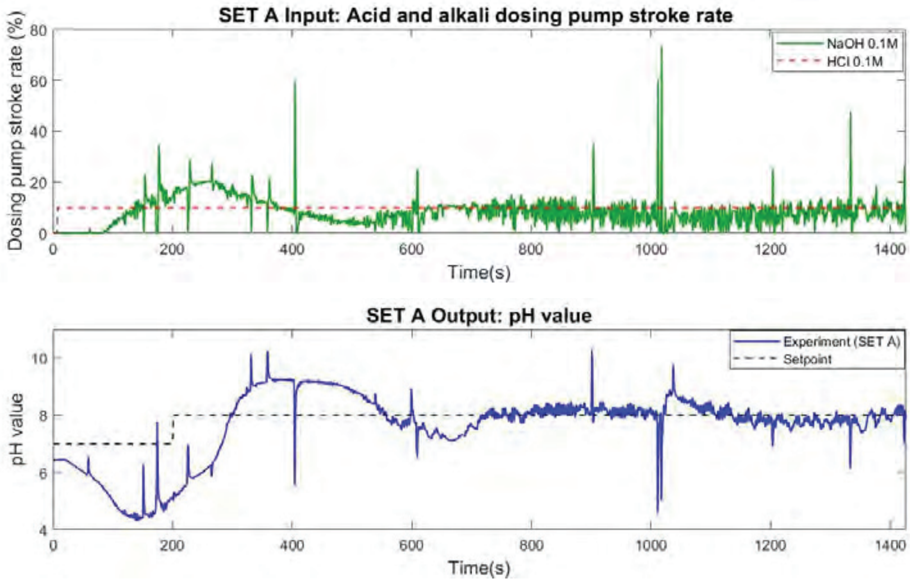

Fig. 6: SET A (10%): The step response and control signal for the closed loop system.

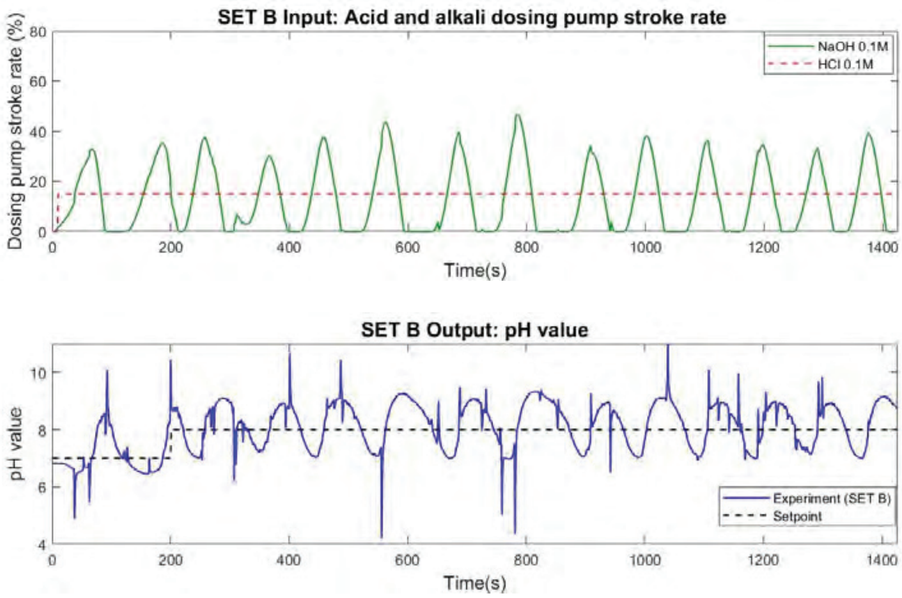

Fig. 7: SET B (15%): The step response and control signal for the closed loop system.

Table 4: Transient performance indexes for the compensated system with PID controller

Transient performance index	The acid dosing stroke rate (%)		
	SET A: 10%	SET B: 15%	SET C: 25%
Rise time, t_r	122.8	74.0	79.0
Peak time, t_p	358	1038	929
5% settling time, t_s	1423.5	-	-
Percentage overshoot (%)	112.04	181.87	301.02

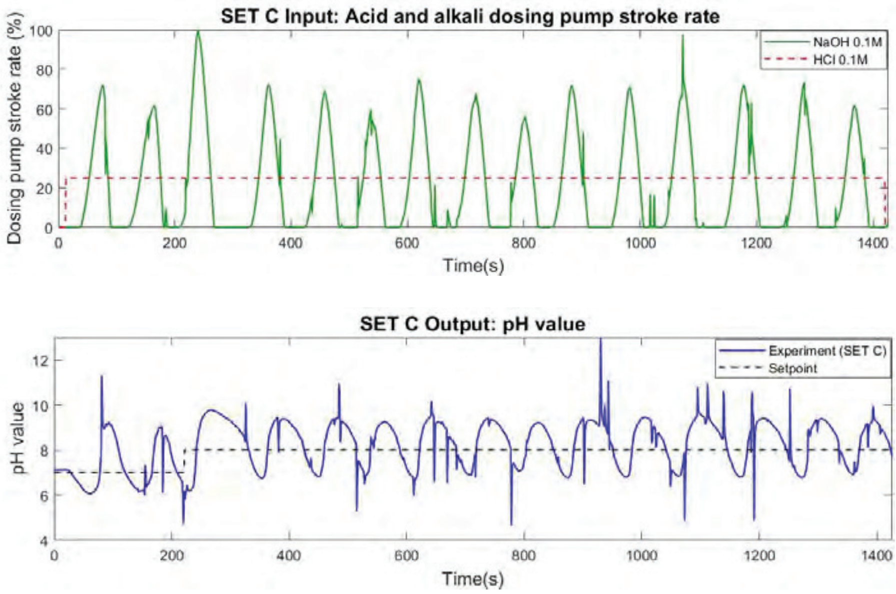

Fig. 8: SET C (25%): The step response and control signal for the closed loop system.

The process model is identified with FOPDT (first order plus dead time) using the System Identification MATLAB Toolbox. 50% of the data sets are used to estimate the models and 50% of the datasets are used to validate the models. The performance of each data set is evaluated based on the quality of fit, or error norm between the measured and estimated outputs. The cost function used is the normalized root mean square error (NRMSE), which is given by Eq. (2).

$$fit(i) = \frac{\|xref(:,i) - x(:,i)\|}{\|xref(:,i) - mean(xref(:,i))\|} \quad (2)$$

Table 5: The fit percentage of obtained model

Data set	FOPDT model	Fit percentage [%]
Set A (Acid dosing pump stroke rate 10%)	$G_1(s) = \frac{0.9674}{1 + 238.45s} e^{-14.519s}$	54.22
Set B (Acid dosing pump stroke rate 15%)	$G_2(s) = \frac{0.6304}{1 + 225.9226s} e^{-5.814s}$	31.85
Set C (Acid dosing pump stroke rate 25%)	$G_3(s) = \frac{0.3725}{1 + 135.1381s} e^{-0.6325s}$	9.691

A fit percentage of 100% indicates a perfect match between reference and estimated outputs. The fit percentage for each data set is shown in Table 5. Set A shows the best fit percentage result, which is 54.22%. From the transient response indexes and the FOPDT model fit percentage, it can therefore be concluded that set A performs better than set B and set C. In addition to the controller tuning, the adjustment of the stroke rate of the acid dosing stroke rate is also important, which can affect the controller performance.

5. CONCLUSIONS

The paper described the use of OPC DA servers for developing real-time process control between MATLAB and PLC. The OPC server enables secure and reliable data acquisition between the various device manufacturers. Instead of the hardware modification, the control system software modification is more effective based on the test result showing the efficient data exchange between the PLC and MATLAB. The PLC-PID controller was tuned using the integrated auto tuning function in the PLC Siemens TIA software. For the pH neutralization process of POME, although the acid dosing stroke rate is set to constant, the parameter value needs to be properly studied because it will affect the controller performance. Based on the transient response results of PLC PID controller, further work is required to develop an advanced process controller that can overcome the nonlinear dynamic response of pH neutralization process.

ACKNOWLEDGEMENT

The authors thank the Universiti Kuala Lumpur Malaysian Institute of Industrial Technology for providing facilities for this study. The project is supported by the Short-Term Research Grant (STRG) no. UniKL/CoRI/str18040 of the Universiti Kuala Lumpur Malaysian Institute of Industrial Technology. This work also is technically supported in part by the Universiti Teknologi Malaysia High Impact University Grant (UTMHI) vote Q.J130000.2451.08G74.

REFERENCES

[1] Lee YS, Chin SY, Lim JW, Witoon T, Cheng CK. (2019). Treatment technologies of palm oil mill effluent (POME) and olive mill wastewater (OMW): A brief review. Environmental Technology & Innovation, 15: 100377. doi:10.1016/j.eti.2019.100377

[2] Iskandar MJ, Baharum A, Anuar FH, Othaman R. (2018). Palm oil industry in South East Asia and the effluent treatment technology - A review. Environmental Technology & Innovation, 9:169-185. doi:10.1016/j.eti.2017.11.003

[3] Bala JD, Lalung J, Ismail N. (2014). Palm Oil Mill Effluent (POME) Treatment "Microbial Communities in an anaerobic Digester": A Review. International Journal of Scientific and Research Publications, 4: 1-24.

[4] Hosseini SE, Abdul Wahid M. (2015). Pollutant in palm oil production process. Journal of the Air & Waste Management Association, 65: 773-78. doi:10.1080/10962247.2013.873092

[5] Poh PE, Chong MF. (2009). Development of anaerobic digestion methods for palm oil mill effluent (POME) treatment. Bioresource Technology, 100: 1-9. doi:10.1016/j.biortech.2008.06.022

[6] Choong YY, Chou KW, Norli I. (2018). Strategies for improving biogas production of palm oil mill effluent (POME) anaerobic digestion: A critical review. Renewable and Sustainable Energy Reviews, 82: 2993-3006. doi:10.1016/j.rser.2017.10.036

[7] Department of Environment, Ministry of Natural Resources and Environment (October 2010) Environmental Requirements: A Guide for Investors. 11th edition, 57-59. Retrieved from https://enviro2.doe.gov.my/ekmc/wp-content/uploads/2016/08/1403056822-A%20Guide%20For%20Investors%20-%202010.pdf

[8] Hermansson AW, Syafiie S. (2015). Model predictive control of pH neutralization process: A review. Control Engineering Practice, 45: 98-109. doi:10.1016/j.conengprac.2015.09.005

[9] Zainal A, Wahab N, Yusof MI, Aliff M. (2020). pH Neutralization Plant Optimization Using Artificial Neural Network. Journal of Advanced Research in Dynamical and Control Systems, 12(SP4): 1466-1472. doi:10.5373/JARDCS/V12SP4/20201625

[10] Fadzlu-llah A, Yusof MI, Zainal A, Azhar A, Karim AH, Aliff M, Safie SI. (2020). Design and Simulation of PID Controller for pH Neutralization Process. International Journal of Innovative Technology and Exploring Engineering, 9(3): 2740-2743. doi:10.35940/ijitee.C9236.019320

[11] Siemens, SIMATIC S7-1200, S7-1500 PID control function manual (2022). 69-86. Retrieved from https://support.industry.siemens.com/cs/document/108210036/simatic-s7-1200-s7-1500-pid-control?dti=0&lc=en-KR on 6 Nov 2022

[12] Gonzalez I, Calderon A, Barragan A, Andujar J. (2017). Integration of Sensors, Controllers and Instruments Using a Novel OPC Architecture. Sensors, 17(7): 1512. doi:10.3390/s17071512

[13] Mahmoodi S, Poshtan J, Jahed-Motlagh MR, Montazeri A. (2009). Nonlinear model predictive control of a pH neutralization process based on Wiener-Laguerre model. Chemical Engineering Journal, 146(3):328-337. doi:10.1016/j.cej.2008.06.010

[14] Stoop F, Ely G, Menna R, Charache G, Gittler T, Wegener K (2019). Smart factory equipment integration through standardized OPC UA communication with companion specifications and equipment specific information models. International Journal of Mechatronics and Manufacturing Systems, 12(3/4): 344-364. doi: 10.1504/ijmms.2019.10025077

[15] Bagal KN, Kadu CB, Parvat BJ, Vikhe PS. (2018). PLC Based Real Time Process Control Using SCADA and MATLAB. In IEEE Fourth International Conference on Computing Communication Control and Automation (ICCUBEA): August 2018; Pune, India. pp 1-5

[16] Gajjar AG, Patel AI, Singh RG. (2017). Real time implementation of MPC in bottle washer machine for small scale beverage industry. In IEEE 6th International Conference on Computer Applications in Electrical Engineering Recent Advances (CERA): October 2017; Roorkee, India. pp 509-514

[17] Bhaskawar T, Chile R, Aole S, Elamvazuthi I. (2019). Remote Monitoring of Coupled Tank Accompanied by PLC-OPC-MATLAB Architecture, In IEEE Student Conference on Research and Development (SCOReD): October 2019; Perak, Malaysia. Pp 328-332

[18] Ahmad B, Prajitno P. (2020). Design of neural network and PLC-based water flow controller, Journal of Physics: Conference Series, 1528 012065.

[19] Zainal NH, Jalani NF, Mamat R, Astimar AA. (2017). A review on the development of palm oil mill effluent (POME) final discharge polishing treatments, Journal of Oil Palm Research, 29(4): 528-540. doi:10.21894/jopr.2017.00012

https://doi.org/10.31436/iiumej.v24i1.2374

SOLAR THERMAL PROCESS PARAMETERS FORECASTING FOR EVACUATED TUBE COLLECTORS (ETC) BASED ON RNN-LSTM

MUHAMMAD ALI AKBAR[1], AHMAD JAZLAN[1], MUHAMMAD MAHBUBUR RASHID[1*], HASAN FIRDAUS MOHD ZAKI[1], MUHAMMAD NAVEED AKHTER[2] AND ABD HALIM EMBONG[1]

[1]*Department of Mechatronics Engineering, Kulliyyah of Engineering, International Islamic University Malaysia, Kuala Lumpur, Malaysia.*
[2]*Department of Electrical Engineering, Rachna College of Engineering and Technology Gujranwala 52250 (A Constituent college of University of Engineering and Technology Lahore), Pakistan*

[*]*Corresponding author: mahbub@iium.edu.my*

(Received: 28th March 2022; Accepted: 22nd August 2022; Published on-line: 4th January 2023)

ABSTRACT: Solar Heat for Industrial Process (SHIP) systems are a clean source of alternative and renewable energy for industrial processes. A typical SHIP system consists of a solar panel connected with a thermal storage system along with necessary piping. Predictive maintenance and condition monitoring of these SHIP systems are essential to prevent system downtime and ensure a steady supply of heated water for a particular industrial process. This paper proposes the use of recurrent neural network-based predictive models to forecast solar thermal process parameters. Data of five process parameters namely - Solar Irradiance, Solar Collector Inlet & Outlet Temperature, and Flux Calorimeter Readings at two points were collected throughout a four-month period. Two variants of RNN, including LSTM and Gated Recurrent Units, were explored and the performance for this forecasting task was compared. The results show that Root Mean Square Errors (RMSE) between the actual and predicted values were 0.4346 (Solar Irradiance), 61.51 (Heat Meter 1), 23.85 (Heat Meter 2), Inlet Temperature (0.432) and Outlet Temperature (0.805) respectively. These results open up possibilities for employing a deep learning based forecasting method in the application of SHIP systems.

ABSTRAK: Penggunaan sumber bersih seperti Tenaga Solar dalam Proses Industri (SHIP) adalah satu kaedah alternatif untuk menhasilkan tenaga yang boleh diperbaharui bagi mengurangkan kesan gas rumah hijau yang terhasil dari proses industri. Sistem SHIP biasanya mengandungi panel solar dan sistem penyimpanan haba yang berhubung melalui paip yang sesuai. Penyelengaraan secara berkala diperlukan bagi memastikan sistem ini sentiasa membekalkan tenaga solar pada kadar bersesuaian dan bekalan tenaga solar yang terhasil berterusan dan tidak menjejaskan sistem pemanasan air bagi sesuatu proses industri. Kajian ini mencadangkan penggunaan model ramalan rangkaian neural berulang bagi meramal parameter proses pemanasan solar. Kelima-lima parameter proses iaitu – Iradiasi Solar, Suhu Saluran Keluar & Masuk Pengumpul Solar dan Bacaan Kalorimeter Fluks pada dua tempat diambil sepanjang empat bulan (dari Julai 2021 sehingga Oktober 2021). Dapatan menunjukkan dua varian RNN termasuk LSTM dan Unit Berulang dapat dibanding prestasinya bagi tugas ramalan ini. Dapatan kajian menunjukkan Ralat Punca Min Kuasa Dua (RMSE) antara bacaan sebenar dan ramalan adalah masing-masing 0.4346 (Iradiasi Solar), 61.51 (Meter Terma 1), 23.85 (Meter

Terma 2), Suhu Salur Masuk (0.432) and Suhu Salur Keluar (0.805). Ini membuka peluang kajian mendalam berdasarkan kaedah ramalan dalam aplikasi sistem SHIP.

KEYWORDS: *evacuated tube collectors; solar irradiance; flux calorimeter; recurrent neural networks; long short term memory*

1. INTRODUCTION

More than 80% of energy generation in today's world is sourced from non-renewable energy resources such as coal, natural gas, and oil [1-3]. The reduction of fossil fuel resources worldwide combined with increased environmental concerns have resulted in a higher demand for renewable and cleaner energy such as solar, wind, hydroelectric, biofuels, piezoelectric and RF energy. Oleochemical industries commonly utilize Natural Gas (NG) for generating low, medium, and high temperature heating, which is required as part of the overall Oleochemical process flow. However, NG-based heating is known to increase undesirable Greenhouse Gas emissions [4].

In Malaysia, solar energy is viewed as a viable, sustainable energy source due to the sunlight availability throughout the year, which is attributed to the tropical climate. Therefore, historically, solar energy has been widely utilized for both residential and commercial water heating applications. Evacuated Tube Collectors (ETC) and Flat Plate Collectors (NC-FPC) are the two most commonly used solar collectors for low to medium temperature industrial and residential water heating applications. These solar collectors are connected to thermal storage systems to allow energy to accumulate. Therefore, when solar irradiation is at its highest during the day, it enables energy to continue to be delivered. On the other hand, solar irradiation is at its lowest or utterly unavailable during rainy weather or at night, therefore, no energy can be delivered. Thermal storage systems consist of various heating equipment such as pumps, heat exchangers, electrical boilers, and gas boilers. A typical complete Solar Heat for Industrial Process (SHIP) system, at its simplest, consists of a control system, water circulation pump with power supply, hot & cold water storage tanks, piping, monitoring systems and a heat exchanger.

To ensure the long-term performance of the overall system and minimize downtime, condition monitoring as well as predictive maintenance of this heating equipment are essential. The ability to forecast, identify, and locate when and where a fault may occur in one part of this equipment and its sub-processes will save maintenance costs and prevent long-term damages to the overall system. Machine learning based models describing an industrial process are useful for applications such as anomaly detection, fault diagnosis and forecasting future system characteristics. The Remaining Useful Life (RUL) of equipment such as pumps, valves, compressors and batteries refers to the time interval before the equipment experiences failure [5-7]. Knowledge about the RUL of an equipment is crucial for maintenance engineering practices and engineering system reliability analysis in a plant. RUL can be forecast using suitable machine learning models. Previous studies have demonstrated the applicability of machine learning models for the analysis of rotating mechanical equipment using sound and vibration measurements, encoder data and temperature measurements [8]. Machine learning models are highly data-driven and therefore require high-quality data of a particular process to generate meaningful results. Effective measurement and data preprocessing methods are essential.

Recurrent Neural Networks (RNN) are a category of Artificial Neural Networks (ANN) that work well with time-series data in various applications such as speech recognition and language translation. RNN are the basis for widely used tools worldwide, namely Google Translate and Siri by Apple [9]. Similarly to convolutional and feedforward neural networks, RNN also use training data for learning. The difference is that RNN utilize information from prior inputs to affect current inputs and outputs. Traditional convolutional and feedforward neural networks also have a disadvantage since inputs and outputs are assumed to be independent of each other. Long Short Term Memory (LSTM) RNN is a modified version of the standard RNN with promising performance. LSTM RNN has successfully been applied in biomedical signal classification, radar target classification, keyword detection, text generation, and video classification [10-15].

This paper presents the design and development of an Evacuated Tube Solar Heat for Industrial Process (SHIP) system to generate the thermal energy required in an oleochemical plant. This plant manufactures fatty acids, glycerin, and soap noodles that are the base material for many types of industrial processes such as the manufacturing of household and toilet detergents. A Long Short-Term Memory Recurrent Neural Network (LSTM-RNN) was used to forecast Solar Irradiance, Solar Collector Inlet/Outlet Temperature, and Flux Calorimeter readings collected throughout a four (4) month period starting from July 2021 and ending in October 2021. Existing studies on forecasting of such parameters were carried out only on smaller-scale experimental prototypes. In contrast, in this study, forecasting was carried out for the first time on a larger scale industrial-grade Evacuated Tube Collector solar thermal system installed in Malaysia. Forecasting of these parameters is essential for the estimation of throughput and of future Return of Investments (ROI).

2. PRELIMINARIES

2.1 Overview of Installed SHIP System and Data Collection

Experimental work and data collection were carried out at an Oleochemical Process Plant based in Malaysia. The Solar Heat for Industrial Process (SHIP) at this factory was implemented using a total of 75 Evacuated Tube Collector Solar Panels (Linuo Ritter - Model CPC 1518). Each of these 75 solar panels consisted of 18 evacuated tubes. In this factory, solar energy heating was utilized as an energy-efficient replacement for existing legacy gas boilers. Evacuated Tube Solar Collectors have a useful life ranging between 20-25 years. Therefore, they are a viable option for achieving a long-term Return of Investment (ROI) [16-18]. This SHIP system was installed at 01°28°57° latitude and 103°54°25° longitude coordinates. This location was selected to avoid the impact of shading effects which would cause a significant reduction of the solar panel efficiency [19-23]. Reviews on various factors affecting solar energy performance and machine learning methods applied in the context of solar energy have been described in previous studies [24-26].

The solar panels were positioned on the roof directly above the boiler at an inclined angle of 10°, as shown in Fig. 1 and Fig. 2. This 10° inclined angle selection was based on the manufacturer's recommendation to maximize the solar energy that can be generated from the solar panels. The cumulative surface area of these 75 solar panels was 225 m^2. The total elevation of the solar panels relative to sea level was 16.35 meters. Solar Irradiance was measured using a Solar Pyranometer Radiation Sensor (RIKA - RK 200-03) which was installed at the roof top close to the ETC. Five process parameters namely Solar Irradiance, Solar Collector Inlet/Outlet Temperatures, and Flux Calorimeter readings from two points were recorded throughout a 4-month period starting from July 2021 until October 2021.

Solar Irradiance and Solar Collector Inlet and Outlet temperature were collected daily starting from 8:00 AM until 7:00 PM with a sampling rate of 15 minutes. Flux Calorimeter readings were collected hourly every day from 8:00 AM until 7:00 PM. The data collected for each process parameter can be represented as a single time series with time steps corresponding to either 15 minutes or 1 hour accordingly. This data was then used in an LSTM network for the prediction of future process data.

Fig. 1: Array of Evacuated Tube Collectors (front view).

Fig. 2: Array of Evacuated Tube Collectors (side view with 10 degree inclination).

2.2 Process Flow and its Description

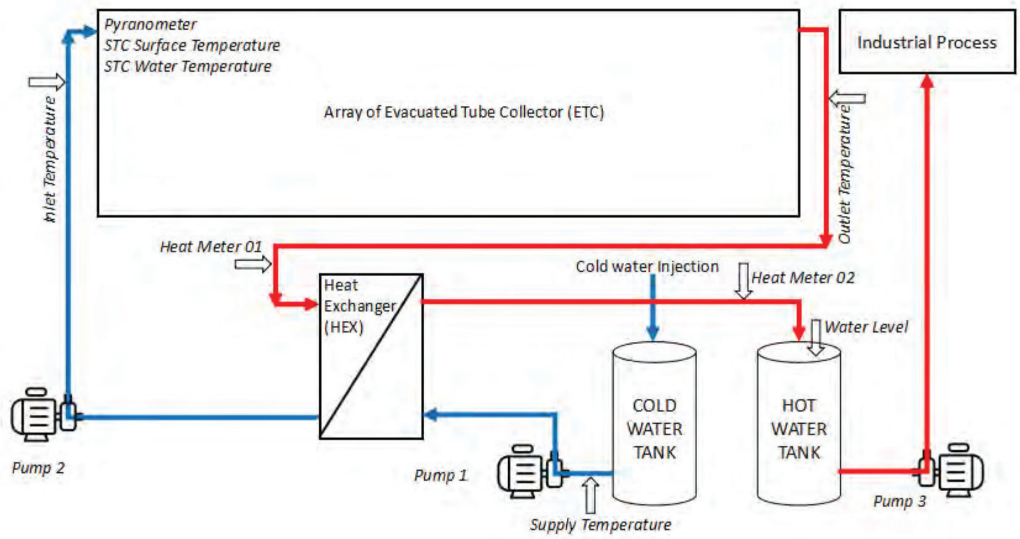

Fig. 3: Overall Process Flow Diagram for SHIP System.

The overall process flow diagram of the Evacuated Tube Solar Heat for Industrial Process (SHIP) System which was implemented at a Malaysian Oleochemical Process Factory is shown in Fig. 3. The blue arrows indicate the flow pipes, whereas the red arrows indicate the return pipes with heated water. The process starts by supplying cold water to the cold-water tank, which can store a maximum volume of 20 m^3 of water (cold water injection). A pump (pump 1) will then control the flow of water from the outlet of the cold storage tank to the inlet of the heat exchanger. The flow rate of the water being transferred from the cold storage tank to the heat exchanger is fixed at 5.5 m^3/hour. A second pump (pump 2) will control the flow of water circulation from the first outlet of the heat exchanger to the array of Evacuated Tube Collectors, generating hot water, which will be delivered to the hot water tank through the heat exchanger.

A flux calorimeter (Heat Meter 1) is used to monitor the thermal energy of the hot water circulating from the array of Evacuated Tube Collectors back into the heat exchanger. This flux calorimeter is equipped with a flow meter and two temperature sensors at both the flow and return pipes. The flux calorimeter device calculates the temperature difference between the flow and return pipes. This temperature difference is multiplied by the volume of the water measured by the flow meter and the hot water's thermal coefficient resulting in the final readings in Kilo-Watt Hour (kWh). The flow rate of the water circulating from the first output of the heat exchanger to the array of Evacuated Tube Collectors and back to the heat exchanger is fixed at 5.5 m^3/hour. The hot water from the heat exchanger is then allowed to flow into a Hot Water Storage Tank, which can store a maximum volume of 20 m^3 of water.

Industrial grade ultrasonic long body sensors are placed at the top of the Hot Water storage tanks for liquid level monitoring. These industrial-grade ultrasonic sensors can work in harsh environments and are unaffected by moisture, debris, or heat. A second flux calorimeter (Heat Meter 2) is used to monitor the thermal energy of the hot water which is circulating from the heat exchanger into the Hot Water Storage Tank. Finally, a third pump (pump 3) will be used to deliver the water from the Hot Water Storage Tank to the oleochemical industrial process. In this process, the input parameters are the Solar Irradiance and ETC inlet temperature. The intermediate parameters are the readings from Heat Meter 1 & 2. The output parameter is the ETC outlet temperature. In this paper, all these 5 parameters will be forecast using an LSTM Regression network.

The data presented in Table 1 shows that the value of Solar Irradiance continuously fluctuates between 50 W/m^2 and 95 W/m^2. This fluctuation is expected since Solar Irradiance commonly peaks during midday before gradually declining in the evening. Furthermore, the Collector Inlet Temperature fluctuates between 26 and 65 degrees Celsius, as reflected in Table 2. The first flux calorimeter (Heat Meter 1) readings have a higher fluctuation range (between 0 kWh and 360 kWh). Whereas the second flux calorimeter (Heat Meter 2) readings vary between 0-125 kWh, as reflected in Tables 1 and 2. Finally, the solar collector outlet temperature which represents the temperature of the water heated by the solar irradiation fluctuates between 25 and 70 degrees Celsius, as reflected in Table 3. This heated water will then be delivered for use at a particular oleochemical processing stage.

Table 1: minimum, maximum, and mean values for solar irradiance and flux calorimeter (Heat Meter 1) readings

Month	**Solar Irradiance (W/m^2)**			**Heat Meter 1 (kWh)**		
	Min	**Max**	**Mean**	**Min**	**Max**	**Mean**
July	54.80	83.70	68.20	2.60	302.80	139.30
August	50.80	86.70	70.10	0.04	283.00	150.40
September	54.80	93.70	72.50	0.03	300.10	144.50
October	53.80	94.60	74.50	0.57	366.70	171.60

Table 2: Minimum, maximum, and mean values for flux calorimeter (Heat Meter 2) and solar inlet temperature readings

Month	**Heat Meter 2 (kWh)**			**Solar Inlet Temperature (Celsius)**		
	Min	**Max**	**Mean**	**Min**	**Max**	**Mean**
July	0.10	98.60	43.80	26.00	65.70	38.00
August	0.05	114.20	38.50	26.00	55.00	37.00
September	0.03	116.40	47.80	27.00	48.00	34.40
October	0.06	124.90	45.20	27.00	48.00	35.00

Table 3: Minimum, maximum, and mean values for solar inlet temperature readings

Month	Solar Outlet Temperature (Celsius)		
	Min	Max	Mean
July	24.90	70.00	40.30
August	26.00	68.70	39.00
September	25.80	63.50	37.80
October	26.80	65.70	38.40

3. METHODOLOGY

3.1 LSTM-RNN based Forecasting

This section describes the forecasting of time series data collected from the Solar Heat for Industrial Process (SHIP) system by using Long Short-Term Memory Networks (LSTM). Future time steps of a time series sequence can be forecast by training a sequence-to-sequence LSTM network such that the outputs to the network are the input sequence shifted ahead by one time step. At a particular time step of the input sequence, the LSTM network learns to forecast the values at the following time step. The time series data of Solar Irradiance, Flux Calorimeters (Heat meters 1 & 2), Solar Collector Inlet & Outlet Temperature were each partitioned into training and test data. In each case the first 90% of the time series data sequence was used as the training data and the remaining 10% of the time series data sequence was used as the testing data. Standardization/Normalization of the training data was performed in order to achieve a better fit and convergence of the LSTM RNN training. Firstly, the mean of the training data is calculated using Eq.(1) as follows:

$$\mu = \frac{\sum X}{N} \tag{1}$$

Where μ is the mean of the training data, $\sum X$ is the summation of all the elements in the training data and N is the total number of elements in the training data. Secondly, the standard deviation of the training data is calculated using Eq.(2) as follows:

$$\sigma = \sqrt{\frac{\sum (X_i - \mu)^2}{N}} \tag{2}$$

Where σ is the standard deviation of the training data and X_i is each element in the training data. The normalization of the training data, $\overline{X_i}$ can then be found using Eq.(3) as follows:

$$\overline{X_i} = \frac{X_i - \mu}{\sigma} \tag{3}$$

Forecasting the values of future time steps in a sequence of data is then done as follows. Two vectors that consist of data extracted from the training data are defined as:

$$\text{Predictors} = [\overline{X}_i, \overline{X}_{i+1}, \overline{X}_{i+2,} \overline{X}_{i+3,} \ldots \overline{X}_{N-1}]$$

$$\text{Responses} = [\overline{X}_{i+1}, \overline{X}_{i+2}, \overline{X}_{i+3,} \overline{X}_{i+4,} \ldots \overline{X}_N]$$

The responses are simply the values of the training data shifted by one time step. The predictors are the training data, excluding the final time step. At a particular time step $\overline{X}_i$, the LSTM Network will learn to forecast the value of the following time step $\overline{X}_{i+1}$. The same process will be repeated where at the time step $\overline{X}_{i+1}$, the LSTM Network will learn to forecast the value of the following time step $\overline{X}_{i+2}$. The final forecast will be done at the time step $\overline{X}_{N-1}$ where the LSTM network will learn to forecast the value at the final time step $\overline{X}_{N}$ and therefore the training will be completed. The LSTM layer was specified to have 200 hidden units. The Adam optimization, a widely used extension of the stochastic gradient descent optimization was utilized for training the LSTM regression network. The LSTM regression network is used due to its high computational efficiency, smaller memory requirements and feasibility for large scale time series forecasting applications. The training was fixed at 250 epochs. The gradient threshold was set to 1 to prevent the gradients from exploding. The initial learning rate was specified to be 0.005 and this learning rate is dropped after 125 epochs by multiplication by a factor of 0.2. The Matlab Deep Learning toolbox is equipped with the '*PredictAndUpdateState'* function to execute this step-by-step prediction when used together with a *'for'* loop.

4. RESULTS

The LSTM networks were then used to forecast Solar Irradiance, Flux Calorimeter (Heat Meter 1 & 2) readings, solar collector inlet, and outlet temperatures. The LSTM forecasting was implemented on a HP 15-bw075AX laptop model with an AMD A12-9720P Radeon R7 processor and 4GB of RAM. The Root Mean Square Error (RMSE) values between the true and predicted values were calculated using Eq. (4) and tabulated in Table 4. The actual and forecast values of Solar Irradiance, Flux Calorimeter (Heat Meter 1 & 2) readings, solar collector inlet and outlet temperatures using test data are shown in Fig. 4, 5, 6, 7, and 8. Solar Irradiance, Collector Inlet and Outlet temperature could be forecast well with a low value of RMSE, which is less than 1. Flux Calorimeter readings could be forecast as well by using an LSTM Network. However, the RMSE values obtained were significantly higher since Flux Calorimeter readings could only be captured hourly. In contrast, Solar Irradiance, Collector Inlet and Outlet temperature are captured every 15 minutes resulting in more training data to be available for the LSTM Network. This result confirms that one of the constraints of forecasting is the sampling rate used by the sensors. If increased accuracy of the forecasting is desired, the sampling rate of the sensors should be increased. For comparison, these simulations were repeated using equivalent Gated Recurrent Units (GRU) instead of LSTM. It was found that lower RMSE values can be achieved using LSTM compared to GRU.

$$RMSE = \sqrt{\frac{\sum_{i=1}^{N}(predicted - actual)^2}{N}} \tag{4}$$

In Fig. 4, the solar irradiance predicted values almost overlap the observed values, resulting in a lower RMSE value (0.43457). The lowest errors were for the samples that were within 1800 to 3000. The largest errors were for the samples with the range 600 to 1700. The largest errors were attributed to the fluctuation in solar irradiance which occurred between samples 600 to 1700 as shown in Fig. 4. The lower errors for samples in the range 1800 to 3000 were attributed to the steady decline in solar irradiance at this period as shown in Fig. 4.

In Fig. 5, the predicted collector outlet temperature values almost overlap the observed values, resulting in a lower RMSE value (0.80517). The error is relatively low throughout the samples except for the presence of an outlier at sample 1050. At this point,

https://doi.org/10.31436/iiumej.v24i1.2374

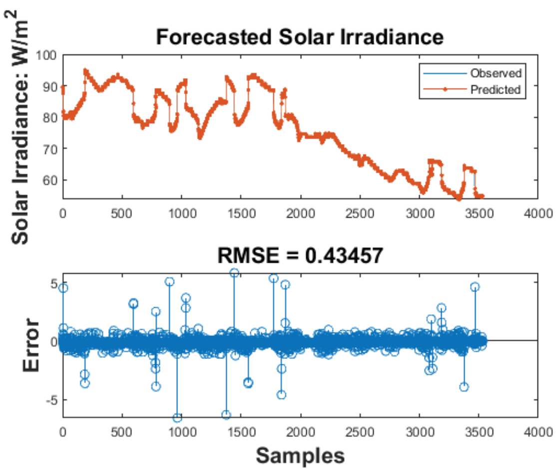

Fig. 4: Actual and Forecast Values of Solar Irradiance with Root Mean Square Error.

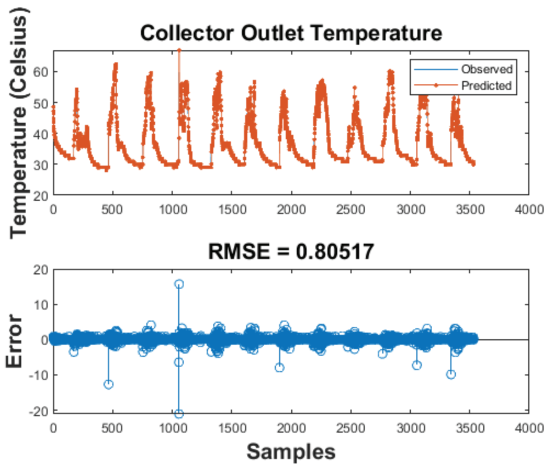

Fig. 5: Actual and Forecast Values of Collector Outlet Temperature with Root Mean Square Error.

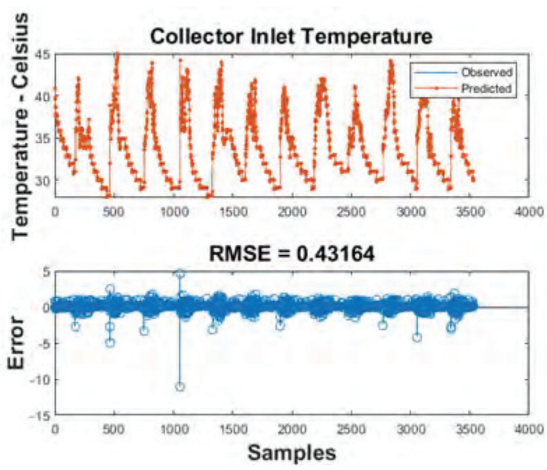

Fig. 6: Actual and Forecast Values of Collector Inlet Temperature with Root Mean Square Error.

there was a sudden rise in the collector outlet temperature and the LSTM model was not able to forecast this sudden rise in the collector outlet temperature accurately as compared to the rest of the samples in this time series data. Similarly in Fig. 6, the predicted collector inlet temperature also overlaps the observed value curves, resulting in a lower

https://doi.org/10.31436/iiumej.v24i1.2374

RMSE value (0.43164). Although the overall error is relatively low, there is an outlier that also occurs at sample 1050 such that the LSTM model could not forecast the sudden rise in collector inlet temperature. The sudden change in the collector inlet and outlet temperature was due to the tripping of pumps that regulate the fluid circulation.

The RMSE values for forecasting Heat Meter 1 and 2 were recorded as 61.5091 & 23.8541 respectively and found to be higher than other parameters (solar irradiance, outlet & inlet temperatures). The main reason is that these energy meter readings are being logged hourly, therefore fewer samples of data are available for training the LSTM model resulting in a higher RMSE value. It can be observed from Fig. 7 that the error is higher for samples in the range from 20-70 but lower in other ranges. In the range from 20-70 the LSTM model had both underestimated and overestimated the readings for Heat Meter 1. The higher error at this range is attributed to the fluctuations in the Heat Meter 1 as well as the limitation in the number of samples of data available. Fig.8 shows the actual and forecast values for Heat Meter 2. A lower RMSE value was obtained for the forecasting of Heat Meter 2 values compared to Heat Meter 1. This lower RMSE value was due to less fluctuations occurring since the Heat Meter 2 readings steadily rise and decline in a predictable cyclic manner. Heat Meter 2 readings represent the final delivery of the water to the hot water tank and, therefore less fluctuations.

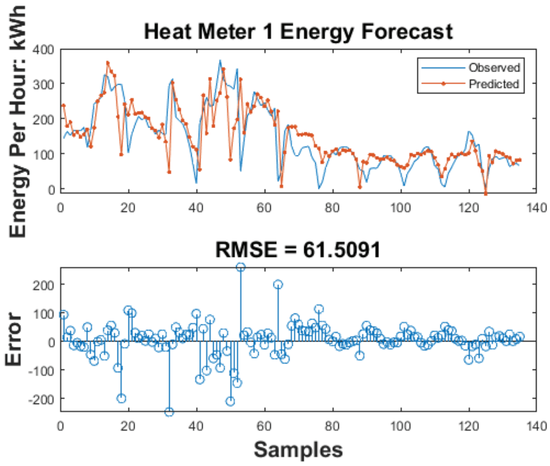

Fig. 7: Actual and Forecast Values of the First Flux Calorimeter Readings (Heat Meter 1) with Root Mean Square Error.

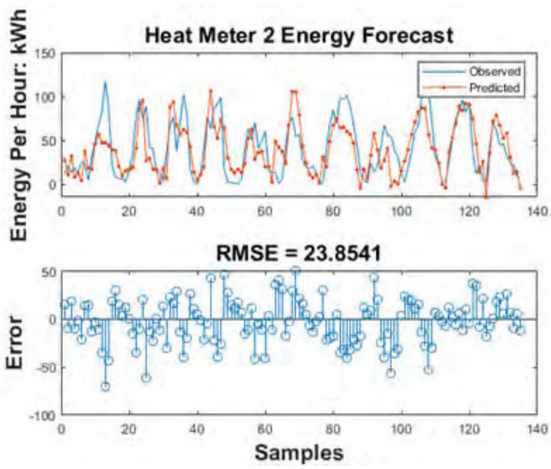

Fig. 8: Actual and Forecast Values of the Second Flux Calorimeter Readings (Heat Meter 2) with Root Mean Square Error.

The results presented in Fig. 4, 5, 6, 7, and 8 are summarized in Table 4. Overall results prove that LSTM is a suitable forecasting method to be applied at the backend of data logging systems for displaying forecast values and preliminary analysis. In particular, the forecast for Heat Meter 2 is beneficial for capacity planning of the factory to plan and meet the day ahead energy demand for their day-to-day operations.

Table 4: Total Number of Data Samples, Training Time and RMSE of LSTM Network Implementation

Parameter (s)	Total Data Samples	Training Time (Minutes)	RMSE (LSTM)	RMSE (GRU)
Solar Irradiance (W/m^2)	35337	410	0.43	0.85
Heat Meter 1 (kWh)	1354	30	61.51	72.34
Heat Meter 2 (kWh)	1354	28	23.85	35.76
Inlet Temperature (Celsius)	35340	430	0.43	0.78
Outlet Temperature (Celsius)	35340	415	0.80	1.53

5. CONCLUSION

In this study, a Solar Heat for Industrial Process (SHIP) system was designed and commissioned for implementation at a Malaysian Oleochemical factory. Five process parameters were recorded throughout a 4-month period namely Solar Irradiance, Solar Collector Inlet/ Outlet Temperature and flux calorimeter readings. In order to incorporate predictive maintenance, condition monitoring, assisting with planning, and commissioning existing renewable and non-renewable resources, two methods were used to forecast future values of these parameters namely LSTM and GRU. It was found that RMSE values obtained by applying LSTM were lower when compared to using Gated Recurrent Units (GRU). The results of this study reveal that LSTM can be integrated into the backend of existing data logging systems used in process industries in order develop websites that display forecasts of both engineering related parameters and also Return of Investments (ROI).

ACKNOWLEDGEMENT

The authors would like to thank the Malaysian Ministry of Higher Education for the funding received for this project under the Fundamental Research Grant Scheme - Grant No: FRGS19-057-0665. Furthermore, the authors would like to thank the IOT SATA Sdn. Bhd, the participating factory, and all supporting agencies for providing the technical data and support to carry out this research.

SUPPLEMENTARY MATERIALS

The codes for performing the forecasting and also the datasets used in this study are publicly available at the following Github repository:
https://github.com/ahmadjazlan/LSTM-Solar-Parameter-Forecasting

REFERENCES

[1] Apergis N, Payne JE. (2012) Renewable and non-renewable energy consumption-growth nexus: Evidence from a panel error correction model, Energy Economics, 34(3): 733-738.

[2] Can Tansel Tugcu, Ilhan Ozturk and Alper Aslan. (2012) Renewable and non-renewable energy consumption and economic growth relationship revisited: Evidence from G7 countries, Energy Economics, 34(6): 1942-1950.
[3] Guney T. (2019) Renewable energy, non-renewable energy and sustainable development, International Journal of Sustainable Development & World Ecology, 26(5): 389-397.
[4] Kim D, Kim KT., Park YK. (2020) A Comparative Study on the Reduction Effect in Greenhouse Gas Emissions between the Combined Heat and Power Plant and Boiler. Sustainability, 12(12): 5144-5155.
[5] Yaguo L, Naipeng L, Liang, Ningbo L, Tao Y and Jing L. (2018) Machinery health prognostics: A systematic review from data acquisition to RUL prediction, Mechanical Systems and Signal Processing. 104: 799-834.
[6] Zhang Y, Xiong R, He H, and Pecht MG. (2018) Long Short-Term Memory Recurrent Neural Network for Remaining Useful Life Prediction of Lithium-Ion Batteries. IEEE Transactions on Vehicular Technology, 67(7): 5695-5705.
[7] Zhao R, Ruqiang Y, Jinjiang W, and Kezhi M. (2017) Learning to monitor machine health with convolutional Bi-directional LSTM networks, Sensors, 17(2): 273-290
[8] Haedong J, Seungtae P, Sunhee W and Seungchul L. (2016). Rotating Machinery Diagnostics Using Deep Learning on Orbit Plot Images, Procedia Manufacturing, 5: 1107-1118.
[9] Wu Y. et al. (2016) Google's neural machine translation system: bridging the gap between human and machine translation. Preprint at https://arxiv.org/abs/1609.08144.
[10] Park K, Kim J and Lee J. (2019) Visual Field Prediction using Recurrent Neural Network. Sci Rep 9: 8385-8397.
[11] Yuan L. (2017). Recurrent neural networks for classifying relations in clinical notes, Journal of Biomedical Informatics, 72: 85-95.
[12] Lyu C, Chen B, Ren Y and Ji D. (2017) Long short-term memory RNN for biomedical named entity recognition. BMC bioinformatics, 18(1): 462-473.
[13] Zhang F, Hu C, Yin Q, Li W, Li H-C and Hong W. (2017) Multi-Aspect-Aware Bidirectional LSTM Networks for Synthetic Aperture Radar Target Recognition. IEEE Access, 5: 26880-26891.
[14] Chen C and Dai J. (2021) Mitigating backdoor attacks in LSTM-based text classification systems by Backdoor Keyword Identification. Neurocomputing, 452: 253-262.
[15] Ogawa T, Sasaka Y, Maeda K and Haseyama M. (2018). Favorite Video Classification Based on Multimodal Bidirectional LSTM, IEEE Access, 6: 61401-61409.
[16] Lan H, Gou Z and Cheng B. (2020) Regional difference of residential solar panel diffusion in Queensland, Australia, Energy Sources, Part B: Economics, Planning, and Policy, 15(1): 13-25.
[17] Tsuchiya Y, Swai TA, Goto F. (2020) Energy payback time analysis and return on investment of off-grid photovoltaic systems in rural areas of Tanzania, Sustainable Energy Technologies and Assessments, 42(2020):100887-100894.
[18] Ozcan O, Ersoz F. (2019) Project and cost-based evaluation of solar energy performance in three different geographical regions of Turkey: Investment analysis application, Engineering Science and Technology, an International Journal, 22(4): 1098-1106.
[19] Gupta AK, Maity T, Anandakumar H, Chauhan YK. (2021) An electromagnetic strategy to improve the performance of PV panel under partial shading, Computers & Electrical Engineering, 90: 106896-106908.
[20] Mert BD, Ekinci F and Demirdelen T. (2019) Effect of partial shading conditions on off-grid solar PV/Hydrogen production in high solar energy index regions, International Journal of Hydrogen Energy, 44(51): 27713-27725.
[21] Niazi K, Khan HA, and Amir F. (2018) Hot-spot reduction and shade loss minimization in crystalline-silicon solar panels. Journal of Renewable and Sustainable Energy 10(3):033506-1 - 033506-8
[22] Torres JPN, Nashih SK, Fernandes CAF and Leite JC. (2018) The effect of shading on photovoltaic solar panels. Energy Systems 9: 195-208.

[23] Wang D, Qi T, Liu Y, Wang Y, Fan J, Wang Y and Du H. (2020) A method for evaluating both shading and power generation effects of rooftop solar PV panels for different climate zones of China, Solar Energy, 205: 432-445.

[24] Akhter MN, Mekhilef S, Mokhlis H and Shah NM. Review on forecasting of photovoltaic power generation based on machine learning and metaheuristic techniques, IET Renewable Power Generation 13(7): 1009-1023

[25] Akhter MN, Mekhilef S, Mokhlis H, Olatomiwa L and Muhammad MA. (2020) Performance assessment of three grid-connected photovoltaic systems with combined capacity of 6.575 kWp in Malaysia. Journal of Cleaner Production, 277: 123242.

[26] Akhter MN, Mekhilef S, Mokhlis H, Ali R , Usama M , Muhammad MA. (2022) A hybrid deep learning method for an hour ahead power output forecasting of three different photovoltaic systems, Applied Energy, 307: 118185

APPENDIX

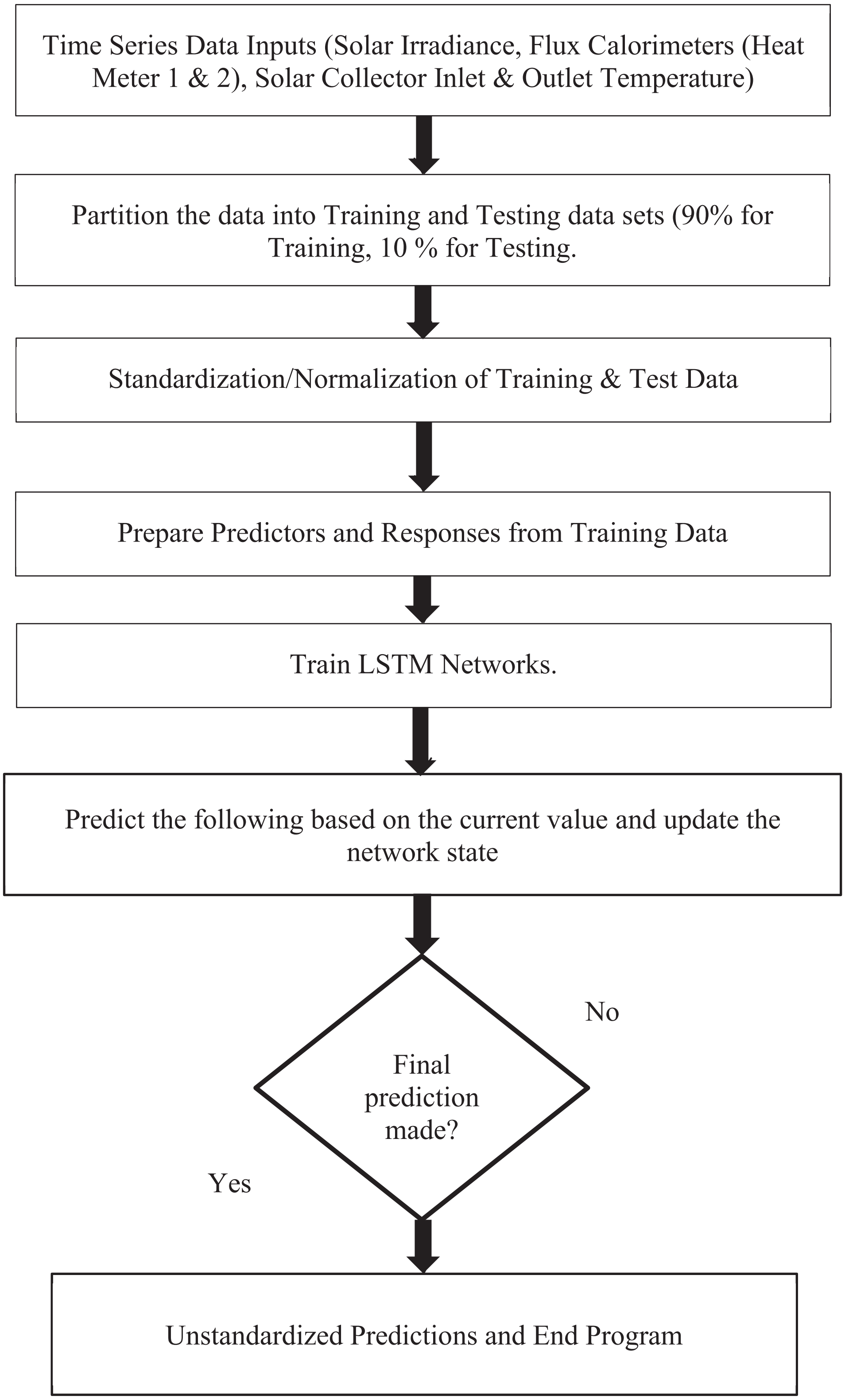

Fig. 9: Flowchart for MATLAB Programming.

https://doi.org/10.31436/iiumej.v24i1.2529

AN INTEGRATED RRT*SMART-A* ALGORITHM FOR SOLVING THE GLOBAL PATH PLANNING PROBLEM IN A STATIC ENVIRONMENT

HERU SUWOYO[1], ANDI ADRIANSYAH[1 *], JULPRI ANDIKA[1], ABU UBAIDAH SHAMSUDIN[2] AND MOHAMAD FAUZI ZAKARIA[2]

[1]*Department of Electrical Engineering, Universitas Mercu Buana, Jakarta, Indonesia*
[2]*Department of Electrical and Electronic Engineering, Universiti Tun Hussein Onn Malaysia, Johor, Malaysia*

[*]*Corresponding author: andi@mercubuana.ac.id*

(Received: 15th July 2021; Accepted: 5th October 2022; Published on-line: 4th January 2023)

ABSTRACT: The use of sampling-based algorithms such as Rapidly-Exploring Random Tree Star (RRT*) has been widely applied in robot path planning. Although this variant of RRT offers asymptotic optimality, its use is increasingly limited because it suffers from convergence rates, mainly when applied to an environment with a poor level of obstacle neatness and a narrow area to the target. Thus, RRT*-Smart, a further development of RRT*, is considered ideal for solving RRT* problems. Unlike RRT*, RRT*-Smart applies a path optimization by removing the redundant nodes from the initial path when it is gained. Moreover, the path is also improved by identifying the beacon nodes used to steer the bias of intelligent sampling. Nevertheless, this initial path is found with termination criteria in terms of a region around the goal node. Consequently, it risks failing to generate a path on a narrow channel. Therefore, a novel algorithm achieved by combining RRT*-Smart and A* is proposed. This combination is intended to switch method-by-method for the exploration process when the new node reaches the region around the goal node. However, before RRT*-Smart is combined with A*, it is improved by replacing the random sampling method with Fast Sampling. In short, by involving A*, the exploration process for generating the Smart-RRT*'s initial path can be supported. It gives the optimal and feasible raw solution for any complex environment. It is logically realistic because A* searches and evaluates all neighbors of a current node when finding the node with low cost to the start and goal node for each iteration. Therefore, the risk of collision with an obstacle in the goal region is covered, and generating an initial path in the narrow channel can be handled. Furthermore, this proposed method's optimality and fast convergence rate are satisfied.

ABSTRAK: Penggunaan algoritma berasaskan pensampelan seperti Rapidly-Exploring Random Tree Star (RRT*) telah digunakan secara meluas dalam perancangan laluan robot. Walaupun varian RRT ini menawarkan keoptimuman tanpa gejala, penggunaannya semakin terhad kerana ia mengalami kadar penumpuan, terutamanya apabila digunakan pada persekitaran dengan tahap kekemasan halangan yang lemah dan kawasan yang sempit ke sasaran. Oleh itu, RRT*-Smart, pembangunan lanjut RRT*, dianggap sesuai untuk menyelesaikan masalah RRT*. Tidak seperti RRT*, RRT*-Smart menggunakan pengoptimuman laluan dengan mengalih keluar nod berlebihan daripada laluan awal apabila ia diperoleh. Selain itu, laluan juga dipertingkatkan dengan mengenal pasti nod suar yang digunakan untuk mengemudi bias pensampelan pintar. Namun begitu, laluan awal ini ditemui dengan kriteria penamatan dari segi rantau di sekeliling nod matlamat. Akibatnya, ia berisiko gagal menjana laluan pada saluran yang sempit. Oleh itu, algoritma baru yang dicapai dengan menggabungkan RRT*-Smart dan A* dicadangkan. Gabungan ini bertujuan untuk menukar kaedah demi kaedah untuk proses penerokaan apabila nod baharu sampai ke kawasan sekitar nod matlamat. Walau bagaimanapun, sebelum RRT*-Smart digabungkan dengan A*, ia diperbaiki dengan menggantikan kaedah persampelan rawak dengan Persampelan Pantas. Pendek kata, dengan melibatkan A*, proses penerokaan dalam menjana laluan awal yang Smart-RRT lakukan* boleh disokong. Ia memberikan penyelesaian mentah yang optimum dan boleh dilaksanakan untuk mana-mana persekitaran yang kompleks. Ia adalah realistik secara logik kerana A* mencari dan menilai semua jiran nod semasa apabila mencari nod dengan kos rendah ke nod permulaan dan matlamat untuk setiap lelaran. Oleh itu, risiko perlanggaran dengan halangan di kawasan matlamat dilindungi, dan menjana laluan awal dalam saluran sempit boleh dikendalikan. Tambahan pula, kaedah optimum yang dicadangkan dan kadar penumpuan yang cepat ini berpuas hati.

KEYWORDS: *path planning; A* algorithm; RRT*-smart algorithm; convergence rate*

1. INTRODUCTION

As an intelligent application, mobile robots have received considerable attention from researchers. The increase in productivity and efficiency offered by the use of mobile robots is behind this concern [1-3]. Therefore, it is not surprising that developments in navigation on mobile robots continue rapidly because navigation is at the core of its intelligence [4,5]. Path planning is the basis of a robotic navigation, namely the ability to plan a path without collisions with obstacles in the environment [6-8]. Although there are several strategies with different exploration representations, grid-based algorithms [9-11] and sampling-based algorithms [12-15] are in great demand because of their ease of implementation. For example, there are A* and RRT* algorithms for these types, respectively. As its advantage, A* offers the completeness and optimality of the resolution which is not guaranteed by RRT*. However, A* algorithm is limited in use, because it consumes much time to solve the problem when applied to high-dimensional state space. Accordingly, RRT* has been chosen to tackle this limitation. Although RRT* in this case is obviously better than A* algorithm, it works infinitely when the region around the goal node is not reached. It is also work based on the probabilistic principle leading the large variance to time which gives its another disadvantage named slow convergence rate. Moreover, RRT* uses the criteria termination in the form of a predefined maximum number of the sampling node and condition when the new explored node reaches the region around the goal node, which increases the processing time.

Referring to this limitation, RRT* have been intensively maintained [16]. This concern not only enhances the optimality of RRT* but also accelerates its convergence rate. There are several algorithms intended to tackle this limitation such as Fast-RRT [17], Connect-RRT [11,15,18], informed RRT*[11], and Smart-RRT*[16,17,19,20]. The most popular algorithm is Smart-RRT* with claims optimality and fast working time. Although it also applies some procedures of RRT*, the Smart-RRT* also executes the path optimization when the initial path is found [21]. This makes RRT*-smart a better solution compared to RRT* in terms of optimality. This optimization is designed to remove the redundant node given by the initial path. Moreover, RRT*-Smart is also completed with an intelligent sampling to replace the conventional random sampling [16]. Conceptually, this sampling is done by biasing it to the beacon node of optimized path, in which the beacon node is identified from the path optimization process. Therefore, once the RRT*-Smart obtains a shorter path compared to the previous one, the optimization is conducted and simultaneously gets the new beacon node. Accordingly, it improves its predecessor named RRT*.

However, due to following some procedures of RRT*, RRT*-Smart takes over the particular characteristic of RRT* namely, the criteria termination [22]. Similar to RRT*, the process of getting the initial path is noticed to break when the newest node is in the region around the goal node. Therefore, both RRT* and RRT*-Smart are still at risk of failure in generating a feasible path when the start and goal node are separated with a narrow channel in the environment [23-26]. Furthermore, terminating the exploration process of Smart-RRT* with a region around a goal node requires the knowledge of any obstacle close to the goal node that would be difficult for the robot to perceive. The reason for this difficulty is because the characteristic of map information that might be given by Simultaneous Localization and Mapping is still categorized as raw. Thus, terminating the process with a trigger of radius will definitely cause RRT*-Smart to make a potential mistake.

For this urgency, it is strongly recommended to improve RRT*-Smart with an ability of connecting the newly expanded node to the goal node when they are closed to each other in the channel environment. Through this paper, aiming to tackle the limitation in terms of optimality and keep the way of determining the optimized path, A* algorithm is proposed to handle the rest task of path planning when the newly expanded node reaches the area closed to the goal node even when a border exists. A* algorithm has been recorded as a searching-based planning method with some advantages such as having optimality and high resolution of tracing procedure [27]. This advantage makes the A* algorithm relevant to be applied as a helper for RRT*-Smart in narrow channels near the goal node so that the time required for search expansion can be further reduced. In general, the search process using this combination begins by using RRT*, part of the RRT*-Smart process, to carry out the exploration stage. In contrast to RRT* and RRT*-Smart, this case uses a fast-sampling technique to replace conventional sampling technique. This is intended to speed up the exploration process and achieve node positions near the goal. For the record, fast sampling is a technique applied to fast-RRT, which performs the exploration process without repeating the placement of sampling nodes in areas close to a group of nodes that have been recorded. While this represents an advantage for searching in a wide environment, the potential difficulty in expanding into narrow channels increases. For this reason, the expansion process needs to be supported by the relevant algorithm, namely A*. The formation of this initial path will be completed after A* makes a connection from the closest node to the goal with the goal node. Furthermore, the proposed algorithm will continue the process by applying path optimization and intelligent sampling from RRT*-Smart, so that optimality is maintained with an increased convergence rate.

2. MATERIAL AND METHODS

As usual, the global problem is defined to show the relation to its existing solution. It is reliable by firstly defining the objective of finding a solution for a path planning problem, which is how to determine the connection from the initial node to the goal node without any collision with any obstacle existing in the environment. Globally, there are two important benchmarks used for evaluating the performance of a path planning algorithm, namely optimality and convergence rate. Respectively, these can be represented by a feasible path and time consumption in generating it. Therefore, by well knowing the problem and these benchmarks, a feasibility of the designed or targeted algorithm could be declared.

Let $Z \in \mathbb{R}^n$ be the representation of state space for a path planning problem, with $n \in N$ being the space dimension, thus $Z = \{Z_{obs,}Z_{free}\}$ is another state space with $Z_{obs} \in Z$ referring to obstacle coordinates and $Z_{free} \in X$ free space. Moreover, if the start node $z_{init} \in Z_{free}$ and goal node $z_{goal} \in Z_{free}$ are given, then referring to Z_{obs}, the path planning algorithm has to find the ideal path to/from those nodes, denoted as $\sigma = [0, T] \rightarrow Z_{free}$with $\sigma(0) = x_{init}$ and $\sigma(T) = Z_{goal}$ where $Z_{goal} = \{z \in Z \| z - z_{goal} \| < r\}$ where r is the radius around goal defined at the beginning.

2.1 A* Algorithm

A* is considered to be a heuristic-based search algorithm with the advantage of optimal path [28], [29]. This algorithm has a main step to assess the direction of travel by referring to the lowest cost/distance value from the neighbor n-th node around the current node $z_{current}$. This cost is obtained by scanning the distance from the current node with eight surrounding nodes to get the value of (n), and also from a heuristic function $h(n)$ that gives the value of h, which is the distance value from the eight nodes around the current node to the destination node, where this distance is calculated by applying Euclidean Distance and $f(n)$ is mathematically determined using Eq. (1).

$$f(n) = g(n) + h(n, z_{goal}) \tag{1}$$

where $g(n)$ is a function that represents the cost of the path required from the start node z_init to the current node $z\_current$. Briefly, the calculation of $g(n)$ refers to the eight costs which are determined based on the position in relation to the current that is the center. While $h(n, z_{goal})$ is a function used to calculate the required cost from the goal node z_{goal} to the n-*th* node. This function applies Euclidean distance which directly calculates the distance to the goal node regardless of whether there is a collision with an obstacle or not. The sum of both is called f_{cost} which is used as the evaluation function of the nth node. In general, there are two sets named $openSet$ and $closedSet$ in A*. All nodes that will be evaluated are placed in $openSet$, and then the nodes that have been evaluated are removed from $openSet$ and moved to $closedSet$. At the start of the process, the start node z_init is placed as a member of the $openSet$ set since the start node is the initial of the search then $g(z\_init) = 0$. Thus f_{cost} for the start node $f(z_{init})$ is the same as $h(z_{init}, z_{goal})$. Furthermore, taking into account all the evaluation costs of f_{cost} for all nodes in the $openSet$, the node with the lowest f_{cost} will be selected as the current node $z_{current}$ and its availability in the $openSet$ is removed and transferred/added to the $closedSet$. As a step in defining the termination criteria, if this current node is a goal node, the process is stopped because it explains that the path has been obtained. Instead, all neighbors of the current node will be checked based on their g_{cost}. In the case of the grid map, there are the eight-neighbor nodes for the current node. Each neighbor node has a specified cost to the current node and is used as the basis for calculating g_{cost}. If the neighbor node is in a $closedSet$ or it is not traversable, the scan is continued on the next neighbor node. The neighbor node with the lowest g_{cost} is determined. The neighbor node with the lowest g_{cost} will then be checked, if it is not in the $openSet$ then it is moved, set its f_{cost}, and set its parent to current node. Furthermore, this series of processes will be repeated until the termination criteria are met and to clarify this description the pseudocode of the A* algorithm is given

Algorithm* 1. A^* *Algorithm

$ClosedSet = [\ \ ]$
$OpenSet = [\ \ ]$
$OpenSet = [z_{init}]$
$g(z_{init}) = 0$
$h(z_{init}) \leftarrow hcalculate(z_{init}, z_{goal})$
$f(z_{init}) \leftarrow 0 + h(z_{init})$
$\boldsymbol{while}\ openSet \neq \emptyset\ \boldsymbol{then}$
  $z_{current} = node\ in\ OpenSet\ lowest\ f_{cost}$
  $remove\ z_{current}\ from\ OpenSet$
  $add\ z_{current}\ to\ ClosedSet$
  $\boldsymbol{if}\ z_{current} = z_{goal}$

    $return$
  $\boldsymbol{endif}$
  $\boldsymbol{foreach}\ z_{neighbour}\ of\ z_{current}$
    $\boldsymbol{if}\ z_{neighbour}\ is\ in\ ClosedSet\ \boldsymbol{or}\ z_{neighbour}\ is\ not\ traversable$
      $continue$
    $\boldsymbol{endif}$
    $\boldsymbol{if}\ newpath\ to\ z_{neighbour}\ is\ shorter\ \boldsymbol{or}\ z_{neighbour}\ is\ not\ in\ OpenSet$
      $set\ f_{cost}\ of\ neighbour$
      $set\ parent\ of\ neighbour\ to\ z_{current}$
      $\boldsymbol{if}\ neighbour\ is\ not\ in\ OpenSet$
        $add\ neighbour\ to\ OpenSet$
      $\boldsymbol{endif}$
    $\boldsymbol{endif}$
  $\boldsymbol{endforeach}$
$\boldsymbol{end}$

2.2 RRT*-Smart

RRT*-Smart is an enhanced version of RRT* that works in the same way as RRT* for finding the initial path [14,20]. Besides that, it undertakes a path optimization procedure once an initial path has been determined. This procedure eliminates unnecessary nodes from the path that was initially discovered. The optimization is supported by the beacon nodes which are determined after conducting a triangular inequality technique when the initial path is found. Intelligent sampling is the second key feature introduced by RRT*- Smart. This sampling differs from random sampling in that it is directed towards optimal path beacon nodes. It sets a radius for intelligent exploration around selected beacons using a Biasing Radius b. RRT*-Smart performs the path optimization procedure again to build additional beacon nodes as soon as it identifies a shorter path. As a result, RRT*-Smart improves path cost and accelerates path convergence.

https://doi.org/10.31436/iiumej.v24i1.2529

$\boldsymbol{Algorithm\ 2. RRT^{*}Smart\ Algorithm}\ \sim\ \boldsymbol{T = (V, E) \leftarrow RRT^{*}Smart(z_{init})}$

1 $T \leftarrow InitializeTree(\,)$
2 $.\, T \leftarrow InsertNode(\emptyset, z_{init}, T)$
3 $.\, \boldsymbol{for}\ i = 1\ \boldsymbol{to}\ N\ \boldsymbol{do}$
4 $\quad \boldsymbol{if}\ i = n + b, n + 2b, n + 3b \dots \boldsymbol{then}$
5 $\quad\quad z_{rand} \leftarrow intelligent\_sampling(i, z_{beacon})$
6 $\quad \boldsymbol{else}$
7 $\quad\quad z_{rand} \leftarrow sampling(i)$
8 $\quad \boldsymbol{endif}$
9 $\quad z_{nearest} \leftarrow nearest(T, z_{rand})$
10 $\quad (z_{new}, u_{new}, T) \leftarrow steer(z_{nearest}, z_{rand})$
11 $\quad \boldsymbol{if}\ obstaclefree(z_{new})\ \boldsymbol{then}$
12 $\quad\quad z_{near} \leftarrow near(T, z_{new}, |V|)$
13 $\quad\quad z_{min} \leftarrow choosenparent(z_{near}, z_{nearest}, z_{new})$
14 $\quad\quad T \leftarrow insertnode(z_{min}, z_{new}, T)$
15 $\quad\quad T \leftarrow rewire(T, Z_{near}, Z_{min}, Z_{new})$
16 $\quad \boldsymbol{endif}$
17 $\quad \boldsymbol{if}\ initialPathfound\ \boldsymbol{then}$
18 $\quad\quad n \leftarrow i$
19 $\quad\quad (T, directcost) \leftarrow pathOptimization\big(T, z_{init}, z_{goal}\big)$
20
21 $\quad \boldsymbol{endif}$
22 $\quad \boldsymbol{if}\ (directcostnew < directcostold)\ \boldsymbol{then}$
23 $\quad\quad Z_{beacons} \leftarrow pathOptimization(T, z_{init}, z_{goal})$
24 $\quad \boldsymbol{endif}$
25 $\quad \boldsymbol{return}\ T$
26 $\boldsymbol{endfor}$

In the initial path-finding stage, RRT*-Smart applies a conventional sampling technique. This technique will randomly generate nodes in the search space referring to the maximum and minimum limits of their representation. Based on these random nodes, the nearest node is determined by applying a Euclidean distance evaluation to the set of nodes. The direction from the nearest node to a random node is then determined as a reference direction for generating new nodes. In addition to referring to the reference direction, the placement of new node locations is also carried out based on the calculated distance between the random node and the nearest node. If the distance is less than or equal to the specified reference distance, then the placement of the new node from the nearest node is as far as the calculated distance. On the other hand, the placement of the new node from the nearest node is equal to the specified reference distance. This process is represented by Algorithm 2 in lines 9 and 10 after the sampling process in line 7 is carried out. Then RRT*-Smart will continue the process by paying attention to the new node. If the location of the new node is not the same as one of the points of the obstacle position and also the line formed from the new node to the nearest node does not intersect with any line from the obstacle, then the new node is connected to the nearest node as an Edge E. This process is called the wiring process in RRT. Furthermore, the nearest node will be temporarily considered as the parent node z_{near} of the new node z_{new} and all neighbor nodes of the new node are then evaluated for their proximity. The node that has the closest distance will be called z_{min} which is also the parent node for the new node. And the new node is linked to z_{min}. This stage is rewiring which simultaneously distinguishes RRT and RRT*, where the process is shown in lines 11 to 15 of Algorithm

2. In RRT*-Smart this series of steps is a process in determining the initial path before this path is optimized by applying Triangular Inequality. In short, this technique builds a new edge by connecting the node to the next node in the node set T if the relationship between the two nodes is free of obstacles and collisions. So, it is clear that in this process, the number of nodes will be reduced. This new set of nodes is called beacons $z_{beacons}$ as lies on line 23 and simultaneously the path formed from start to goal is connecting all these beacons with its costs termed $directcost$. Finding this initial path will trigger intelligent sampling with a number of samples spawned around $z_{beacons}$. This is done as an effort to reduce path costs by optimizing new nodes that are potentially better than the beacon position without having to do time-consuming sampling. Finally, the path correction is conducted in the global looping once the lower $directcost$ is found.

3. PROPOSED METHOD – RRT*SMART-A* ALGORITHM

In a high-dimensional space, as a sampling-based algorithm, RRT is indeed better and faster in finding the initial path. However, by observing more deeply, precisely by taking random samples, the variance of the search time is so large that it has the potential to take a long time to determine a feasible path. This is even more so in the narrow channel scenario, which of course will take a lot of time, because each path is formed randomly due to random sampling. It is this basis upon which RRT* is introduced. As previously mentioned, the difference between the two is that there are two operations on the RRT*, namely neighbors search and rewiring step after wiring step is done. The parent, which is always updated every time a new node is generated, certainly makes RRT* have the advantage of maintaining the optimality of the path. RRT*-Smart applies this to initial path determination. However, this kind of determination requires a lot of time and memory usage to achieve a truly optimal path. Accordingly, a new method with the name An Integrated RRT*Smart-A* Algorithm is introduced in this paper.

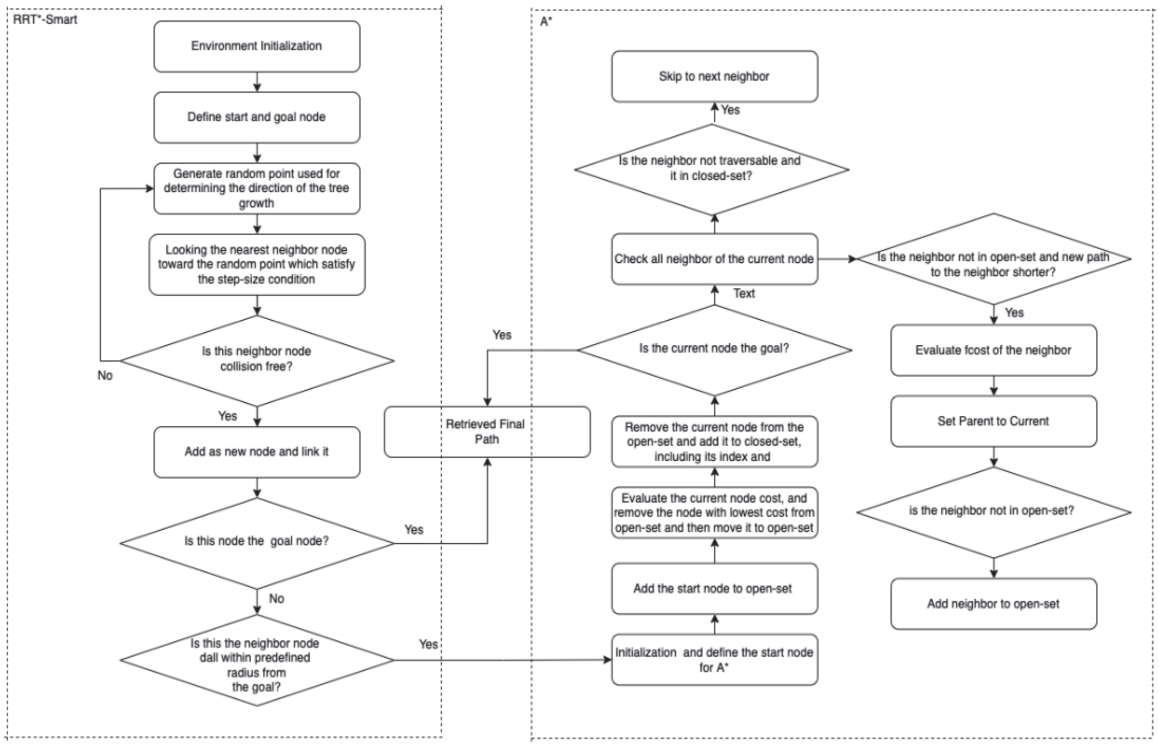

Fig. 1: Flowchart of Proposed Method (An Integrated RRT*-Smart A* Algorithm)

As seen in Fig. 1, in addition to integrating two different approaches referring to the proximity of the last exploration node to the goal node, conventional sampling techniques in the early stages of RRT*-Smart were replaced with fast-sampling techniques. Instead of expanding on a new exploration area, random sampling is not limited to the possibility of falling on the explored area. This reason underlies the replacement of conventional sampling with fast sampling. Where fast-sampling applies restrictions in generating samples, random samples obtained will be rejected if their position is in the explored area, and only random samples are in the new exploration area (see Fig. 2 and Algorithm 3 lines 7 up to 10).

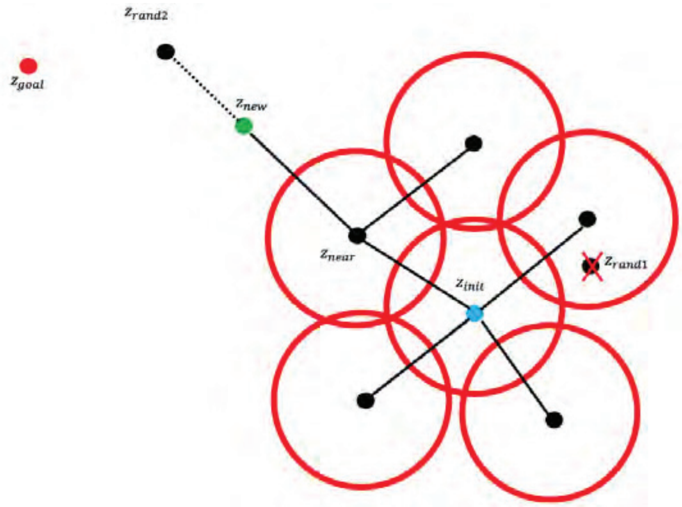

Fig. 2: Illustration of Fast-Sampling Technique. The red circle is the explored area. When random node z_{rand1} falls on the explored area it is rejected and random sampling is repeated. When the random node z_{rand2} is obtained, the wiring and rewiring process is carried out.

Furthermore, new nodes z_{new} formed during expansion will continue to be observed. If it is close to the goal node z_{node}, A* will take over determining this initial path. This aims to minimize the consumption of expansion time in narrow channels (see Algorithm 4 from lines 21 to 24). Furthermore, when the initial path is obtained, all feasible nodes will be directly connected by applying triangular equality. This application is intended to shorten the path as an optimization step. Iteration in this process starts from z_{goal} and moves to z_{init} by observing the direct connection to the parent sequentially until the connection of two different nodes is declared a collision on the obstacle. When the order of observations reaches z_{init} then no more nodes can be connected directly. To provide clarity on this process Fig. 3 and Algorithm 4 are given (see Algorithm 3).

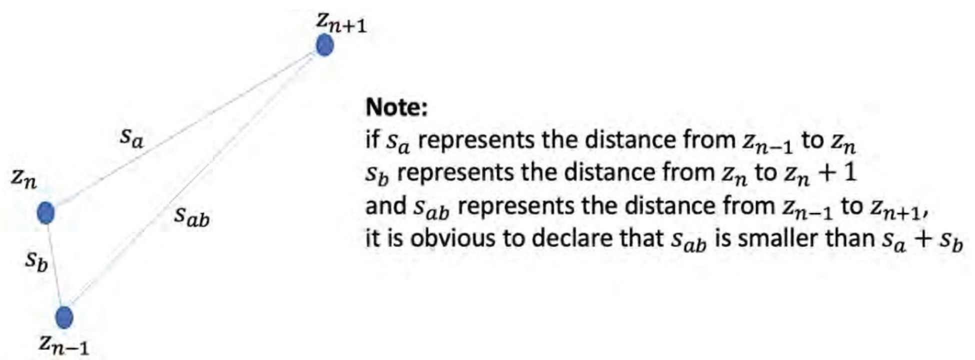

Fig. 3: The Principle of Triangular Inequality.

Algorithm 3. $Zbeacons \leftarrow \boldsymbol{PathOptimization}(\boldsymbol{T}, \boldsymbol{z_{init}}, \boldsymbol{z_{goal}})$

$Z_{beacons} = [\ \ ]$
$zn_{beacon} = z_{goal}$
$add\ zn_{beacon} to\ Zbeacons$
$\boldsymbol{for\ i = 2\ to}\ length(T)\ \boldsymbol{do}$
  $\boldsymbol{if}\ obstacleFree(zn_{beacon}, T(i))$
    $\boldsymbol{continue}$
  $\boldsymbol{else}$
    $add\ T(i-1)\ to\ Z_{beacons}$
    $update\ cost\ of\ zn_{beacon}$
    $zn_{beacon} = T(i-1)$
  $\boldsymbol{endif}$
  $\boldsymbol{return}\ Z_{beacons}$
$\boldsymbol{endfor}$

Along with getting this optimized path, the *directcost* will be calculated which will then be compared each time *pathOptimization* is performed. Once this path optimization occurs at the end of performance A* and will only repeat when the new *directcost* is better than the previous one. At the same time, when two conditions are met, n, the sampling bias variable, will be updated. Based on its magnitude and its relationship to the number of iterations, a number of samples will be generated around $Z_{beacons}$ as is the case with RRT*-Smart in general. This is intended to reduce the path again as an effort to maintain the optimality of the proposed method. Furthermore, this series of processes will be repeated until the maximum value of the iteration is met. To clarify the series of this process, Algorithm 4 is given as follows.

Algorithm 4. $\boldsymbol{RRT^{*}Smart - A*\ \ Algorithm}$

$T \leftarrow InitializeTree(\ )$
$T \leftarrow InsertNode(\emptyset, z_{init}, T)$
$initialPathFound = false$
$\boldsymbol{for}\ i = 1\ \boldsymbol{to}\ N\ \boldsymbol{do}$
  $\boldsymbol{if}\ i = n + b, n + 2b, n + 3b \ldots \boldsymbol{then}$
    $z_{rand} \leftarrow intelligent\_sampling(i, z_{beacon})$
  $\boldsymbol{else}$
    $z_{rand} \leftarrow sampling(i)$
    $\boldsymbol{while}\ z_{rand} \in Z_{explored}$
      $z_{rand} \leftarrow sampling(i)$
    $\boldsymbol{endwhile}$
  $\boldsymbol{endif}$
  $z_{nearest} \leftarrow nearest(T, z_{rand})$
  $(z_{new}, u_{new}, T) \leftarrow steer(z_{nearest}, z_{rand})$
  $\boldsymbol{if}\ obstaclefree(z_{new})\ \boldsymbol{and}\ {\sim}initialPathFound\ \boldsymbol{then}$
    $z_{near} \leftarrow near(T, z_{new}, |V|)$
    $z_{min} \leftarrow choosenparent(z_{near}, z_{nearest}, z_{new})$
    $T \leftarrow insertnode(z_{min}, z_{new}, T)$
    $T \leftarrow rewire(T, Z_{near}, Z_{min}, Z_{new})$
    $\boldsymbol{if}\ z_{nearest} \in Z_{goal}$
      $T \leftarrow astart(z_{nearest}, z_{goal})$

```
            initialPathFound = true
            n ← i
        endif
    endif
    if initialPathfound then
        (T, directcost) ← pathOptimization(T, z_init, z_goal)
        if (directcostnew < directcostold) then
            Z_beacons ← pathOptimization(T, z_init, z_goal)
            n ← i
        endif
    endif
    return T
endfor
```

4. RESULTS AND DISCUSSION

In this section, experimental results of different algorithms such as RRT*, RRT*-Smart, and the proposed algorithm are presented. In this experiment, the three algorithms were performed to solve the global path planning problem in some different environments that consists of a narrow channel and several barriers. They are compared to each other in terms of optimality and degree of convergence by observing the cost/distance from z_{init} to z_{goal} number of iterations, respectively.

For the first scenario, the start node is in the field area and the goal node is in a certain place. Before being tested, parameter equations were carried out to provide good observations and comparisons. This parameter includes eps which is the distance allowed to place a new node when the nearest node and a random node are given. In the first scenario experiment, eps was set to 3 for both RRT*, RRT*-Smart, and RRT*-Smart-A*. In addition, the parameter in determining the neighbor of the new node is also the same, which is set to $r_n = 3$. It should be noted that the second parameter is intended to provide equalities in the rewiring process of the three algorithms.

The next parameter equalization is the parameter used only for RRT*-Smart and the proposed algorithm, namely the beacon radius which is used for intelligent sampling performance after the initial path is found and every time the direct cost improves. In the experiment in this first scenario, the beacon radius is set equal to $r_{beacon} = 3$. In detail, the position of the start node and goal node are respectively at coordinates (5,5) and (50,65) in an environment as shown in Figure 4. The complexity of the environment is not so high, so all the algorithms compared have the ability to get the optimal path. And the optimality of this path will be observed based on the cost of each iteration and its dynamic value.

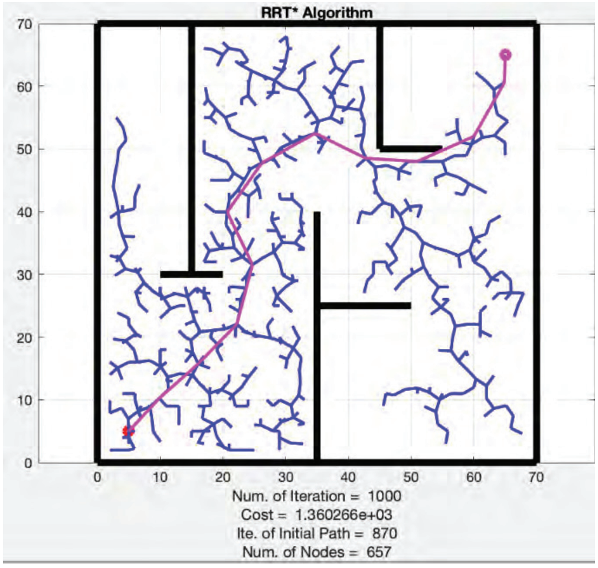

Fig. 4: Performance of RRT* Algorithm (1st Case).

Figure 4 shows a graphical result representing the performance of the RRT* Algorithm. Generally, the RRT* has succeeded in determining the collision-free path from z_{init} to z_{goal}. However, as shown in the graph and the cost value of 1360.3, the optimality of RRT* is still lacking. This is strongly relevant to the underlying theory that using simple random sampling the expansion of the nodes becomes diffuse and not centered. So, it is reasonable for a limited number of iterations, interconnecting feasible nodes is not enough to generate the optimal path.

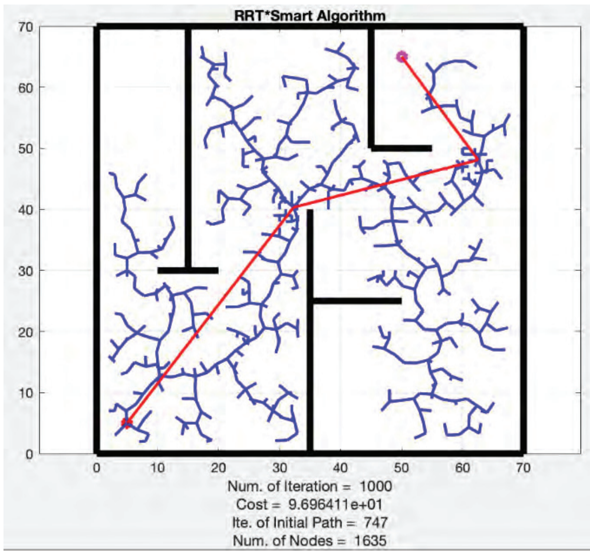

Fig. 5: Performance of RRT*-Smart Algorithm (1st Case).

In the same case, the effect of using conventional sampling on the initial path determination also makes RRT*-Smart take time to provide the optimal path. This is because the path optimization time is getting narrower when RRT*-Smart works at a limited time. This phenomenon can be seen in the need for repetition of 747 times in finding the initial path (see Fig. 5). So, it is not surprising that the final solution with a given cost of 95 can actually be increased if the application time of intelligent sampling is sufficient. However, this performance is enough to prove that RRT*-Smart has better optimality than RRT*.

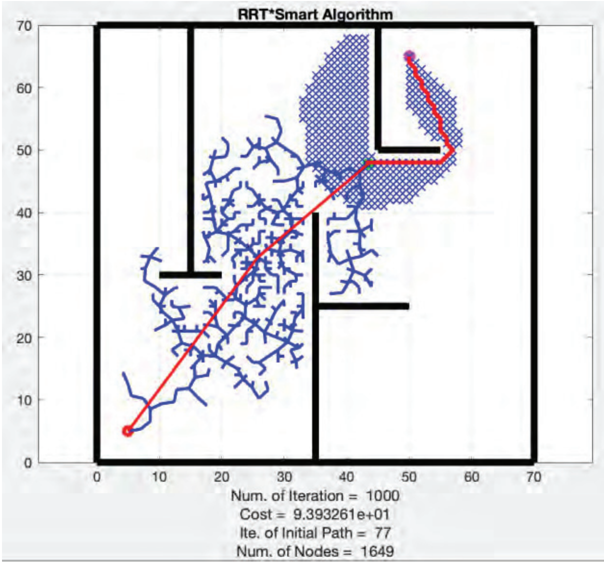

Fig. 6: Performance of RRT*Smart-A* Algorithm.

Next in this first scenario, the RRT*-Smart A* Algorithm is performed. As shown in Fig. 6, the proposed algorithms that involve fast-sampling only need 77 iterations to explore from z_{init} to Z_{goal}. This achievement is ideal because it will provide a long duration to apply intelligent sampling and path optimization to the next process. This can be seen from the distribution of samples in the area near the beacon used to assist the path optimization. Although the path optimization is not intended to repair the offered path of A, the cost is 93, it is enough to prove that in term of optimality the proposed method is better than RRT* and RRT*-Smart. Additionally, the number of nodes generated in a finite duration implies that optimization can occur iteratively, so the potential for generating shorter paths is possible.

Fig. 7: Performance of RRT* Algorithm (2nd Case).

Figure 7 shows a graphical result representing the performance of the RRT* Algorithm for the second scenario. It can be seen from Fig. 7, the RRT* needs more than 8000 iterations to get initially optimal path before it is optimized. This situation shows that the RRT* algorithm does not have ability or is improper to solve the environment with narrow channel. Besides that, it can be seen from the path cost after optimization, the cost is high. It represents that its optimality is still lacking for this second case.

Fig. 8: Performance of RRT*-Smart Algorithm (2nd Case).

Since the conventional sampling is used for obtaining the initial path, the RRT*-smart has the similar level for its convergence speed as RRT*. It indicates that the convergence rate of RRT*-smart strongly depends on the initial sampling method. As can be seen from Fig. 8, unfortunately the RRT*-Smart does not obtain the initial path even if the number of iterations is increased and the number of nodes reaches more than 4000 nodes. For this inconsistency and limitation, the RRT*-Smart improves by replacing the conventional sampling with a fast sampling in the second case. Graphically its performance can be seen as follows.

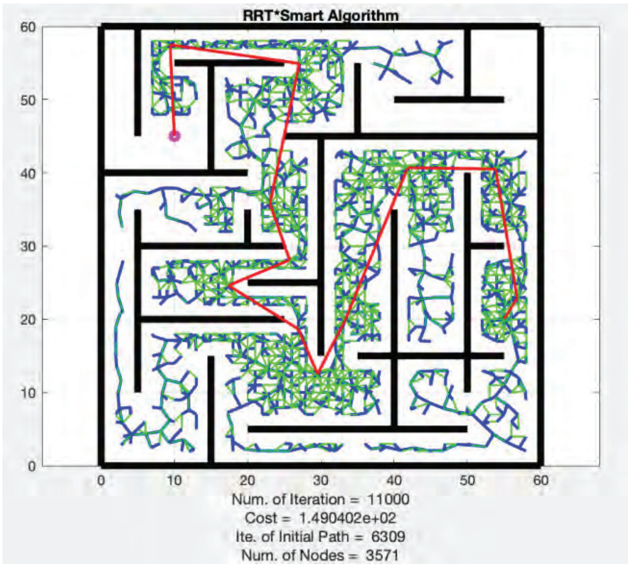

Fig. 9: Performance of RRT*-Smart with A Fast Sampling (2nd Case).

Referring to Fig. 9, the RRT*-Smart with a fast sampling is also limited. It can be observed based on the number of iterations and the iteration indicating the initial path found. The diversity between these values represents that the optimization, which is an advantage of RRT*-Smart, has a short duration. Therefore, the generated nodes have small number compare to RRT* or its predecessor. For this reason, the proposed method is introduced and its performance can be presented as follows.

Fig. 10: Performance of RRT*-Smart-A* Algorithm (2nd Case).

It can be seen from Fig. 10, the proposed method finds the initial path in the iterations of 2643 within 6000 iterations. It indicates more than 3000 iterations that are allocated for optimization only. This small number of iterations also implies that the proposed method has a better convergence speed than its predecessor. Next, although the cost is high compared to its predecessor, it is only because of the dynamicity of the exploration process. Therefore, in terms of convergence rate and optimality, the proposed method is validated by this result.

5. CONCLUSION

Due to the limitation of RRT*-Smart when it is used in environments containing some narrow channels, the conventional sampling is improper. For this reason, it is improved by replacing the conventional sampling with A* sampling. Moreover, if a wide enough time frame is provided for its optimization, it is integrated with the A* algorithm. Henceforth, it is called An Integrated RRT*Smart-A* Algorithm. It is used to solve the global path planning problem. By comparing with its predecessors, RRT* and RRT*-Smart, the proposed method has shown better efficiency in terms of convergence rate and optimal cost.

ACKNOWLEDGEMENT

This research is supported by Universitas Mercu Buana.

REFERENCES

[1] Satapathy SC, Biswal BN, Udgata SK, Mandal JK. (2014). Proceedings of the 3rd International Conference on Frontiers of Intelligent Computing: Theory and Applications (FICTA) 2014. Advances in Intelligent Systems and Computing, 327: 175-183. https://doi.org/10.1007/978-3-319-11933-5.

[2] Adriansyah A, Suwoyo H, Tian Y. (2019). Jurnal Teknologi IMPROVING ROBOT. 3: 119-126.
[3] Tian Y, Suwoyo H, Wang W, Li L. (2019). An ASVSF-SLAM Algorithm with Time-Varying Noise Statistics Based on MAP Creation and Weighted Exponent. Mathematical Problems in Engineering, 2019(1): 1-17. https://doi.org/10.1155/2019/2765731.
[4] Al-Mutib K, Faisal M, Alsulaiman M, Abdessemed F, Ramdane H, Bencherif M. (2017). Obstacle avoidance using wall-following strategy for indoor mobile robots. 2016 2nd IEEE International Symposium on Robotics and Manufacturing Automation, ROMA 2016, 1-6. https://doi.org/10.1109/ROMA.2016.7847817.
[5] Siegwart, R., Nourbakhsh, I. R., & Scaramuzza, D. (2011). Introduction to autonomous mobile robots. MIT press.
[6] Kümmerle, R. (2013). State estimation and optimization for mobile robot navigation (Doctoral dissertation, Verlag nicht ermittelbar).
[7] Jeong IB, Lee SJ, Kim JH. (2019). Quick-RRT*: Triangular inequality-based implementation of RRT* with improved initial solution and convergence rate. Expert Systems with Applications, 123: 82-90. https://doi.org/10.1016/j.eswa.2019.01.032.
[8] Baglivo L, Bellomo N, Miori G, Marcuzzi E, Pertile M, Cecco MDe. (2008). An object localization and reaching method for wheeled mobile robots using laser rangefinder. 2008 4th International IEEE Conference Intelligent Systems, IS 2008. 1. 5-6. https://doi.org/10.1109/IS.2008.4670429.
[9] Chen W, Qin H. (2011). Path planning of mobile robot based on hybrid cascaded genetic algorithm. Proceedings of the World Congress on Intelligent Control and Automation (WCICA), 501-504. https://doi.org/10.1109/WCICA.2011.5970564.
[10] Kim T, Wang Y, Sahinoglu Z, Wada T, Hara S, Qiao W. (2014). State of charge estimation based on a realtime battery model and iterative smooth variable structure filter. IEEE Innovative Smart Grid Technologies - Asia, ISGT ASIA 2014, 132-137. https://doi.org/10.1109/ISGT-Asia.2014.6873777.
[11] Mashayekhi R, Idris MYI, Anisi MH, Ahmedy I, Ali I. (2020). Informed RRT∗-Connect: An Asymptotically Optimal Single-Query Path Planning Method. IEEE Access, 8: 19842-19852. https://doi.org/10.1109/ACCESS.2020.2969316.
[12] Qureshi AH, Ayaz Y. (2016). Potential functions based sampling heuristic for optimal path planning. Autonomous Robots, 40(6): 1079-1093. https://doi.org/10.1007/s10514-015-9518-0.
[13] Perez A, Karaman S, Shkolnik A, Frazzoli E, Teller S, Walter MR. (2011). Asymptotically-optimal path planning for manipulation using incremental sampling-based algorithms. IEEE International Conference on Intelligent Robots and Systems, 4307-4313. https://doi.org/10.1109/IROS.2011.6048640.
[14] Yi G, Zhou C, Cao Y, Hu H. (2021). Hybrid assembly path planning for complex products by reusing a priori data. Mathematics, 9(4): 1-13. https://doi.org/10.3390/math9040395.
[15] Chen J, Zhao Y, Xu X. (2021). Improved RRT-Connect Based Path Planning Algorithm for Mobile Robots. IEEE Access, 9: 145988-145999. https://doi.org/10.1109/ACCESS.2021.3123622.
[16] Nasir J, Islam F, Malik U, Ayaz Y, Hasan O, Khan M, Muhammad MS. (2013). RRT*-Smart: A rapid convergence implementation of RRT*,. International Journal of Advanced Robotic Systems. https://doi.org/10. 299. 10.5772/56718.
[17] Liao B, Wan F, Hua Y, Ma R, Zhu S, Qing X. (2021). F-RRT*: An improved path planning algorithm with improved initial solution and convergence rate. Expert Systems with Applications. 184. 115457. 10.1016/j.eswa.2021.115457.
[18] Mashayekhi R, Idris MYI, Anisi MH, Ahmedy I. (2020). Hybrid RRT: A semi-dual-tree RRT-based motion planner. IEEE Access, 8: 18658-18668. https://doi.org/10.1109/ACCESS.2020.2968471.
[19] Noreen I, Khan A, Habib Z. (2016). A Comparison of RRT, RRT* and RRT*-Smart Path Planning Algorithms. IJCSNS International Journal of Computer Science and Network Security, 16(10): 20-27. http://cloud.politala.ac.id/politala/1. Jurusan/Teknik Informatika/19. e-journal/Jurnal Internasional TI/IJCSNS/2016 Vol. 16 No. 10/20161004_A

Compar ison of RRT, RRT and RRT - Smart Path Planning Algorithms.pdf

[20] Islam F, Nasir J, Malik U, Ayaz Y, Hasan O. (2012). RRT*-Smart: Rapid convergence implementation of RRT* towards optimal solution. 2012 IEEE International Conference on Mechatronics and Automation, ICMA 2012, 1651-1656. https://doi.org/10.1109/ICMA.2012.6284384.

[21] Noreen, I., Khan, A., Asghar, K., & Habib, Z. (2019). A Path-Planning Performance Comparison of RRT*-AB with MEA* in a 2-Dimensional Environment. Symmetry, 11(7), 945. MDPI AG. Retrieved from http://dx.doi.org/10.3390/sym11070945.

[22] Prince, C.G. (2004). Book Review: Computational Principles of Mobile Robotics. Minds and Machines 14, 407–414. https://doi.org/10.1023/B:MIND.0000035501.55990.99.

[23] Barfoot, T. (2017). State Estimation for Robotics. Cambridge: Cambridge University Press. https://doi.org/10.1017/9781316671528.

[24] Fernández-Madrigal J-A. (2012). Simultaneous Localization and Mapping for Mobile Robots: Introduction and Methods. IGI global. https://doi.org/10.4018/978-1-4666-2104-6.

[25] Gao Z, Mu D, Zhong Y, Gu C, Ren C. (2019). Adaptively Random Weighted Cubature Kalman Filter for Nonlinear Systems. Mathematical Problems in Engineering. 2019. 1-13. 10.1155/2019/4160847.

[26] Kocijan, J. (2016). Modelling and control of dynamic systems using Gaussian process models (pp. 33-38). Cham: Springer International Publishing .https://doi.org/10.1007/978-3-319-21021-6.

[27] Ni J, Wang K, Huang H, Wu L, Luo C. (2016). Robot path planning based on an improved genetic algorithm with variable length chromosome. 2016 12th International Conference on Natural Computation, Fuzzy Systems and Knowledge Discovery, ICNC-FSKD 2016, 145-149. https://doi.org/10.1109/FSKD.2016.7603165.

[28] Magzhan K, Jani H. (2013). A Review And Evaluations Of Shortest Path Algorithms. International Journal of Scientific & Technology Research, 2(6): 99-104. http://www.ijstr.org/final-print/june2013/A-Review-And-Evaluations-Of-Shortest-Path-Algorithms.pdf.

[29] Rachmawati D, Gustin L. (2020). Analysis of Dijkstra's Algorithm and A* Algorithm in Shortest Path Problem. Journal of Physics: Conference Series. 1566. 012061. https://doi.org/10.1088/1742-6596/1566/1/012061.

https://doi.org/10.31436/iiumej.v24i1.2604

CONTROL STRATEGY FOR POWER ASSIST UPPER LIMB REHABILITATION ROBOT WITH THE THERAPIST'S MOTION INTENTION PREDICTION

ZULIKHA AYOMIKUN ADEOLA-BELLO[1], NORSINNIRA ZAINUL AZLAN[1*] AND SALMAH ANIM ABU HASSAN[2]

[1]Department of Mechatronics Engineering, Kulliyyah of Engineering, International Islamic University Malaysia, Jalan Gombak, 53100 Kuala Lumpur, Malaysia
[2]Department of Orthopaedics, Traumatology and Rehabilitation, Kulliyyah of Medicine, International Islamic University Malaysia Kuantan Campus, Jalan Sultan Ahmad Shah, Bandar Indera Mahkota, 25200 Kuantan, Pahang, Malaysia

**Corresponding author: sinnira@iium.edu.my*

(Received: 15th September 2022; Accepted: 1st December 2022; Published on-line: 4th January 2023)

ABSTRACT: Currently, fully automated rehabilitation robots can assist therapists in providing rehabilitation therapy, hence the patients could get hurt. On the other hand, manual treatment may cause less patient injury but it is tiresome, and there are not enough therapists in most countries. Power assist rehabilitation robots can support the therapists in conducting the treatment and may help to alleviate this problem. The goal of this study is to develop a control strategy for the robot to assist the therapist's movement in a power assist upper limb rehabilitation treatment. The system combines the advantages of robotic and manual rehabilitation therapy. Torque and position sensors fitted on the power assist upper limb rehabilitation robot arm are used for motion intention estimation. The amount of angular velocity necessary to be delivered to the feedback controller will be determined by predicting the therapist's motion intention using the impedance control method. The resulting velocity from the motion intention estimator is incorporated into the Sliding Mode Control - Function Approximation Technique (SMC-FAT) based adaptive controller. The SMC-FAT based adaptive controller in the feedback loop, overcomes the uncertain parameters in the combination of the robot and the human arm. The motion intention estimator forecasts the movement of therapists. The proposed controller is used to regulate elbow flexion and extension motion on a power assist upper limb rehabilitation robot with one degree of freedom (DOF). The proposed control system has been tested using MATLAB simulation and hardware experimental tests. The outcomes demonstrate the effectiveness of the proposed controller in directing the rehabilitation robot to follow the desired trajectory based on the therapist's motion intention, with maximum errors of 0.002rad/sec, 0.005rad/sec and 0.02rad/sec for sinusoidal, constant torque values, and hardware experiment respectively.

ABSTRAK: Pada masa ini, robot rehabilitasi automatik sepenuhnya dapat membantu ahli terapi dalam menyediakan terapi pemulihan, tetapi pesakit berkemungkinan tercedera. Sebaliknya, rawatan manual berkemungkinan mengurangkan kecederaan pesakit tetapi ia memenatkan, dan terdapat kurang ahli terapi yang mencukupi di kebanyakan negara. Robot pembantu rehabilitasi dapat membantu ahli terapi dalam menjalankan pemulihan dan mengurangkan masalah ini. Sistem ini menggabungkan kelebihan terapi pemulihan robotik dan manual. Alat pengesan tork dan kedudukan diletakkan pada anggota atas lengan robot rahabilitasi yang digunakan bagi mengesan anggaran jarak pergerakan ahli terapi. Anggaran halaju sudut diperlukan bagi kawalan gerak balas dan dapat diketahui melalui anggaran niat gerakan ahli terapi menggunakan kaedah kawalan impedans. Halaju yang terhasil daripada anggaran niat gerakan diadaptasi ke dalam pengawal adaptif berasaskan Kawalan Mod

Gelongsor - Teknik Anggaran Fungsi (SMC-FAT). Pengawal penyesuaian berasaskan SMC-FAT dalam gelung maklum balas, mengatasi parameter yang tidak pasti dalam gabungan robot dan lengan manusia. Penganggar niat gerakan meramalkan gerakan ahli terapi. Pengawal yang dicadangkan digunakan bagi mengawal lenturan siku dan gerakan lanjutan pada robot rehabilitasi dengan satu darjah kebebasan (DOF). Sistem kawalan yang dicadangkan telah diuji menggunakan simulasi MATLAB dan ujian eksperimen perkakasan. Dapatan kajian menunjukkan keberkesanan pengawal yang dicadangkan dalam mengarahkan robot rehabilitasi mengikut trajektori yang dikehendaki berdasarkan niat gerakan ahli terapi, dengan ralat maksimum masing-masing 0.002rad/s dan 0.005rad/s bagi sinusoidal, nilai tork malar, dan eksperimen perkakasan masing-masing.

KEYWORDS: *Upper Limb rehabilitation; Motion intention estimator; uncertainties; therapist assistance; rehabilitation robot*

1. INTRODUCTION

Stroke victims frequently lose their ability to do daily tasks with their hands. Stroke is regarded as one of the most serious diseases and a vital issue in the nation because of the large number of its victims. Patients can restore arm functions and resume doing routine and essential daily tasks after intensive practice that is repeated and massed over the rehabilitation process. The two categories of power assist upper limb rehabilitation robots are end-effector and exoskeleton robots. These robots can conduct a variety of actions and undertake rehabilitation training activities to help patients complete certain therapies [1]. Additionally, it offers a consistent and demanding physical treatment, relieving physical therapists of a substantial amount of labor. End-effector systems may move limbs in space without requiring the patient's and robot's joints to be aligned by using footplates or grips.

Manual rehabilitation therapy and robotic rehabilitation therapy are two rehabilitation approaches. A global issue with manual rehabilitation treatment is its inconsistency and its low therapist-to-patient ratio. The entirely autonomous nature of earlier rehabilitative equipment increases the potential for patient injury. This issue can be solved by a rehabilitation robot that combines manual and automated functions. The study focuses on a new control approach for a power assist rehabilitation robot that aids the therapist in moving the patient's arm during rehabilitation exercises, allowing the system to combine the advantages of completely robotic and manual rehabilitation treatment. In this manner, the system may provide patients with a rehabilitation program that is both safe and comfortable [2].

This paper presents a new control approach for the therapist, allowing them to actively intervene in the treatment, taking into account the robot and patient's parameter uncertainties. The controller consists of a motion intention estimator for the therapist based on the impedance controller. The resulting output velocity is fed into the FAT-SMC based adaptive controller to cater to the uncertainties. The novelty of this paper is a new control strategy that focuses on assisting the therapist's movement with a motion intention estimator combined with SMC-FAT based adaptive controller in the feedback loop for a power assist upper limb rehabilitation robot.

The rest of the paper is organized as follows. Section 2 presents the summary of previous works on upper limb rehabilitation robot and motion intention estimation. Section 3 describes the methods and equations used in deriving the proposed control strategy. The simulation results and hardware experimental analysis are discussed in Section 4. Section 5 presents the conclusion of the paper.

2. PREVIOUS WORKS ON UPPER LIMB REHABILITATION ROBOT AND MOTION INTENTION ESTIMATION

Due to the lack of a direct therapist intervention during training, the use of totally robotic rehabilitation treatment may increase the risk of patients' injuries and may be uncomfortable for the patients [3]. Additionally, mistakes in the treatment robot's actuation are possible. Thus, this paper presents a new control strategy for the upper limb rehabilitation robot that is not fully robotic and assists the therapist based on their motion intention to realize a smooth movement in the rehabilitation. This section represents the previous work in power assist upper limb rehabilitation robot and motion intention estimation methods.

2.1. Power Assist Upper Limb Rehabilitation Robot

Power assist devices are created and intended to help physically challenged persons with everyday chores and self-rehabilitation. Tang et al. [4] developed an upper-limb power-assist exoskeleton actuated by pneumatic muscles. The exoskeleton may now be controlled in real time depending on the user's intended movements thanks to the development of proportional myoelectric control. The feature extraction technique and classification were utilized to create an electromyogram (EMG)-angle model for pattern recognition.

An approach for perception-assist that modifies the user's mobility as necessary to help their movement and interaction with their environment was proposed [5]. A study on a power-assist robot arm using pneumatic artificial rubber muscles (PARMs) with a balloon sensor was published to help with upper-limb and back motions. The elbow and wrist joints may be moved by a single PARM, and the movement of the various arm portions is similar to that of the bi-articular muscle. According to the independent joint control paradigm, an ideal linear quadratic Gaussian torque controller (LQG) with integral action for an upper limb rehabilitation robot was introduced. The controller's goals are to simplify the control design process, guarantee the best robust torque control, and prevent modeling uncertainties.

2.2. Motion Intention Estimation Methods

The intended velocity, which serves as a proxy for human intention is determined in real-time using the robot's location, speed, and interaction force as well as contact point movement characteristics [6]. Impedance control, which enables the robot to follow a specified path, may be used for interaction control. The techniques for changing the assistance lever of the impedance parameters are often employed in various applications of human-robot shared control systems.

The Radial-based Function Neural Network (RBFNN) model for evaluating the cooperation intention in touch human-robot collaboration has been developed. Lee et al. [7] suggested a new classifier based on force information measured by the robot's Force/Torque sensor and surface EMG signals from muscle activation to extract human intention during interaction with external force. The degree of external force produced by the encounter may be determined using the suggested classifier. In order to validate the suggested methodology, a simple control method is developed based on the proposed classifier to support the intention-based motion.

A device that produce the intended trajectory based on the designer's assessment of the user's motion intention was introduced. Motion intention was proposed as a workable solution since it takes a lot of energy for a person to move the exoskeleton arm, especially if the difference between the robot's true position and the human's motion intention is large. The subject's desired intention of motion (DIM) must be determined via an indirect force control loop. The identification of DIM can be accomplished using the Damped Least Square technique (DLS).

A wearable double-shell robotic exoskeleton for upper-limb power assist was proposed by Huang et al. [8], based on an online assessment of the wearer's motion intention.

A unique method for identifying human body motion intention for active power-assist lower limb exoskeleton robots (APAL) was investigated [9]. Both the inverse dynamics approach (IDA), which uses a dynamic model of the human body, and the sensing system integrated within an exoskeleton robot (APAL), which was developed to gather motion data and foot contact force, were used to do online estimations of the human joint torque. An approach to evaluate interaction motion intention for perception-assist with an upper-limb wearable power-assist robot was given in a work by [10]. The power-assist wearable robot user was given instructions to use visual information from the camera that was worn to assess the other person's motion intention in this approach.

The problem of tracking the user's motion intentions when they were using an upper-limb power-assist wearable robot in planned social interactions with other people was addressed by [11]. If the interaction is inappropriate, the power-assist wearable robot's user motion can be automatically changed to guarantee excellent interaction performance or to prevent unforeseen mistakes when using the device.

Surface electromyography (SEMG), a bioelectrical signal created when a neuron conveys human motion intention information directly to a related muscle, is an example of artificial intelligence-based estimate. Therefore, without any information loss or delay, the motion's purpose may be fully inferred. Due to its wealth of data, superior collecting technology, and noninvasiveness, human motion intention recognition based on SEMG will become widely used. Machine learning (ML) based motion and SEMG-driven musculoskeletal (MS) model-based motion are the two methods of SEMG-based motion intention recognition. The most important aspect of the entire procedure is determining human motion intentions [12].

A neuro-fuzzy technique for accurately anticipating the motion intention of the power-assist rehabilitation robot user was proposed, taking the effect of the difference in posture into consideration. It seems that many sensor modalities are needed for sophisticated device control given the challenges of providing reliable control with simply EMG. An EMG-based admittance controller (EAC) was created to address the problem. Determining the human purpose for a multifunctional device's successful use and effective operation presents a number of challenges, though. The primary rationale is the time-varying and noisy character of the EMG signals [13]. In addition, there is a complicated non-linear connection between the output forces of the various muscles.

Extreme Learning Machine (ELM), a revolutionary approach, was suggested as a solution to these problems [14]. Using radial basis function networks, single and multi-hidden layer neural networks, feed-forward neural networks may be generalized effectively. However, because these approaches are sluggish when simulating a broad class of natural occurrences, they are unsuitable for applications like discerning human purpose. The need to fine-tune each network parameter is the fundamental reason for this delayed learning. Based on information from force sensors, joint current location, and current moving speed, ELM can quickly assess desired goals, learn human motion patterns, and forecast future movement. In assistive robotics and rehabilitation, this desired motion may be used to increase performance and robot compliance. An exoskeleton-style rehabilitation or assistance robot may be managed more successfully and comfortably by the user by utilizing the recommended interface, intention estimate, and intention-based control algorithms [15]. The rehabilitation power-assisted robot must be able to increase its output proportionally to the amount of mobility required.

Utilizing EMG data, a lower limb neuromusculoskeletal model was used to determine the torque at each human joint before applying an admittance control strategy to attain the desired position. A synchronized and robust Human-Robot Interaction (HRI) was produced using an EMG-based admittance controller (EAC). Wang et al. [16] employed neural networks to discover model parameters online before adding the desired trajectory into the impedance control of an upper-limb humanoid robot. To illustrate the expected course of human mobility, they created a model of an upper human limb. When the human motion intention is unsure and the robot dynamics are unknown, an interactive robot utilizes adaptive impedance control. It was found that the joint torque of the human body fits the essential requirements of motion intention estimate for the active power-assist after looking at the conduction path and numerous stage manifestations of motion intention in the human body. Joint torque is also said to create real-time, continuous output, precede human limb movements, and indicate the intensity and direction of the wearer's efforts. This calls for the need for an accurate model, an evaluation of human intent, and a method for measuring human joint torque.

Conventional control systems based on force/torque sensors have difficulty interpreting human intentions and are typically susceptible to misreading or distorting such intentions because of external contact force interruptions, such as those experienced in daily activities. Therefore, a power-assist robot controller cannot accurately evaluate the real human force. Force/torque sensors are used to measure the overall amount of applied force, which includes both human intention and unidentified environmental factors. The power assist robot may also employ motion sensors on the user to facilitate the anticipated actions. For a power support exoskeleton robot arm, a motion intention-based bionic control system was suggested [17]. To pre-process the recorded motion signal, filtering is utilized.

An improved robot skill learning system that took motion production and trajectory tracking into account, was suggested by [18]. During robot learning demonstrations, dynamic movement primitives (DMPs) were used to imitate robotic mobility. Each DMP is composed of a number of dynamic systems that act in concert to increase the stability of the motion toward the aim. A hybrid force/position control approach for robotic arms based on the stiffness estimation of an unknowable environment was developed to provide precise control and a stable system. Predicting human intent necessitates human-robot interaction.

The primary aspect affecting the creation of upper limb rehabilitation robots is human motion intention. Since assistive or rehabilitative robots must move in line with the wearer's request, estimating the wearer's motion intention is a key challenge. For Power support systems for wearables, it is extremely important to design an effective identification method for identifying the wearer's motion intention. Thus, in this research, the impedance control interaction strategy is used for motion intention estimation of the therapist and SMC-FAT-adaptive controller is used to cater for the parameter uncertainties for a power assist upper limb rehabilitation robot with patient's arm.

3. PROPOSED CONTROL STRATEGY

The block diagram for the proposed control strategy is shown in Fig. 1. The motion intention controller calculates the therapists' motion prediction, and it is integrated into the SMC-FAT controller. This controller acts as the feedback controller to cater to the patient's arm parameter uncertainties [19]. It takes the information of the desired trajectory, x_d , actual angular velocity, $\dot{q}$, and therapist's torque, τ_h to calculate the desired velocity, $\dot{q_d}$, for the therapist's motion intention estimation. The value is then passed to the SMC-FAT controller. The outcome is integrated into the lumped rehabilitation robot and human arm plant.

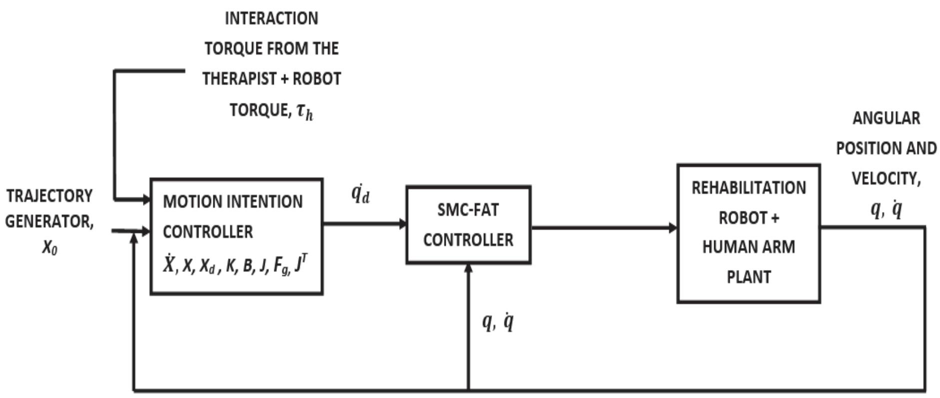

Fig. 1. Block diagram of control strategy

Fig. 2 shows the block diagram of the experimental setup. The angular position of the robot's joints with the patient's arm and therapist's torque exerted will be measured using encoders and torque sensors respectively, and supplied to the microcontroller. The amount of desired angular velocity based on the motion prediction of the therapist will be calculated. The necessary amount of voltage required for assisting the therapist will be provided to the upper limb rehabilitation robot from the SMC-FAT based adaptive controller.

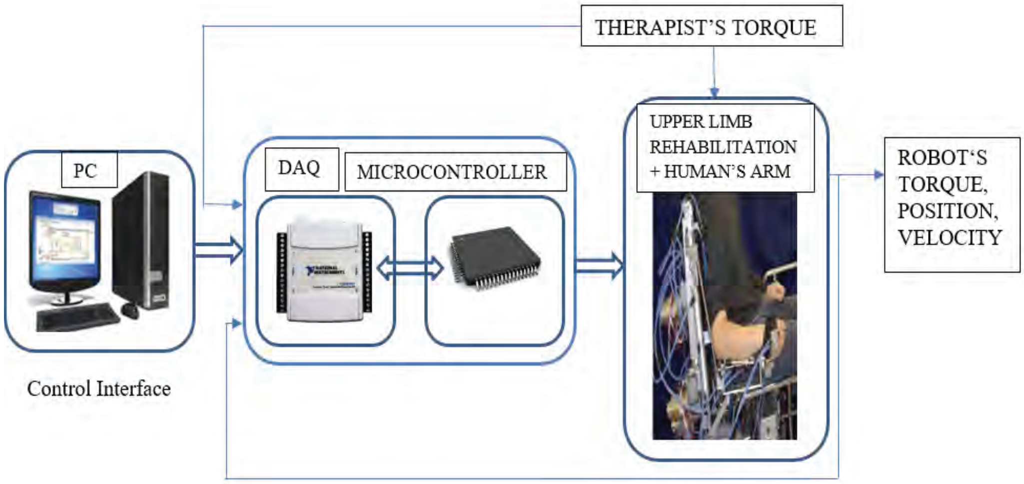

Fig. 2. Block diagram of the experimental architecture

In this research, torque and position sensor measurements are used to calculate the therapist's motion intention prediction. The therapist's torque exerted and the robot joint's angular position are the quantities that will be measured. The therapist's torque is calculated using constant torque and sinusoidal value. The robot torque and position trajectory of the robot can only be derived from the output of the lumped upper limb rehabilitation robot and human arm, after the implementation of motion intention estimator and SMC-FAT- adaptive controller. The DAQ helps to communicate between the computer (PC) and the robot. In this research, a serial communication DAQ (NI USB-6211) is used, and it is connected to the Upper limb rehabilitation robot. The role of the PC is to program the controller and also serve as interface to help tune and display the control parameters. The LabVIEW and the NI-DAQmx driver are installed into the PC to test the proposed controller on the power assist upper limb rehabilitation robot. Simulation and hardware experimental tests are used to evaluate the performance of the project with the aid of MATLAB and LabVIEW softwares.

https://doi.org/10.31436/iiumej.v24i1.2604

3.1. Dynamic Model of the Integrated Power Assist Upper Limb Rehabilitation Robot with Human Arm

The dynamic model of the upper limb rehabilitation robot with human arm can be written below. The mathematical model of the system is adopted from [20].

$$\dot{X}_B = A_B X_B(t) + B_B U_s(t) + F_B T(t) + W_B \dot{T}(t) \tag{1}$$

where, A_B, B_B, F_B, W_B are the system, input, load distribution, and rate of load distribution matrices with acceptable dimensions respectively. $X_B(t)$ is the vector consisting of the angular position, velocity, and acceleration of the electrical motor. $U_s(t)$ is an input vector, $T(t)$ is the mechanical link torque and $\dot{T}(t)$ is its time derivative.

where,

$$X_B(t) = [x_1 \quad x_2 \quad x_3] \tag{2}$$

$$= [x^1{}_B \quad x^2{}_B \quad x^3{}_B] \tag{3}$$

$$= [q \quad \dot{q} \quad \ddot{q}\ ] \tag{4}$$

$$A_B = \begin{bmatrix} 0 & 1 & 0 \\ 0 & 0 & 1 \\ 0 & a_{B32} & a_{B33} \end{bmatrix}$$

$$B_B = \begin{bmatrix} 0 \\ 0 \\ b_B \end{bmatrix} \qquad F_B = \begin{bmatrix} 0 \\ 0 \\ f_B \end{bmatrix} \tag{5}$$

$$W_B = \begin{bmatrix} 0 \\ 0 \\ w_B \end{bmatrix} \qquad U(t) = [U(t)]$$

$$T(t) = [T(t)] \qquad \dot{T}(t) = [T(t)]$$

The non-zero elements of the A_B, B_B, F_B and W_B matrices are as follows [20]:

$$a_{B32} = -\frac{k_v k_t + B_v R}{J_m L} \qquad a_{B33} = -\frac{B_v L + J_m R}{J_m L}$$

$$b_B = \frac{k_t}{J_m L N} \tag{6}$$

$$f_B = -\frac{R_2}{N^2 J_m L} \qquad w_B = -\frac{1}{N^2 J_m}$$

where,

J_m is the moment of inertia, R is the armature resistance, L is the armature inductance, B_v is the viscous friction constant, k_v is the Back Emf constant, and N is the inverse of gear ratio [20].

The dynamic equation of the mechanical links of the 1 DOF rehabilitation robot with human arm can be written as follows.

$$T(t) = M(q(t),\zeta)\ddot{q}(t) + \bar{D}(q(t),\zeta)\hat{V}(\dot{q}) + G(q(t),\zeta) + F_c\, sgn(\dot{q})s + V_c \dot{q}(t) \tag{7}$$

where,

$$q(t) = [q(t)]^T \tag{8}$$

$$T(t) = [T(t)]^T \tag{9}$$

$$M(q,\zeta) = [M] \tag{10}$$

$$\bar{D}(q,\zeta) = [\bar{D}_{11} \quad 0 \quad 0 \quad 0 \quad \bar{D}_{15} \quad \bar{D}_{16}]$$

$$\hat{V}(\dot{q}) = [\dot{q}], \qquad G(q) = [G] \tag{11}$$

$$Fc = [F_C] \qquad Vc = [V_C] \tag{12}$$

where,
q is the joint angular position
$\dot{q}$ is the joint angular velocity
$\ddot{q}$ is the joint angular acceleration
$M(q,\zeta)$ is the positive definite inertia matrix.
$\bar{D}(q,\zeta)$ is the Coriolis and Centrifugal torques.
$G(q,\zeta)$ is the gravitational torque.
ζ is the uncertain human arm mass carried by the rehabilitation robot.
T is the control input torque from the actuators.
Fc and Vc are the coulomb friction coefficients and viscous friction coefficients respectively.
The terms $\bar{D}(q,\zeta)\,\hat{V}(\dot{q})$ and $G(q,\zeta)$ in Eq. (7) can be modified as $\widehat{D}(q,\dot{q},\zeta)\,\dot{q}$ and $\hat{G}(q,\zeta)q$ respectively. Hence, the lumped 1DOF rehabilitation robot with human arm dynamic model can be rewritten as:

$$T(t) = M(q(t),\zeta)\ddot{q}(t) + \widehat{D}(q(t),\dot{q}(t),\zeta)\dot{q}(t) + \hat{G}(q(t),\zeta)q(t) + F_c[sgn(\dot{q})q(t)] + V_c\dot{q}(t) \tag{13}$$

where,

$$\widehat{D}(q,\dot{q},\zeta) = [D\dot{q}] \tag{14}$$

$$\hat{G}(q,\zeta) = \left[\frac{G}{q}\right] \quad \widehat{sgn}(\dot{q}) = \left[\frac{sgn(\dot{q})}{q}\right] \tag{15}$$

The derivative of the torque with respect to time for 1 DOF rehabilitation robot with human arm from Eq. (13) can be written as

$$\dot{T}(t) = M(q,\zeta)\ddot{q}(t) + \tilde{C}(q,\dot{q},\zeta)\ddot{q}(t) + \widetilde{D}(q,\dot{q},\zeta)\dot{q}(t) + F_c[sgn(\dot{q})\dot{q}(t)] + F_c q\frac{d}{dt}(sgn(\dot{q})) + V_c\ddot{q}(t) \tag{16}$$

By substituting Eq. (13) and Eq. (16) into the augmented actuator dynamic Eq. (1), the integrated dynamic model of a 1-DOF rehabilitation robot with human arm can be obtained in the following form. Only one joint of rehabilitation robot is considered in this study, which is the elbow for flexion and extension. The robot and human arm are considered as lumped body. The dynamic model is taken from [20] and can be written as:

$$\dot{X}_B(t) = A_B(X_B,\zeta,t)X_B(t) + B_B(X_B,\zeta,t)U(t) \tag{17}$$

where,

$$A_B(X_B,\zeta,t) = [I_3N - W_BM(X_B,\zeta,t)Z_B]^{-1}\{A_B + [F_BM(X_B,\zeta,t) + W_B\tilde{C}(X_B,\zeta,t) + W_BV_C]Z_B + [F_B\widehat{D}(X_B,\zeta,t) + F_BV_C(X_B,\zeta,t) + W_B\widetilde{D}(X_B,\zeta,t) + W_BF_C\widehat{sgn}(\dot{q}) +$$

$$W_B\hat{d}(t)]Z_{B1} + [F_B\hat{G}(X_B,\zeta,t) + F_BF_C\, sgn(\dot{q}) + F_B\hat{d}(t) + W_B\dot{\hat{d}}(t) + W_BF_C\left[\frac{d}{dt}((\dot{q}))\right]Z_{B2}\} \quad (18)$$

$$B_B(X_B,\zeta,t) = [I_3N - W_BM(X_B,\zeta,t)Z_B]^{-1}B_B \quad (19)$$

Then, the integrated model of the 1-DOF robot manipulator can be obtained and has the following form:

$$`\dot{X}_B(t) = A(X_B,\zeta,t)X_B(t) + B(X_B,\zeta,t)U(t) \quad (20)$$

where,

$$A_B(X_B,\zeta,t) = \begin{bmatrix} 0 & 1 & 0 \\ 0 & 0 & 1 \\ a_{B31} & a_{B32} & a_{B33} \end{bmatrix} \quad (21)$$

$$B(X_B,\zeta,t) = [b] \quad (22)$$

A detailed explanation of the dynamic model of the rehabilitation robot exoskeleton with human arm can be found in [20] , which will serve as a guide for the derivation of the integrated model of the 1 DOF robot arm.

3.2. Motion Intention Controller

For the motion intention controller, the impedance control is adopted [21]. Impedance control is defined as the relationship between the motion state of the endpoint and applied force. The relationship between the therapist's torque, τ_h, contact force, F_{ext} and transpose form of the Jacobian vector of the exoskeleton is given as [22].

$$\tau_h = J^TF_{ext} \quad (23)$$

The target impedance adopted from [22] is given as a second-order differential equation and can be written as

$$M(\ddot{X} - \ddot{X}_d) + B(\dot{X} - \dot{X}_d) + K(X - X_d) = -F_{ext} \quad (24)$$

For this research, only one degree of freedom is used. To overcome some practical challenges in impedance control, F_g is the extra gravity compensated force is considered [23]. Eq. (24) is modified as.

$$M(\ddot{X} - \ddot{X}_d) + B(\dot{X} - \dot{X}_d) + K(X - X_d) = -F_{ext} - F_g \quad (25)$$

$M(\ddot{X} - \ddot{X}_d)$ is omitted for simplicity. Therefore, Eq. (25) can be written as.

$$B(\dot{X} - \dot{X}_d) + K(X - X_d) = -F_{ext} - F_g \quad (26)$$

where,
M is the moment of inertia
$\ddot{X}$ is the actual acceleration
$\ddot{X}_d$ is the desired acceleration
$\dot{X}$ is the actual velocity
$\dot{X}_d$ is the desired velocity
X is the actual position
X_d is the desired position
B is the damping coefficient
K is the stiffness
F_g is the extra gravity compensated force.

A relationship between the target speed and the interaction torque of each joint is necessary to obtain the motion intention estimation [24]. Thus, the angular velocity needs to be converted to the velocity of the endpoint of the robotic arm by using the Jacobian matrix [24]. Hence, Eq. (26) is multiplied by the Jacobian matrix, J^T

$$J^T B(\dot{X} - \dot{X}_d) + J^T K(X - X_d) = -J^T F_{ext} - J^T F_g \tag{27}$$

Substituting Eq. (23). into Eq. (27) yields.

$$J^T B(\dot{X} - \dot{X}_d) + J^T K(X - X_d) = -\tau_h - J^T F_g \tag{28}$$

Expand and simplify Eq. (28) will result in.

$$J^T B\dot{X} - J^T B\dot{X}_d + J^T K(X - X_d) = -\tau_h - J^T F_g \tag{29}$$

$$J^T B\dot{X}_d = \tau_h + J^T F_g + J^T K(X - X_d) + J^T B\dot{X} \tag{30}$$

Substituting $\dot{X}_d = J\dot{q}_d$ [23] into Eq. (30) to obtain the velocity of the endpoint, gives.

$$J^T BJ\dot{q}_d = \tau_h + J^T F_g + J^T K(X - X_d) + J^T B\dot{X} \tag{31}$$

Eq. (31) is simplified to derive the equation for the motion intention estimator

$$\dot{q}_d = \frac{\tau_h + J^T F_g + J^T [B\dot{X} + K(X - X_d)]}{B\, J^T J} \tag{32}$$

where,
τ_h is the interaction torque from the therapist
J is the Jacobian matrix

$$J = \begin{bmatrix} -l\sin q \\ l\cos q \\ l \end{bmatrix} \tag{33}$$

According to the equation, each joint's intended velocity will change throughout active training sessions as the interaction torques from the associated joint change. Contact torques, departure from the endpoint's reference trajectory, and the damping impedance coefficient B, all have an impact on the rate of current changes. The desired velocity of each joint modifies when the endpoint position deviates from the prescript trajectory, bringing the subject back to the reference trajectory, indicating $X_d \neq X$. The adjustment range is determined by the stiffness and damping impedance coefficients $K$and B [24]. The interaction controller outputs the required joint velocity $\dot{q}_d$, which the SMC-FAT adaptive controller will use. Fig.3 shows the block diagram for the motion intention controller.

3.3.SMC-FAT-based Adaptive Controller

The motion intention estimator is integrated into the SMC-FAT based adaptive controller to get the desired motion and cater to the uncertainties in the lumped robot and human arm plant. The SMC-FAT controller equation used in the proposed control law for the feedback loop is written as [25].

$$X_a = [q \quad \dot{q} \quad \ddot{q}]^T \tag{34}$$

$$X_{da} = [q_d \quad \dot{q}_d \quad \ddot{q}_d]^T \tag{35}$$

$$U_s(t) = U_{eq} + U_{PI} + U_a \tag{36}$$

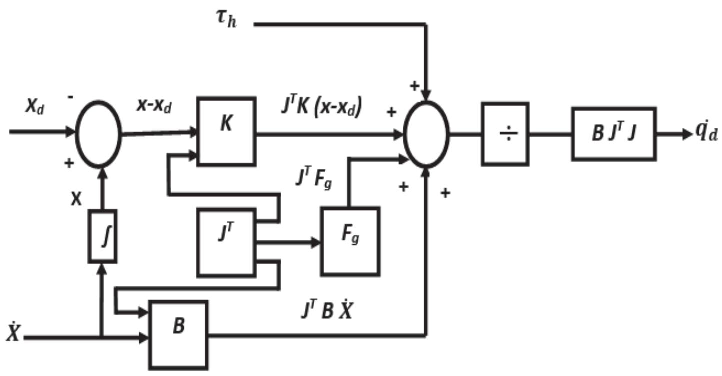

Fig. 3. Block diagram of motion intention estimator

The measured (actual trajectory) and desired (desired trajectory) state variables can be represented by vectors X_a and X_{da} respectively.
where, U_s , U_{eq} , U_{PI} and U_a terms of the proposed controller are described below. The U_s is the control signal supplied to the plant. The equivalent control term U_{eq} is considered for the approximately known nominal system [25].

$$U_{eq} = \bar{B_B}^{-1}(\dot{X}_r - \bar{A_B}X_a) \tag{37}$$

where, $\bar{A_B}$ and $\bar{B_B}$ represent the nominal matrices of A_B and $B_B$respectively.
X_a is the actual trajectory
$\dot{X}_r$ is the reference acceleration and it is denoted by the term $\dot{X}_{da} - \frac{\lambda_2{}^2 e}{2\lambda_1}$

The second term of the control strategy U_{PI} is a sort of PI (Proportional Integral) controller that is required to increase closed-loop stability and transient performance.

$$U_{PI} = -\bar{B_B}^{-1}K_1S(t) = -\bar{B_B}^{-1}K_1(2\lambda_1 e + \lambda_2{}^2 \int edt) \tag{38}$$

where, K_1 is a positive definite constant and $S(t)$ is the sliding surface of the controller
λ_1 and λ_2 are $n \times n$ diagonal positive definite matrix
$e = X_a - X_{da}$ is the tracking error vector
The term U_a is the term used to describe the process of removing approximation errors.

$$U_a = -\bar{B_B}^{-1}K_0\hat{\alpha}_0[sgn(S(t))] \tag{39}$$

where, K_0 is a constant, $\hat{\alpha}_0$is the estimation of α_0, and the upper bound of the uncertainties.

Substituting Eq. (37), Eq. (38), and Eq. (39), into Eq. (36), as shown below.

$$U_s(t) = \bar{B_B}^{-1}(\dot{X}_r - \bar{A}X_a - K_1S - K_0\hat{\alpha}_0[sgn(S(t))]) \tag{40}$$

A detailed explanation of the derivation and stability proof of the controller can be found in [25].

3.4.Simulation Results

The simulation was carried out using different values of the constant and sinusoidal waveform for the torque exerted by the therapist. This research focuses on a 1 DOF upper limb rehabilitation arm, therefore only one motor is used in the verification experiment. The motion intention estimator based on impedance control as in Section 3.2, is adopted for the motion intention controller. The impedance parameters of the motion intention controller are set as $K = 0.34$ N/m and $B = 50Ns$/m. The extra gravity compensated force is set at $F_g = [0; 0; 0]$

https://doi.org/10.31436/iiumej.v24i1.2604

N initially. The SMC-FAT controller parameters are set as $\lambda_1 = 50$, $\lambda_2 = 1$, $K_0 = 1$ and $K_1 = 337$.

Fig. 4 and 5 shows the tracking performance of the motion intention controller using a constant torque and sinusoidal waveform respectively. The range of the constant torque was calculated using the formula in Eq. (41) and the sinusoidal formula to represent the torque from the therapist is shown in Eq. (42).

$$\tau_h = F \times r \tag{41}$$

$$\tau_h = \mathrm{A}\sin(t) + \emptyset \tag{42}$$

In Fig.4 the red line shows the actual angular velocity and the dash blue line represents the desired angular velocity. It can be seen that the actual angular velocity follows the desired angular velocity that is calculated using the therapist's motion intention estimation based on his/her input torque τ_h. This result shows that the proposed control strategy has successfully calculated the therapist's motion intention and the robot follows the prescribed velocity trajectory under the SMC-FAT based adaptive controller.

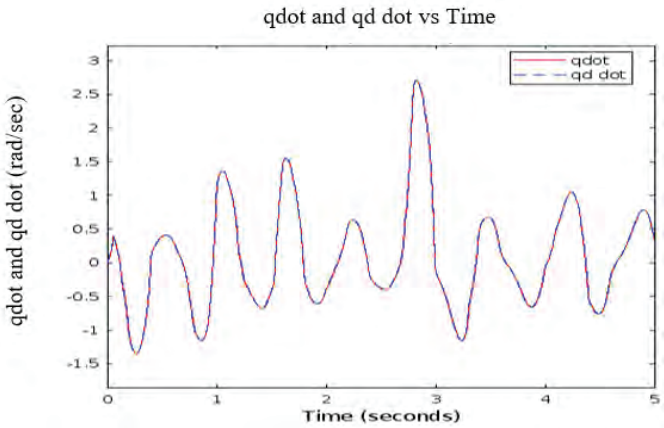

Fig.4. Tracking performance of the proposed control strategy at constant τ_h

Fig. 5 shows the tracking performance of the motion intention estimator using the sinusoidal equation, $\tau_h = \sin(2) + 11.76\ Nm$ to represent variation in the torque exerted by the therapist. It can be seen in Fig. 5 below that the actual angular velocity follows the desired angular velocity resulting from the motion intention estimator, under the proposed control law strategy.

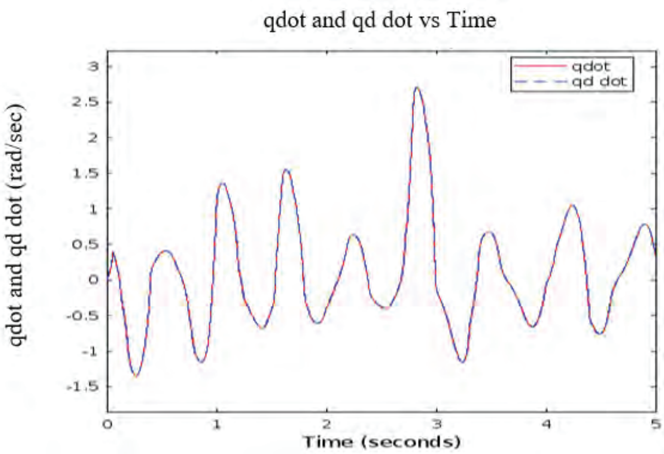

Fig.5. Tracking performance of the proposed control strategy at sinusoidal torque

From the simulation results, it can be observed that the proposed controller is effective. The motion intention estimator produces the desired velocity based on the therapist's torque. This

https://doi.org/10.31436/iiumej.v24i1.2604

value was fed into the SMC-FAT controller and the robot follows the desired trajectory precisely. The average percentage error at sample time of 5 seconds is 0.002rad/sec and 0.005rad/sec for constant and sinusoidal therapist‘s torque respectively.

4. SIMULATION RESULTS AND EXPERIMENTAL ANALYSIS

The simulation of the motion controller has been conducted using MATLAB Simulink for different inputs of torque and the experimental analysis is done with the aid of LabVIEW from National Instruments (NI).

4.1.Experimental Results

The experimental setup consists of 1 DOF robot arm and computer installed with LabVIEW to control the robot arm with the proposed motion intention estimator. LabVIEW is used to test and analyze the proposed motion intention controller on the robot arm. The National Instruments Data Acquisition (NI DAQmx) driver has been installed along with LabVIEW into the computer to aid the communication between the robot and the computer. The computer that is installed with LabVIEW is connected to the robot using the NI USB-6211 DAQ. The schematic diagram of the control strategy and motion intention estimator has been built in LabVIEW and run to check for errors. After the schematic has been verified, the robot is powered on, and the LabVIEW programming is launched. The robot motor torque, robot position, actual angular velocity, and desired angular velocity are displayed on the interface of the LabVIEW on the computer.

The motion intention controller impedance parameters are set as $K = 0.34$ N/m and $B = 50Ns$/m. The gravity force is set at $F_g = [0; 0; 0]$ N at first. The SMC-FAT controller parameters are set as $\lambda_1 = 50$, $\lambda_2 = 1$, $K_0 = 1$ and $K_1 = 337$. The experimental result of the robot's joint angular velocity is shown in Fig. 6.

Fig. 6 shows the desired angular velocity trajectory based on the therapist's motion intention estimation, $\dot{q}_d$ and the actual angular velocity $\dot{q}$, under the control of the SMC-FAT controller.

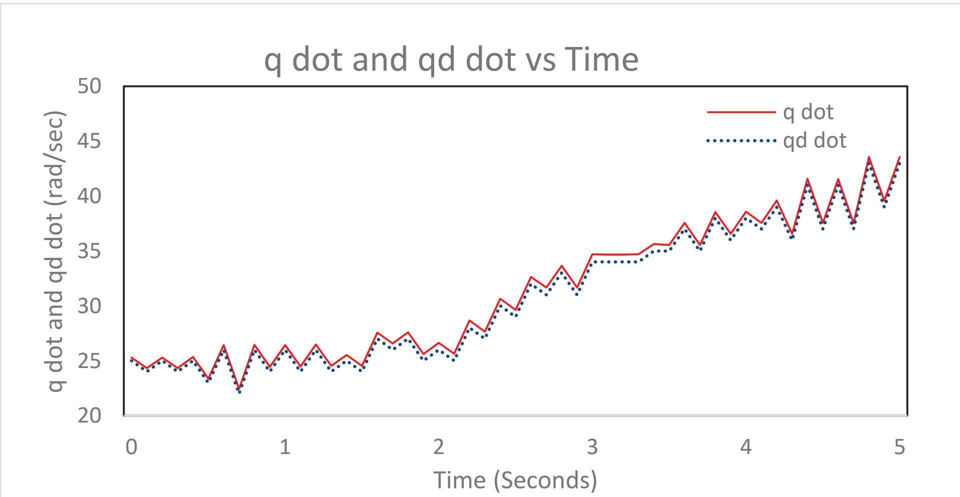

Fig.6. Experimental result of actual angular velocity and desired angular velocity against time using human torque

Fig.7 shows the corresponding therapist's torque during the experiment. The result shows that the controller produces the estimated motion intention based on the torque exerted by the therapist and drives the robot to track the resulting desired trajectory.

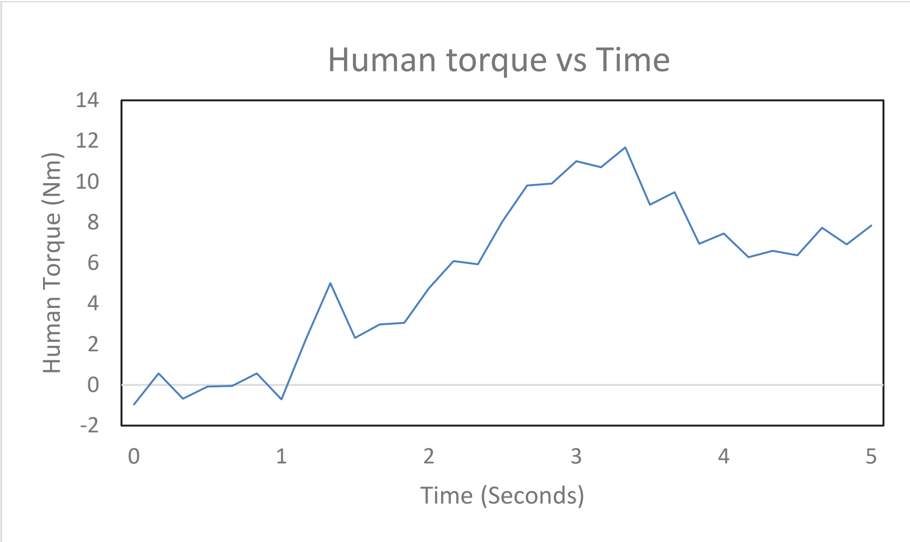

Fig.7. Therapist's torque input in hardware experimental test

From the simulation results and hardware experiment, it can be observed that the proposed controller is effective in generating the desired angular velocity, $\dot{q}_d$ based on the motion intention of the therapist and controlling the upper limb rehabilitation robot to follow the desired trajectory. The results verify that the proposed control strategy is successful. The therapist's motion intention can be predicted for the upper limb rehabilitation robot based on the torque exerted by the therapist under the proposed technique. The SMC-FAT - based adaptive controller integrated into the motion intention estimator can overcome the uncertainties in the robot and human arm parameters. The maximum error is 0.02rad for the hardware experiments.

5. CONCLUSION

A new control method has been formulated for therapists' motion intention estimation in a power assist upper limb rehabilitation robot based on impedance controller. The controller uses the therapist's interaction torque to estimate his/her motion intention and produces the desired angular velocity for the feedback controller. The SMC-FAT adaptive controller implemented in the feedback loop overcomes the uncertainties, in the lumped rehabilitation robot and human arm plant. Integrating the formulated motion intention estimator and SMC-FAT Adaptive control yields high tracking accuracy with the therapist's motion intention. The simulation results and hardware experiment validated that the proposed control strategy is successful in producing the motion intention estimation and accurate trajectory tracking with a maximum error of 0.005 rad/sec and 0.02 rad/sec respectively. In future work, the integrated motion intention controller and SMC-FAT controller can be used for a higher DOF of the upper limb rehabilitation robot arm system. Other types of uncertainties can also be considered in future studies.

ACKNOWLEDGEMENT

The authors would like to thank International Islamic University Malaysia (IIUM) for sponsoring this study under grant number P-RIGS 18-019-0019.

REFERENCES

[1] Eiammanussakul, T., and Sangveraphunsiri, V. (2018). A lower limb rehabilitation robot in sitting position with a review of training activities. Journal of Healthcare Engineering, 2018, 1–18.
[2] Bogue, R. (2018). Rehabilitation robots. Industrial Robot, 45(3), 301–306.
[3] Alrabghi, L., Alnemari,R., Aloteebi, R., Alshammari, H., Ayyad, M., Al Ibrahim,M., Alotayfi, M., Bugshan, T., Alfaifi, A., and Aljuwayd, H. (2018). Stroke types and management. International Journal Of Community Medicine And Public Health, 5(9), 3715.
[4] Tang, Z., Zhang, K., Sun, S., Gao, Z., Zhang, L., and Yang, Z. (2014). An upper-limb power-assist exoskeleton using proportional myoelectric control. Sensors (Switzerland), 14(4), 6677–6694.
[5] Kadota, K., Akai, M., Kawashima, K., and Kagawa, T. (2009). Development of power-assist robot arm using pneumatic rubber muscles with a balloon sensor. Proceedings - IEEE International Workshop on Robot and Human Interactive Communication, 546–551.
[6] Liu, Z., and Hao, J. (2019). Intention Recognition in Physical Human-Robot Interaction Based on Radial Basis Function Neural Network. Journal of Robotics, 2019, 1–8.
[7] Lee, J., Kim, M., Ko, H., and Kim, K. (2014). A control method of power-assisted robot for upper limb considering intention-based motion by using sEMG signal. 2014 11th International Conference on Ubiquitous Robots and Ambient Intelligence, URAI 2014, 385–390.
[8] Huang, J., Huo, W., Xu, W., Mohammed, S., and Amirat, Y. (2015). Control of Upper-Limb Power-Assist Exoskeleton Using a Human-Robot Interface Based on Motion Intention Recognition. IEEE Transactions on Automation Science and Engineering, 12(4), 1257–1270.
[9] Li, M., Deng, J., Zha, F., Qiu, S., and Wang, X. (2018). Motion Intention Estimation for Active Power-Assist Lower Limb Exoskeleton Robot (APAL). Preprints, 1–20.
[10] Chathuramali, K. G. M., and Kiguchi, K. (2020). Real-time detection of the interaction between an upper-limb power-assist robot user and another person for perception-assist. Cognitive Systems Research, 61, 53–63.
[11] Struk, S., Correia, N., Guenane, Y., Revol, M., and Cristofari, S. (2018). Full-thickness skin grafts for lower leg defects coverage: Interest of postoperative immobilization. Annales de Chirurgie Plastique Esthetique, 63(3), 229–233.
[12] Wang, X., Li, X., and Wang, J. (2015). Modeling and identification of the human-exoskeleton interaction dynamics for upper limb rehabilitation. Lecture Notes in Electrical Engineering, 338, 51–60.
[13] Lee, J., Kim, M., and Kim, K. (2017). A control scheme to minimize muscle energy for power assistant robotic systems under unknown external perturbation. IEEE Transactions on Neural Systems and Rehabilitation Engineering, 25(12), 2313–2327.
[14] Nomura, S., Takahashi, Y., Sahashi, K., Murai, S., Taniai, Y., and Naniwa, T. (2019). Power assist control based on human motion estimation using motion sensors for powered exoskeleton without binding legs. Applied Sciences (Switzerland), 9(1), 14–16.
[15] Zhuang, Y., Yao, S., Ma, C., and Song, R. (2019). Admittance Control Based on EMG-Driven Musculoskeletal Model Improves the Human-Robot Synchronization. IEEE Transactions on Industrial Informatics, 15(2), 1211–1218.
[16] Wang, W., Zhang, J., Kong, D., Su, S., Yuan, X., & Zhao, C. (2022). Research on control method of upper limb exoskeleton based on mixed perception model. Robotica, 1–17.
[17] Wang, W., Qin, L., Yuan, X., Ming, X., Sun, T., and Liu, Y. (2019). Bionic control of exoskeleton robot based on motion intention for rehabilitation training. Advanced Robotics, 33(12), 590–601.
[18] Yang, C., Chen, C., He, W., Cui, R., and Li, Z. (2019). Robot Learning System Based on Adaptive Neural Control and Dynamic Movement Primitives. IEEE Transactions on Neural Networks and Learning Systems, 30(3), 777–787.
[19] Shanta, M. N. T., and Azlan, N. Z. (2015). Function Approximation Technique based Sliding Mode Controller Adaptive Control of Robotic Arm with Time-Varying Uncertainties. Procedia Computer Science, 76, 87–94.

https://doi.org/10.31436/iiumej.v24i1.2604

[20] Osman, J. (1990). Modeling and control of robot manipulators. Dissertation, City University London.https://openaccess.city.ac.uk/id/eprint/7758/1/Decentralized_and_hierarchical_control_of_robot_manipulators.pdf

[21] Adeola-Bello, Z., & Azlan, N. (2022). Power Assist Rehabilitation Robot and Motion Intention Estimation. International Journal of Robotics and Control Systems, 2(2), 297-316.

[22] Song, P., Yu, Y., and Zhang, X. (2019). A Tutorial Survey and Comparison of Impedance Control on Robotic Manipulation. Robotica, 37(5), 801-836.

[23] Xing, L., Wang, X., and Wang, J. (2017). A motion intention-based upper limb rehabilitation training system to stimulate motor nerve through virtual reality. International Journal of Advanced Robotic Systems, 14(6), 1–8.

[24] Topini, A., Sansom, W., Secciani, N., Bartalucci, L., Ridolfi, A., andAllotta, B. (2022). Variable Admittance Control of a Hand Exoskeleton for Virtual Reality-Based Rehabilitation Tasks. Frontiers in neurorobotics, 15, 789743.

[25] Shanta, M. N. T., and Azlan, N. Z. (2016). Adaptive sliding mode control with radial basis function neural network for time dependent disturbances and uncertainties. ARPN Journal of Engineering and Applied Sciences, 11(6), 4123–4129.

https://doi.org/10.31436/iiumej.v24i1.2577

NON-VERBAL HUMAN-ROBOT INTERACTION USING NEURAL NETWORK FOR THE APPLICATION OF SERVICE ROBOT

Zubair Adil Soomro[1], Abu Ubaidah bin Shamsudin[1*], Ruzairi bin Abdul Rahim[1], Andi Adriansyah[2], Mohd Hazeli[3]

[1] *Department of Electronic Engineering, Faculty of Electrical and Electronic Engineering, Universiti Tun Hussein Onn Malaysia, Batu Pahat, Malaysia*
[2] *Universitas Mercu Buana, Jakarta, Indonesia*
[3] *Move Robotic SDN BHD*

**Corresponding author: ubaidah@uthm.edu.my*

(Received: 22nd August 2022; Accepted: 4th December 2022; Published on-line: 4th january 2023)

ABSTRACT: Service robots are prevailing in many industries to assist humans in conducting repetitive tasks, which require a natural interaction called Human Robot Interaction (HRI). In particular, nonverbal HRI plays an important role in social interactions, which highlights the need to accurately detect the subject's attention by evaluating the programmed cues. In this paper, a conceptual attentiveness model algorithm called Attentive Recognition Model (ARM) is proposed to recognize a person’s attentiveness, which improves the accuracy of detection and subjective experience during nonverbal HRI using three combined detection models: face tracking, iris tracking and eye blinking. The face tracking model was trained using a Long Short-Term Memory (LSTM) neural network, which is based on deep learning. Meanwhile, the iris tracking and eye blinking use a mathematical model. The eye blinking model uses a random face landmark point to calculate the Eye Aspect Ratio (EAR), which is much more reliable compared to the prior method, which could detect a person blinking at a further distance even if the person was not blinking. The conducted experiments for face and iris tracking were able to detect direction up to 2 meters. Meanwhile, the tested eye blinking model gave an accuracy of 83.33% at up to 2 meters. The overall attentive accuracy of ARM was up to 85.7%. The experiments showed that the service robot was able to understand the programmed cues and hence perform certain tasks, such as approaching the interested person.

ABSTRAK: Robot perkhidmatan lazim dalam banyak industri untuk membantu manusia menjalankan tugas berulang, yang memerlukan interaksi semula jadi yang dipanggil Interaksi Robot Manusia (HRI). Khususnya, HRI bukan lisan memainkan peranan penting dalam interaksi sosial, yang menonjolkan keperluan untuk mengesan perhatian subjek dengan tepat dengan menilai isyarat yang diprogramkan. Dalam makalah ini, algoritma model perhatian konseptual yang dipanggil Model Pengecaman Perhatian (ARM) dicadangkan untuk mengenali perhatian seseorang, yang meningkatkan ketepatan pengesanan dan pengalaman subjektif semasa HRI bukan lisan menggunakan tiga model pengesanan gabungan: pengesanan muka, pengesanan iris dan mata berkedip. . Model penjejakan muka telah dilatih menggunakan rangkaian saraf Memori Jangka Pendek Panjang (LSTM), yang berdasarkan pembelajaran mendalam. Manakala, pengesanan iris dan mata berkelip menggunakan model matematik. Model mata berkelip menggunakan titik mercu tanda muka rawak untuk mengira Nisbah Aspek Mata (EAR), yang jauh lebih dipercayai berbanding kaedah sebelumnya, yang boleh mengesan seseorang berkelip pada jarak yang lebih jauh walaupun orang itu tidak berkelip. Eksperimen yang dijalankan untuk pengesanan muka dan iris dapat mengesan arah sehingga 2 meter. Sementara itu, model berkelip mata yang diuji memberikan ketepatan

83.33% sehingga 2 meter. Ketepatan perhatian keseluruhan ARM adalah sehingga 85.7%. Eksperimen menunjukkan bahawa robot perkhidmatan dapat memahami isyarat yang diprogramkan dan seterusnya melaksanakan tugas tertentu, seperti mendekati orang yang berminat.

KEYWORDS: *Attentive Recognition Model (ARM), Long-Short-Term Memory (LSTM), Human Robot Interaction (HRI), Eye Aspect Ratio (EAR)*

1 INTRODUCTION

As service robots are starting to coexist with humans, they ought to deal with two fundamental aspects: sturdy navigation in cluttered environments [1, 2] and effective human-robotic interaction (HRI). There have been many research conducted in navigation area whereas, a significant amount of problems in HRI field need to be addressed. Therefore, there are two primary forms of communication in robotics for establishing an accurate interaction between a robot and a human being within physical and psychological contexts. Human verbal interaction is expressed using thoughts, ideas, and feelings through spoken or written language. Meanwhile, in kinesics, nonverbal communication is defined through body movements, positioning, facial expressions, and gestures [17]. In particular, this research is based on head movement and oculesics, a subcategory of kinesics, which is the study of eye movement, behaviour, gaze, and eye-related nonverbal communication. An important perceptual variable in the analysis of nonverbal cues is the focus of attention, which indicates the person is attending to something and is often used to convey interpersonal intent. It often happens that people turn toward their focus of attention, thereby physically expressing their attention by means of head orientation. In most cases, head orientation is directly related to the visual gaze estimate since the perceived gaze direction is determined by the orientation of the head. Inspired by this human behaviour, an Attentive Recognition Model (ARM) is proposed that corresponds to social cues, namely, face tracking, iris tracking and eye blinking, characterised by effective non-verbal human interaction.

In the prior method for attentiveness architecture, body components were represented as cylindrical shapes using the Top View Re-projection (TVR) concept [3]. The hypothesis with the highest score provides the presumed pose and the location of the joints after the pose has been measured against a scoring system. Meanwhile, another method uses mutual gaze [4] as a social cue by making iCub capable of recognizing eye contact events while interacting online with a human partner. Other than that, Hand Gesture Recognition in [5] was also considered one of the non-verbal cues used to get the attention of a robot. The methods in the literature are limited to the use of stationary robots and are not considered to be a combined model of different cues. Therefore, this paper will focus on the face tracking, iris tracking and eye blinking cues, which are mainly important because they develop social awareness. Furthermore, both portrayals of robots and embodied robots activate social cognitive mechanisms that rely on interpreting others' gaze direction, such as gaze cueing. The significance of a glance in a particular direction can only be completely understood if the gaze's objective and the agent's mental state are known in relation to that target [6]. Author in [7] presented a study on social cues being taking into account to enable the robot by deciding socially, at which human it should direct its gaze.

The author in [8] used a performance improved eye tracking system for a more efficient human-robot collaboration than a comparable head tracking approach. Paper [9] introduced an approach for accurate and robust eye center localization by using image gradients. This method yields low computational complexity and is invariant to rotation and linear changes in illumination. It was also tested in [10], where a Partially-Observable Markov Decision Process (POMDP) was proposed to plan the navigation in the dynamic (crowded) environment by using sensor fusion and filtering techniques.

In addition, the previous method in [11] for the eye blinking model used vertical and horizontal lines to calculate blinking ratio, which limited its capability to detect blinks at a further distance. Moreover, it was also added to help the robot show more realistic eye gazes. Nevertheless, the overall accuracy of the system is not precise enough for different light intensity environments for altogether algorithms.

On the other hand, the previous method in [12, 13] for the face tracking model uses Support Vector Machine (SVM) and Constrained Local Models (CLM) to train the data, respectively. Although the former option provides enough precision in gaze detection, the latter avoids any tedious calibration procedure and makes it possible to interact with people with no prior preparation. Thus, a new Long Short-Term Memory (LSTM) neural network was considered to train the 468 extracted keypoints from the face. This network is an extension of RNN, designed to avoid the long-term dependency issue. It can also remember data for long periods. This happens as it allows back-propagation through time by connecting events that appear far apart in the input data without their weight being diluted between the forget gate, input gate and output layers.

The main objectives of this work are as mentioned below:

- To propose an attentive gaze algorithm by fusing iris, face tracking and eye blinking data.
- To develop face tracking model using LSTM neural network.
- To optimize previous eye blinking model using a new variable
- To validate the feasibility of the method in real world for service robot.

2 PROPOSED ARM METHOD

The service robots in a café operate in close proximity with humans, which raises social behavioural skills typical of human–human interactions, which is still a challenge [4]. This research proposes an attentive gaze algorithm by estimating the face direction, iris direction and eye blinking as a fundamental social cue in face-to-face interactions. These models were integrated into the service robot to maximize its capability to recognize the stare of a person, which potentially gives it an advantage in communicating by reducing false negative errors. The data of trained LSTM keypoints in 4.4 were used to detect the possibility of the face posing classification. Based on the face detected in a person, the iris and eye blinking models were implemented. The ARM algorithm was tested in 4.5 by facing straight at the camera. When the face was facing away from the camera, the algorithm was not able to detect the attentiveness from the person, hence there was no response from the system. When a person showed some cues, such as facing straight at the camera with direct eye contact by aligning the iris position and no eye blinking, the system gave a response of '!!ATTENTIVE!!' as shown in Fig 1. The experimentation for face, iris tracking and eye blinking was conducted in Sections 4.2, 4.3 and 4.4, respectively. This shows that the attentive gaze algorithm can be used to gain a person's interest. This combined model was important as it could execute all of the important cues altogether without having multiple files.

https://doi.org/10.31436/iiumej.v24i1.2577

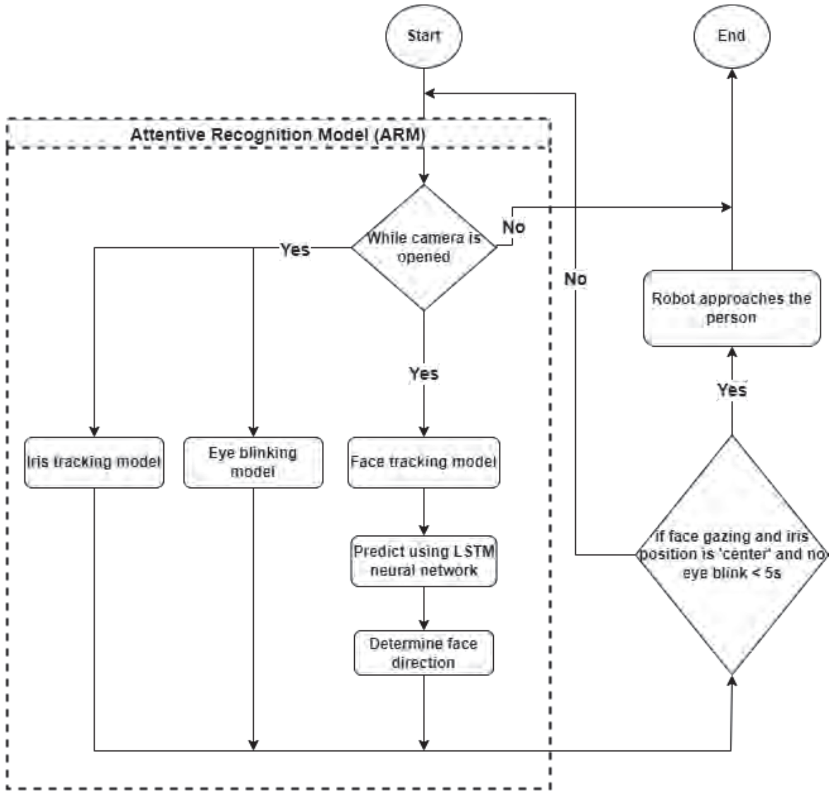

Fig. 1: Overall flowchart of ARM

3 METHODOLOGY

3.1 Data collection

A participant was recruited for data collection (age = 23) for a face tracking model using a Lenovo S410p laptop camera. A total of 20 number of frames were extracted from the 20 raw video sequences for each of the action namely right, left and center. The data collection was conducted at the Universiti Tun Hussein Onn Malaysia.

Fig. 2. Human interaction with robot

3.2 Environment setup

Hussein, a service robot developed by the UTHM RoboCup team, was used in this experiment as shown in Fig. 2. It was located in the middle of the room and was surrounded by chairs and tables to look like a café environment. A Logitech C920 high-definition (HD) webcam was used for tracking, which provides a clear image up to 3 meters away. It was mounted on the robot at a height of 130 cm from the ground to detect different heights of a person's face. The developed software modules were integrated within the ROS environment, which was needed to initiate the robot's navigation system.

3.3 Task

A total of 7 participants (mean age = 22.5) were chosen to test the ARM algorithm. They were asked to sit in front of the robot at a distance of around 2 meters and establish mutual gaze.

3.4 Measurement

The measurements of this experiment have been separated into two categories:

1. Testing of each models in indoor and outdoor environment
2. Accuracy of ARM detection

3.5 Face tracking

For the active eye contact recognition, the face location is tracked. For this purpose, state-of-the-art real-time face mesh approach was utilized from Google Research, which is implemented in MediaPipe-framework. This approach differs from [15] by using machine learning to infer 3D surface geometry that estimates 468 3D face landmarks in real-time from a single frame and facilitates fast and robust requiring only a single camera input and no separate depth sensor as shown in Fig 3. It is able to utilize lightweight model designs and CPU acceleration across the pipeline to achieve real-time performance, which is crucial for live experiences [16]. This ML pipeline operates on the captured video using OpenCv library and computes face positions and a 3D face landmark model that uses those locations to predict the approximate surface geometry via regression. This also have advantage of greatly reducing the requirement for typical data augmentations such as affine transformations, which include rotations, translations, and scale modifications.

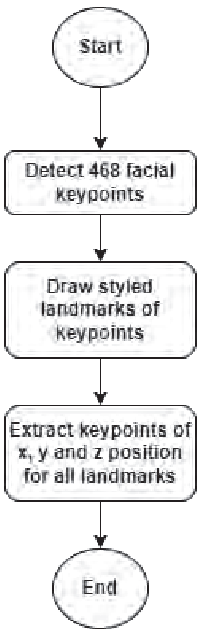

Figure 3: Flowchart for face tracking model

Theoretically, the line linking the eye centres with the rectangle's horizontal axis is aligned by rotating a facial rectangle using the bounding rectangles produced by the camera's frame. To create the input for the mesh prediction neural network, this is then clipped and resized. A vector of 3D landmark coordinates can then be generated by the model and mapped back into the original image's coordinate system. The facial rectangles of a real-world frame were covered using a 3D Morphable Model (3DMM) technique, and the ground truth vertex coordinates are now readily available thanks to a previously established relationship between the 468 mesh points and a subset of 3DMM vertices.

This mesh model pays special attention to semantically significant face regions, resulting in more accurate landmark predictions around the mouth, eyes, and irises at the cost of average computation as it resulted in 4.2. The start of algorithm for the face tracking process was detected for specified class and gathering landmarks keypoints. Those keypoints were saved in their respective classes such as 'center', 'left' and 'right'.

3.6 Iris tracking

Meanwhile it was known that the horizontal iris diameter of the human eye is fairly constant throughout the population at 11.7±0.5 mm [17]. Due to restricted processing resources, fluctuating lighting conditions, and the presence of occlusions, such as people squinting, it was a difficult assignment to complete. Moreover iris tracking had 10 additional iris landmark which gave accurate estimation for features affecting the iris, pupil, and eye contours in real time using just a single RGB camera and no specialist hardware [18]. It was also able to utilize for determining the metric distance of the camera to the user with relative error less than 10%. Fig. 4 displays a face mesh containing over 468 main keypoints which is represented by the dots (junction between lines).

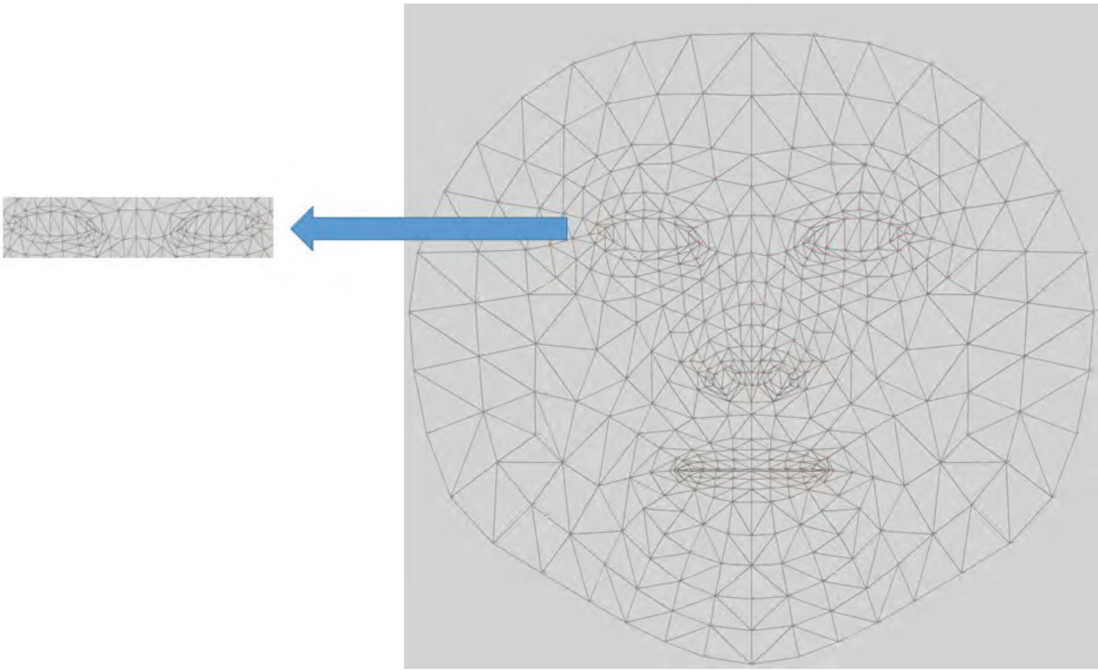

Fig. 4. Eyes landmarks with marked numbers

This was achieved by using the Euclidean distance formula as shown in equation 2.1 where each point reflects the mesh points with notations and corresponding descriptions in Table 1:

$$euclidean\ distance = \sqrt[2]{(x2 - x1)^2 + (y2 - y1)^2} \quad (2.1)$$

Table 1: Notations and corresponding descriptions

Symbol	Description
x1	x-coordinate of point1
y1	y-coordinate of point1
x2	x-coordinate of point2
y2	y-coordinate of point2

The iris model predicts both eye landmarks (along the eyelid) and iris landmarks (along the iris contour) from an image patch of the eye region. An array of mesh points such as 33, 133, 362 and 263 were generated for x and y coordinates of eyes which was based on the frame size of image captured by the camera as shown in Fig 5. These mesh points then provided the position for left and right eyes for x and y position coordinates respectively to extract the radius and center as resulted in 4.3.

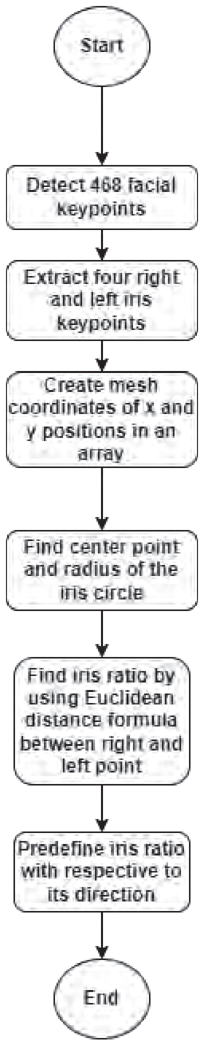

Fig. 5: Flowchart for iris tracking model

3.7 Eye blinking

Although blinking may appear to be an unconscious habit, new research by Paul Hömke and colleagues reveals that when humans are conversing, they unconsciously receive eye blinks as nonverbal indicators [14]. Furthermore, research have revealed that blinks frequently occur during natural pauses in discourse. Hömke wondered if, like nodding one's head, a movement as little and subconscious as blinking may work as verbal feedback. Speakers were able to detect a minor difference between short and long blinks, with longer blinks prompting significantly shorter responses from volunteers. More broadly, the discovery may help us understand the origins of how humans communicate their mental states, which has evolved into an important component of everyday social interactions. In this algorithm, a different approach have been used to calculate for eye blinking.

The right and left eyes coordinates were used to find vertical ratio of right and left eye respectively as shown in Fig. 6. As to differentiate this method with previous ways, it was by using the random coordinate landmarks which was in the nose area to get overall ratio. The vertical distance between those coordinates was calculated using the Euclidean distance formula. The calculated blink ratio was utilized by comparing it with a threshold of 0.7 which was determined by using trial and error method as experimented in 4.4.

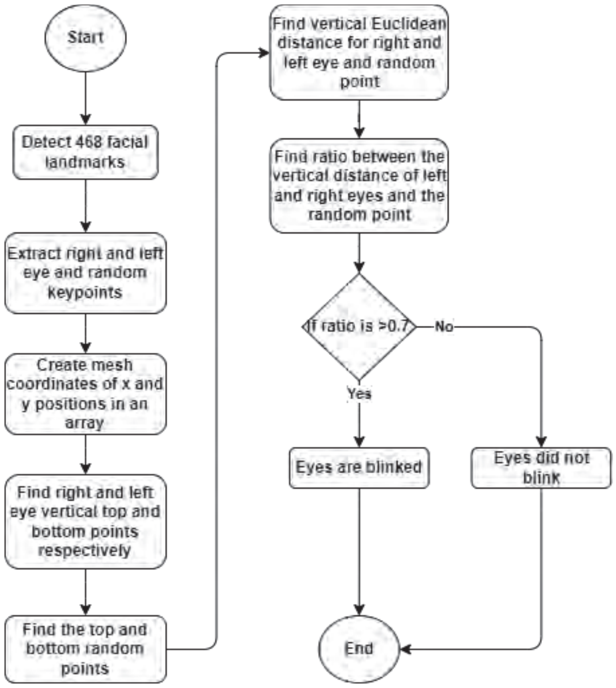

Fig. 6: Flowchart for eye blinking model

3.8 Long-Short-Term Memory (LSTM) Neural Network

In a crowded environment, datasets for people cues detection to identify a large number of human motion data [18] increases linearly and often difficult to interpret due to involvement of sequential data. LSTM is a method capable of learning order dependence in sequence prediction problems by enabling persistent error back-propagation within its inner memory cells. It remembers its input, due to an internal memory, which makes it perfectly suited for machine learning problems that involve sequential data. This will help to reduce the computational costs by reducing number of dimensions of the feature space by extracting a subspace that describes the data best [19]. Hence, reducing number of training data. This study uses LSTM neural network model to process and identify a face direction position. For example, the model proposed in the study is divided into three directions, namely, right, left and center. These directions are used to distinguish the attentiveness of the system function. The collected data was diversified into right, left and center. To train the model, the dataset used in this experiment was based on the personal dataset collection, which is conducive to reflecting the accuracy of LSTM neural network model. The tactile model was trained using sequences of images. It employs three LSTMs to shape temporal data by progressive

https://doi.org/10.31436/iiumej.v24i1.2577

codification of its vector. The output classification probability distribution was provided by a fully-connected layer with 3 neurons and a Softmax function after the second LTSM. A modified LSTM neural network was constructed which consist of LSTM, dropout and dense layers as shown in Fig. 7.

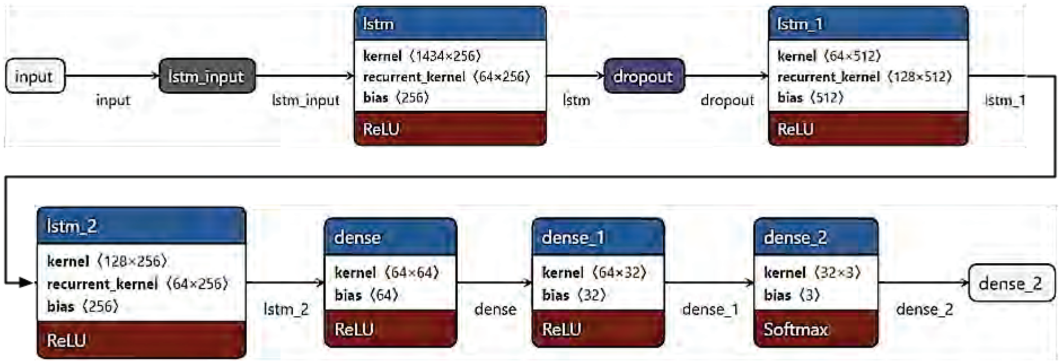

Fig. 7. LSTM neural network architecture

The data was spliced into training and testing keypoints which made it easier to evaluate the trained data. For this case, the original data for each category have been split into 30% of testing and 70% of training. The LSTM neural network trained the data for all of the classes according to the right, left and center face movement classification in 4.5. This type of neural network was powerful as it was capable to create a more descriptive and abstract result to let the network learn all sorts of features from scratch, by arranging them in layers, the network can recycle/reuse features such that low-level features combine to form mid-level features and mid-level features combine to form high-level features.

4 RESULTS AND ANALYSIS

4.1 Face tracking experiment and result

The face detection model was developed to execute the face tracking recognition as cues for attentive model for specified face mesh annotations. This was able to produce more nodes on face which can easily be observed by the joints in tessellation, while previous method [16] consists of smaller number of landmarks which were used for cues to be trained which in this case makes it to have less precision. This was tested in both indoor and outdoor conditions for 2 meters as you can see in the Fig. 8 below.

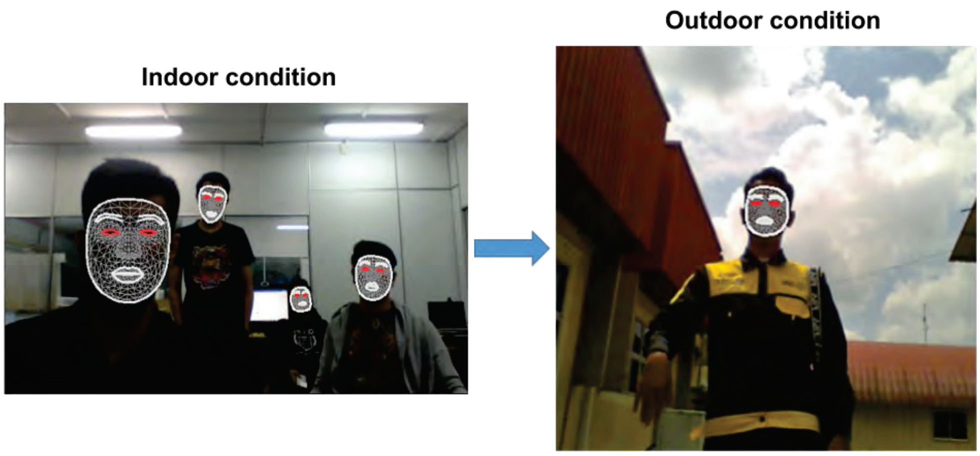

Fig. 8. Face detection model

https://doi.org/10.31436/iiumej.v24i1.2577

From the experiment, it was shown that the model was able to detect the multiple face mesh with limitation roughly up to 2 meters in both indoor and outdoor environment. This could be due to the fact that it was affected by the luminance in the room preventing it to recognize the people. Even though, for outdoor condition the light intensity was higher than the indoor, the model was detected due to the camera's capability to auto calibrate lens adjustment which allows it to adjust the light entering its aperture and detect a person's face. The face tracking model was limited by the amount of data needed to be trained, therefore it is suggested to use larger dataset to have better prediction. This is summarized in the following Table 2.

Table 2: Overall face detection

Participant	Environment	Estimated distance of detection (m)
1	Indoor/Outdoor	2
2 (wearing spectacles)	Indoor/Outdoor	2
3 (wearing spectacles)	Indoor/Outdoor	2

4.2 Iris tracking experiment and result

As there are people in real life who face straight forward but at the same time look the other way which causes the unnaturalness in communication with the robot therefore, an iris tracking model is introduced to create a natural eye to eye contact feature. This algorithm was proposed to extract the iris landmark from the specified face mesh annotations. The ratio for determining the iris positions are classified as in following Table 3.

Table 3: Iris position based on specified ratio

Ratio	Iris position
0 – 0.42	Right
0.42 – 0.57	Center
0.57 – 1.0	Left

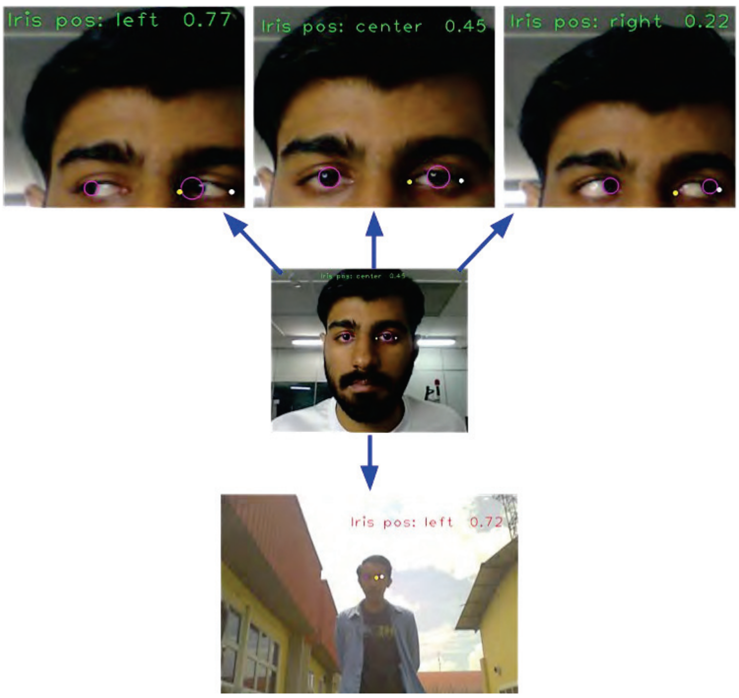

Fig. 9. Iris tracking model

These values were determined by conducting several trials in both indoor and outdoor environments as shown in Fig. 9. This was calculated using the Euclidean distance equation. The model was able to detect the participant's iris at 2 meters from the camera.

4.3 Eye blinking experiment and result

The eye blinking was tested for squinting and blinking action to test the model's robustness as shown in Fig 10. The state of eye being closed shows that the person was blinking.

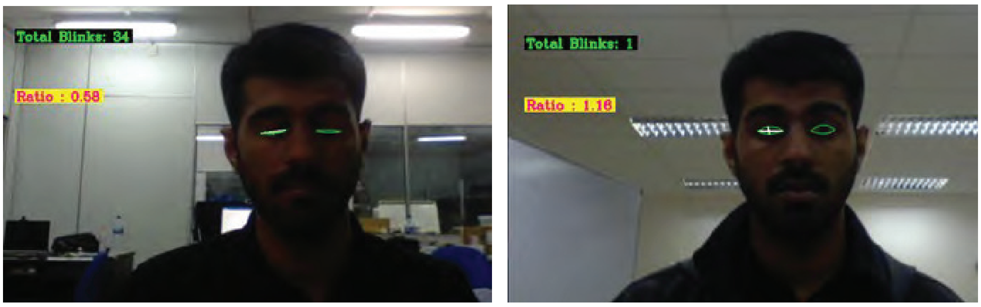

Fig. 10. Eye blinking model

The data also consisted of different positions of face during squinting so that the camera was able to take record of those eyes movement keypoints at most of the positions in camera's stereo vision. The vertical distance used for right, left eyes and random landmarks at nose area is illustrated in Fig 11. These points were chosen due to their availability in such position that can give maximum distance value to get the correct distance measurement. Thus enabling by giving flexibility to test the model for further distance.

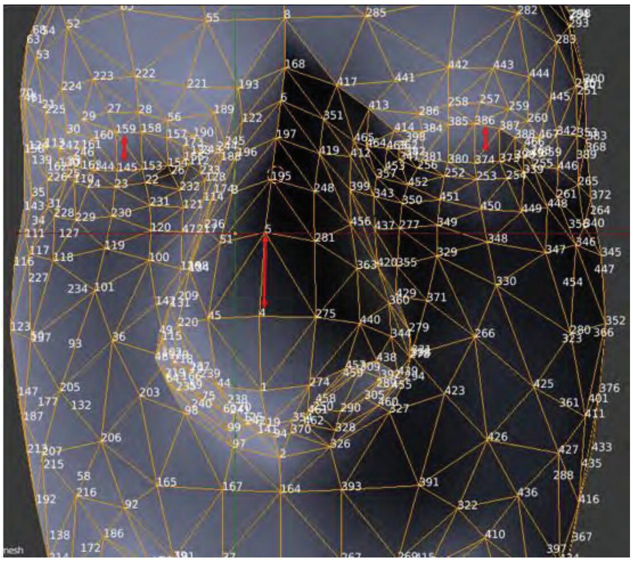

Fig. 11. Vertical distance measurement [14]

From the Fig. 12, it shows that even when a person was standing at farther distance from the camera the ratio is roughly same as of sitting in front of camera. This outlines that the vertical distance between the 2 landmarks of eyes have similar observation in terms of value compared to the vertical distance between the 2 random landmarks chosen. This mathematical method enabled the algorithm to differentiate between eyes open and closed even at further distance.

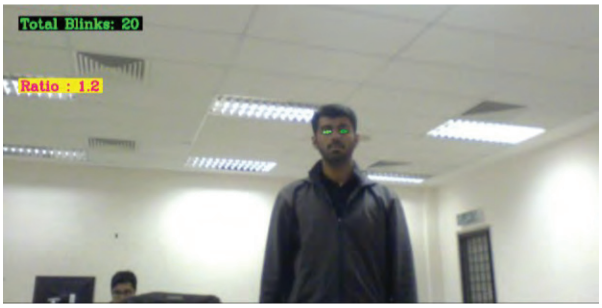

Fig. 12. Eyes open at 2 meters distance

Additionally, participants 2 and 3 wore spectacles to test the capability of the eye blinking model with respect to lenses distortion detection as shown in Fig 13. The previous method [14] of ratio calculation had some drawbacks which was noticed when a person moved further away from the camera, the ratio decreases causing the blinking counter to continuously moves. This was because when a person moves away from camera, the pixels that covers the eyes reduces which causes the distance to be reduced making the counter to increment.

Fig. 13: Testing participant 2 and 3

Table 4 explains the statistics on the prediction and true set for each participants. Statistics for participant 1 on the prediction set show that the number of eyes continue to open for 2 samples, and the number of blinks was 2 samples for EAR threshold 0.7. However, statistics on the test set describe the number of eyes continue to open was 2 samples, and the number of blinks was 2 samples. Furthermore, participant 2 and 3 had eyes continue to open for 2 samples, and the number of blinks was 2 samples for EAR threshold 0.7. Meanwhile, during prediction of blinking only 1 sample was present, and predicted eyes open was 2 samples.

Table 4: Statistics on the prediction and true set for each participant

Participants	True eyes open	Predicted Eyes remains open	True eyes blink	Predicted eyes blink	EAR
1	2	2	2	2	0.7
2	2	2	2	1	0.7
3	2	2	2	1	0.7

Based on the table, a confusion matrix was drawn as shown in Table 5. This experiment exhibited an accuracy of 83.33% by using calculation as shown in equation 3.1 which justifies its practicality. Based on this, it had been concluded that, the experiment achieves the best performance for all datasets.

Table 5: Confusion matrix for 3 participants

	True positive	True negative
Predicted positive	6	2
Predicted negative	0	4

$$ACC = \frac{(TP+TN)}{(TP+TN+FP+FN)} \times 100\% = \frac{(6+4)}{(6+4+2+0)} = 83.33\% \quad (3.1)$$

The F1 score of this method was calculated as shown in equation 3.2 which resulted in 0.86. For easier comparison, this was later compared with the previous datasets by extracting their precision-recall value and tabulating them as shown in Table 6.

$$F1 = 2 \times \frac{precision \times recall}{precision + recall} = \frac{TP}{TP + \frac{1}{2}(FP+FN)} \quad (3.2)$$

$$= \frac{6}{6 + \frac{1}{2}(2+0)} = 0.86$$

Table 6: Results obtained for blink detection using the proposed method

Dataset	ZJU	TF (Talking Face)	Our
Precision	0.98	1.0	0.75
Recall	0.898	1.0	1.0
F1	0.94	1	0.86

The accuracy of the blinking model for the proposed method were compared with previous methods as shown in Table 7.

Table 7: Results obtained for blink detection using the proposed method

Methods	Accuracy (%)
Proposed method	83.33
Dlib+CNN	97

Based on the results, it was concluded that the percentage for accuracy dropped due to the person was wearing glasses or the effect from outdoor environment. As the recall was able to get full percentage, it showed that the eye blinking model had the ability to correctly predict the positives out of actual positives. The glasses might have caused the ratio calculation to be off by a certain margin which leads to misreading in eye blinking cue. Other than that, the response time for the camera to be able to detect a person's face took a longer period which resulted in less precise. This outlines, even eyes are capable to be detected in different light conditions due to the capability of the camera's auto calibrating lens adjustment which allows it to detect a person's face and eyes.

4.4 Long-Short-Term Memory (LSTM) Neural Network experiment and result

The face tracking model dataset was trained with 97% of accuracy and 3% of loss as shown in Figure 14 and 15. It was seen that the error was propagated at 30 to 40 steps throughout the entire network to compute gradients with respect to inputs early in a long sequence. Such models will often overfit on the training set and lose generalizability and accuracy on the test set. Therefore, a dropout regularization with a dropout probability of p = 0.5 had been employed in the output layer and between recurrent layers to combat this. Dropout regularization independently sets each weight in consideration to zero with probability p. In response to this, the network cannot rely on a few weights per-example to predict an outcome, lest those weights get pruned in a training step. The model is thus forced to employ many weights to process and predict each example, reducing overfitting. It was deliberately avoided using of dropout on weights between time steps, as doing so effectively eliminates long-range memory

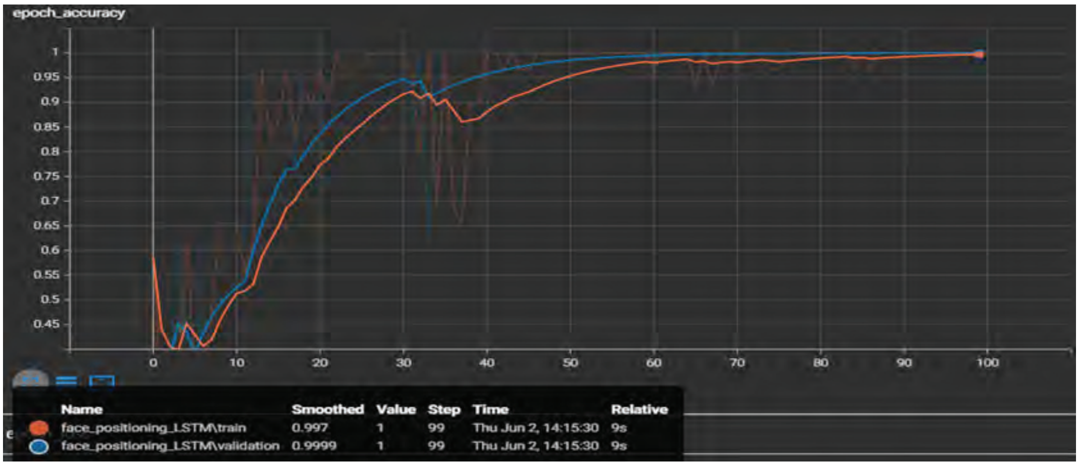

Fig. 14. Training and validation accuracy graph

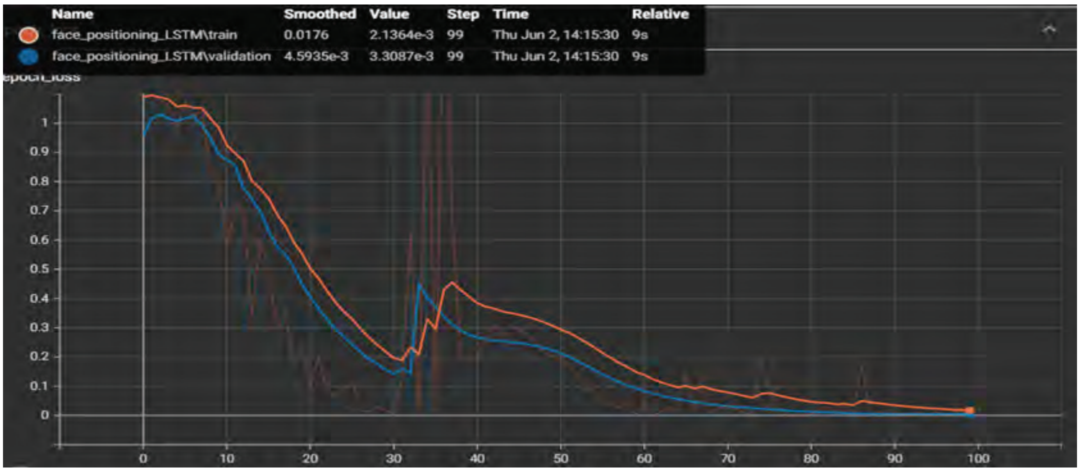

Fig. 15. Training and validation loss graph

4.5 ARM experiment and result

The overall coding for ARM was able to be constructed by combining the mentioned subsection 3.4, 3.5 and 3.6 together. Table 8 demonstrates that the attention mesh runs 80.6% faster than the cascade of separate face and region models on a typical modern mobile device. This performance had been measured using the inference time. Based on this, it could be due

https://doi.org/10.31436/iiumej.v24i1.2577

to during separate execution of the program, it had to run the same coding in other python file rather than using the same line of code form previous saved history such as for the cascaded version of algorithm.

Table 8: Performance on models

Model	Inference Time (ms)
Face mesh tracking	113.98
Iris tracking	37.9
Eye blinking	3.997
Total	155.877
Cascade (ARM)	125.65

7 participants were used to test the system response as tabulated in Table 9. The confusion matrix was formed which showed that the system had 85.7% of accuracy which was due to only one of the participant which had been predicted wrong as shown in equation 3.3. This could be due to the fact that the position of the person was in the right side of the video frame. Therefore, the face was not detected as aligned with the camera's stereo vision.

Table 9: The confusion matrix

	Predicted positive	Predicted negative
Actual positive	4	1
Actual negative	0	2

$$ACC = \frac{(4+2)}{(4+2+0+1)} \times 100\% = 85.7\% \tag{3.3}$$

Recall (R) indicates the ratio of the positive samples which were correctly classified, and presented in equation 3.4.

$$R = \frac{4}{(4+1)} = 0.8 \tag{3.4}$$

Precision (P) as in equation 3.5 was the proportion of actual positive instance in the samples which were classified as positive samples.

$$P = \frac{4}{(4+0)} = 1 \tag{3.5}$$

Intersection over Union (IoU) was calculated for a standard performance measure for the face segmentation problem. IoU represented the overlap between the candidate face mesh and the ground truth face mesh, namely, the ratio of their intersection and union. This showed that, the value was greater due to the closer correlation. Given a set of images, the IoU measurement gave the similarity between the predicted area of the candidate's face mesh presented in the set of images and the ground truth area, which was defined by equation 3.6.

https://doi.org/10.31436/iiumej.v24i1.2577

$$IoU = \frac{area\ of\ overlap}{area\ of\ union} = \frac{4}{(4+0+1)} = 0.8 \tag{3.6}$$

Mean average precision (mAP) for a set of classes was the mean of average precision as in equation 3.7, where N denoted as the number of classes and C meant the class.

$$mAP = \frac{\sum average\ precision}{N(classes)} = \frac{1}{3} = 0.33 \tag{3.7}$$

The accuracy of the ARM was compared with previous methods as shown in Table 10.

Table 10: Results obtained for ARM

Methods	Accuracy (%)
Proposed method	85.7
Scalable HMM	76
OpenPose [5]	97

Based on the result, the accuracy of proposed method was positioned at the middle compared to Scalable HMM and OpenPose. The OpenPose method scored the highest which could be due to its limitation of using eye blinking model to gain attention for attentive model. The literature experiment was conducted based on the study of eye contact. Other than that, it could also be the effect from light which caused the accuracy to drop. This method lacks the iris tracking and eye blinking detection of multiple people at the same time in one frame which is essential for the robot in a crowded place.

5 CONCLUSIONS

In this paper, face tracking, iris tracking and eye blinking models were combined to propose an attentive model known as ARM to improve a robot's attention model performance in determining the most attentive person and prioritizing people based on attentiveness. Moreover, the accuracy of attentiveness prediction was evaluated at different light intensities in order to validate the feasibility of these methods in the real world. This project was expected to provide the best HRI experience with low computational complexity and to be invariant to rotation and linear changes in illumination. Experimentation results concluded that face tracking and an eye blinking model were achieved successfully. This was validated by applying the program inside the service robot and testing it in the real world. Hence, it could be operated in a café environment on a trial basis.

In the future, the current algorithm will be modified to enable it to detect all the important cues of various people at the same time. Additionally, some modifications to the face positioning training data would be done to increase its detection ratio for people at a further distance from the camera.

Acknowledgement: Communication of this research is made possible through monetary assistance by Universiti Tun Hussein Onn Malaysia and the UTHM Publisher's Office via Publication Fund E15216

REFERENCES

[1] Haider, MH, Wang Z, Khan AA, Ali H, Zheng H, Usman S, Kumar R, Bhutta MUM, Zhi P. (2022) Robust mobile robot navigation in cluttered environments based on hybrid adaptive neuro-fuzzy inference and sensor fusion. Journal of King Saud University-Computer and Information Sciences. https://doi.org/10.1016/j.jksuci.2022.08.031

[2] Hacene N, Mendil B. (2021) Behavior-based autonomous navigation and formation control of mobile robots in unknown cluttered dynamic environments with dynamic target tracking. International Journal of Automation and Computing, 18: 766-786. https://doi.org/10.1007/s11633-020-1264-x

[3] Sigalas M, Pateraki M, Trahanias P. (2015, July) Visual estimation of attentive cues in HRI: the case of torso and head pose. International Conference on Computer Vision Systems, vol (9163): pp 375-388. https://doi.org/10.1007/978-3-319-20904-3_34

[4] D'Eusanio A, Simoni A, Pini S, Borghi G, Vezzani R, Cucchiara R. (2020, November) A Transformer-Based Network for Dynamic Hand Gesture Recognition. 2020 International Conference on 3D Vision (3DV): pp. 623-632. https://doi.org/10.1109/3DV50981.2020.00072

[5] Lombardi M, Maiettini E, De Tommaso D, Wykowska A, Natale L. (2022) Toward an Attentive Robotic Architecture: Learning-Based Mutual Gaze Estimation in Human–Robot Interaction. Frontiers in Robotics and AI, 9, 770165. https://doi.org/10.3389/frobt.2022.770165

[6] Hömke P, Holler J, Levinson SC. (2018) Eye blinks are perceived as communicative signals in human face-to-face interaction. PLoS ONE, 13(12): e0208030. https://doi.org/10.1371/journal.pone.0208030

[7] Keiling H. (2019, February 28) 9 Types of Nonverbal Communication and How To Understand Them. Indeed Career Guide [https://www.indeed.com/career-advice/career-development/nonverbal-communication-skills#:~:text=Nonverbal%20communication%20is%20important%20because]

[8] Khan ZH, Siddique A, Lee CW. (2020) Robotics Utilization for Healthcare Digitization in Global COVID-19 Management. International Journal of Environmental Research and Public Health, 17(11): 1-23. https://doi.org/10.3390/ijerph17113819

[9] Timm F, Barth E. (2011) Accurate eye centre localisation by means of gradients. VISAPP 2011 - Proceedings of the International Conference on Computer Vision Theory and Application, 125-130.

[10] Li J, Liu R, Kong D, Wang S, Wang L, Yin B, Gao R. (2021) Attentive 3D-Ghost Module for Dynamic Hand Gesture Recognition with Positive Knowledge Transfer. Computational Intelligence and Neuroscience, 2021(5044916): pp 1–12. https://doi.org/10.1155/2021/5044916

[11] Attiah AZ, Khairullah EF. (2021) Eye-Blink Detection System for Virtual Keyboard. National Computing Colleges Conference (NCCC), pp 1-6. https://doi.org/10.1109/NCCC49330.2021.9428797.

[12] Shen Z, Elibol A, Chong NY. (2020) Understanding nonverbal communication cues of human personality traits in human-robot interaction. IEEE/CAA Journal of Automatica Sinica, 7(6): 1465-1477. https://doi.org/10.1109/JAS.2020.1003201

[13] Palinko O, Rea F, Sandini G, Sciutti A. (2016, October) Robot reading human gaze: Why eye tracking is better than head tracking for human-robot collaboration. International Conference on Intelligent Robots and Systems (IROS), pp. 5048-5054. https://doi.org/ 10.1109/IROS.2016.7759741

[14] Chandra B, Sharon HLU, Vignesh CP, Sriram R. (2020) Eye Blink Controlled Virtual Interface Using Opencv And Dlib. European Journal of Molecular & Clinical Medicine, 7(8), pp 2119–2126. https://ejmcm.com/article_4542.html

[15] Pasternak K, Wu Z, Visser U, Lisetti C. (2021) Let's be friends! A rapport-building 3D embodied conversational agent for the Human Support Robot. ArXiv preprint ArXiv:2103.04498. https://doi.org/10.48550/arXiv.2103.04498

[16] Saran A, Majumdar S, Short ES, Thomaz A, Niekum S. (2018, October 1) Human Gaze Following for Human-Robot Interaction. 2018 IEEE/RSJ International Conference on Intelligent Robots and Systems (IROS), pp 8615-8621. https://doi.org/10.1109/IROS.2018.8593580

[17] Saunderson S, Nejat G. (2019) How Robots Influence Humans: A Survey of Nonverbal Communication in Social Human–Robot Interaction. International Journal of Social Robotics, 11(4): 575–608. https://doi.org/10.1007/s12369-019-00523-0
[18] Li X. (2021) Design and implementation of human motion recognition information processing system based on LSTM recurrent neural network algorithm. Computational Intelligence and Neuroscience. https://doi.org/10.1155/2021/3669204
[19] Laghrissi FE, Douzi S, Douzi K, Hssina B. (2021) Intrusion detection systems using long short-term memory (LSTM). Journal of Big Data, 8(1): 1-16. https://doi.org/10.1186/s40537-021-00448-4

https://doi.org/10.31436/iiumej.v24i1.2642

REPURPOSING A SAMPLING-BASED PLANNER FOR A SIX-DEGREE-OF-FREEDOM MANIPULATOR TO AVOID UNPREDICTABLE OBSTACLES

HAFIZ IMAN* AND MD RAISUDDIN KHAN

*Department of Mechatronics Engineering, Kulliyyah of Engineering,
International Islamic University Malaysia, Jalan Gombak,
53100 Kuala Lumpur, Malaysia*

**Corresponding author: hafiz.ghazman@gmail.com*

(Received: 3rd November 2022; Accepted: 4th December 2022; Published on-line: 4th january 2023)

ABSTRACT: This paper presents the use of a sampling-based planner as a reactive planning scheme to avoid obstacles between a robotic arm and a moving obstacle. Based on a planner benchmark on an obstacle-ridden environment, a rapidly-exploring random tree (RRT) planner has been used to populate the trajectories of the task space and map them into a configuration space using a Newton-Raphson-based inverse kinematic solver. Two robot poses are defined in a cycle of back-and-forth motion; the initial and the goal poses. The robot repeatedly moves from the starting pose to the end pose via the midpoint pose. Each set of trajectories is unique. We define this unique solution within the context of the configuration space as a cycle space. We impose a periodically occurring synthetic obstacle that moves in and out of the robot arm workspace defined in a simulated environment. Within the robot's workspace, the obstacle moves and cuts through the cycle space to emulate a dynamic environment. We also ran a benchmark on the available sampling planner in the OMPL library for static obstacle avoidance. Our benchmark shows that the RRT has the lowest time planning time at 0.031 s compared with other sampling-based planners available in the OMPL library, RRT implicitly avoids singularities within the cycle space, and reactively attempts to avoid synthetic moving objects near the robot hardware. This research intends to further investigate on the use of RGB-D sensor and LiDAR to track moving obstacles while abiding by the task space commands described by the initial and goal poses.

ABSTRAK: Kertas kerja ini membentangkan penggunaan perancang berasaskan persampelan sebagai skim perancangan reaktif untuk mengelakkan halangan antara lengan robot dan halangan yang bergerak. Berdasarkan penanda aras perancang pada persekitaran yang dipenuhi halangan, perancang pokok rawak (RRT) penerokaan pantas telah digunakan untuk mengisi trajektori ruang tugas dan memetakannya ke dalam ruang konfigurasi menggunakan penyelesai kinematik songsang berasaskan Newton-Raphson. Dua pose robot ditakrifkan dalam kitaran gerakan bolak-balik; pose awal dan matlamat. Robot berulang kali bergerak dari pose permulaan ke pose akhir melalui pose titik tengah. Setiap set trajektori adalah unik. Kami mentakrifkan penyelesaian unik ini dalam konteks ruang konfigurasi sebagai ruang kitaran. Kami mengenakan halangan sintetik yang berlaku secara berkala yang bergerak masuk dan keluar dari ruang kerja lengan robot yang ditakrifkan dalam persekitaran simulasi. Dalam ruang kerja robot, halangan bergerak dan memotong ruang kitaran untuk meniru persekitaran yang dinamik. Kami juga menjalankan penanda aras pada perancang pensampelan yang tersedia dalam perpustakaan OMPL untuk mengelakkan halangan statik. Penanda aras kami menunjukkan bahawa RRT mempunyai masa perancangan masa terendah pada 0.031 s berbanding dengan perancang berasaskan pensampelan lain yang terdapat dalam perpustakaan OMPL, RRT secara tersirat mengelakkan singulariti dalam ruang kitaran, dan secara reaktif cuba mengelakkan objek bergerak sintetik yang menghampiri perkakasan robot. Melangkah ke hadapan, penyelidikan ini berhasrat untuk menyiasat lebih lanjut mengenai penggunaan penderia RGB-D dan LiDAR untuk mengesan halangan bergerak sambil mematuhi arahan ruang tugas yang diterangkan oleh pose awal dan matlamat.

KEYWORDS: *mechatronics; robot manipulator; planner; motion planning; dynamic environment*

1. INTRODUCTION

Given its rigid and massive construction, a small-sized industrial robot imposes significant hazards on the people that work near it. Hence, robotic manufacturers build robot manipulators that are more compliant and designed to cooperatively without risking their safety [1]. Regardless, a robot manipulator imposes occupational hazards in the workspace during a collision with foreign objects or a person [2]. The collision also warrants expensive maintenance and repairs. An industrial robot system implements a certain degree of planning algorithm specifically for the movement of the manipulator.

A robot motion planner can provide a collision-free motion solution for a manipulator if a solution is defined as the collection of waypoints and trajectories that avoid collision between the robot and the obstacle as will be demonstrated by this paper in the following section. A global planner, an offline approach to motion planning, takes in a set of initial and goal positions, $t \in \mathbb{R}^3$, or as set of initial and goal poses, $p \in \boldsymbol{SE(3)}$, as its input constraint-informed trajectory as intermediate waypoints for the robot to follow [3]. However, a global planner is offline, which implies that the trajectories are set before the task commences. The global planner also assumes a static workspace. Any unplanned changes in the workspace over the global planning scheme, such as an unplanned introduction of a stationary object or a moving object into the robot workspace, renders the offline-planned trajectory outdated and, consequently, requires replanning.

Hence, a compliant manipulator or cooperative manipulator must have an efficient online motion planner because of the dynamic aspect of their workspace. However, this requires replanning which is computationally expensive and time-consuming. To relax the computational strain, algorithms are designed stochastically by implementing sampling of plausible solution in specific solution space [4]. Unfortunately, sampling-based planner trade completeness and optimality with efficiency where the planner may fail to provide a solution [5]. Also, if a solution exists under its metric space, the waypoints may not be the least cost path to a goal [6].

Regardless of the lack of completeness and optimality, sampling-based planners excel at maintaining reasonable usage of computational resources that pave the way to the near-online planning scheme. The sampling-based planners for robot motion are a family of planners that use probabilistic approach to generate graph structures that encode the free space and the robot configuration space. The samplings are stochastic, such that resampling will give a unique solution to the previous sampling. Most sampling-based planners are tractable in higher-dimensional configurations and task space. Nonetheless, sampling-based planners also assume a static workspace.

This paper uses sampling-based motion planning, the rapidly-exploring random tree motion planning, to address operation tasks in a dynamic environment in Euclidean space, Our method leverages the efficiency and the computationally reserved sampling-based motion planning without needing to apply a purely reactive motion planning approach so that computational resources can be delegated to other tasks, i.e., motion-tracking, state estimation, mapping, localization, and motion control. In the following sections of this report, we will assume sampling planners to provide solutions in higher dimensional configuration space, which implicates a solution with a set of poses represented by the special Euclidean group $\boldsymbol{SE(3)}$.

2. RELATED WORK

The research done in [5] is the seminal work on the use of a probability model for sampling the configuration space for holonomic robot motion such as a manipulator robot. The planner is called the probabilistic roadmap (PRM). The algorithm constructs a graph structure to find a path between an initial pose to a goal pose in a two-dimensional configuration space, $n = 2$. A more general solution for higher dimensional configuration space, $n > 2$, were also proved using the PRM in their work. With graph structure, more than one path connects the initial pose to the goal pose. Therefore, PRM is a multi-query type planner.

The work in [6] improved PRM by redefining the distance metric of a robot manipulator so that the robot can move around a moving obstacle in real-time. Their approach performs well in an uncluttered environment. They also redefined the distance function of the PRM to address dynamic objects, such as a walking person, into a two-dimensional map. Although the configuration space of the manipulator is in $\mathbb{R}^3$, the map, constructed from a two-dimensional LiDAR scan, is in, $\mathbb{R}^2$.

In retrospect, the RRT was formulated for non-holonomic motion targeting problems addressed in differential-constrained motion such as a car on a plane [7]. However, given the model of its metric space and consequently the configuration space, RRT is tractable for the higher dimensional problem such as manipulator motion in 3D space. RRT assumes a static environment but investigation in [8], successfully changed the way RRT samples a robot metric space so that it is fast enough to react to a changing environment. Also, unlike PRM, RRT works well in a cluttered environment because of the randomized sampling on the robot configuration space in the context of the metric space.

Apart from the works in [6] and [8], few have applied their planning algorithms on a robot manipulator despite having RRT and PRM algorithms provide a mathematical framework for planning for multi-body and multi-frame systems. In this paper, we will use the method demonstrated by [6] and [8] to design a moving obstacle avoidance algorithm with the implementation of the vanilla RRT to solve motion for a robot manipulator in three-dimensional space, $\mathbb{R}^3$. Our method implements the vanilla RRT where we do not represent the obstacle configuration space unlike in [8].

3. FORMULATION AND ALGORITHMS

This paper will use the superscript notation to refer to the control space and the subscript as the equivalent representation in the configuration space. For example, C^{ee}, refers to the control space of the end-effector where the controlling pipelines would take in $c^{ee} = (\theta_1, \ldots, \theta_6) \in C^{control}$, and the equivalent pose is in the configuration space, C_{ee}. Since the revolute joint topology is the 1-hypersphere, S^1, we will assume that, for the case of 6R robot, its joints are limited to a certain range which makes, $c^{ee} \in \mathbb{R}^{6\times 1}$.

https://doi.org/10.31436/iiumej.v24i1.2642

3.1 The Geometry of a Compliant Robotic Arm, r_mini

We prototype and build a 3D-printed robot called Richard Mini (*r_mini*, see Fig. 1(a) and 1(b)) based on the condition addressed by Pieper [9], which entails three collated joints sharing the same cross point of their, *z-axes*, shown in Fig. 2.

(a) *r_mini* hardware assemblage (b) r_mini Computer Aided Design (CAD) construction

Fig. 1: A 3D-printed compliant manipulator, *r_mini*, designed to replicate a common industrial robot construction.

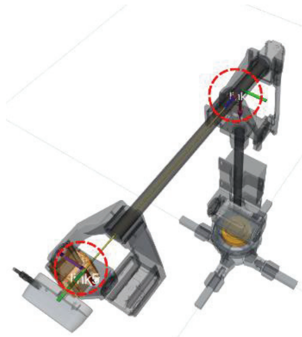

Fig. 2: *r_mini* wrist conforms to Pieper condition where axes of rotation for joint4, joint5, and joint6 share points of intercept. The dashed circles in the diagram refer to point of intercepts. Both points are valid frames for constructing the DH-table.

r_mini has six revolute axes, $(\theta_1, \ldots, \theta_6)$. The first three axes move the task space from one point to another representing the translation vector, $t \in \mathbb{R}^3$. The last three axes of the manipulator rotate the task space representing the rotation operation about the task space frame, $R \in \mathbb{R}^{3\times3}$. Hence the complete transformation of the task space via the joint movement is represented by the homogenous transformation matrix, $T \in \boldsymbol{SE(3)}$, where $\boldsymbol{SE(3)}$ is homomorphic to $(R, \boldsymbol{t})$; $\boldsymbol{SE(3)} = \mathbb{R}^3 \times \boldsymbol{SO(3)}$. The matrix representation of the homogenous transformation is shown in Eq. (1).

$$T = \left[\begin{array}{c:c} R & \boldsymbol{t} \\ \hdashline \mathbf{0} & 1 \end{array}\right] \quad (1)$$

The kinematic model of the r_mini follows the Denavit-Hartenberg (DH) formulation [10]. The DH-parameters are shown in Table 1 and the visualization of these parameters in the form of frames transformation is shown in Fig. (3).

Table 1: DH-parameter table for *r_mini*

Link (i)	a_i	α_i	d_i	θ_i
1	0	0	0.196	θ_1
2	0	$-90°$	0	θ_2
3	-0.373	0	0	θ_3
4	-0.08	$-90°$	0	θ_4
5	0	$-90°$	0.391	θ_5
6	0	$-90°$	0	θ_6

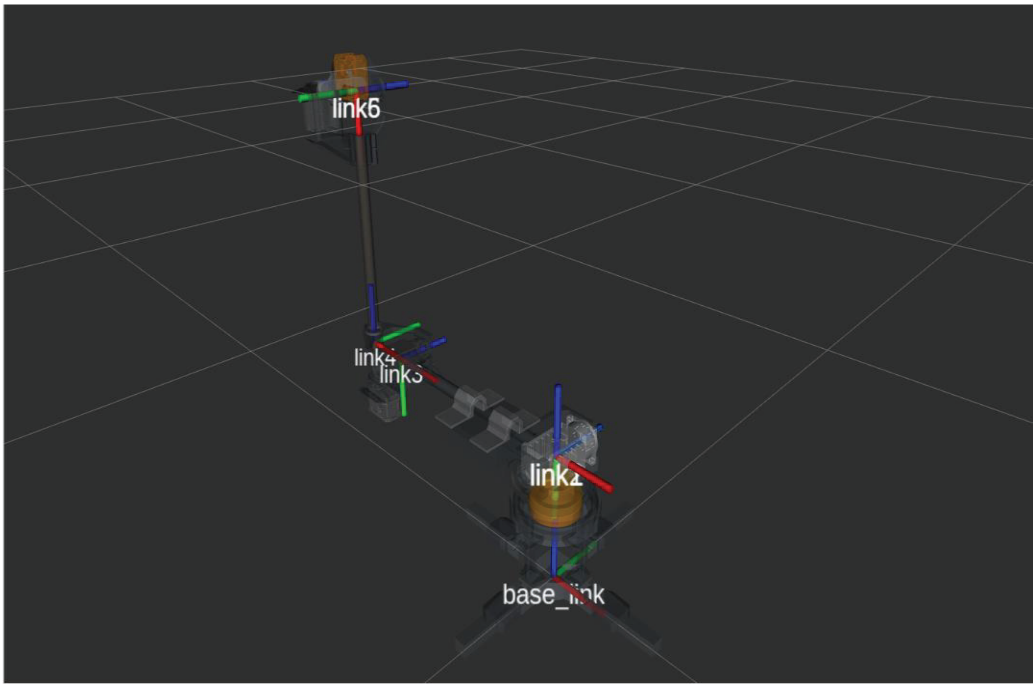

r_mini build completion

Fig. 3: The location and orientation of *r_mini*. The choice of orientation for each frame is based on Denavit-Hartenberg convention. The joints' values are represented by the angle between the *x-axis* around the *z-axis* (the rotation axis of each joint) of the actuator.

Following the DH-convention, each link rotates about the *z-axis* of each frame it is attached to, where $(joint_1, \ldots, joint_6)$, corresponds to $(\theta_1, \ldots, \theta_6)$ respectively. In Table 1, each row represents elements of homogeneous transformation, used in Eq. (2):

$$T_i = T(R_z(\theta_i))T(t_z(d_i))T(t_x(a_i))T(R_x(\alpha_i)) \quad (2)$$

where, $R_z, R_x \in \boldsymbol{SO(3)}$, are the rotation operations about the *z-axis* and the *x-axis* respectively, and $t_z, t_x \in \mathbb{R}^3$ are the translation vector on the *z-axis* and the *x-axis* respectively, while, $d, a, \alpha \in \mathbb{R}$, are scalars. The homogeneous transformation between the origin of the base of the robot into the end-effector of the robot, which coincides with $joint_6$ is shown in Eq. (3),

$$\begin{bmatrix} t_{ee} \\ 1 \end{bmatrix} = \left(\prod_{n=0}^{6-n>0} T_i \right) \begin{bmatrix} t_0 \\ 1 \end{bmatrix} \quad (3)$$

where $t_{ee} \in \mathbb{R}^3$, is the point location of the end effector in 3D space, and $t_0 \in \mathbb{R}^3$ is the origin of the base of the robot. Since the rotation involve in Eq. (3) includes the rotation about the origin of the local frames, the orientation of the end-effector can be represented by,

$$R_{ee} = \prod_{n=0}^{6-n>0} R_z(\theta_n) R_x(\theta_n) \quad (4)$$

Here the operation is closed. Often, to reduce computation expenses and trailing errors due to matrix-matrix multiplication, the rotation operation of *r_mini* are done over the quaternion (Eq. (5)),

$$\boldsymbol{q}_{ee} = \prod_{n=0}^{6-n>0} \boldsymbol{q}_z(\theta_n) \boldsymbol{q}_x(\theta_n) \quad (5)$$

where the Eq. (2) and Eq. (3) represent the forward kinematic solution for the end-effector of *r_mini*.

The self-collision, robot collision checking is delegated to a collision and proximity query library, the Flexible Collision library (FCL). Later in the algorithm formulation of the RRT and the cycle space, the subroutine from the FCL will be invoked to check collisions between the manipulator and the moving obstacles. The robot manipulator and the obstacles are encoded inside the collision scene which resides in the planning scene, $\mathcal{M}$, when the RRT datastructure is initialized (refer to Algorithm 2 line 1).

We use the Newton-Raphson method to find the inverse kinematic solution of *r_mini*, $\hat{c}^{ee}$. The generalization of the method uses the current value of the robot's encoder, $c^{current}$, and the termination value, $\epsilon = 0.005$, to end the iteration. Algorithm 1 delineates the method:

Table 2: The Newton-Raphson algorithm for *r_mini*'s inverse kinematic solver

Algorithm 1: getInverseKinematics

Input: c_{goal}, $c^{current}$, ϵ
Output: $\hat{c}_{ee}$

1. $e \leftarrow$ getForwardKinematic($c^{current}$)
2. **while** $\|e\| \neq \epsilon$ **do**
3. $\hat{c}^{estimate} \leftarrow c^{current} +$ getInverseJacobian($c^{current}$)e
4. $e \leftarrow C_{goal} -$ getForwardKinematic($c^{estimate}$)
5. $c^{current} \leftarrow c^{estimate}$
6. $\hat{c}^{ee} = c^{current}$
7. **return** $\hat{c}$

3.2 The Rapidly-Exploring Random Trees and its Mathematical Background

This research uses RRT implementation provided by the OMPL library packaged in the MoveIt software. The algorithm for the purpose of this research is shown in Algorithm 2:

Where k represents the number of nodes in the tree generated by the RRT; $\mathcal{M}$ represents the collision space of the planning scene where all RRT sampling takes place and, $\mathcal{T}$ is the tree that points to a non-colliding space. In this RRT implementation, the map is loaded or queried in line 1 each time the *generateRRT()* is invoked. Line 3 generates a random state bias towards the C_{goal}. Line 4 invokes the k-nearest neighbor to find a selection of nodes that is close to the state configuration, c_{random}. Line 5 is the core of the RRT sampling where it represents the controlling input of the robot motion. Since the robot is controlled in the joint-configuration space, the angular joint limit addresses the shape of the workspace. However, given the angular velocity, these limits are translated into the configuration space via the kinematic Jacobian which requires information on the Δt. The limits implicitly ensure that the RRT, by executing Line 5 within the context of the robot's Jacobian, does not pass through the singularities of the robot. Hence, the configuration space of the manipulator also includes, C_{limit}, containing configuration that abides the joint-configuration space range and angular velocity limit.

Table 3: The RRT algorithm

Algorithm 2: generateRRT

Input: $C_{initial}, C_{goal}, \Delta t, k, \mathcal{M}$
Output: $\mathcal{T}$
1 $\mathcal{T}$.initialize($C_{initial}, C_{goal}, \mathcal{M}$)
2 **while** $c_{new} \neq C_{goal}$ **do**
3 $\quad c_{random} \leftarrow$ randomState()
4 $\quad c_{near} \leftarrow$ kNearestNeighbor($k, c_{random}, \mathcal{T}$)
5 $\quad \boldsymbol{u} \leftarrow$ selectInput(c_{random}, c_{near})
6 $\quad c_{new} \leftarrow$ newConfiguration($c_{near}, \Delta t$)
7 $\quad \mathcal{T}$.append($c_{new}, c_{near}, \boldsymbol{u}$)
8 **return** $\mathcal{T}$

The configuration space where sampling occurs is modified in this paper where, the rotation representation and its sampling is in $R \in \mathbb{H}$, such that the parameterization of the Hamiltonian-space is the quaternions, $\boldsymbol{q} \in \mathbb{R}^4$. Therefore, the representation of the robot poses and also the non-colliding poses, $(\boldsymbol{q}, \boldsymbol{t})$, are explained in Eq. (6).

$$c_{pose} = \begin{bmatrix} \boldsymbol{q} \\ \cdots \\ \boldsymbol{t} \end{bmatrix} \quad (6)$$

The RRT sampling involves a query into a map, that stores objects that are prone to collision. This is the planning scene, denoted as the collision map, where the RRT sampling occurs. The query is invoked when both the initial pose and a goal pose are sent to the RRT planner input. The output of the pipeline is a set of non-colliding space where from another pipeline, transform the configuration space into a control space. We will define the control space in the following section.

3.3 The Cyclical Space

The cyclical space is the subset of the planner solution where the RRT algorithm is invoked twice. During the generation of the cyclical space, the RRT output a trajectory from the initial pose, $c_{initial}$ to the goal pose, c_{goal}, into a controlling pipeline. The trajectories are then mapped from the configuration space into the joint-configuration space via the Newton-Raphson inverse kinematic solver (see algorithm 1). To complete the set of the cyclical space, the entries in the initial pose and the goal pose are swapped, while invoking the query into the collision map,

$$\tau = (C^{control}, t) \quad (7)$$

https://doi.org/10.31436/iiumej.v24i1.2642

which forms a cyclical motion between the initial pose and the goal pose. Here,

$$C_{cycle} = \overbrace{C_{initial\rightarrow goal}}^{\text{see algorithm 3 line 4}} + \overbrace{C_{goal\rightarrow initial}}^{\text{see algorithm 3 line 7}}$$

Algorithm 3 block explains how the C_{cycle} space is constructed.

The control space is represented by the trajectory in the joint-configuration space $C^{control} \subset C^{cycle} \in S$, where S is the 6-hypersphere homomorphic to $\mathbb{R}^6$ because each joint is constrained to its angle limit. In Eq. (7), the joint-configuration space is equivalent to the configuration space in Eq. (6). The control space is the direct controlling parameters for the movement of *r_mini* where it only handles the control space (or joint-state space). The sampling of the RRT to generate the tree data structure, $\mathcal{T}$, are done within the $\boldsymbol{SO(3)} \times \mathbb{R}^3$topology. The free configuration space, or the non-colliding pose, is represented by,$C_{free} = C_{workspace}/C_{obstacle}$. According to LaValle et al. [7], this also covers the physical constraint of the non-holonomic movement of the robot. However, in the case of an articulated robot arm in this research, the configuration limitations are the range of the joints and the angular velocity limits. Since, these measurements are in the 6-space, to map them into the $\boldsymbol{SO(3)} \times \mathbb{R}^3$, we use the kinematic Jacobian.

Table 4: The cycle space generator where the movement within the constraint of the cycle space (also, a cyclical space) is dependent on the map, $\mathcal{M}$.

Algorithm 3: generateCycleSpace

Input: $c_{initial}$,c_{goal},Δt
Output: success_status

1 **Function** generateCycleSpace(c_{goal}, $c_{initial}$):
2 success_status $\leftarrow$ false
3 **while** *within iteration* **do**
4 $\mathcal{T}_{initial\rightarrow goal} \leftarrow$ generateRRT($c_{initial}$,c_{goal},Δt)
5 success_status $\leftarrow$ moveRobot($\mathcal{T}_{initial\rightarrow goal}$,$\Delta t$)
6 **if** *success_status* $=$ *true* **then**
7 $\mathcal{T}_{goal\rightarrow initial} \leftarrow$ generateRRT(c_{goal},$c_{initial}$,Δt)
8 success_status $\leftarrow$ moveRobot($\mathcal{T}_{goal\rightarrow initial}$,$\Delta t$)
9 **return** success_status
10 **Function** moveRobot($\mathcal{T}$, Δt):
11 **for** *all index in* $\mathcal{T}$*.vertices* **do**
12 c^{cycle}(index) $\leftarrow$ getIK($\mathcal{T}$.vertex(index))
13 $t \leftarrow \mathcal{T}.\boldsymbol{u}$.(index)$\Delta t$
14 $\mathcal{T}$.append(c^{cycle}, t)
15 success_status $\leftarrow$ TrajectoryController(τ)

4. METHODOLOGY

The methodology starts with the benchmarking of sampling-based planners available in the OMPL library and comparing the performance of the planners with the RRT. The benchmark is followed by experimentation in the simulated environment with a simulated robotic arm (*r_mini*) followed by the coupling of the simulated environment with *r_mini* hardware. The experimentation involves the moving obstacle that is introduced synthetically in the collision space. This was necessary since, at the time of this experimentation, the feedback from the mapping sensors was unavailable.

4.1 Benchmarking of Sampling-Based Motion Planners

In this research, the planner for the dynamic obstacle avoidance is selected based on the performance of a benchmarking activity. Two poses were set for the benchmark, pose initial were represented in the form of Eq. (6). The following vectors explain the numerical value of these poses concerning the frame attached to the base of *r_mini*.

$$c_{initial} = \begin{bmatrix} 1.0 \\ 1.71 \\ 1.0 \\ 1.71 \\ \hdashline 1.43 \\ 1.25 \\ 1.42 \end{bmatrix} \quad c_{goal} = \begin{bmatrix} 1.0 \\ 1.71 \\ 1.0 \\ 1.71 \\ \hdashline 1.46 \\ 1.29 \\ 1.43 \end{bmatrix} \tag{8}$$

A box, with dimension, 0.5 m × 0.05 m × 0.575 m, was placed in front of the robot, its pose was described by the vector in Eq. (9),

$$c_{box} = \begin{bmatrix} 0 \\ 0 \\ 0 \\ 1 \\ \hdashline 0.45 \\ 0 \\ 0.2874 \end{bmatrix} \tag{9}$$

Figure 4 shows the simulation setup and the planning motion in action. The simulation was run for 50 requests from the initial pose to the goal pose. Time processing was given a 10 s limit. The memory limit was set to 1 Mb. The time limit for a request, including the motion and the processing time was set to 3637 s (about 1 hour). This paper also uses the default configuration of each planner in MoveIt to start the benchmarking.

4.2 Experiment Design

The cyclical space is populated by the RRT-Newton-Raphson pipeline where the generated trajectories are then passed to the control pipeline where the controller will spline the sparse trajectory waypoints. Two poses are defined in this experimentation which has been described in Eq. (8). A moving obstacle is placed in front-view of the robot. The obstacle is a cylinder with a 0.1 m radius base at 1 m height. The obstacle moves from 0.3 m to 1.7 m away from the robot in oscillation. The period of motion is harmonic, such that, the robot follows $1 + 0.7 \sin(2\pi(0.0006)\Delta t)$ along the *x-axis*. Two velocities ($\mathcal{V}$) values were used: 50% and 10% scale from the maximum velocity of the end-effector.

The planner is invoked five seconds before the obstacle is placed into the planning scene. As described previously, the cylinder is directly placed into the planning scene (i.e., collision space) such that no motion tracking via mapping sensor feedback is necessary for this research. The planner is requested to provide a solution for the motion described by the cycle space. Twenty iterations were done with each given a five-minute runtime. The metric used for this experiment was the time on the first collision where, when the prototype touches the cylinder, the iteration is terminated. This experimentation was done, both, in simulation, and with the real robot hardware coupled with the simulated environment. To reiterate, for both the simulation and the hardware validation, the obstacle was augmented in simulated environment.

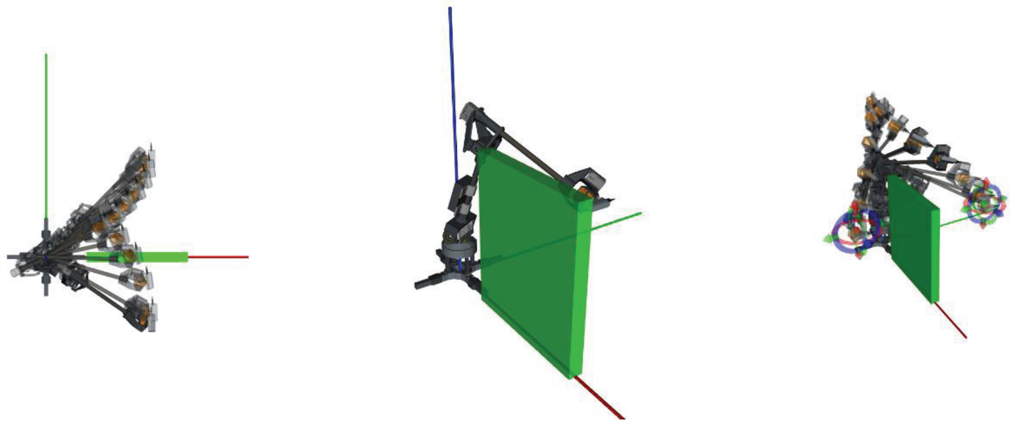

(a) (b) (c)

Fig. 4: (a) Top view of the simulation shown, (b) Isometric view of the benchmark setup, (c) *r_mini* attempts to move around the static obstacle placed in its immediate configuration workspace.

5. RESULTS AND DISCUSSION

There are two parts of the results in this paper, the first dealing with the benchmarking result to ascertain the best sampling-based planner. The second part delve into the performance of the selected planner from the benchmarking on a moving obstacle.

5.1 Benchmark Result

Figure 5 shows the compiled statistics of the time the solutions that were passed to the controller (in this case a virtual controller for the simulation of *r_mini* in the simulated environment).

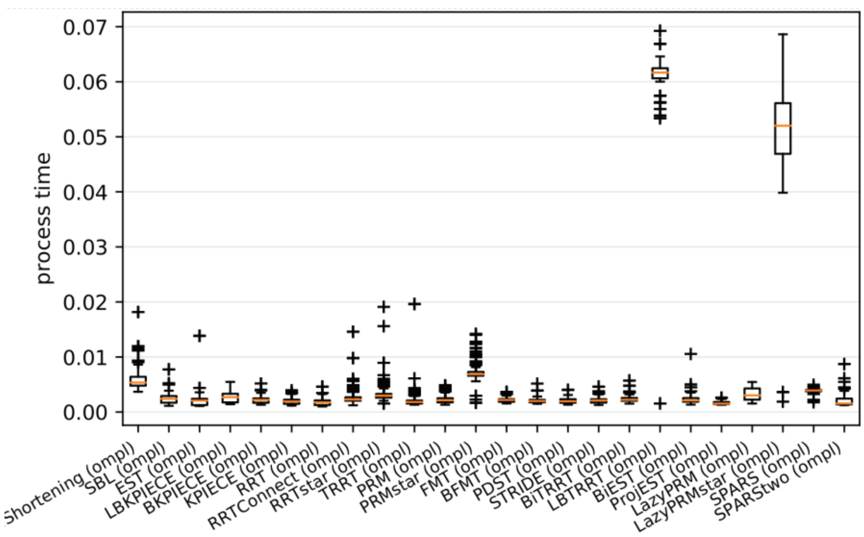

Fig. 5: The benchmark result when two configurations are defined and passed to the OMPL planner pipeline. All planners completed a 50-cycle query from an initial pose to a goal pose. RRT required the least amount of processing time at finding the motion planning solution, followed by the PRM.

RRT requires on average, 0.031 planning time while PRM requires 0.035 planning time from the initial pose to the goal pose when subjected to an obstacle close to the robot.

Wei & Ren [8] explained that the improved RRT algorithms, such as the bi-RRT, and the RRT-connect, solve a query faster. However, based on our benchmarking and in the case of this experimentation setup, vanilla RRT, or base-RRT, and PRM outperformed their improved variants when completing the path query between an initial pose and a goal pose. To that end, this research uses vanilla RRT as the scheme for the high-level local planner. This result helps us select the motion planner for dynamic obstacle avoidance.

5.2 The Performance of RRT on a Dynamic Environment

Table 5 shows the recorded time to the collision of 20 iterations. The average time to the collision was 40 s. There were two iterations where no collision was recorded. This performance is subjected to Algorithm 3, specifically in line 4 and line 7, when RRT is invoked. Within this call (refer to Algorithm 2: line 1), the random tree initialization considers an obstacle map that is outdated, given the cylinder moving further toward the manipulator when the RRT is executed. Within the RRT algorithm, there is no mechanism for the robot to stop or move at a lower rate to avoid the cylinder. Fig. 6 shows the sequence when the end-effector collided with the cylinder.

Table 5: The simulated and hardware-connected result of the performance of RRT in a dynamic environment. NC stands for *No Collision* after five minute runtime

	time to 1^{st} collision,(s)				
condition\iteration	1^{st}	2^{nd}	3^{th}	4^{th}	5^{th}
$\text{simulation}_{0.5\nu}$	64	NC	NC	133	18
$\text{hardware}_{0.1\nu}$	205	16	17	134	13
$\text{simulation}_{0.5\nu}$	13	23	11	9	13
$\text{hardware}_{0.1\nu}$	17	4	15	7	10

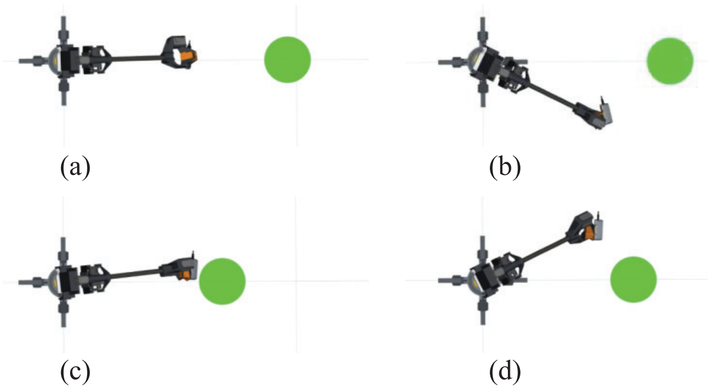

Fig. 6: These sequences show the manipulator follows an outdated trajectory and collides with the cylinder despite an attempt to move away from the moving cylinder.

Despite the obstacle collision when the moving cylinder approaches the robot, specifically when the centroid of the cylinder is nearing the *x-axis* of the $c_{initial}$ and c_{goal}, the planner reacts to the obstacles when lines 4 and 7 in Algorithm 3 are invoked by attempting to move around the cylinder.

The planner shows reactive behavior (local planning) when the cyclical space is initialized via Algorithm 3. Figure 7 illustrates such behavior in the simulated environment, and Fig. 8 shows the same behavior in the hardware reiteration of the experimentation. The reactive behavior is illustrated in Fig. 9, where the change we observed changes in movement range and a range in movement rate.

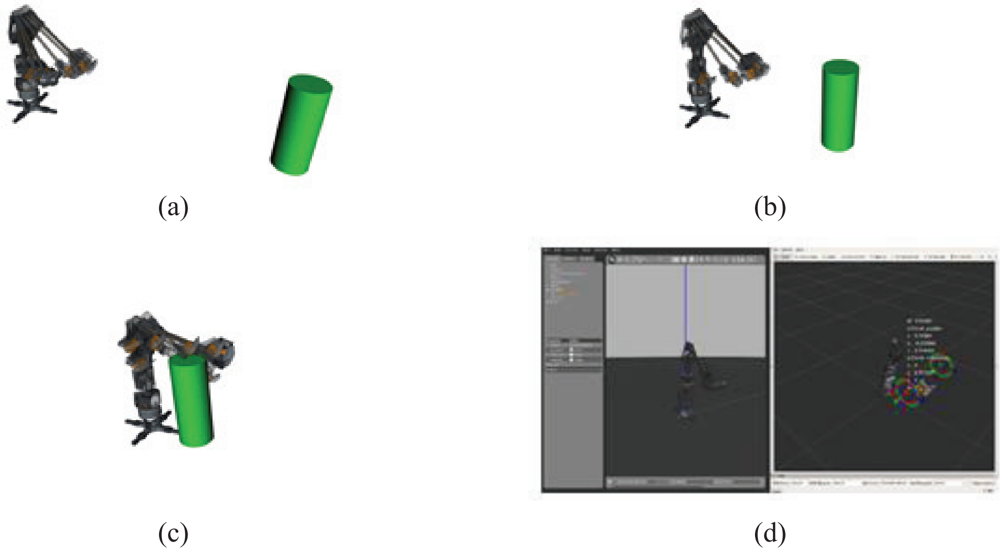

Fig. 7: The chronology of the attempt at avoiding a moving obstacle. (a) and (b) When the obstacle approaches the robot, (c) The planner successfully provides a non-colliding solution when the cylinder is moving away from the robot. (d) Experimentation is defined in a simulated setup using Gazebo with the ODE physic engine to replicate the robot hardware and encoders feedback and the cyclical space initialization.

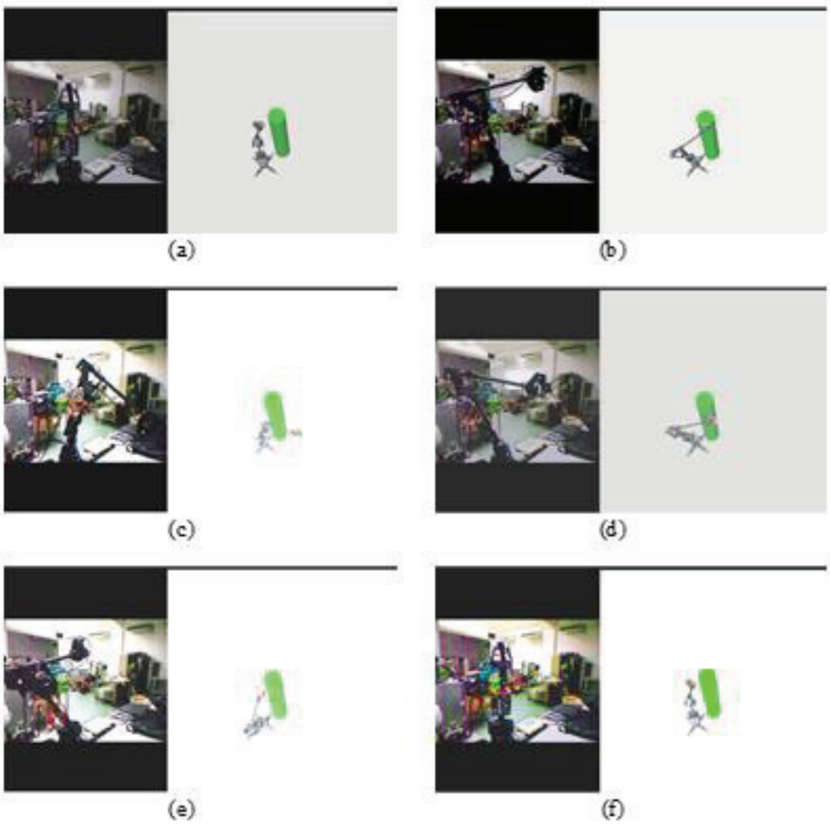

Fig. 8: The sequence of motion when *r_mini* successfully avoids a moving obstacle when the obstacle is at a turning point to move away from the hardware.

No significant changes are observed for $joint_4$, $joint_5$ and $joint_6$. This is the implication of the Pieper-condition manipulator design where, none of the *z-axis* from the first three joints shares the same crossing point, which suggests the actuation on these joints are not a linear transformation as the case for affine translation. Due to the offset (affine transformation) of the joints' axis of rotation, there is a bijection mapping of these joints to the task-space specifically reserved for translation changes in space. Also, changes are observed in the orientation of the frame attached to the end-effector, however, there is no bijection mapping of the three joints to the task-space's orientation.

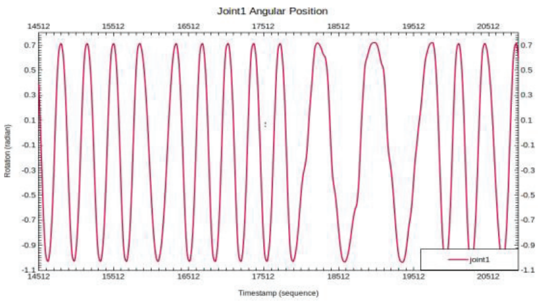

(a)

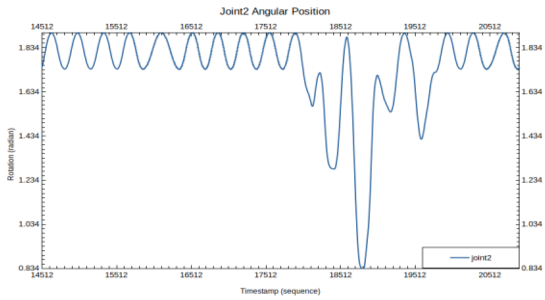

(b)

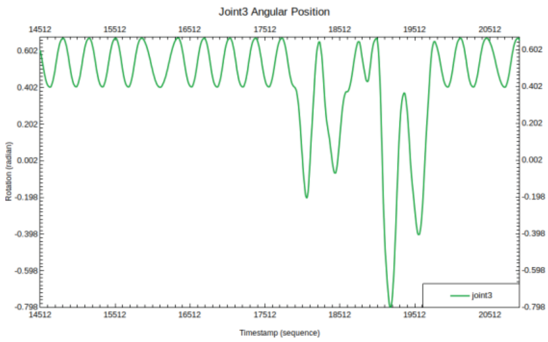

(c)

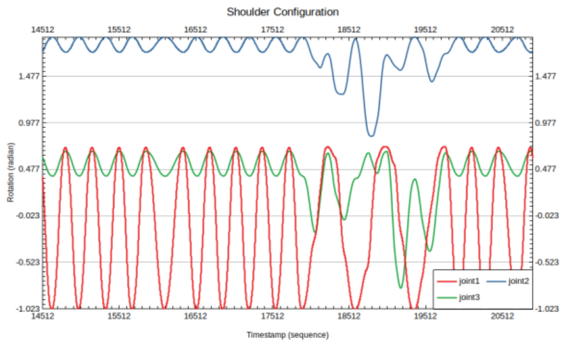

(d)

Fig. 9: Joint angle position against timestamp due to reactions of the planner. (a) Joint 1, (b) Joint 2, (c) Joint 3, and (d) Joints 1,2, and 3 on a single graph.

6. CONCLUSION AND RECOMMENDATION

We conclude that the RRT outperformed other sampling-based planners when the workspace of a manipulator is subjected to static obstacles. We observe that the RRT reacts to a moving object under the cycle space on a dynamic setup. We also concluded that with velocity-constrained configuration within the RRT, the planners generate a singularity-denied trajectory. To improve the time-to-collision value, we proposed an obstacle-tracking pipeline via mapping sensors such as an RGB-D sensor or a LiDAR. It is also recommended that more than one intermediate pose capable of reacting with the environment between the initial pose and the goal pose should be defined in the cycle space.

REFERENCES

[1] Hägele M, Nilsson K, Pires JN, Bischoff R. (2016) Industrial Robotics, in Springer Handbook of Robotics, Springer International Publishing, pp. 1385-1421. doi: 10.1007/978-3-319-32552-1_54.

[2] Matthias B, Kock S, Jerregard H, Källman M, Lundberg I. (2011) Safety of collaborative industrial robots: Certification possibilities for a collaborative assembly robot concept, in Proceedings - 2011 IEEE International Symposium on Assembly and Manufacturing (ISAM) pp. 1-6. doi: 10.1109/ISAM.2011.5942307.

[3] Deng H, Xia Z, Xiong J. (2016) Robotic manipulation planning using dynamic RRT," in 2016 IEEE International Conference on Real-Time Computing and Robotics, RCAR 2016, Dec. 2016, pp. 500-504. doi: 10.1109/RCAR.2016.7784080.

[4] Elbanhawi M, Simic M. (2014) Sampling-based robot motion planning: A review. Institute of Electrical and Electronics Engineers Inc., 2: 56-77. doi: 10.1109/ACCESS.2014.2302442.

[5] Kavraki LE, Kolountzakis MN, Latombe JC. (1998) Analysis of probabilistic roadmaps for path planning. IEEE Trans. Robot. Autom., 14(1): 166-171. doi: 10.1109/70.660866.

[6] Kunz T, Reiser U, Stilman M, Verl A. (2010) Real-time path planning for a robot arm in changing environments. IEEE/RSJ 2010 Int. Conf. Intell. Robot. Syst. IROS 2010 - Conf. Proc., pp. 5906-5911. doi: 10.1109/IROS.2010.5653275.

[7] LaValle SM. (1998) Rapidly-Exploring Random Trees: A New Tool for Path Planning. Accessed: Sep. 25, 2022. [Online]. Available: https://www.cs.csustan.edu/~xliang/Courses/CS4710-21S/Papers/06 RRT.pdf

[8] Wei K, Ren B. (2018) A method on dynamic path planning for robotic manipulator autonomous obstacle avoidance based on an improved RRT algorithm. Sensors (Switzerland), 18(2):571. doi: 10.3390/s18020571.

[9] Pieper DL. (1968) The Kinematics of Manipulators Under Computer Control. Stanford University.

[10] Denavit J, Hartenberg RS. (1955) A Kinematic Notation for Lower-Pair Mechanisms Based on Matrices. J. Appl. Mech., 22(2): 215-221. doi: 10.1115/1.4011045.